

## **INFORMATION TO USERS**

This manuscript has been reproduced from the microfilm master. UMI films the text directly from the original or copy submitted. Thus, some thesis and dissertation copies are in typewriter face, while others may be from any type of computer printer.

**The quality of this reproduction is dependent upon the quality of the copy submitted.** Broken or indistinct print, colored or poor quality illustrations and photographs, print bleedthrough, substandard margins, and improper alignment can adversely affect reproduction.

In the unlikely event that the author did not send UMI a complete manuscript and there are missing pages, these will be noted. Also, if unauthorized copyright material had to be removed, a note will indicate the deletion.

Oversize materials (e.g., maps, drawings, charts) are reproduced by sectioning the original, beginning at the upper left-hand corner and continuing from left to right in equal sections with small overlaps.

Photographs included in the original manuscript have been reproduced xerographically in this copy. Higher quality 6" x 9" black and white photographic prints are available for any photographs or illustrations appearing in this copy for an additional charge. Contact UMI directly to order.

ProQuest Information and Learning  
300 North Zeeb Road, Ann Arbor, MI 48106-1346 USA  
800-521-0600

**UMI<sup>®</sup>**



# THE REST-FRAME OPTICAL PROPERTIES OF HIGH REDSHIFT GALAXIES

by  
Gregory Howard Rudnick

---

A Dissertation Submitted to the Faculty of the  
DEPARTMENT OF ASTRONOMY  
In Partial Fulfillment of the Requirements  
For the Degree of  
DOCTOR OF PHILOSOPHY  
In the Graduate College  
THE UNIVERSITY OF ARIZONA

2001

UMI Number: 3031412

UMI<sup>®</sup>

---

UMI Microform 3031412

Copyright 2002 by Bell & Howell Information and Learning Company.

All rights reserved. This microform edition is protected against  
unauthorized copying under Title 17, United States Code.

---

Bell & Howell Information and Learning Company  
300 North Zeeb Road  
P.O. Box 1346  
Ann Arbor, MI 48106-1346

THE UNIVERSITY OF ARIZONA @  
GRADUATE COLLEGE

As members of the Final Examination Committee, we certify that we have  
read the dissertation prepared by Gregory Howard Rudnick  
entitled The Rest-Frame Optical Properties of High Redshift Galaxies

and recommend that it be accepted as fulfilling the dissertation  
requirement for the Degree of Doctor of Philosophy

Hans-Walter Rix

Hans-Walter Rix

Nov. 2, 2001  
Date

Marijn Frank

Marijn Frank

Nov 2, 2001  
Date

Robert C. Kennicutt, Jr.

Robert C. Kennicutt, Jr.

10-2-01  
Date

\_\_\_\_\_  
Date

\_\_\_\_\_  
Date

Final approval and acceptance of this dissertation is contingent upon  
the candidate's submission of the final copy of the dissertation to the  
Graduate College.

I hereby certify that I have read this dissertation prepared under my  
direction and recommend that it be accepted as fulfilling the dissertation  
requirement.

Hans-Walter Rix


Dissertation Director, Hans-Walter Rix

Nov 2, 2001  
Date

### STATEMENT BY AUTHOR

This dissertation has been submitted in partial fulfillment of requirements for an advanced degree at The University of Arizona and is deposited in the University Library to be made available to borrowers under rules of the Library.

Brief quotations from this dissertation are allowable without special permission, provided that accurate acknowledgment of source is made. Requests for permission for extended quotation from or reproduction of this manuscript in whole or in part may be granted by the head of the major department or the Dean of the Graduate College when in his or her judgment the proposed use of the material is in the interests of scholarship. In all other instances, however, permission must be obtained from the author.

SIGNED: 

## DEDICATION

This dissertation is dedicated to three people. First to my parents, who taught me compassion, responsibility, and the need to do what is right. Their support has been unwavering and their love unconditional. I owe this all to them.

I also dedicate this dissertation to my cousin Lilly. We love her and we all miss her and her wonderful smile.

## ACKNOWLEDGEMENTS

None of this work would have been remotely possible without the advice, brilliance, encouragement, and understanding of my advisor and mentor Hans-Walter Rix. From the first day of my first visit to Steward, I knew that our collaboration would be special, but I had no idea how rewarding. HW, thanks for showing me how to be a good scientist, how to ask the right questions (not only in colloquium), and how to know when good was good enough. HW and MB, thanks for your friendship, honesty, hikes in the mountains, salmon steaks at 8000 feet, dampfnudels in the Alps, Phish Concerts, and practice in flood control.

I have many wonderful collaborators; Marijn, thanks for welcoming me into the FIRES team and for providing your input, experience, and amazing scientific intuition, all of which were so crucial in completing this thesis. Thanks also for your financial support of my trips to Leiden. Thanks to the rest of FIRES team, especially Ivo Labbé for his excellent work in getting the HDF-S data ready and his help on Chapter 4 and Alan Moorwood for insisting that something wasn't quite right with the redshift distribution in Chapter 2. Thanks to Rob Kennicutt for always telling me that I was good enough.

Many people both in Tucson and Germany enriched my time and made it fun. Grateful thanks to Ed Olzewski for the music and Don McCarthy for the wonderful Astronomy Camp experiences. Thanks to Michelle, Catalina, Joy, Susan, Ursula, and everyone else in offices on both sides of the Atlantic for always having the right answers or knowing where I could get them. There were, of course, the friends who shared the whole "experience" with me and who saw to it that I was always entertained. The Tucsonites: my first officemate Anne, Craig and Groppi for all their computer support, Audra and Aimee for the great halloween costumes, my roommate Chris Gottbrath, my academic sister Joannah, Phil, Val, Rose, Jen, my academic brother Dan, and Rory. Mike, Jaime, Stacey, and Joanna, thanks for giving me a life outside of astronomy. Of course, there were also the people in Heidelberg: Roland, Marc, Tom, Adrienne, Elena. Thanks to Thilo and Nicolas for all the great conversations, italian wine, and forest walks after lunch. Thanks to Babi for all of the great home cooking and wonderful friendship. My roommates Matthias, Jens, and Bärbel put up with the guy who was never around and still thought he was cool enough to throw a party for him.

I owe who I am to the love I have received. I could not wish for a better, more caring family than the one I have. I cherish their support now more than ever and thank them for everything.

Finally, but most importantly, I thank Elke. She has been the shining light of the last year of my life and I thank her for having the courage to fall in love with a stressed out graduate student in the last year of his studies. Schatze, I look forward to spending many less stressful times with you in years to come.



# TABLE OF CONTENTS

LIST OF FIGURES . . . . .	9
ABSTRACT . . . . .	10
CHAPTER 1. INTRODUCTION . . . . .	12
1.1. IMPORTANT STEPS AT $z \gtrsim 0.5$ : GALAXIES BEFORE THE MID-LIFE	13
1.1.1. Optical Imaging Surveys . . . . .	13
1.1.2. Near Infrared Imaging Surveys . . . . .	15
1.1.3. Spectroscopic Surveys . . . . .	16
1.2. PHOTOMETRIC REDSHIFTS . . . . .	18
1.3. HIGH REDSHIFT GALAXIES: WHAT IS KNOWN? . . . . .	20
1.3.1. Optical Studies . . . . .	21
1.3.2. High Redshift Galaxy Evolution in the NIR . . . . .	22
1.4. THE THEORETICAL CONTEXT . . . . .	24
1.5. THE FAINT INFRARED EXTRAGALACTIC SURVEY . . . . .	26
1.6. OUTLINE . . . . .	27
CHAPTER 2. A K-BAND SELECTED PHOTOMETRIC REDSHIFT CATALOG IN THE HDF-S: SAMPLING THE REST-FRAME V-BAND TO $z = 3$ . . . . .	29
2.1. MOTIVATION . . . . .	29
2.2. OBSERVATIONS AND DATA . . . . .	29
2.2.1. Observations . . . . .	29
2.2.2. Data Reduction . . . . .	30
2.2.3. Photometric calibration . . . . .	31
2.2.4. Object Detection and Photometry . . . . .	32
2.2.5. Completeness . . . . .	34
2.3. PHOTOMETRIC REDSHIFTS . . . . .	39
2.3.1. Template Choice . . . . .	39
2.3.2. Template Based Estimates of the Redshift . . . . .	40
2.3.3. Comparison With Spectroscopic Redshifts . . . . .	41
2.4. RESULTS . . . . .	47
2.4.1. SED Fits . . . . .	47
2.4.2. The Redshift Distribution . . . . .	52
2.4.3. Rest-Frame Luminosities . . . . .	57
2.5. SUMMARY . . . . .	63

TABLE OF CONTENTS—*Continued*

CHAPTER 3. OPTICAL SPECTROSCOPY OF GALAXIES IN THE HDF-S . . .	<b>66</b>
3.1. MOTIVATION . . . . .	66
3.2. OBSERVATIONS & DATA REDUCTION . . . . .	67
3.2.1. Object Selection . . . . .	67
3.2.2. Observations . . . . .	68
3.2.3. Data Reduction . . . . .	69
3.3. SPECTROSCOPIC REDSHIFTS . . . . .	70
3.4. TESTING THE PHOTOMETRIC REDSHIFT TECHNIQUE . . . . .	79
3.4.1. Comparing Photometric and Spectroscopic Redshifts . . . . .	80
3.4.2. Measuring the Uncertainty in $z_{phot}$ . . . . .	85
3.4.3. Accuracy of Photometrically Derived Rest-Frame Luminosities . . . . .	89
3.5. A LARGE, DISK-LIKE LYMAN BREAK GALAXY AT $z \sim 3$ . . . . .	89
3.6. SUMMARY . . . . .	92
CHAPTER 4. OBSERVATIONS, DATA REDUCTION, SOURCE DETECTION, AND PHOTOMETRY OF A $K_{s,AB}^{tot} < 26$ CATALOG IN THE HDF-S . . . . .	<b>94</b>
4.1. OBSERVATIONS . . . . .	94
4.2. DATA REDUCTION . . . . .	95
4.2.1. Flatfield Construction . . . . .	96
4.2.2. Photometric Calibration . . . . .	96
4.2.3. Combination . . . . .	97
4.3. THE IMAGES . . . . .	98
4.3.1. Quality of the Images . . . . .	98
4.4. SOURCE DETECTION AND PHOTOMETRY . . . . .	98
4.4.1. Detection . . . . .	99
4.4.2. Photometry . . . . .	99
4.4.3. The Catalogs . . . . .	100
CHAPTER 5. MEASURING THE REST-FRAME OPTICAL COLORS AND STELLAR MASSSES OF $K$ -BAND SELECTED GALAXIES . . . . .	<b>102</b>
5.1. MOTIVATION . . . . .	102
5.2. REDSHIFTS . . . . .	104
5.2.1. The Photometric Redshift Distribution . . . . .	104
5.3. REST-FRAME LUMINOSITIES AND COLORS . . . . .	107
5.3.1. Rest-Frame Photometric System . . . . .	108
5.3.2. Rest-Frame Magnitudes and Luminosities . . . . .	109
5.3.3. Color Measurement Techniques . . . . .	115
5.3.4. Color Uncertainties and Method Comparison . . . . .	116
5.4. REST-FRAME COLOR ANALYSIS . . . . .	121
5.4.1. Local Comparison . . . . .	121

TABLE OF CONTENTS—*Continued*

5.4.2. Objects Missed by the Lyman Break Technique . . . . .	126
5.4.3. Redshift Evolution of the Color . . . . .	127
5.5. STELLAR MASS-TO-LIGHT RATIOS AND MASSES . . . . .	131
5.5.1. Rest-Frame Optical $\mathcal{M}/L$ 's . . . . .	135
5.5.2. The Stellar Mass . . . . .	141
5.5.3. Comparison with Studies of the LBG Population . . . . .	144
5.5.4. The Stellar Mass Budget . . . . .	146
5.6. SUMMARY . . . . .	154
CHAPTER 6. SUMMARY AND OUTLOOK . . . . .	<b>157</b>
6.1. Summary . . . . .	157
6.2. Outlook . . . . .	159
APPENDIX A. TABLES . . . . .	<b>162</b>
REFERENCES . . . . .	<b>238</b>

## LIST OF FIGURES

FIGURE 2.1.	$K_s$ -band Image . . . . .	35
FIGURE 2.2.	Detection Completeness . . . . .	37
FIGURE 2.3.	$z_{phot}$ vs. $z_{spec}$ Comparison – HDF-N . . . . .	42
FIGURE 2.4.	$z_{phot}$ vs. $z_{spec}$ Comparison – HDF-S . . . . .	45
FIGURE 2.5.	Example Template Fits . . . . .	48
FIGURE 2.6.	Model Fit Residuals . . . . .	49
FIGURE 2.7.	The Usefulness of NIR Data . . . . .	50
FIGURE 2.8.	$K_{s,AB}^{tot} \leq 23.5$ Redshift Histogram . . . . .	53
FIGURE 2.9.	$K_{s,AB}^{tot}$ vs. $z_{phot}$ . . . . .	54
FIGURE 2.10.	$K_{s,vega} < 21$ Cumulative Redshift Histogram . . . . .	56
FIGURE 2.11.	$L^{rest}$ vs. $z_{phot}$ . . . . .	58
FIGURE 3.1.	Spectra With $z_{spec}$ Determinations . . . . .	72
FIGURE 3.2.	Photometric vs. Spectroscopic Redshift Comparison . . . . .	81
FIGURE 3.3.	HDFS1-36 Image Tiles . . . . .	90
FIGURE 4.1.	Full $K_s$ -band Image . . . . .	101
FIGURE 5.1.	$K_{s,AB}^{tot} < 26$ $z_{phot}$ Histogram . . . . .	105
FIGURE 5.2.	$K_{s,AB}^{tot}$ vs. $z_{phot}$ for $K_{s,AB}^{tot} < 26$ sample . . . . .	106
FIGURE 5.3.	$L^{rest}$ vs. $z_{phot}$ for $K_{s,AB}^{tot} < 26$ sample . . . . .	112
FIGURE 5.4.	Method Color Comparison . . . . .	118
FIGURE 5.5.	Color Comparison at $z_{spec}$ vs. $z_{phot}$ . . . . .	120
FIGURE 5.6.	$(U - B)_{rest}$ vs. $(B - V)_{rest}$ . . . . .	123
FIGURE 5.7.	Model SED Fits to Red $z > 2$ Galaxies . . . . .	124
FIGURE 5.8.	Rest-Frame Color vs. $L^{rest}$ . . . . .	128
FIGURE 5.9.	Rest-Frame Color vs. $z_{phot}$ . . . . .	132
FIGURE 5.10.	Origin of Color vs. $\mathcal{M}/L$ Relation . . . . .	137
FIGURE 5.11.	Effects of Bursts on $\mathcal{M}/L$ . . . . .	138
FIGURE 5.12.	Stellar $\mathcal{M}/L$ vs. $z_{phot}$ . . . . .	140
FIGURE 5.13.	Stellar Mass vs. $z_{phot}$ . . . . .	142
FIGURE 5.14.	Stellar $\mathcal{M}/L$ vs. Stellar Mass . . . . .	143
FIGURE 5.15.	Rest-Frame Optical Luminosity Density . . . . .	148
FIGURE 5.16.	Stellar Mass Density . . . . .	152

## ABSTRACT

We present the first results from the **F**aint **I**nfra-**R**ed **E**xtragalactic **S**urvey (FIRES) of the Hubble Deep Field (HDF) South. Using a combination of very deep ground-based near infrared (NIR) data with the WFPC2 Hubble Space Telescope data, we constructed a  $K_s$ -band selected sample to  $K_{s,AB} \leq 26.0$ . To interpret this data, we developed a new photometric redshift technique and tested it using spectroscopic redshifts in the HDF-N and HDF-S. Our accuracy was  $\Delta z / (1 + z) \approx 0.07$  for  $z < 6$ . We derived realistic error estimates in  $z_{phot}$  by accounting both for template mismatch and for the dependence of the redshift uncertainty on the photometric errors. We estimated the rest-frame optical luminosities from an initial NIR data set and found 90 times more galaxies at  $2 < z < 3.5$  and  $L_B^{rest} > 5 \times 10^{10} h^{-2} L_{\odot,B}$  than are expected from local luminosity functions. This discrepancy can be explained if  $L_{*,B}$  increases by a factor of 2.4-3.2 with respect to locally determined values. Using all available NIR data in the HDF-S, we then derived the rest-frame colors  $(U - B)_{rest}$ ,  $(B - V)_{rest}$ , and  $(U - V)_{rest}$  of all galaxies with  $K_{s,AB} < 25$ . Eight of the 12 rest-frame optically reddest galaxies at  $2 < z_{phot} < 3.2$  would have been missed by the  $U$ -dropout selection criteria. Three of the galaxies at  $z > 2$  have strong rest-frame optical breaks with colors corresponding to those of present day Sbc's. Using theoretical relations between the color and stellar mass-to-light ratio  $\mathcal{M}/L$ , we estimated the  $\mathcal{M}/L$  and stellar mass  $\mathcal{M}$ . Using these estimates, we found that the most massive galaxies at any redshift are those with the reddest rest-frame colors and those that would be missed by the  $U$ -dropout technique. We also found that the stellar mass budget at  $z < 3.2$  has significant contributions from galaxies redder than local Scd's. There are, however, large uncertainties in the  $\mathcal{M}/L$  analysis and we have a relatively small field. Confirmation of these results will require additional modeling, observations over a larger area, and extensive spectroscopic follow-up.

We found an intrinsically bright ( $L_V^{rest} = 5.10 \times 10^{10} h^{-2} L_{\odot, V}$ ) U-dropout galaxy in the HDF-S with  $z_{spec} = 2.793$ . This galaxy has an extended ring-like morphology, and a co-moving diameter of  $\gtrsim 9.4 h^{-1}$  Kpc for a  $\Omega_M = 0.3$ ,  $\Omega_\Lambda = 0.7$  cosmology. The light profile appears more centrally concentrated and symmetric at longer wavelengths and this object may have an older population superimposed on a star-forming disk.

## CHAPTER 1

## INTRODUCTION

Understanding how present day galaxies evolved from their birth to their current state is a necessary step in understanding the evolution of the universe as a whole. Tinsley (1980) said, “Essentially everything of astronomical interest is either part of a galaxy, or from a galaxy, or otherwise relevant to the origin and evolution of galaxies.” In addition to studying “fossil” evidence in nearby galaxies, another means to study galaxy evolution are direct look-back observations that take advantage of light travel time effects to observe galaxies at times when the universe was a small fraction of its current age ( $t \lesssim 0.5 t_{\text{hub}}$ ). The focus of these look-back studies were strongly coupled to the technology available at the time. The first effort to quantify the evolution in the properties of faint galaxies (Sandage, 1961) was undertaken in photographic surveys primarily to correct effects which would bias the determination of cosmological parameters. Research on galaxy evolution has since blossomed from merely a “correction” to a full-blown field of astronomy.

In §1.1, I will outline the landmark steps in direct look-back observations of galaxy evolution at moderate to high redshifts  $z > 0.5$ . I will review in §1.2 the use of broadband photometry to constrain the redshifts of galaxies. In §1.3, I will give a brief summary of the current state of the observations and will discuss the relevant theoretical developments in §1.4. The work in this dissertation is largely based on the faint infrared extragalactic survey (FIRES), which I will introduce in §1.5. An outline of the dissertation will be presented in §1.6.

## 1.1 Important Steps at $z \gtrsim 0.5$ : Galaxies Before the Mid-Life

Observations at high redshifts allow astronomers to study galaxies when they were at a fraction of their present age. For example, at  $z \sim 0.5$  or  $0.8$  the look-back time is 50% the age of the universe (for an  $\Omega_m = 1.0, \Omega_\Lambda = 0$  cosmology or an  $\Omega_m = 0.3, \Omega_\Lambda = 0.7$  cosmology respectively) and the galaxies at these redshifts are therefore at most this old. The recent, rapid development of the field of high redshift galaxy evolution is evidenced in the surging number of papers published on the subject (Ellis, 2001). We cannot hope to make a review of all of the pertinent literature but, rather, we summarize below some of the most important imaging and spectroscopic studies of galaxy evolution at  $z \gtrsim 0.5$  when galaxies were younger than 50% of their current age.

### 1.1.1 Optical Imaging Surveys

A pioneering search for galaxies at significant look-back times was made by Tyson (1988) using three broad-band filters and modern Charge Coupled Device (CCD) detectors. The high quantum efficiency, linear response, and stability of these detectors allowed Tyson to take images in  $B_J$ ,  $R$ , and  $I$  bands with  $B_J$  limits two magnitudes fainter than previous work with photographic plates (Koo, 1986). Differential number counts  $N(m)$  in the blue at these faint magnitudes confirmed, from photographic work, the presence of a population of  $B_J > 25$  galaxies (known as faint blue galaxies; FBGs) 5-15 times more numerous than what is predicted by no evolution models. It was not clear from the data if these galaxies were an intrinsically bright population at high redshift seen in the redshifted rest-frame ultraviolet (UV) or an intrinsically faint population of  $z < 1$  galaxies undergoing a starbursting phase. To constrain the redshift distribution of the faintest FBGs Guhathakurta, Tyson, & Majewski (1990) used even deeper  $U$ ,  $B_J$ , and  $R$  images to see if any of their detected objects had the very red ( $U - B_J$ ) color and blue ( $B_J - R$ ) color indicative of a  $z > 3$  star-forming



galaxy. This fairly unique color combination is the signature of a rest-frame UV break at  $912\text{\AA}$  redshifted into the  $U$  filter. This break, called the “Lyman break” (LB), is caused by the absorption from foreground neutral hydrogen of Lyman continuum photons ( $\lambda < 912\text{\AA}$ ) produced by very young ( $t \lesssim 10^6\text{yrs}$ ) stars. Guhathakurta, Tyson, & Majewski (1990) found that none of the galaxies in their sample had colors characteristic of a redshifted LB and concluded that  $> 93\%$  of the the FBGs were therefore at  $z < 3$ . The first high- $z$  candidate galaxies detected by the presence of a LB were found by Steidel & Hamilton (1992) who used custom designed filters corresponding to  $U$ ,  $B$ , and  $R$  to detect the signature of a redshifted LB in  $z \sim 3$  galaxies. The refinement of this photometric technique and the extensive spectroscopic follow-up (discussed in §1.1.3), has revolutionized the study of galaxies at high redshift.

The most recent milestones in deep optical imaging were the Hubble Deep Field (HDF) North and South (Williams et al., 1996; Casertano et al., 2000) programs. Using the WFPC2 camera on the Hubble Space Telescope (HST), these projects imaged “empty” fields in the northern and southern hemispheres in four optical bands ( $U_{300}$ ,  $B_{450}$ ,  $V_{606}$ , and  $I_{814}$ ) to  $10\sigma$  AB magnitude limits of  $27 - 28$ . These surveys gave an unprecedented look at the high redshift universe in great detail and opened the doors to the study of intrinsically faint galaxies at  $z > 2$ . Despite their extreme usefulness, the HDFs originally only had optical imaging available over small areas. When drawing conclusions from studies of these fields, it is crucial to remember that the effects of large scale structure (LSS) may make it difficult to interpret the observations of one field in a global context. Furthermore, even  $I_{814}$  only probes the rest-frame UV at  $z \gtrsim 1.5$ . Unfortunately, rest-frame UV light is subject to uncertain, possibly large, amount of extinction and probes only the youngest, most massive stars which contribute very little to the stellar mass. Hence selection at rest-frame UV wavelengths will miss galaxies with little UV light, such as evolved or heavily extinguished objects. In addition, comparison with local samples is difficult because UV observations of local galaxies are scant. Optimal studies of galaxy evolution should

compare “apples to apples” over a large range in redshift i.e., both select and observe galaxies at the same rest-frame wavelength, preferably at or redder than the rest-frame optical. To reach rest-frame optical wavelengths at  $z \gtrsim 1.5$ , however, near infrared (NIR) observations are required.

### 1.1.2 Near Infrared Imaging Surveys

NIR observations have always lagged behind their optical counterparts in depth and area. First among the reasons was the difficulty in building NIR arrays, but almost as important was the very bright and variable night sky in the NIR, which forces very long series of short integration exposures to reach faint limiting magnitudes. Cowie, Gardner, Lilly, & McLean (1990) initiated the first NIR survey theoretically deep enough to pick out normal galaxies at high redshifts. These authors appreciated the importance of selecting galaxies at high redshift by their rest-frame optical light i.e., in the same way that they are selected at low redshifts. The newly available NIR array detectors made their program possible. This survey was followed four years later by a combination survey of deep  $K$ -band imaging and optical spectroscopy of a  $K < 20$  sample (Cowie et al., 1994; Songaila, Cowie, Hu, & Gardner, 1994). The authors found that their objects lay almost exclusively at  $z \lesssim 1$  although there were a substantial population (30%) of red ( $I - K$ ) objects which had flat, featureless optical spectra that could not be identified. Their work demonstrated that a  $K < 20$  sample was sufficient to get out to  $z \sim 1$ , but implied that much deeper imaging and spectroscopy was required to push the limits to  $z > 2$ . An important step in the development of NIR imaging techniques for crowded fields was made by Stanford, Eisenhardt, & Dickinson (1995). This was to prove a necessary skill in later, much deeper NIR imaging projects.

The culmination of these advances in techniques and detectors was the deep Keck imaging in the  $K$ -band of a small portion of the HDF-N (Hogg et al., 1997) and the

publically available Kitt Peak 4 meter  $J$ ,  $H$ , and  $K$ , imaging of the central WFPC2 pointing (Dickinson, 2001a). These new NIR images were deep enough to detect the population of LBGs in these fields and, for the first time, gave access to rest-frame optical wavelengths at high redshifts where significant samples of optically selected galaxies had already been amassed by the LB technique.

### 1.1.3 Spectroscopic Surveys

$z < 1$

Spectroscopic follow-up observations of faint objects detected in deep imaging surveys has always been difficult. The total system throughput of spectrographs is typically  $< 10 - 15\%$  and traditional long-slit methods only allow a few galaxies to be observed with a given instrument setup. An alternative method is to use a multi-object spectrograph (MOS) to observe many objects at once with a set of fibers or slitlets. The first use of a MOS unit to obtain spectra of faint ( $b_J < 21.5$ ) field galaxies was made by Broadhurst, Ellis, & Shanks (1988) on a sample selected from photographic plates, although they only probed  $z < 0.5$ . The first spectroscopic survey that probed  $z > 0.5$  used the low dispersion survey spectrograph (LDSS) (Colless, Ellis, Taylor, & Hook, 1990). Like Broadhurst, Ellis, & Shanks (1988) the LDSS survey team also selected their galaxies from photographic plates, but went one magnitude deeper and measured galaxies with redshifts out to  $z \lesssim 0.7$ .

A large step forward was taken by the Canada-France Redshift Survey (CFRS; Lilly et al. 1995a). The depth of this survey ( $17.5 \leq I_{AB} \leq 22.5$ ) was designed to push spectroscopy to the limit using 4 meter class telescopes and to obtain spectra of galaxies out to  $z \sim 1$ . Its main strength, however, lie in its selection process. Broadhurst, Ellis, & Shanks (1988) and Colless, Ellis, Taylor, & Hook (1990) selected galaxies by their  $B$ -band light and hence in the rest-frame UV for  $z > 0.5$ . This poses a problem because very little was (and is) known about the UV properties of

nearby galaxies and comparison with local samples is difficult. In addition, and as a result of the former problem, theoretical galaxy SED models are poorly constrained in the UV. By using the *I*-band the CFRS gain access to the rest-frame *B*-band for  $z < 1$  and their galaxies can be compared directly to local samples. The number of spectroscopically confirmed galaxies (591) in the CFRS also increased by a factor of  $\sim 4$  the number of galaxies obtained in the LDSS survey. Lilly et al. (1995b) used the CFRS sample to measure the rest-frame *B* luminosity function out to  $z \sim 1$  and, for the first time, were able to study galaxies in a constant rest-frame wavelength over half of the age of the universe. Using the rest-frame *B*-band and  $2800\text{\AA}$  luminosity functions calculated in Lilly et al. (1995b), Lilly, Le Fevre, Hammer, & Crampton (1996) concluded that the rest-frame *B*-band luminosity density increased by a factor of three between a redshift of zero and unity while the global star formation rate (SFR) increased by a factor of seven over the same redshift range.

$z > 1$

Although small numbers of galaxies were confirmed at  $z > 1$  in the early 90's (e.g., Lowenthal et al. 1991, Hu et al. 1991), the next major advance in survey depth and redshift was only attainable with the advent of 8-10 meter class telescopes (Keck, VLT). These studies skipped entirely the redshift regime from  $z = 1.3 - 2$  and moved directly to  $z \sim 3$  (Steidel et al., 1996), for a very simple reason, no strong emission lines or other significant spectral features with which to measure a redshift are visible in the optical over the range  $z = 1.3 - 2$ . Selection of star-forming galaxies at  $z > 2$ , however, is feasible by picking objects with  $(U - B)$  and  $(B - R)$  colors consistent with a redshifted LB in a star-forming galaxy. Using the filter set and selection technique developed by Steidel & Hamilton (1992), combined with extensive spectroscopic follow-up on Keck, Steidel et al. (1996) refined the LB technique and identified a star-forming population of galaxies at  $z \sim 3$ . The LB technique has been heavily exploited and there are currently  $\sim 900$  spectroscopically confirmed galaxies

at  $z \gtrsim 2.5$  (Steidel et al., 1996, 1999).

## 1.2 Photometric Redshifts

Most of the work discussed above would have been impossible without some form of photometric pre-selection, specifically methods which yield a prior estimate of the redshift such as the LB technique. Given an object with a faint apparent magnitude, there is always the confusion over whether it is an intrinsically faint object at low redshift, or an intrinsically bright object at high redshift. Because differential galaxy number counts have a steep slope ( $d\log N/dm = 0.34$  in the I-band; Tyson 1988), it is impractical to obtain spectra of all faint objects and photometric pre-selection is required to differentiate the redshifts of objects with similar apparent magnitudes. The most commonly used method to estimate a galaxy's redshift based on photometry is the “photometric redshift” technique (see contributions in Weymann et al. 1999). This method operates like  $R \sim 3 - 10$  spectroscopy, where the resolution elements are medium/broad-band filters, and the analog of spectral features are mostly large scale shape variations in the SED (breaks).

Baum (1962) first used broad-band photometry to constrain the redshift of galaxies (in the cluster 3C395) using nine-band photometry and assuming that the SEDs were well represented by those of ellipticals. Later, Puschell, Owen, & Laing (1982) fit empirical and theoretical spectral templates to the optical/NIR SEDs of radio galaxies. They made the important point that accurate photometric redshifts could not be derived if all the galaxies were fit with an identical model SED. Rather, a range of model SEDs had to be used to fit the data well. Later, Koo (1985) used theoretical and observed galaxy templates to predict the position of redshifted galaxies in a color-color plot. In comparison to spectroscopic redshifts  $z_{\text{spec}}$ , his estimates of the photometric redshift  $z_{\text{phot}}$  were accurate to  $\lesssim 0.05$  at  $z < 0.6$ . The first application of photometric redshifts to large samples ( $\sim 1000$ ) of “ordinary” field galaxies using

CCD data was done by Loh & Spillar (1986) who fitted six band fluxes with a set of three local SED templates. This early work almost entirely falls into the class of “template fitting” techniques, which fit model SEDs directly to the observed flux points.

Little work was done on photometric redshifts in the late 1980’s and early 1990’s, but the technique was revisited by Connolly et al. (1995) who explored an alternative method of estimating the redshift called “empirical fitting”. In this method, a set of galaxies with  $z_{spec}$  measurements and photometry are plotted in color-color space and a function (originally a 2<sup>nd</sup> order polynomial) is then fit to the distributions of color, apparent magnitude and redshift. This technique yields redshifts accurate to within  $\lesssim 0.05$  using only four broad-band optical colors. Although very accurate  $z_{phot}$  estimates are possible, this technique has the disadvantage that it requires a training set of objects with spectroscopic redshifts which span all expected spectral types. At high redshifts, where suitable training sets are not available, this technique cannot be applied. Since Connolly et al. (1995), the field of photometric redshifts has blossomed (Lanzetta, Yahil, & Fernandez-Soto, 1996; Sawicki, Lin, & Yee, 1997; Wang, Bahcall, & Turner, 1998; Hogg et al., 1998; Giallongo et al., 1998; Fernández-Soto, Lanzetta, & Yahil, 1999; Wolf, 1999; Fontana et al., 2000; Budavári et al., 2000; Mobasher & Mazzei, 2000; Bolzonella, Miralles, & Pelló, 2000; Thompson, Weymann, & Storrie-Lombardi, 2001). Because it doesn’t rely on large training sets, almost all of the work at high redshifts has shifted to the template fitting method, although some groups still use spectroscopic datasets to optimize the exact template colors for an improved  $z_{phot}$  estimate. Regardless of the exact method, both photometric redshift techniques take advantage of breaks in the rest-frame SEDs to fix the redshift. These are either the 4000Å/Balmer breaks in the optical or the LB in the UV. The observed wavelength of the break fixes the redshift to a small set of values and the color of the galaxy on either side of these breaks helps to identify the galaxy SED type and removes the degeneracy between breaks with different redshifts, but with

nearly identical observed colors. These studies have shown that three improvements in the data are needed to move the  $z_{phot}$  technique forward: large sets of galaxies with spectroscopic redshifts and matching photometry are needed at all SED types to test the accuracy of  $z_{phot}$  estimates, high  $S/N$  imaging data is needed to minimize the effects of photometric errors on the uncertainty in  $z_{phot}$ , and large wavelength coverage which extend into the NIR is needed to increase both the accuracy of  $z_{phot}$  and give access to the  $z = 1 - 2$  redshift range, where rest-frame optical breaks are shifted into the NIR and where the LB is still in the UV. All of these goals require the use of large telescopes with high throughput spectrographs in conjunction with deep optical/NIR imaging.

### 1.3 High Redshift Galaxies: What is Known?

Observations of high redshift galaxies has already yielded a wealth of knowledge about their sizes, metallicities, clustering, luminosities, instantaneous SFRs, and star formation histories (SFHs). The knowledge that one can extract from the observations is highly dependent on the wavelength at which they were carried out and most observations (e.g. Steidel et al. 1996) have been carried out in the optical, which samples the rest-frame UV at  $z \gtrsim 1.5$ , is most sensitive to very young massive stars, and can be severely effected by dust extinction. We will discuss below some of the information gleaned at high redshift from optical and NIR observations. The latter allow the study of galaxies in the rest-frame optical, where the light has more contributions from older stars and where dust extinction effects are reduced. Selection of high redshift galaxies in the NIR should also be able to find objects with little rest-frame UV flux that would be missed by the LB technique.

### 1.3.1 Optical Studies

As discussed above, deep optical imaging and extensive spectroscopic follow-up have resulted in the assembly of a large, well-defined sample of  $z \gtrsim 2$ , star-forming, Lyman break galaxies (LBGs; Steidel et al. 1996). Additional samples at similar redshifts have been selected using the  $U$  and  $B$ -dropout techniques on HST data in the HDF-N (Madau et al., 1996). Under the assumption of an initial mass function (IMF), the inferred rest-frame UV luminosity, or conversely the number of high mass stars, can be converted to the instantaneous SFR. Using rest-frame UV luminosities which were not corrected for extinction, Steidel et al. (1996) derived modest SFRs of  $3 - 20 h^{-2} M_{\odot} yr^{-1}$  (for  $q_0 = 0.05$ ) for LBGs while spectroscopy of the lensed LBG MS 1512-cB58 seem to imply modest extinctions of  $E(B - V) = 0.1 - 0.3$  (Pettini et al., 2000). The sizes of these objects from HST observations seem to be rather small with half-light radii of  $1.2 - 1.8 h^{-1} kpc$  (for  $q_0 = 0.05$ ) and a high degree of axisymmetry (Giavalisco, Steidel, & Macchetto, 1996). Their clustering however seems to indicate that these galaxies are associated with massive dark matter halos (Giavalisco et al., 1998).

Using the integrated SFRs of  $U$ -dropouts in the HDF-N Madau et al. (1996) extended the Lilly, Le Fevre, Hammer, & Crampton (1996) global SFR( $z$ ) measurements out to  $z \sim 4$  and found tentative evidence for a decline in the global SFR after a redshift of 2. These measurements, however, were highly uncertain and even when corrected for incompleteness, the inferred global SFRs suffer from unknown extinction corrections. This problem is underscored by recent submillimeter observations with the Submillimeter Common-User Bolometer Array (SCUBA) instrument which have revealed a population of heavily obscured star-forming galaxies which may dominate the global SFR at high redshifts (Barger et al., 1998, 1999). Adelberger & Steidel (2000) argued that the normal LBG population has enough obscuration to account for the measured Sub-mm number counts, but there are still Sub-mm detected galaxies



which would simply not be selected by the LB technique.

### 1.3.2 High Redshift Galaxy Evolution in the NIR

The first author who took advantage of the new NIR data in the HDF-N (Dickinson, 2001a) and combined it with the pre-existing HST optical data used the surface density of red ( $V_{606} - K_s$ ) objects to constrain the numbers of passively evolving elliptical galaxies (Zepf, 1997). He found that far fewer objects were found than were expected by these simple models and claimed that elliptical galaxies either had to form at low to moderate redshifts, be significantly enshrouded by dust at early ages, or be assembled by many smaller mergers. The new NIR data gave Zepf (1997) the ability to not only see the light from the youngest stars, but also from stars of ages  $t \gtrsim 1$  Gyr which contribute most of their light redward of the age-sensitive Balmer break. His work was followed by that of Sawicki & Yee (1998; hereafter SY98) who used a combination of optical and NIR data in the HDF-N to constrain the SFHs of LBGs. They used SEDs corresponding to simple SFHs to model the observed fluxes taking into account the effects of dust extinction, metallicity, and IMF. They concluded that the light at  $1600\text{\AA}$  was extinguished by a factor of  $\sim 16$ , requiring a large correction to the SFRs derived only from the rest-frame UV light. They also found that the ages of the dominant stellar populations in almost all LBGs (even those at  $z \sim 2$ ) were quite young ( $t < 0.2$  Gyr) and that a bursty star formation history was required to hide the old stars built up from previous episodes of SF. Evolved galaxies could be present, but would not be detectable with the Kitt Peak NIR data. The inferred stellar masses were 1/15 to 1/20 the mass of a present L<sub>\*</sub> galaxy and were rather insensitive to the exact details of the SFH.

Even though the Dickinson (2001a) data on the HDF-N was the best at the time, it still was much shallower than the deep WFPC2 exposures and had much poorer spatial resolution. To produce datasets in the NIR which were comparable in quality

to the deepest datasets in the optical, Thompson, Weymann, & Storrie-Lombardi (2001) used the NICMOS instrument on HST to image a small section of the HDF-N in F110W and F160W (approximately  $J$  and  $H$  respectively) to similar depths as the optical images while Dickinson (2001b) imaged the entire WFPC2 field in these two filters but to slightly shallower depths. Thompson, Weymann, & Storrie-Lombardi (2001) used their extremely deep NIR data in conjunction with the optical HST data to measure  $z_{phot}$  for galaxies in the field and then determine their SFRs and extinctions. With this analysis, they re-visited the Madau plot and found that corrections due to dust and incompleteness allowed for a flat  $SFR(z)$  at  $z > 2$ , in agreement with the LBG studies of Steidel et al. (1999) based solely on optical data. This indicated that the instantaneous SFR was dependent on information blueward of the Balmer Break and was not significantly improved by the NIR data. As SY98 had shown however, the NIR data was very important in constraining the presence of older populations which presumably dominate the stellar mass of galaxies.

Utilizing the best optical/NIR data available over the largest area (F110W and F160W from Dickinson 2001b and  $K_s$  from Dickinson 2001a), Papovich, Dickinson, & Ferguson (2001; hereafter P01) studied the SFHs of the spectroscopically confirmed LBGs in the HDF-N, many of which were the same as studied by SY98. The results of P01 were not incompatible with those of SY98 but tended to favor lower extinctions ( $\langle A_{1700} \rangle = 1.2$  mag for  $Z = Z_\odot$  vs.  $\langle A_{1700} \rangle = 2.7$  for Sawicki & Yee), and slightly older ages ( $t \sim 1$  Gyr). The inferred stellar masses were similar to SY98, as expected since both authors found that the stellar mass values were not very dependent on the exact SFHs. Like SY98, P01 showed that bursty SFHs were needed to explain the lack of red objects with high estimated redshifts. P01's data however went much deeper than that used by SY98 and the limits on the numbers of these objects were correspondingly much tighter. In fact, only one object (HDF-N J123656.3+621322 from Dickinson et al. 2000) was found to have colors consistent with a dusty galaxy at  $z \gtrsim 2$  or an evolved population at  $z \gtrsim 3$ . Work by Shapley et al. (2001) using

G, R,  $J_s$ , and  $K_s$  data on a set of LBGs brighter than those of P01 came to similar conclusions as P01 although the brighter galaxies in their sample had correspondingly larger inferred masses than those measured for the faint HDF-N LBGs.

Despite the high quality of the data used by P01, there remained a few weaknesses. The first was that P01 used the Kitt Peak  $K_s$  data which was significantly shallower than the F110W and F160W NICMOS data. The  $K_s$ -band data however is most useful in constraining the presence of old populations which contribute most of their light redward of the Balmer break. In addition, P01 only performed their analysis on the relatively bright, spectroscopically confirmed LBGs, which are known to be actively star-forming and are selected by their rest-frame UV light. It is not obvious whether a fainter sample would yield similar results. Finally, the HDF-N is only one small field and large scale structure may play a dominant role in applying the P01 results to the total galaxy population.

The high redshift studies seems to overwhelmingly indicate a long, drawn out formation history for galaxies. Faint number counts fail to show the enhancement at  $B_J = 21 - 22$  predicted by monolithic collapse models (Tyson, 1988), and the detailed SFHs of LBGs indicate that their SFHs are bursty (Sawicki & Yee, 1998; Papovich, Dickinson, & Ferguson, 2001; Shapley et al., 2001). Assembly may have started at  $z \sim 6$  but has evidently continued to the present day (e.g., via merging; Brinchmann & Ellis 2000).

## 1.4 The Theoretical Context

In addition to the wealth of new observations, the theoretical models necessary to explain them are also rapidly improving, mostly in the context of a hierarchical galaxy formation scenario, where galaxies are assembled over time from many smaller sub-clumps. These advances have come primarily down two avenues. First, very high resolution N-body/hydrodynamic simulations are now being performed on the most

powerful supercomputers at scales of  $\gtrsim 1$  Gpc (the VIRGO consortium; e.g., Pearce et al. 1999) and the detailed properties of galaxies are being simulated at higher resolution and on smaller scales (e.g., Steinmetz & Navarro 1999; Moore et al. 1999). Equally important has been the development of semi-analytical techniques which follow the statistical merging histories galaxy halos and combine then with physically motivated recipes for gas cooling, star formation, and feedback (e.g., White & Frenk 1991; Kauffmann & White 1993; Kauffmann, White, & Guiderdoni 1993; Cole et al. 1994; Baugh, Cole, Frenk, & Lacey 1998; Somerville & Primack 1999; Somerville, Primack, & Faber 2001). In this theoretical context, there seems to be two different scenarios for the formation of massive present day galaxies (Baugh, Cole, Frenk, & Lacey, 1998). Galaxies could have been mostly assembled at high redshift and increased mass since then by accreting low mass galaxies and by passively forming stars. Alternatively, they could form at relatively recent times through the merger of two massive progenitors.

The most recent models have increased their usefulness by predicting observable quantities. Through their combination with stellar population synthesis databases (e.g., Bruzual A. & Charlot 1993; Fioc & Rocca-Volmerange 1997) the modelers can use their generated SFHs, dust contents, and abundances to predict the emergent SEDs, luminosities (Kauffmann & Charlot, 1998), and emission and absorption line kinematics (Haehnelt, Steinmetz, & Rauch, 1998). Using these theoretical predictions, several authors have now compared them directly to the observed sizes, luminosity functions, and redshift distributions of galaxies out to  $z \sim 4$  (Poli et al., 1999; Fontana et al., 1999; Giallongo et al., 2000). They have found that the redshift distributions, luminosity functions, and size-luminosity distributions are broadly consistent with hierarchical models, but that there are too many faint, small galaxies at all redshifts  $z \sim 0.5 - 3$  compared to the model predictions. Because the SF and feedback prescriptions of the models are highly uncertain, and because the rest-frame optical luminosities are fairly robust, observations which probe the rest-frame optical

are most likely to constrain the different theories.

## 1.5 The Faint Infrared Extragalactic Survey

The key to tracing galaxy evolution consistently over a large redshift range is observing galaxies at identical rest-frame wavelengths. To trace the stellar *mass* of the universe as opposed to the SFR it is necessary to select galaxies as red as possible in the rest-frame. While the HDF-N, with its extremely deep optical and NICMOS imaging, has greatly improved the situation, it has only moderately deep *K*-band data and the NICMOS data is proprietary. In addition, it has a small area making it difficult to interpret results in the broader context of galaxy formation given the possibly large influence of LSS. We realized the need by the community for a survey which combines the deepest data that optical imaging had to offer with the deepest  $1 - 2.5\mu m$  data obtainable on the world's largest telescopes. This dataset should push the depths and image quality obtainable with ground based observatories, should cover multiple fields to mitigate the effects of cosmic variance, should allow the construction of a very faint *K*-band selected sample which has wide wavelength coverage, should be accessible to the largest telescopes for spectroscopic follow-up, and should be publically available. The Faint InfraRed Extragalactic Survey<sup>1</sup> (FIRES; Franx et al. 2000) is a project which uses the Infrared Spectrograph And Array Camera (ISAAC; Moorwood et al. 1997) at the VLT to image the HDF-S and the  $z = 0.83$  cluster MS1054-03 in  $J_s$ ,  $H$ , and  $K_s$ , combining some of the deepest HST optical data, with  $\sim 200$  hours of NIR imaging (with no proprietary rights) over a total area of  $\sim 30$  square arcminutes. 100 hours of the total exposure time will be devoted to the WFPC2 field of the HDF-S alone providing us with the deepest ground-based  $J_s$ , and  $H$  data and the overall deepest  $K_s$  band data in any field allowing us to reach

---

<sup>1</sup>Based on observations with the NASA/ESA *Hubble Space Telescope*, obtained at the Space Telescope Science Institute, which is operated by the AURA, Inc., under NASA contract NAS5-26555. Also based on observations collected at the European Southern Observatories on Paranal, Chile as part of the ESO programme 164.O-0612

rest-frame optical luminosities in the  $V$ -band of  $\sim 0.4 L_*$  at  $z \sim 3$ . The data were taken in service mode under the best possible seeing conditions and showcase the best that the VLT has to offer.

Including myself, the FIRES team members (Marijn Franx, Ivo Labbé, Hans-Walter Rix, Alan Moorwood, Paul van der Werf, Huub Röttgering, Konrad Kuijken, Pieter van Dokkum, Lottje van Starkenburg, and Arjen van de Wel) plan on pursuing a variety of research topics including, but not limited to (and not in order of importance): selection of galaxies in the NIR and comparison to optically selected samples i.e., looking for objects missed by optical selection, estimation of photometric redshifts for the whole sample across a large redshift range and the characterization of the redshift distribution of  $K$  selected sources, searching for evolved or extremely red galaxies at high redshift, measuring the rest-frame optical colors and stellar masses of objects out to  $z \lesssim 3$ , tracing the build-up of the stellar mass as a function of  $z$  and rest-frame color, measuring the sizes and morphologies of objects in the rest-frame optical over a large redshift range, exploring the optical/NIR SEDs of galaxies selected at other wavelengths (e.g., Rigopoulou et al. 2000), tracing the evolution of the rest-frame optical luminosity function, comparing the rest-frame luminosities, sizes, and redshift distributions in an  $K$  selected sample with the predictions of galaxy formation models, studying the dwarf galaxy population in MS0154-03, and the selection of interesting candidates for spectroscopic follow-up.

## 1.6 Outline

In this dissertation, we will present the first scientific results from the FIRE survey in the HDF-S. In Chapter 2 we will present a  $K_s$ -band selected ( $K_{s,AB} < 23.5$ ) catalog of seven band data ( $0.3 - 2.2\mu m$ ) and constructed to give accurate colors. We will describe in detail a template based photometric redshift code, discuss its accuracy, and use it to estimate the redshifts  $z_{phot}$  of the entire sample. We will also discuss

our determination of realistic uncertainties on  $z_{phot}$  and their dependence on the photometric errors. Using our set of redshifts and large wavelength coverage, we determine rest-frame luminosities for our sample and discuss the redshift evolution of the rest-frame  $V$ -band luminosity function.

In Chapter 3 we present VLT optical spectroscopy of candidate high redshift galaxies in the HDF-S. We use these spectroscopic redshifts along with all available redshifts in the HDF-S to refine our  $z_{phot}$  estimates and our  $z_{phot}$  uncertainties given the FIRES photometry. We also discuss a large, disk-like LBG which is spectroscopically confirmed to lie at  $z = 2.793$ .

The full 101.5 hours of FIRES integration is presented in Chapter 4. We discuss the NIR data reduction and the construction of a preliminary multi-color,  $K_s$ -band selected ( $K_{s,AB} < 26$ ) 2-arcsecond aperture flux catalog.

The full FIRES dataset is used in Chapter 5 to derive the rest-frame optical luminosities and colors of a  $K_{s,AB} < 25$  subsample of the total catalog. We estimate the uncertainties in these quantities which come from our uncertainty in the redshift. We then use these colors to compare our galaxies directly to local samples and show that there are red  $K_s$ -band selected galaxies which would not be identified by the Lyman Break technique. Using theoretical relations between the rest-frame colors and mass-to-light ratios  $\mathcal{M}/L$ , we derive the rest-frame optical  $\mathcal{M}/L$ 's and stellar masses for our galaxies and make uncertainty estimates. Finally we address the global properties of our sample out to  $z < 3.2$  and infer the rest-frame optical luminosity density and stellar mass density of the bright galaxies with secure redshifts.

## CHAPTER 2

# A K-BAND SELECTED PHOTOMETRIC REDSHIFT CATALOG IN THE HDF-S: SAMPLING THE REST-FRAME V-BAND TO $z = 3$

## 2.1 Motivation

In this chapter we present initial results from observations the HDF-S obtained as part of FIRES. With these data, we derive photometric redshifts with accompanying uncertainties and determine the rest-frame U, B, and V-band luminosities for galaxies with  $z \leq 3$  in a  $K_s$ -band selected sample. Our current data are deep enough to probe galaxies at  $z = 2$  with rest-frame luminosities  $L^{\text{rest}} \geq 10^{10} L_{\odot}$ . With our data we place new constraints on the redshift distribution in the HDF-S for  $1 < z < 2.5$ . In §2.2, we present the observations and data. In §2.3 we discuss our new photometric redshift technique including a discussion of its reliability. We show and discuss the redshift distribution of our sample and the  $L^{\text{rest}}$  values of our galaxies in §2.4. We summarize in §2.5. We adopt a  $\Lambda$ -cosmology throughout the paper with  $\Omega_M = 0.3$ ,  $\Omega_{\Lambda} = 0.7$ , and  $H_0 = 100 \text{ km s}^{-1} \text{ Mpc}^{-1}$ . If  $h$  is omitted, assume  $h = 1.0$ .

## 2.2 Observations and Data

### 2.2.1 Observations

We present the first data taken on the HDF-S in the fall of 1999. The total exposure times were 6.7, 5.7, and 7.5 hours in  $J_s$ ,  $H$ , and  $K_s$  respectively. The field was centered at 22h32m55.03s, 60°33'09".8 (J2000). All these data were taken in service mode at the Antu telescope on the nights of 1999 October 21-29, 1999 November 19, and 1999 December 18-19, before its primary mirror was re-coated. Despite the



reduced sensitivity, the data were of exceptional quality. Most of the nights had excellent seeing in all bands and the combined images had a median image quality of  $0''.55$  ( $J_s$ -band),  $0''.50$  ( $H$ -band), and  $0''.50$  ( $K_s$ -band). ISAAC has a pixel scale of  $0''.147 \text{ pix}^{-1}$  and a field of almost  $150 \times 150''$  which almost perfectly matches the size of the WFPC2 field.

Our observing strategy followed established procedures for ground-based NIR work. We dithered the images randomly in a  $20''.0$  box to allow the construction of sky frames with minimal object contamination. This works well for a field such as the HDF-S which contains no large, bright objects. Our exposure times were 120s, 120s, and 60s split into 4, 6, and 6 integrations for  $J_s$ ,  $H$ , and  $K_s$  respectively.

For our optical data, we used the version 2 (Casertano et al., 2000), reduced, calibrated  $U_{300}$ ,  $B_{450}$ ,  $V_{606}$ , and  $I_{814}$  WFPC2 images from the HDF-S. In §2.2.4 we used these images in conjunction with the reduced NIR images to construct a multi-band catalog.

### 2.2.2 Data Reduction

We reduced our ground based images with IRAF<sup>1</sup> using the DIMSUM<sup>2</sup> package within IRAF and ECLIPSE<sup>3</sup>. We give a brief summary of our data reduction below. For further details see the presentation of our full dataset (Labbé et al., 2001). For each individual science exposure in a given Observing Block (OB), a sky image was constructed from a maximum of 8 temporally adjacent images and subtracted from the science frame. Cosmic rays were identified from the individual sky-subtracted frames and all the sky-subtracted frames in a given OB were then aligned and com-

---

<sup>1</sup>IRAF is distributed by the National Optical Astronomical Observatories, which are operated by AURA, Inc. under contract to the NSF.

<sup>2</sup>DIMSUM is the Deep Infrared Mosaicing Software package developed by Peter Eisenhardt, Mark Dickinson, Adam Stanford, and John Ward, and is available via ftp to <ftp://iraf.noao.edu/iraf/contrib/dimsumV2/dimsum.tar.Z>

<sup>3</sup>ECLIPSE is a software package written by Devillard which is available at <http://www.eso.org/projects/aot/eclipse/>

bined. DIMSUM created a mask marking all pixels belonging to objects by applying a threshold to the combined image. Sky-subtraction and cosmic-ray identification were repeated for the individual frames using the newly created object mask to exclude object pixels. We modified DIMSUM to account for the time-dependent bias in the ISAAC frames by subtracting the median, on a line-by-line basis, excluding from the median calculation all object pixels in the object mask. The sky-subtracted frames were then flatfielded before the final registration and combination. The flatfield images were created from a time sequence of twilight sky images using the ECLIPSE software. Individual frames for a given OB were registered and added together using the imcombine task in IRAF. The NIR images from all OBs for a given filter were then combined into a total image. Finally, we applied the documented geometric distortion correction to the combined image while simultaneously interpolating the final NIR images to 4 times the WFPC pixel scale ( $0''.159 \text{ pix}^{-1}$ ).

A weight map was constructed for each NIR passband to reflect the exposure time at every pixel and hence the noise. For the HST data we used the weight maps publically distributed along with the science frames. These weight maps were used in all subsequent detection and photometry steps.

### 2.2.3 Photometric calibration

Magnitude zeropoints were derived from standard star observations taken as part of the normal VLT calibration routine. For each standard star, in each filter, and on each night, we measured the flux in a circular aperture of radius  $\sim 3''$  (20 pixels) and used the magnitude of that star as given in Persson et al. (1998) to establish our zeropoint for that star. We derived a nightly zeropoint by combining all standard star observations in a given night and filter. By comparing these derived nightly zeropoints to the median zeropoints over all nights we identified non-photometric nights. We used the mean of the zeropoints on the photometric nights to determine the zeropoint

for each bandpass. The uncertainties in the final zeropoints were  $\sim 0.02$ . Using these zeropoints, we derived the magnitudes of bright stars in the field for the OB's on the photometric nights, and used them to calibrate the final combined and distortion corrected image. All magnitudes in this paper are given in the AB system unless stated explicitly otherwise. For the NIR data, the adopted transformations from the Vega system to the AB system are taken from Bessell & Brett (1988;  $J_{s,vega} = J_{s,AB} - 0.90$ ,  $H_{vega} = H_{AB} - 1.37$ ,  $K_{s,vega} = K_{s,AB} - 1.88$ ).

In our final reduced images, the  $10\sigma$  magnitude limits in a  $2''.0$  circular aperture are  $m_{AB} = 23.8$ ,  $23.0$ , and  $23.2$  in  $J_s$ ,  $H$ , and  $K_s$  respectively. The  $3\sigma$  limits are  $m_{AB} = 25.1$ ,  $24.4$ , and  $24.5$ . Our data are  $\sim 0.25$ ,  $0.1$ , and  $0.2$  magnitudes deeper in  $J_s$ ,  $H$ , and  $K_s$  respectively than the data on the HDF-N taken at the Kitt Peak 4-meter with the IRIM camera in April of 1996 (Dickinson, 2001a). The F110W and F160W HDF-N NICMOS data (Dickinson, 2001b) goes  $1.1$  and  $1.9$  magnitudes deeper respectively than our  $J_s$  and  $H$  data. In the HDF-S our data are  $\sim 1$ ,  $2.1$ , and  $2.1$  magnitudes deeper in  $J_s$ ,  $H$ , and  $K_s$  respectively than the EIS data from da Costa (1998).

#### 2.2.4 Object Detection and Photometry

Our first goal is to construct a  $K_s$ -band flux-limited catalog of objects. We used the SExtractor software (Bertin & Arnouts, 1996) to detect objects from the final  $K_s$  image, using the  $K_s$ -band weight image. Faint objects are detected against a noisy background after convolving the image with a kernel representing the typical expected object size. Because SExtractor allows only one convolution kernel per detection pass, we must optimize the detection for a particular object size, biasing ourselves against faint objects of very different sizes. We choose a  $0''.48$  FWHM Gaussian convolution kernel, extending over  $0''.8 \times 0''.8$  which represents the size of the seeing disk. As in all deep surveys, deblending of overlapping or close object pairs is difficult and to some

extent subjective. An ideal deblending algorithm will not “oversplit” single galaxies with knotty internal structure, but will split close groupings of separate galaxies. We settled on a single set of deblending parameters that nearly eliminate the over splitting of galaxies: `DEBLEND_NTHRESH` = 32, `DEBLEND_MINCONT` = 0.0002. These parameters set the number of deblending sub-thresholds and the minimum contrast needed to deblend two objects, respectively.

To obtain consistent photometry across the full seven bands, we need to account for the vastly different pixel scales and resolutions between our space-based and ground-based images. To this end, we first resampled all of the data to the same pixel scale, fitted the PSF in the NIR images with a double Gaussian, whose equally weighted components have  $\text{FWHM} = 0''.38$  and  $\text{FWHM} = 0''.75$  respectively, and convolved this with the optical data. To measure colors over identical angular scales in each band, we choose to measure the fluxes of all objects in a fixed  $2''.0$  diameter aperture whose position was chosen from the  $K_s$ -band image. For the largest objects this aperture misses some flux, but this choice lessens the chance of measuring flux from two separate objects. Still, there are 6 pairs of objects whose  $2''.0$  apertures overlap (IDs=98,99; 117,127; 187,188; 354,364; 372,373; 397,398). For some of these objects, the flux measurements of the galaxy might be strongly affected by the light from its nearest neighbor. In calculating the flux errors in all the images, we used the weight images discussed in (§2.2.2).

We used SExtractor to detect objects using a detection threshold of 0.8 times the standard deviation of the background. The relative strength of the background at each pixel was given by the  $K_s$ -band weight image. For an object to enter the initial catalog we required that a minimum of five contiguous pixels lie above the detection threshold. From the resulting initial catalog of 615 objects detected in the  $K_s$ -band image, we constructed a catalog optimized for photometric redshift estimates based on three criteria. 1) To homogenize the data quality, the value of the exposure time weight must exceed 0.5 and 0.25 for the VLT and HST images respectively

(this cut reduces our total usable image area to  $4.3 \text{ arcmin}^2$ ). 2) To differentiate between stars and galaxies, we examined the FWHM and magnitude of objects in the  $I_{814}$  image. Objects were identified as stars if they satisfied either of the following two criteria:  $\text{FWHM} < 6 \text{ pixels}$  and  $I_{814, \text{AB}} < 27$  or  $\text{FWHM} < 15 \text{ pixels}$  and  $I_{814, \text{AB}} < 22$ . The second of these criteria was used to eliminate saturated stars. 3) To limit ourselves to magnitudes where the completeness is greater than 50%, we require that the object must have a total magnitude (the “AUTO” magnitude from SExtractor with a minimum  $2''$  diameter) of  $K_{s, \text{AB}}^{\text{tot}} \leq 23.5$ , roughly a  $6\sigma$  detection (see §2.2.5). The exposure time criterion reduced the initial catalog to 316 objects and the removal of all point sources in the  $I_{814}$  image left 293. Of these, 136 objects had  $K_{s, \text{AB}}^{\text{tot}} \leq 23.5$  and were entered into our final catalog (see Tables A.1 and A.2). The  $K_s$ -band image is shown in Figure 2.1 along with all 136 objects and their ID numbers from the final catalog. All flux measurements are summarized in Tables A.1 and A.2 .

### 2.2.5 Completeness

The issue of completeness must be addressed in every survey for faint, extended objects. The detectability of an object depends not only on its apparent magnitude, but also on its morphology and mean surface brightness. The detection algorithm used by SExtractor looks for continuously connected pixels above a certain threshold with respect to the background. Relatively bright objects of low surface brightness may be missed by this technique. To understand our detection completeness we added objects to the  $K_s$ -band image and then determined how successful we were at detecting them. We constructed three different types of model objects: An elliptical galaxy with a de Vaucouleurs profile and an axis ratio of  $b/a = 0.7$  and two exponential galaxies with  $b/a = 0.4$  and  $b/a = 0.8$ . For each of these three profile types, we made a magnitude grid of  $K_{s, \text{AB}} = 20, 21, 22, 23, 24$ , and  $25$  and a size grid of  $R_H = 0''.25, 0''.5, 0''.8$ , and

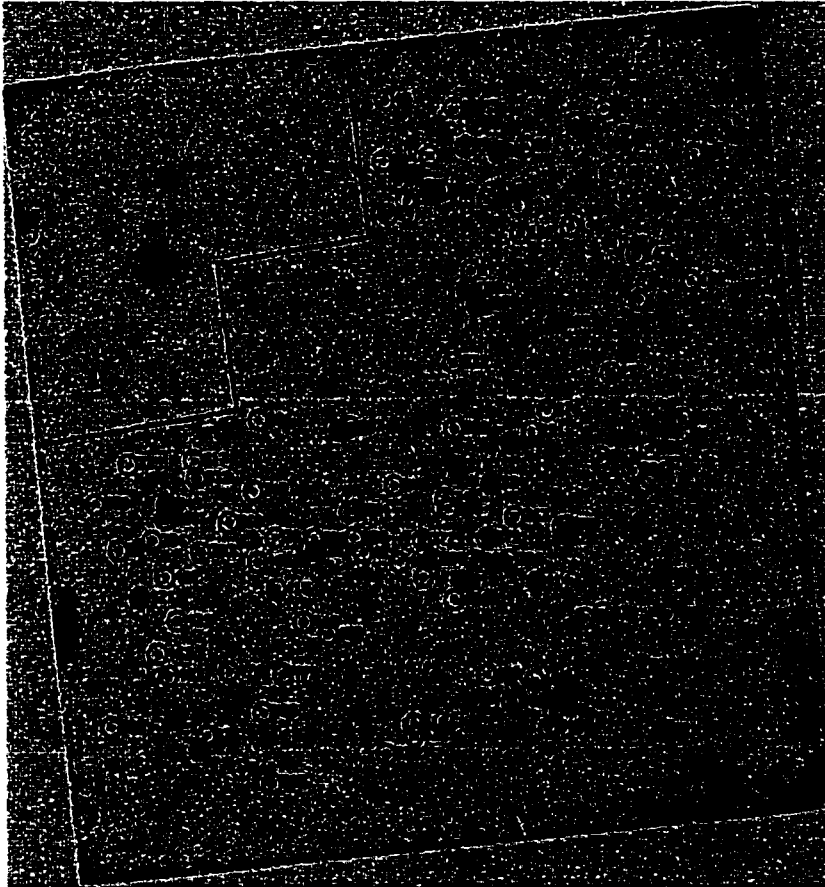


FIGURE 2.1. The reduced  $K_s$ -band image. All 136 objects in the final catalog are marked, and the numbers are the ID numbers in the catalog shown in Table A.1. The outline of the WFPC2 field of the HDF-S is shown.

1".6 where  $R_H$  is the half-light radius. For each profile type, magnitude, and size, we convolved the synthetic galaxy images with the seeing (see §2.4) and inserted about 50 such objects into the  $K_s$  image at simple grid positions. We then ran SExtractor on the new image and counted how many of the model objects were detected for each set of parameters and how well these parameters (apparent magnitude and size) were recovered. Figure 2.2a shows how the completeness depends on surface brightness, parameterized by both input magnitude and size, for a given profile shape and axial ratio. For a fixed size Figure 2.2b shows how little completeness changes with profile shape.

To assess the actual 50% completeness limit for our sample we must select size parameters most applicable to galaxies near our flux limit. To map the input sizes used in Figure 2.2 to the sizes returned by SExtractor for the model images, we compared, for different magnitudes,  $R_H$  to

$$R_{out} = \sqrt{R_{kron}^2 - R_{seeing}^2} . \quad (2.1)$$

Here  $R_{kron}$  is the Kron radius (Kron 1980) calculated by SExtractor, and  $R_{seeing}$  is the FWHM/2 of the actual observations. At the faintest level where we could both retrieve the input magnitude and also see a defined relation between input and output size ( $K_{s,AB} \sim 22$ ), we measured that objects had a typical  $R_{kron}$  of 0".6. Using our input-output size relations, averaged over profile type, we associated this measured radius with an intrinsic  $R_H$  of 0".8. As a choice of profile type we conservatively chose the curve for which we are least complete, the exponential disk with  $b/a = 0.8$  (see Figure 2.2b). Using this curve (see Figure 2.2a), we established a 50% completeness limit at  $K_{s,AB} = 23.5$  and note that we are 90% complete for  $K_{s,AB} < 22.0$ . For this flux limit our conclusions are insensitive to completeness corrections, and so we make no such corrections.

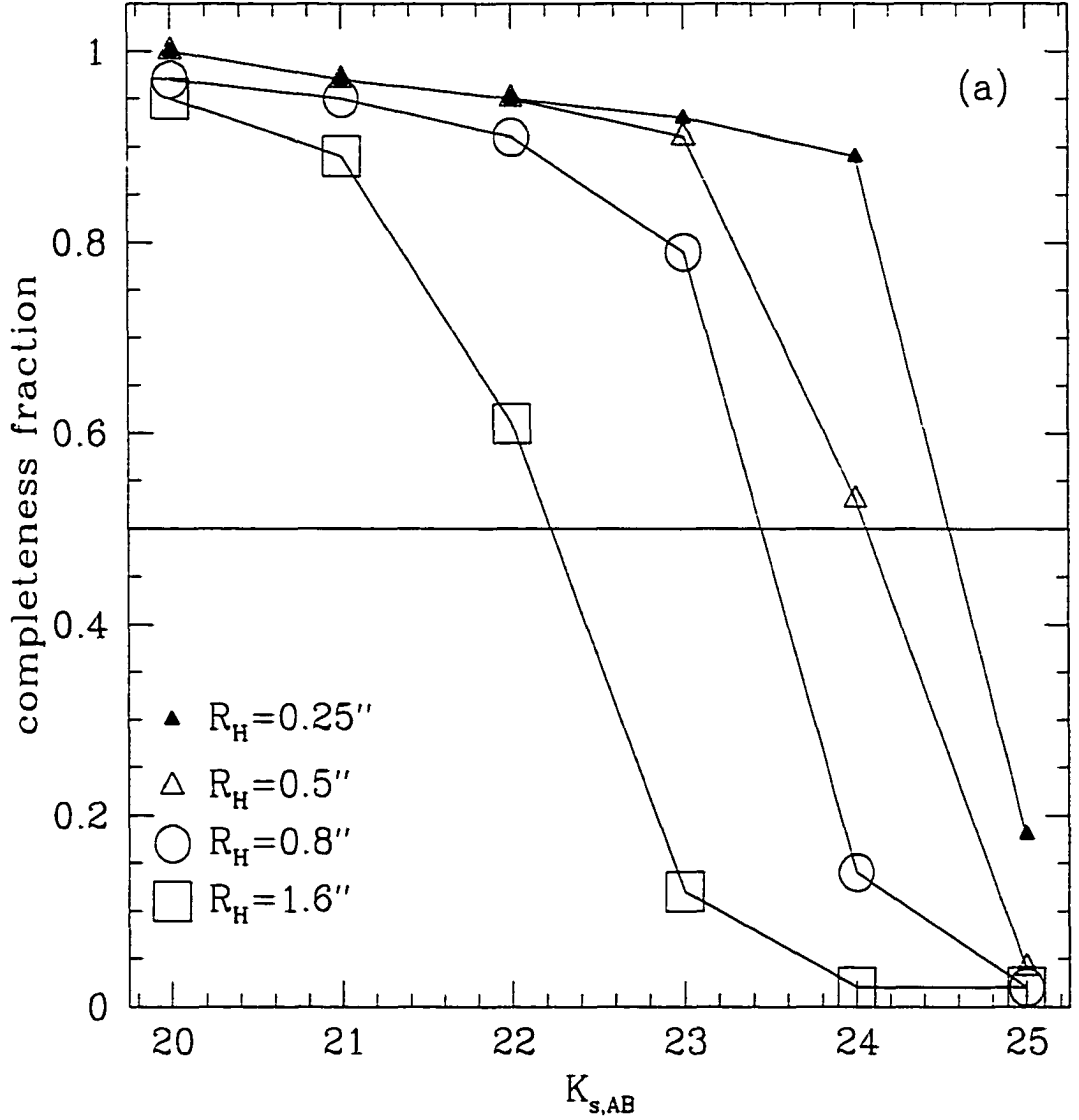
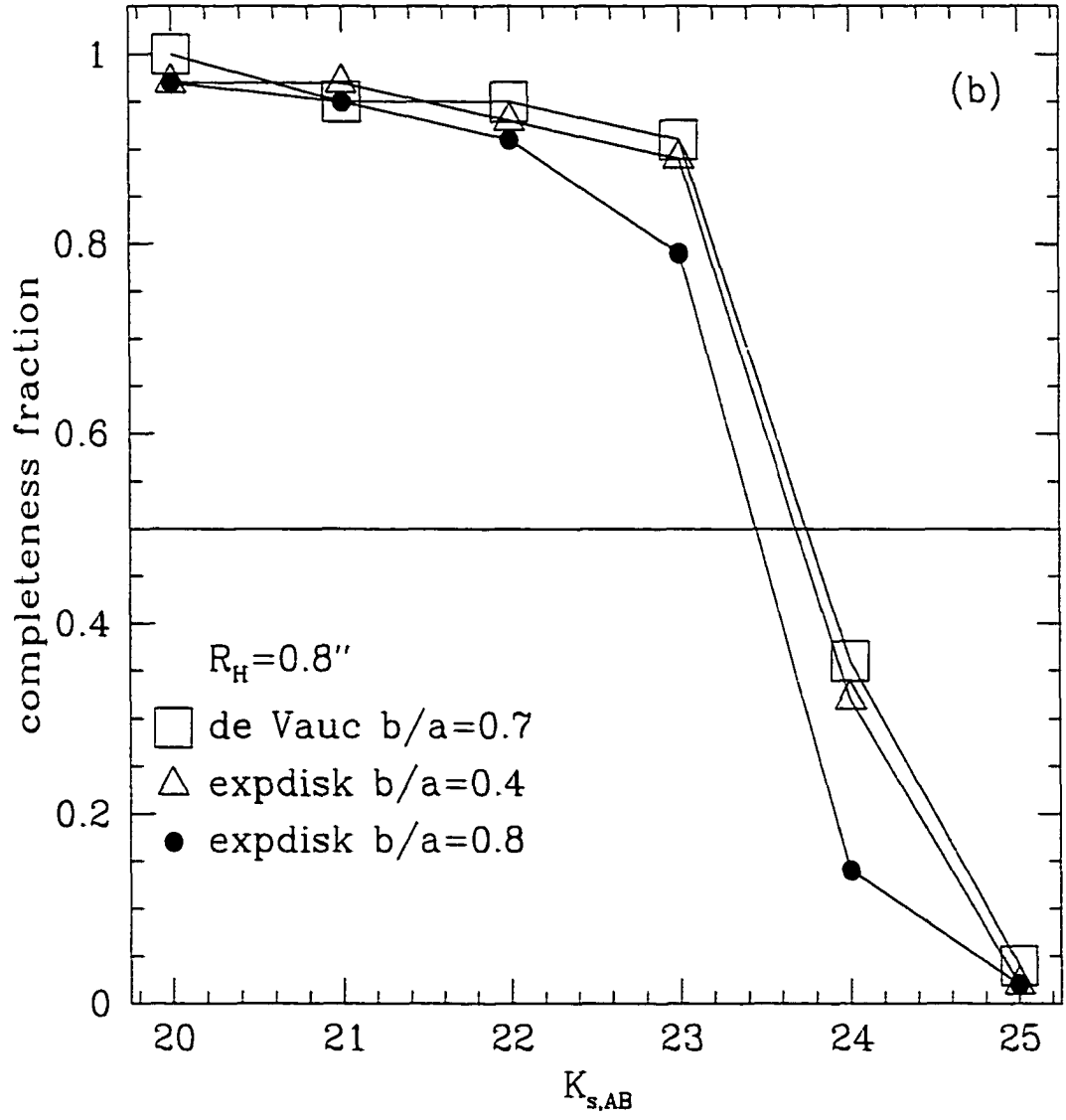


FIGURE 2.2. Estimates of the  $K_s$ -band completeness limit. a) Completeness against  $K_{s,AB}$  magnitude for galaxies with an exponential profile and an axis ratio,  $b/a = 0.8$ . Different points represent different galaxy half-light radii  $R_H$ . Note how the completeness depends greatly on the object size. b) Completeness vs.  $K_{s,AB}$  magnitude, at the typical faint object radius of  $R_H = 0''.8$ , for three different profile shapes. The completeness is relatively insensitive to the exact profile shape. In both plots, the horizontal line shows the 50% completeness limit.





## 2.3 Photometric Redshifts

### 2.3.1 Template Choice

The next step in the analysis is to convert the flux measurements of objects in the seven bands into an estimate of their redshift. We estimate the redshifts of our galaxies by modeling their rest-frame colors by a combination of empirical spectral templates. We used Hubble type templates E, Sbc, Scd, and Im from Coleman, Wu, & Weedman (1980; hereafter CWW) and the two starburst templates with a low derived reddening, designated SB1 and SB2, from Kinney et al. (1996). For the two starburst templates, the color excess  $E(B - V)$  with respect to the expected colors of an unreddened galaxy is  $\leq 0.10$  and  $0.11 \leq E(B - V) \leq 0.21$  respectively. These templates are needed because many galaxies even in the nearby universe have colors bluer than the bluest CWW templates and the inclusion of SB1 and SB2 significantly improves the photometric redshift estimate (see also Sawicki, Lin, & Yee 1997; Benítez 2000).

To extend the CWW and starburst templates from their published short-wavelength limits (1400Å and 1232Å respectively) to below the Lyman break, we extrapolated blueward a power law fit to the 1400-1800Å and 1240-1740Å wavelength ranges, respectively. To account for intervening absorption from neutral cosmic hydrogen, we applied to all our template spectra, the redshift dependent cosmic mean opacity taken from Madau (1995). We accounted for the internal hydrogen absorption of the galaxy by setting the flux blueward of 912Å to zero. To extend the templates to the IR, we used the latest stellar population synthesis code of Bruzual & Charlot (2001). We constructed NIR SED extensions for each template by using the stellar population ages, star formation timescales, and initial mass functions for each template Hubble type from Pozzetti, Bruzual, & Zamorani (1996; see Table A.3). We verified that these SEDs matched the optical colors of our templates.

In addition to the “natural” reddening already included in the templates, addi-

tional reddening may be present. We will examine the effect of reddening on the determination of  $z_{phot}$  in Labbé et al. (2001).

### 2.3.2 Template Based Estimates of the Redshift

We cannot assume *a priori* that distant galaxies have SEDs identical to any one of our empirical SEDs. In fact, even within a single galaxy there may be spatial variations in the stellar populations and SFR. Our goal is to fit the observed flux points as well as possible with minimal assumptions about the galaxy's SFH. Therefore, we attempt to model the observed SED by a *linear combination* of redshifted templates. We estimate the likelihood that a galaxy lies at a given redshift by calculating

$$\chi^2(z) = \sum_{i=1}^{N_{filter}} \left[ \frac{F_i^{data} - F_i^{model}}{\sigma_i^{data}} \right]^2, \quad (2.2)$$

where  $F_i^{data}$  is the measured flux value, in units of  $f_\lambda$ , in the  $i$ th color bandpass,  $\sigma_i^{data}$  is its associated  $1\sigma$  uncertainty and

$$F_i^{model} = \sum_{j=1}^{N_{template}} C^j \times F_i^j(z), \quad (2.3)$$

where the  $F_i^j(z)$  is the flux of the  $j$ th template, redshifted to  $z$ , adjusted for intervening cosmic hydrogen absorption, and integrated over the transmission curve of the  $i$ th filter. For every redshift we determine the non-negative coefficients  $C^j$  which minimize  $\chi^2$  and the most likely photometric redshift,  $z_{phot}$ , which is the minimum of  $\chi^2(z)$ . To determine how our photometric errors propagate to errors in  $z_{phot}$ , we performed a Monte-Carlo simulation where, for each object, we create 200 synthetic photometry measurements distributed like a Gaussian around the observed flux, with a width  $\sigma = \sigma_i^{data}$ . For each object's Monte-Carlo set of fluxes, we determined, individually, the values of  $z_{phot}$  and calculated its 68% confidence limits  $\delta z_{MC}$  from the resulting distribution. We added a systematic error component in §2.3.3 to obtain the final error estimate  $\delta z_{phot}$ . From this point on, all values of  $z_{phot}$  will refer to those

calculated directly from the catalog data. The values of  $z_{phot}$  and  $\delta z_{phot}$  are given in Table A.4.

### 2.3.3 Comparison With Spectroscopic Redshifts

#### *The Hubble Deep Field North*

We gauged the precision and accuracy of our photometric redshift technique against spectroscopic redshifts, using the data set provided by Cohen et al. (2000) on the HDF-N. This field has optical data from HST (Williams et al., 1996) and  $J$ ,  $H$ , and  $K_s$  data from the IRIM camera on the Kitt Peak 4-meter telescope taken by Dickinson (2001a) in April of 1996. Using the photometry of Fernández-Soto, Lanzetta, & Yahil (1999; hereafter FLY99) we derive the photometric redshifts of all the  $I_{814}$  selected objects in the HDF-N using our code. There are a total of 150 objects common between the Cohen et al. spectroscopic sample and the FLY99 photometric sample. The comparison between our photometric redshifts  $z_{phot}$  and the spectroscopic redshifts  $z_{spec}$  for this sample is shown in Figure 2.3. The redshift error bars here are those calculated from the Monte Carlo simulation  $\delta z_{MC}$  (see §2.3.2). We choose for our measure of photometric redshift accuracy

$$\Delta z = |z_{spec} - z_{phot}|. \quad (2.4)$$

Our mean value is  $\Delta z \approx 0.14$  for  $z \leq 1.5$  and  $\Delta z \approx 0.44$  for  $z > 1.5$ . We also note that the value  $\Delta z / (1 + z)$  is nearly constant with redshift with  $\Delta z / (1 + z) \approx 0.09$  for the whole sample. This was first noted by FLY99 and likely stems from the effect that the filter spacing is roughly constant in  $\ln(\lambda)$  and the redshift determination is equivalent to finding a constant shift  $\ln(1 + z)$  for the spectrum if it is expressed as a function of  $\ln(\lambda)$ .

We note that there are a few objects ( $\lesssim 3\%$ ) for which  $z_{phot}$  and  $z_{spec}$  are greatly different, in part because there appear to be galaxies whose SEDs cannot be represented by our template set. Also, Fernández-Soto et al. (2001; hereafter FS01)

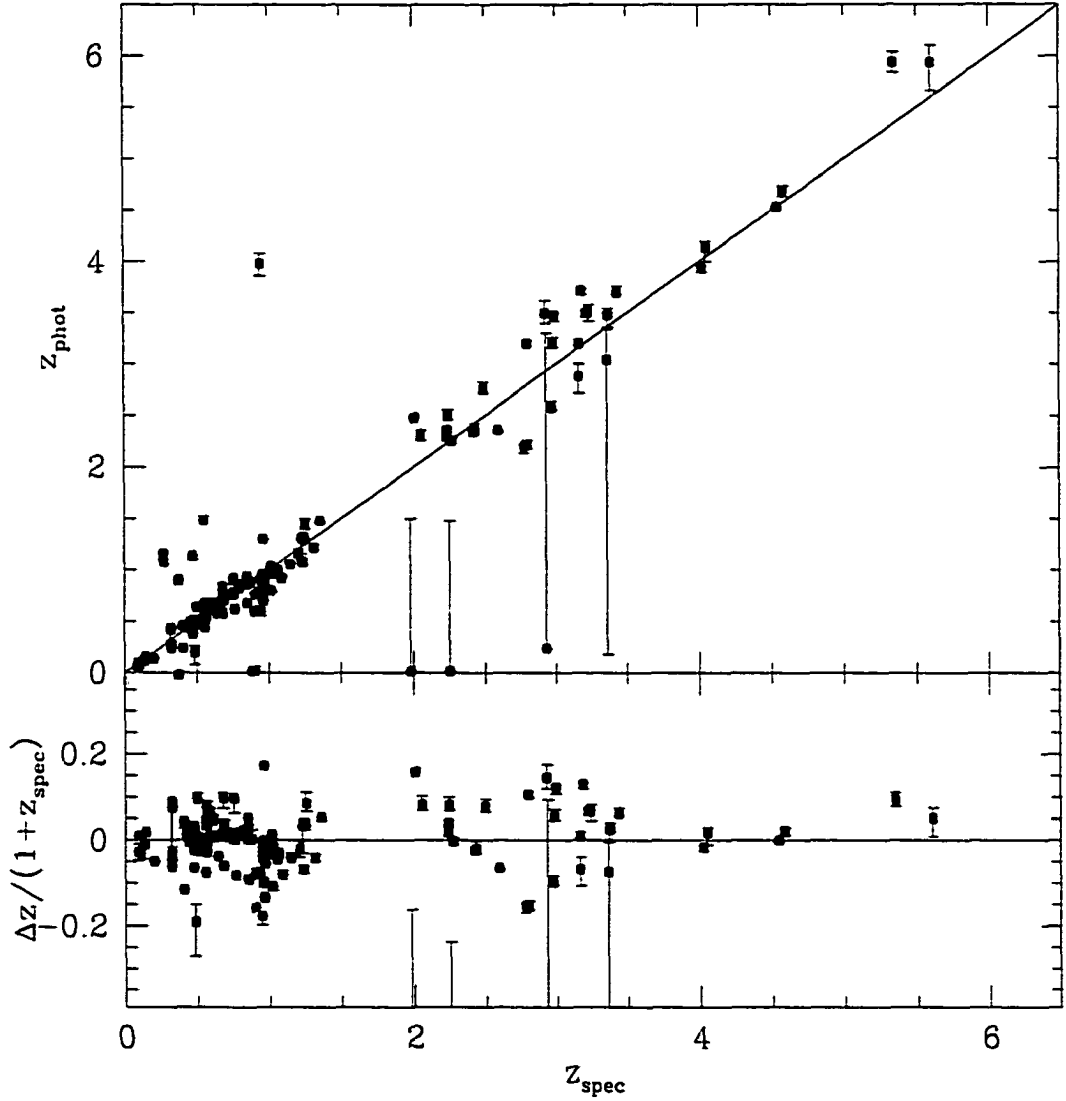


FIGURE 2.3. A comparison of  $z_{\text{phot}}$  to  $z_{\text{spec}}$  for objects in the WFPC2 field of the HDF-N. The error bars are derived from our Monte-Carlo simulations. The top panel shows a direct comparison between  $z_{\text{phot}}$  and  $z_{\text{spec}}$ . The diagonal line corresponds to a one-to-one relation to guide the eye. The bottom panel shows how  $z_{\text{spec}}$  relates to the difference between  $z_{\text{phot}}$  and  $z_{\text{spec}}$  normalized by  $1 + z_{\text{spec}}$ . The agreement is excellent for  $z_{\text{spec}} < 6.0$  with only  $\lesssim 3\%$  of the sample having  $|z_{\text{spec}} - z_{\text{phot}}| > 1.0$  and with  $\Delta z / (1 + z) = 0.07$ . The Monte-Carlo errors serve as a good indication of possible catastrophic failures of the  $z_{\text{phot}}$  determination. The one outlier with  $z_{\text{spec}} = 1$  and  $z_{\text{phot}} = 4$  has a spectroscopic redshift considered in error by FS01.

suggested that five of the published spectroscopic redshifts may be in error. One of these objects (FS01 ID number HDF36441.1410) has a  $z_{spec} = 2.267$  and is found by FS01 to have  $z_{phot} = 0.01$ . We however find  $z_{phot} = 2.26$ , in excellent agreement with the spectroscopic redshift. Eliminating HDF36441.1410 causes almost no change in  $\Delta z$  or  $\Delta z / (1 + z)$  for  $z > 1.5$ . Four objects remain<sup>4</sup> for which we found that our  $z_{phot}$  values do not agree well with the published  $z_{spec}$  values. These objects all lie at  $z_{spec} < 1$ . When eliminating these four objects, we found that  $\Delta z$  decreased to  $\approx 0.10$  for  $z \leq 1.5$ . With these four objects removed the mean  $\Delta z / (1 + z)$  for the redshift range  $z < 6$  is 0.07. There are three objects with  $z_{spec} = 2.931$ , 2.250, and 1.980 which are not flagged by FS01 as having an incorrect spectroscopic redshifts (FS01 IDs HDF36478.1255, HDF36446.1227, and HDF36498.1415) for which we find  $z_{phot} = 0.024$ , 0.02, and 0.02 and for which FS01 find  $z_{phot} = 0.26$ , 2.47, and 1.64. In all three of these cases,  $\delta z_{MC}$  is large and so in general, may provide a good indicator of discrepant  $z_{phot}$  values.

To test the importance of the NIR data in determining the correct redshift, we compare the accuracy of  $z_{phot}$  in the HDF-N as derived with and without NIR data. The NIR data is excluded from the fit by setting the error term to infinity in the  $\chi^2$  sum. For  $z_{spec} \leq 1.5$  the advantage of the NIR data is obvious, with the mean value of  $\Delta z$  increasing from 0.10 to 0.21 when the NIR data is not included. For two galaxies (FS01 ID HDF36498.1415, HDF36446.1227) with  $z_{spec} = 1.98$  and  $z_{spec} = 2.25$  however, excluding the NIR data causes  $z_{phot}$  to change from 0.20 to 2.24 and from 0.20 to 2.20 respectively. The original estimates were obviously wrong. In both of these cases, the inclusion of the NIR data forces the code to incorrectly identify a Lyman break, just entering the  $U_{300}$  band, as a rest-frame optical break. When leaving out these two galaxies,  $\Delta z$  at  $z_{spec} > 1.9$  remains unchanged by the omission of the NIR data. We should expect that the NIR data should improve the accuracy of the redshifts, but it is possible that the flux errors in the NIR have been underestimated

---

<sup>4</sup>FS01 ID numbers: HDF36396.1230, HDF36494.1317, HDF36561.1330, and HDF36569.1302

by FLY99 and that these data may overly contribute to the  $\chi^2$ . Unfortunately, the importance of the NIR data cannot be assessed in the redshift range  $1.3 < z < 2$  due to the lack of spectroscopic redshifts. In this regime however, only rest-frame optical breaks are observable and the NIR data is needed to constrain their position.

### *The Hubble Deep Field South*

For the HDF-S we selected all the objects in our catalog with publically available spectroscopic redshifts. These include five objects detected by ISOCAM (Rigopoulou et al., 2000) with spectroscopic redshifts from ISAAC, two objects from the FORS1 commissioning data (Cristiani et al., 2000), and four objects with unpublished spectra taken with the Anglo Australian Telescope (AAT; Glazebrook et al. 2001; hereafter G01; available at <http://www.aao.gov.au/hdfs/>), all of which lie in our area with “good photometry”. Two of the objects from G01 also had spectra from Rigopoulou et al. (2000) which yielded identical values of  $z_{spec}$ . The comparison of our  $z_{phot}$  to  $z_{spec}$  for these objects is shown in Figure 2.4. We find excellent agreement between  $z_{phot}$  and  $z_{spec}$  with  $\Delta z \approx 0.05, 0.18$  for  $z \leq 1.0$  and  $z > 1.0$  respectively.

### *Template Mismatch and Redshift Uncertainties*

The photometric redshift error bars derived solely from the Monte Carlo simulation described in §2.3.2 significantly underestimate the true variance of  $z_{phot}$  when compared to  $z_{spec}$ . This is because the galaxies with spectroscopic redshifts are among the brightest galaxies in our sample, with very small formal flux errors. The resulting range of statistically acceptable redshifts and SEDs is very small and our coarse and finite set of templates significantly distorts  $z_{spec}$ , but is not modeled by our Monte Carlo estimates. At the faint end, the photometric errors become large, and dominate the uncertainty in the redshift, implying realistic error estimates. Both effects were noted by FLY99.

We first attempted to compensate for this “template mismatch” in the bright galaxies by using a minimum photometric error of 10% chosen such that our Monte

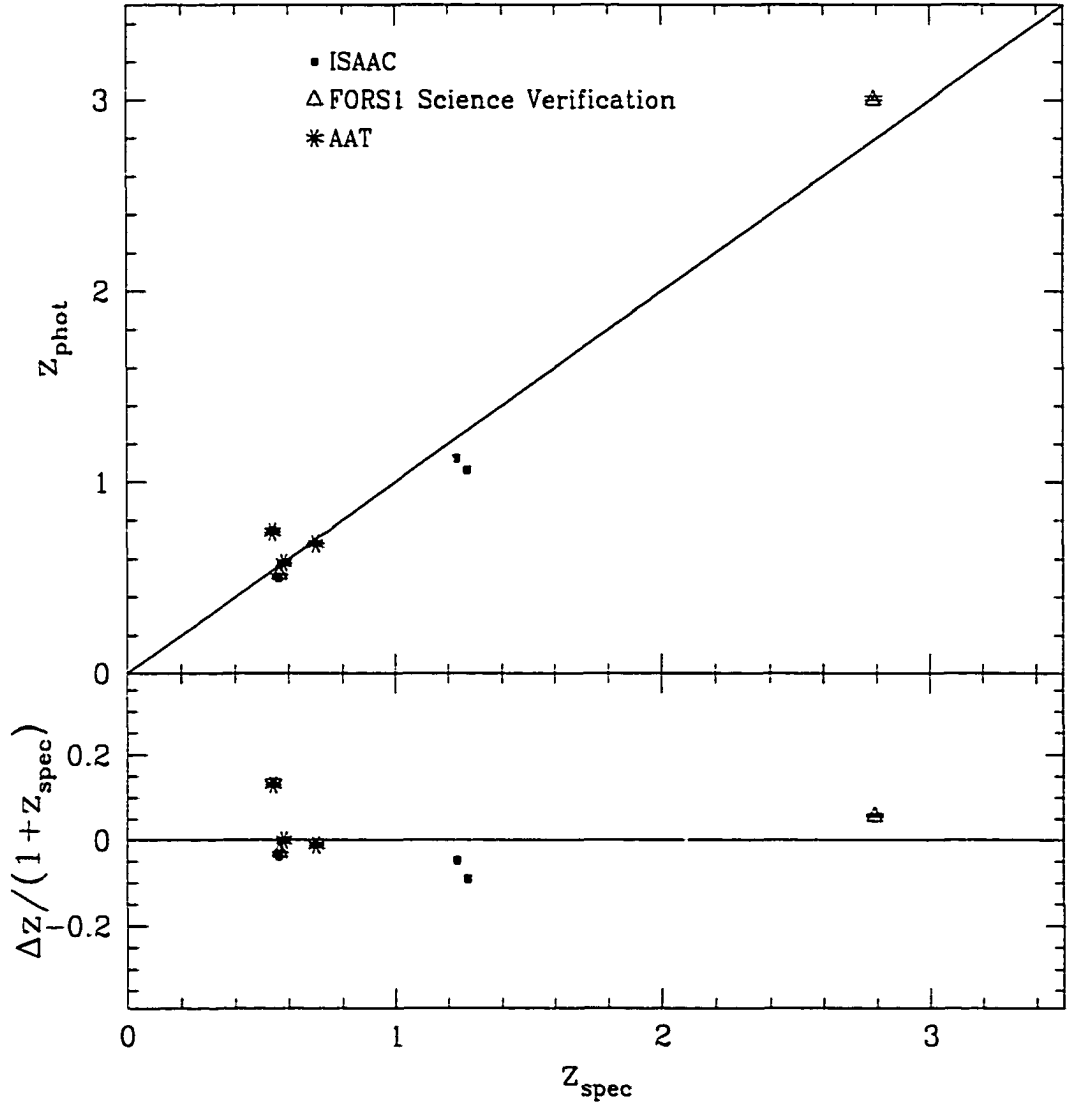


FIGURE 2.4. A comparison of  $z_{\text{phot}}$  to  $z_{\text{spec}}$  for objects in the WFPC2 field of the HDF-S. The explanation of this figure is identical to Figure 2.3.  $z_{\text{phot}}$  and  $\delta z_{\text{phot}}$  are derived from a Monte-Carlo simulation using the formal photometric errors. Two objects with  $z_{\text{spec}} = 0.58$  measurements from the AAT both have values of  $z_{\text{phot}} = 0.58$ .



Carlo error bars reflect the deviation of  $z_{phot}$  from  $z_{spec}$ . By introducing a minimum flux error we lessen the relative contribution of the high S/N HST data points to the  $\chi^2$  budget - which in turn changes the formal best-fit redshift. A detailed examination of this effect in the HDF-N and HDF-S data showed that while this minimum photometric error brought the  $z_{phot}$  values into statistical agreement with  $z_{spec}$ , the actual best-fit values of  $z_{phot}$  agreed worse with  $z_{spec}$  than when using the formal photometric errors. In fact,  $\sim 20\%$  of the galaxies in both the HDF-N and HDF-S have  $z_{phot}$  values calculated with the formal flux errors which lie outside the 68% confidence limits allowed with the boosted flux errors.

Hence, a proper estimate of the uncertainty in  $z_{phot}$  must take into account both systematic uncertainties arising from template mismatch and the uncertainties in  $z_{phot}$  which result from the photometric errors. We define the total uncertainty in  $z_{phot}$  as

$$\delta z_{phot} \equiv \sqrt{\langle |\Delta z| \rangle^2 + \delta z_{MC}^2}, \quad (2.5)$$

where  $\langle |\Delta z| \rangle$  is the value of  $(1+z_{phot})$  times the mean value of  $\Delta z / (1+z) = 0.07$  as derived from the HDF-N and  $\delta z_{MC}$  is again the 68% confidence limit of  $z_{phot}$  as derived from the Monte-Carlo simulation. Note that  $\delta z_{MC}$  need not be symmetric around  $z_{phot}$  and that we add  $\Delta z$  in quadrature separately for the upper and lower error bars. Again, the values of  $\delta z_{phot}$  are listed in Table A.4.

In addition to providing realistic error bars it is also informative to flag objects with secondary minima in their  $\chi^2(z)$  distributions. Although some secondary minima in  $\chi^2(z)$  are reflected by large values of  $\delta z_{MC}$ , some objects with small  $\delta z_{MC}$  may have a finite fraction of the Monte-Carlo realizations which end up at a rather different redshift. In fact some of the objects with large  $\Delta z$  in the HDF-N have secondary minima close to  $z_{spec}$  which are too small to be included in  $\delta z_{MC}$ . In addition to supplying the error bars which define the range of a galaxy's most likely redshifts, we flag in Table A.4 the 20 objects for which  $\geq 1\%$  of the Monte-Carlo realizations lie

greater than unity in redshift away from  $z_{phot}$ .

## 2.4 Results

In the section below, we use our estimates of  $z_{phot}$  to examine the redshift distribution of galaxies in the HDF-S. We also use our estimate of  $z_{phot}$ , coupled with our broad wavelength coverage, to determine the rest-frame optical SEDs and luminosities of our galaxies across a wide range in redshift.

### 2.4.1 SED Fits

In Figure 2.5 we show 10 examples of SED fits to the seven-band photometry ( $0.3 - 2.2\mu\text{m}$ ) for galaxies in the HDF-S. In our analysis of  $K_s$ -band selected galaxies in the HDF-S we find galaxies with a range of SEDs at all redshifts  $0 < z < 3$  with SED shapes ranging from very blue starburst templates to earlier Hubble type templates. As is shown in Figure 2.5 we also find galaxies with strong rest-frame  $4000\text{\AA}$  breaks or Balmer breaks at  $z > 1$ . These breaks signal that the rest-frame optical light is dominated by stars at least as old as  $A$  stars. Note that the small flux errors of the  $V_{606}$  and  $I_{814}$  data force the best-fit SED at any redshift to pass always through these two points. This is best shown in Figure 2.6 where, for each of our 136 galaxies, we plot the fractional difference between the measured flux and the model flux of our best-fit SED as a function of  $K_{s,AB}$ . At all magnitudes, the residuals are lowest in the  $V_{606}$  and  $I_{814}$  bands even if they are very large in other bands. This plot is also useful for finding systematic differences between the SEDs and the data. For example, it is seen that the best-fit SED slightly overpredicts the  $U_{300}$  flux at all magnitudes.

To demonstrate the effect of the inclusion of deep NIR data in the redshift range  $1.5 < z < 2$ , we show in Figure 2.7 two galaxies fit with and without the NIR information. Even where the  $V - I$  color is well constrained, and hence the possible redshifts severely limited, the NIR data can fix the break position.

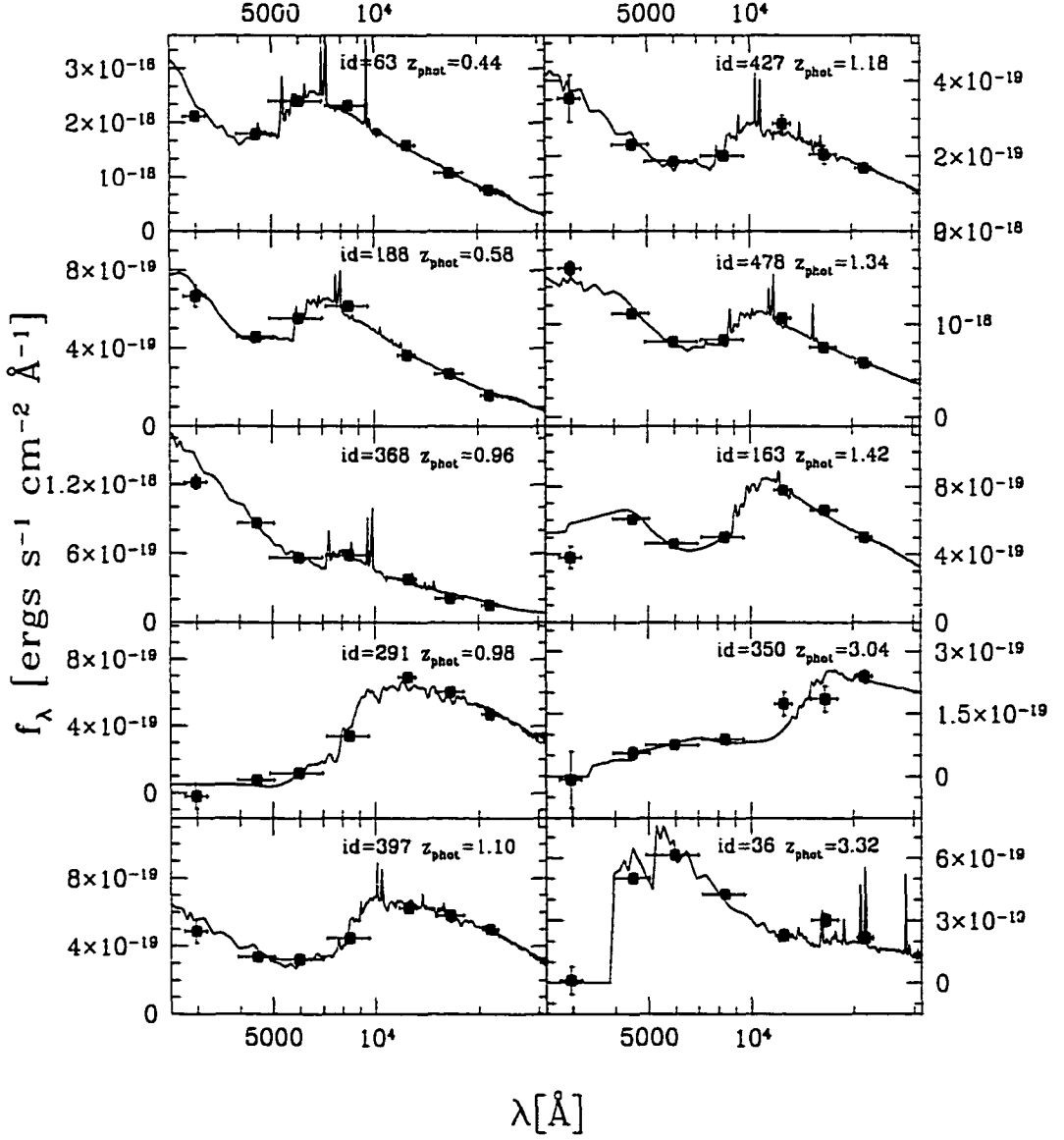


FIGURE 2.5. A sample of template fits to photometric data for 10 objects in the HDF-S. The measured  $z_{\text{phot}}$  increases down and to the right. In addition to blue, star-forming galaxies, there are many galaxies at  $z > 1$  with strong Balmer or  $4000\text{\AA}$  breaks.

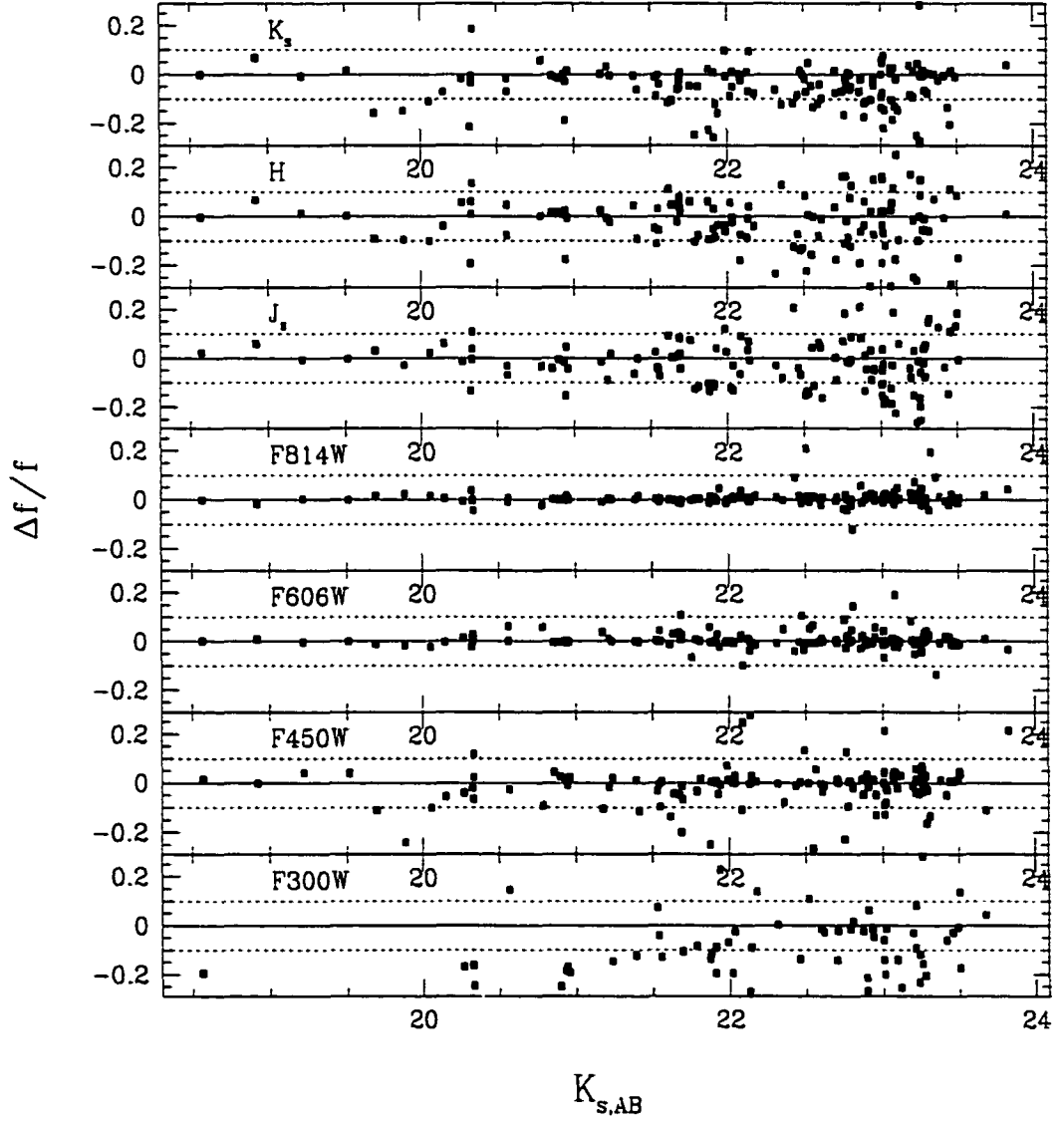


FIGURE 2.6. The fractional difference between the observed and model fluxes at the best-fit redshift as a function of  $K_{s,AB}$ . The horizontal dotted lines are at  $\pm 10\%$  to guide the eye. The high signal-to-noise of the  $I_{814}$  and  $V_{606}$  data forces the best-fit SED to always pass close to these points.

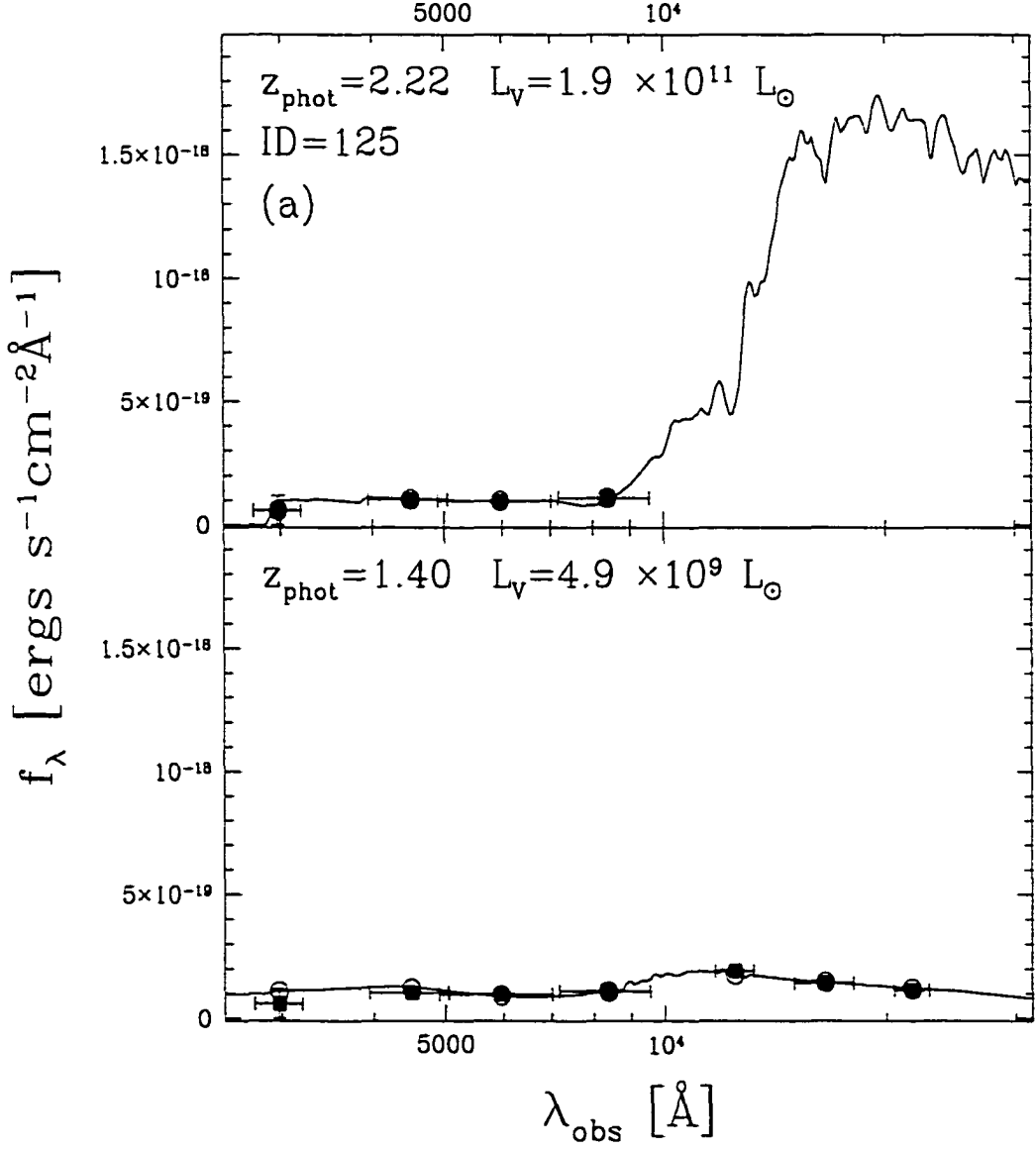
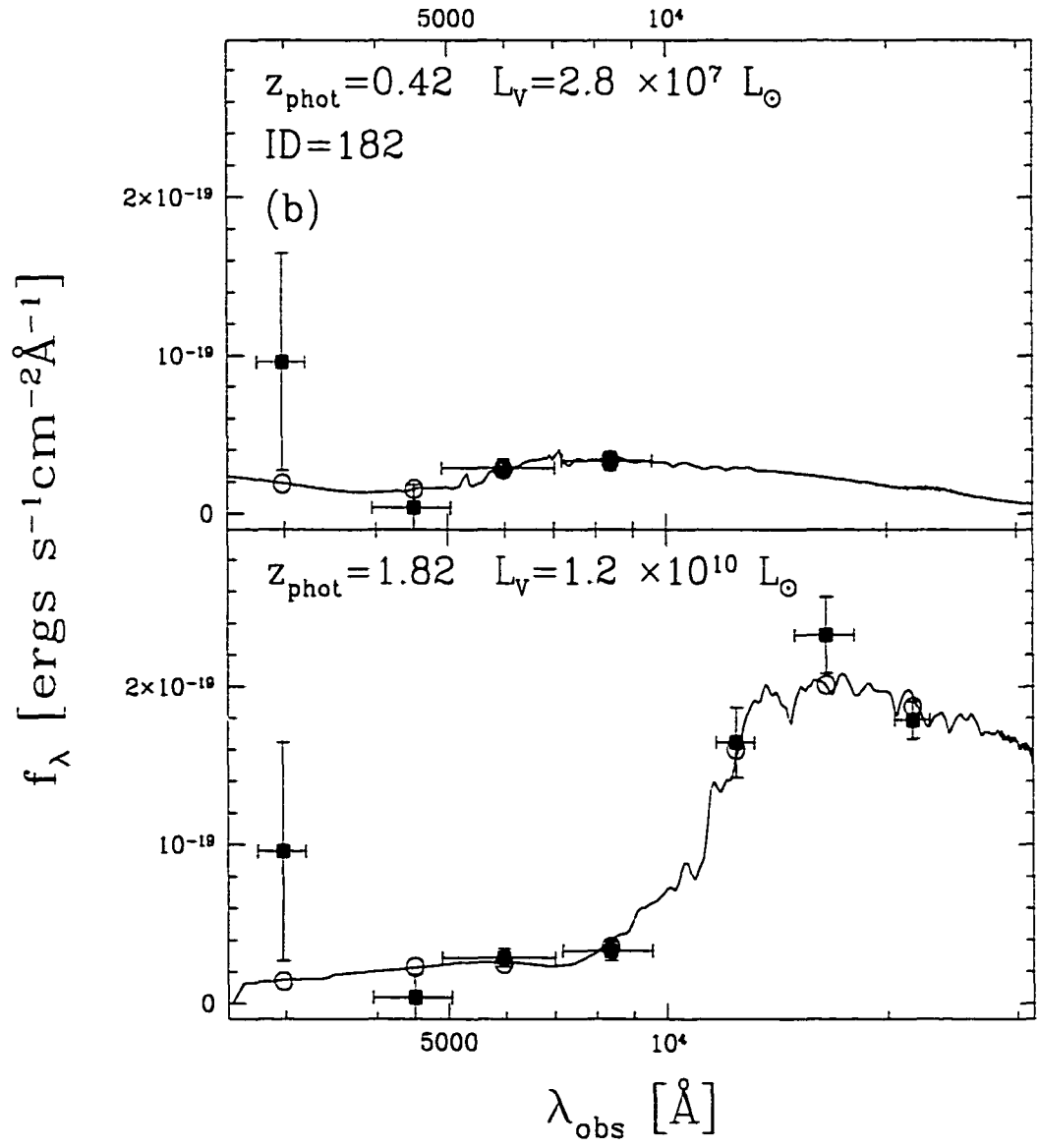


FIGURE 2.7. Two examples of how the inclusion of near infrared data helps to measure the correct  $z_{\text{phot}}$ . Obviously, the inferred  $L^{\text{rest}}$  is strongly coupled to  $z_{\text{phot}}$ . The top panels for each object contain the fit using only data from the four optical HST filters. The bottom panels contain the fit using all seven bands. The solid points are the data and the empty points are the model fluxes.



The three highest redshift objects in our sample (objects 542, 424, and 45) have  $z_{phot} = 3.86, 4.82, \text{ and } 5.34$  and  $K_{s,AB}^{tot} = 22.75, 23.29, \text{ and } 23.16$  respectively. Object 542 has 68% redshift confidence limits of  $z_{phot} = 0.42\text{--}3.88$ . In general, while the observed SED of object 424 is fit well, there is flux blueward of the predicted 912Å break position. The high redshift is chosen by the technique because the red  $H\text{--}K_s$  color indicates the presence of a rest-frame optical break. No Monte-Carlo realizations end up in a secondary minimum, but when fit using only the optical data, a redshift of 1.1 is found. Object 45 has a poor fit in the NIR, and has a redshift of 1.34 when fit with only the optical data. We do not consider these objects in any of our analyses.

## 2.4.2 The Redshift Distribution

In Figure 2.8 we show the histogram of the photometric redshifts listed in Table A.4. The three sets of lines represent galaxies with different photometric redshift precision. This figure also reveals structure in the redshift histogram with a sharp peak at  $z_{phot} \approx 0.5$  and a broad enhancement at  $1 \leq z_{phot} \leq 1.4$ . The redshift peak at  $z \approx 0.5$  was first noticed by G01 from AAT spectroscopic redshifts taken over a larger field centered on the HDF-S. To examine the luminosity distribution of galaxies in these enhancements, we plot  $z_{phot}$  vs.  $K_{s,AB}^{tot}$  in Figure 2.9, revealing that they are prominent in very bright galaxies,  $K_{s,AB}^{tot} < 21.5$ . These strong features in our redshift distribution are also seen in a  $K_{s,AB}^{tot} \leq 23.5$  subsample of the HDF-S data from Fontana et al. (2000). HDF-N contains several peaks, but they are not as strong as the features in the HDF-S (Cohen et al., 1996).

We can use the overall redshift distribution of galaxies in our sample to test the predictions of theoretical models of galaxy formation. In Figure 2.10 we directly compare our cumulative redshift distribution for galaxies with  $K_{s,vega} < 21$  to the theoretical predictions for  $\Lambda$ CDM ( $\Omega_m = 1.0, \Lambda = 0.0, h = 0.5$ ),  $\Lambda$ CMD ( $\Omega_m = 0.3, \Lambda = 0.7, h = 0.6$ ) and Pure Luminosity Evolution (PLE) models calculated

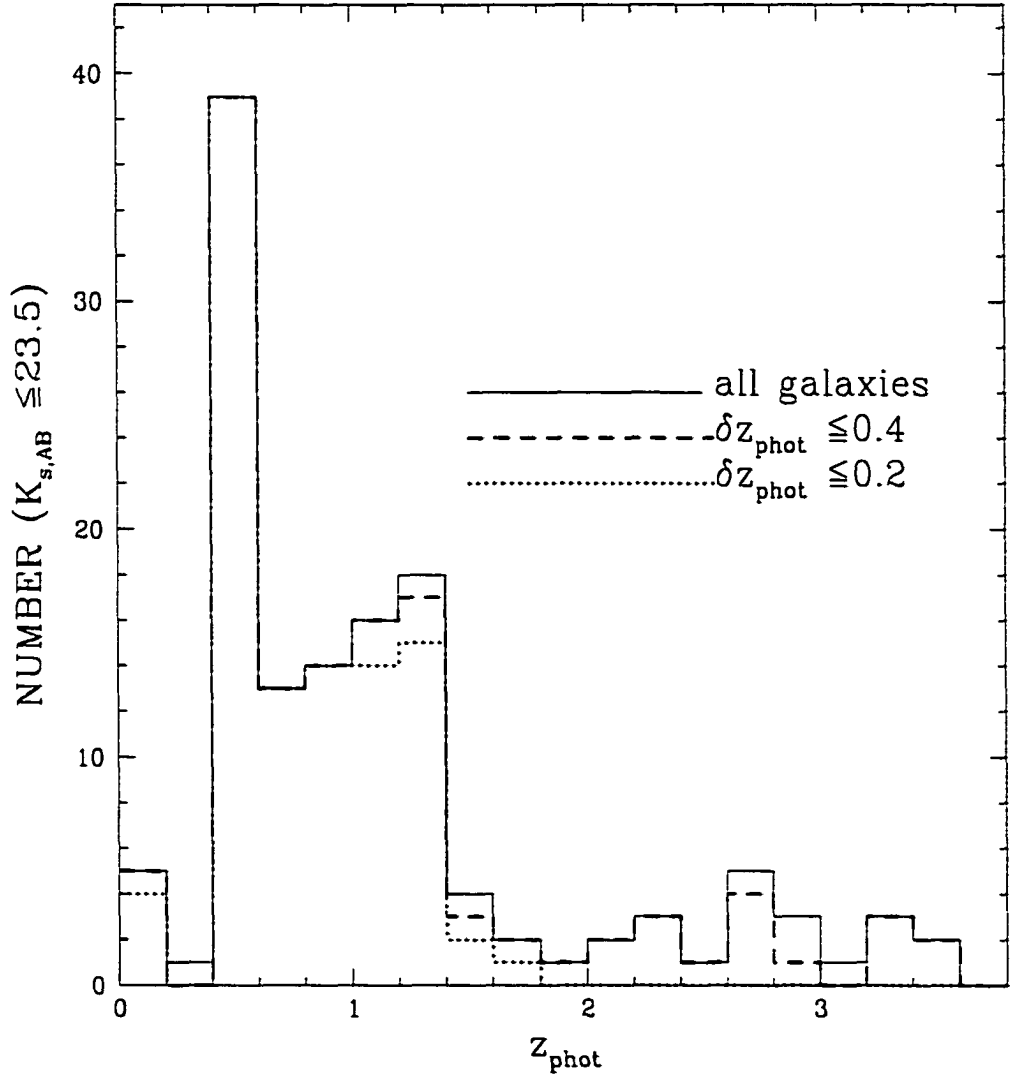


FIGURE 2.8. The redshift histogram of all 132 objects in our catalog with reliable redshifts (solid line). The two other histograms show the redshift distributions for all objects with  $\delta z_{\text{phot}} \leq 0.4$  (dashed line) and all objects with  $\delta z_{\text{phot}} \leq 0.2$  (dotted line) where the photometric redshift errors are the combination of those calculated using our Monte Carlo technique with the systematic errors determined from the HDF-N.



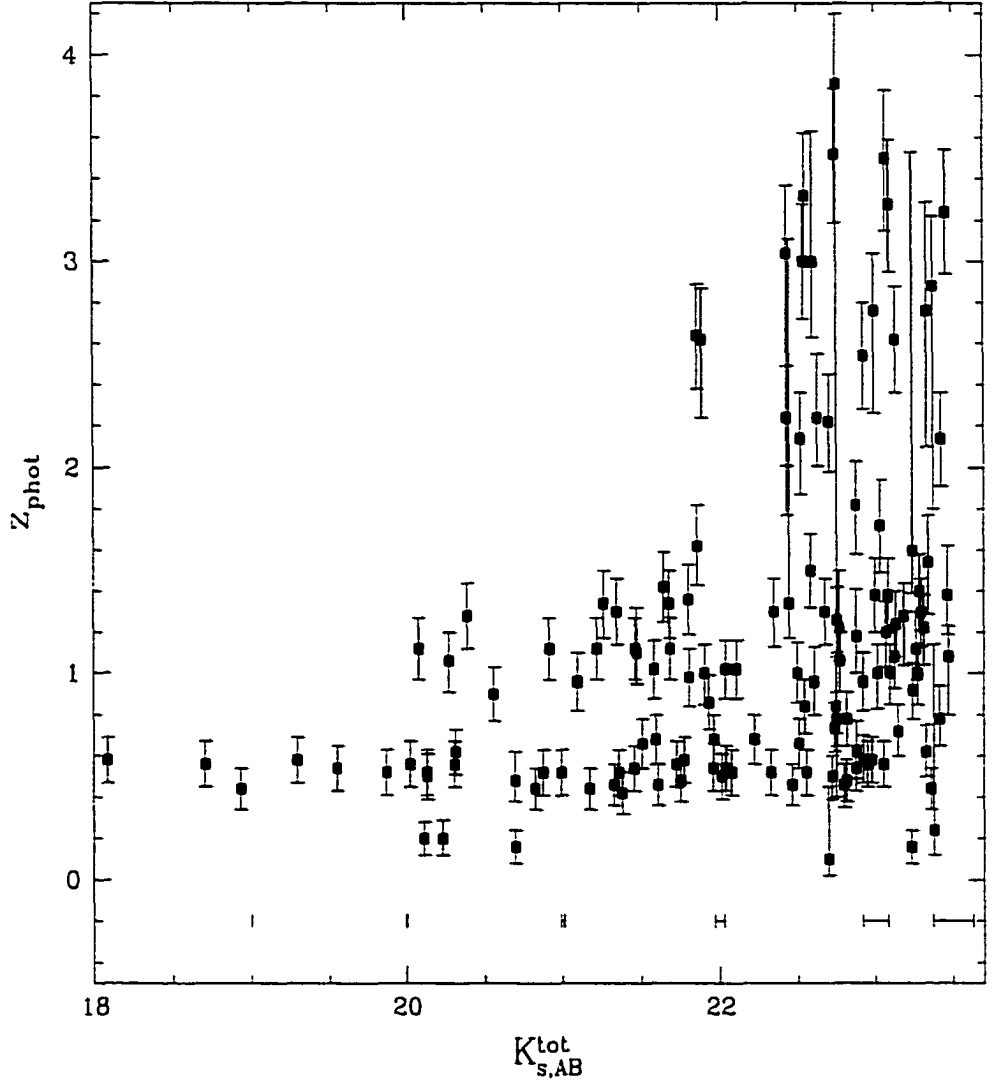


FIGURE 2.9. The  $K_{s,AB}^{\text{tot}}$  magnitude of our objects vs.  $z_{\text{phot}}$ . The photometric redshift errors are a combination of those calculated using our Monte Carlo technique and the systematic errors calculated from agreement with spectroscopic redshifts in the HDF-N. At the bottom of the graph, we show the typical photometry errors of objects of different magnitude.

by Fontana et al. (1999; hereafter F99) following slightly modified versions of the “Durham” prescriptions (e.g., Cole et al. 1994). At almost all redshifts, SCDM underpredicts the fraction of galaxies which lie at high redshifts, while the  $\Lambda$ CDM model provides a much better description of the data. Both CDM models reproduce the median redshift of the data ( $z \sim 0.8$ ) reasonably well. The difference between the CDM models can be understood because galaxy formation occurs at higher redshift in a  $\Lambda$  dominated universe. It is also interesting to note that the PLE models severely overpredict the abundance of bright galaxies at all redshifts. Our data has a low ( $\lesssim 1\%$ ) K-S probability of being drawn from any of the models. This is likely due to the clustering of galaxies in our small volume as the CDM models reproduce the general trends well. We note however that the models do not take into account any of the observational biases and incompleteness that may occur for IR selected galaxies. NIR selection is generally thought to be less prone to extinction effects and less dependent on the current SFR than optical selection. However surface brightness dimming and the bright IR sky can limit detection efficiency for extended objects. In addition, the F99 models represent only one point in the parameter space of the models which match local galaxy populations. Different parameter combinations may change the predictions.

We now compare our results directly with those of F99 and the SUNY group. F99 claims that in a  $K_{s,vega} < 21$  sample, only 2% of the galaxies lie at  $z_{phot} \geq 2$  in the HDF-S and 6% in the NTT Deep Field. In contrast, we find in our data that 12% of the galaxies with  $K_{s,vega} < 21$  lie at  $z_{phot} \geq 2$ . Using a  $K_{s,vega} < 21$  subsample of the SUNY Stonybrook HDF-S photometric redshift catalog we find that the fraction of galaxies lying at  $z_{phot} \geq 2$  is identical to ours. The differences between us and F99 are not due to small sample selection issues. There are 5 galaxies with  $K_{s,vega} < 21$  which F99 place at  $1.5 < z < 2$  but which we find at  $2 < z < 3$ . The exact differences between the high-redshift fractions measured by different photometric redshift techniques can depend rather sensitively on the redshift threshold used to discriminate

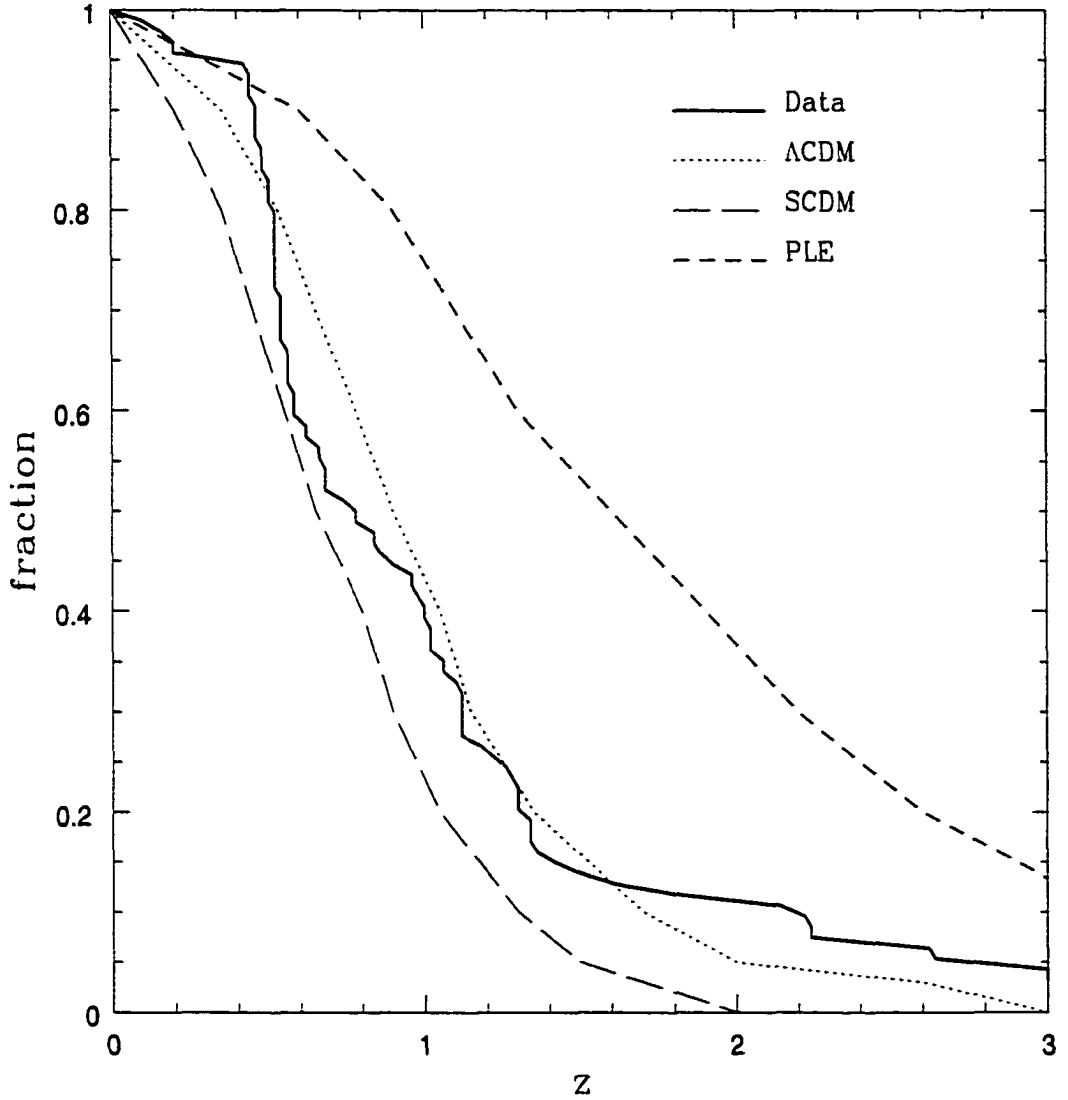


FIGURE 2.10. The cumulative redshift histogram for the 95 galaxies in our sample with  $K_{s,vega} < 21$  as indicated by the solid curve. The other curves are semi-analytical model predictions from Fontana et al. (1999) for an SCDM ( $\Omega_m = 1.0$ ,  $\Lambda = 0.0$ ,  $h = 0.5$ ; long dashed curve),  $\Lambda$ CDM ( $\Omega_m = 0.3$ ,  $\Lambda = 0.7$ ,  $h = 0.6$ ; dotted curve), and PLE model. The data are generally consistent with hierarchical models of formation while the PLE model significantly overpredicts the number of bright galaxies at high redshift.

between “high” and “low” redshift galaxies. For example, although there is disagreement on the fraction of galaxies at  $z_{phot} \geq 2$  both F99 and we are in agreement about the fraction of the  $K_{s,vega} < 21$  galaxies ( $\sim 14 - 15\%$ ) in the HDF-S which lie at  $z_{phot} \geq 1.5$ . It is also worth mentioning that all groups have small samples. F99 have 2 out of 92 galaxies with  $K_{s,vega} < 21$  and  $z_{phot} \geq 2$  while we have 11 out of 94. We used a bootstrapping technique drawn from a  $K_{s,AB}^{tot} < 23.5$  subsample of both ours and the F99 data to estimate the uncertainty in the measured fraction which was due to counting errors. The fractions differed by  $\sim 2 - 3\sigma$ . F99 is also using K-band data which is 2.1 magnitudes shallower than ours and which has known sky subtraction problems. These discrepancies will be eventually resolved with extensive spectroscopy in the NIR and the blue optical.

### 2.4.3 Rest-Frame Luminosities

Our long wavelength baseline allows us to observe a given rest-frame wavelength over a large range in redshift. From the best-fit SED at the best-fit redshift we measured the rest-frame luminosity in the U, B, and V bands for our galaxies and plot this as a function of enclosed volume and redshift in Figure 2.11. As reference to solar values, we take  $2.73 \times 10^{29}$ ,  $5.10 \times 10^{29}$ , and  $4.94 \times 10^{29}$  ergs  $s^{-1} \text{\AA}^{-1}$  for  $L_{\odot}^U$ ,  $L_{\odot}^B$ , and  $L_{\odot}^V$  respectively (assuming  $M_U = +5.66$ ,  $M_B = +5.47$ , and  $M_V = +4.82$  in Johnson magnitudes; Cox 2000). Using the distribution of  $L^{rest}$  values measured over  $\delta z_{phot}$ , we calculate an errorbar in  $L^{rest}$  for each galaxy. While we differentiate points in Figure 2.11 based on their values of  $\delta z_{phot}$ , the errors in  $L^{rest}$  are tightly coupled with the values of  $\delta z_{phot}$  and so are not presented on this plot. This coupling is demonstrated by the two cases in Figure 2.7 where the main uncertainty in  $L^{rest}$  stems from the uncertainty in  $z_{phot}$ , not from the specific values of the NIR data. All values of  $L^{rest}$  and their associated uncertainties are presented in Table A.4.

Because our fluxes are measured in uncorrected 2'' apertures, we may be missing

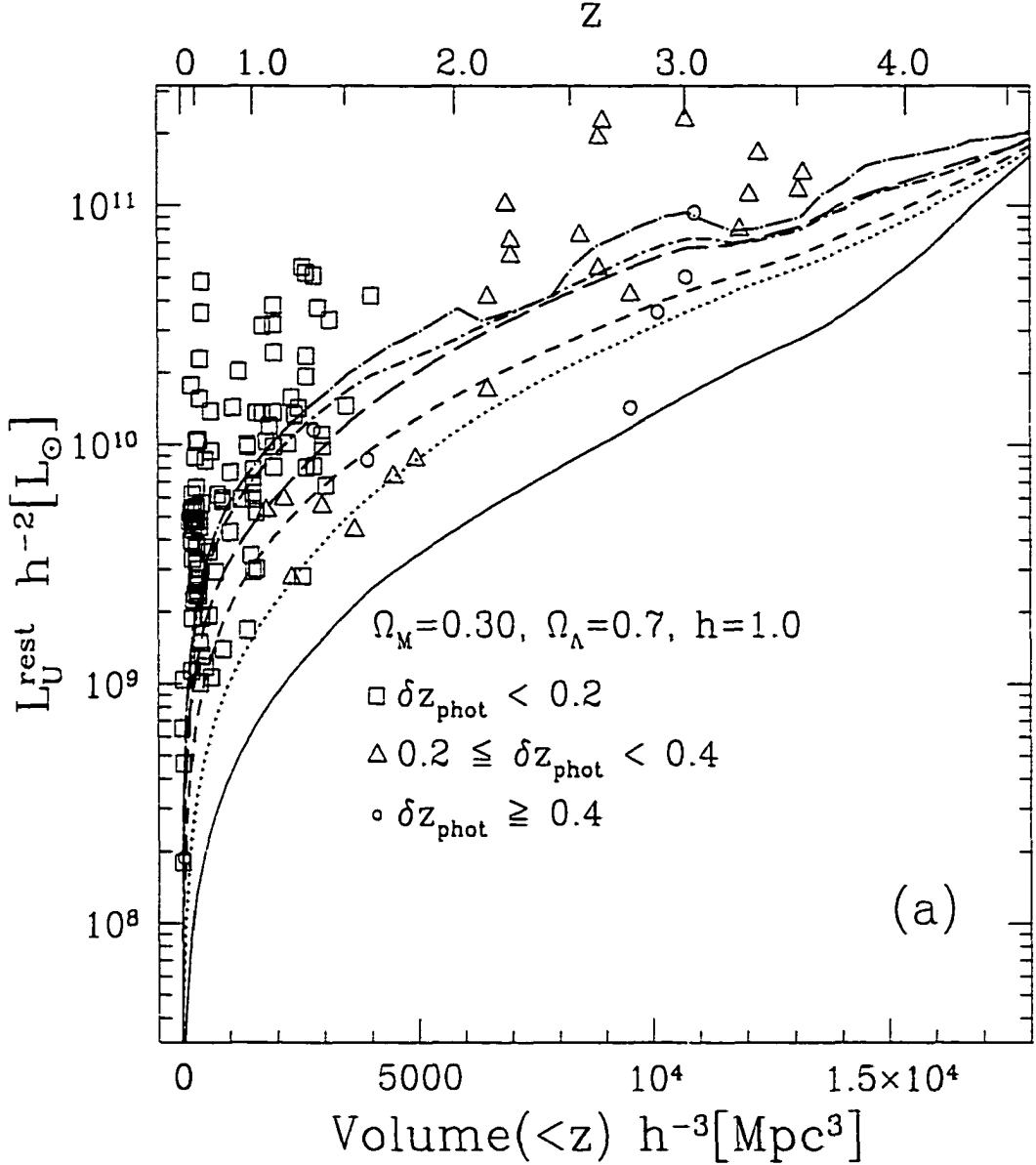
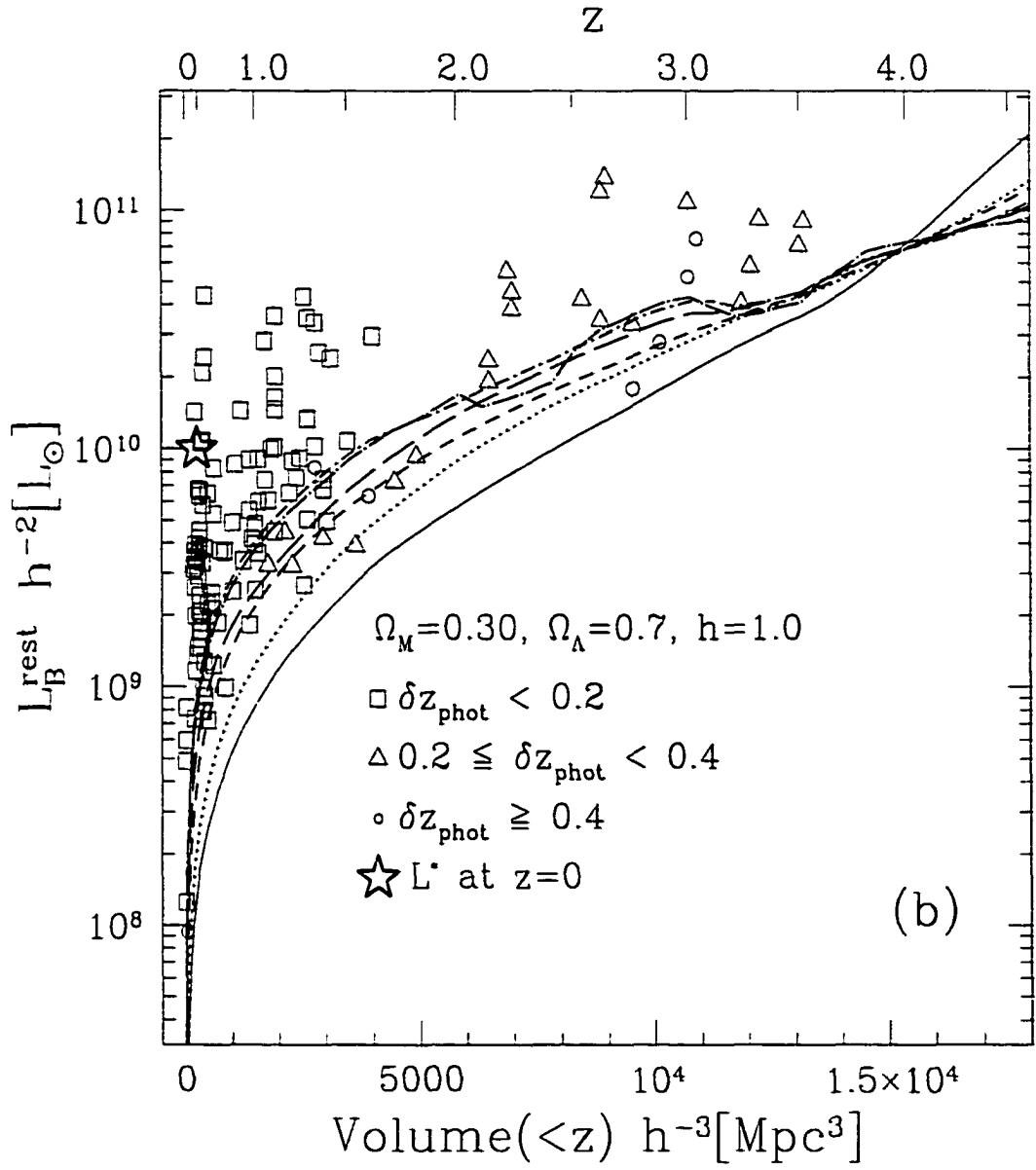
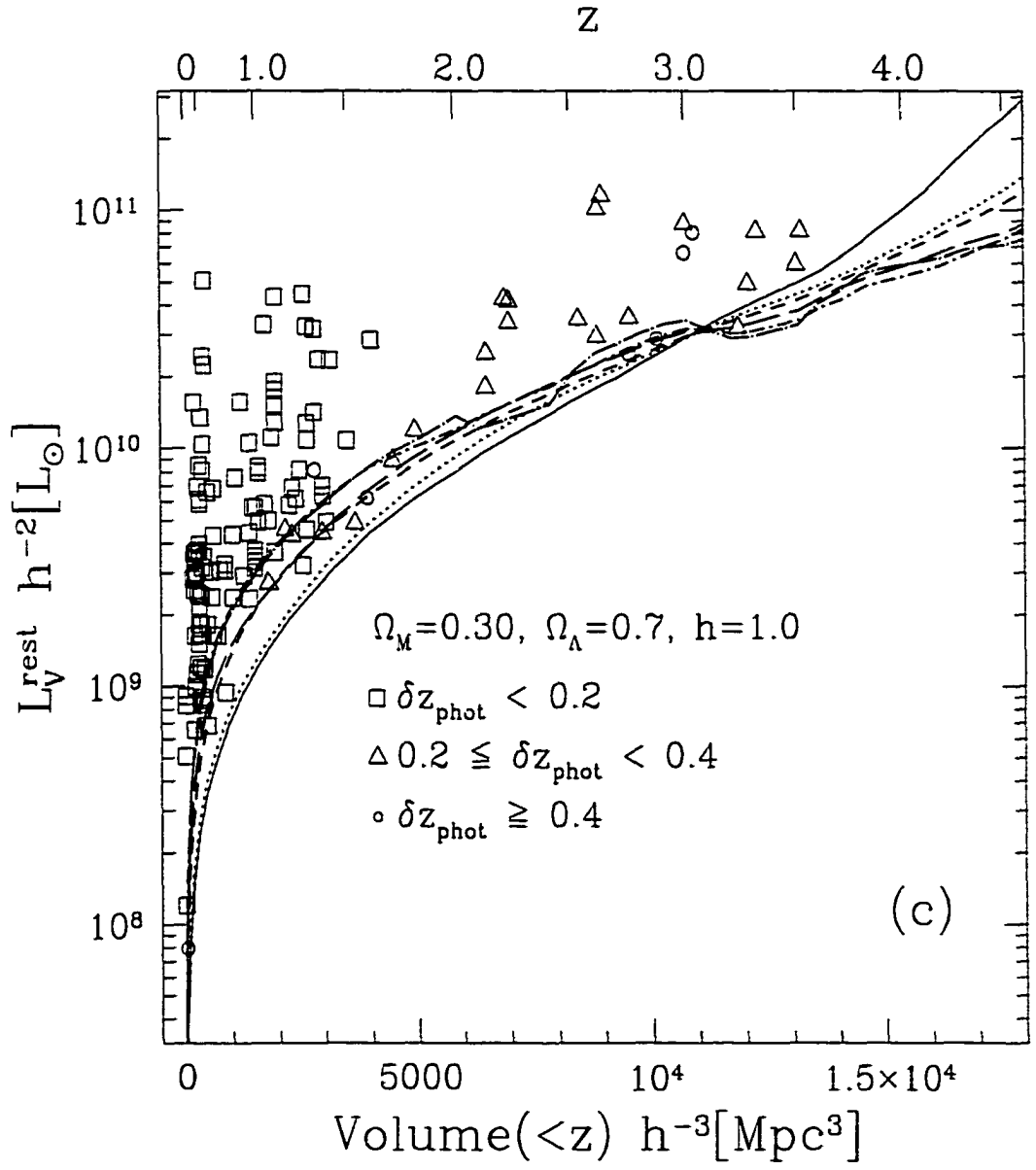


FIGURE 2.11. The distribution of rest-frame U, B, and V-band luminosities as a function of enclosed co-moving volume and  $z_{phot}$  is shown in figures a, b, and c respectively. We show all 132 galaxies with  $K_{s,AB} \leq 23.5$  and reliable redshift estimates. Note the large number of galaxies at  $z_{phot} \geq 2$  with  $L^{rest} \geq 5 \times 10^{10} L_{\odot}$ . The tracks represent the values of  $L^{rest}$  for each of our six template spectra normalized at each redshift to  $K_{s,AB} = 23.5$ . The large star in b) indicates the value of  $L_{*,B}$  from local surveys. The specific tracks correspond to the E (solid), Sbc (dot), Scd (short dash), Irr (long dash), SB1 (dot-short dash), and SB2 (dot-long dash) templates.





flux for the larger galaxies. Therefore, we correct all values of  $L^{\text{rest}}$  by the ratio (in the  $K_s$ -band) of the SExtractor total flux to the 2''0 aperture flux. The median correction factor is 1.05 with 68% confidence limits of 0.97 and 1.25. The largest correction is by a factor of 1.72. To quantitatively assess the goodness of our SED fits we compared the luminosities derived from the best-fit SED to the luminosities derived from a linear interpolation between the observed filters shifted to the desired redshift, and found the RMS differences to be  $\lesssim 10\%$  in all bands.

Perhaps the most interesting feature of Figure 2.11 is the presence of intrinsically luminous galaxies ( $L^{\text{rest}} \geq 5 \times 10^{10} h^{-2} L_{\odot}$ ) in all passbands at high redshifts. The apparent lack of low luminosity galaxies at high redshift in Figure 2.11 merely reflects our  $K_s$  magnitude limit translated to a rest-frame luminosity limit. Also apparent in Figure 2.11, at  $z > 1$ , is the increasing range in  $L^{\text{rest}}$  toward shorter rest-frame wavelengths. This is due to our magnitude limit in  $K_s$ , combined with the variation in intrinsic galaxy colors. We demonstrate this by showing the  $L^{\text{rest}}$ - $z$  tracks of our 6 galaxy templates normalized to  $K_{s,AB} = 23.5$ .

We use the local B-band luminosity function to estimate the evolution in the bright high-redshift galaxies. We find 9 galaxies with  $L_B^{\text{rest}} \geq 5 \times 10^{10} h^{-2} L_{\odot,B}$  which lie in a volume of  $7.29 \times 10^3 h^{-3} \text{Mpc}^3$  between  $2 \leq z \leq 3.5$ . We should be at least 50% complete for all galaxy types over this redshift and luminosity range. The number of galaxies at the bright end of the luminosity function is especially sensitive to variations in  $L_*$  and we try to measure evolution in the luminosity function by holding  $\alpha$  and  $\phi^*$  constant and changing  $L_*$  to match the observed counts. We use the local luminosity functions derived from the Sloan Digital Sky Survey (SDSS; Blanton et al. 2001) and the 2d Field Galaxy Redshift Survey (2dFGRS; Folkes et al. 1999) to predict the number of galaxies expected in this volume. The 2dFGRS luminosity function is in  $b_j$  magnitudes and Blanton et al. (2001) provide a conversion of their SDSS luminosity function to this system. With  $B = b_j + 0.2$  for a typical galaxy color of  $(B - V) \approx 0.6$ , the SDSS luminosity function then gives  $L_{*,B} =$



$9.7 \times 10^9 h^{-2} L_{\odot,B}$ ,  $\phi^* = 2.69 \times 10^{-2} h^3 \text{Mpc}^{-3}$ , and  $\alpha = -1.22$  while the 2dFGRS gives  $L_{*,B} = 1.0 \times 10^{10} h^{-2} L_{\odot,B}$ ,  $\phi^* = 1.69 \times 10^{-2} h^3 \text{Mpc}^{-3}$ , and  $\alpha = -1.28$ . The predicted numbers of galaxies in this volume are  $\approx 0.1$  for both the SDSS and 2dFGRS luminosity functions. If  $L_{*,B}$  is increased by a factor of 2.7 or 3.2 for the SDSS and 2dFGRS luminosity functions, respectively, then 9 galaxies are predicted. Because of the small co-moving volumes enclosed in this redshift range, these numbers may not be indicative of the galaxy population as a whole. Furthermore, random errors in the photometric redshifts will tend to produce a bias in the derived luminosities, as the luminosity function declines very steeply towards higher luminosities, and the smoothing will increase the number of observed very luminous galaxies. We estimate this effect by convolving the Schechter function with a Gaussian of width 0.3 magnitudes characteristic of our errors. As a result, the required increase in  $L_*$  decreases to 2.4-2.9 with respect to locally determined values. It is clear that spectroscopic confirmation of the photometric redshifts of these bright galaxies is desirable.

Another striking feature is the lack of galaxies with  $L_V^{\text{rest}} \gtrsim 1.4 \times 10^{10} h^{-2} L_{\odot}$  and  $1.5 < z < 2$ . Given the observed redshift structure in our field, this may simply be due to clustering. It is interesting however to note that Dickinson (2001b) found a similar paucity of intrinsically luminous galaxies at  $1.4 < z < 2$  in the HDF-N. The photometric redshifts in this regime are particularly uncertain however, as spectroscopic redshifts are rarely available. The derived  $z_{\text{phot}}$  between  $1.5 < z < 2.5$  is very sensitive to the  $U$ -band photometry, as the Lyman break moves into the  $U$ -band. We tested how  $z_{\text{phot}}$  changes if the  $U$ -band data is omitted. The largest changes occur for galaxies with  $2 < z < 2.5$ , and their newly derived  $z_{\text{phot}}$  are systematically lower. This suggests that  $z_{\text{phot}}$  might be biased if the bluest band falls just above the rest-frame Lyman break.

## 2.5 Summary

We have presented the initial results from the **Faint Infra-Red Extragalactic Survey** (FIRES) obtained with ISAAC at the VLT. We assembled a  $K_s$ -band selected catalog of galaxies in the HDF-S from the deepest NIR data taken of this field. Our catalog consists of 136 galaxies with  $K_{s,AB} \leq 23.5$  and photometry in seven bands from  $0.3\mu\text{m}$  to  $2.2\mu\text{m}$ . Our unique combination of ultra-deep optical data from HST with our deep NIR data allows us to sample the rest-frame V-band in galaxies for  $z \leq 3$  and to select galaxies in a way less dependent on the current SFR than the rest-frame UV.

To interpret these data, we have developed a new photometric redshift algorithm which models the galaxy colors with a linear combination of empirical templates and in so doing, makes minimal *a priori* assumptions about the galaxies' SFH. Testing our method on galaxies with spectroscopic redshifts from the HDF-N and HDF-S, we find that our technique is precise and robust for all  $z_{spec} < 6$  having a mean  $\Delta z \approx 0.10$  for  $z \leq 1.5$  and  $\Delta z \approx 0.44$  for  $z > 1.5$  with catastrophic errors in  $\lesssim 3\%$  of the sample. The results from the HDF-S also confirm that our photometry is adequate for good  $z_{phot}$  estimates. We find that in almost all cases that our best-fit SED matches the observed fluxes well.

We developed a Monte-Carlo code to estimate the uncertainty in  $z_{phot}$  arising from the flux errors. In agreement with previous work by other groups, we found that the uncertainty in  $z_{phot}$  is dominated at the faint end by photometric uncertainty, and at the bright end by template mismatch. For bright galaxies, where spectroscopic redshifts are available, the uncertainty in  $z_{phot}$  is severely underestimated when it is derived solely from the flux uncertainties although large values of  $\delta z_{MC}$  can help identify catastrophic errors in  $z_{phot}$ . To provide realistic, individual estimates on the accuracy each galaxy's  $z_{phot}$  we added our Monte-Carlo errors in quadrature with the mean disagreement with  $z_{spec}$  as measured from the HDF-N and also flag galaxies with secondary minima in their  $\chi^2(z)$  profiles.

Although the redshift is primarily constrained by the high signal-to-noise HST optical data, the deep NIR data can break degeneracies between different template combinations at different redshifts, which have identical  $V - I$  colors. While the NIR data greatly improves the redshift estimation at  $z < 1.5$ , it can actually worsen the  $z_{phot}$  estimate at high redshifts by causing the mis-identification of a Lyman break as a rest-frame optical break. The effect of the NIR should become increasingly important when the signal-to-noise is dramatically improved, such as in the very deep exposures planned for FIRES. By fixing the position of rest-frame optical breaks at  $z > 1$ , our NIR data also allows us to probe the redshift distribution of all galaxy types at these epochs. We use our photometric redshift technique to estimate  $z_{phot}$  and its accompanying uncertainty for our entire  $K_s$ -band selected sample.

Applying these techniques, we have found a sharp peak in the redshift distribution at  $z \approx 0.5$  and an broad peak at  $1 \leq z_{phot} \leq 1.4$ . The  $z \approx 0.5$  spike was first noticed by G01 using spectroscopic redshifts obtained with the AAT.

To compare our redshift distribution with the predictions of hierarchical galaxy formation models, we measured the fraction of galaxies at  $z > 2$  in a  $K_{s,vega} < 21$  sample to be 12%. We find that this fraction is much greater than that predicted by KC98 and F99 for a CDM universe with  $\Omega_m = 1$  although it is in better agreement with a  $\Lambda$ CDM model. At all redshifts we find far fewer bright galaxies than predicted by PLE models. We also find however, that different groups working with similar datasets find different fractions of galaxies above a certain redshift threshold. This disagreement stems from differences in  $z_{phot}$  determinations between groups.

Taking advantage of our extended wavelength coverage, we measure the rest-frame luminosity  $L^{rest}$  in the U, B, and V bands for the galaxies in our sample, regardless of their redshift. Many high-redshift galaxies have  $L^{rest} \geq 5 \times 10^{10} h^{-2} L_\odot$  in all bands, however we find a paucity of galaxies with  $L_V^{rest} \geq 1.4 \times 10^{10} h^{-2} L_\odot$  between  $1.5 < z < 2$ . A similar deficit in the redshift distribution of intrinsically luminous galaxies was noted by Dickinson (2001b) using NICMOS data on the HDF-

N. However, the photometric redshifts in this regime are uncertain and spectroscopic confirmation of this deficit is required. At higher redshifts the densities increase and we find 9 galaxies with  $L_B^{rest} \geq 5 \times 10^{10} h^{-2} L_{\odot,B}$  which lie between  $2 \leq z \leq 3.5$ . These numbers can be accounted for if  $L_*$  in the B-band increases by a factor of 2.7-3.2 with respect to SDSS and 2dFGRS values. When accounting for uncertainties in the rest-frame luminosity, the required increase is 2.4-2.9. The redshifts and nature of these intrinsically bright galaxies at high- $z$  needs to be verified with spectroscopic follow-up.

Observational evidence seems to indicate that galactic disks were already in place and with present sizes by  $z \sim 1$  (Lilly, Le Fevre, Hammer, & Crampton, 1996) but the morphologies of most Lyman Break Galaxies at  $z > 2$  tentatively suggests that they are not similar to present day galactic disks (Giavalisco, Steidel, & Macchetto, 1996). If galactic disks were indeed not formed at  $z > 2$  then it is tempting to associate the increase in the number density of bright galaxies seen at  $z < 1.5$  compared to  $1.5 < z < 2$  with the onset of disk formation. Spectroscopic studies of larger volumes are necessary to rule out that cosmic variance, or uncertainties in the photometric redshifts dominate this effect.

## CHAPTER 3

## OPTICAL SPECTROSCOPY OF GALAXIES IN THE HDF-S

## 3.1 Motivation

Photometric redshifts provide an effective way to analyze deep imaging surveys, however, galaxies with known spectroscopic redshifts and photometric redshift estimates are needed to calibrate  $z_{phot}$  and its reliability. Ideally, calibrating spectra should be available across all redshifts and SED types. While  $\sim 150$  spectroscopic redshifts exist in the HDF-N, fewer than 20 are currently available in the area of the HDF-S with FIRES photometry. As part of a program to spectroscopically confirm astrophysically interesting objects in the HDF-S using FORS1 on the VLT, we also improved the general spectroscopic situation in the HDF-S increased the number of spectroscopically confirmed galaxies against which we can test our  $z_{phot}$  technique and calibrate our uncertainty estimates.

Spectroscopy of high redshift galaxies, however, is a difficult task; even on 8-10 meter class telescopes with state of the art spectrographs,  $I \sim 24$  is the practical limit of spectroscopic redshifts based on absorption lines. Emission line spectroscopy allows one to reach fainter magnitudes, but no strong spectral features are observable in the optical for  $1.3 \lesssim z \lesssim 2$  and successful narrow-band imaging emission line searches at high- $z$  have been rare (Hu, McMahon, & Cowie, 1999), mostly because Lyman- $\alpha$  emission is easily suppressed by small amounts of dust or neutral gas. An additional complication is that most deep surveys cover small areas (the area of the HDF-S WFPC2 field is  $\sim 6$  square arcminutes) and that most MOSs can only fit a limited number of apertures (fibers or slitlets) in such a small field. Thus, spectroscopic follow-up in very deep fields, where the photometric data is best, is time consuming. The situation, however, is improving; large format CCDs with improved

throughputs across the whole wavelength range allow large spectral coverage at moderate resolution and even provide the ability to observe rest-frame UV absorption lines for objects with  $z < 2$  where the Lyman break (LB) and Lyman- $\alpha$  are not visible from the ground.

Drawing on these advances, we have used a  $K_s$ -band selected catalog from the initial FIRES data on the WFPC2 field of the HDF-S (Chapter 2) to select candidates for spectroscopic follow-up with FORS1 on the VLT. Combined with spectroscopic redshifts of galaxies in the HDF-S obtained by other groups, our spectroscopic redshifts allow us to test the accuracy of the photometric redshifts and of the rest-frame luminosities discussed in Chapter 2. In §3.2 we present our selection strategy, a description of the observations, and data reduction technique. In §3.3 we discuss the determination of the redshifts and the spectral characteristics. We discuss the agreement with  $z_{spec}$  in §3.4, develop a new method for measuring the photometric redshift uncertainty, and comment on the accuracy of the  $L^{rest}$  measurements made in Chapter 2. In §3.5 we discuss a large, spectroscopically confirmed disk-like LBG. We summarize in §3.6.

## 3.2 Observations & Data Reduction

### 3.2.1 Object Selection

The number of objects which can be observed with one instrument configuration (slitlet configuration and spectral range) is limited in the HDF-S by the size of the field. On the basis of the photometric redshift analysis of Chapter 2, we choose objects based their usefulness in testing the  $z_{phot}$  estimates and on their astrophysical interest. Specifically, we selected galaxies in the WFPC2 field of the HDF-S that had:

- $I_{814} < 25$

- Photometric redshifts estimates (Chapter 2) of  $1.5 < z_{phot} < 4$  if  $B_{450} < 25$  or  $2.5 < z_{phot} < 4$  if  $V_{606} < 25.5$ .
- Luminosity weighted mean template types earlier than Scd/Im drawing from our six spectral templates from Chapter 2.
- Large predicted stellar masses. These were roughly estimated from the template weights in the best-fit template combination (Chapter 2) by normalizing the templates to  $1 M_{\odot}$  using a  $(V - I)$  vs.  $\mathcal{M}/L$  relation derived from Bruzual and Charlot models.

The application of these selection criteria, in addition to the limited on the number of slitlets which could fit in the WFPC2 field, allowed us to select a total of nine target objects.

### 3.2.2 Observations

The observations were performed with FORS1 using the 300V+10 grism with the GG375 order separation filter in MOS mode. We first obtained a short image for accurate slit mask design. Eight “science” slitlets with a  $1''.0$  width were placed on the nine target galaxies and two  $5''.0$  width slitlets above and below the science area were placed on compact sources to verify the telescope pointing. The slitlets range in length from 19-22 arcseconds. A short acquisition image was taken before almost every science exposure to verify our pointing. While the exact wavelength range of each slitlet depends on its position, our spectra typically extend from  $3700\text{\AA}$  to  $8500\text{\AA}$ . The spectral sampling is  $2.64\text{\AA}$  per pixel corresponding to a resolution for extended sources of  $R \sim 500$ .

Our objects were observed in service mode during dark time on UT dates 27, 29, 30 June 2000, and 8 July 2000. The seeing on the four nights, as measured from the acquisition image, was  $0''.9$ ,  $1''.2$ ,  $1''.0$ , and  $0''.8$  on the 27, 29, 30 June 2000, and 8 July

2000 respectively. The transparency also varied over the nights with July 8 having the best conditions and the June 29 having the worst. The total exposure time was seven hours split into 30 minute segments. The telescope pointing was randomly dithered along the slit between exposures with maximum shifts of  $\pm 3''.5$  from the reference pointing.

### 3.2.3 Data Reduction

We reduced the raw spectra with IRAF<sup>1</sup>. For each night the 2D spectra were first bias and overscan subtracted, split up into 12 individual 2D spectra (one for each slitlet; 8 science and 4 acquisition/pointing), and then flatfielded. Parasitic light in the flatfields was removed by pairwise combination of flatfields with each pair containing exposures obtained using both lamps. Residual structure along the slit was removed with the *fit1d* task in IRAF. The individual exposures were cleaned of cosmic rays using the method described in Rudnick, Rix, & Kennicutt (2000). The individual slitlet spectra were then wavelength calibrated and rectified from the lamp spectra, and then background subtracted. From the strong night sky lines, we verified our wavelength calibration to be within  $\lesssim 0.5\text{\AA}$ . We registered and combined the exposures for each slitlet using the *imcombine* task with integer shifts in the spatial direction measured from spectra of the brightest objects. We removed residual cosmicrays in a two-step process. For each slitlet we first made two combined images - one with and one without a minmax rejection applied. We took the difference between these two images and set all low pixels to zero in the resultant difference to create an image consisting just of residual cosmic rays. We then subtracted this cosmic ray image from the uncleaned combined image to obtain the final combined 2D spectra. To deal with the varying data quality, we weighted each exposure by the 2nd power of the maximum signal-to-noise ( $S/N$ ) as determined from a bright guide

---

<sup>1</sup>IRAF is distributed by the National Optical Astronomical Observatories, which are operated by AURA, Inc. under contract to the NSF.



star in one of the wide slitlets. We then repeated a background subtraction to remove any residual sky. Finally, the 1D spectra were extracted using the *apextract* package in IRAF, weighting by the inverse of the expected variance derived from a smooth fit to data.

### 3.3 Spectroscopic Redshifts

A total of 17 objects were visible on our eight science slitlets, of which nine were on our original target list. In the end, we measured  $z_{spec}$  successfully for seven of these 17 objects, three of which (HDFS1-36, HDFS1-104, and HDFS1-386) were in our targeted list and four of which serendipitously fell in our slits. In Figure 3.1 we show the spectra of these seven objects. Only one of these seven galaxies<sup>2</sup> had a strong emission line which we identified with Lyman- $\alpha$  at  $z = 2.804$ . In all other cases, the redshift was measured by visual inspection of the absorption lines and comparison with high  $S/N$ , rest-frame UV and optical spectra of both low redshift and high redshift galaxies (e.g., Pettini et al. 2000; Walborn et al. 2000; González Delgado et al. 1999; Kulkarni et al. 1999; Ponder et al. 1998, Steidel et al. 1996; Bonatto, Bica, & Alloin 1995). No single UV galaxy template spanned the whole rest-wavelength range covered by our high-redshift spectra and we had to use a combination of the templates to access our complete wavelength range. Strong absorption lines were identified by visual inspection in the 2D spectra to discriminate against sky subtraction artifacts; their positions were measured in the extracted spectra with *splot*. Once a possible redshift was determined based on the positions of the easily identified lines, the 2D images and 1D extracted spectra were searched for the presence of further expected lines at  $z_{spec}$ . Except for HDFS2-865, all of the objects had more than 6 identifiable absorption lines at the spectroscopic redshift. Our redshift accuracy  $\delta z_{spec}$  is typically 0.001 – 0.003, or a few pixels, measured from the rms of the identified lines about the predicted

---

<sup>2</sup>This object was too faint to be included in the Chapter 2 catalog, but has the ID HDFS2-865 in the Chapter 4 catalog.

position given  $z_{spec}$ . The spectroscopic and photometric redshifts, coordinates, and  $I_{814}$  magnitudes of these seven objects are given in Table A.5. Objects which failed to yield  $z_{spec}$  determinations were either too faint to detect any convincing features or had too few features to determine a unique redshift.

There are spectral features in some objects which we could not identify. In object HDFS1-334, there is a strong absorption feature at  $4498\text{\AA}$  which would lie at  $1969\text{\AA}$  rest-wavelength for  $z_{spec} = 1.283$ . A similar unidentified feature appears in the Bonatto, Bica, & Alloin (1995) composite UV spectra of young stellar clusters. In addition, there is a weak absorption feature in HDFS1-334 at  $5135\text{\AA}$  (rest-wavelength  $2249\text{\AA}$ ) and a weak, probable emission line observed at  $7434\text{\AA}$  (rest-wavelength  $3255\text{\AA}$ ) which we cannot identify. The redshift of HDFS1-334 is clearly correct as the eight identified absorption lines yield a redshift solution with an rms of  $\delta z_{spec} = 0.001$ . In object HDFS1-360, there is an unidentified absorption feature at  $4789\text{\AA}$  ( $1960\text{\AA}$  rest-wavelength) which again has an unlabeled analog in the Bonatto, Bica, & Alloin (1995) spectra. In object HDFS-104, there is an unidentified feature at  $4318\text{\AA}$  ( $1690\text{\AA}$  rest-wavelength). As an alternative to being features at  $z_{spec}$ , these absorption features may be associated with intervening systems (Pettini et al., 2000).

Three additional serendipitous galaxies fell on the wide acquisition slitlets and were located at  $z_{spec} = 0.509$ ,  $z_{spec} = 0.520$ , and  $z_{spec} = 0.184$  based on the presence of emission lines. We also found that one of our acquisition objects was in fact a galaxy at  $z = 0.514$ . Our FIRES imaging does not cover these objects and we did not perform an independent astrometric calibration on the FORS1 image used to design our slit mask. Instead we used the world coordinates written in the header of our mask design image to determine the object coordinates. Comparison with the positions of ESO guide stars in the field showed that these positions are accurate to within  $<1''5$ . The coordinates and spectroscopic redshifts of these four serendipitous objects are given at the end of Table A.5.

Other spectroscopic redshifts in the HDF-S have been collected by Glazebrook

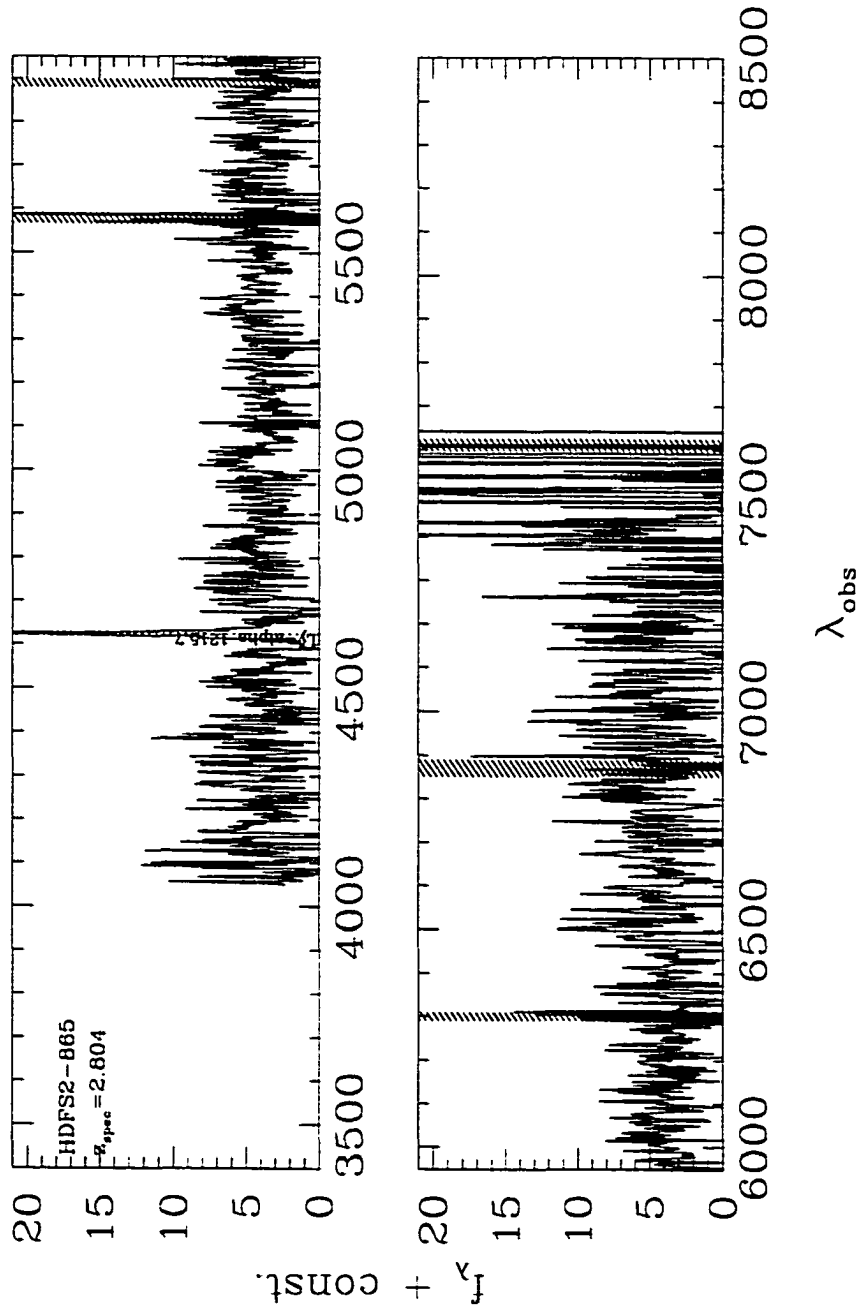
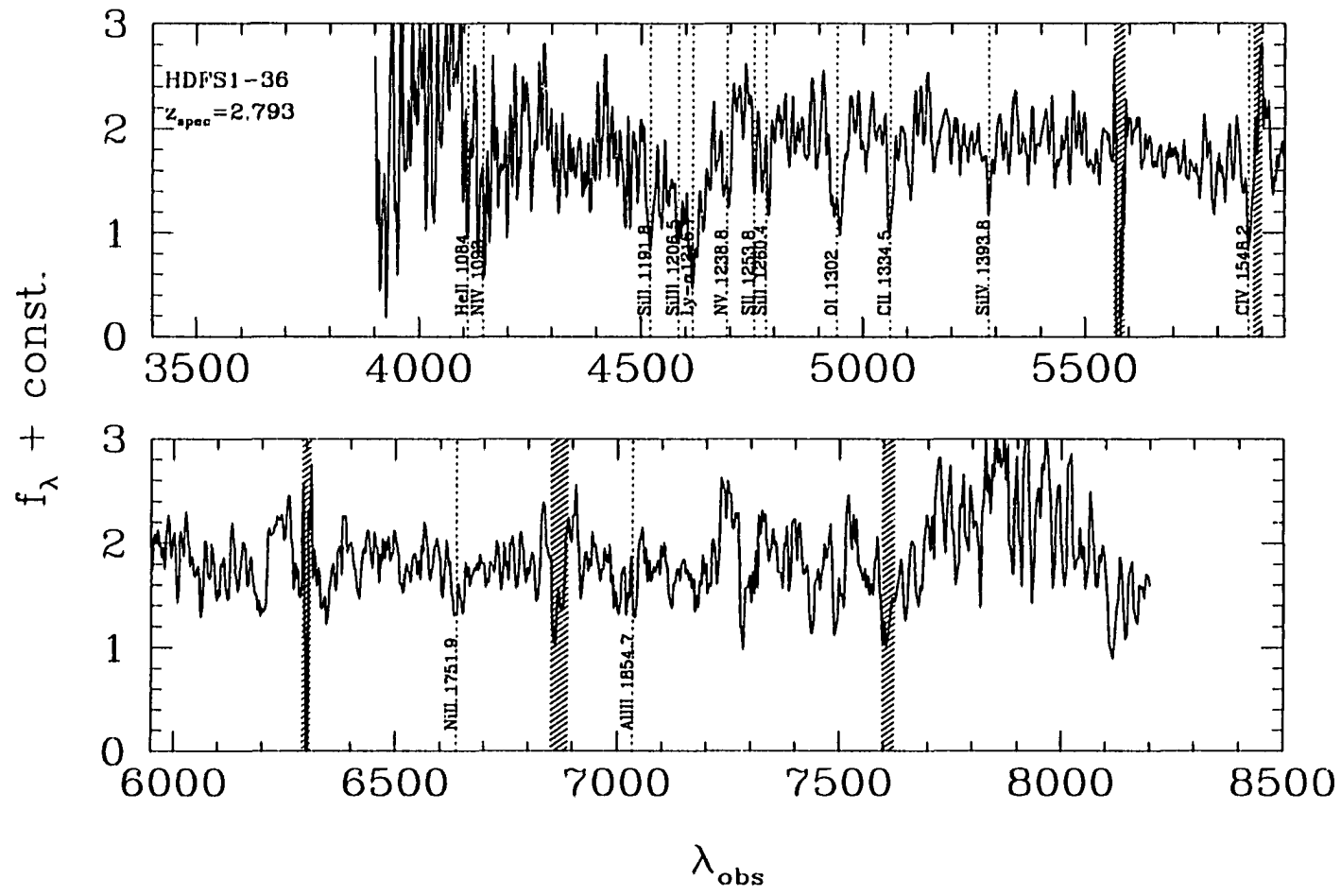
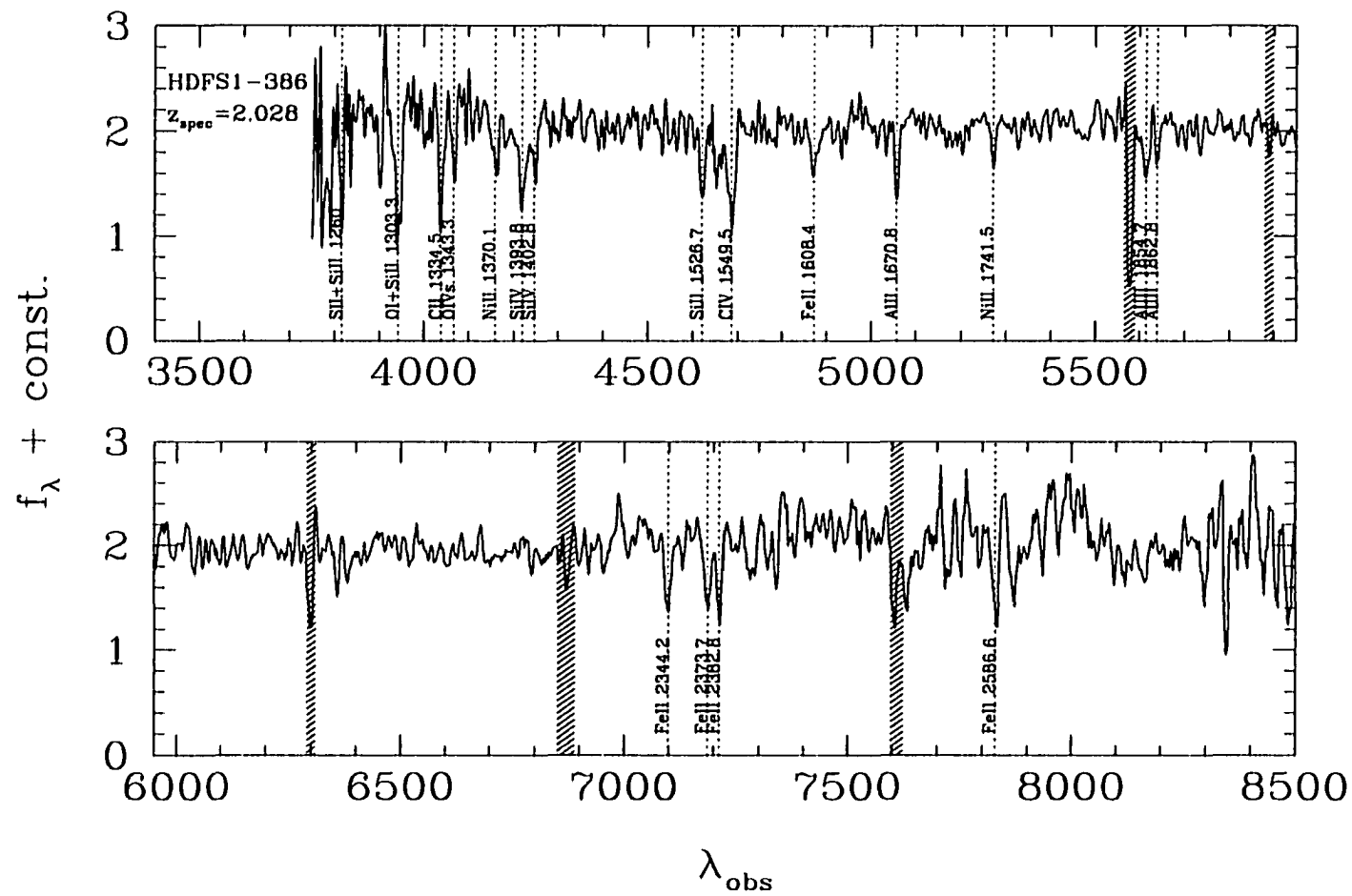
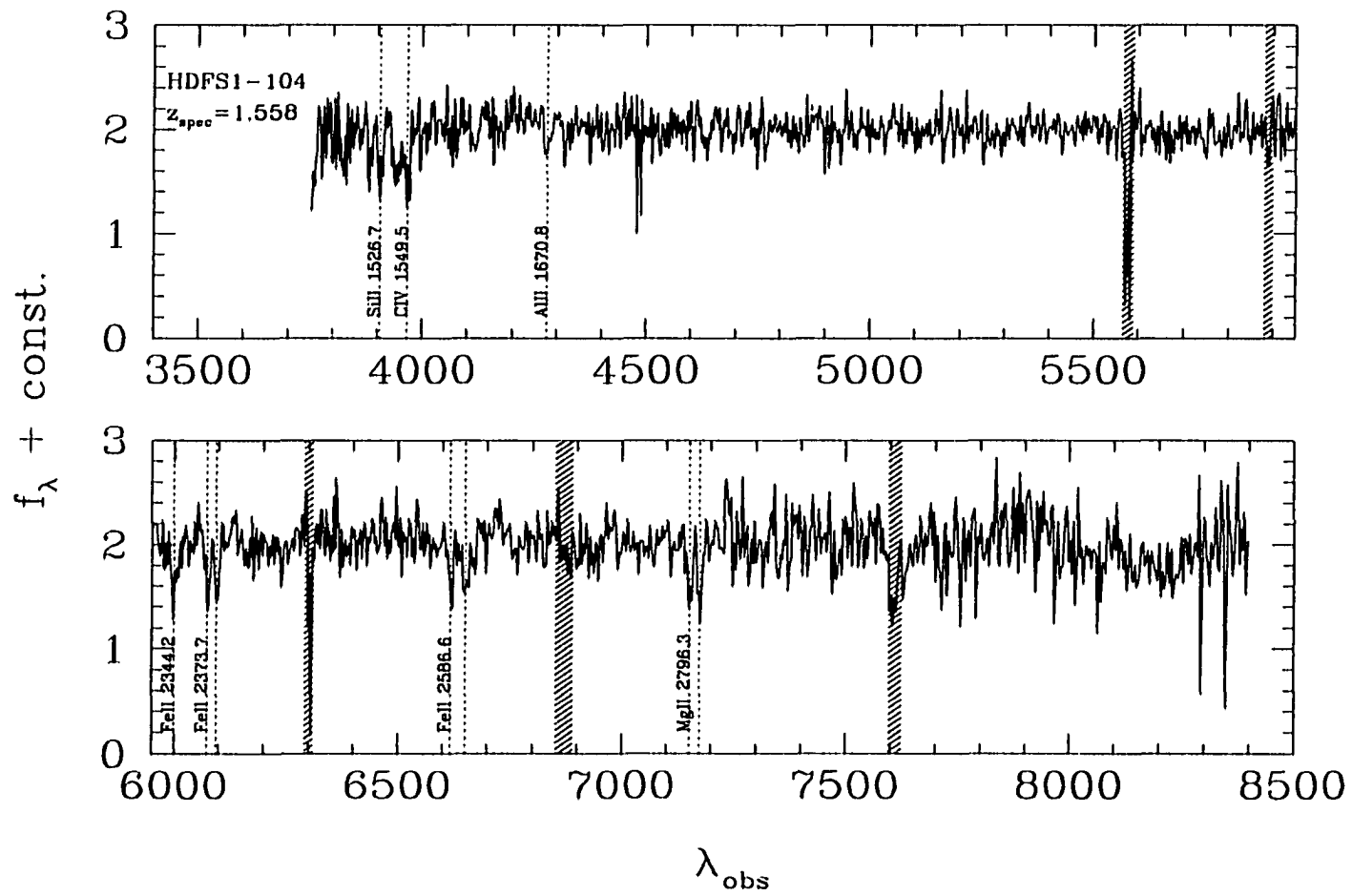
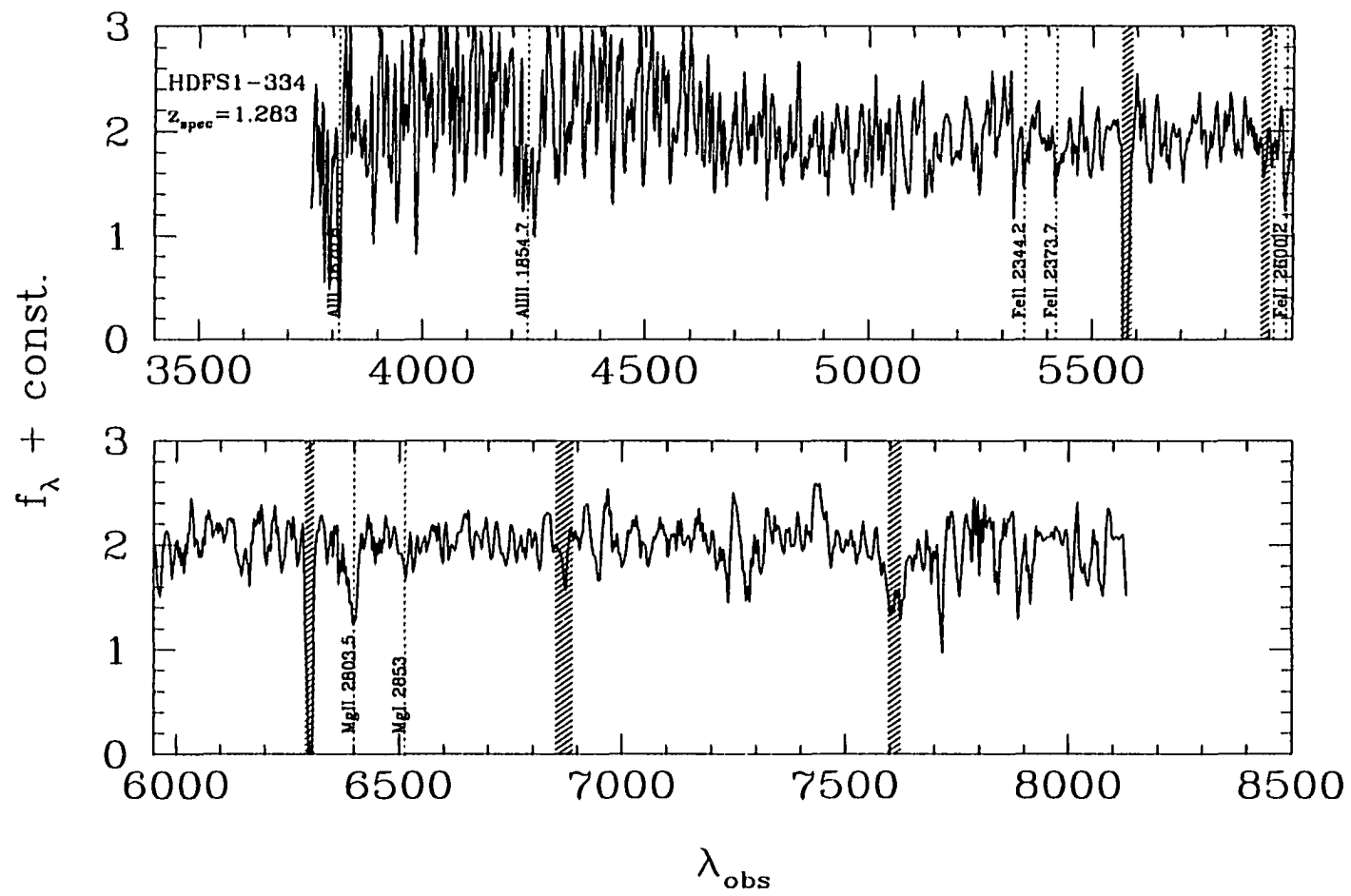


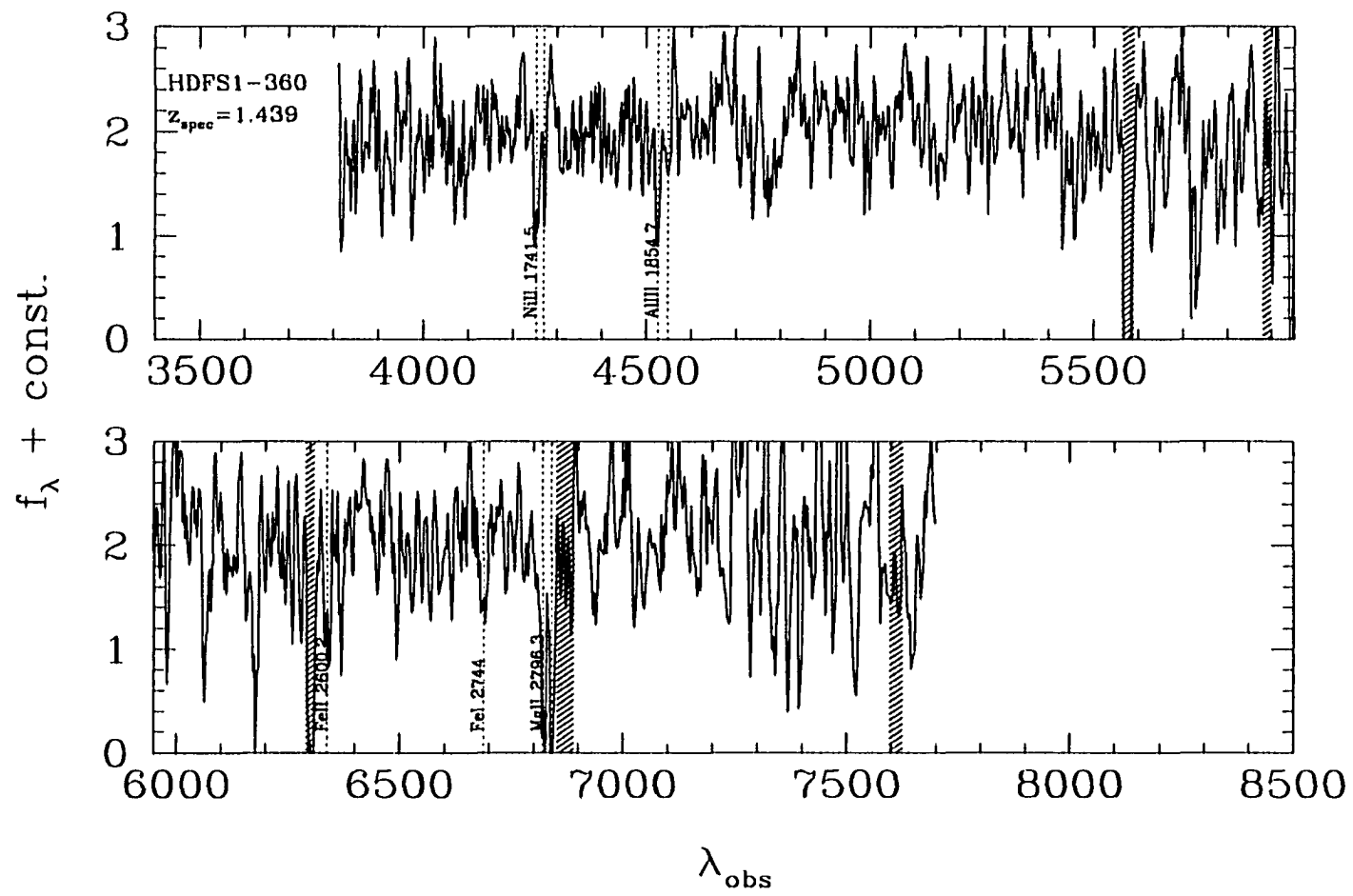
FIGURE 3.1. The optimally extracted spectra of the seven galaxies which fell on science slitlets and for which redshifts were obtainable, sorted by decreasing redshift. Improperly subtracted night sky lines have been interpolated out. All lines which were successfully identified in both the 1D and 2D spectra are shown. For clarity we have only shown the line ID of only one line in all doublets. Despite our efforts to properly subtract out the night sky, some residuals remained and for clarity, we marked the location of strong sky emission and absorption features. Some spectra have also been boxcar smoothed by  $\leq 3$  pixels. The  $S/N$  of the spectra decline rapidly to the blue and red and in some cases, for clarity, they were truncated at the edge of the wavelength range



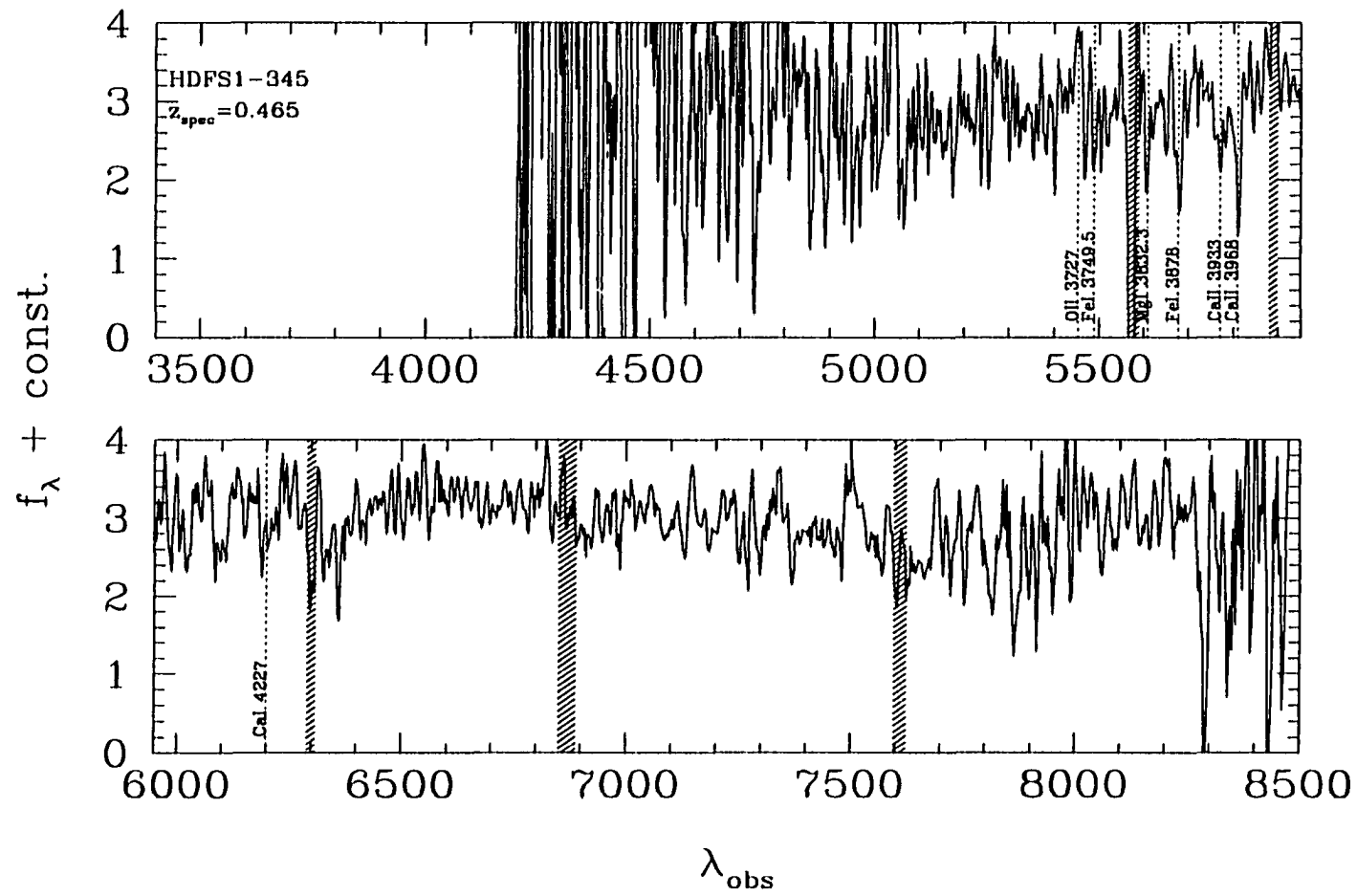












(2001; available at <http://www.aao.gov.au/hdfs/>), Cristiani et al. (2000), and Rigopoulou et al. (2000), bringing to 21 the total number of galaxies with  $z_{\text{spec}}$  and with FIRES photometry. We duplicate one spectroscopic measurement and our spectroscopic redshifts increase by  $\sim 40\%$  the number of spectroscopically confirmed galaxies in the WFPC2 field of the HDF-S. A direct comparison with the duplication reveals a discrepancy. Glazebrook (2001) find a redshift of 0.7525 for HDF-S1-104 (ID 821 from the AAT catalog) and measure  $R = 22.93$ . The AAT redshift disagrees with our redshift of 1.558. This is one of our highest  $S/N$  objects and the redshift was based on the identification of 11 absorption lines with an rms of  $\delta z_{\text{spec}} = 0.001$ . The Glazebrook (2001) identification is based on “HK, weak absorption” and has a quality of two i.e. a  $\sim 50\%$  chance that the redshift is correct. In light of our high quality spectrum and the many identified lines, we believe our redshift is correct.

### 3.4 Testing the Photometric Redshift Technique

Using the photometric redshift method described in Chapter 2, we derived  $z_{\text{phot}}$  from the  $K_{s,\text{AB}}^{\text{tot}} \leq 23.5$  catalog obtained from the initial FIRES data. We also derive  $z_{\text{phot}}$  for the  $K_{s,\text{AB}}^{\text{tot}} < 26$   $K_s$ -band selected catalog created in Chapter 4 (the  $z_{\text{phot}}$  catalog is presented in Chapter 5). This catalog is based on all available ISAAC imaging of the HDF-S with exposure times of 33.6, 32.3, and 35.6 hours in the  $J$ ,  $H$ , and  $K_s$  filters respectively. In brief review, our photometric redshift method attempts to model the observed flux points, at all redshifts, with a linear combination of six empirical local galaxy templates. The redshift with the lowest  $\chi^2$  value is then chosen as the most likely  $z_{\text{phot}}$ . Uncertainties in  $z_{\text{phot}}$  due to photometric errors,  $\delta z_{\text{MC}}$ , were calculated from the Monte-Carlo simulation (see Chapter 2). We use the E, Sbc, Scd, and Im templates from Coleman, Wu, & Weedman (1980) and the two least extinguished starburst templates, SB1 and SB2, from Kinney et al. (1996). These were extended into the ultraviolet using a power law extrapolation and into the NIR using models

from Bruzual & Charlot (2001).

### 3.4.1 Comparing Photometric and Spectroscopic Redshifts

In Figure 3.2a we plot the photometric redshifts derived from the initial FIRES data (Chapter 2) compared to all of the available spectroscopic redshifts in the HDF-S. This plot also includes objects which did not satisfy the good photometry requirements of Chapter 2 or Chapter 4 but which are included to show  $z_{phot}$  predictions for photometric measurements of different quality. In this comparison, we only consider objects that were not flagged as point sources in the WFPC2 F814W image (Chapter 2). In Figure 3.2a we find a qualitatively good agreement with the spectroscopic redshifts over all redshift ranges. To judge the accuracy of  $z_{phot}$ , we use  $\langle \Delta z / (1 + z) \rangle$  where

$$\Delta z = |z_{spec} - z_{phot}|. \quad (3.1)$$

$\langle \Delta z / (1 + z) \rangle$  was shown in Chapter 2 and Fernández-Soto, Lanzetta, & Yahil (1999) to be roughly constant with redshift. When considering all objects, regardless of their photometric quality,  $\langle \Delta z / (1 + z) \rangle = 0.24$  for  $z_{spec} \leq 3.2$ . All of the outliers in Figure 3.2a are those which do not satisfy our good photometry requirements and for which we did not expect to measure accurate photometric redshifts. When we only consider objects with good photometry our disagreement with  $z_{spec}$  becomes  $\langle \Delta z / (1 + z) \rangle = 0.07$ . This is identical to the value measured in the HDF-N from Chapter 2 using spectra obtained by Cohen et al. (2000) and optical/NIR imaging and photometry from Williams et al. (1996), Dickinson (2001a), and Fernández-Soto, Lanzetta, & Yahil (1999). This agreement between the  $z_{phot}$  accuracy using the HDF-N and the initial FIRES data is not surprising given the nearly identical survey depths and filters for these two data sets. One of the objects with a spectroscopic redshift (HDFS2-865) was too faint to be detected in the original FIRES data and is not shown in Figure 3.2a.

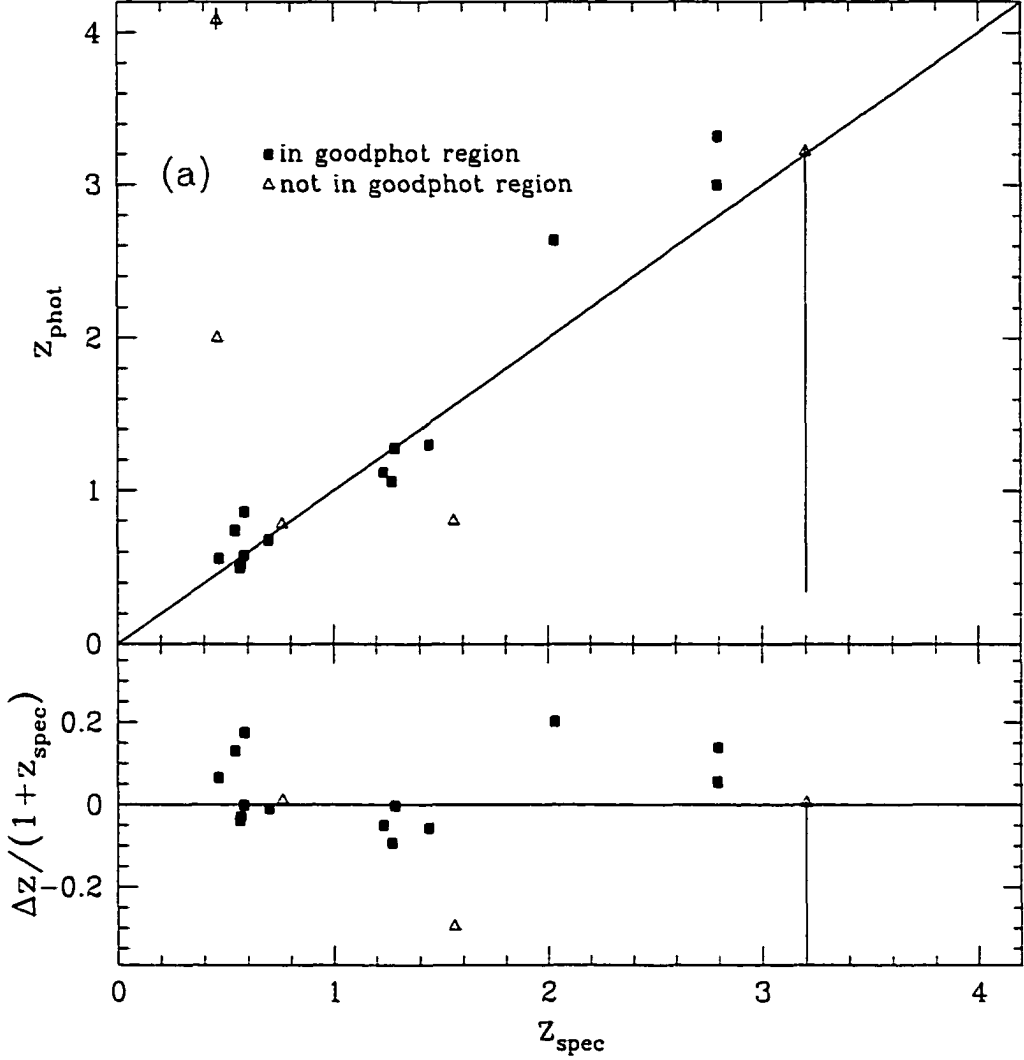
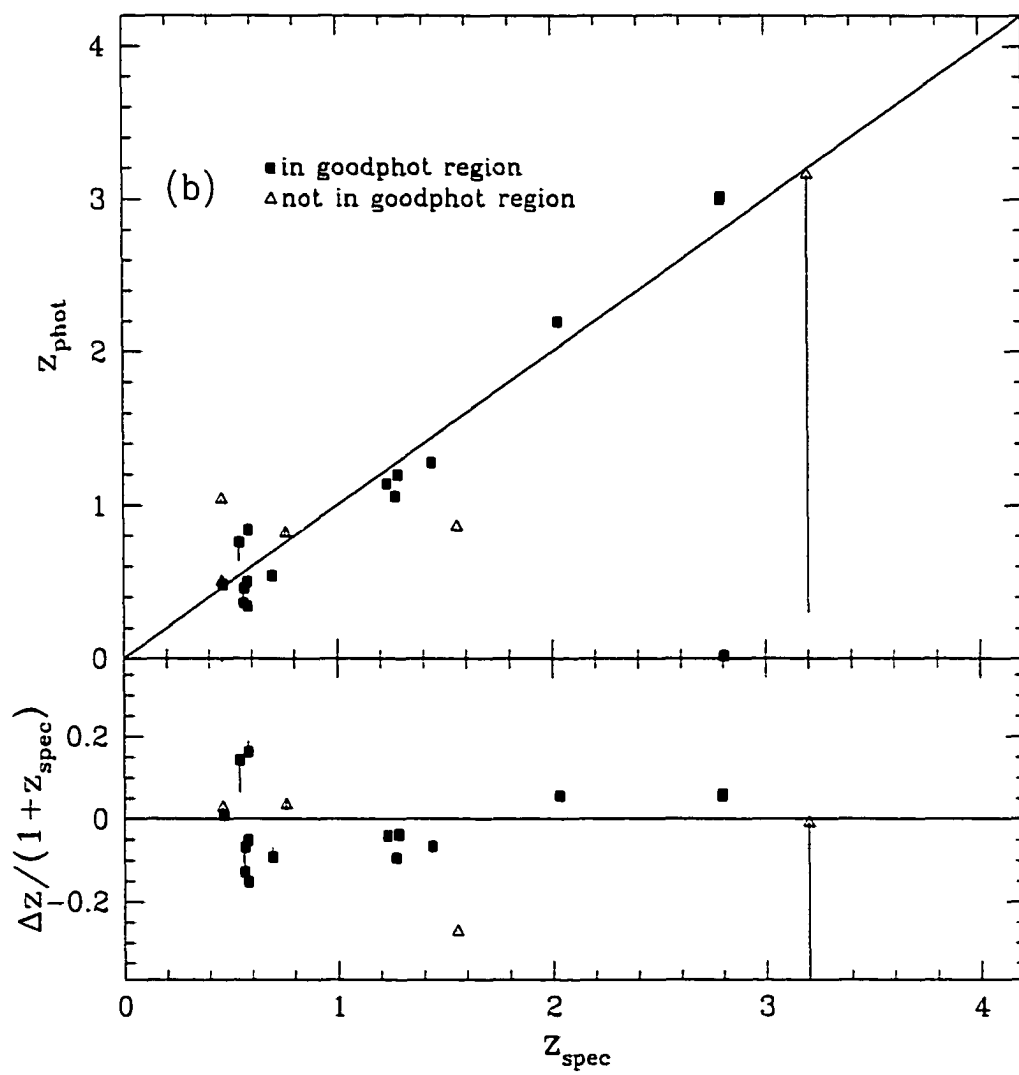


FIGURE 3.2. Plots of  $z_{\text{spec}}$  vs.  $z_{\text{phot}}$  for all measured spectroscopic redshifts in the HDF-S. The top panel shows a direct comparison between  $z_{\text{phot}}$  and  $z_{\text{spec}}$ . The diagonal line corresponds to a one-to-one relation to guide the eye. The bottom panel shows how  $z_{\text{spec}}$  relates to the difference between  $z_{\text{phot}}$  and  $z_{\text{spec}}$  normalized by  $1 + z_{\text{spec}}$ . Objects with solid and open symbols lie respectively inside and outside regions with good photometry as defined from the weight images. In a) we show  $z_{\text{phot}}$  as measured from the photometry of Chapter 2 while in b)  $z_{\text{phot}}$  was measured from the much deeper NIR photometry of Chapter 4. In a) and b) the redshift error bars are derived from the formal flux errors and are obviously underestimated. In c), we  $z_{\text{phot}}$  was derived from the complete FIRES data with an additional very blue template added to the empirical template set. The new photometric redshift errors  $\delta z'_{\text{phot}}$  in this figure were calculated by boosting the flux errors to account for the systematic mismatch between the templates and our data.



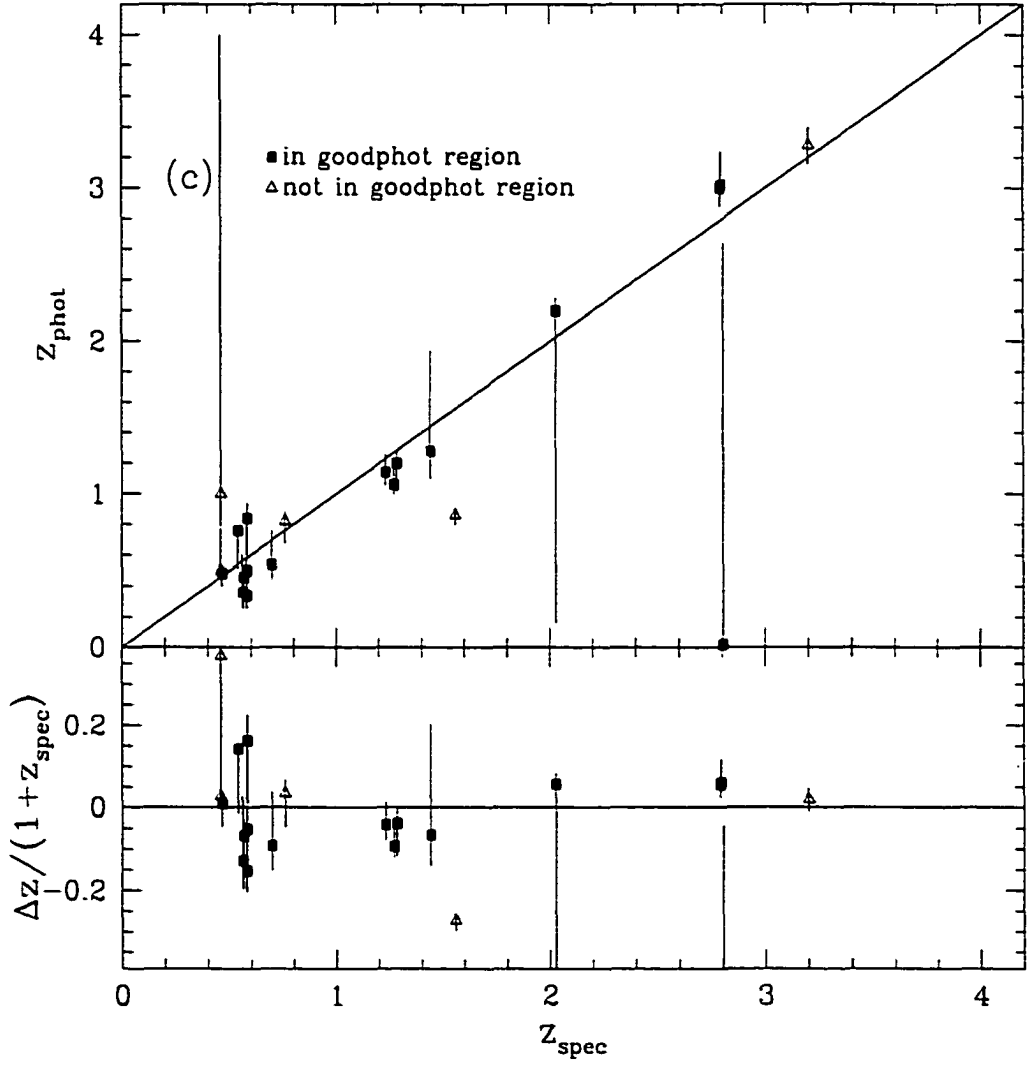


Figure 3.2b shows the  $z_{spec}$  vs.  $z_{phot}$  comparison using the complete 101.5 hours of FIRES data on the HDF-S. As can be seen, most of the  $z_{phot}$  values for galaxies at  $z < 2$  do not change with the use of the much deeper NIR data. Two objects (HDFS1-540 and HDFS1-541) which do not satisfy our good photometry requirements experience  $z \gtrsim 1$  changes in  $z_{phot}$  between the two data sets. In both cases the increase in the depth of the NIR data allows for a more accurate  $z_{phot}$  determination in comparison to the spectroscopic value. For all objects with  $z_{spec} \leq 3.2$  which were detected in the Chapter 2 catalog,  $\langle \Delta z / (1 + z) \rangle = 0.10$  and  $\langle \Delta z / (1 + z) \rangle$  decreases to 0.08 when only objects with good photometry are considered. Compared to the Chapter 2 data, the Chapter 4 data yield a substantial improvement in the  $z_{phot}$  accuracy at  $z_{spec} > 2$  with  $\langle \Delta z / (1 + z) \rangle$  increasing from 0.13 to 0.06. For both datasets all of the objects with  $z_{spec} > 2$  and good photometry have  $z_{phot}$  systematically higher than  $z_{spec}$ .

There is one object at  $z_{spec} = 2.804$  (HDF2-865) which was not detected in the Chapter 2 catalog but for which we have good photometry in the Chapter 4 catalog and for which we find  $z_{phot} = 0.02$ . From the observed spectral energy distribution (SED) this object appears to be an obvious  $U$ -dropout at  $z > 2$ , however, at these high redshifts, our current template set cannot reproduce the high  $S/N$  blue ( $B - V$ ) color and, at  $z \approx 0$ , the  $U$ -Band flux is significantly overpredicted by the best-fit template. Our technique gives more weight to the higher signal-to-noise  $B$  and  $V$  data and mistakenly identifies the observed break as a weak  $4000\text{\AA}$ /Balmer break at  $z \approx 0$ . We also noticed this phenomena in the broadband SEDs of several galaxies from Chapter 4 for which no spectroscopic data exists. This problem was noted by Thompson, Weymann, & Storrie-Lombardi (2001) who found that many galaxies observed in the HDF-N with NICMOS needed a template bluer than the Kinney et al. (1996) templates to fit the observed fluxes optical-NIR fluxes. Using this statement as a guide, we attempted to remedy our problem by adding a solar metallicity, 10 Myr old, single age burst template from the stellar population synthesis code of Bruzual

& Charlot (2001) with a mass range of  $0.1 - 100M_{\odot}$  and a Salpeter (1955) initial mass function. This template is significantly bluer than the Kinney et al. (1996) SB1 template. At high redshift  $z > 2$  the very hot young stars in this template can produce very blue ( $B - V$ ) colors while the attenuation from intervening neutral Hydrogen absorption (Madau, 1995) can at the same time give very red ( $U - B$ ) colors. The inclusion of this blue template failed to change the photometric redshift of HDFS2-865 (or the  $z_{phot}$  of any of the galaxies in the spectroscopic sample) although, as will be discussed in §3.4.2, the spectroscopic redshift is contained in the 68% redshift confidence limits. There are however galaxies in our  $K_{s,AB}^{tot} < 26$  sample with observed SEDs very similar to that of HDFS2-865 and  $z_{phot} \sim 0$ . For almost all of these galaxies, the inclusion of the very blue template moved  $z_{phot}$  to  $\sim 2 - 2.5$  and greatly improved the  $\chi^2$ . When including the blue template, but excluding HDFS2-865, the  $z_{phot}$  accuracy for all objects and only those with good photometry remains at  $\langle \Delta z / (1 + z) \rangle = 0.10$  and  $0.08$  respectively. The spectroscopic and photometric redshifts for all galaxies are given in Table A.6.

It is apparent that the large increase in depth between the initial and final FIRES datasets does not result in a large increase in the  $z_{phot}$  accuracy at low redshifts. It is important to remember, however, that the galaxies with  $z_{spec}$  determinations are almost exclusively very bright; the photometric errors for these bright galaxies are very small and the residuals from the template fit are dominated by template mismatch. While, at this time, we cannot confirm this with spectra, we expect that the much deeper exposures of the final FIRES data set improve our  $z_{phot}$  determinations for fainter objects where the photometric uncertainties still dominate the  $z_{phot}$  accuracy.

### 3.4.2 Measuring the Uncertainty in $z_{phot}$

It is clear from Figure 3.2a and 3.2b (see also Chapter 2) that our Monte-Carlo errorbars  $\delta z_{MC}$  severely underestimate the uncertainty in  $z_{phot}$ . This occurs because



the galaxies for which spectroscopic redshifts are available are typically bright and therefore have very small flux errors; the resulting range of statistically acceptable redshifts is likewise very small and our finite set of templates significantly distorts  $z_{phot}$ , but is not modeled by our Monte-Carlo technique. At fainter magnitudes, the uncertainty in  $z_{phot}$  is dominated by the errors in the photometry (Fernández-Soto, Lanzetta, & Yahil, 1999) and our Monte-Carlo technique should accurately estimate the uncertainty in  $z_{phot}$ . Experience from Chapter 2 showed that setting a minimum fractional flux error of 10% to account for this “template mismatch” effect gave more realistic  $\delta z_{phot}$  estimates, but resulted in a less accurate measure of  $z_{phot}$  in comparison to  $z_{spec}$ . In an attempt to produce realistic errorbars for  $z_{phot}$  we constructed  $\delta z_{phot}$  (Chapter 2) from a combination of the Monte-Carlo errors and from the redshift dependent systematic errors derived from a comparison of  $z_{phot}$  to  $z_{spec}$  for galaxies in the HDF-N with spectra obtained by Cohen et al. (2000) and optical/NIR photometry from Williams et al. (1996), Dickinson (2001a), and Fernández-Soto, Lanzetta, & Yahil (1999). This method has the disadvantage that the systematic component of  $\delta z_{phot}$  is only true in the mean and that individual galaxies, depending on their SED shapes, can have very different values for  $\delta z_{phot}$  at a given redshift and magnitude.

To improve this situation, we tried to estimate the photometric redshift uncertainty in our data directly using the FIRES photometry and testing our  $\delta z_{phot}$  estimates with the full set of spectroscopic redshifts in the HDF-S. Given a set of formal flux errors, one way to broaden the redshift confidence interval without degrading the accuracy (as noticed in Chapter 2) is to lower the absolute  $\chi^2$  of every  $\chi^2(z)$  curve without changing its shape (or the location of the minimum). By scaling up all the flux errors by a constant factor, we retain the relative weights of the points in the  $\chi^2$  without changing the best fit redshift and SED, but we do enlarge the redshift interval over which the templates can satisfactorily fit the flux points. Since we believe the disagreement between  $z_{spec}$  and  $z_{phot}$  is due to our finite template set, this factor should reflect the degree of template mismatch in our sample i.e. the degree by which

our models fail to fit the flux points. To estimate this factor we first computed the fractional difference between the model and the data  $\Delta_{i,j}$  for the  $j^{\text{th}}$  galaxy in the  $i^{\text{th}}$  filter,

$$\Delta_{i,j} = \frac{(f_{i,j}^{\text{mod}} - f_{i,j}^{\text{dat}})}{f_{i,j}^{\text{dat}}} \quad (3.2)$$

where  $f^{\text{mod}}$  are the predicted fluxes of the best-fit template combination and  $f^{\text{dat}}$  are our actual data. We then averaged over all galaxies in our complete FIRES sample with  $K_{s,\text{AB}}^{\text{tot}} < 24$  to obtain

$$\Delta_i = \frac{1}{N_{\text{gal}}} \sum_{j=1}^{N_{\text{gal}}} |\Delta_{i,j}|. \quad (3.3)$$

To determine the mean deviation of all of the flux points from the model  $\Delta_{\text{dev}}$ , we then averaged  $\Delta_i$  over  $N_{\text{filt}} - 1$  filters

$$\Delta_{\text{dev}} = \frac{2}{N_{\text{filt}}} \sum_{i=1}^{N_{\text{filt}}-1} \Delta_i \quad (3.4)$$

where we have ignored the contributions of the  $U$ -band. While the  $U$ -band is important in finding breaks in the SEDs, the exact shapes of the templates are poorly constrained blueward of the rest-frame  $U$ -band and the  $U$ -data often deviates significantly from the best-fit model fluxes. We find  $\Delta_{\text{dev}} \approx 5\%$ , which includes both random and systematic deviations from the model. We modified the Monte-Carlo simulation of Chapter 2 by calculating, for each object  $j$ ,

$$\left\langle \frac{S}{N} \right\rangle_j = \sqrt{\frac{\sum_{i=2}^{N_{\text{filt}}} \left( \frac{f_i}{\delta f_i} \right)^2}{N_{\text{filt}} - 1}} \quad (3.5)$$

again excluding the  $U$ -Band. We then scaled the flux errors, for each object, using the following criteria:

$$\delta f'_i = \begin{cases} \delta f_i & : \left\langle \frac{S}{N} \right\rangle_j \leq \frac{1}{2\Delta_{\text{dev}}} \\ \delta f_i \frac{2\Delta_{\text{dev}}}{\left\langle \frac{S}{N} \right\rangle_j} & : \left\langle \frac{S}{N} \right\rangle_j > \frac{1}{2\Delta_{\text{dev}}} \end{cases} \quad (3.6)$$

where we have multiplied  $\Delta_{\text{dev}}$  by a factor of 2 to be more conservative in our error estimate. The new photometric redshift error  $\delta z'_{\text{phot}}$  is computed from the  $\delta f'_i$ 's. Note that this procedure will not modify the errors of the objects with low  $S/N$  where  $\delta z'_{\text{phot}}$  is dominated by the formal photometric errors. Figure 3.2c shows the comparison of  $z_{\text{phot}}$  to  $z_{\text{spec}}$  using the new errorbars and including the blue template. For these bright galaxies, it is remarkable that our new photometric redshift errors bars come so close to predicting the disagreement between  $z_{\text{phot}}$  and  $z_{\text{spec}}$ . We do notice however, using full  $z_{\text{phot}}$  catalog for the  $K_{s,\text{AB}}^{\text{tot}} < 26$  sample, that there are galaxies with  $K_{s,\text{AB}}^{\text{tot}} > 25$  but with  $\langle \Delta z / (1 + z) \rangle < 0.05$ , an unrealistically low value. Even though these galaxies have  $\langle \frac{S}{N} \rangle_j \leq \frac{1}{2\Delta_{\text{dev}}}$ , they still have high  $S/N$  in the  $B_{450}$  or  $V_{606}$  bandpasses and hence have steep chisquared curves and small inferred redshift uncertainties.

We have worked hard and found it difficult to develop a scheme for measuring realistic photometric redshift uncertainties over all regimes. The  $\delta z'_{\text{phot}}$  estimate derives the  $z_{\text{phot}}$  uncertainties individually for each object, but can underpredict the uncertainties in some cases. Compared to  $\delta z_{\text{phot}}$ , however, a method based completely on the Monte-Carlo technique is preferable because it has a straightforwardly computed redshift probability function. This trait is desirable for estimating the errors in the rest-frame luminosities and colors (Chapter 5) and for this reason we will use  $\delta z'_{\text{phot}}$  in all subsequent chapters.

Even though the 68% confidence limits for many objects are small, there can still be a secondary minima in the  $\chi^2(z)$  curve. To identify secondary minima which were not reflected in the 68% confidence limits, we determined (see Chapter 2) the fraction of the Monte-Carlo redshift iterations  $z_{\text{MC}}$  for which  $|z_{\text{MC}} - z_{\text{phot}}| > 1$ . We refer to this fraction as  $\gamma_{\text{alt}}$ . With this new technique for measuring the photometric redshift uncertainty, the  $\chi^2(z)$  curves broaden and  $\gamma_{\text{alt}}$  increases. In Table A.6 we indicate when a galaxy's 90% confidence limits are very large by flagging objects with  $\gamma_{\text{alt}} > 10\%$ .

### 3.4.3 Accuracy of Photometrically Derived Rest-Frame Luminosities

In Chapter 2 we pointed out the overabundance of intrinsically luminous,  $L_B^{\text{rest}} > 5L_{*,B}$   $K_s$ -band selected galaxies at  $z > 2$  compared to the local luminosity function. This overabundance has also been noted by Shapley et al. (2001) from NIR studies of spectroscopically confirmed LBGs and may indicate that the luminosity function at high redshift had a brighter turnover than in the local universe. Our statements in Chapter 2 hinge upon the accuracy of our photometric redshifts as we measured  $L^{\text{rest}}$  for each object by using the luminosity of the best-fit template at  $z_{\text{phot}}$ . We tested these  $L^{\text{rest}}$  measurements by fixing the redshift at  $z_{\text{spec}}$  and re-computing the rest-frame luminosity. At  $z > 2$  (excluding object HDFS2-865)  $z_{\text{spec}}$  is systematically lower than  $z_{\text{phot}}$  by  $\approx 0.15$  (§3.4.1) and  $L^{\text{rest}}$  correspondingly decreases by  $\approx 10 - 15\%$  when measured at  $z_{\text{spec}}$ . This small decrease in  $L^{\text{rest}}$  does not change our  $L_*$  brightening estimate.

## 3.5 A Large, Disk-Like Lyman Break Galaxy at $z \sim 3$

One of our targeted galaxies, HDFS1-36, is an LBG with  $z_{\text{phot}} = 3.02_{-0.08}^{+0.22}$ , a non-axisymmetric ring-like structure, and a large apparent diameter of  $\sim 1''.7$ . In Figure 3.3a, you can see the image tiles of HDFS1-36 in the F606W through  $K_s$ -bands with a  $1''.7$  diameter circle drawn for reference and centered at the centroid of the  $K_s$ -band image. We measured  $z_{\text{spec}} = 2.793 \pm 0.003$  for this galaxy and can assign its apparent size a co-moving physical diameter of  $9.4h^{-1}$  kpc for  $\Omega_M = 0.3$ ,  $\Omega_\Lambda = 0.7$  and  $6.3h^{-1}$  kpc for  $\Omega_M = 1.0$ ,  $\Omega_\Lambda = 0.0$ . At this redshift, the I-band samples a rest-frame wavelength of  $2150\text{\AA}$ , where the light is dominated completely by massive, very young stars and where the observed morphology is heavily affected by dust extinction. Still, the size of the ring implies at least that some kind of vigorous and possibly coherent star formation is occurring over a large co-moving distance.

It is interesting to note how the observed structure changes with wavelength. As is

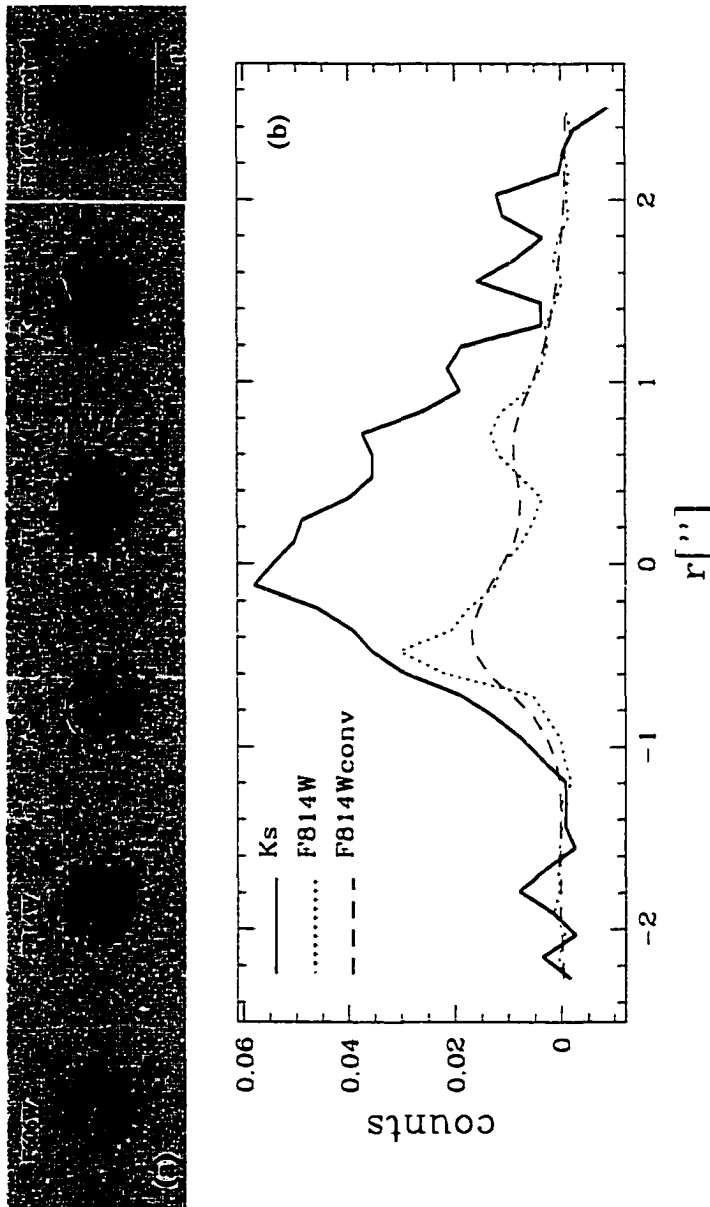


FIGURE 3.3. a) Image tiles of object HDFS1-36 normalized to a zeropoint of  $m(AB) = 25$ . The  $U_{300}$  and  $B_{450}$  filters are not shown. The last tile is convolved to the ground-based seeing of  $0''.45$  (see Chapter 4) for direct comparison with the  $K_s$ -band image. In the unconvolved images, a plus sign is painted at the location of the  $K_s$ -band centroid, and a circle is drawn around this point to demonstrate the circularity of the star formation ring. In b) we show a column average of the central 5 columns for the  $K_s$ , F814W, and convolved F814W images. These column cuts are also normalized to a zeropoint of  $m(AB) = 25$ . The  $K_s$ -band image appears more concentrated and symmetric than both the unconvolved and convolved F814W images.

shown in Figure 3.3a, the size of HDFS1-36 does not appear to change dramatically as one moves from the observed optical to the NIR. In the NIR bands, the prominent ring structure does appear to diminish however and the light appears more concentrated and symmetric than in the optical. Both the centrally concentrated and symmetric NIR image, and the near circular morphology of the optical ring conflict with a merger scenario. By convolving the HST image to the ground-based seeing of  $0''.47$  (Chapter 4) we tested whether the change in morphology with observed wavelength could be accounted for by the decrease in spatial resolution when going from the optical HST images to the ground-based NIR images. This test shows that the optical ring-like structure would still be obvious when observed at the ground-based resolution and, unlike in the  $K_s$ -band image, would have a brightness distribution which peaks significantly off-center (Figure 3.3a). In Figure 3.3b we have plotted the average of the central five columns along the  $K_s$ , F814W, and convolved F814W images. The  $K_s$  profile appears to be more concentrated than that of the F814W image and shows only a little evidence of the ring structure. One way to explain this difference in morphology is by invoking a radial dust gradient superimposed on a background source. Because of its redder wavelength, the  $K_s$ -band image suffers from less extinction than the F814W image and so would appear more concentrated. Another possibility is that the increased concentration seen in the  $K_s$ -band image is real and that we are seeing an intrinsically redder, more centrally concentrated population contributing heavily to the rest-frame optical light. It is tempting to associate this redder population with a spheroidal component sitting in the middle of a star forming disk.

The size of HDFS1-36 ( $R \approx 4.7h^{-1}$  kpc) is much larger than the typical LBG half-light radii of  $1.0 - 1.5h^{-1}$  kpc (for  $\Omega_m = 0.3$ ,  $\Omega_\Lambda = 0.7$ ) measured by Giavalisco, Steidel, & Macchetto (1996) from HST images. The large size also contradicts theoretical predictions of LBG sizes. Hierarchical pictures of galaxy formation (e.g., Kauffmann, White, & Guiderdoni 1993; Baugh, Cole, Frenk, & Lacey 1998) predict

that galaxies form over time from the merger and accretion of small sub-galactic clumps. In this framework, large galaxies did not have time to form at high redshift and should be very rare (if at all present). Using semi-analytic models of galaxy formation, Baugh, Cole, Frenk, & Lacey (1998) predict half-light radii of only  $0.4 - 0.6 h^{-1}$  kpc for LBGs at  $z \approx 3$ . While low number statistics must be taken into account when interpreting the significance of this large object, hierarchical galaxy formation models clearly need to produce objects of comparable size.

### 3.6 Summary

In this chapter we present results from optical spectroscopic observations of the WPFC2 field of the HDF-S taken as follow-up to the deep NIR imaging of the FIRES project. We obtained 11 spectroscopic redshifts of which seven had accompanying optical/NIR photometry from the FIRES data set. For six out of these seven galaxies, spectroscopic redshifts were measured using interstellar and stellar absorption lines. All but one of these seven galaxies had  $z > 1$  and three had  $z > 2$ .

Our spectroscopic redshifts increased by 40% the number of spectroscopically confirmed galaxies in the HDF-S. We used our spectroscopic redshifts in combination with others taken from the literature to test the photometric redshift technique presented in Chapter 2. Good agreement is found between  $z_{phot}$  and  $z_{spec}$  using the initial FIRES photometry (Chapter 2) with  $\langle \Delta z / (1 + z) \rangle = 0.07$ . Using the much deeper NIR data from the complete FIRES catalog (Chapter 4) we find that  $\langle \Delta z / (1 + z) \rangle$  at low redshift remains unchanged when we do not count the one galaxy which was too faint to be included in the Chapter 2 photometric catalog and which had a very wrong  $z_{phot}$  estimate. The accuracy of  $z_{phot}$  at  $z > 2$  doubles however, likely because the deeper NIR data better constrains the position of the 4000Å/Balmer break.

We improved upon the uncertainty estimate for  $z_{phot}$  described in Chapter 2 by deriving a method based solely on our photometric data which accounts for tem-

plate mismatch effects. Instead of applying a mean systematic error component to all galaxies, this method incorporates information about each object's SED in the determination of the redshift uncertainties. We find that the new errors  $\delta z'_{phot}$  reflect much more accurately the disagreement between  $z_{phot}$  and  $z_{spec}$ .

To test how our redshift errors effect our measurements of  $L^{rest}$  at high redshift, where we measured an overabundance (in Chapter 2) of intrinsically bright galaxies, we determined  $L^{rest}$  at  $z=z_{spec}$  for our spectroscopically confirmed galaxies at  $z > 2$ . We found that  $L^{rest}$  decreased by only 10 – 15% in comparison to the values derived at  $z_{phot}$ .

One of our galaxies at  $z = 2.793$  has a very extended morphology in both the HST optical images and in the ground-based NIR images. The rest-frame ultraviolet ring observed in the HST images has a co-moving diameter of  $\gtrsim 9.4(6.3) h^{-1}$  Kpc for a  $\Omega_M = 0.3$ ,  $\Omega_\Lambda = 0.7$  ( $\Omega_M = 1.0$ ,  $\Omega_\Lambda = 0.0$ ) cosmology. The  $K_s$ -band light appears more concentrated and symmetric than the I-band light and its shape seems inconsistent with a mere convolution of the I-band image to the ground-based seeing. While this effect could in part stem from extinction effects, it is tempting to associate the large star-forming ring with an extended disk and the concentrated NIR light as a redder bulge population. If this is indeed the case, it presents a challenge to hierarchical galaxy formation scenarios which predict few if any large disk galaxies at high redshifts.



## CHAPTER 4

OBSERVATIONS, DATA REDUCTION, SOURCE  
DETECTION, AND PHOTOMETRY OF A  $K_{s,AB}^{\text{tot}} < 26$   
CATALOG IN THE HDF-S

A primary goal of the FIRES program is to construct a  $K_s$ -band selected sample with photometry in seven filters. While reduced versions of the optical HST bandpasses were presented in Casertano et al. (2000) we had to first process our NIR data before a multi-color catalog could be constructed. The reduction of the full FIRES dataset, presentation of the final images, and the construction of the final multicolor catalogs will be discussed in Labbé et al. (2001) as part of Labbé's Doctoral Dissertation. Because Chapters 3 and 5 are based on a preliminary version of the final data products, we present here the penultimate reduction version, images, and catalog and briefly outline the reduction, source detection, and photometry steps. In §4.1 we discuss the observations. The data reduction itself is explained in §4.2. In §4.3 we present the reduced NIR images. We discuss the source detection and present the catalog in §4.4.

#### 4.1 Observations

The FIRES data were obtained at the VLT using the Infrared Spectrometer And Array Camera (ISAAC; Moorwood 1997). This instrument has a  $1024 \times 1024$  Hawaii Rockwell detector (HgCdTe), covers the spectral range from 1-5  $\mu m$ , and is designed primarily for wide-field imaging ( $2.5 \times 2.5$  arcmin) and long-slit low- and medium-resolution spectroscopy.

The NIR FIRES data were taken in two sets; one at the end of 1999 (Chapter 2) and one from April through October of 2000. The second block of data was centered on the WFPC2 field of the HDF-S albeit at a slightly different position (22h32m55.46s

and  $-60^{\circ}33'5''.01$ ) than the first block (see Chapter 2) and one which better matched the position of the HST pointing. The total exposure time was 101.5 hours with 33.6, 32.3, and 35.6 hours in the  $J_s$ ,  $H$ , and  $K_s$  filters respectively. The  $J_s$ -band exposures were split into 4-30s detector integration times (DITs), the  $H$ -band into 6-20s DITs, and the  $K_s$ -band into 6-10s DITs. The exact observation parameters such as integration time, filters and telescope offsets were defined a priori in the Observation Blocks (OBs) via an observation template. We used the **ISAACSW\_img\_obs\_AutoJitter** template which moves the telescope between exposures (dithers/jitters) in a random pattern of offsets (in a  $20''.0$  box) that is generated within the template. It is the best choice for deep integrations on fields that do not contain extended sources and are uncrowded.

## 4.2 Data Reduction

The dominance of the variable sky background and the large amount of jittered exposures require a careful treatment in order to produce very deep ground based images. The reduction process for the short-wavelength imaging template

**ISAACSW\_img\_obs\_AutoJitter** included the following steps: quality verification, flat-field construction, bad pixel correction, sky estimation and subtraction, flatfield correction, distortion correction, frame offset detection and registration, zeropoint calibration, combining to a single frame, and post-processing. We used a modified version of the DIMSUM<sup>1</sup> package in IRAF<sup>2</sup> for sky subtraction and the ECLIPSE<sup>3</sup> package for creating the flatfields and bad pixel masks. In addition, several corrections were applied to remove instrumental features, contamination by scattered light,

---

<sup>1</sup>DIMSUM is the Deep Infrared Mosaicing Software package developed by Peter Eisenhardt, Mark Dickinson, Adam Stanford, and John Ward, and is available via ftp to <ftp://iraf.noao.edu/contrib/dimsumV2/>

<sup>2</sup>IRAF is distributed by the National Optical Astronomy Observatories, which are operated by the AURA, Inc., under cooperative agreement with the NSF.

<sup>3</sup>ECLIPSE is an image processing package written by N. Devillard, and is available at <ftp://ftp.hq.eso.org/pub/eclipse/>

satellite trails, or other unmistakable artifacts.

Several versions of the reductions were made with increasing level of sophistication, leading to a final version that is registered directly to the WFPC2 F814W image. Labbé et al. (2001) will present the multiple reduction passes and we will summarize the final pass below.

#### 4.2.1 Flatfield Construction

We generated flatfields using a technique similar to that described in Chapter 2. From a time series of twilight images we generated flatfields for each filter, on each night of the observations, using the *flat* routine in ECLIPSE. This software also produced bad pixel maps flagging pixels with a non-linear response. The nightly flats were combined to form monthly flatfield images excluding individual frames with obvious scattered light. We quantified the long-term stability of the flats by dividing one monthly flat by another; the disagreement was typically 0.5%. If no flatfield was available in a given month, we used the average flatfield over all good nights.

#### 4.2.2 Photometric Calibration

The observations of standard stars were taken following the VLT calibration plan. The calibration procedure followed that in Chapter 2 with the modification that we used the magnitudes of non-saturated stars on photometric nights to scale all of the distortion corrected frames to the same zeropoint before combining. The zeropoints were measured from the distorted frames, but since the standard stars are located close to the center of the array the differential distortion correction is small and this effect should be minor. The derived zeropoints have an RMS of  $\approx 1 - 2\%$  over all OBs and magnitudes of bright stars measured from the Chapter 2 data set are within 1% of magnitudes measured from the final catalog.

### 4.2.3 Combination

The varying sky background requires dithering of many short exposures and the subtraction procedure is intended to filter out these low-frequency time dependent variations. A brief summary of how this was accomplished with the *reduce* task in DIMSUM and how cosmic rays were removed was presented in Chapter 2.

#### *Distortion Correction, Registration, and Combination*

In a single step the individual sky subtracted images are distortion corrected, rotated, scaled, and registered directly to the  $3 \times 3$  blocked WFPC2 F814W image. Using the distortion correction<sup>†</sup>, we computed the inverse transformation which maps a position on the blocked WFPC2 image to a position on the distorted ISAAC frame. In addition to the distortion correction, we also used the positions of a few hundred objects which were common in both the  $J_s$  and F814W images to compute the rotation and scaling which maps one onto the other. The new pixel scale ( $0''.119 \text{ pix}^{-1}$ ) somewhat oversamples the original ISAAC scale ( $0''.147 \text{ pix}^{-1}$ ). After applying the transformation, we used a bicubic interpolation scheme to compute the flux at the new pixel.

The shifts between the individual ISAAC frames were recalculated after the correction of the measured positions of the stars for geometric distortion. Correcting for distortion in our shift determination, we achieved an alignment accuracy of  $0''.03$  RMS (0.25 original ISAAC pixels) over all frames.

All sky subtracted images, which were individually transformed and registered to the blocked WFPC2 F814W image, were scaled to the same zeropoint and were then directly combined per filter into the final images. In the final frames, the RMS offset in positions with respect to the F814W image is  $0''.03$  with a maximum amplitude of  $0''.09$ .

---

<sup>†</sup>available at <http://www.eso.org/instruments/isaac/problems.tips.html>

## 4.3 The Images

### 4.3.1 Quality of the Images

The combined  $K_s$  image which is registered to the blocked F814W image is presented in Figure 4.4.3. This image should be compared to the much shallower  $K_s$  image shown in Chapter 2. The FWHM of the seeing in the combined images is  $0''.48$ ,  $0''.48$ , and  $0''.47$  in  $J_s$ ,  $H$ , and  $K_s$  respectively.

We list in Table A.7 the  $5\sigma$  formal sensitivity limits (without aperture corrections) of the images in both a  $0''.7$  and  $2''.0$  aperture. We find that our  $J_s$  and  $H$  data are 0.2 magnitudes deeper and 0.4 magnitudes shallower than the deep NICMOS images of the HDF-N from Dickinson (2001b) while our  $K_s$  data is 1.7 magnitudes deeper than that taken by Dickinson (2001a) on the HDF-N at the Kitt Peak 4-meter<sup>5</sup>. We point out however that the smaller point-spread function of NICMOS results in deeper point source limits than those calculated just from the background RMS. Our adopted conversions from Vega system to the AB system are  $J_{s,vega} = J_{s,AB} - 0.90$ ,  $H_{vega} = H_{AB} - 1.38$ , and  $K_{s,vega} = K_{s,AB} - 1.86$ .

## 4.4 Source Detection and Photometry

As discussed in Chapter 2, it is always necessary to make trade-offs between completeness and reliability when constructing catalogs from deep images. We present one such combination here whose detection process is optimized for point sources and which suffers minimal contamination from spurious detections.

---

<sup>5</sup>available at  
[http://www.stsci.edu/ftp/science/hdf/clearinghouse/irim/irim\\_hdf.html](http://www.stsci.edu/ftp/science/hdf/clearinghouse/irim/irim_hdf.html)

#### 4.4.1 Detection

To construct our  $K_s$ -band selected catalog we used SExtractor version 2.2.1 (Bertin & Arnouts, 1996) to perform detection on the  $K_s$  image and photometry on all the bands. The dithering of the observations has led to significant S/N variations across the image caused mainly by the large differences in exposure times near the edge of the image. Therefore, we divided the  $K_s$  image by the square root of the exposure time (weight) map to create an S/N image and ran SExtractor with a S/N criterion. SExtractor detects objects after convolving the image with a Gaussian FWHM= $0''.46$  kernel, optimizing the S/N for sources of that particular size. At the same time this introduces a slight bias against extended low-SB objects, but the majority of objects to be picked up near the detection limit are expected to be compact. Merging multiple catalogs created with different kernels is not a viable option because it severely complicates our detection sensitivity. The adopted deblending parameters in SExtractor are `DEBLEND_NTHRESH` = 32 and `DEBLEND_MINCONT` = 0.0002. With these settings SExtractor fails to pick up galaxies near the brightest stars in the image.

The detection threshold was set so that at least 1 pixel was above  $\approx 5$  times the standard deviation in the background of the convolved detection image. Simulations (Labbé et al., 2001) show that spurious sources detected close to the detection limit are not a problem.

#### 4.4.2 Photometry

SExtractor was run in dual-image mode, detecting in the  $K_s$  S/N image and measuring in  $U_{300}$ ,  $B_{450}$ ,  $V_{606}$ ,  $I_{814}$ ,  $J_s$ ,  $H$ , and  $K_s$  using identical apertures. The measurement images are precisely aligned and on the same pixel scale ( $0''.119 \text{ pix}^{-1}$ ). To ensure accurate color measurements, the optical PSFs were matched to the NIR PSF (FWHM= $0''.48$ ) by convolving the WFPC2 images by a kernel specially constructed to match the complicated space-based PSF structure to the smooth ground-based

seeing dominated ISAAC PSF.

#### 4.4.3 The Catalogs

Tables A.8 and A.9 contain the the catalog of the 495 objects detected with SExtractor which had  $K_{s,AB}^{\text{tot}} < 26$ , were not identified as point sources in Chapter 2, and had weights  $w > 0.2$  in exposure time weight maps. We choose a magnitude limit of  $K_{s,AB}^{\text{tot}} < 26$  because it is at roughly this magnitude that our number counts turn over. The list below gives the definitions for the individual columns in the two tables:

- ID: The catalog ID number
- R.A., Decl.: The right ascension and declination in J2000 coordinates. The transformation from pixel coordinates to R.A. and Decl. was computed from the astrometry of Fernández-Soto, Lanzetta, & Yahil (1999). The objects are listed in order of increasing declination.
- $f_i \pm \sigma_i$ : The flux  $f_i$  in the  $i$ -band ( $f_i = \{ U_{300}, B_{450}, V_{606}, I_{814}, J_s, H, K_s \}$ ) and its uncertainty ( $\sigma_i$ ). The fluxes refer to that within a  $2''.0$  diameter circular aperture centered on the location of the  $K_s$ -band image. The fluxes are in units of  $10^{-31} \text{ ergs s}^{-1} \text{ Hz}^{-1} \text{ cm}^{-2}$ .
- $K_{s,AB}^{\text{tot}} \pm \sigma(K_{s,AB}^{\text{tot}})$ : Total  $K_s$ -band flux and its uncertainty. The total magnitude is defined as either SExtractor's BEST flux or a  $0.7''$  diameter circular aperture, whichever has the largest area. SExtractor's BEST flux is either the AUTO flux, the sum of counts within an elliptical aperture (Kron, 1980), or the ISOCOR flux, the corrected isophotal flux. The semi-major axis of the Kron aperture is  $2.5 \times$  the first moment of the flux distribution within an ellipse of about twice the isophotal radius, with a minimum semi-major axis of 4.5 pixels. The correction applied to isophotal flux depends on profile, according to the SExtractor manual.



FIGURE 4.1. The  $K_s$ -band image. This image involves a total exposure time of 35.6 hours and has a FWHM seeing of  $0''.47$ .



## CHAPTER 5

MEASURING THE REST-FRAME OPTICAL COLORS AND  
STELLAR MASSES OF  $K$ -BAND SELECTED GALAXIES

## 5.1 Motivation

Look-back observations of galaxy evolution should ideally compare luminous galaxy properties at constant rest-wavelength across a range of cosmic epochs. A weakness in most existing studies of high-redshift galaxies has been that optical selection chooses high redshift galaxies on the basis of flux in the rest-frame UV, a wavelength regime where precious little information has been gathered in the local universe. Using deep NICMOS  $J$  and  $H$  data in the HDF-N, supplemented with moderately deep  $K_s$ -band, and in the optical the WFPC2 data, Papovich, Dickinson, & Ferguson(2001; hereafter P01) performed a detailed analysis of the stellar populations and star formation histories (SFHs) of 33 optically selected, spectroscopically confirmed, Lyman Break Galaxies (LBGs) using the broad-band photometry. This work was closely followed by Shapley et al. (2001; hereafter S01) who performed a similar analysis on a sample of 81 brighter LBGs using ground based  $G$ ,  $R$  and  $J$ , and  $K_s$  data much shallower than that of P01. Both of these works had the advantage of working with a set of galaxies with spectroscopic redshifts - removing the redshift uncertainties as a contributing source of error in the population modeling. Even with this advantage, the SFHs they derived were highly degenerate. The total stellar masses were less degenerate, but still suffer from considerable uncertainties.

Despite the lack of spectroscopic redshifts for most of our galaxies, the FIRES sample enjoys advantages over both of these datasets. With 71 galaxies at  $2 < z < 3.2$  and  $K_{s,AB}^{\text{tot}} < 25$  (where our color uncertainties are not dominated by the photometric errors; see §5.3.4), our sample has worse  $J$  and  $H$  data, but is larger than that of P01

and has much deeper  $K_s$ -band data in comparison with the the P01 detection limit of  $K_{s,AB}^{\text{tot}} \approx 23.8$ . Our  $J_s$  and  $K_s$  data are much deeper than that of S01 (who almost always used NIR exposure times of  $\sim 1$  hour) and we have observations through more filters. Our very deep  $K_s$ -band data allow us to better constrain the stellar mass-to-light ratios  $\mathcal{M}/L$  simply because they are more stable in the red. These deep  $K_s$ -band data also give us a higher sensitivity to galaxies with red SEDs that would not be selected by the presence of a strong LB. Finally, we are not limited by the LB technique to  $z > 2$ , but rather can use our photometric redshift technique to identify galaxies at all redshifts and use our broad wavelength coverage to compare these galaxies at identical rest-frame wavelengths. Unfortunately, however,  $z_{\text{phot}}$  estimates can have considerable errorbars and our analyses must take the realistic redshift uncertainties into account.

This limitation forces us to take a simpler approach than S01 or P01. From our deep near-infrared (NIR) data we measure the rest-frame optical colors and luminosities redward of the Balmer/4000Å break for all galaxies  $z \lesssim 3.2$  and compare them to galaxies in the local universe. Drawing on theoretical relations between the rest-frame color and stellar  $\mathcal{M}/L$  (Bell & de Jong 2001; hereafter BJ01), we then estimate the  $\mathcal{M}/L$  and consequently the stellar masses of our galaxies. In conjunction with our  $K_s$ -band selection, these  $\mathcal{M}/L$  and mass estimates help us to answer several questions. Is there a quiescent phase of star formation in galaxies at high redshift? At any given redshift, do “red” or “blue” galaxies dominate the stellar mass? How does the total stellar mass content of the universe evolve with redshift? To properly address these questions, we will not only have to measure the rest-frame colors and stellar masses of our galaxies, but also assess whether we detect objects not found in deep, optically selected samples.

In §5.2, we present the  $z_{\text{phot}}$  distribution of our sample. In §5.3, we will discuss the different methods for measuring the rest-frame colors and their uncertainties. We discuss the derived rest-frame colors in §5.4. In §5.5 we discuss the measurement of

the mass-to-light ratios and stellar masses and discuss their significance.

## 5.2 Redshifts

### 5.2.1 The Photometric Redshift Distribution

We derive the photometric redshifts  $z_{phot}$ , and their uncertainties  $\delta z'_{phot}$  for our entire  $K_{s,AB}^{tot} < 26$  sample (see Chapter 4) using the method described in Chapters 2 and 3. These are listed in Table A.10. We exclude all objects identified as stars in Chapter 2. In Figure 5.1 we show the redshift histogram for all 492 galaxies with  $K_{s,AB}^{tot} < 26$  and  $z_{phot} < 5.9$  (The three galaxies with  $z_{phot} \geq 5.9$  are believed to have erroneous photometric redshifts; see below). The sharp peak in the redshift distribution at  $z \approx 0.5$  which was discussed in Chapter 2 is still present. The broad enhancement seen in Chapter 2 from  $1 < z < 1.4$  appears absent. To examine if this disappearance is simply due to our deeper magnitude cut we plot, in Figure 5.2, the  $K_{s,AB}^{tot}$  of galaxies vs. their  $z_{phot}$ . From this plot it is clear that the broad enhancement of galaxies at  $1 < z < 1.4$  discussed in Chapter 2 is still present when using the  $K_{s,AB}^{tot} < 23.5$  cut from Chapter 2, but that this enhancement disappears at fainter magnitudes. We must also remind the reader that the field of the HDF-S is small and that cosmic variance can effect the redshift distribution.

There three galaxies for which the accuracy of the photometric redshift may be in doubt. Object HDFS2-813 has  $K_{s,AB}^{tot} = 23.35$ ,  $z_{phot} = 5.9$ , and a small value of  $\delta z'_{phot}$ . This object, however, has a poor SED fit and a secondary  $\chi^2(z)$  minima at  $z_{phot} = 0.55$ . Additionally, object 813 is very compact in the HST F814W image and is likely a star which was not properly identified in Chapter 2. There are two galaxies (HDFS2-254 and HDFS2-409) which have  $z_{phot} > 9$ . Both of these objects have very large values of  $\delta z'_{phot}$ , secondary  $\chi^2(z)$  minima at  $z \sim 2$  and may simply be lower redshift, faint ellipticals. We do not consider any of these 3 objects in our subsequent analyses.

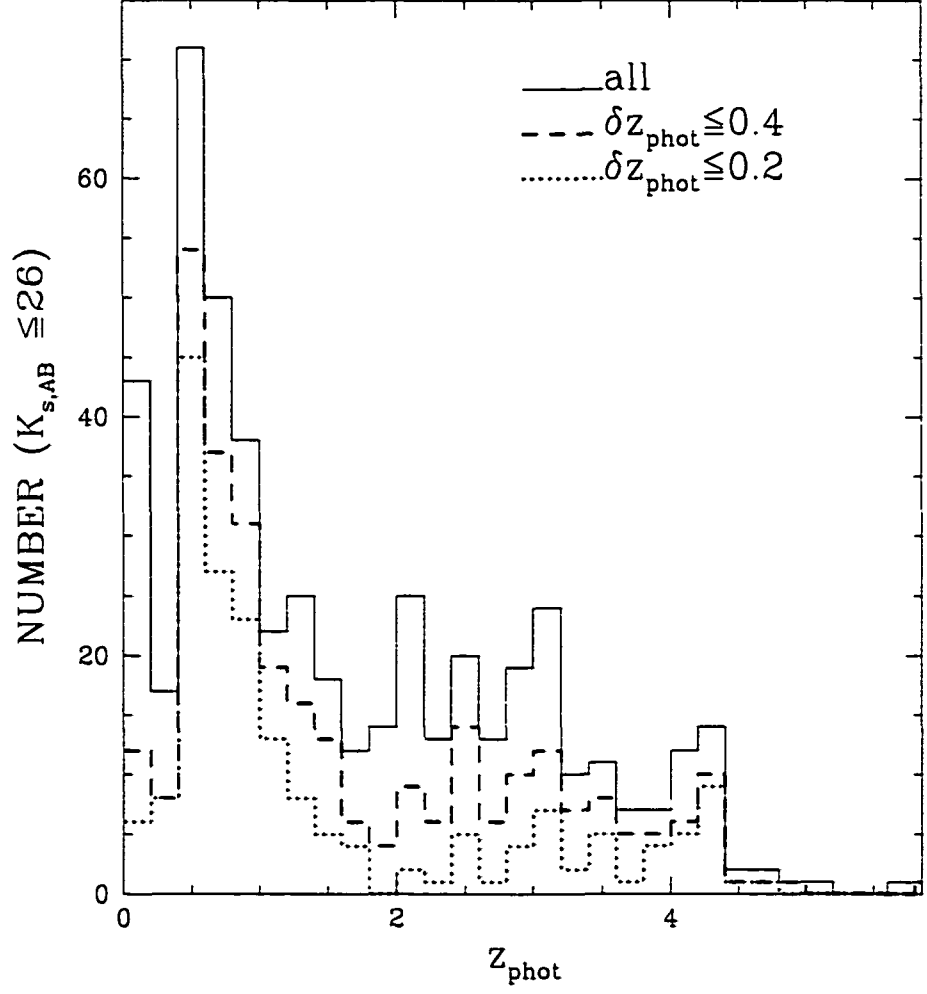


FIGURE 5.1. The photometric redshift histogram for the 492 galaxies in the  $K_{s,AB}^{\text{tot}} < 26$  sample with  $z_{\text{phot}} < 5.9$ . The different lines represent different uncertainty thresholds in  $z_{\text{phot}}$ . There are two galaxies at  $z_{\text{phot}} > 9$  and one at  $z_{\text{phot}} = 5.9$  for which we doubt the redshift accuracy and which we do not plot.

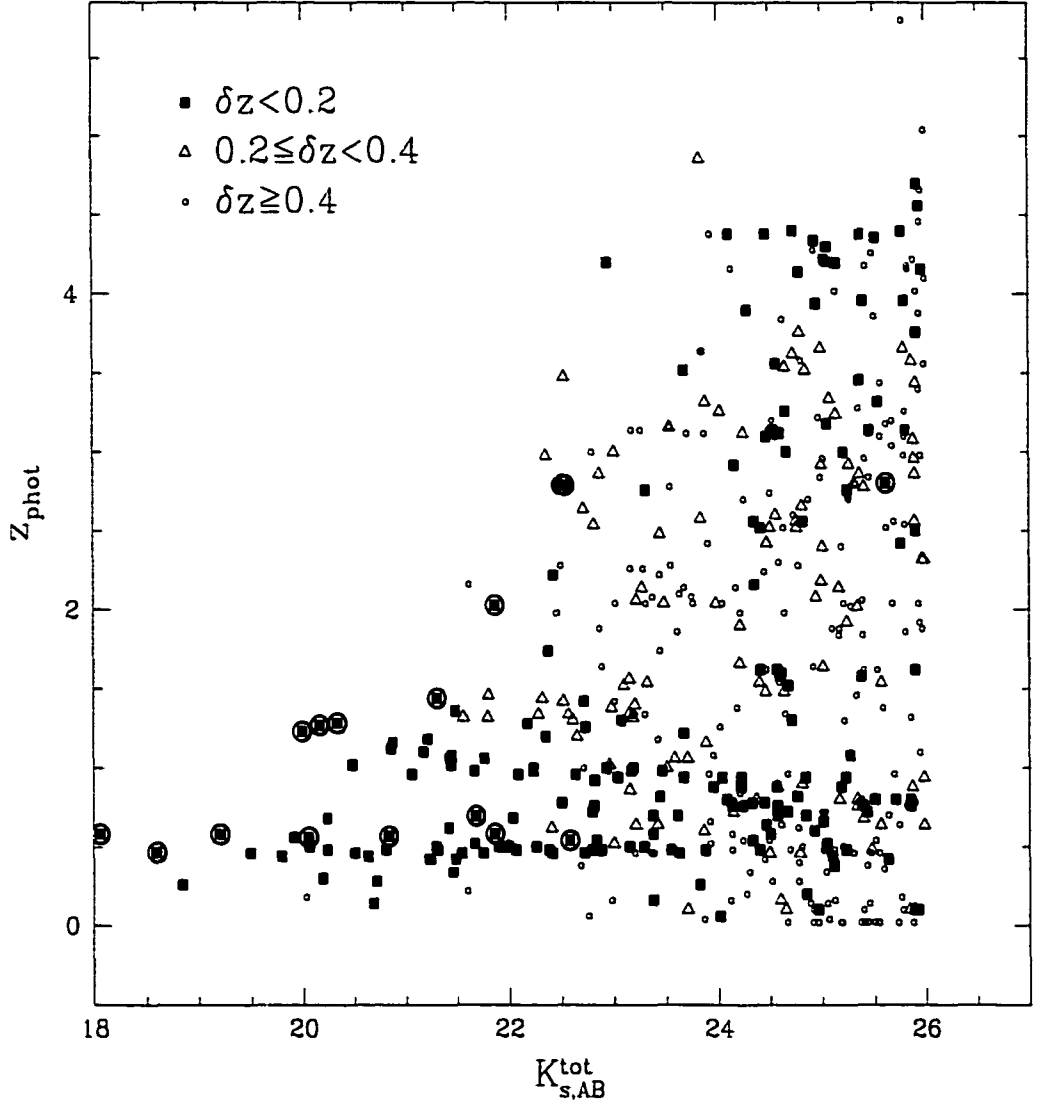


FIGURE 5.2. The photometric redshift vs. the K-band magnitude for the 492 galaxies in the  $K_{s,AB}^{\text{tot}} < 26$  sample with  $z_{\text{phot}} < 5.9$ . Points are circled which have spectroscopic redshifts. The broad enhancement at  $1 < z < 1.4$  seen in Chapter 2 is still there for the bright galaxies although it is not present in the fainter population. There are two galaxies at  $z_{\text{phot}} > 9$  and one at  $z_{\text{phot}} = 5.9$  for which we doubt the redshift accuracy and which we do not plot.

### 5.3 Rest-Frame Luminosities and Colors

To measure the rest-frame color and luminosity  $L^{\text{rest}}$  of a galaxy one must combine the redshift of the galaxy with the observed spectral energy distribution (SED), to estimate the intrinsic SED. To convert a redshift and an observed SED into a set of rest-frame luminosities and colors, it is necessary to make some assumptions about the intrinsic SED. In Chapter 2 we described our technique for measuring the rest-frame luminosity and will review it below. In this section we also describe two methods to measure the rest-frame colors and explain their advantages and disadvantages. Both methods calculate fluxes in redshifted, rest-frame filters based on the observed fluxes and then use sets of these rest-frame fluxes to compute the rest-frame colors. We will conclude this section with a discussion of how we estimate the uncertainty in the rest-frame color given an uncertainty in the redshift.

In this section we choose to study the rest-frame  $(U - B)$ ,  $(B - V)$ , and  $(U - V)$  colors ( $(U - B)_{\text{rest}}$ ,  $(B - V)_{\text{rest}}$ , and  $(U - V)_{\text{rest}}$ ) of our sample galaxies as these are historically the most commonly used colors for studying nearby galaxies and will better facilitate a direct comparison with local samples. The  $(U - V)_{\text{rest}}$  color combines the advantages of the  $(U - B)_{\text{rest}}$  and  $(B - V)_{\text{rest}}$  color; it samples the rest-frame optical redward of the Balmer/4000Å break, but also straddles the break itself, which is sensitive to the ratio of light which comes from stars older and younger than 1 Gyr. Because of its long wavelength baseline, this color is also less susceptible to small photometric errors. In §5.5 we will use  $(B - V)_{\text{rest}}$  to exploit theoretical relations between the color and stellar mass-to-light ratio.

How to best determine the rest-frame luminosities and colors from the observed quantities is not straightforward. Therefore, we describe it in some detail below.

### 5.3.1 Rest-Frame Photometric System

We measure  $U$ ,  $B$ , and  $V$  fluxes using the filter definitions defined by Bessell (1990). Specifically, we use the  $UX$ ,  $B$ , and  $V$  filters from Bessell (1990) and the zeropoints tabulated therein. The Bessell zeropoints are given as magnitude offsets with respect to a source which has constant  $f_\nu$  and  $AB = 0$ . The  $AB$  magnitude is defined as

$$AB_\nu = -2.5 * \log_{10} \langle f_\nu \rangle - 48.58 \quad (5.1)$$

where  $\langle f_\nu \rangle$  is the flux  $f_\nu(\nu)$  observed through a filter  $T$  and in units of  $\text{ergs s}^{-1} \text{cm}^{-2} \text{Hz}^{-1}$ . Given the zeropoint offset  $ZP_\nu$  for a given filter, the Vega magnitude  $m_\nu$  is then

$$m_\nu = AB_\nu - ZP_\nu = -2.5 * \log_{10} \langle f_\nu \rangle - 48.58 - ZP_\nu. \quad (5.2)$$

All of our observed fluxes and rest-frame template fluxes are expressed in  $f_\lambda$ . To obtain rest-frame magnitudes in the Bessell (1990) system, we must calculate the conversion from  $f_\lambda$  to  $f_\nu$  for the redshifted rest-frame filter set. The flux density of an SED with  $f_\lambda(\lambda)$  integrated through a given filter with transmission curve  $T(\lambda)$  is

$$\langle f_\lambda \rangle = \frac{\int f_\lambda(\lambda') T'(\lambda') d\lambda'}{\int T'(\lambda') d\lambda'} \quad (5.3)$$

or

$$\langle f_\nu \rangle = \frac{\int f_\nu(\nu') T'(\nu') d\nu'}{\int T'(\nu') d\nu'}. \quad (5.4)$$

Since

$$\int f_\lambda(\lambda') T'(\lambda') d\lambda' = \int f_\nu(\nu') T'(\nu') d\nu' \quad (5.5)$$

we can convert to  $\langle f_\nu \rangle$  through

$$\langle f_\nu \rangle = \langle f_\lambda \rangle * \frac{\int T'(\lambda') d\lambda'}{\int T'(\nu') d\nu'} \quad (5.6)$$

and use  $\langle f_\nu \rangle$  to calculate the apparent rest-frame Vega magnitude through the redshifted filter via Eq. 5.2.

### 5.3.2 Rest-Frame Magnitudes and Luminosities

In Chapter 2 we described a method to measure the rest-frame luminosities of a galaxy  $L_U^{rest}$ ,  $L_B^{rest}$ , and  $L_V^{rest}$  by integrating the best-fit template combination at  $z_{phot}$ . From now on we refer to this as the DTI (direct template integration) method. This method makes the strong assumption that the intrinsic SED is well modeled by our template set and that the templates span the full range of galaxy SEDs. We know that for many galaxies the best-fit template is good at matching qualitatively the position and strength of the spectral breaks and the general shape of the SED. There are, however, galaxies in our sample which are poorly fit by any template combination. But even for the qualitatively good fits, the model and observed flux points can differ by  $\sim 10\%$ . These mismatches between the data and the templates will lead to corresponding errors in the derived rest-frame colors. Therefore, we define below an alternative rest-frame luminosity estimate called the color-color relation (CCR) method, that relies less heavily on model templates.

#### *The Color-Color Relation Method*

We derive for any given redshift, the relation between the apparent AB magnitude  $m_{\lambda_z}$  of a galaxy through a redshifted rest-frame filter, its observed fluxes  $\langle f_{\lambda_i, obs} \rangle$  in the different filters  $i$ , and the colors of the spectral templates. At redshift  $z$ , the rest-frame filter with effective wavelength  $\lambda_{rest}$  has been shifted to an observed wavelength

$$\lambda_z = \lambda_{rest} \times (1 + z) \quad (5.7)$$

and we can define the adjacent observed bandpasses with effective wavelengths  $\lambda_l$  and  $\lambda_h$  which satisfy

$$\lambda_l < \lambda_z \leq \lambda_h. \quad (5.8)$$

We now define

$$C_{obs} \equiv m_{obs, \lambda_l} - m_{obs, \lambda_h} \quad (5.9)$$



where  $m_{obs,\lambda_l}$  and  $m_{obs,\lambda_h}$  are the AB magnitudes which correspond to the fluxes  $\langle f_{\lambda_l,obs} \rangle$  and  $\langle f_{\lambda_h,obs} \rangle$  respectively. We then shift each template in wavelength to the redshift  $z$  and compute,

$$C_{templ} \equiv m_{templ,\lambda_l} - m_{templ,\lambda_h}, \quad (5.10)$$

where  $m_{templ,\lambda_l}$  and  $m_{templ,\lambda_h}$  are the AB magnitudes through the  $\lambda_l$  and  $\lambda_h$  observed bandpasses (including the atmospheric and instrument throughputs). We sort the templates by their  $C_{templ}$  values,  $C_{templ,a}$ ,  $C_{templ,b}$ , etc., and find the two templates such that

$$C_{templ,a} \leq C_{obs} < C_{templ,b}. \quad (5.11)$$

We then define for the  $a^{\text{th}}$  template

$$C_{\lambda_l,z,a} \equiv m_{templ,\lambda_l} - m_{templ,\lambda_z} \quad (5.12)$$

where  $m_{templ,\lambda_z}$  is the apparent AB magnitude of the  $a^{\text{th}}$  template through the redshifted  $\lambda_{rest}$  filter. We point out that because our computations always involve colors, they are not dependent on the actual template normalization (which cancels out in the difference). Taking our observed color  $C_{obs}$  and the templates with adjacent “observed” colors  $C_{templ,a}$  and  $C_{templ,b}$ , we can interpolate between  $C_{\lambda_l,z,a}$  and  $C_{\lambda_l,z,b}$

$$m_{obs,\lambda_l} - m_{\lambda_z} = C_{\lambda_l,z,a} + (C_{obs} - C_{templ,a}) \times \left( \frac{C_{\lambda_l,z,b} - C_{\lambda_l,z,a}}{C_{templ,b} - C_{templ,a}} \right) \quad (5.13)$$

and solve for  $m_{\lambda_z}$ .

When  $C_{obs}$  lies outside the range of the  $C_{templ}$ ’s, we simply take the two nearest templates in observed  $C_{templ}$  space and extrapolate Eq. 5.13 to compute  $m_{\lambda_z}$ .

Equation 5.13 has the feature that  $m_{\lambda_z} \approx m_{obs,\lambda_l}$  when  $\lambda_z = \lambda_l$  (and hence when  $C_{\lambda_l,z,a}$  and  $C_{\lambda_l,z,b} \approx 0$ ). While this method still assumes that the templates are reasonably good approximations to the true shape of the SEDs it has the advantage that it does not rely on exact agreement. Galaxies whose observed colors fall outside the range of the templates can also be easily flagged. A final advantage of this method

is that the uncertainty in  $m_{\lambda_z}$  can be readily calculated from the errors in the observed fluxes.

From the apparent magnitude through the redshifted  $\lambda_{rest}$  filter,  $m_{\lambda_z}$ , we compute the rest-frame luminosity by applying the K-correction and converting to luminosity units

$$\frac{L^{rest}}{L_{\odot}} = 10^{-0.4(m_{\lambda_z} - M_{\odot, \lambda_{rest}} - ZP_{\lambda_{rest}})} \times \left( \frac{D_L}{10pc} \right)^2 \times (1+z)^{-1} \times h^{-2} \quad (5.14)$$

where  $M_{\odot, \lambda_{rest}}$  is the absolute magnitude of the sun in the  $\lambda_{rest}$  filter

( $M_{\odot, U} = +5.66$ ,  $M_{\odot, B} = +5.47$ , and  $M_{\odot, V} = +4.82$  in Vega magnitudes; Cox 2000),  $ZP_{\lambda_{rest}}$  is the zeropoint in that filter (as in Eq. 5.2 but expressed at  $\lambda$  and not at  $\nu$ ), and  $D_L$  is the distance modulus in parsecs. As in Chapter 2, we correct this luminosity by the ratio of the  $K_s^{tot}$  flux to the  $2''0$  diameter aperture flux. This adjustment factor has a mean of 40% and a median of 24%.

Using this method, we now plot in Figure 5.3 the rest-frame luminosities vs. redshift and enclosed volume for the galaxies in the  $K_{s, AB}^{tot} < 26$  FIRES sample. The points represent different ranges of redshift uncertainty. Since the derived luminosity is tightly coupled to the redshift, we do not plot  $L^{rest}$  errorbars. The tracks indicate our  $L^{rest}$  detection limit for different SEDs shapes. The intersection of the tracks in each panel indicates the redshift at which the rest-frame filter passes through our  $K_s$ -band detection filter. At all redshifts there is a wide range in rest-frame luminosities. As expected, we are much more sensitive than in Chapter 2 and are complete at  $z \approx 2$  to approximately  $0.1-0.2 L_*$  (as defined from local samples; Folkes et al. 1999; Blanton et al. 2001). We find that there are many galaxies at  $z > 2$ , in all bands, with  $L^{rest} \geq L_*$ . As noticed in Chapter 2, we also find a deficit of bright galaxies at  $1.5 \lesssim z \lesssim 2$  although this deficit is not as pronounced at lower values of  $L^{rest}$ . The values of  $L^{rest}$  are listed in Table A.10.

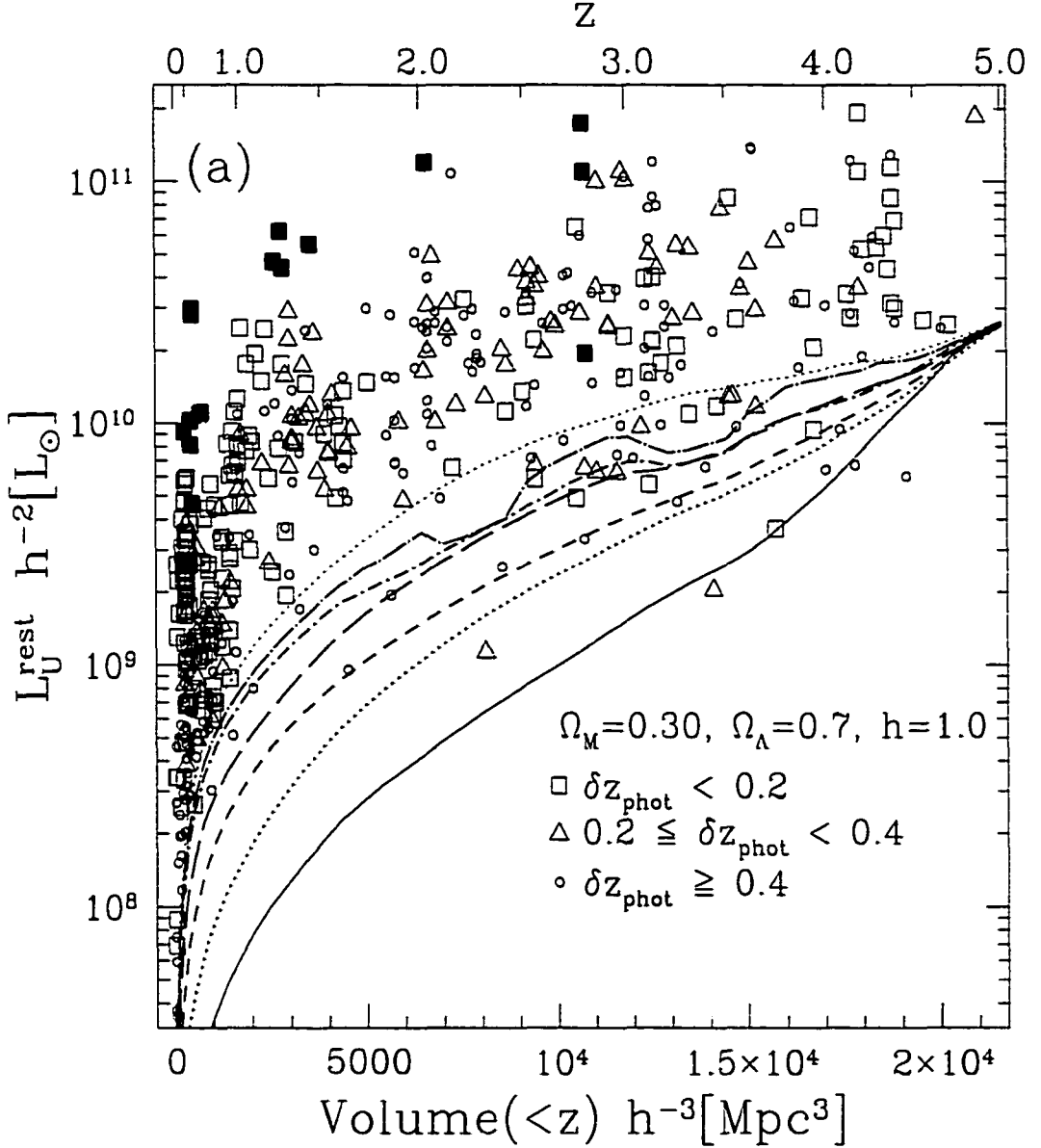
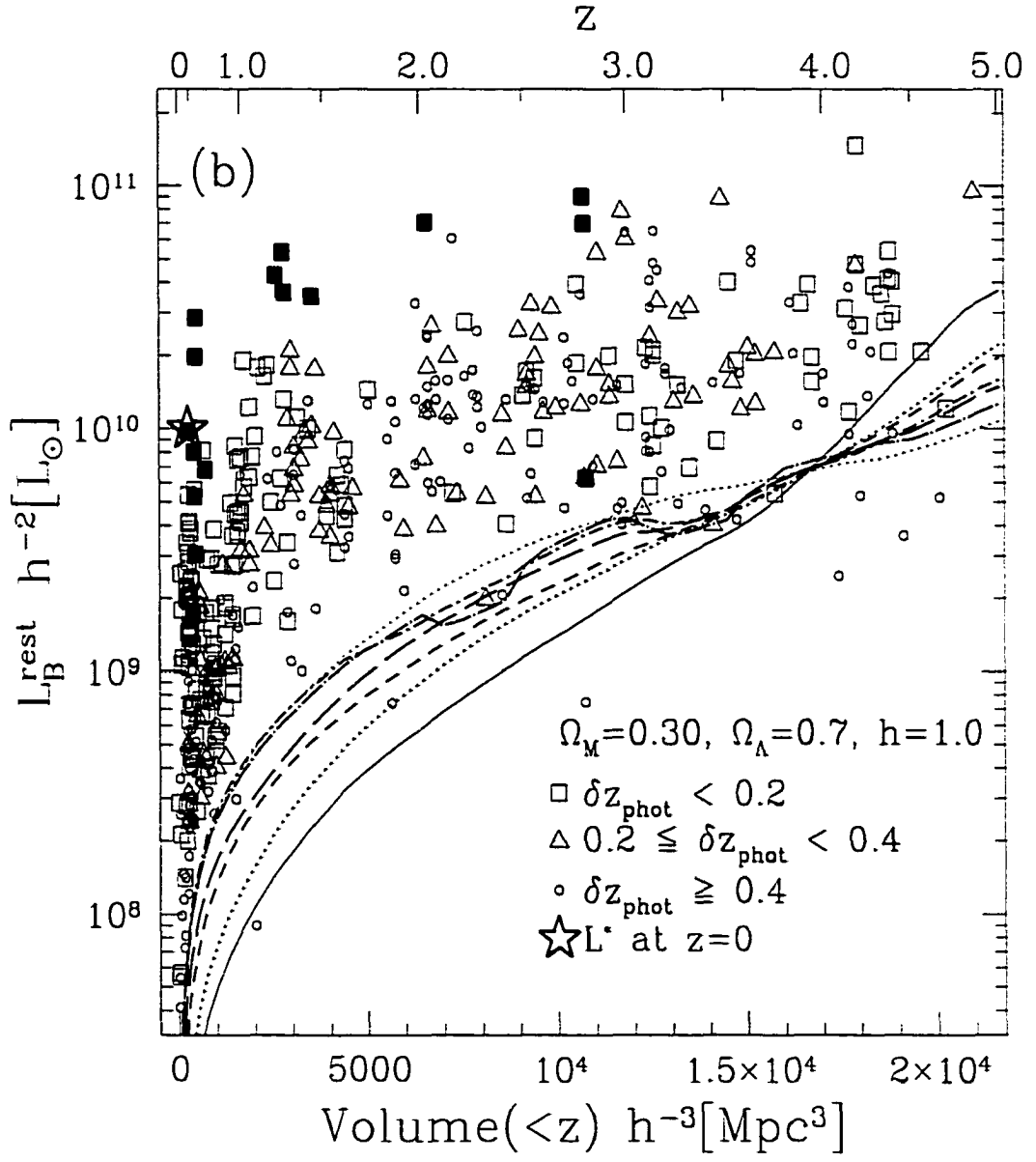
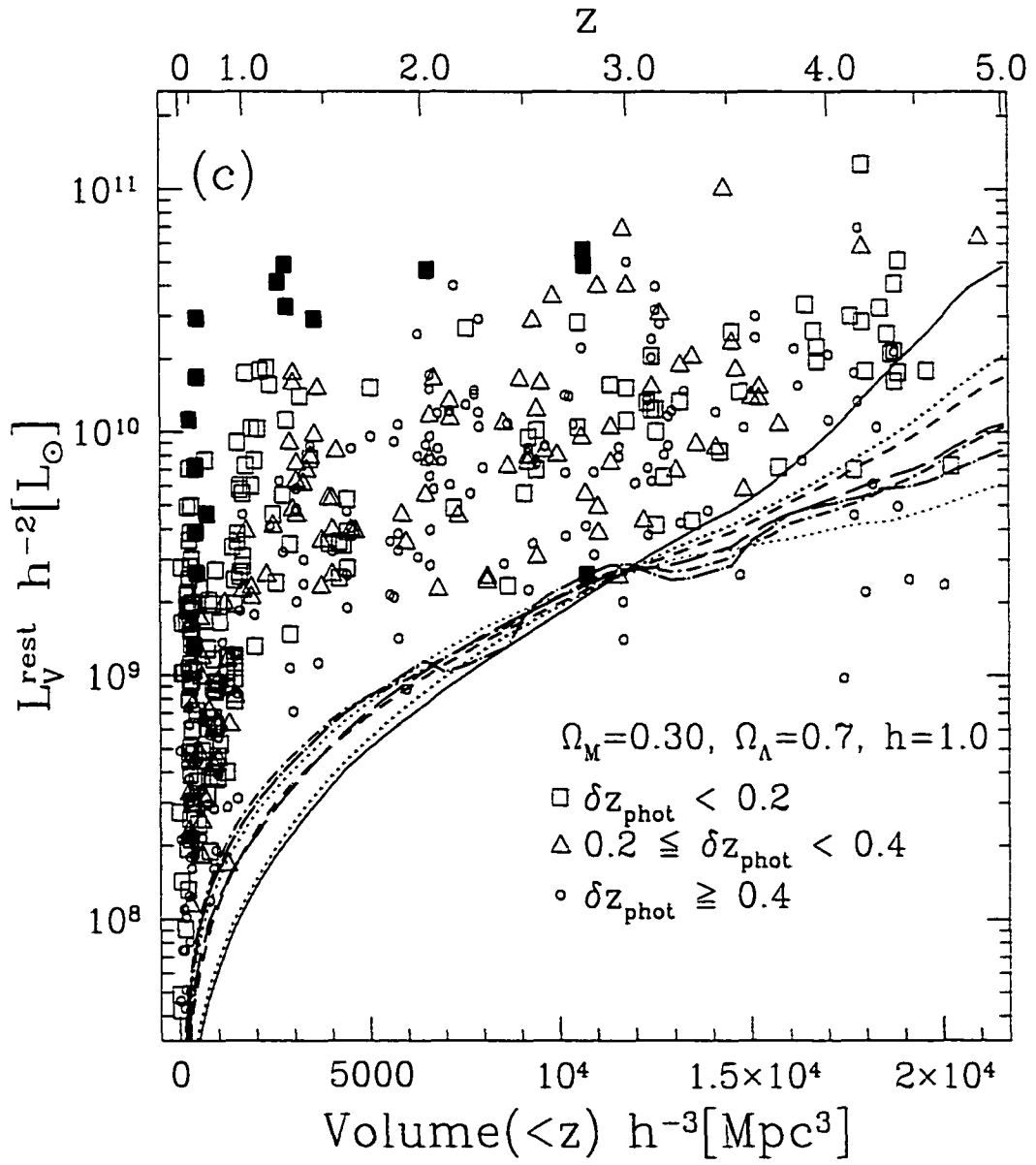


FIGURE 5.3. The distribution of rest-frame U, B, and V-band luminosities as a function of enclosed co-moving volume and  $z_{\text{phot}}$  is shown in figures a, b, and c respectively. We show all galaxies with  $K_{s,AB}^{\text{tot}} < 26$ . Galaxies which have spectroscopic redshifts are represented by solid points. Note the presence of galaxies at  $z_{\text{phot}} \geq 2$  with  $L^{\text{rest}} \geq 5 \times 10^{10} h^{-2} L_\odot$ . The tracks represent the values of  $L^{\text{rest}}$  for each of our six template spectra normalized at each redshift to  $K_{s,AB}^{\text{tot}} = 26$ . The large star in b) indicates the value of  $L_{*,B}$  from local surveys. The specific tracks correspond to the E (solid), Sbc (dot), Scd (short dash), Irr (long dash), SB1 (dot-short dash), SB2 (dot-long dash), and 10my (dot) templates.





### 5.3.3 Color Measurement Techniques

Using both methods described in §5.3.2 we computed the rest-frame colors from the rest-frame magnitudes (after expressing the DTI rest-frame luminosities in magnitudes). We first converted all the  $m_{\lambda_z}$ 's to Vega magnitudes by applying the Bessel zeropoints and then define, for example,  $m_{B,z}$  as the apparent magnitude  $m_{\lambda_z}$  through the redshifted  $B$ -band filter. We then calculate the rest-frame colors from e.g.,

$$(B - V)_{rest} \equiv m_{B,z} - m_{V,z}. \quad (5.15)$$

#### *Emission Lines*

There will be emission line contamination of the rest-frame broad-band colors when rest-frame optical emission lines contribute significantly to the flux in our observed filters. Huchra (1977) found that this effect was not significant for nearby, morphologically normal galaxies. Eisenhardt & Dickinson (1992) found, however, that the emission line contributions to NIR filters can be significant for high redshift radio galaxies although lines in these galaxies can be unusually strong. P01 estimated the effect of emission lines in the NICMOS F160W filter and the  $K_s$  filter using emission line strengths from the nearby starburst templates of Kinney et al. (1996) and from the rest-frame optical spectra of Pettini et al. (2001). They found that redshifted, rest-frame optical emission lines, whose equivalent widths are at the maximum end of those observed for starburst galaxies (rest-frame equivalent width  $\sim 200\text{\AA}$ ), can contribute up to 0.2 magnitudes in the NIR filters. They concluded, however, based on the fitting of templates to observed LBG SEDS, that the emission lines in typical high redshift star-forming galaxies did not noticeably effect their fits. Without knowing beforehand the strength of emission lines in any of our galaxies we can only acknowledge that the emission lines might introduce color changes of  $\lesssim 0.2$  for the bluest galaxies.

### 5.3.4 Color Uncertainties and Method Comparison

The uncertainty in the derived color has contributions both from the uncertainty in the observed fluxes and from the uncertainty in the redshift, which causes  $\lambda_z$  to move with respect to the observed filters. The first effect is estimated by propagating the observed flux errors through Eq. 5.13, including the covariances (Press, Vetterling, Teukolsky, Flannery, 1992). Because different rest-frame magnitudes can and do rely on the same observed passbands, the errors in the rest-frame magnitudes are correlated and cross terms must not be ignored; in practice, the resulting color error will be less than that assumed if one ignored the off-diagonal terms in the covariance matrix. To reduce the contributions of the flux errors to the color errors we will consider only objects with  $K_{s,AB}^{\text{tot}} < 25$  when determining colors; this is one magnitude brighter than our limiting magnitude and corresponds to a  $K_s$ -band signal-to-noise of  $\approx 7$  in our 2''0 aperture.

To account for the redshift dependent error in the calculated color, we use the Monte-Carlo simulation described in chapters 2 and 3. For each Monte-Carlo iteration we calculate the rest-frame colors and determine their 68% confidence limits. We find that the contributions to the total error budget are dominated by the redshift errors rather than by the flux errors and we choose for simplicity, to consider only the redshift dependent errors. The 68% confidence limits in color can be highly asymmetric, just as for  $z_{\text{phot}}$ . The rest-frame colors and their errors for all objects with  $K_{s,AB}^{\text{tot}} < 25$  are shown in Table A.11.

To assess the agreement between the two different color measurement techniques we plot in Figure 5.4 as a function of redshift the difference between rest-frame colors derived using the “direct template integration” (DTI) method and the “color-color relation” (CCR) method. We separate the data both by a magnitude cut and by a threshold in the derived color error. We extend each plot to the highest redshift where the rest-frame filters are still bracketed by our observed set ( $z \leq 4.0$  for  $(U - B)_{\text{rest}}$

and  $z \leq 3.2$  for  $(B - V)_{rest}$ . As can be seen from Figure 5.4, for most redshifts there is little or no systematic offset between the two methods, although the  $(U - B)$  template colors are systematically bluer at higher redshifts. In both plots, the scatter tends to decrease with the more stringent quality cut, although this is most evident for  $(B - V)$ . Most of the improvement in the scatter comes from the  $K_{s,AB}^{tot}$  cut although some far outliers are flagged by the color error threshold. Objects with large differences in color as measured with the CCR and DTI methods are always fit poorly by the best-fit SED in the rest-frame optical and may have large contributions from emission lines. These few objects will not effect the following analyses.

When separating the points in Figure 5.4 by their rest-frame color we find for both  $(U - B)_{rest}$  and  $(B - V)_{rest}$ , that the rest-frame optically blue galaxies have CCR colors which are systematically bluer than those derived by the DTI method and that the rest-frame optically red galaxies have CCR colors which are systematically redder than those derived by the DTI method. This effect likely occurs because our templates, with their limited color range, artificially truncate the true color distribution at the blue and red ends while the CCR method is allowed to freely extrapolate to redder and blue colors.

### *The Effect of Redshift Errors*

Errors in  $z_{phot}$  will also cause errors in the rest-frame color estimate. To determine the magnitude of these errors, we plot in Figure 5.5  $(B - V)_{rest}$  determined at  $z_{spec}$  vs.  $(B - V)_{rest}$  determined at  $z_{phot}$  for all of the objects in the HDF-S with  $z_{spec}$  determinations and good photometry (Chapter 3). The colors measured at  $z_{phot}$  lie  $\approx 0.07$  above those measured at  $z_{spec}$  but the disagreement is matched by the size of our color errors; the mean disagreement decreases to  $\lesssim 1\%$  when only considering the three galaxies with  $z_{spec} > 2$ .



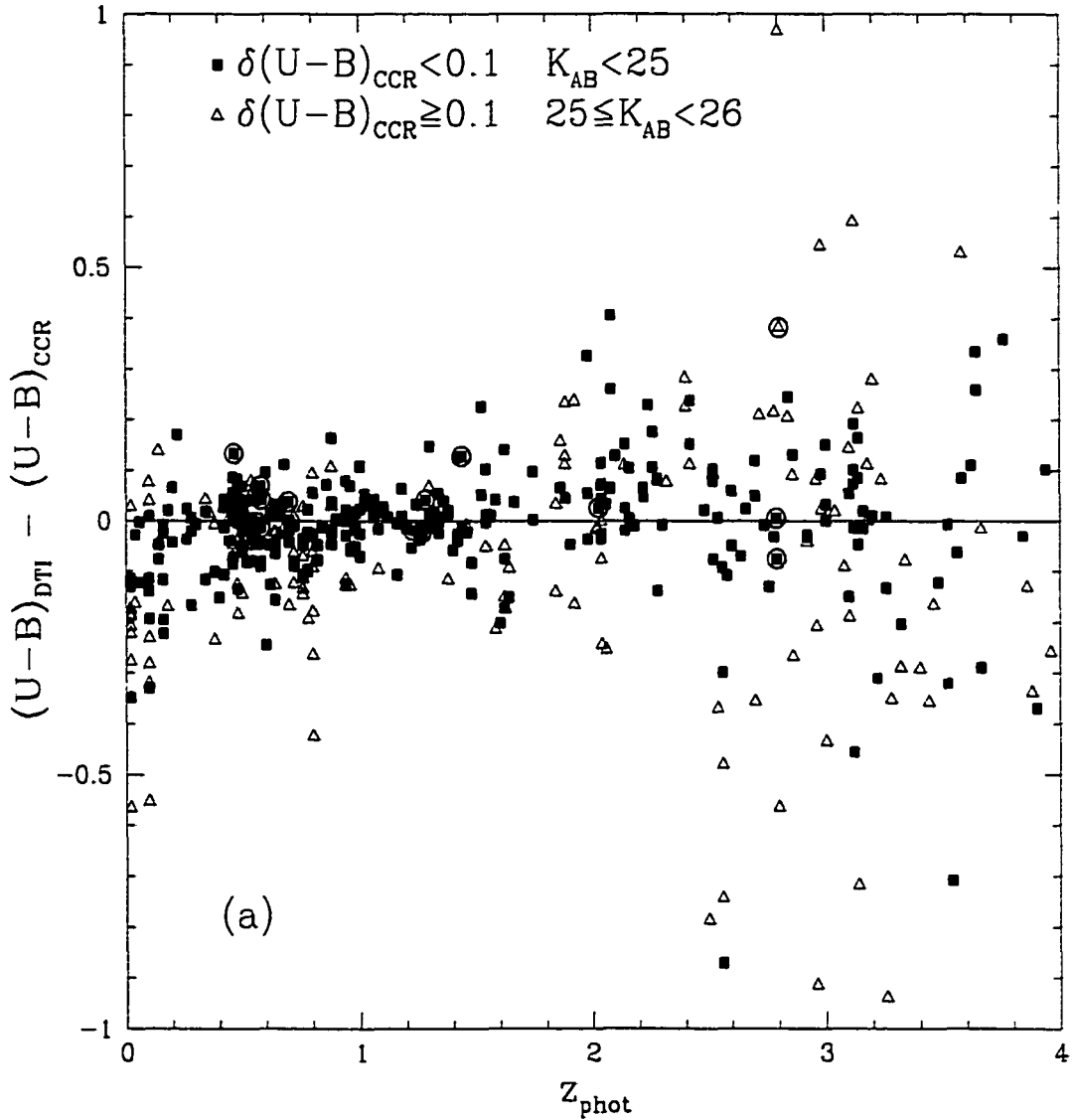
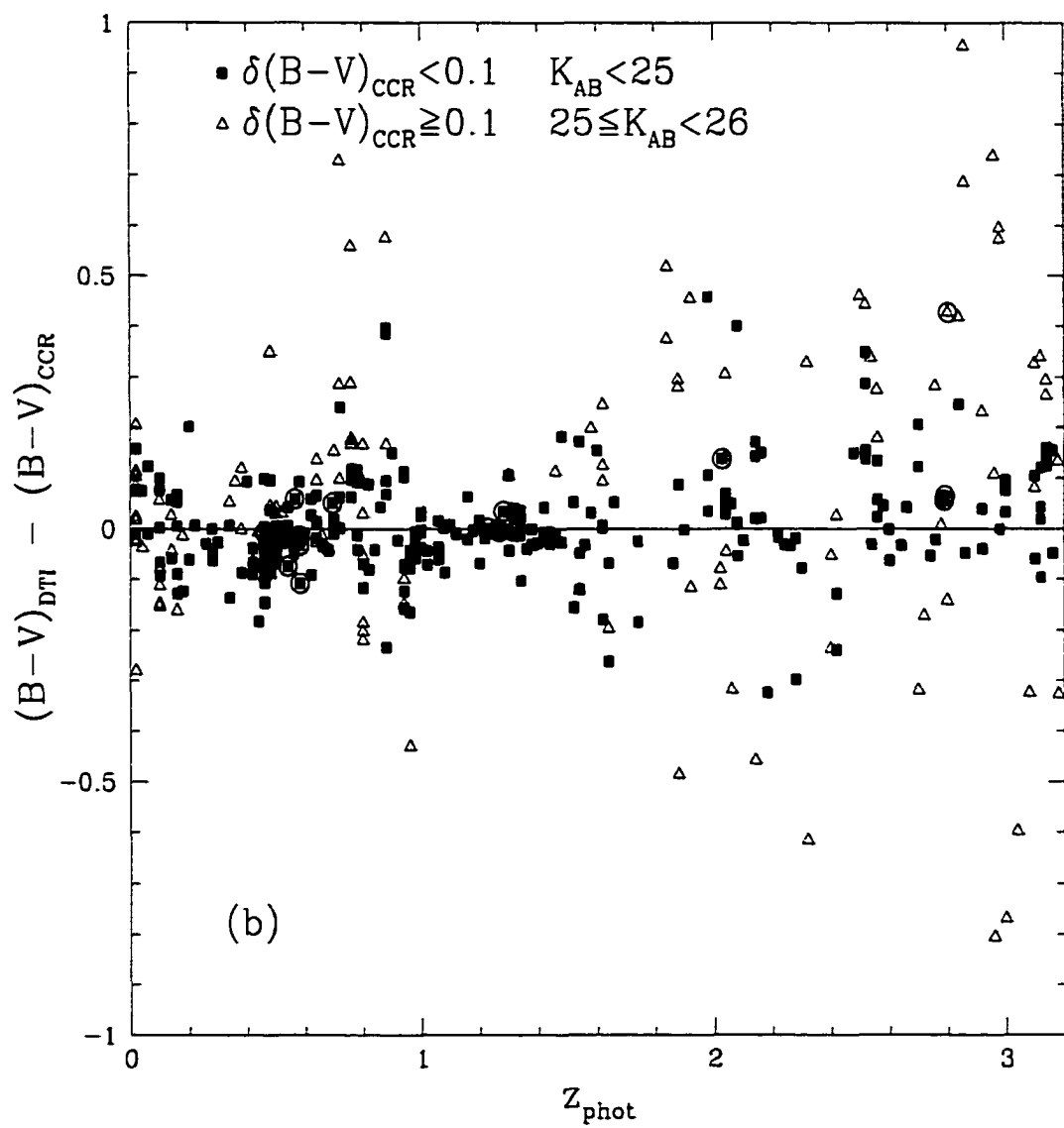


FIGURE 5.4. A comparison, as a function of redshift, of the difference in rest-frame colors derived from the “direct template integration” (with  $_{DTI}$  subscript) versus the colors derived from the “Color-Color Relation” method (with  $_{CCR}$  subscript). Objects are divided both by their apparent magnitude and by their derived color error. Objects with spectroscopic redshifts have circled points. In **a**) we show the  $(U - B)$  color while in **b**) we show the  $(B - V)$  color. Both plots are extended to the highest redshift where the reddest rest-frame filter in that color remains inside the  $K_s$ -band transmission curve. The two types of points represent two different quality regimes. Most of the improvement in the scatter of the solid points comes from the magnitude cut.



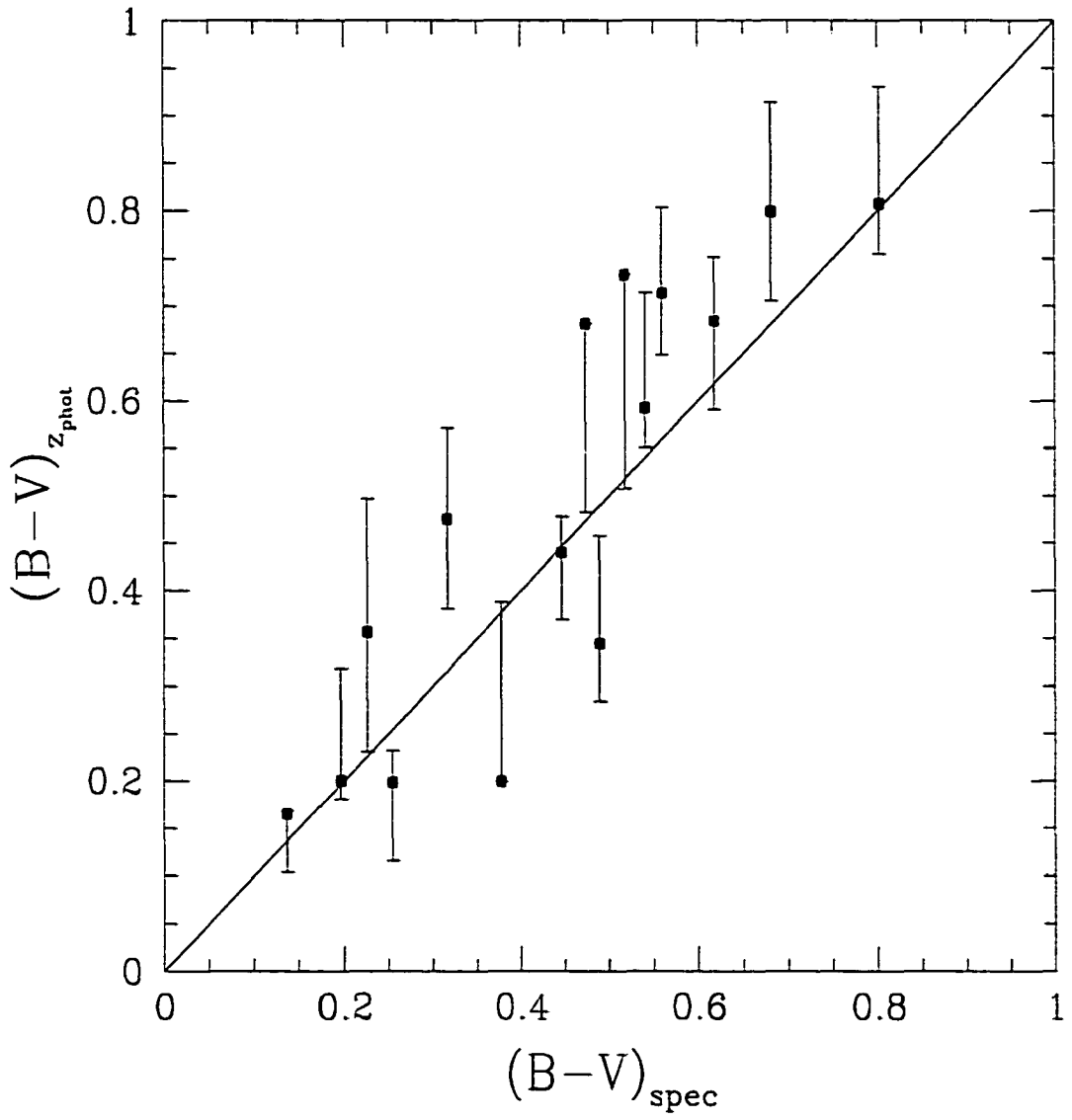


FIGURE 5.5. A comparison of the  $(B-V)_{\text{rest}}$  colors derived at  $z_{\text{phot}}$  and at  $z_{\text{spec}}$ .

## 5.4 Rest-Frame Color Analysis

We now take our set of rest-frame colors, luminosities, and redshift estimates over a wide range in  $z$ , compare them to local values, examine their interrelationships, and study their evolution with redshift.

### 5.4.1 Local Comparison

Larson & Tinsley (1978) pointed out that morphologically normal galaxies follow a tight sequence in  $(U - B)$  vs.  $(B - V)$  space and that the general shape and scatter of the relationship can be explained by simple monotonic SFHs. The position of a galaxy on this sequence is a function of its specific SFH, initial mass function (IMF), dust content, and metallicity. The tight relation occurs for galaxies with monotonically declining SFHs because changes in the IMF, age, dust extinction, and metallicity tend to move galaxies parallel to the relation. A relation of similar shape, but higher scatter, was shown to exist for members of the *Atlas of Peculiar Galaxies* (Arp, 1966; Larson & Tinsley, 1978). The higher scatter was interpreted as being due to very large dust extinctions and the effects of complex SFHs including large bursts of recent star formation.

In Figure 5.6 we plot the  $(U - B)_{rest}$  colors vs. the  $(B - V)_{rest}$  colors for our  $K_{s,AB}^{tot} < 25$  sample out to  $z = 3.2$  for two different  $z$  and  $L^{rest}$  ranges. Our  $z = 2$  division between the low and high redshift panels divides the total FIRES survey volume out to  $z = 3.2$  in half. The points are coded by their color errorbars. The solid line represents the locus of nearby morphologically normal galaxies from Tinsley (1980). For  $L_V^{rest} \leq 10^{10} h^{-2} L_\odot$ , the Tinsley (1980) trend is followed at low redshift and the galaxies cover the entire locally defined color range but seem to be concentrated at the blue end. There is no obvious difference between the color distributions of intrinsically faint galaxies at low and at high redshifts. The intrinsically bright galaxies at low redshift lie directly on the locally defined locus, have a very small scatter, but do not

span the full range of normal, local galaxy colors. This, however, may simply be due to our poor statistics in this regime. In the high redshift bin, the intrinsically luminous galaxies still follow the local relation, but have a bluer mean color than those at low redshift. Even with the bluer mean color, however, there are still galaxies with high  $L^{\text{rest}}$  which lie at the red end of the sequence. Once better colors are available, by obtaining spectroscopic redshifts, we will be able to quantify the scatter in different luminosity and redshift bins and use this to determine how important starbursts are in the SFHs of our sample. We note that one object (HDFS2-163) has a very red  $(U - B)_{\text{rest}}$  color in comparison to its  $(B - V)_{\text{rest}}$  color. The  $(J_s - H)$  color for this object is very red, the  $(H - K_s)$  color is very blue and the NIR fluxes are fit poorly by the best-fit template. We regard the rest-frame color for this object to be unreliable and exclude it from all analyses.

To see how well the SEDs of the reddest galaxies at high redshift can be described by those of local galaxies we plot in Figure 5.7 the best-fit SEDs at  $z_{\text{phot}}$  for the 12 galaxies with  $2 < z_{\text{phot}} < 3.2$ ,  $K_{s,\text{AB}}^{\text{tot}} < 25$ ,  $(B - V)_{\text{rest}} > 0.4$ , and  $\delta z'_{\text{phot}} < 0.5$ . The observed SEDs are in general fit well by our local galaxy templates and some display strong, sharp breaks in their SEDs. Many of these SEDs with sharp breaks rise again to the blue giving some indication that the red rest-frame colors should be interpreted in the context of an older stellar population and not as a very high dust extinction. Only HDFS2-469 has very red colors and monotonically declines to the blue with no sign of a break, indicating that the rest-frame color is possibly due to a highly extincted stellar population. If this is true then the  $z_{\text{phot}}$  uncertainty may be underestimated. The values of  $z_{\text{phot}}$  for the other 11 galaxies are fairly secure, with almost all having small  $\delta z'_{\text{phot}}$  values and only HDFS2-699 having  $\gamma_{\text{alt}} > 10\%$ . Out of the six reddest galaxies, only the reddest galaxy, HDFS2-368, is fit very poorly in the rest-frame optical. Correspondingly, the differences between the DTI and CCR colors for this galaxy are very large and we consider this color measurement to be unreliable. We remove objects HDFS2-469 and HDFS2-368 from all analyses.

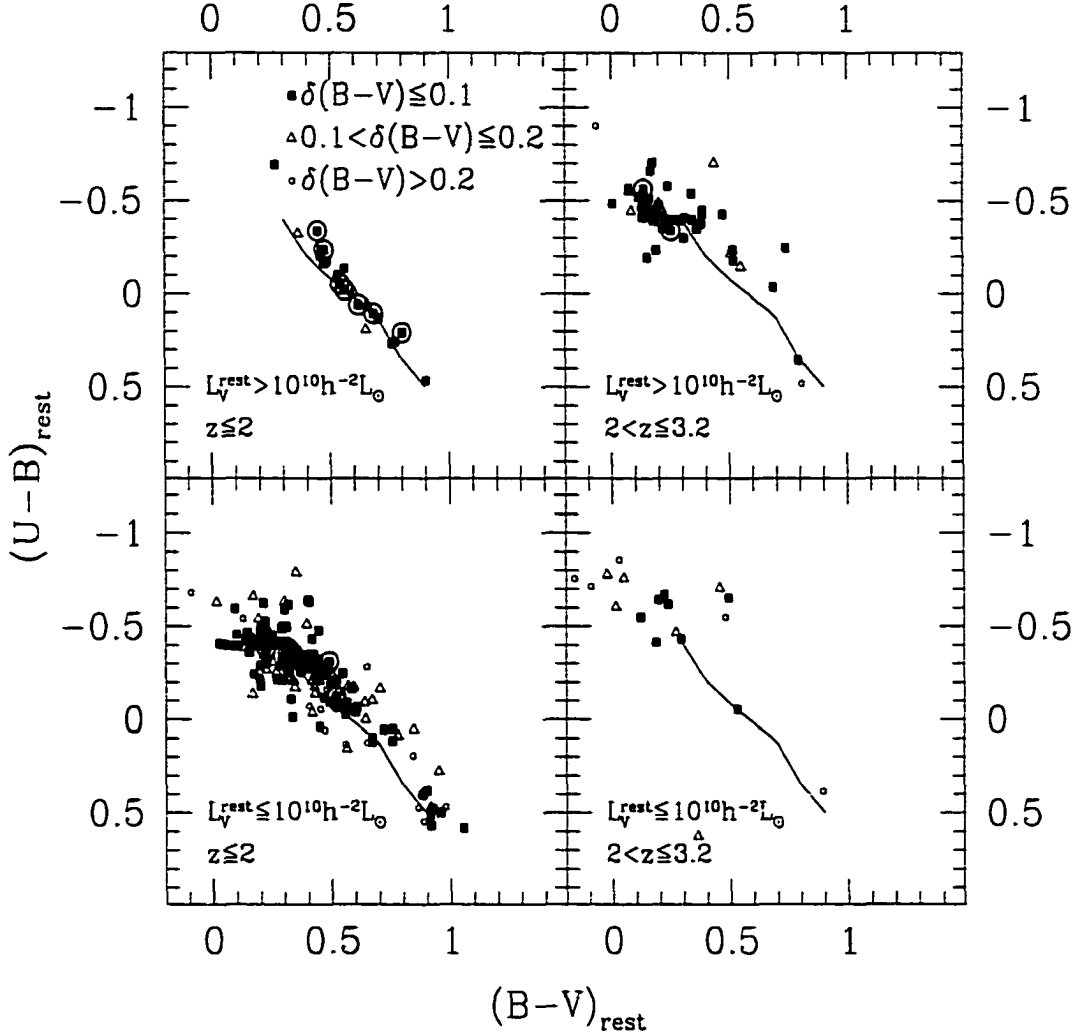


FIGURE 5.6. A comparison of  $(U - B)_{rest}$  to  $(B - V)_{rest}$  for the 294 galaxies with  $K_{s,AB}^{tot} < 25$  and  $z_{phot} < 3.2$ . The points represent different rest-frame color errorbars. Objects with spectroscopic redshifts have circled points. The black line is the locus of morphologically normal galaxies from Tinsley (1980). Our redshift separation divides the the total survey volume in half. The top panels contains objects with higher  $L_V^{rest}$  values, while the lower panels contain intrinsically fainter objects. Object HDFS2-163 at  $z_{phot} = 2.560$  in the lower-right panel has a normal  $(B - V)_{rest}$  but a very red  $(U - B)_{rest}$  caused by a very red observed  $(J_s - H)$  color.

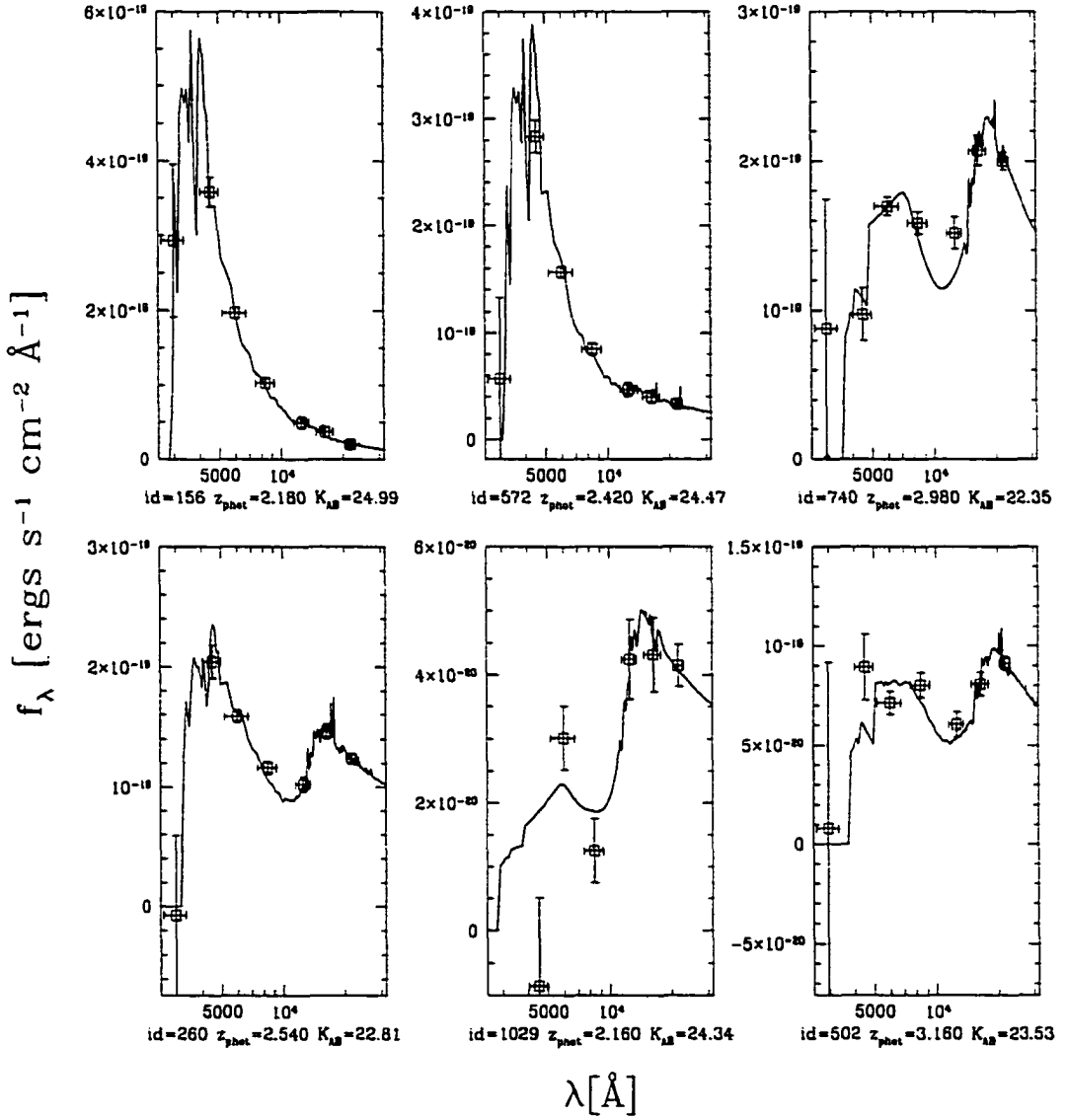
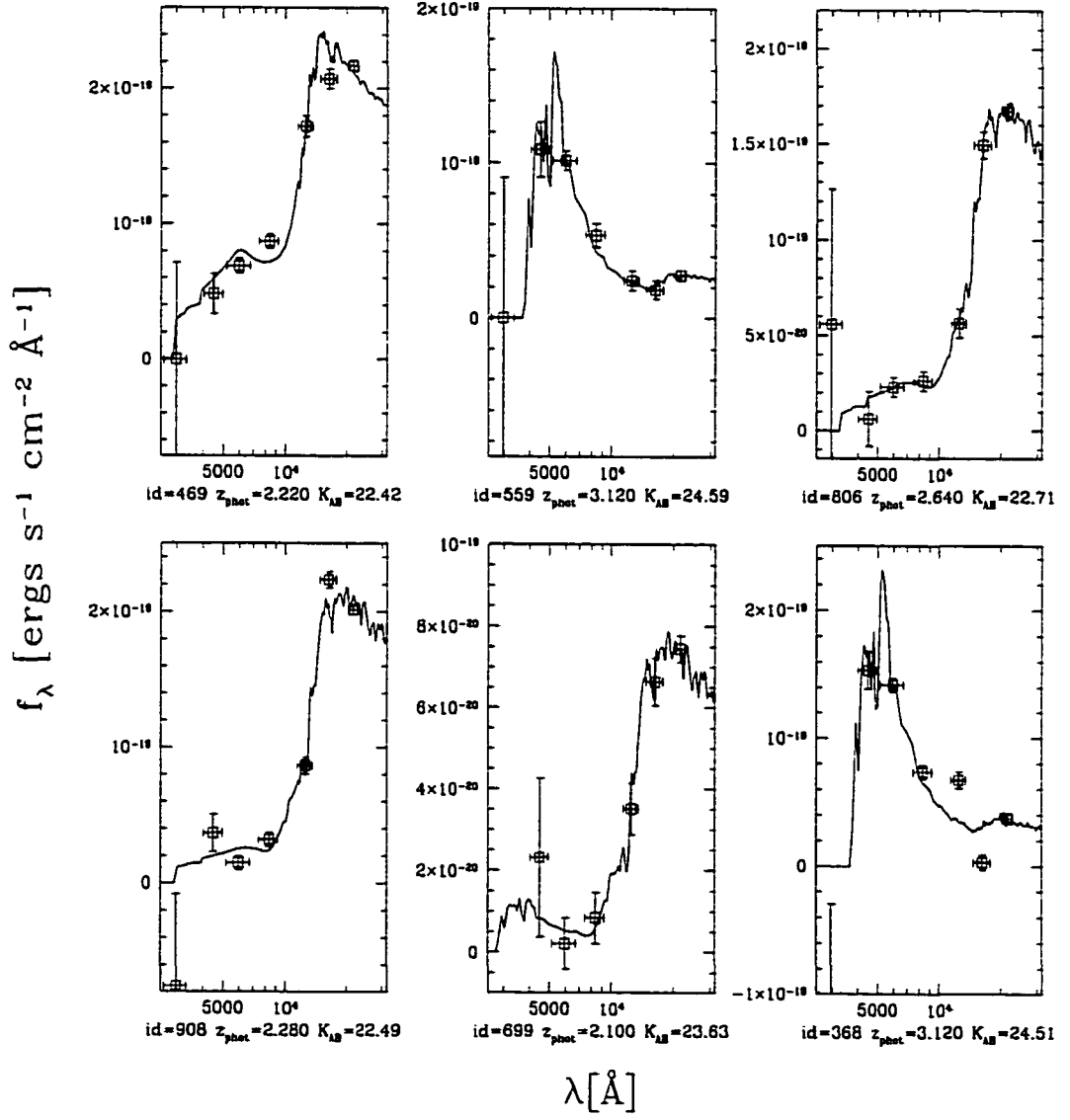


FIGURE 5.7. Plots of the best-fit spectral templates, at  $z_{\text{phot}}$ , to the 12 galaxies with the reddest  $(B - V)_{\text{rest}}$  colors,  $K_{s,\text{AB}}^{\text{tot}} < 25$ , and  $2 < z_{\text{phot}} < 3.2$ . The colors increase to the right and down in both panels. The observed SEDs are fit, in general, well by our local galaxy templates and only our reddest galaxy, HDFS2-368, has an obviously poor fit in the rest-frame optical.





### 5.4.2 Objects Missed by the Lyman Break Technique

In §5.4.1 we selected red galaxies based on their rest-frame optical colors. High redshift galaxies, however, have traditionally not been selected by their rest-frame optical flux, but by a strong observed break in their rest-frame UV SED (Steidel et al., 1996, 1999). We can use our data to search for galaxies which may have been missed by the  $U$ -dropout technique and to measure their rest-frame optical colors. Drawing on their very deep NICMOS data from HST P01 state that there are almost no galaxies at  $z > 2$  which would have been missed by the Lyman Break identification technique. We look for just such galaxies in the HDF-S by applying the  $U$ -dropout criteria of Madau et al. (1996):  $U_{300} - B_{450} > 1.3$ ,  $U_{300} - B_{450} > B_{450} - I_{814} + 1.2$ ,  $B_{450} - I_{814} < 1.5$ ,  $B_{450} < 26.79$ , and  $V_{606} < 28.0$ , where all magnitudes and colors are given in the AB magnitude system. In Tables A.10 and A.11 we indicate the galaxies flagged by the  $U$ -dropout criteria and compare the subset of this list with  $z_{phot} > 2$  to the galaxies with  $(B - V)_{rest} > 0.4$  and  $\delta z'_{phot} < 0.5$  that were shown in Figure 5.7. Of these 12 galaxies, four (HDFS2-260, 368, 559, and 572) would have been identified by the  $U$ -dropout technique and the others, which in many cases have large NIR magnitudes and  $L^{rest}$ , would not be selected even though they are bright enough to show up in the WFPC2 images. Three galaxies in particular (HDFS2-806, 699, and 908) have SEDs with strong rest-frame optical breaks and little or no flux in the rest-frame UV. These galaxies have  $(V_{606} - H)$  colors  $> 4$  and galaxies of this magnitude and color have not been found by P01 in the HDF-N. Their  $(V_{606} - H)$  colors are similar to the very red object HDF-N J123656.3+621322 from Dickinson et al. (2000), however they are significantly brighter ( $H_{AB} = 24.3$ , 23.4, and 23.0 for HDFS2-806, 699, and 908 respectively), and their  $(H - K_s)$  colors are significantly bluer. Unlike the Dickinson object, they also have  $S/N \gtrsim 5$  in the  $I_{814}$  band and their SEDs are fit well by a nearby Sbc galaxy. If we interpret the red colors of these objects as coming from a stellar population and not from excessive dust extinction, they are examples of evolved

galaxies at high redshifts. Red objects this bright would have been easily detected in the NICMOS sample but are not and their presence in the HDF-S highlights the field-to-field variance in small area surveys. Objects with fit well by Elliptical templates and de Vaucouleurs profiles were detected by Benítez et al. (1999) and Broadhurst & Bouwens (2000) at  $1 \lesssim z \lesssim 2$  with number and luminosity densities similar to that of nearby early type galaxies. Our three reddest galaxies (HDFS2-806, 699, and 908) which are fit by slightly later type templates might be interpreted as the higher redshift progenitors of these evolved galaxies at  $z \lesssim 2$ .

### 5.4.3 Redshift Evolution of the Color

To show the distribution of luminosities and colors we plot in Figure 5.8,  $L^{\text{rest}}$  vs. rest-frame color for three different redshift bins. In all figures the vertical, dotted line indicates the rest-frame color of our Scd template. As in Figure 5.3, the lack of intrinsically faint galaxies at high redshift is due to our magnitude limit, while the lack of intrinsically luminous galaxies in the low-redshift bin is due to the small co-moving volumes at  $z < 1$  in the HDF-S. This plot provides similar information as Figure 5.6; although most galaxies are blue at any redshift, in the highest redshift bins there are still intrinsically bright galaxies with colors of nearby, normal spirals and ellipticals.

#### *Comparison with Simple Models*

We next compared the redshift distribution of the rest-frame colors to a set of simple models. In Figure 5.9 we plot the rest-frame color vs. redshift for our  $K_{s,AB}^{\text{tot}} < 25$  sample in two different luminosity bins. We attempted to model the distribution of colors at different redshifts by creating tracks corresponding to simple exponential SFHs with  $z_{\text{form}} = 1000$  and exponential timescales  $\tau = 0.01, 1, 3$  Gyr, and  $\infty$ . We used the latest release of the Bruzual & Charlot models (Bruzual A. & Charlot, 1993; Liu, Charlot, & Graham, 2000) to construct color- $z$  tracks of galaxies with

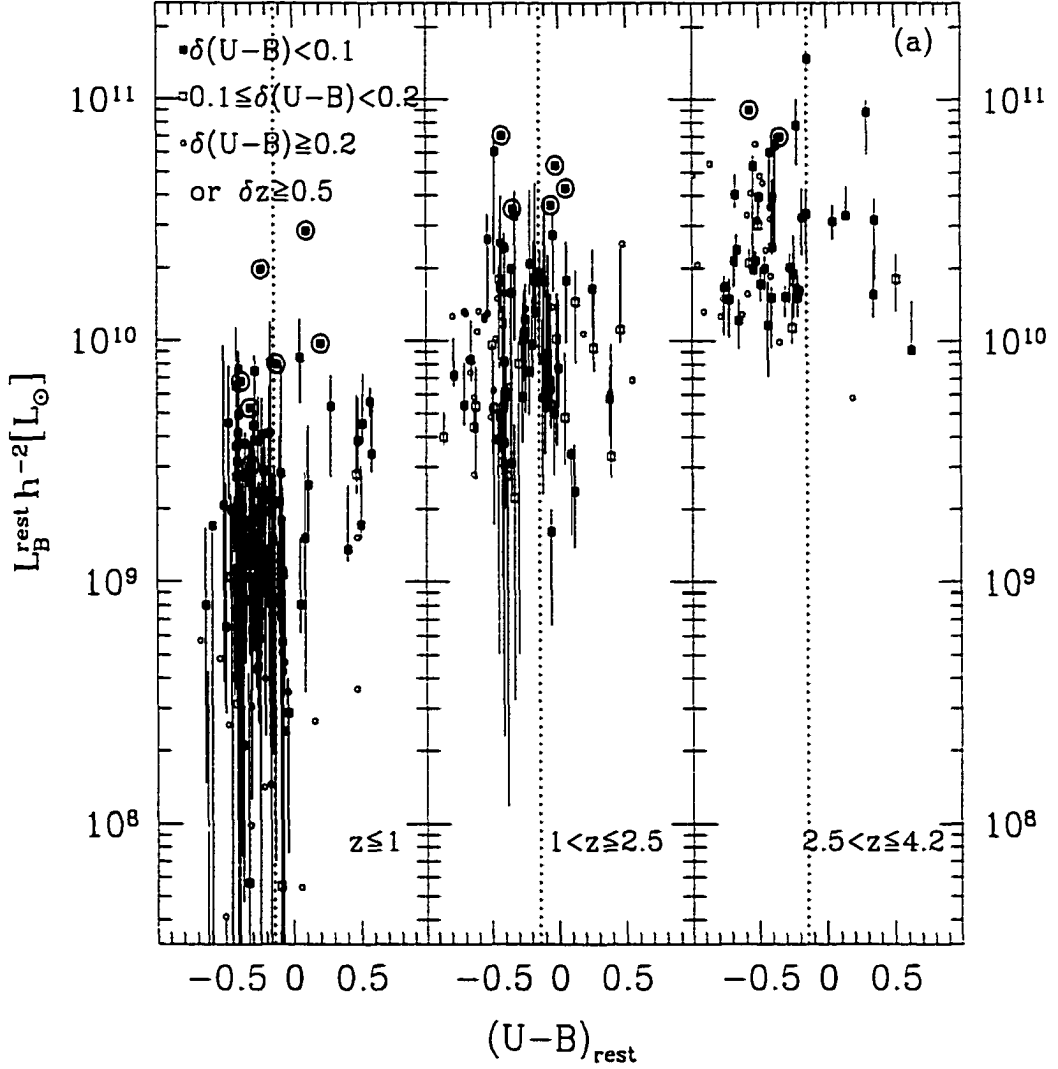
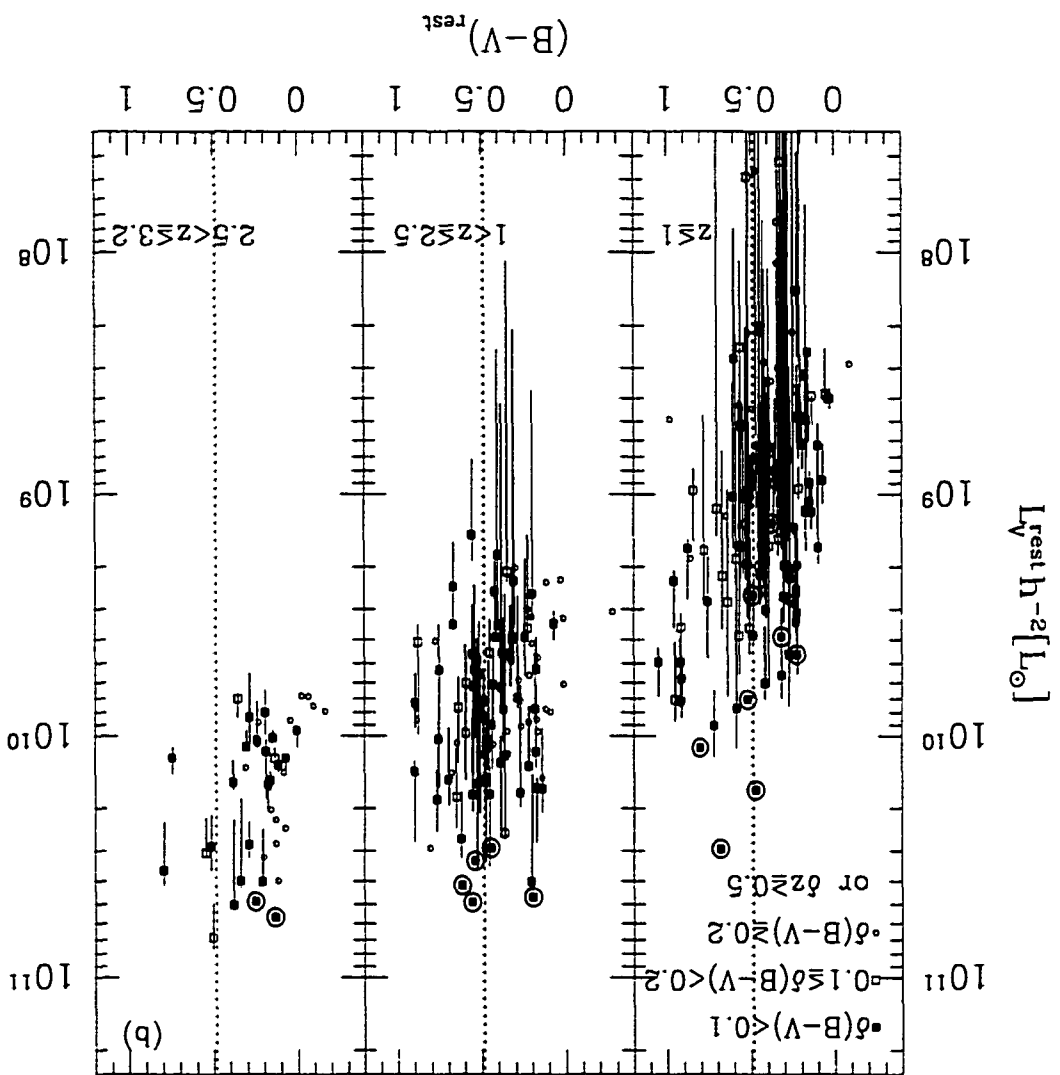
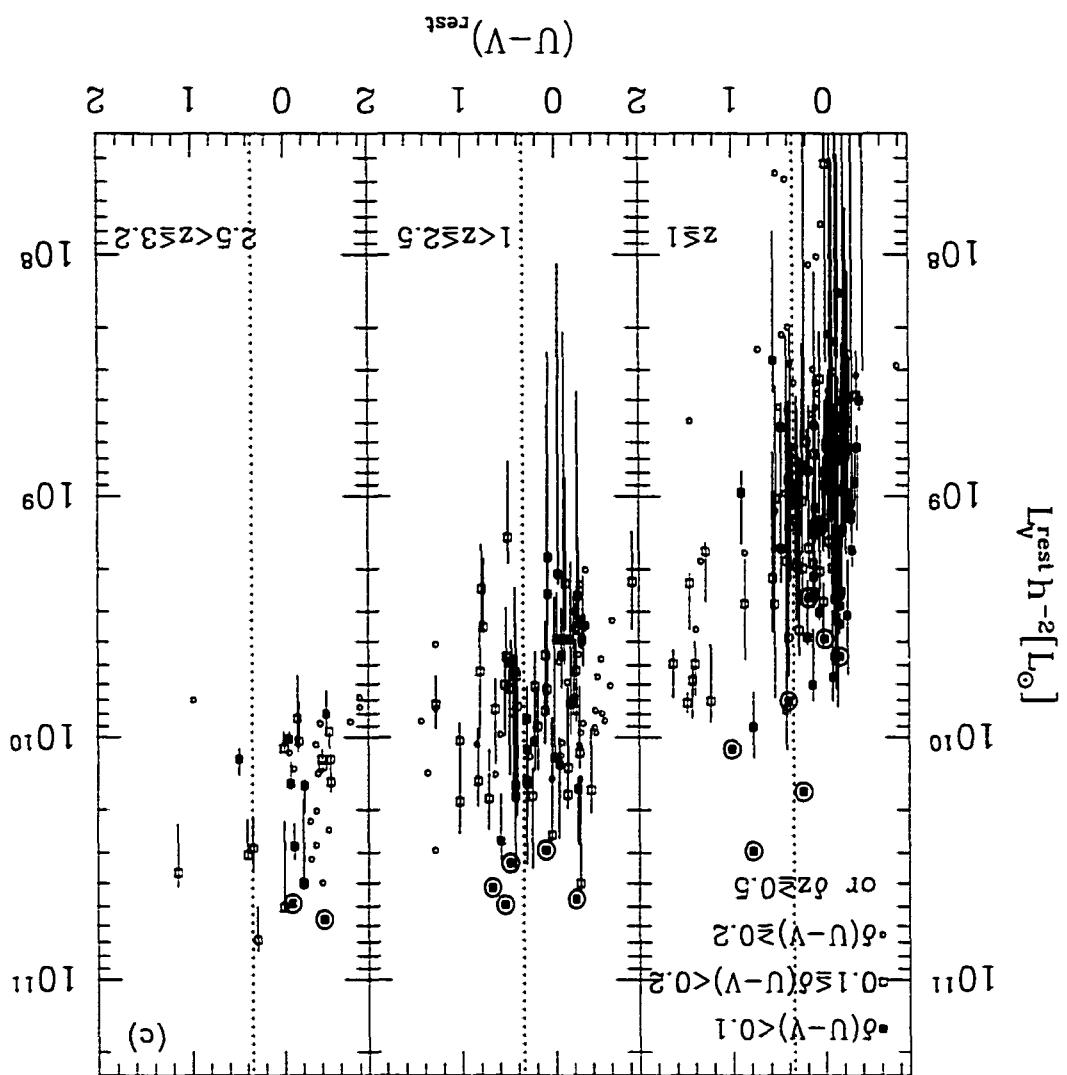


FIGURE 5.8. Rest-frame color vs. rest-frame luminosity for all galaxies with  $K_{s,AB}^{\text{tot}} < 25$ . In a) we plot  $(U-B)_{\text{rest}}$ , in b), and in c) we plot  $(U-V)_{\text{rest}}$ . We divide each plot into three redshift bins to highlight the redshift evolution of the color. The points are coded by the size of the redshift or color uncertainties. Objects with spectroscopic redshifts have circled points. The vertical dotted lines indicate the color of our Scd template. The different plots extend to different redshift limits reflecting the observed wavelength of the redder rest-frame filter. The lack of high luminosity galaxies at low redshift is mostly due to the low co-moving volume at  $z < 1$  while the lack of low luminosity galaxies at high redshift is due to our apparent magnitude limit. Note there are, at almost all redshifts and luminosities, galaxies as red as local spirals and ellipticals.





solar metallicity, a Salpeter (1955) IMF, and a  $0.1 - 100M_{\odot}$  mass range. Because we restricted ourselves to solar metallicity, we were able to use the empirical stellar spectra to generate our tracks and hence remove our dependence on the accuracy of the stellar atmosphere models. In Figure 5.9 we see that many of the galaxies fall within the range of colors defined by the simple evolutionary models although there are galaxies which fall outside the range of the tracks, especially to the blue.

To test how well the intrinsically bright galaxies can be described by these model tracks, we counted in two redshift bins the fraction of galaxies which lie in-between adjacent tracks and outside of the model color range. If these models describe the SFHs of the intrinsically bright galaxies, then the fractions between the tracks should be roughly constant with redshift i.e. the colors of galaxies whose SFHs are described by these tracks should follow lines of similar shape in color- $z$  space. We constructed 68% confidence limits on this fraction using a bootstrap technique where we resampled 300 times (with replacement) the full  $K_{s,AB}^{\text{tot}} < 26$  catalog and recounted the numbers of galaxies which satisfied our redshift and  $K_{s,AB}^{\text{tot}} < 25$  magnitude limit, and which lay in-between and outside the tracks. For all three rest-frame colors, the fraction of galaxies which lie above the reddest track and between the  $\tau = 0.01 - 1\text{Gyr}$  tracks remains constant with redshift at the  $1-\sigma$  level. It is hard to conclude much from this without information from the full SED. It is comforting to see that the galaxies get bluer with increasing redshift as expected.

## 5.5 Stellar Mass-to-Light Ratios and Masses

We have derived rest-frame colors for our sample of galaxies and identified galaxies at all redshifts with red rest-frame optical colors and high rest-frame optical luminosities. These red galaxies are less numerous than their blue counterparts but have high  $L^{\text{rest}}$  values and if coupled with a high  $\mathcal{M}/L$ , can contribute significantly to the stellar mass budget at a given redshift. In this section we describe how we derive rest-

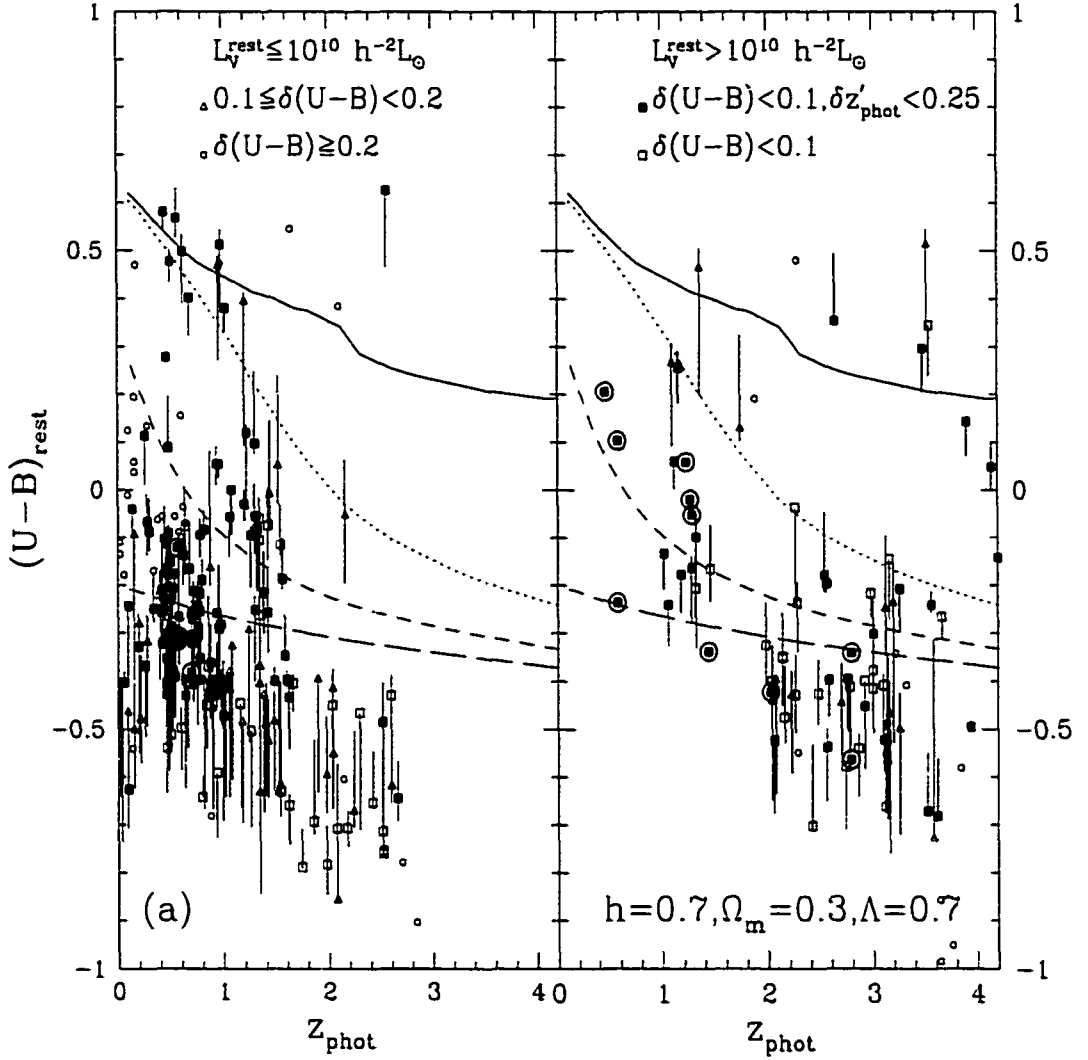
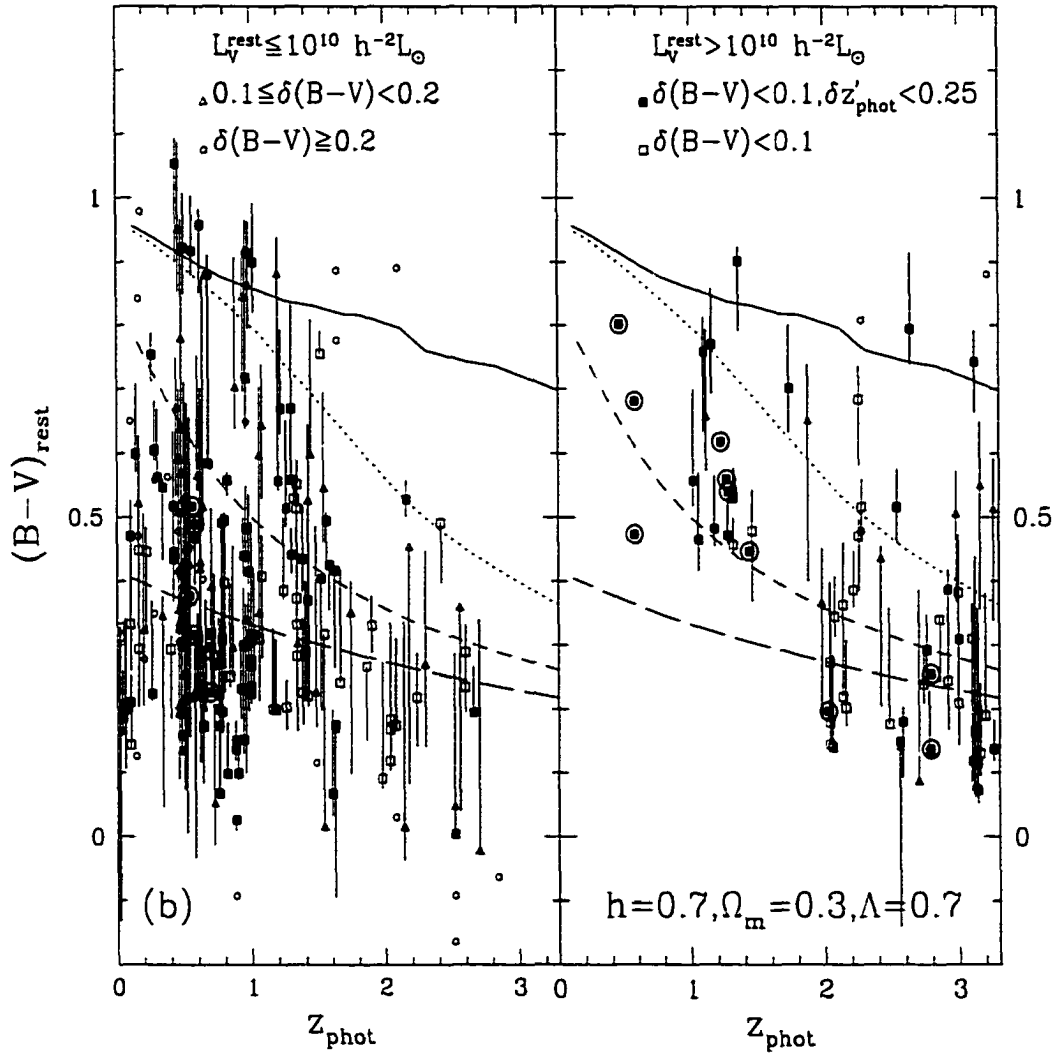
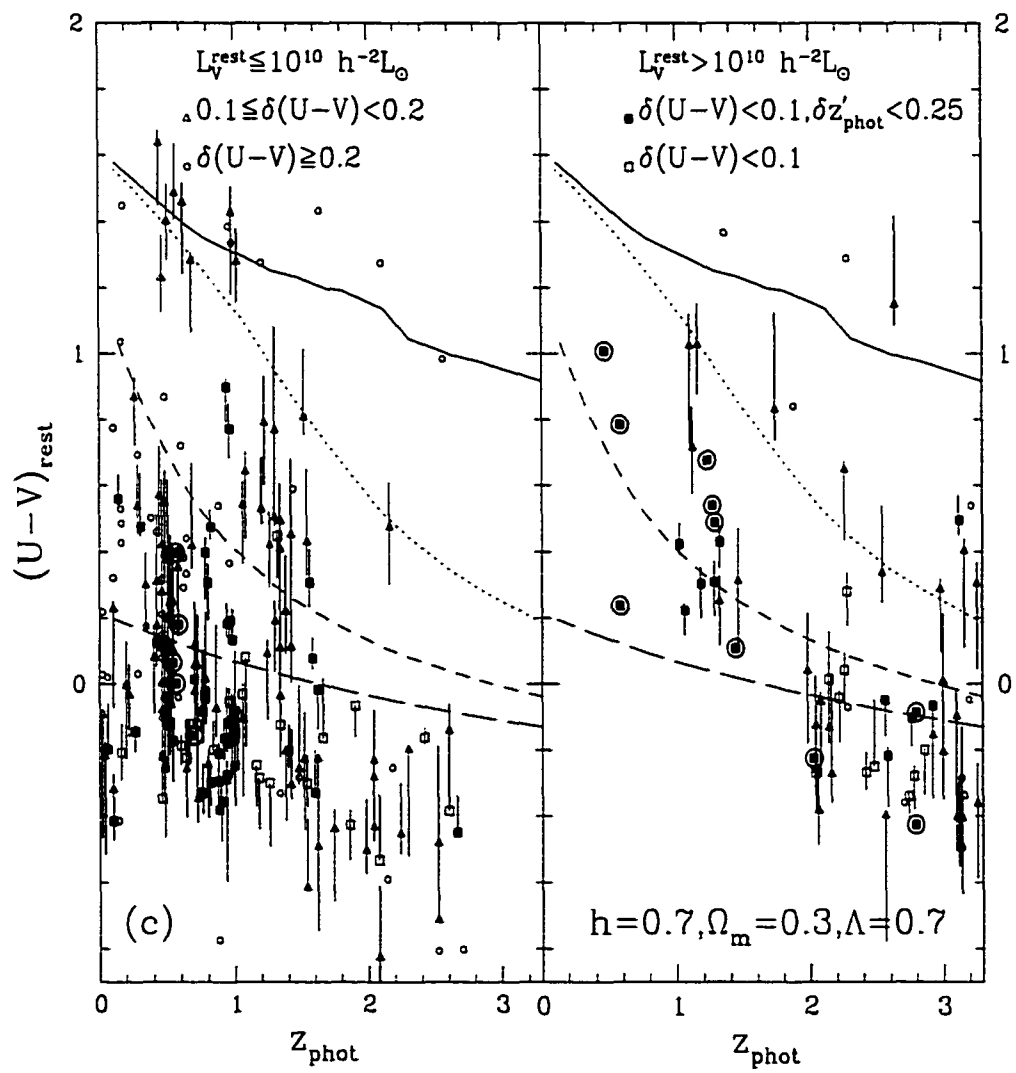


FIGURE 5.9. Rest-frame color vs. redshift for all galaxies with  $K_{s,AB}^{\text{tot}} < 25$ . In **a**) we plot  $(U - B)_{\text{rest}}$ ; in **b**) we plot  $(B - V)_{\text{rest}}$ , and in **b**) we plot  $(U - V)_{\text{rest}}$ . The left and right panels correspond respectively to intrinsically faint and luminous galaxies. The points are coded by the redshift and color uncertainties. The redshifts for each plot extend to where the reddest rest-frame filter shifts redward of the  $K_s$  filter. Objects with spectroscopic redshifts have circled points. The four lines correspond to simple exponential star formation histories of solar metallicity with  $z_{\text{form}} = 1000$  and exponential timescales of 0.01 Gyr (solid line), 1 Gyr (dotted line), 3 Gyr (short-dashed line). We also show a constant star formation rate model, and  $\infty$  (long-dashed line). For clarity, points with color uncertainties  $\geq 0.2$  do not have their errorbars shown.







frame optical  $\mathcal{M}/L$  values for our  $K_{s,AB}^{\text{tot}} < 25$  subsample from theoretical relations. We then use these  $\mathcal{M}/L$  values coupled with the our measures of  $L^{\text{rest}}$  to derive the stellar mass of each galaxy and examine the rest-frame color distribution of the most massive galaxies at all redshifts.

### 5.5.1 Rest-Frame Optical $\mathcal{M}/L$ 's

As shown by Tinsley (1980), the  $\mathcal{M}/L$  depends on a large number of parameters including IMF, metallicity, and age. Recently models have been constructed for the composite stellar populations of galaxies by BJ01 who used custom-built spectrophotometric galaxy models constructed to match the relations between the observed radial color gradients of local galactic disks and their structural parameters. Using these models, BJ01 found a tight, linear relation between optical color and  $\log_{10}(\mathcal{M}/L)$ . The cause for this correlation is seen in Figure 5.10 which is adapted from Figure 2 of BJ01 and which plots  $\mathcal{M}/L_B$  vs. color for a set of exponentially declining Bruzual & Charlot models. This relation is preserved in the presence of dust, metallicity, and SFH variations because these effects slide galaxies roughly parallel to the locus, changing their colors, but at the same time resulting in different  $\mathcal{M}/L$ 's. The zero-point and slope of this relation are insensitive to variations in the exact galaxy model used and are even insensitive low-level bursts of star formation in the SFH (BJ01). In addition, the slope of this relation is robust against different assumptions about the IMF and the specific population synthesis codes. Varying these assumptions however (particularly the IMF), changes the zeropoint by up to 0.5 dex and causes the absolute  $\mathcal{M}/L$ 's to be correspondingly uncertain. Unfortunately, we do not know which IMF to use since the nature of the IMF at high redshift is even more uncertain than in the local universe. While Pettini et al. (2000) found that the detailed rest-UV spectra of the LBG MS 1512-cB58 is described very well by a Salpeter IMF, Broadhurst & Bouwens (2000) speculate that the IMF is truncated at  $M > 2 M_{\odot}$  for early type

galaxies. Without considering truncation, further changing the slope of the IMFs leads to changes in the  $\mathcal{M}/L$  at a given color. Since more information on the IMF at high redshift does not exist we assume a universal IMF for simplicity's sake and adopt the Salpeter IMF. Even though the absolute masses may therefore be in error, under this assumption of a universal IMF we may still use the BJ01 relations to explore the *relative* masses of galaxies with different rest-frame colors assuming that the colors reflect the stellar populations which dominate the mass.

A problem arises because the BJ01 relations were derived using models of quiescently star-forming disks with only small bursts of star formation. Large bursts of star formation degrade the relationship between  $\mathcal{M}/L$  and color. In Figure 5.11 (adapted from Figure 5a of BJ01) we show the effect of a burst on the  $\mathcal{M}/L_B$  of an exponentially declining Bruzual & Charlot galaxy population. Bursts of star formation which produce 10% of the final galaxy mass will make objects rapidly bluer and can lower  $\log_{10}(\mathcal{M}/L_B)$  by a maximum of  $\sim 0.5$  dex. The effect of a burst on  $\mathcal{M}/L$  is greatest and most long lasting for red models, where the young population contributes a much larger fraction of the total luminosity (BJ01). For the bluer models, the effect is small but the  $\mathcal{M}/L$ 's can still be lowered by  $\sim 0.15$  dex. A galaxy with a given color will have its  $\mathcal{M}/L$  overestimated by the BJ01 technique if it is undergoing a burst of star formation. Because the colors of red galaxies become so readily blue in the presence of a burst, the fact that we still find galaxies with very red rest-frame colors indicates that the amount of recent star formation in bursts is small (or that the galaxy is very dusty) and that the BJ01 relation can be more reliably applied. The situation is not as clear for the blue galaxies. P01 found evidence for large bursts in the SFHs in LBGs and these inferred bursts, if present in the LBGs we observe, will cause us to underestimate their true  $\mathcal{M}/L$  and hence their stellar mass. Our data does not allow us to constrain the presence of bursts, so we can only apply the BJ01 relation with the caveat that our  $\mathcal{M}/L$ 's and masses will be lower if strong bursts of star formation are present.

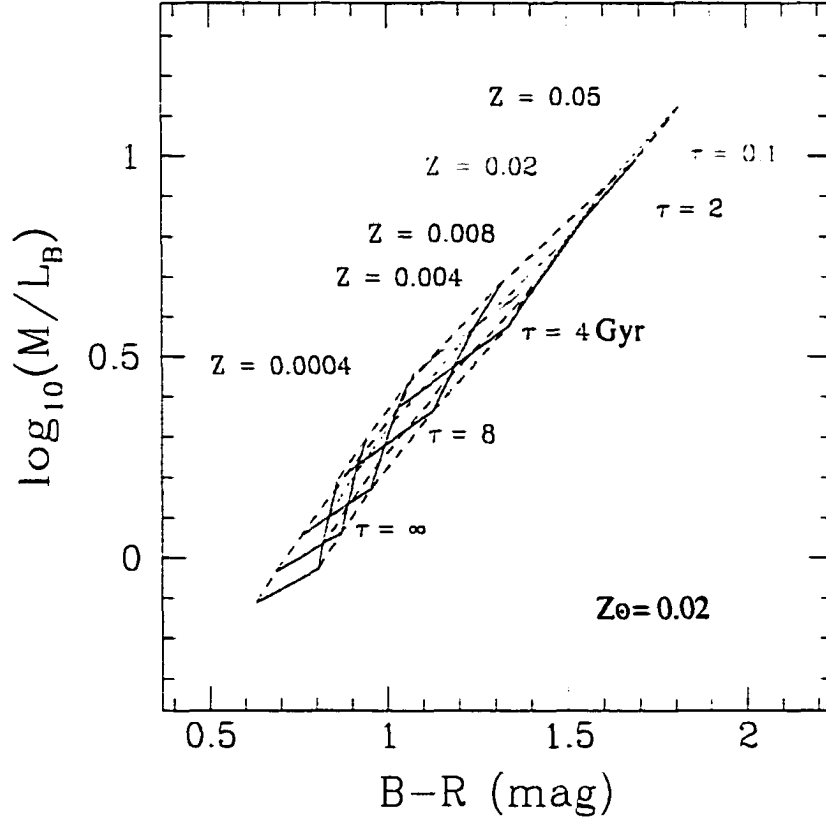


FIGURE 5.10. An example of the correlation between  $\log_{10}(M/L_B)$  and color adapted from Figure 2 of Bell & de Jong (2001). The color is different from that which we use, but still illustrates the relation. The tracks were generated using exponentially declining SFHs with different  $e$ -folding times and metallicities. Models with identical  $\tau$ 's are connected with solid lines and models with identical metallicity are connected by dotted lines.

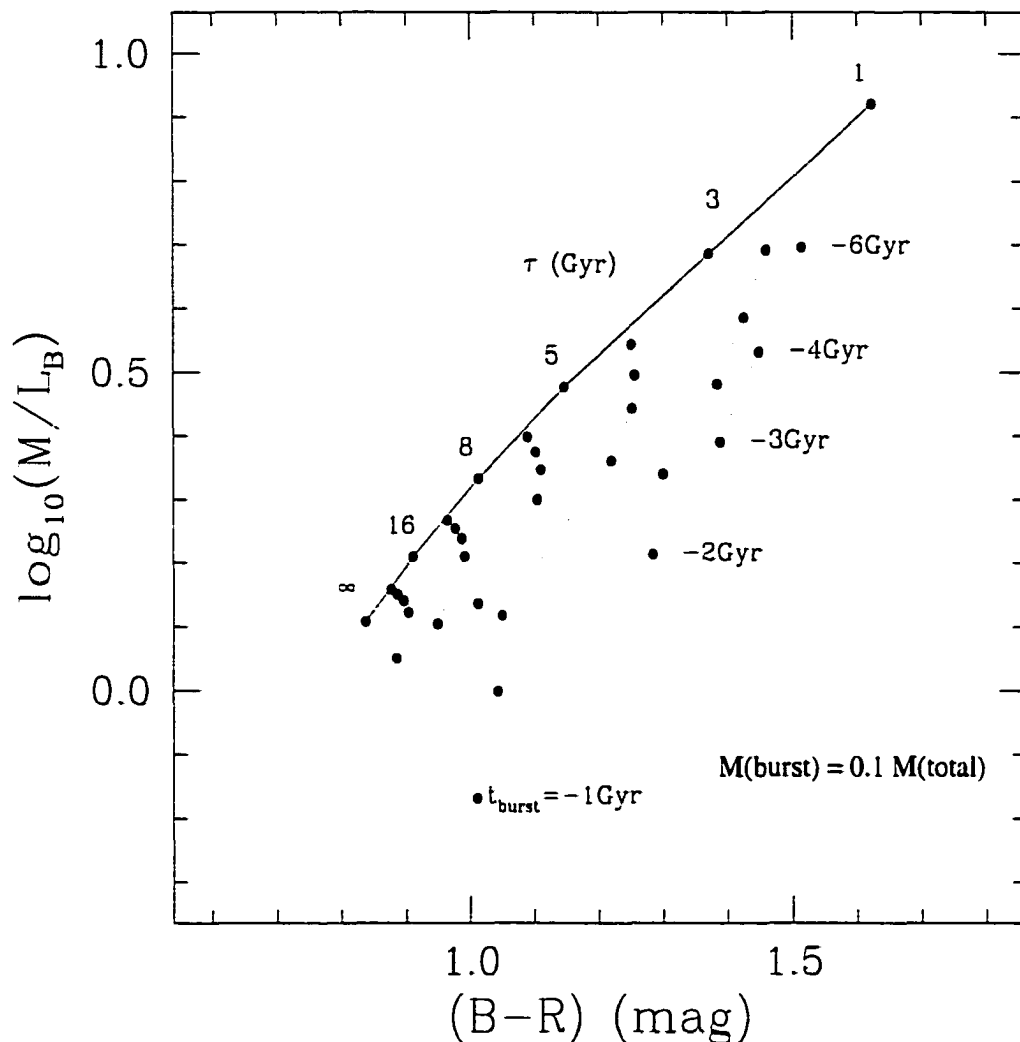


FIGURE 5.11. An example of the effect of a burst of star formation on the  $M/L$  of a 12 Gyr old, Solar metallicity, exponentially declining population adapted from Figure 5a of Bell & de Jong (2001). The mass of the burst is 10% the mass of the final population, and the burst lasts for 0.5 Gyr. The solid line connects models with different  $e$ -folding SFH's and the dotted lines connect models with the same  $\tau$  but with the object observed 1, 2, 3, 4, and 6 Gyr after the burst. The color is not our adopted  $(B - V)$  but the plot still illustrates the change in  $M/L_B$  for a burst of a given strength.

Using our measure of  $(B-V)_{rest}$ , we calculate both the values of  $\mathcal{M}/L_B$  and  $\mathcal{M}/L_V$  for our sample using the BJ01 relations for a mass dependent formation epoch with bursts. The correlation between  $\mathcal{M}/L$  and color is valid even for simple exponentially declining SFHs, but the relation is not very dependent on which exact SFH is used. Because BJ01 give no color- $\mathcal{M}/L$  relation for  $(U-B)$ , we must use  $(B-V)_{rest}$  to derive  $\mathcal{M}/L$ , and hence are limited to  $z < 3.2$ , where our observed wavelength range still encompasses the redshifted V-band. To calculate the  $\mathcal{M}/L$ 's from the rest-frame colors we use the relations from BJ01

$$\log_{10}(\mathcal{M}/L_B) = -0.844 + 1.804 * (B - V)_{rest} \quad (5.16)$$

and

$$\log_{10}(\mathcal{M}/L_V) = -0.584 + 1.404 * (B - V)_{rest} \quad (5.17)$$

where the units of  $\mathcal{M}/L$  are  $M_\odot/L_\odot$  and we calculate the uncertainty in  $\mathcal{M}/L$ ,  $\delta\mathcal{M}/L$ , from a modified version of our Monte-Carlo redshift simulation. Because it was difficult to estimate the scatter in their theoretical relations, no scatter in the  $\mathcal{M}/L$ -color relation was quoted in BJ01. Using their range of model  $\mathcal{M}/L$ 's at a given  $(B-V)$  color and the fact that bursts can change the  $\mathcal{M}/L$ 's of blue galaxies (where the SFH's are thought to be bursty) by  $\sim 0.15$  dex, we decided to adopt a scatter of  $\sigma_{\mathcal{M}/L} = 0.15$  dex in  $\log_{10}(\mathcal{M}/L)$ . At every redshift iteration, we derive the  $\mathcal{M}/L$  from the color 20 times with the  $\mathcal{M}/L$  values drawn randomly from a Gaussian centered on the BJ01 relation with a scatter of  $\sigma_{\mathcal{M}/L}$ . We obtain our 68% confidence limits on  $\mathcal{M}/L$  from the total distribution.

In Figure 5.12, we show  $\mathcal{M}/L_V$  plotted against redshift for two different  $L^{\text{rest}}$  ranges. The points are delineated by rest-frame color error, by  $\delta z'_{phot}$ , and by the colors difference between the DTI and CCR methods. At all redshifts there are a large range of  $\mathcal{M}/L_V$  values and at  $z > 2$  and  $L^{\text{rest}} > 10^{10} h^{-2} L_\odot$ , we find objects with high  $\mathcal{M}/L_V$  values which correspond to the red, intrinsically luminous objects from Figure 5.9.

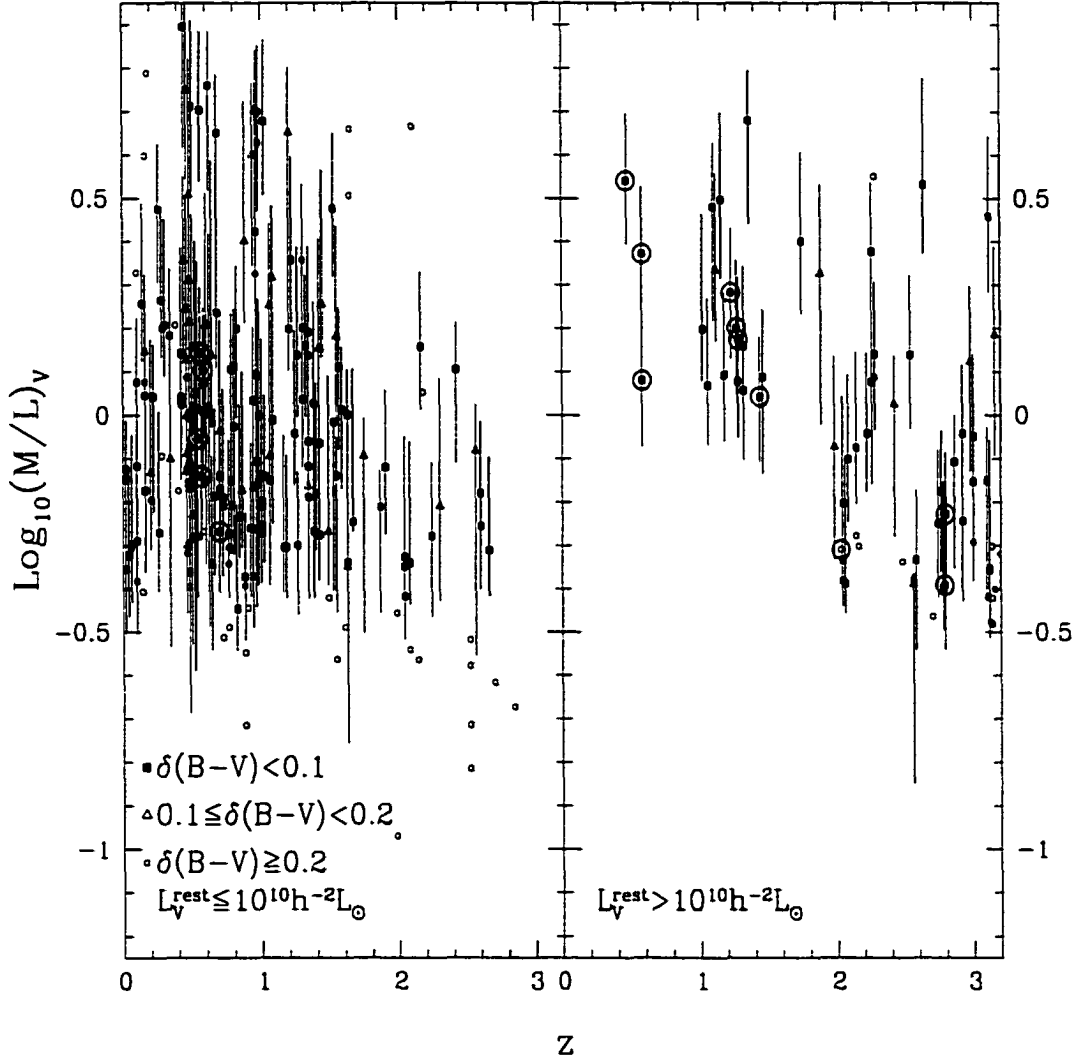


FIGURE 5.12.  $M/L_V$  vs. redshift for all galaxies with  $K_{s,AB}^{\text{tot}} < 25$ . The left and right panels correspond respectively to intrinsically faint and luminous galaxies. Objects with spectroscopic redshifts have circled points. The points are coded by the redshift and rest-frame color uncertainties. The empty circle is used if the objects has a large color error, if  $|(B-V)_{\text{DTI}} - (B-V)_{\text{CCR}}| > 0.2$ , or if  $\delta z'_{\text{phot}} > 0.5$ .

### 5.5.2 The Stellar Mass

Using our measured  $L^{\text{rest}}$  values we then converted the  $\mathcal{M}/L$  to a stellar mass  $\mathcal{M}$  through

$$\mathcal{M} = \mathcal{M}/L_V * L_V^{\text{rest}}. \quad (5.18)$$

We list the inferred  $\mathcal{M}/L_V$ 's and  $\mathcal{M}$ 's in Table A.11. In Figure 5.13, we plot the stellar mass of galaxies as a function of redshift and enclosed volume. The error bars were calculated from the same Monte-Carlo simulation used to measure  $\delta\mathcal{M}/L$ . We notice first that the uncertainties in the mass  $\delta\mathcal{M}$ , are significantly smaller than either  $\delta\mathcal{M}/L$  or  $\delta L^{\text{rest}}$ . The small size of the mass errorbars can be understood by examining in detail the  $L^{\text{rest}}$  and rest-frame color trends of a given galaxy as the photometric redshift increases given the observed magnitudes. At higher redshifts the derived  $L^{\text{rest}}$  increases, but at the same time, the derived  $(B - V)_{\text{rest}}$  of a galaxy usually becomes bluer (and the derived  $\mathcal{M}/L_V$  therefore becomes lower) as one moves to higher redshifts. At a redshift away from  $z_{\text{phot}}$ , the  $\mathcal{M}/L_V$  and luminosity may be very different from the best-fit values, but they are different in opposite directions and the resultant  $\mathcal{M}/L_V$  and  $L^{\text{rest}}$  distributions largely cancel out and produce small confidence limits on the mass.

From Figure 5.13 it is also apparent that the most massive galaxies at any redshift are those with the reddest optical colors (or highest  $\mathcal{M}/L$  values). This relation of  $\mathcal{M}/L$  and mass can also be seen in Figure 5.14 where we plot  $\mathcal{M}/L$  vs. the stellar mass. Even though the mean  $\mathcal{M}/L$  decreases with redshift, the most massive galaxies always have the highest  $\mathcal{M}/L$ 's. This must not necessarily be the case; if the red galaxies were much fainter than the blue galaxies, this correlation would weaken or disappear.

The second most massive galaxy in our sample is HDFS2-908 which has  $z_{\text{phot}} = 2.28$ , a stellar mass of  $\mathcal{M} = 7.6 \times 10^{10} h^{-2} M_{\odot}$ , and  $K_{s,AB}^{\text{tot}} = 22.5$ . This galaxy has a large redshift error with a secondary  $\chi^2$  minima at  $z > 9$  where the large break



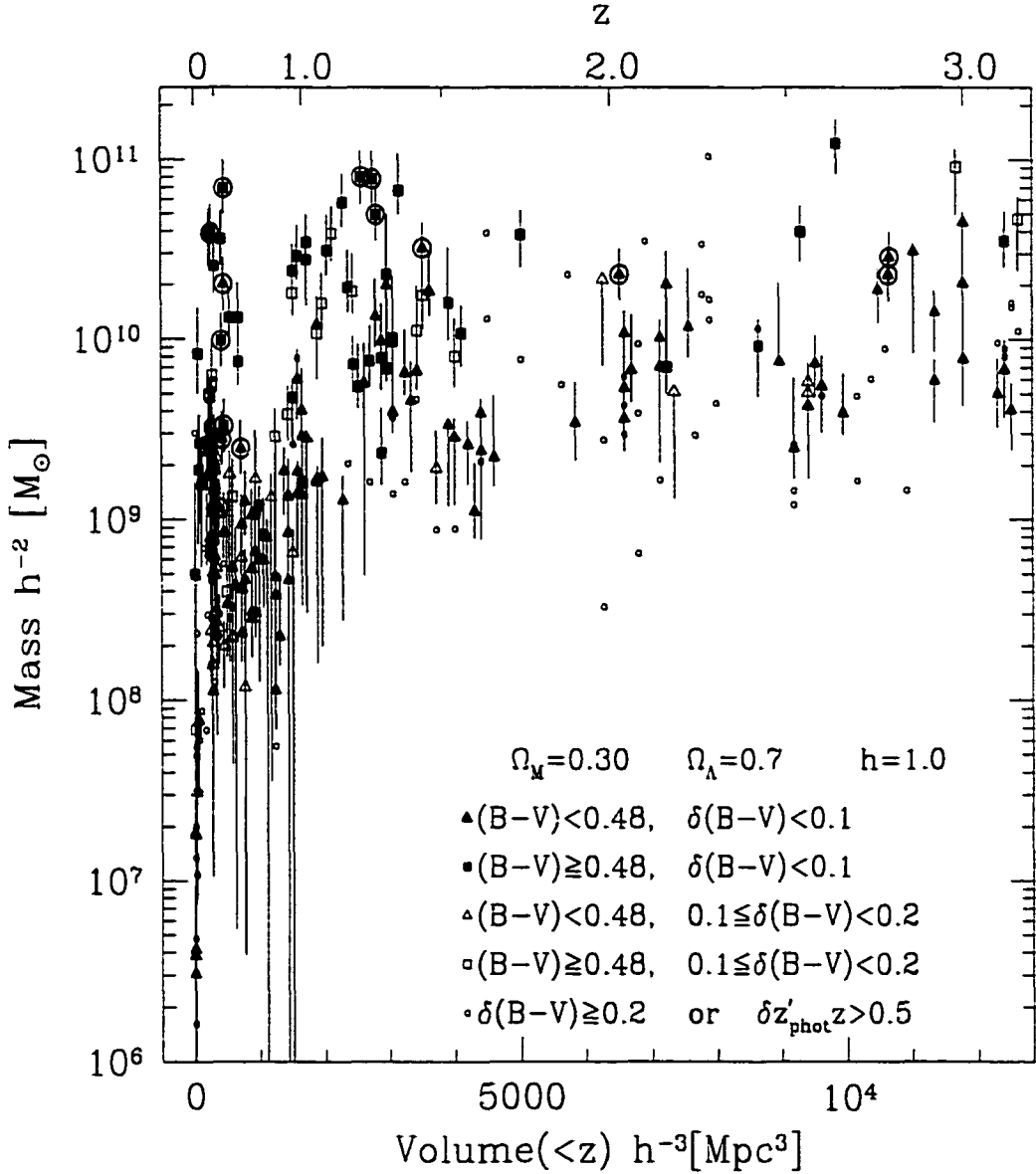


FIGURE 5.13. A plot of the stellar mass as a function of redshift and enclosed volume. The squares and triangles represent rest-frame optically red and blue objects respectively. The solid and empty symbols respectively represent lower and higher rest-frame color errors. Small circles have very high color or redshift errors. Objects with spectroscopic redshifts have circled points. Note that the most massive galaxies at any redshift are rest-frame optically red.

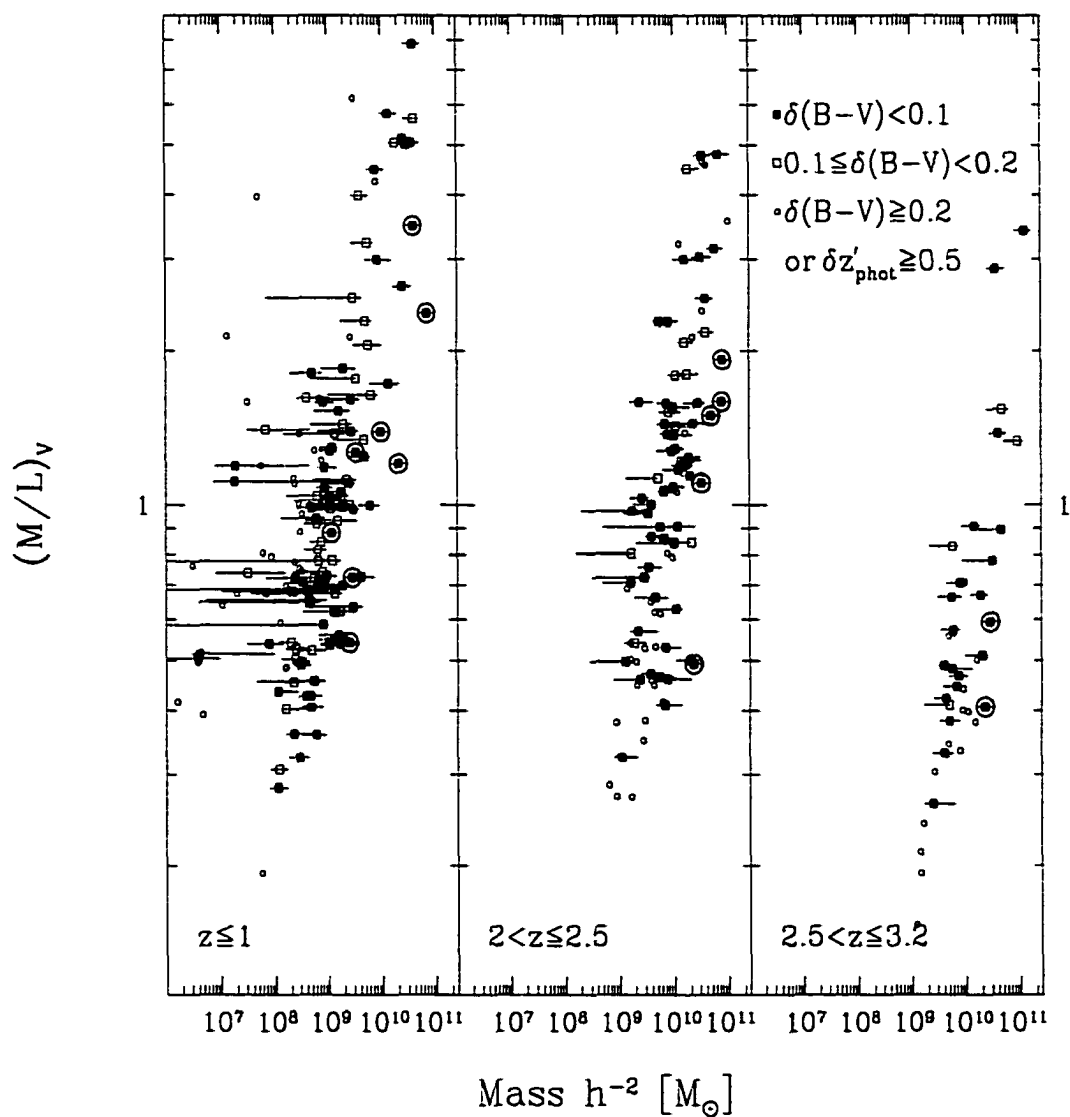


FIGURE 5.14. A plot of the stellar  $\mathcal{M}/L_V$  as a function of stellar mass. The point type represents different rest-frame color and redshift uncertainties. Objects with spectroscopic redshifts have circled points. At every redshift, the most massive galaxies have the highest  $\mathcal{M}/L_V$ .

in the SED is interpreted as a Lyman Break. The  $K_s$ -band magnitude, however, is bright and at  $z > 9$  the extrapolated  $L_V^{\text{rest}}$  is  $\gtrsim 10^{12} h^{-2} L_\odot$ . This extremely high  $L^{\text{rest}}$  is very unlikely and we assume that the best interpretation is of an evolved galaxy with a strong Balmer/4000Å break. Even though we do not believe the secondary minima to be true, we remain consistent with our  $\delta z'_{\text{phot}} < 0.5$  quality cut and do not include this object in following analyses.

### 5.5.3 Comparison with Studies of the LBG Population

To estimate the consistency between different mass measurement methods, we compared our  $\mathcal{M}$  to the stellar masses derived in P01 and S01. After converting  $\mathcal{M}$  and the masses of S01 to the  $h=0.7$  scale used by P01 we find that our median  $\mathcal{M}$  lies 0.1 dex lower than S01 and 0.3 dex higher than P01. We note that S01 finds similar masses to P01 when measured over similar rest-frame UV luminosity ranges. It is not surprising that our sample has a lower median mass than that of S01 as they used a LBG subsample with a mean apparent magnitude significantly brighter than ours and in fact significantly brighter than the mean apparent magnitude of the entire optically selected LBG sample. More interesting is our disagreement with P01. A Kolmogorov-Smirnov test shows that the two distributions have only a  $\lesssim 1\%$  chance of being drawn from the same parent population, but yet they occupy a similar range in apparent magnitude with our magnitude distribution having a faint tail absent in the P01 sample (likely due to the magnitude threshold in P01 imposed by spectroscopic follow-up requirements). Our higher median mass is not due to a few massive galaxies which were missed by the LBG technique (although these galaxies do exist e.g., HDFS2-806 and HDFS-699) but rather to a systematic shift in the distribution of our masses. This offset could be due to differences between this work and P01 in the sample selection, the mass measurement technique, or the photometry; to disentangle these effects, we determined the rest-frame colors,  $\mathcal{M}/L$ 's, and masses for two

galaxies (NIC ID 814 and 503 with  $z_{spec} = 2.931$  and  $2.233$  respectively) from the P01 spectroscopically confirmed LBG sample which have fluxes published in P01. When measured at  $z_{spec}$  we found that our  $\mathcal{M}$ 's were greater than those of P01 by  $\sim 0.2$  dex, where we used P01's mass estimates for a Salpeter IMF and solar metallicity. A similar offset is also present in our mass estimates at  $z_{spec}$  for five galaxies from P01 for which the NICMOS photometry was not presented, but for which we could use the KPNO 4-meter NIR photometry from Fernández-Soto, Lanzetta, & Yahil (1999). While our masses are systematically higher than those of P01, there is still a  $\approx 95\%$  Spearman-Rank probability that the two estimates are correlated.

Because we used the same objects as P01 (some with identical photometry) to compare our mass estimates and still found an offset, we must conclude that the mass disagreement comes from differences in the two techniques. One simple difference between the two techniques is the wavelength regime over which each derives its  $\mathcal{M}/L$ 's. Our  $\mathcal{M}/L$  estimates are based on  $(B - V)_{rest}$ , which is determined only from the observed filters which straddle the redshifted rest-frame optical bandpasses (the NIR for  $z \gtrsim 0.8$ ). P01 on the other hand determined the mass by fitting the entire SED redward of the LB, including light significantly blueward of the Balmer/4000Å break. In galaxies which are forming stars, light from even relatively few massive stars will contribute more to the optical passbands than to the NIR ones and might drive the  $\mathcal{M}/L$ 's and masses downward compared to the masses that would be derived solely from the NIR data. This effect might be exacerbated since P01 only have moderately deep  $K_s$  band data. This hypothesis could be tested by applying the P01 technique to our data. There may be a residual systematic effect between the models used by P01 and BJ01.

The differences between the mass determinations of P01 and our method, which may be in disagreement by at least a factor of  $\sim 1.5$  (0.2 dex), highlight the model dependence of such estimates and necessitate caution in interpreting not only the absolute masses determined by us and P01 but also those determined by S01 (who

estimate the mass in a similar way to P01).

#### 5.5.4 The Stellar Mass Budget

The instantaneous  $\text{SFR}(z)$  of the universe has been constrained by different observational data sets over a large range in redshift and matched by a large suite of theoretical models. One requirement of any such  $\text{SFR}(z)$  curve should be that its integral over time minus mass loss produce the total mass of *observed* stars at any epoch. For the first time we can use a single technique over a large range in redshift to measure the total stellar mass at any epoch.

##### *The Rest-Frame Optical Luminosity Density of Bright Galaxies*

Using our  $L^{\text{rest}}$  estimates (§5.3.2) from the  $K_{s,\text{AB}}^{\text{tot}} < 26$  catalog (Chapter 4), we first derived the rest-frame luminosity density of the intrinsically bright galaxies with well determined redshifts. This quantity is less model dependent than the stellar mass density. Other groups have measured the redshift evolution of the UV luminosity density (e.g., Lilly et al. 1996; Madau et al. 1996) and converted it to an estimate of the  $\text{SFR}(z)$ , but this is the first attempt to measure the rest-frame optical luminosity density in a consistent way over a redshift range greater than two. Because we do not at present (although we could easily do so) measure rest-frame UV luminosities, we do not convert our luminosity densities to a  $\text{SFR}(z)$  estimate. In a given redshift interval, we estimated the luminosity density from our most reliable subsample by adding up the rest-frame luminosities of the individual galaxies which satisfied our  $\delta z'_{\text{phot}}$  and  $L^{\text{rest}}$  criteria. We imposed an  $L^{\text{rest}}$  cut of  $10^{10}$ ,  $10^{9.7}$ , and  $10^{9.6} \text{ h}^{-2} L_{\odot}$  in  $U_{\text{rest}}$ ,  $B_{\text{rest}}$ , and  $V_{\text{rest}}$  respectively to ensure that we are complete at all redshifts  $z < 3.2$  (Figure 5.3). Uncertainties in the luminosity density are based solely on counting errors and are computed by bootstrapping from the full  $K_{s,\text{AB}}^{\text{tot}} < 26$  catalog. The results are shown in Figure 5.15. Because we exclude galaxies with uncertain redshifts, faint rest-frame luminosities, or low apparent magnitudes, and do not correct

for incompleteness, our estimates should be regarded as lower limits on the true luminosity density. Including all galaxies with  $K_{s,AB}^{\text{tot}} < 26$  raises the points typically by 0.15-0.3 dex. The dip in the inferred luminosity density in the second lowest redshift bin of all the panels of Figure 5.15 can be traced to the lack of intrinsically luminous galaxies at  $z \sim 1.5-2$  (§5.3.2; Chapter 2). In Figure 5.15b, we show the local  $B$ -band luminosity density  $\rho_B$  from the summary of Fukugita, Hogan, & Peebles (1998) and from Blanton et al. (2001) using the Sloan Digital Sky Survey (SDSS) Data. We fail to see the factor of  $\sim 3$  rise in  $\rho_B$  between redshift of zero and unity seen by Lilly, Le Fevre, Hammer, & Crampton (1996) and Fried et al. (2001). This disagreement is partially accounted for by the exclusion of galaxies by our quality cut. Our lowest redshift  $\rho_B$  estimate increased by a factor of about 1.5 when we include all of the galaxies rejected by our  $L^{\text{rest}}$  and  $\delta z'_{\text{phot}}$  cuts. Almost all of this increase comes from galaxies which fell below our  $L^{\text{rest}}$  cut and our  $K_{s,AB}^{\text{tot}} = 26$  limit makes us roughly complete to  $L_B^{\text{rest}} \approx 0.05L_*$  at  $z < 1$  so that we only expect to miss about 10% of the total luminosity with our magnitude limit. It is also possible that we are missing light from individual galaxies. For  $h = 0.7$  our  $2''0$  diameter aperture is larger than the half-light diameter of an exponential disk with  $r_{\text{exp}} = 3$  kpc (10 kpc) when  $z > 0.35$ . We do however, correct our rest-luminosities by estimating the amount of flux missed by our  $2''0$  aperture (Chapter 2; §5.3.2). The remainder of the disagreement may simply be an effect of cosmic variance due to the small co-moving volume in the HDF-S at  $z < 1$ . Whatever the reasons, it seems that we are still underestimating the luminosity density at low redshifts and this must be taken into account when we interpret the inferred co-moving stellar mass densities. At higher redshifts, we agree better agreement with other estimates, finding a similar  $\rho_V$  as that of S01.

### *The Stellar Mass Densities of Bright Galaxies*

By using our individual mass estimates, we quantified the stellar mass density at  $z \leq 2$  and  $2 < z \leq 3.2$  (which divide the survey volume in half) for galaxies with

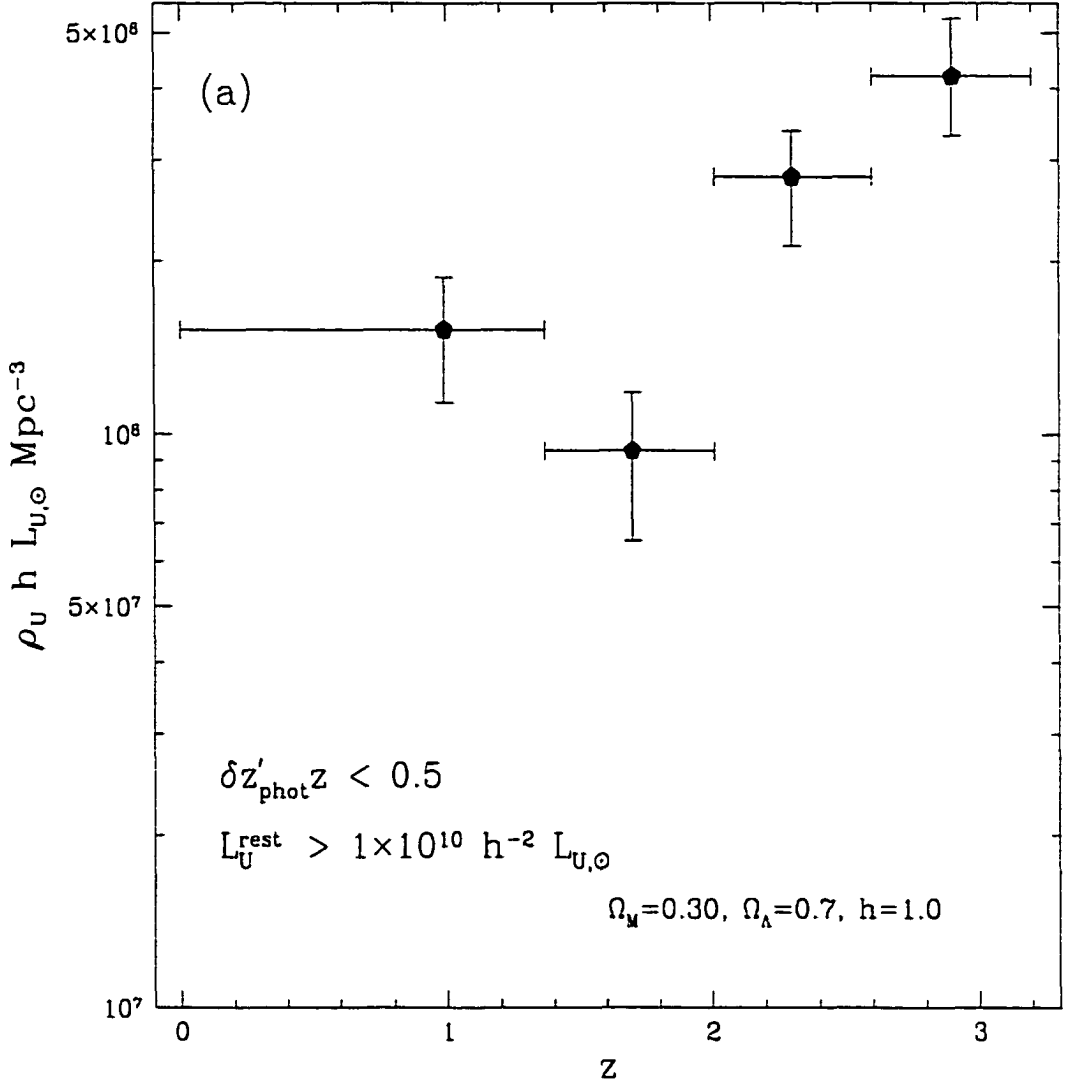
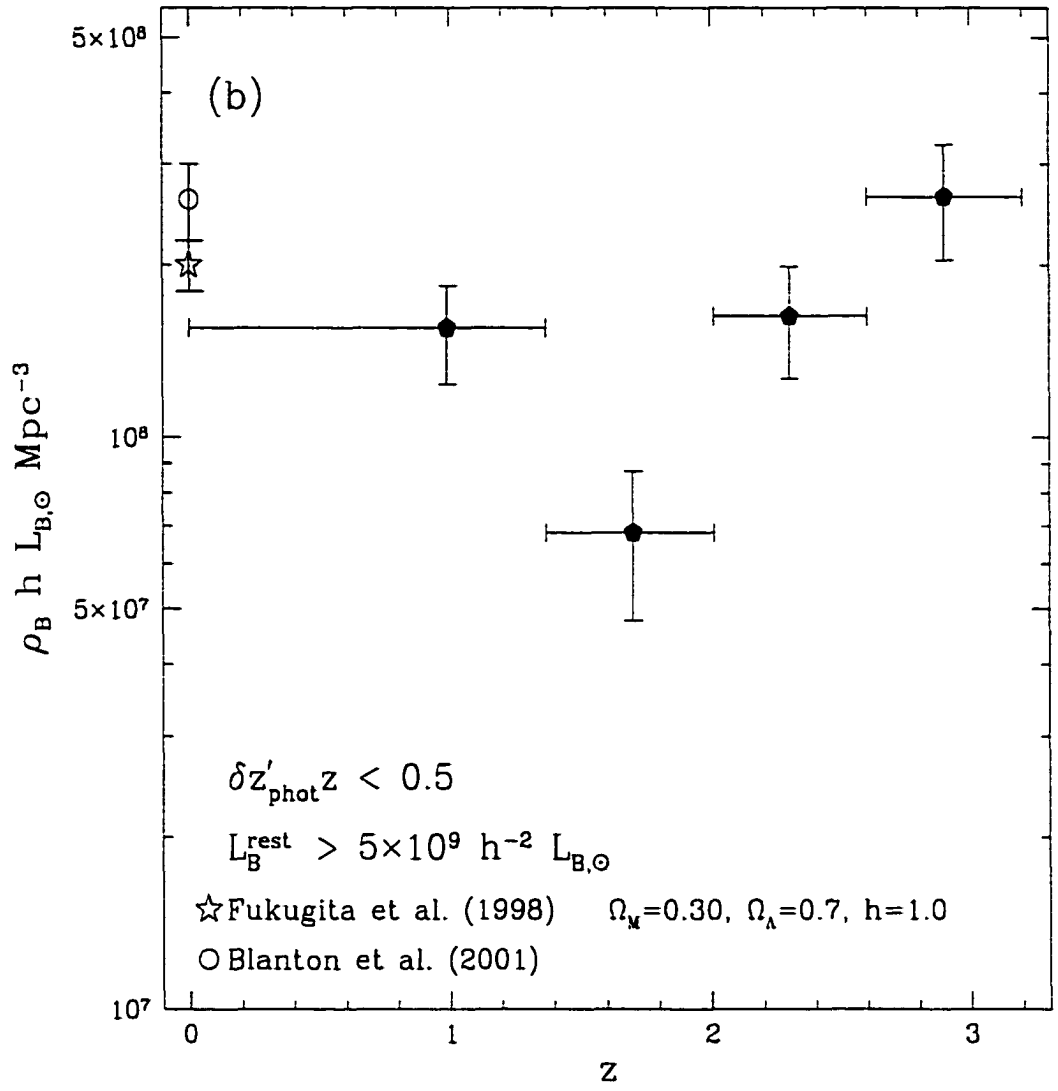
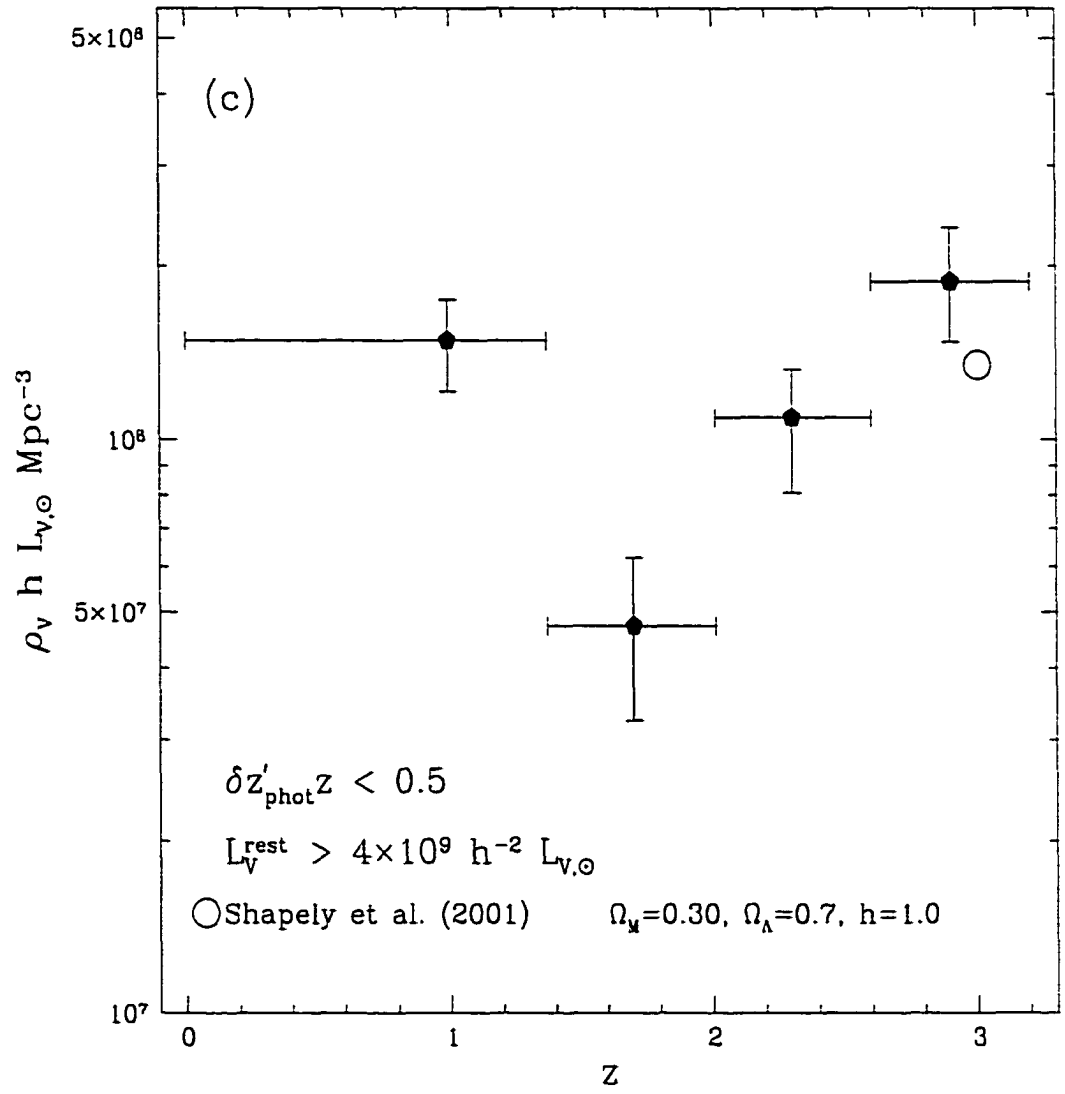


FIGURE 5.15. The luminosity density from intrinsically bright galaxies with  $K_{s,AB}^{\text{tot}} < 26$  and well determined redshifts. The data are split into redshift intervals containing equal co-moving volumes. The dip in the density at  $z \sim 1.5 - 2$  is a direct consequence of the lack of luminous galaxies in this range (§5.3.2; Chapter 2). The star in b) indicates the locally derived  $B$ -band luminosity density from the summary of Fukugita, Hogan, & Peebles (1998) and the circle in b) indicates the LBG  $V$ -band luminosity density from Shapley et al. (2001). Including all galaxies with  $K_{s,AB}^{\text{tot}} < 26$  raises the total densities by 0.15-0.3 dex. No correction for incompleteness has been made for our values.







$K_{s,AB}^{tot} < 25$ ,  $\delta z'_{phot} \leq 0.5$ ,  $\delta(B - V)_{rest} \leq 0.2$ , and  $L_V^{rest} > 10^{9.6} h^{-2} L_\odot$ . The last criterion was imposed so that we are equally complete at all redshifts (Figure 5.3 and §5.5.4). We obtained our errors using bootstrapping (with replacement) from the full  $K_{s,AB}^{tot} < 26$  sample. In Figure 5.16 we show the mass density computed from 112 objects which passed our quality criteria. The data were divided into two redshift bins which contained equal co-moving volumes. There are many effects which may introduce errors in our mass density estimates. It is known from our comparison in Figure 5.15 that we find a factor of  $\sim 3$  too little light at  $z \lesssim 1$  compared to other work. This discrepancy is also likely manifest in our mass density determinations but may be more severe because here we impose an additional color uncertainty quality cut and a brighter apparent magnitude limit. We know that the low luminosity galaxies rejected by our  $L_V^{rest}$  cut contribute substantially to the numbers and rest-frame luminosity density at low redshift, but very little to the mass density because removing our  $L^{rest}$  threshold only increases the mass density at  $z < 2$  by 15%. We must keep in mind, however, that we now limit ourselves to galaxies one magnitude brighter than in §5.5.4 and are hence miss even more galaxies. At high redshift the mass density remains unchanged if we remove the  $L_V^{rest}$  limit because this limit was defined a priori for high redshift completeness. An additional source of error in the mass density could be that we have errors in the mass determinations of individual galaxies. For one, the BJ01 zeropoint is uncertain and depends strongly on the IMF. Also, Sawicki & Yee (1998) and later P01 showed that the SFHs of LBGs are likely bursty. This latter concern will cause errors in the  $\mathcal{M}/L$ 's estimated from models with exponentially declining SFHs.

For comparison, we also plot the stellar mass density estimates of Cole et al. (2001) and Brinchmann & Ellis (2000) and adjust all the points to  $h = 0.65$  after Brinchmann & Ellis ignoring the small differences between our cosmology and theirs ( $\Omega_M = 0.35$ ,  $\Omega_\Lambda = 0.65$ ). If corrected to our cosmology, their density estimates increase by  $\approx 10\%$ . We also compared the mass density estimates all groups to the

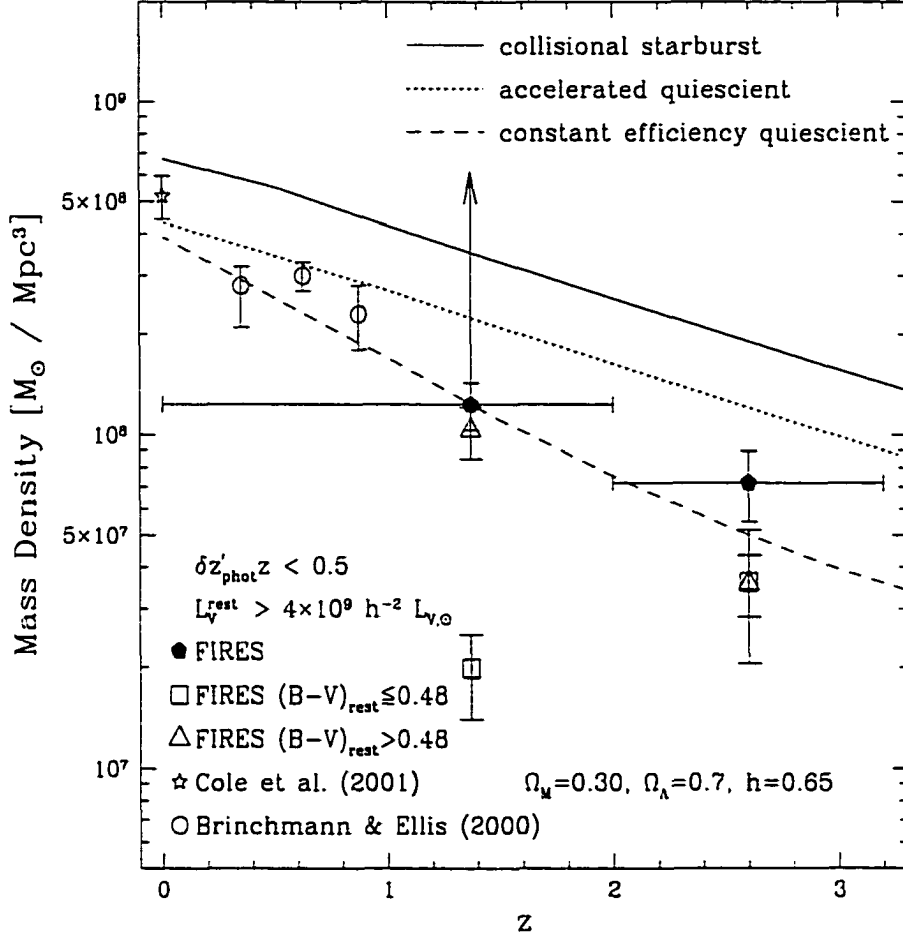


FIGURE 5.16. A plot of the stellar mass density vs. redshift for the intrinsically brightest galaxies with the most secure redshifts. Each of the FIRES points are derived over an equal volume, and are plotted at the redshifts which divide the volumes  $z < 2$  and  $2 < z \leq 3.2$  in half. The horizontal errorbars define the redshift range over which the mass density was determined. The upwards arrow on our low redshift point indicates how much we would need to correct this mass density estimate to account for the disagreement of our  $\rho_B$  measurement (Figure 5.15b) with the Blanton et al. (2001) point at  $z = 0$  given a factor of  $\sim 3$  rise in  $\rho_B$  between  $z = 0$  and unity (Lilly, Le Fevre, Hammer, & Crampton, 1996). The lines represent the predictions of semi-analytic models from Somerville, Primack, & Faber (2001) for three different star formation scenarios. The lowest four redshift points were taken from estimates of Cole et al. (2001) and Brinchmann & Ellis (2000). Our values and those of Cole et al. were scaled to  $h = 0.65$  for comparison with the Brinchmann & Ellis values.

predictions of Somerville, Primack, & Faber (2001; hereafter SPF01) by integrating their  $\text{SFR}(z)$  curves over redshift, to obtain  $\text{Mass}(z)$  curves for their three different models (Figure 5.16): the “constant efficiency quiescent” (CE), the “accelerated quiescent” (ACC), and the “collisional starburst” (CSB) model. The CE model uses a constant SF efficiency in a quiescent mode, the ACC model includes an efficiency which increases with look-back time, and the CSB model includes bursts of star formation from both major and minor mergers. These models assume that all the mass from stars with  $M > 8M_{\odot}$  is returned to the interstellar medium (this recycles 14% of the mass formed at any given time). No recycling is included for less massive stars. We decrease our  $\text{Mass}(z)$  curves by 14% to account for the SPF01 recycling but note that uncertainties in the exact recycling prescription will change the normalization of the  $\text{SFR}(z)$  and  $\text{Mass}(z)$  tracks. SPF01 claim that only the CSB model fits the observed number counts, luminosity functions, and  $\text{SFR}(z)$  derived from optically selected high redshift galaxy samples. We find, however, that the mass density estimates fall at the lower end of the model envelope, close to the CE curve. In light of all of the uncertainties discussed above, it is not feasible, at this time, to rule out any of the models based only the FIRES data. The measurements of Brinchmann & Ellis and Cole et al., however, use only galaxies with  $z_{\text{spec}}$  measurements and sample redder rest-frame wavelengths than the FIRES data so their mass estimates should be more reliable. They also have been corrected for incompleteness. The CSB model is not consistent with the Brinchmann & Ellis and Cole et al. points.

Even though our absolute stellar masses may be in error, we can still use the BJ01 relation to estimate the relative mass contributions of galaxies of different rest-frame color. We divided our sample into objects with colors redder and bluer than a present day Scd ( $(B - V)_{\text{rest}} = 0.48$ ) and plotted the separate contributions in Figure 5.16. At high redshifts, objects with the colors of present day, quiescent galaxies appear to contribute comparable amounts of mass as bluer presumably star forming galaxies while at lower redshifts the intrinsically red objects completely dominate the mass

budget. In addition to dividing our sample by rest-frame color, we also investigated the mass contributions of optically vs. NIR selected galaxies at high redshift via the application of the  $U$ -dropout criteria. The  $U$ -dropout galaxies in our sample mostly have blue rest-frame optical colors, but a few can still be fairly red (e.g., HDFS2-260) and it is not obvious how they contribute to the total stellar mass budget. If, instead of counting mass in subsamples split by their rest-frame color we counted mass in subsamples split by their classification as a  $U$ -dropout, we find for  $2 < z < 3.2$  that the mass density is still equally split between the two object categories.

The conclusions above are of course again subject to our assumption that the blue galaxies do not have large amounts of older stars hidden under the glare of younger populations. Once spectroscopic redshifts have been obtained for more high-redshift galaxies in the HDF-S, the detailed analysis of P01 can be repeated using our much deeper  $K_s$ -band data and better constraints on the total mass can be obtained. Due, however, to the dominance of light from young populations even at rest-frame optical wavelengths, a definitive answer will not be reached until the rest-frame NIR is observed in these high redshift galaxies with the upcoming SIRTf mission.

## 5.6 Summary

Using our deep  $K_s$ -band selected data coupled with our  $0.3 - 2.2\mu m$  wavelength coverage, we have measured the photometric redshifts for a  $K_{s,AB}^{\text{tot}} < 26$  sample of galaxies which for  $z < 4$  are selected by their rest-frame optical light. The photometric redshift of these galaxies displays a sharp peak at  $z \approx 0.5$ . This peak was first seen in spectroscopic studies in the HDF-S taken over a larger field and again in Chapter 2. The broad overdensity from  $1 < z < 1.4$  discussed in Chapter 2, is still seen in galaxies with  $K_{s,AB}^{\text{tot}} < 23.5$ , but is not evident in the fainter galaxy population.

We measured the rest-frame luminosities of our galaxies using the techniques described in Chapter 2 and find we are sensitive to galaxies with  $L_V^{\text{rest}} < 0.3 L_*$ .

at  $z \lesssim 3$ . We found that there are many galaxies with  $L^{\text{rest}} > L_*$ , in all bands and at all redshifts. We also confirmed the deficit of bright galaxies with  $1.5 < z < 2$  seen in Chapter 2 although this strong deficit is not apparent at lower values of  $L^{\text{rest}}$ .

We developed techniques to measure the rest-frame colors of our galaxies and their uncertainties by combining their observed SEDs with their photometric redshift and its probability distribution. We found in a  $K_{s,AB}^{\text{tot}} < 25$  subsample (where photometric errors are small) that there are intrinsically luminous galaxies ( $L^{\text{rest}} > L_*$ ) at all redshifts  $z < 4$  which have rest-frame colors equal to present day spirals and ellipticals. Although a few of these red galaxies would be included in optically selected samples, eight of the 12 reddest objects are not selected by the  $U$ -dropout technique and have observed SEDs fit well by spiral/early type templates. If these red rest-frame colors correspond to evolved stellar populations at these redshifts, we are seeing a quiescent phase of the star formation associated with the more numerous vigorously star-forming galaxy population.

We derived the rest-frame optical stellar mass-to-light ratios of galaxies with  $K_{s,AB}^{\text{tot}} < 25$  using theoretical relations between the rest-frame optical color and  $\mathcal{M}/L$  (BJ01). We found that there are galaxies at all redshifts  $z < 3.2$  which are rest-frame optically red and which have correspondingly large  $\mathcal{M}/L$  values. These same galaxies can be intrinsically luminous and have large inferred stellar masses. In fact the most massive galaxies at any redshift are those with the highest  $\mathcal{M}/L$  and the reddest rest-frame colors.

We computed the rest-frame luminosity and stellar mass density as a function of redshift for the intrinsically luminous galaxies with well constrained redshifts and rest-frame colors. We find that our luminosity density measurements fail to reproduce the rapid rise in  $\rho_B$  and  $z < 1$  seen in Lilly, Le Fevre, Hammer, & Crampton (1996) and Fried et al. (2001) however we find a similar  $\rho_V$  to the LBG population at  $z \sim 3$  (S01). Noting our substantial uncertainties we combine our estimates with the low redshift measurements of Cole, Lacey, Baugh, & Frenk (2000) and Brinchmann &

Ellis (2000) and make a comparison with semi-analytic model predictions. Our mass density estimates are not corrected for completeness and our low redshift point may go up by a factor of  $\sim 3$  if our missing luminosity compared to Lilly, Le Fevre, Hammer, & Crampton (1996) is taken into account. Cosmic variance may also make it difficult to interpret our data, especially at  $z < 1$  where the co-moving volume of the HDF-S is small. Still, the Cole et al. and Brinchmann & Ellis points seem to contradict the favored semi-analytic model.

We also estimate the fraction of the stellar mass budget which comes from galaxies redder and bluer than present day Scd's. The red galaxies contribute to the stellar mass budget equally as the blue galaxies at high redshift and dominate the mass budget at lower redshifts.

## CHAPTER 6

## SUMMARY AND OUTLOOK

## 6.1 Summary

In this dissertation, we have presented early science results from the FIRES program at the VLT. Specifically we have used 101.5 hours of  $J_s$ ,  $H$ , and  $K_s$  imaging of the WFPC2 field of the HDF-S and developed techniques to interpret this data set. We have combined the extremely deep optical images of the HDF-S with our high quality NIR images, an unprecedented combination of depth and wavelength coverage. From this dataset we constructed a seven band  $K_s$ -band selected catalog ( $K_{s,AB} < 26$ ) designed to give accurate colors. We also developed a new photometric redshift technique and explored ways to derive realistic uncertainties in the photometric redshifts. Our  $z_{phot}$  estimates are accurate to  $\langle \Delta z / (1 + z) \rangle = 0.08$  when compared to spectroscopic redshifts. Using our  $z_{phot}$  estimates and our broad wavelength coverage, we derived the rest-frame optical luminosities and colors of galaxies out to  $z = 5.2$  in a  $K_{s,AB} < 25$  subsample. Our major results are:

- At  $z > 2$  we find galaxies in all rest-frame bands with  $L^{rest} \geq 5 \times 10^{10} h^{-2} L_{\odot}$ . We find 9 galaxies with  $L_B^{rest} \geq 5 \times 10^{10} h^{-2} L_{\odot,B}$  which lie between  $2 \leq z \leq 3.5$  while local luminosity functions predict only 0.1 galaxies. The differences can be accounted for if  $L_*$  in the  $B$ -band increases by a factor of 2.4-2.9. The redshifts and nature of these intrinsically bright galaxies at high- $z$  needs to be verified with spectroscopic follow-up.
- There is an intrinsically bright ( $L_V^{rest} = 5.10 \times 10^{10} h^{-2} L_{\odot,V}$ )  $U$ -dropout galaxy in the HDF-S with a secure spectroscopic redshift at  $z_{spec} = 2.793$ . In the optical, this galaxy has an non-axisymmetric ring like structure and a co-moving



diameter of  $\gtrsim 9.4(6.3) h^{-1} Kpc$  for a  $\Omega_M = 0.3$ ,  $\Omega_\Lambda = 0.7$  ( $\Omega_M = 1.0$ ,  $\Omega_\Lambda = 0.0$ ) cosmology. The morphology becomes more concentrated and symmetric as one moves to the ground-based NIR images. This change in morphology, however, is not solely due to the lower resolution in the ground based data and seems to indicate a true morphological dependence on the wavelength. A tentative interpretation is that of a star-forming disk with a superimposed, spheroidal population.

- The rest-frame optical colors of our  $K_{s,AB} < 25$  galaxies lie on the  $(U - B)$  vs.  $(B - V)$  locus defined from local galaxy samples. There are rest-frame optically red, intrinsically luminous galaxies at all redshifts  $z < 3.2$ , some of which have SEDs indicative of evolved populations with little ongoing star formation. Eight of our twelve rest-frame optically reddest galaxies at  $2 < z_{phot} < 3.2$  would have been identified in the F814W image, but would have been missed by the  $U$ -dropout selection technique.
- Using theoretical relations between  $(B - V)_{rest}$  and the stellar mass-to-light ratio  $\mathcal{M}/L$ , we estimate the stellar masses for galaxies in our sample and determine their uncertainties in the face of our  $z_{phot}$  uncertainties. The most massive galaxies at any redshift are those with the reddest rest-frame optical colors and galaxies with  $(B - V)_{rest}$  colors redder and bluer than present day Scd's contribute comparable amounts to the stellar mass budget at high redshift. The absolute  $\mathcal{M}/L$  determinations may be highly uncertain as they rely on models with monotonically declining SFHs, something ruled out by other high redshift studies. Still, the relative  $\mathcal{M}/L$ 's of galaxies of different rest-frame color should be more reliable. Studying the effects of bursty SFHs on the derived  $\mathcal{M}/L$ 's is required before more secure mass estimates can be obtained.
- We make preliminary estimates of the luminosity and stellar mass density as

a function of redshift which comes from intrinsically bright galaxies with reliable  $z_{phot}$  determinations. Our estimates of the luminosity density at  $z < 1$  fall a factor of five short of those predicted by other studies over much larger volumes. It does not appear that the discrepancy can be made up by galaxies missed from our survey or from light missed in detected objects and is likely a result of large scale structure effects in the very small HDF-S volume at  $z < 1$ . Detailed simulations of our incompleteness and data over larger volumes will help to determine the origin of this discrepancy. At  $z \sim 3$  our rest-frame luminosity density estimates agree with those derived from the Lyman break galaxy population. The uncertainties in our luminosity density translate into correspondingly large uncertainties in our stellar mass density determinations. Still, taken together with estimates from other groups, our results are broadly consistent with theoretical predictions of the build-up of stellar mass from hierarchical galaxy formation.

## 6.2 Outlook

The work presented here suffers from two uncertainties which need to be addressed in the future: (i) To what effect are our results affected by large scale structure (ii) How sensitive are the results to the presence of very high dust extinction ?

Any attempt to interpret results from pencil beam surveys in the greater context of galaxy evolution must consider whether such a survey, over a given redshift interval, encompasses a representative volume of the universe. Surveys with too small enclosed volumes will be dominated by LSS and strong conclusions about the population must be made with caution. At  $z < 1$  FIRES in the HDF-S only contains  $\sim 2/3$  the co-moving volume of the local supercluster (for  $\Omega_m = 0.3, \Omega_\Lambda = 0.7$ , and  $h = 0.7$ ) and the deficit in the luminosity density which we see at low redshifts could easily be attributable to variations in the galaxy density on the supercluster scale. Things

are slightly better at  $2 < z < 3.5$ , where the co-moving volume is  $\sim 4$  times that of the local supercluster (again for  $h = 0.7$ ) and our conclusions there should be more indicative of the global galaxy population. The redshift distribution is especially susceptible to LSS effects because in its construction one is essentially splitting an already small survey into a set of even smaller redshift slices. The lack of galaxies in the HDF-S at  $1.5 < z < 2$  may simply result from the effects of LSS in a volume slightly smaller than the local supercluster. That is, we may simply be encountering a void similar to those seen in the local universe. The inferred co-moving volumes become even smaller for  $\Omega_m = 1$  cosmologies.

Our next step should be to construct a survey which not only has rest-frame luminosity sensitivity and wavelength coverage comparable to FIRES, but which also encompasses co-moving volumes significantly larger than the local supercluster. Such surveys should also probe distinct lines of sight to control the effects of cosmic variance. These requirements will be partly fulfilled by the FIRES imaging of the MS1054-03 field, which covers four times the area of the HDF-S to slightly shallower depths. Even then however, at  $z < 1$  the volume will be  $< 3$  times that of the local supercluster. One possibility to remedy the situation is to combine very deep pencil beam surveys with slightly shallower surveys over larger areas. Due to the large volume elements at  $z > 1$  in a  $\Lambda$ -dominated universe, new pencil beam surveys along different lines of sight can rapidly improve the situation at high-redshift. Wider field surveys at lower redshifts don't need to go as deep to reach similar rest-frame luminosities and so should not require any more telescope time than the pencil beam ones. These surveys should be possible with current and upcoming instrument/telescope combinations. In the optical, the advanced camera for surveys (ACS) on HST will provide deep, high resolution imaging from  $0.3 - 1.0\mu m$  with 10 times the survey speed of WFPC2. NIR imaging on 8-meter class telescopes and with the refurbished NICMOS camera on HST can perform the NIR component out to  $2.2\mu m$ . The wider field, but shallower NIR studies can be made with substantial investments of time on 4-meter

class telescopes with new wide field NIR detectors (i.e., Omega 2000 on the Calar Alto 3.5-meter).

The second major step is to better understand the effects of dust extinction and reddening on our results. We claim in Chapter 5 that the rest-frame optically reddest galaxies have SEDs consistent with evolved or quiescently star-forming populations, primarily based on the presence of large breaks in the SEDs coupled with rising flux in the blue. Large amounts of dust extinction ( $E(B - V) \gtrsim 2$ ) however, can indeed produce abrupt breaks in the observed SED and we must examine whether the red rest-frame optical colors of our galaxies can fit better by templates with large amounts of reddening.

In addition to studying the effects of extreme reddening we must also consider how our results are effected by adding small amounts of extinction on top of the extinction already present in our empirical templates. Because dust slides galaxies roughly parallel to the BJ01 relations, small amounts of additional extinction should not effect our  $\mathcal{M}/L$  estimates at a fixed redshift. Additional dust may however effect the redshift estimates themselves. Photometric redshift techniques rely on the presence of a break in the SED to determine the redshift and the position of the break will not be changed by small amounts of reddening. The colors on either side of the break, however, will change and in the presence of dust the code may incorrectly identify the break (e.g., 4000Å break, Balmer break, or LB).

## APPENDIX A

## TABLES

Table A.1: Optical Photometry –  $K_{s,AB}^{\text{tot}} \leq 23.5$  sample

ID	F300W <sup>a</sup>	F450W <sup>a</sup>	F606W <sup>a</sup>	F814W <sup>a</sup>
HDFS1 – 30	17.5 ± 2.0	62.4 ± 1.0	81.7 ± 0.7	140.4 ± 1.2
HDFS1 – 33	19.2 ± 1.9	37.6 ± 1.0	45.2 ± 0.7	93.9 ± 1.2
HDFS1 – 31	6.9 ± 1.9	11.7 ± 1.0	21.9 ± 0.6	41.1 ± 1.2
HDFS1 – 36	0.3 ± 2.0	34.9 ± 1.0	73.8 ± 0.7	90.5 ± 1.2
HDFS1 – 37	4.6 ± 2.0	1.0 ± 1.0	3.5 ± 0.7	6.2 ± 1.2
HDFS1 – 45	1.9 ± 2.0	1.4 ± 1.0	9.6 ± 0.7	71.4 ± 1.2
HDFS1 – 50	0.3 ± 1.9	2.0 ± 1.0	5.4 ± 0.7	18.3 ± 1.2
HDFS1 – 52	30.9 ± 1.9	53.8 ± 1.0	60.1 ± 0.6	85.1 ± 1.2
HDFS1 – 54	16.2 ± 1.9	23.5 ± 1.0	31.6 ± 0.6	52.4 ± 1.2
HDFS1 – 62	7.7 ± 1.9	28.6 ± 0.9	37.3 ± 0.6	75.3 ± 1.2
HDFS1 – 58	4.3 ± 1.9	4.3 ± 1.0	17.5 ± 0.6	75.1 ± 1.2
HDFS1 – 63	62.9 ± 1.9	124.9 ± 0.9	287.9 ± 0.6	491.4 ± 1.2
HDFS1 – 69	22.3 ± 1.9	32.6 ± 0.9	46.6 ± 0.6	92.8 ± 1.2
HDFS1 – 74	8.9 ± 1.9	22.0 ± 0.9	51.7 ± 0.6	166.1 ± 1.2
HDFS1 – 79	25.2 ± 1.9	83.7 ± 0.9	99.7 ± 0.6	120.1 ± 1.2
HDFS1 – 80	–0.3 ± 1.9	23.6 ± 0.9	44.2 ± 0.6	57.0 ± 1.2
HDFS1 – 83	103.7 ± 1.9	163.8 ± 0.9	338.9 ± 0.6	534.6 ± 1.2
HDFS1 – 86	14.4 ± 3.1	93.2 ± 1.2	177.8 ± 0.9	256.5 ± 1.7
HDFS1 – 87	2.0 ± 1.9	5.4 ± 1.0	12.3 ± 0.6	19.4 ± 1.2
HDFS1 – 92	8.3 ± 2.0	16.7 ± 1.0	24.7 ± 0.7	41.4 ± 1.2
HDFS1 – 98	2.3 ± 2.0	38.6 ± 1.0	221.7 ± 0.6	846.6 ± 1.2
HDFS1 – 105	–3.6 ± 1.9	3.1 ± 0.9	2.1 ± 0.6	7.5 ± 1.2
HDFS1 – 107	34.3 ± 1.9	48.0 ± 0.9	60.6 ± 0.6	101.8 ± 1.2
HDFS1 – 99	16.1 ± 1.8	27.7 ± 0.9	44.1 ± 0.6	89.5 ± 1.1
HDFS1 – 119	35.4 ± 1.9	50.4 ± 0.9	75.9 ± 0.6	166.4 ± 1.2
HDFS1 – 111	7.0 ± 1.9	50.8 ± 0.9	251.3 ± 0.6	802.5 ± 1.2
HDFS1 – 112	15.2 ± 1.9	43.8 ± 0.9	52.8 ± 0.6	64.5 ± 1.2
HDFS1 – 113	–2.1 ± 1.9	11.2 ± 0.9	21.1 ± 0.6	38.7 ± 1.2
HDFS1 – 117	5.8 ± 1.9	5.8 ± 0.9	6.2 ± 0.6	12.9 ± 1.2
HDFS1 – 115	22.6 ± 1.9	49.8 ± 0.9	114.4 ± 0.6	228.3 ± 1.2
HDFS1 – 127	25.7 ± 1.9	38.5 ± 0.9	55.5 ± 0.6	113.3 ± 1.2
HDFS1 – 121	48.4 ± 2.0	63.8 ± 1.0	117.0 ± 0.6	181.6 ± 1.2
HDFS1 – 125	1.8 ± 1.8	7.2 ± 0.9	11.8 ± 0.6	23.5 ± 1.1
HDFS1 – 131	5.2 ± 1.9	19.0 ± 0.9	28.0 ± 0.6	45.7 ± 1.2
HDFS1 – 139	5.1 ± 1.9	38.5 ± 1.0	54.9 ± 0.6	77.7 ± 1.2
HDFS1 – 141	72.3 ± 1.9	103.2 ± 1.0	183.8 ± 0.7	293.6 ± 1.2
HDFS1 – 148	–4.1 ± 1.9	2.0 ± 0.9	3.8 ± 0.6	9.6 ± 1.2

Table A.1: Optical Photometry – continued

ID	F300W <sup>a</sup>	F450W <sup>a</sup>	F606W <sup>a</sup>	F814W <sup>a</sup>
HDFS1 – 152	$-1.9 \pm 1.9$	$11.1 \pm 0.9$	$31.4 \pm 0.6$	$40.7 \pm 1.2$
HDFS1 – 160	$2.5 \pm 1.9$	$97.1 \pm 0.9$	$150.4 \pm 0.6$	$176.0 \pm 1.1$
HDFS1 – 163	$11.3 \pm 1.9$	$42.2 \pm 0.9$	$55.6 \pm 0.6$	$106.4 \pm 1.2$
HDFS1 – 173	$19.0 \pm 1.9$	$29.0 \pm 0.9$	$32.9 \pm 0.6$	$52.9 \pm 1.2$
HDFS1 – 182	$2.8 \pm 2.0$	$0.3 \pm 1.0$	$3.5 \pm 0.7$	$7.0 \pm 1.2$
HDFS1 – 186	$89.2 \pm 1.9$	$234.9 \pm 0.9$	$577.6 \pm 0.6$	$963.1 \pm 1.2$
HDFS1 – 194	$4.5 \pm 2.0$	$12.6 \pm 1.0$	$35.3 \pm 0.6$	$48.1 \pm 1.2$
HDFS1 – 187	$32.5 \pm 1.9$	$71.2 \pm 0.9$	$136.3 \pm 0.6$	$317.6 \pm 1.2$
HDFS1 – 188	$19.8 \pm 1.6$	$31.8 \pm 0.8$	$66.5 \pm 0.5$	$130.6 \pm 1.0$
HDFS1 – 207	$25.6 \pm 2.0$	$116.9 \pm 1.0$	$478.8 \pm 0.6$	$1439.3 \pm 1.2$
HDFS1 – 232	$94.7 \pm 2.1$	$149.3 \pm 1.0$	$308.3 \pm 0.7$	$498.4 \pm 1.2$
HDFS1 – 236	$42.8 \pm 2.4$	$59.9 \pm 1.2$	$112.0 \pm 0.7$	$179.1 \pm 1.4$
HDFS1 – 237	$40.2 \pm 2.4$	$73.1 \pm 1.1$	$153.6 \pm 0.7$	$298.7 \pm 1.4$
HDFS1 – 276	$13.1 \pm 2.3$	$38.3 \pm 1.1$	$46.9 \pm 0.7$	$78.6 \pm 1.5$
HDFS1 – 283	$12.2 \pm 2.3$	$30.5 \pm 1.1$	$43.1 \pm 0.7$	$70.9 \pm 1.4$
HDFS1 – 286	$17.6 \pm 3.3$	$51.4 \pm 1.6$	$57.1 \pm 0.9$	$84.4 \pm 1.9$
HDFS1 – 287	$64.9 \pm 2.5$	$94.3 \pm 1.3$	$132.8 \pm 0.8$	$271.7 \pm 1.7$
HDFS1 – 302	$12.9 \pm 2.4$	$34.0 \pm 1.1$	$118.3 \pm 0.7$	$307.7 \pm 1.6$
HDFS1 – 289	$233.6 \pm 2.6$	$498.0 \pm 1.3$	$989.8 \pm 0.8$	$1917.0 \pm 1.8$
HDFS1 – 291	$-0.6 \pm 2.2$	$5.4 \pm 1.0$	$14.2 \pm 0.7$	$72.1 \pm 1.3$
HDFS1 – 299	$77.2 \pm 2.1$	$156.7 \pm 1.0$	$346.1 \pm 0.7$	$688.6 \pm 1.2$
HDFS1 – 306	$2.0 \pm 2.1$	$19.8 \pm 1.0$	$24.6 \pm 0.7$	$40.3 \pm 1.3$
HDFS1 – 313	$39.5 \pm 2.1$	$59.8 \pm 1.0$	$117.5 \pm 0.7$	$201.4 \pm 1.2$
HDFS1 – 317	$-3.4 \pm 2.1$	$7.8 \pm 1.1$	$11.4 \pm 0.7$	$31.3 \pm 1.4$
HDFS1 – 318	$13.2 \pm 2.1$	$141.6 \pm 1.0$	$546.9 \pm 0.7$	$1140.3 \pm 1.2$
HDFS1 – 335	$5.6 \pm 2.3$	$42.6 \pm 1.1$	$58.7 \pm 0.7$	$71.1 \pm 1.4$
HDFS1 – 326	$56.3 \pm 2.1$	$69.0 \pm 1.0$	$111.8 \pm 0.7$	$193.5 \pm 1.2$
HDFS1 – 332	$61.1 \pm 2.0$	$170.2 \pm 1.0$	$415.1 \pm 0.7$	$725.6 \pm 1.2$
HDFS1 – 334	$10.1 \pm 2.1$	$38.1 \pm 1.0$	$86.6 \pm 0.7$	$231.1 \pm 1.2$
HDFS1 – 340	$39.9 \pm 3.8$	$67.8 \pm 1.4$	$131.6 \pm 0.9$	$228.2 \pm 1.8$
HDFS1 – 342	$50.0 \pm 1.9$	$69.0 \pm 1.0$	$101.2 \pm 0.6$	$193.5 \pm 1.2$
HDFS1 – 346	$28.6 \pm 2.1$	$47.1 \pm 1.0$	$94.0 \pm 0.7$	$143.0 \pm 1.2$
HDFS1 – 347	$5.2 \pm 2.1$	$19.7 \pm 1.0$	$41.1 \pm 0.7$	$52.9 \pm 1.2$
HDFS1 – 345	$41.1 \pm 1.9$	$207.3 \pm 1.0$	$821.0 \pm 0.7$	$2147.5 \pm 1.2$
HDFS1 – 350	$-0.2 \pm 2.0$	$3.9 \pm 1.0$	$9.1 \pm 0.7$	$19.0 \pm 1.2$
HDFS1 – 355	$3.9 \pm 2.1$	$4.6 \pm 1.0$	$5.7 \pm 0.7$	$12.2 \pm 1.2$
HDFS1 – 354	$3.4 \pm 1.6$	$9.6 \pm 0.8$	$12.0 \pm 0.5$	$22.1 \pm 1.0$

Table A.1: Optical Photometry – continued

ID	F300W <sup>a</sup>	F450W <sup>a</sup>	F606W <sup>a</sup>	F814W <sup>a</sup>
HDFS1 – 364	81.1 ± 1.9	117.4 ± 0.9	164.0 ± 0.6	274.9 ± 1.2
HDFS1 – 363	50.1 ± 2.0	115.3 ± 1.0	158.0 ± 0.7	268.8 ± 1.2
HDFS1 – 360	27.1 ± 1.9	86.4 ± 1.0	114.0 ± 0.6	198.9 ± 1.2
HDFS1 – 368	36.1 ± 1.9	60.0 ± 0.9	67.7 ± 0.6	123.8 ± 1.2
HDFS1 – 372	32.4 ± 1.8	75.8 ± 0.9	172.0 ± 0.6	336.5 ± 1.1
HDFS1 – 373	34.1 ± 1.8	70.7 ± 0.9	112.0 ± 0.6	202.1 ± 1.1
HDFS1 – 378	9.2 ± 2.0	72.6 ± 1.0	98.4 ± 0.7	130.4 ± 1.2
HDFS1 – 379	38.0 ± 2.1	67.8 ± 1.0	124.7 ± 0.7	345.9 ± 1.2
HDFS1 – 377	2.1 ± 2.1	15.7 ± 1.0	34.2 ± 0.7	130.2 ± 1.3
HDFS1 – 380	−3.1 ± 1.9	8.8 ± 0.9	23.7 ± 0.6	101.9 ± 1.2
HDFS1 – 381	18.4 ± 1.9	37.3 ± 0.9	45.5 ± 0.6	83.8 ± 1.2
HDFS1 – 382	−2.7 ± 1.9	24.9 ± 0.9	31.2 ± 0.6	45.8 ± 1.2
HDFS1 – 386	13.7 ± 1.9	102.0 ± 0.9	139.6 ± 0.6	191.4 ± 1.2
HDFS1 – 383	65.3 ± 1.9	119.3 ± 0.9	266.5 ± 0.6	412.6 ± 1.2
HDFS1 – 424	0.0 ± 1.9	2.3 ± 0.9	7.6 ± 0.6	35.7 ± 1.2
HDFS1 – 393	5.0 ± 1.9	33.0 ± 0.9	47.7 ± 0.6	75.6 ± 1.2
HDFS1 – 394	4.5 ± 1.9	25.6 ± 1.0	63.6 ± 0.6	109.9 ± 1.2
HDFS1 – 395	73.1 ± 2.1	291.9 ± 1.0	603.1 ± 0.7	930.9 ± 1.2
HDFS1 – 397	14.4 ± 2.1	23.4 ± 1.0	38.7 ± 0.7	94.8 ± 1.2
HDFS1 – 399	57.9 ± 2.0	89.7 ± 1.0	180.2 ± 0.7	315.6 ± 1.2
HDFS1 – 404	27.3 ± 2.9	43.4 ± 1.2	70.1 ± 0.8	112.3 ± 1.5
HDFS1 – 405	5.1 ± 1.9	3.3 ± 0.9	9.2 ± 0.6	47.5 ± 1.2
HDFS1 – 398	1.1 ± 1.9	1.8 ± 0.9	5.0 ± 0.6	24.1 ± 1.1
HDFS1 – 406	118.8 ± 2.1	343.0 ± 1.0	1174.0 ± 0.7	3242.7 ± 1.2
HDFS1 – 411	11.1 ± 2.2	6.6 ± 1.1	16.2 ± 0.7	41.3 ± 1.3
HDFS1 – 427	10.5 ± 1.9	16.1 ± 0.9	22.5 ± 0.6	42.8 ± 1.2
HDFS1 – 414	26.6 ± 2.0	89.1 ± 1.0	236.7 ± 0.7	526.1 ± 1.2
HDFS1 – 410	85.3 ± 2.0	144.6 ± 1.0	285.7 ± 0.7	491.4 ± 1.2
HDFS1 – 415	61.0 ± 1.9	116.1 ± 0.9	252.7 ± 0.7	415.9 ± 1.2
HDFS1 – 421	121.1 ± 1.9	428.1 ± 0.9	1243.9 ± 0.6	2490.1 ± 1.2
HDFS1 – 426	13.0 ± 2.1	15.4 ± 1.0	33.9 ± 0.7	85.1 ± 1.2
HDFS1 – 434	15.6 ± 2.0	15.9 ± 1.0	41.1 ± 0.7	84.0 ± 1.2
HDFS1 – 435	1.6 ± 2.0	13.8 ± 1.0	37.6 ± 0.7	89.5 ± 1.2
HDFS1 – 437	49.1 ± 2.0	69.2 ± 1.0	81.6 ± 0.7	127.7 ± 1.2
HDFS1 – 439	93.5 ± 1.9	140.1 ± 0.9	212.6 ± 0.6	382.9 ± 1.2
HDFS1 – 440	6.2 ± 1.9	0.1 ± 0.9	6.7 ± 0.6	33.9 ± 1.2
HDFS1 – 448	31.5 ± 2.3	62.4 ± 1.1	71.2 ± 0.8	100.2 ± 1.4



Table A.1: Optical Photometry – continued

ID	F300W <sup>a</sup>	F450W <sup>a</sup>	F606W <sup>a</sup>	F814W <sup>a</sup>
HDFS1 – 450	20.0 ± 1.7	27.1 ± 0.9	65.5 ± 0.6	102.8 ± 1.1
HDFS1 – 463	–0.5 ± 1.9	15.4 ± 0.9	20.5 ± 0.6	26.9 ± 1.2
HDFS1 – 484	6.0 ± 2.1	64.3 ± 1.0	353.4 ± 0.7	1138.1 ± 1.3
HDFS1 – 472	12.2 ± 2.1	36.7 ± 1.0	74.9 ± 0.7	168.4 ± 1.2
HDFS1 – 476	27.0 ± 1.8	49.8 ± 0.9	59.1 ± 0.6	97.2 ± 1.2
HDFS1 – 480	–2.5 ± 2.1	2.3 ± 1.0	0.3 ± 0.7	1.7 ± 1.3
HDFS1 – 479	5.7 ± 1.9	12.1 ± 0.9	26.3 ± 0.7	47.0 ± 1.2
HDFS1 – 483	4.4 ± 1.8	34.1 ± 0.9	43.9 ± 0.6	58.8 ± 1.2
HDFS1 – 487	3.0 ± 2.1	1.8 ± 1.0	4.4 ± 0.7	16.4 ± 1.2
HDFS1 – 488	42.3 ± 2.1	92.3 ± 1.0	235.8 ± 0.7	493.2 ± 1.2
HDFS1 – 492	19.7 ± 2.1	31.9 ± 1.0	44.5 ± 0.7	57.7 ± 1.3
HDFS1 – 489	46.1 ± 2.2	96.0 ± 1.0	236.3 ± 0.7	513.2 ± 1.3
HDFS1 – 478	47.4 ± 2.2	77.4 ± 1.0	97.1 ± 0.7	176.7 ± 1.3
HDFS1 – 505	2.3 ± 1.9	35.3 ± 1.0	50.0 ± 0.6	93.3 ± 1.2
HDFS1 – 511	28.5 ± 2.3	63.3 ± 1.1	97.3 ± 0.7	190.9 ± 1.3
HDFS1 – 516	48.9 ± 3.4	68.8 ± 1.4	126.7 ± 0.9	188.2 ± 1.7
HDFS1 – 542	3.7 ± 2.4	28.3 ± 1.1	81.2 ± 0.8	139.0 ± 1.3
HDFS1 – 521	80.4 ± 2.8	177.6 ± 1.3	427.4 ± 0.9	875.4 ± 1.5
HDFS1 – 522	13.2 ± 2.0	29.7 ± 1.0	58.3 ± 0.7	109.2 ± 1.2
HDFS1 – 530	26.2 ± 3.5	52.3 ± 1.6	73.6 ± 1.0	158.6 ± 1.8
HDFS1 – 536	25.1 ± 1.9	43.8 ± 1.0	66.0 ± 0.7	144.9 ± 1.2
HDFS1 – 527	31.0 ± 2.0	59.3 ± 1.0	104.5 ± 0.7	299.5 ± 1.2
HDFS1 – 538	97.8 ± 2.4	162.6 ± 1.1	294.2 ± 0.8	504.3 ± 1.4
HDFS1 – 548	12.9 ± 2.3	8.5 ± 1.1	41.6 ± 0.8	174.2 ± 1.3
HDFS1 – 555	–5.9 ± 3.0	8.5 ± 1.5	22.7 ± 1.1	95.6 ± 1.6

<sup>a</sup> Flux measured with a 2''0 diameter aperture.

Note – All fluxes in units of  $10^{-31}$  ergs s<sup>–1</sup>Hz<sup>–1</sup>cm<sup>–2</sup>.

Table A.2: NIR Photometry –  $K_{s,AB}^{\text{tot}} \leq 23.5$  sample

ID	$J_s^a$	$H^a$	$K_s^a$	$K_s^{\text{tot } b}$
HDFS1 – 30	$465.8 \pm 15.2$	$528.4 \pm 29.2$	$629.7 \pm 24.8$	$700.4 \pm 39.6$
HDFS1 – 33	$128.3 \pm 15.1$	$195.7 \pm 29.0$	$184.7 \pm 24.7$	$186.5 \pm 24.5$
HDFS1 – 31	$71.1 \pm 14.1$	$119.7 \pm 27.4$	$184.1 \pm 23.1$	$261.5 \pm 38.4$
HDFS1 – 36	$119.4 \pm 13.5$	$275.2 \pm 26.2$	$337.0 \pm 22.0$	$353.4 \pm 28.0$
HDFS1 – 37	$11.3 \pm 14.7$	$119.1 \pm 28.3$	$281.7 \pm 24.0$	$337.1 \pm 37.1$
HDFS1 – 45	$228.4 \pm 14.7$	$225.4 \pm 28.4$	$216.9 \pm 24.1$	$201.1 \pm 22.4$
HDFS1 – 50	$132.0 \pm 12.4$	$247.2 \pm 23.6$	$294.2 \pm 19.9$	$289.0 \pm 20.2$
HDFS1 – 52	$139.0 \pm 13.4$	$151.8 \pm 25.9$	$146.9 \pm 21.8$	$174.4 \pm 26.5$
HDFS1 – 54	$98.0 \pm 13.0$	$127.7 \pm 24.9$	$159.0 \pm 21.1$	$150.8 \pm 28.7$
HDFS1 – 62	$131.4 \pm 11.3$	$140.9 \pm 21.6$	$220.0 \pm 18.2$	$230.4 \pm 29.9$
HDFS1 – 58	$388.1 \pm 12.1$	$576.8 \pm 23.1$	$782.9 \pm 19.5$	$858.8 \pm 29.7$
HDFS1 – 63	$823.6 \pm 11.5$	$986.8 \pm 22.0$	$1179.9 \pm 18.5$	$1255.0 \pm 26.3$
HDFS1 – 69	$193.9 \pm 11.5$	$248.7 \pm 22.0$	$308.5 \pm 18.5$	$294.5 \pm 18.2$
HDFS1 – 74	$536.9 \pm 11.5$	$858.4 \pm 22.0$	$1248.0 \pm 18.5$	$1349.0 \pm 26.6$
HDFS1 – 79	$211.8 \pm 11.5$	$236.9 \pm 22.0$	$249.8 \pm 18.5$	$306.6 \pm 28.0$
HDFS1 – 80	$80.2 \pm 11.5$	$63.5 \pm 22.0$	$165.0 \pm 18.5$	$153.0 \pm 17.2$
HDFS1 – 83	$739.3 \pm 11.5$	$784.4 \pm 22.0$	$896.1 \pm 18.5$	$1087.8 \pm 30.1$
HDFS1 – 86	$308.0 \pm 13.0$	$312.9 \pm 24.5$	$184.1 \pm 20.6$	$188.3 \pm 22.1$
HDFS1 – 87	$83.6 \pm 11.5$	$79.6 \pm 22.1$	$196.8 \pm 18.6$	$187.0 \pm 18.0$
HDFS1 – 92	$134.6 \pm 11.5$	$216.8 \pm 22.0$	$231.2 \pm 18.5$	$216.0 \pm 17.2$
HDFS1 – 98	$2035.4 \pm 11.5$	$2785.0 \pm 22.0$	$3513.2 \pm 18.5$	$3620.1 \pm 26.7$
HDFS1 – 105	$45.4 \pm 11.5$	$235.4 \pm 22.0$	$368.2 \pm 18.6$	$363.0 \pm 19.5$
HDFS1 – 107	$156.7 \pm 11.5$	$232.0 \pm 22.0$	$195.1 \pm 18.5$	$181.0 \pm 17.2$
HDFS1 – 99	$145.3 \pm 10.6$	$152.6 \pm 20.3$	$180.7 \pm 17.1$	$203.9 \pm 26.5$
HDFS1 – 119	$304.0 \pm 11.5$	$305.8 \pm 22.0$	$339.7 \pm 18.5$	$354.3 \pm 21.8$
HDFS1 – 111	$1931.8 \pm 11.5$	$2662.9 \pm 22.0$	$3228.2 \pm 18.5$	$3267.8 \pm 26.2$
HDFS1 – 112	$131.9 \pm 11.4$	$183.6 \pm 22.0$	$153.4 \pm 18.5$	$157.2 \pm 30.2$
HDFS1 – 113	$186.3 \pm 11.5$	$218.6 \pm 22.0$	$354.2 \pm 18.5$	$342.4 \pm 20.0$
HDFS1 – 117	$57.5 \pm 11.4$	$148.6 \pm 21.9$	$183.8 \pm 18.5$	$170.4 \pm 17.1$
HDFS1 – 115	$373.3 \pm 11.5$	$470.6 \pm 22.0$	$568.7 \pm 18.6$	$564.2 \pm 22.5$
HDFS1 – 127	$147.7 \pm 11.5$	$129.4 \pm 22.0$	$192.0 \pm 18.5$	$276.3 \pm 35.2$
HDFS1 – 121	$228.9 \pm 11.5$	$204.1 \pm 22.1$	$256.1 \pm 18.6$	$276.5 \pm 21.9$
HDFS1 – 125	$99.5 \pm 10.5$	$131.5 \pm 20.1$	$179.3 \pm 16.9$	$178.7 \pm 23.6$
HDFS1 – 131	$141.8 \pm 11.5$	$179.4 \pm 22.0$	$244.3 \pm 18.5$	$233.5 \pm 19.7$
HDFS1 – 139	$226.1 \pm 11.5$	$294.4 \pm 22.0$	$395.2 \pm 18.5$	$393.3 \pm 26.0$
HDFS1 – 141	$381.5 \pm 11.5$	$353.1 \pm 22.0$	$440.7 \pm 18.5$	$577.6 \pm 29.6$
HDFS1 – 148	$79.8 \pm 11.5$	$191.7 \pm 22.0$	$244.4 \pm 18.6$	$226.6 \pm 17.2$

Table A.2: NIR Photometry – continued

ID	J <sub>s</sub> <sup>a</sup>	H <sup>a</sup>	K <sub>s</sub> <sup>a</sup>	K <sub>s</sub> <sup>tot b</sup>
HDFS1 – 152	70.6 ± 11.5	171.0 ± 22.0	176.0 ± 18.5	219.0 ± 26.6
HDFS1 – 160	199.7 ± 11.1	286.4 ± 21.4	365.2 ± 18.0	356.9 ± 22.1
HDFS1 – 163	402.9 ± 11.5	601.6 ± 22.0	781.1 ± 18.5	812.1 ± 26.3
HDFS1 – 173	106.4 ± 11.5	88.8 ± 22.0	148.9 ± 18.5	182.9 ± 33.7
HDFS1 – 182	85.2 ± 11.5	211.3 ± 22.0	279.8 ± 18.5	261.7 ± 18.1
HDFS1 – 186	1605.1 ± 11.5	1933.2 ± 22.0	2194.5 ± 18.5	2992.2 ± 37.2
HDFS1 – 194	109.0 ± 11.5	156.7 ± 22.0	289.2 ± 18.5	295.6 ± 27.3
HDFS1 – 187	858.0 ± 11.5	1201.0 ± 22.0	1794.9 ± 18.5	2208.2 ± 32.7
HDFS1 – 188	189.0 ± 9.9	245.9 ± 19.1	248.3 ± 16.0	237.8 ± 17.0
HDFS1 – 207	3169.8 ± 11.5	4177.3 ± 22.0	4909.9 ± 18.6	5594.4 ± 34.5
HDFS1 – 232	630.5 ± 11.5	728.9 ± 22.0	715.6 ± 18.5	735.2 ± 24.3
HDFS1 – 236	244.1 ± 11.5	244.9 ± 22.0	281.0 ± 18.5	301.7 ± 33.7
HDFS1 – 237	418.8 ± 11.5	583.9 ± 22.1	576.1 ± 18.6	721.1 ± 29.2
HDFS1 – 276	189.8 ± 11.5	247.7 ± 22.0	287.5 ± 18.5	232.4 ± 24.9
HDFS1 – 283	158.1 ± 11.5	256.2 ± 22.0	232.2 ± 18.5	213.4 ± 19.3
HDFS1 – 286	152.3 ± 11.5	213.0 ± 22.0	218.4 ± 18.5	206.2 ± 17.7
HDFS1 – 287	491.0 ± 10.8	492.8 ± 20.8	592.0 ± 17.5	622.7 ± 23.8
HDFS1 – 302	611.2 ± 11.5	797.7 ± 22.0	1006.4 ± 18.5	967.5 ± 22.5
HDFS1 – 289	3402.5 ± 11.5	4810.0 ± 22.0	5790.5 ± 18.5	7104.0 ± 37.7
HDFS1 – 291	358.2 ± 11.5	547.6 ± 22.1	733.7 ± 18.6	700.0 ± 19.6
HDFS1 – 299	1139.6 ± 11.5	1435.2 ± 22.0	1619.5 ± 18.5	2788.3 ± 44.4
HDFS1 – 306	103.1 ± 11.5	95.0 ± 22.0	181.2 ± 18.5	177.3 ± 18.0
HDFS1 – 313	249.6 ± 11.5	328.6 ± 22.0	333.4 ± 18.5	351.2 ± 25.6
HDFS1 – 317	23.4 ± 11.3	81.7 ± 21.7	109.4 ± 18.3	159.1 ± 26.4
HDFS1 – 318	2001.0 ± 11.5	2422.8 ± 22.0	2745.0 ± 18.6	3336.3 ± 34.5
HDFS1 – 335	91.6 ± 11.5	213.1 ± 22.1	233.1 ± 18.6	250.0 ± 24.8
HDFS1 – 326	175.9 ± 11.5	277.8 ± 22.0	191.7 ± 18.5	172.5 ± 17.4
HDFS1 – 332	1140.3 ± 11.5	1462.2 ± 22.0	1681.7 ± 18.5	1727.9 ± 26.5
HDFS1 – 334	873.6 ± 11.5	1478.9 ± 22.0	2203.7 ± 18.5	2577.4 ± 33.0
HDFS1 – 340	315.4 ± 11.5	350.1 ± 22.0	384.4 ± 18.6	433.6 ± 24.5
HDFS1 – 342	254.3 ± 11.5	259.2 ± 22.0	307.0 ± 18.6	297.6 ± 19.7
HDFS1 – 346	161.6 ± 11.5	187.3 ± 22.0	214.6 ± 18.5	280.7 ± 32.4
HDFS1 – 347	60.7 ± 11.5	162.8 ± 22.0	179.3 ± 18.5	214.5 ± 27.1
HDFS1 – 345	5113.4 ± 11.5	8029.0 ± 22.1	10027.0 ± 18.6	12210.0 ± 38.4
HDFS1 – 350	90.0 ± 14.7	169.1 ± 27.8	373.7 ± 23.7	393.7 ± 28.1
HDFS1 – 355	12.2 ± 11.5	106.0 ± 22.0	169.3 ± 18.5	165.1 ± 17.4
HDFS1 – 354	77.4 ± 9.4	203.5 ± 18.0	155.8 ± 15.2	151.6 ± 21.3

Table A.2: NIR Photometry – continued

ID	J <sub>s</sub> <sup>a</sup>	H <sup>a</sup>	K <sub>s</sub> <sup>a</sup>	K <sub>s</sub> <sup>tot b</sup>
HDFS1 – 364	388.1 ± 11.4	452.9 ± 21.9	515.8 ± 18.5	606.4 ± 35.9
HDFS1 – 363	580.5 ± 11.5	705.6 ± 22.0	791.4 ± 18.5	781.4 ± 21.8
HDFS1 – 360	561.7 ± 11.4	776.6 ± 21.9	817.3 ± 18.4	1071.2 ± 34.3
HDFS1 – 368	195.2 ± 11.5	190.1 ± 22.0	232.7 ± 18.5	250.7 ± 23.4
HDFS1 – 372	483.2 ± 10.4	593.5 ± 20.0	700.0 ± 16.9	754.1 ± 23.2
HDFS1 – 373	388.1 ± 10.3	445.5 ± 19.7	595.3 ± 16.6	607.9 ± 21.9
HDFS1 – 378	311.1 ± 11.5	422.2 ± 22.1	499.1 ± 18.6	648.2 ± 40.3
HDFS1 – 379	1373.1 ± 11.5	2079.8 ± 22.0	2726.2 ± 18.5	2881.6 ± 28.2
HDFS1 – 377	700.4 ± 11.5	1090.0 ± 22.0	1551.8 ± 18.5	1590.3 ± 24.9
HDFS1 – 380	291.4 ± 11.5	408.5 ± 22.0	518.0 ± 18.6	478.4 ± 20.0
HDFS1 – 381	121.8 ± 11.5	184.8 ± 22.0	219.2 ± 18.5	213.9 ± 21.5
HDFS1 – 382	70.6 ± 11.4	121.7 ± 21.9	191.8 ± 18.4	206.7 ± 24.9
HDFS1 – 386	462.9 ± 11.5	575.7 ± 22.0	620.5 ± 18.5	665.6 ± 26.6
HDFS1 – 383	543.2 ± 11.5	642.0 ± 22.0	656.8 ± 18.5	1037.5 ± 44.3
HDFS1 – 424	31.3 ± 11.5	48.8 ± 22.0	152.9 ± 18.5	177.3 ± 35.0
HDFS1 – 393	284.3 ± 11.5	352.9 ± 22.0	544.6 ± 18.5	664.9 ± 30.4
HDFS1 – 394	161.7 ± 13.0	198.9 ± 25.0	188.0 ± 21.1	308.1 ± 41.0
HDFS1 – 395	1321.3 ± 11.5	1516.6 ± 22.1	1554.7 ± 18.6	1947.7 ± 33.0
HDFS1 – 397	323.4 ± 11.5	526.9 ± 22.1	778.5 ± 18.6	952.8 ± 34.7
HDFS1 – 399	410.7 ± 11.5	532.8 ± 22.0	568.3 ± 18.5	546.5 ± 23.4
HDFS1 – 404	151.1 ± 11.5	153.3 ± 22.0	186.8 ± 18.6	261.2 ± 33.6
HDFS1 – 405	258.1 ± 11.5	341.2 ± 22.0	541.7 ± 18.5	565.7 ± 25.5
HDFS1 – 398	84.8 ± 10.7	141.2 ± 20.4	231.5 ± 17.2	335.1 ± 31.0
HDFS1 – 406	7359.3 ± 11.5	10974.2 ± 22.0	13863.9 ± 18.5	21541.4 ± 49.5
HDFS1 – 411	134.5 ± 11.5	235.4 ± 22.0	361.3 ± 18.5	370.4 ± 28.9
HDFS1 – 427	148.6 ± 11.5	186.9 ± 22.0	264.1 ± 18.5	261.3 ± 20.2
HDFS1 – 414	1248.8 ± 11.5	2030.9 ± 22.1	2714.7 ± 18.6	2770.6 ± 26.2
HDFS1 – 410	671.5 ± 11.5	782.2 ± 22.0	882.8 ± 18.5	1481.1 ± 41.1
HDFS1 – 415	552.8 ± 11.5	673.8 ± 22.0	637.9 ± 18.5	839.5 ± 33.0
HDFS1 – 421	4647.2 ± 11.6	6378.8 ± 22.3	7614.6 ± 18.7	9886.4 ± 40.3
HDFS1 – 426	259.9 ± 11.5	465.1 ± 22.1	659.7 ± 18.6	639.4 ± 21.6
HDFS1 – 434	119.2 ± 11.5	170.4 ± 22.0	230.1 ± 18.5	250.1 ± 20.6
HDFS1 – 435	139.1 ± 11.5	193.4 ± 22.0	227.9 ± 18.6	244.0 ± 31.9
HDFS1 – 437	201.1 ± 11.5	226.5 ± 22.1	285.0 ± 18.6	288.0 ± 23.0
HDFS1 – 439	496.9 ± 11.5	610.1 ± 22.0	637.5 ± 18.5	851.0 ± 36.3
HDFS1 – 440	284.0 ± 11.5	569.8 ± 22.0	781.8 ± 18.5	785.1 ± 24.6
HDFS1 – 448	198.3 ± 11.8	264.2 ± 22.5	258.6 ± 19.0	314.4 ± 28.7

Table A.2: NIR Photometry – continued

ID	$J_s^a$	$H^a$	$K_s^a$	$K_s^{\text{tot } b}$
HDFS1 – 450	$88.8 \pm 10.7$	$78.6 \pm 20.6$	$125.8 \pm 17.3$	$167.4 \pm 29.7$
HDFS1 – 463	$69.1 \pm 11.5$	$87.9 \pm 22.0$	$216.9 \pm 18.6$	$234.5 \pm 21.0$
HDFS1 – 484	$2428.7 \pm 11.5$	$3465.8 \pm 22.0$	$4114.4 \pm 18.5$	$4158.8 \pm 26.3$
HDFS1 – 472	$253.0 \pm 11.5$	$339.9 \pm 22.0$	$350.5 \pm 18.5$	$367.6 \pm 21.9$
HDFS1 – 476	$186.9 \pm 11.5$	$193.6 \pm 22.0$	$210.5 \pm 18.5$	$208.1 \pm 27.9$
HDFS1 – 480	$16.8 \pm 11.5$	$70.4 \pm 22.0$	$174.6 \pm 18.5$	$171.6 \pm 20.0$
HDFS1 – 479	$156.2 \pm 11.5$	$217.7 \pm 22.0$	$378.9 \pm 18.5$	$388.5 \pm 21.4$
HDFS1 – 483	$155.8 \pm 11.5$	$185.6 \pm 22.1$	$266.2 \pm 18.6$	$328.1 \pm 28.8$
HDFS1 – 487	$55.2 \pm 11.5$	$187.5 \pm 22.0$	$213.5 \pm 18.5$	$196.5 \pm 17.8$
HDFS1 – 488	$873.6 \pm 11.5$	$1245.4 \pm 22.0$	$1533.3 \pm 18.5$	$1947.3 \pm 32.3$
HDFS1 – 492	$105.6 \pm 11.5$	$100.6 \pm 22.0$	$147.5 \pm 18.5$	$164.7 \pm 24.0$
HDFS1 – 489	$934.6 \pm 11.5$	$1322.8 \pm 22.0$	$1568.4 \pm 18.6$	$1647.6 \pm 26.6$
HDFS1 – 478	$553.1 \pm 11.5$	$682.6 \pm 22.0$	$907.6 \pm 18.5$	$1157.7 \pm 37.3$
HDFS1 – 505	$265.1 \pm 11.5$	$438.4 \pm 22.0$	$423.6 \pm 18.5$	$425.5 \pm 20.3$
HDFS1 – 511	$451.0 \pm 11.5$	$669.7 \pm 22.1$	$889.9 \pm 18.6$	$962.4 \pm 26.5$
HDFS1 – 516	$205.6 \pm 11.5$	$268.6 \pm 22.0$	$229.7 \pm 18.5$	$381.8 \pm 37.0$
HDFS1 – 542	$216.4 \pm 11.5$	$195.7 \pm 22.0$	$291.6 \pm 18.5$	$293.5 \pm 23.1$
HDFS1 – 521	$1620.2 \pm 11.6$	$2313.2 \pm 22.3$	$2721.3 \pm 18.8$	$3263.4 \pm 35.4$
HDFS1 – 522	$145.8 \pm 15.6$	$111.6 \pm 29.3$	$232.5 \pm 25.1$	$222.4 \pm 26.0$
HDFS1 – 530	$357.5 \pm 11.5$	$395.9 \pm 22.0$	$520.6 \pm 18.5$	$531.7 \pm 24.6$
HDFS1 – 536	$203.9 \pm 11.5$	$257.9 \pm 22.0$	$258.4 \pm 18.5$	$294.0 \pm 32.1$
HDFS1 – 527	$1278.7 \pm 11.5$	$2125.7 \pm 22.0$	$2883.0 \pm 18.6$	$3437.7 \pm 35.1$
HDFS1 – 538	$706.7 \pm 11.5$	$962.7 \pm 22.1$	$1025.3 \pm 18.6$	$1059.7 \pm 25.0$
HDFS1 – 548	$508.4 \pm 11.5$	$787.7 \pm 22.1$	$835.5 \pm 18.6$	$922.8 \pm 30.2$
HDFS1 – 555	$427.0 \pm 12.7$	$743.0 \pm 24.5$	$1202.9 \pm 20.5$	$1204.0 \pm 26.4$

<sup>a</sup> Flux measured with a  $2''$ 0 diameter aperture.

<sup>b</sup> Flux measured from SExtractor BEST aperture with a  $2''$ 0 minimum diameter

Note – All fluxes in units of  $10^{-31} \text{ ergs s}^{-1} \text{ Hz}^{-1} \text{ cm}^{-2}$ .

TABLE A.3. NIR Template Extension Parameters

Template	Age Gyr	IMF	SFR
E/S0	12.7	Scalo	$\tau = 1$ Gyr
Sbc	12.7	Scalo	$\tau = 8$ Gyr
Scd	12.7	Salpeter	Constant
Irr	0.1	Salpeter	Constant
SB1	0.1	Salpeter	Constant
SB2	0.1	Salpeter	Constant

Table A.4:  $z_{phot}$  Catalog –  $K_{s,AB}^{tot} \leq 23.5$  sample

ID	RA (22h) J2000	DEC ( $-60^\circ$ ) J2000	$z_{phot}$	$L_U^{rest}$ $10^{10} L_\odot$	$L_B^{rest}$ $10^{10} L_\odot$	$L_V^{rest}$ $10^{10} L_\odot$
HDFS1 – 30	32 : 52.26	31 : 52.7	$1.36_{0.17}^{0.17}$	$3.74_{1.40}^{1.43}$	$2.53_{0.94}^{1.00}$	$2.36_{0.86}^{0.96}$
HDFS1 – 33	32 : 52.69	31 : 53.0	$0.92_{0.14}^{0.13}$	$0.59_{0.25}^{0.27}$	$0.34_{0.13}^{0.18}$	$0.29_{0.11}^{0.17}$
HDFS1 – 31	32 : 52.04	31 : 54.1	$0.62_{0.13}^{0.15}$ <sup>a</sup>	$0.12_{0.06}^{0.09}$	$0.07_{0.04}^{0.05}$	$0.07_{0.03}^{0.05}$
HDFS1 – 36	32 : 48.84	31 : 54.1	$3.32_{0.31}^{0.30}$	$16.53_{0.98}^{4.64}$	$9.21_{0.38}^{2.50}$	$8.13_{0.49}^{3.08}$
HDFS1 – 37	32 : 53.38	31 : 54.5	$3.00_{0.37}^{0.63}$ <sup>a</sup>	$5.06_{1.92}^{4.47}$	$5.25_{1.99}^{4.64}$	$6.62_{2.50}^{5.88}$
HDFS1 – 45 <sup>b</sup>	32 : 56.18	31 : 56.6	$5.34_{0.45}^{0.44}$	$59.89_{14.96}^{11.84}$	$32.92_{6.75}^{0.11}$	$27.59_{6.67}^{0.08}$
HDFS1 – 50	32 : 49.45	31 : 58.1	$1.22_{0.16}^{0.28}$	$0.28_{0.12}^{0.40}$	$0.32_{0.13}^{0.33}$	$0.43_{0.17}^{0.35}$
HDFS1 – 52	32 : 54.06	31 : 58.1	$1.22_{0.18}^{0.16}$	$1.57_{0.51}^{0.49}$	$0.89_{0.33}^{0.24}$	$0.69_{0.25}^{0.19}$
HDFS1 – 54	32 : 52.98	31 : 58.4	$1.08_{0.28}^{0.15}$	$0.53_{0.29}^{0.25}$	$0.32_{0.20}^{0.15}$	$0.27_{0.16}^{0.15}$
HDFS1 – 62	32 : 50.35	32 : 01.0	$1.00_{0.17}^{0.14}$	$0.63_{0.26}^{0.29}$	$0.40_{0.18}^{0.21}$	$0.35_{0.16}^{0.19}$
HDFS1 – 58	32 : 53.38	32 : 01.3	$1.02_{0.14}^{0.14}$	$0.52_{0.26}^{0.39}$	$0.60_{0.27}^{0.30}$	$0.79_{0.33}^{0.31}$
HDFS1 – 63	32 : 50.28	32 : 03.5	$0.44_{0.10}^{0.10}$	$0.40_{0.21}^{0.26}$	$0.26_{0.13}^{0.16}$	$0.25_{0.12}^{0.13}$
HDFS1 – 69	32 : 48.80	32 : 03.5	$0.84_{0.13}^{0.24}$	$0.43_{0.18}^{0.48}$	$0.25_{0.10}^{0.32}$	$0.24_{0.08}^{0.29}$
HDFS1 – 74	32 : 53.70	32 : 06.0	$0.96_{0.14}^{0.14}$	$1.01_{0.48}^{0.85}$	$0.90_{0.40}^{0.58}$	$1.05_{0.42}^{0.50}$
HDFS1 – 79	32 : 49.06	32 : 06.0	$2.22_{0.24}^{0.23}$	$10.13_{2.31}^{2.32}$	$5.54_{1.20}^{0.99}$	$4.26_{0.94}^{0.81}$
HDFS1 – 80	32 : 51.86	32 : 06.0	$3.24_{0.30}^{0.30}$	$8.00_{0.67}^{1.48}$	$4.07_{0.23}^{0.28}$	$3.21_{0.14}^{0.26}$
HDFS1 – 83	32 : 52.73	32 : 07.1	$0.46_{0.10}^{0.10}$	$0.62_{0.30}^{0.40}$	$0.39_{0.19}^{0.20}$	$0.35_{0.15}^{0.17}$
HDFS1 – 86	32 : 46.68	32 : 07.1	$0.16_{0.08}^{0.08}$	$0.02_{0.01}^{0.03}$	$0.01_{0.01}^{0.02}$	$0.01_{0.01}^{0.02}$
HDFS1 – 87	32 : 54.82	32 : 08.2	$1.60_{0.21}^{0.93}$ <sup>a</sup>	$0.87_{0.30}^{6.98}$	$0.63_{0.23}^{5.03}$	$0.62_{0.23}^{4.87}$
HDFS1 – 92	32 : 56.26	32 : 09.6	$1.38_{0.18}^{0.18}$	$0.99_{0.40}^{0.40}$	$0.68_{0.25}^{0.28}$	$0.63_{0.21}^{0.27}$
HDFS1 – 98	32 : 55.72	32 : 11.4	$0.56_{0.11}^{0.11}$	$0.45_{0.23}^{0.46}$	$0.58_{0.29}^{0.40}$	$0.80_{0.40}^{0.46}$
HDFS1 – 105	32 : 49.24	32 : 11.8	$2.14_{0.27}^{0.22}$	$1.70_{0.73}^{0.67}$	$1.91_{0.73}^{0.67}$	$2.50_{0.89}^{0.82}$
HDFS1 – 107	32 : 51.65	32 : 12.5	$1.00_{0.15}^{0.14}$	$0.79_{0.25}^{0.39}$	$0.46_{0.19}^{0.19}$	$0.37_{0.15}^{0.19}$
HDFS1 – 99	32 : 55.75	32 : 13.6	$0.72_{0.12}^{0.13}$	$0.29_{0.13}^{0.17}$	$0.19_{0.08}^{0.10}$	$0.16_{0.06}^{0.09}$
HDFS1 – 119	32 : 52.01	32 : 15.0	$0.84_{0.13}^{0.13}$	$0.77_{0.31}^{0.35}$	$0.49_{0.19}^{0.23}$	$0.43_{0.16}^{0.21}$

Table A.4:  $z_{phot}$  Catalog – continued

ID	RA (22h) J2000	DEC ( $-60^\circ$ ) J2000	$z_{phot}$	$L_U^{rest}$ $10^{10} L_\odot$	$L_B^{rest}$ $10^{10} L_\odot$	$L_V^{rest}$ $10^{10} L_\odot$
HDFS1 – 111	32 : 54.82	32 : 15.4	$0.52^{0.11}_{0.11}$	$0.38^{0.41}_{0.21}$	$0.45^{0.33}_{0.24}$	$0.61^{0.35}_{0.31}$
HDFS1 – 112	32 : 54.42	32 : 15.4	$2.14^{0.22}_{0.23}$	$4.15^{0.97}_{0.85}$	$2.35^{0.47}_{0.49}$	$1.79^{0.37}_{0.34}$
HDFS1 – 113	32 : 52.58	32 : 15.4	$1.50^{0.18}_{0.18}$	$1.45^{0.53}_{0.52}$	$1.08^{0.40}_{0.40}$	$1.08^{0.39}_{0.40}$
HDFS1 – 117	32 : 52.91	32 : 15.7	$1.54^{0.23}_{0.25}$	$0.44^{0.25}_{0.18}$	$0.39^{0.22}_{0.17}$	$0.48^{0.25}_{0.21}$
HDFS1 – 115	32 : 48.88	32 : 16.1	$0.54^{0.11}_{0.11}$	$0.26^{0.17}_{0.13}$	$0.19^{0.10}_{0.09}$	$0.18^{0.09}_{0.08}$
HDFS1 – 127	32 : 53.05	32 : 17.2	$0.78^{0.13}_{0.13}$	$0.60^{0.27}_{0.25}$	$0.37^{0.17}_{0.15}$	$0.31^{0.14}_{0.12}$
HDFS1 – 121	32 : 55.54	32 : 17.5	$0.48^{0.10}_{0.10}$	$0.22^{0.12}_{0.10}$	$0.14^{0.07}_{0.06}$	$0.11^{0.05}_{0.05}$
HDFS1 – 125	32 : 48.16	32 : 18.2	$1.40^{0.18}_{0.19}$	$0.68^{0.29}_{0.31}$	$0.50^{0.21}_{0.20}$	$0.49^{0.21}_{0.17}$
HDFS1 – 131	32 : 52.08	32 : 18.6	$1.38^{0.18}_{0.18}$ <sup>a</sup>	$1.10^{0.44}_{0.43}$	$0.75^{0.30}_{0.28}$	$0.70^{0.29}_{0.24}$
HDFS1 – 139	32 : 47.80	32 : 19.7	$2.24^{0.25}_{0.23}$	$7.16^{1.93}_{1.69}$	$4.52^{1.42}_{0.89}$	$4.16^{1.22}_{0.83}$
HDFS1 – 141	32 : 56.08	32 : 20.4	$0.50^{0.11}_{0.11}$	$0.48^{0.28}_{0.23}$	$0.29^{0.15}_{0.15}$	$0.24^{0.12}_{0.11}$
HDFS1 – 148	32 : 50.50	32 : 22.6	$1.72^{0.22}_{0.23}$	$0.74^{0.38}_{0.33}$	$0.73^{0.33}_{0.30}$	$0.89^{0.38}_{0.33}$
HDFS1 – 152	32 : 52.01	32 : 24.4	$3.50^{0.33}_{0.35}$	$11.65^{2.88}_{1.83}$	$7.12^{2.31}_{1.18}$	$5.94^{4.15}_{0.73}$
HDFS1 – 160	32 : 49.16	32 : 26.2	$3.00^{0.28}_{0.28}$	$22.84^{4.28}_{3.03}$	$10.85^{1.58}_{0.72}$	$8.77^{1.18}_{0.43}$
HDFS1 – 163	32 : 48.44	32 : 28.7	$1.42^{0.17}_{0.17}$	$3.32^{1.18}_{1.35}$	$2.39^{0.85}_{0.89}$	$2.34^{0.84}_{0.76}$
HDFS1 – 173	32 : 53.52	32 : 31.9	$1.12^{0.18}_{0.15}$	$0.81^{0.41}_{0.27}$	$0.45^{0.22}_{0.16}$	$0.37^{0.21}_{0.12}$
HDFS1 – 182	32 : 46.79	32 : 33.7	$1.82^{0.21}_{0.24}$	$0.87^{0.40}_{0.41}$	$0.93^{0.38}_{0.39}$	$1.19^{0.44}_{0.45}$
HDFS1 – 186	32 : 53.66	32 : 35.9	$0.20^{0.09}_{0.08}$	$0.10^{0.16}_{0.08}$	$0.08^{0.11}_{0.06}$	$0.09^{0.12}_{0.06}$
HDFS1 – 194	32 : 48.37	32 : 38.0	$3.52^{0.32}_{0.33}$	$13.69^{2.61}_{2.73}$	$9.03^{3.12}_{1.80}$	$8.16^{5.88}_{1.55}$
HDFS1 – 187	32 : 53.34	32 : 39.1	$0.90^{0.13}_{0.13}$	$2.03^{0.97}_{0.85}$	$1.45^{0.81}_{0.59}$	$1.56^{0.75}_{0.58}$
HDFS1 – 188	32 : 53.12	32 : 39.1	$0.58^{0.11}_{0.11}$	$0.19^{0.11}_{0.09}$	$0.13^{0.06}_{0.06}$	$0.12^{0.06}_{0.05}$
HDFS1 – 207	32 : 50.89	32 : 43.1	$0.54^{0.11}_{0.11}$	$1.05^{0.92}_{0.66}$	$1.07^{0.71}_{0.57}$	$1.34^{0.75}_{0.64}$
HDFS1 – 232	32 : 54.06	32 : 51.7	$0.48^{0.10}_{0.10}$	$0.54^{0.31}_{0.26}$	$0.34^{0.17}_{0.16}$	$0.30^{0.14}_{0.13}$
HDFS1 – 236	32 : 47.65	32 : 52.4	$0.50^{0.10}_{0.11}$	$0.24^{0.15}_{0.11}$	$0.15^{0.08}_{0.07}$	$0.12^{0.06}_{0.05}$
HDFS1 – 237	32 : 49.24	32 : 53.5	$0.58^{0.11}_{0.11}$	$0.57^{0.33}_{0.26}$	$0.38^{0.18}_{0.18}$	$0.35^{0.17}_{0.15}$
HDFS1 – 276	32 : 51.18	33 : 01.4	$1.26^{0.16}_{0.16}$	$1.42^{0.46}_{0.51}$	$0.91^{0.30}_{0.33}$	$0.81^{0.27}_{0.28}$



Table A.4:  $z_{phot}$  Catalog - continued

ID	RA (22h) J2000	DEC ( $-60^\circ$ ) J2000	$z_{phot}$	$L_U^{rest}$ $10^{10} L_\odot$	$L_B^{rest}$ $10^{10} L_\odot$	$L_V^{rest}$ $10^{10} L_\odot$
HDFS1 – 283	32 : 47.04	33 : 02.9	$1.20^{0.15}_{0.17}$	$1.02^{0.35}_{0.41}$	$0.65^{0.23}_{0.26}$	$0.58^{0.21}_{0.22}$
HDFS1 – 286	33 : 0.04	33 : 04.0	$1.24^{0.16}_{0.16}$ a	$1.33^{0.36}_{0.44}$	$0.76^{0.23}_{0.24}$	$0.62^{0.18}_{0.20}$
HDFS1 – 287	32 : 57.26	33 : 05.4	$0.86^{0.13}_{0.13}$	$1.43^{0.58}_{0.58}$	$0.86^{0.40}_{0.33}$	$0.75^{0.34}_{0.28}$
HDFS1 – 302	32 : 54.02	33 : 05.4	$0.54^{0.11}_{0.11}$	$0.23^{0.19}_{0.14}$	$0.21^{0.13}_{0.11}$	$0.24^{0.12}_{0.11}$
HDFS1 – 289	32 : 57.59	33 : 06.1	$0.58^{0.11}_{0.11}$	$3.57^{2.24}_{1.61}$	$2.42^{1.15}_{1.16}$	$2.23^{1.10}_{0.92}$
HDFS1 – 291	32 : 51.68	33 : 06.1	$0.98^{0.14}_{0.14}$	$0.35^{0.33}_{0.17}$	$0.42^{0.27}_{0.19}$	$0.57^{0.28}_{0.25}$
HDFS1 – 299	32 : 52.30	33 : 08.3	$0.56^{0.11}_{0.11}$	$1.55^{0.97}_{0.75}$	$1.08^{0.56}_{0.52}$	$1.04^{0.51}_{0.45}$
HDFS1 – 306	32 : 48.05	33 : 09.4	$1.30^{0.16}_{0.17}$ a	$0.81^{0.27}_{0.31}$	$0.51^{0.20}_{0.19}$	$0.46^{0.18}_{0.17}$
HDFS1 – 313	32 : 49.49	33 : 11.2	$0.52^{0.11}_{0.11}$	$0.27^{0.17}_{0.13}$	$0.17^{0.08}_{0.08}$	$0.15^{0.08}_{0.07}$
HDFS1 – 317	33 : 2.02	33 : 12.6	$0.78^{0.16}_{0.13}$ a	$0.14^{0.11}_{0.07}$	$0.10^{0.07}_{0.04}$	$0.09^{0.07}_{0.04}$
HDFS1 – 318	32 : 53.92	33 : 13.3	$0.20^{0.08}_{0.08}$	$0.05^{0.10}_{0.03}$	$0.06^{0.10}_{0.04}$	$0.08^{0.11}_{0.06}$
HDFS1 – 335	33 : 4.00	33 : 13.7	$2.54^{0.26}_{0.26}$	$7.55^{1.44}_{1.50}$	$4.22^{1.08}_{0.87}$	$3.49^{0.97}_{0.75}$
HDFS1 – 326	32 : 48.55	33 : 14.0	$0.62^{0.13}_{0.12}$	$0.37^{0.25}_{0.15}$	$0.22^{0.12}_{0.10}$	$0.18^{0.10}_{0.07}$
HDFS1 – 332	33 : 1.94	33 : 16.2	$0.44^{0.10}_{0.10}$	$0.52^{0.36}_{0.28}$	$0.37^{0.22}_{0.19}$	$0.36^{0.19}_{0.17}$
HDFS1 – 334	32 : 52.91	33 : 16.9	$1.28^{0.16}_{0.16}$	$5.56^{2.53}_{2.58}$	$4.34^{1.95}_{1.71}$	$4.45^{1.99}_{1.44}$
HDFS1 – 340	32 : 55.90	33 : 17.6	$0.52^{0.11}_{0.11}$	$0.32^{0.20}_{0.15}$	$0.21^{0.11}_{0.10}$	$0.18^{0.09}_{0.08}$
HDFS1 – 342	33 : 0.18	33 : 18.7	$0.74^{0.12}_{0.12}$	$0.62^{0.26}_{0.25}$	$0.37^{0.15}_{0.14}$	$0.31^{0.12}_{0.11}$
HDFS1 – 346	32 : 54.31	33 : 20.2	$0.46^{0.10}_{0.11}$	$0.19^{0.13}_{0.10}$	$0.12^{0.07}_{0.06}$	$0.10^{0.05}_{0.05}$
HDFS1 – 347	32 : 53.12	33 : 20.2	$3.28^{0.31}_{0.33}$	$11.08^{1.64}_{1.60}$	$5.83^{0.82}_{0.48}$	$4.92^{1.15}_{0.36}$
HDFS1 – 345	33 : 2.81	33 : 22.0	$0.56^{0.11}_{0.11}$	$2.29^{1.87}_{1.41}$	$2.09^{1.32}_{1.09}$	$2.43^{1.22}_{1.09}$
HDFS1 – 350	33 : 5.00	33 : 22.0	$3.04^{0.33}_{1.27}$	$9.39^{3.24}_{7.74}$	$7.60^{2.59}_{6.21}$	$8.04^{2.74}_{6.53}$
HDFS1 – 355	32 : 54.24	33 : 22.3	$2.88^{0.34}_{1.08}$	$3.61^{1.44}_{3.00}$	$2.80^{1.05}_{2.25}$	$2.88^{1.09}_{2.20}$
HDFS1 – 354	32 : 57.26	33 : 23.0	$1.38^{0.24}_{0.19}$	$0.55^{0.38}_{0.24}$	$0.42^{0.27}_{0.17}$	$0.44^{0.27}_{0.17}$
HDFS1 – 364	32 : 57.08	33 : 23.0	$0.68^{0.12}_{0.12}$	$0.94^{0.49}_{0.35}$	$0.53^{0.22}_{0.22}$	$0.43^{0.18}_{0.16}$
HDFS1 – 363	32 : 52.15	33 : 23.8	$1.12^{0.15}_{0.15}$	$3.19^{1.26}_{1.22}$	$2.01^{0.84}_{0.77}$	$1.75^{0.77}_{0.66}$
HDFS1 – 360	33 : 2.88	33 : 25.2	$1.30^{0.16}_{0.16}$	$5.26^{1.82}_{1.92}$	$3.52^{1.23}_{1.26}$	$3.25^{1.15}_{1.13}$

Table A.4:  $z_{phot}$  Catalog – continued

ID	RA (22h) J2000	DEC ( $-60^\circ$ ) J2000	$z_{phot}$	$L_U^{rest}$ $10^{10} L_\odot$	$L_B^{rest}$ $10^{10} L_\odot$	$L_V^{rest}$ $10^{10} L_\odot$
HDFS1 – 368	33 : 0.94	33 : 25.6	$0.96^{0.14}_{0.14}$	$0.99^{0.49}_{0.36}$	$0.55^{0.29}_{0.20}$	$0.44^{0.26}_{0.17}$
HDFS1 – 372	32 : 50.57	33 : 25.9	$0.56^{0.11}_{0.11}$	$0.49^{0.29}_{0.24}$	$0.33^{0.17}_{0.16}$	$0.32^{0.15}_{0.14}$
HDFS1 – 373	32 : 50.71	33 : 25.9	$0.54^{0.12}_{0.11}$	$0.30^{0.19}_{0.15}$	$0.17^{0.12}_{0.08}$	$0.16^{0.10}_{0.07}$
HDFS1 – 378	32 : 50.68	33 : 28.4	$2.62^{0.25}_{0.38}$	$19.36^{4.57}_{5.42}$	$11.99^{2.83}_{3.78}$	$10.14^{2.39}_{2.98}$
HDFS1 – 379	32 : 53.05	33 : 28.4	$1.06^{0.14}_{0.15}$	$3.15^{2.09}_{1.41}$	$2.82^{1.46}_{1.28}$	$3.31^{1.33}_{1.38}$
HDFS1 – 377	32 : 55.00	33 : 28.8	$1.12^{0.15}_{0.15}$	$1.37^{0.95}_{0.65}$	$1.46^{0.70}_{0.63}$	$1.89^{0.66}_{0.75}$
HDFS1 – 380	32 : 57.12	33 : 28.8	$0.68^{0.12}_{0.12}$	$0.11^{0.09}_{0.06}$	$0.12^{0.08}_{0.06}$	$0.16^{0.09}_{0.08}$
HDFS1 – 381	32 : 59.50	33 : 28.8	$1.00^{0.14}_{0.15}$	$0.68^{0.30}_{0.24}$	$0.40^{0.20}_{0.15}$	$0.33^{0.18}_{0.13}$
HDFS1 – 382	32 : 58.31	33 : 29.2	$2.62^{0.26}_{0.26}$	$5.48^{1.41}_{1.19}$	$3.44^{0.90}_{0.74}$	$2.95^{0.79}_{0.62}$
HDFS1 – 386	33 : 3.24	33 : 29.5	$2.64^{0.25}_{0.26}$	$22.52^{5.21}_{4.13}$	$13.77^{3.17}_{2.96}$	$11.50^{2.63}_{2.22}$
HDFS1 – 383	32 : 58.24	33 : 31.3	$0.42^{0.10}_{0.10}$	$0.48^{0.33}_{0.25}$	$0.31^{0.18}_{0.16}$	$0.28^{0.15}_{0.14}$
HDFS1 – 424 <sup>b</sup>	32 : 56.83	33 : 31.7	$4.82^{0.41}_{0.41}$	$28.02^{10.54}_{6.91}$	$24.97^{6.74}_{11.23}$	$31.13^{7.16}_{18.65}$
HDFS1 – 393	33 : 1.80	33 : 31.7	$1.62^{0.20}_{0.19}$	$4.21^{1.52}_{1.35}$	$2.96^{1.07}_{1.02}$	$2.85^{1.04}_{1.00}$
HDFS1 – 394	33 : 4.28	33 : 31.7	$0.10^{0.35}_{0.08}$	$0.00^{0.13}_{0.00}$	$0.00^{0.09}_{0.00}$	$0.00^{0.08}_{0.00}$
HDFS1 – 395	32 : 54.71	33 : 33.1	$0.16^{0.08}_{0.08}$	$0.07^{0.12}_{0.05}$	$0.05^{0.08}_{0.04}$	$0.05^{0.08}_{0.04}$
HDFS1 – 397	32 : 53.41	33 : 33.1	$1.10^{0.22}_{0.15}$	$1.20^{1.33}_{0.50}$	$1.00^{0.88}_{0.42}$	$1.11^{0.78}_{0.41}$
HDFS1 – 399	32 : 52.37	33 : 33.1	$0.52^{0.11}_{0.11}$	$0.37^{0.24}_{0.18}$	$0.24^{0.12}_{0.12}$	$0.22^{0.11}_{0.10}$
HDFS1 – 404	32 : 55.75	33 : 33.5	$0.54^{0.11}_{0.11}$	$0.24^{0.14}_{0.10}$	$0.15^{0.07}_{0.07}$	$0.12^{0.06}_{0.05}$
HDFS1 – 405	33 : 0.04	33 : 33.8	$1.02^{0.14}_{0.14}$	$0.30^{0.23}_{0.14}$	$0.36^{0.19}_{0.16}$	$0.49^{0.20}_{0.21}$
HDFS1 – 398	32 : 53.30	33 : 34.9	$0.96^{0.17}_{0.16}$ <sup>a</sup>	$0.17^{0.18}_{0.10}$	$0.18^{0.14}_{0.09}$	$0.23^{0.14}_{0.11}$
HDFS1 – 406	32 : 47.65	33 : 36.0	$0.58^{0.11}_{0.11}$	$4.83^{3.83}_{2.83}$	$4.38^{2.70}_{2.23}$	$5.08^{2.49}_{2.23}$
HDFS1 – 411	32 : 54.96	33 : 36.7	$1.00^{0.15}_{0.14}$	$0.30^{0.22}_{0.12}$	$0.26^{0.15}_{0.11}$	$0.31^{0.14}_{0.13}$
HDFS1 – 427	33 : 2.88	33 : 37.1	$1.18^{0.23}_{0.18}$	$0.59^{0.54}_{0.24}$	$0.44^{0.34}_{0.20}$	$0.46^{0.30}_{0.19}$
HDFS1 – 414	32 : 51.50	33 : 37.4	$0.62^{0.11}_{0.11}$	$0.86^{0.50}_{0.44}$	$0.65^{0.33}_{0.30}$	$0.66^{0.31}_{0.27}$
HDFS1 – 410	32 : 53.77	33 : 37.4	$0.52^{0.11}_{0.11}$	$1.03^{0.67}_{0.49}$	$0.66^{0.33}_{0.33}$	$0.59^{0.31}_{0.26}$

Table A.4:  $z_{phot}$  Catalog – continued

ID	RA (22h) J2000	DEC ( $-60^\circ$ ) J2000	$z_{phot}$	$L_U^{rest}$ $10^{10} L_\odot$	$L_B^{rest}$ $10^{10} L_\odot$	$L_V^{rest}$ $10^{10} L_\odot$
HDFS1 – 415	32 : 59.46	33 : 39.6	$0.46^{0.10}_{0.10}$	$0.49^{0.29}_{0.25}$	$0.32^{0.17}_{0.16}$	$0.29^{0.15}_{0.13}$
HDFS1 – 421	33 : 3.64	33 : 41.4	$0.44^{0.10}_{0.10}$	$1.76^{1.43}_{1.00}$	$1.43^{0.95}_{0.77}$	$1.55^{0.82}_{0.77}$
HDFS1 – 426	32 : 54.02	33 : 41.4	$1.00^{0.14}_{0.15}$	$0.59^{0.39}_{0.27}$	$0.48^{0.27}_{0.21}$	$0.56^{0.23}_{0.24}$
HDFS1 – 434	32 : 49.45	33 : 43.9	$0.58^{0.12}_{0.11}$	$0.13^{0.10}_{0.06}$	$0.09^{0.06}_{0.04}$	$0.09^{0.05}_{0.04}$
HDFS1 – 435	32 : 47.47	33 : 44.3	$0.56^{0.11}_{0.11}$	$0.10^{0.07}_{0.05}$	$0.08^{0.05}_{0.04}$	$0.08^{0.04}_{0.04}$
HDFS1 – 437	32 : 49.99	33 : 45.0	$1.06^{0.14}_{0.15}$	$1.35^{0.56}_{0.42}$	$0.74^{0.26}_{0.30}$	$0.58^{0.25}_{0.23}$
HDFS1 – 439	33 : 2.52	33 : 46.4	$0.68^{0.12}_{0.12}$	$1.38^{0.66}_{0.59}$	$0.83^{0.35}_{0.34}$	$0.68^{0.29}_{0.26}$
HDFS1 – 440	32 : 58.63	33 : 46.4	$1.34^{0.16}_{0.17}$	$0.82^{0.50}_{0.33}$	$1.03^{0.47}_{0.39}$	$1.41^{0.55}_{0.53}$
HDFS1 – 448	32 : 45.56	33 : 47.2	$1.30^{0.16}_{0.16}$	$2.35^{0.59}_{0.74}$	$1.34^{0.35}_{0.40}$	$1.08^{0.27}_{0.33}$
HDFS1 – 450	32 : 57.88	33 : 49.0	$0.44^{0.10}_{0.10}$	$0.11^{0.07}_{0.06}$	$0.07^{0.04}_{0.04}$	$0.07^{0.03}_{0.03}$
HDFS1 – 463	33 : 3.10	33 : 53.3	$2.76^{0.28}_{0.50}$	$4.26^{1.25}_{1.22}$	$3.31^{1.07}_{1.24}$	$3.53^{1.25}_{1.55}$
HDFS1 – 484	32 : 46.90	33 : 54.7	$0.52^{0.11}_{0.11}$	$0.55^{0.56}_{0.32}$	$0.63^{0.45}_{0.33}$	$0.85^{0.49}_{0.43}$
HDFS1 – 472	32 : 48.26	33 : 55.1	$0.66^{0.12}_{0.12}$	$0.36^{0.20}_{0.17}$	$0.25^{0.12}_{0.11}$	$0.24^{0.11}_{0.10}$
HDFS1 – 476	33 : 0.90	33 : 56.9	$1.08^{0.15}_{0.15}$	$1.03^{0.41}_{0.37}$	$0.61^{0.26}_{0.23}$	$0.50^{0.23}_{0.20}$
HDFS1 – 480	32 : 53.02	33 : 56.9	$2.76^{0.53}_{0.66}$ a	$1.43^{1.54}_{0.85}$	$1.79^{1.73}_{1.06}$	$2.47^{2.25}_{1.46}$
HDFS1 – 479	32 : 59.24	33 : 57.2	$1.34^{1.77}_{0.17}$ a	$1.16^{11.35}_{0.48}$	$0.84^{8.05}_{0.32}$	$0.81^{7.82}_{0.27}$
HDFS1 – 483	33 : 2.74	33 : 58.0	$2.24^{0.31}_{0.23}$	$6.19^{1.90}_{1.36}$	$3.84^{1.27}_{0.79}$	$3.37^{1.05}_{0.67}$
HDFS1 – 487	32 : 51.54	33 : 58.3	$1.28^{0.16}_{0.24}$ a	$0.28^{0.15}_{0.17}$	$0.27^{0.12}_{0.14}$	$0.32^{0.13}_{0.16}$
HDFS1 – 488	32 : 52.15	33 : 59.4	$0.48^{0.14}_{0.10}$	$0.44^{0.53}_{0.23}$	$0.35^{0.34}_{0.18}$	$0.37^{0.29}_{0.17}$
HDFS1 – 492	32 : 51.32	34 : 01.6	$0.24^{0.90}_{0.12}$ a	$0.02^{0.81}_{0.02}$	$0.01^{0.46}_{0.01}$	$0.01^{0.36}_{0.01}$
HDFS1 – 489	32 : 52.26	34 : 02.6	$0.52^{0.11}_{0.11}$	$0.48^{0.37}_{0.26}$	$0.37^{0.24}_{0.20}$	$0.40^{0.20}_{0.19}$
HDFS1 – 478	32 : 50.96	34 : 04.8	$1.34^{0.16}_{0.17}$	$5.12^{1.83}_{2.03}$	$3.37^{1.36}_{1.19}$	$3.17^{1.27}_{1.03}$
HDFS1 – 505	32 : 59.86	34 : 05.5	$1.30^{0.16}_{0.17}$	$1.92^{0.76}_{0.76}$	$1.33^{0.54}_{0.52}$	$1.27^{0.52}_{0.48}$
HDFS1 – 511	32 : 49.85	34 : 06.2	$1.12^{0.15}_{0.15}$	$2.43^{1.11}_{1.01}$	$1.64^{0.79}_{0.64}$	$1.52^{0.78}_{0.53}$
HDFS1 – 516	32 : 55.28	34 : 07.7	$0.46^{0.10}_{0.10}$	$0.33^{0.19}_{0.16}$	$0.20^{0.10}_{0.09}$	$0.16^{0.08}_{0.07}$
HDFS1 – 542	32 : 51.11	34 : 08.0	$3.86^{0.34}_{3.46}$	$31.10^{6.03}_{31.03}$	$15.42^{1.61}_{15.36}$	$12.60^{1.02}_{12.55}$

Table A.4:  $z_{phot}$  Catalog – continued

ID	RA (22h) J2000	DEC ( $-60^\circ$ ) J2000	$z_{phot}$	$L_U^{rest}$ $10^{10} L_\odot$	$L_B^{rest}$ $10^{10} L_\odot$	$L_V^{rest}$ $10^{10} L_\odot$
HDFS1 – 521	32 : 47.58	34 : 08.8	$0.50^{0.11}_{0.11}$	$0.89^{0.67}_{0.48}$	$0.67^{0.43}_{0.36}$	$0.69^{0.36}_{0.33}$
HDFS1 – 522	33 : 4.50	34 : 08.8	$0.56^{0.11}_{0.11}$	$0.15^{0.09}_{0.07}$	$0.10^{0.05}_{0.05}$	$0.09^{0.04}_{0.04}$
HDFS1 – 530	32 : 55.25	34 : 10.2	$1.02^{0.14}_{0.14}$	$1.36^{0.60}_{0.52}$	$0.90^{0.37}_{0.37}$	$0.83^{0.36}_{0.32}$
HDFS1 – 536	33 : 1.58	34 : 10.6	$0.78^{0.13}_{0.13}$	$0.58^{0.28}_{0.25}$	$0.37^{0.18}_{0.15}$	$0.33^{0.16}_{0.13}$
HDFS1 – 527	33 : 1.80	34 : 13.4	$1.12^{0.15}_{0.15}$	$3.83^{2.51}_{1.67}$	$3.59^{1.74}_{1.55}$	$4.33^{1.56}_{1.71}$
HDFS1 – 538	32 : 56.11	34 : 14.2	$0.52^{0.11}_{0.11}$	$0.66^{0.43}_{0.30}$	$0.42^{0.22}_{0.21}$	$0.37^{0.19}_{0.16}$
HDFS1 – 548	33 : 0.54	34 : 17.4	$0.66^{0.12}_{0.12}$	$0.19^{0.17}_{0.10}$	$0.23^{0.15}_{0.11}$	$0.30^{0.17}_{0.14}$
HDFS1 – 555	32 : 59.60	34 : 20.3	$1.12^{0.15}_{0.15}$	$0.98^{0.63}_{0.51}$	$1.02^{0.50}_{0.43}$	$1.28^{0.52}_{0.46}$

<sup>a</sup>  $\geq 1\%$  of Monte-Carlo realizations have  $z$  more than unity away from  $z_{phot}$

<sup>b</sup>  $z_{phot}$  may be incorrect

Note, – Units of right ascension are minutes and seconds, and units of declination are arcminutes and arcseconds

TABLE A.5. Newly Obtained Spectroscopic Determinations

ID	RA (22h) J2000	DEC ( $-60^\circ$ ) J2000	$I_{814}$ AB	$K_s$ AB	$z_{\text{phot}}$	$z_{\text{spec}}$	Q <sup>a</sup>
HDFS1-345	33:02.81	33:22.0	20.26	18.67	$0.48^{0.04}_{0.08}$	$0.465 \pm 0.002$	1
HDFS1-334	32:52.91	33:16.9	22.82	20.42	$1.20^{0.08}_{0.18}$	$1.283 \pm 0.001$	1
HDFS1-360	33:02.88	33:25.2	22.89	21.41	$1.28^{0.66}_{0.18}$	$1.439 \pm 0.002$	1
HDFS1-104 <sup>b</sup>	32:56.94	32:12.1	21.14	22.16	$0.86^{0.02}_{0.06}$	$1.558 \pm 0.001$	1
HDFS1-386	33:03.24	33:29.5	23.26	21.96	$2.20^{0.08}_{2.04}$	$2.028 \pm 0.002$	1
HDFS1-36	32:48.84	31:54.1	23.89	22.60	$3.02^{0.22}_{0.08}$	$2.793 \pm 0.003$	1
HDFS2-865	32:49.45	32:02.0	26.08	25.96	$0.02^{0.00}_{2.62}$	2.804	3
HDFSext-4 <sup>c</sup>	33:03.06	34:39.6	...	...	...	$0.184 \pm 0.001$	2
HDFSext-2 <sup>c</sup>	32:47.59	30:55.1	...	...	...	0.509	3
HDFSext-1 <sup>c</sup>	32:43.14	30:59.5	...	...	...	$0.514 \pm 0.001$	1
HDFSext-3 <sup>c</sup>	32:48.49	31:16.1	...	...	...	$0.520 \pm 0.001$	2

<sup>a</sup> 1 - redshift definite, with 6 or more identified lines;

2 - redshift probable, with 2 or more identified lines;

3 - redshift uncertain, with only 1 identified line.

<sup>b</sup> Does not meet good photometry requirements.

<sup>c</sup> No FIRES photometry available; Positional accuracy to within  $<1''5$ .

TABLE A.6. Compilation of Spectroscopically Confirmed Galaxies in HDF-S

ID	$z_{\text{spec}}$	$z_{\text{phot}}$	specID <sup>a</sup>	Source <sup>b</sup>
HDFS1-540 <sup>c</sup>	0.46	$0.50^{3.50}_{0.02}$ <sup>d</sup>	23	1
HDFS1-541 <sup>c</sup>	0.4606	$1.00^{0.02}_{0.06}$	389-3	3
HDFS1-345	0.465	$0.48^{0.04}_{0.08}$	....	4
HDFS1-342	0.5402	$0.76^{0.02}_{0.24}$	919-2	3
HDFS1-521	0.56	$0.36^{0.24}_{0.10}$	28	1
HDFS1-410	0.565	$0.46^{0.06}_{0.20}$	ANON09	2
HDFS1-289	0.58	$0.34^{0.24}_{0.08}$	53	1
HDFS1-406	0.5803	$0.50^{0.08}_{0.06}$	469-4	3
HDFS1-287	0.5823	$0.84^{0.10}_{0.24}$	841-4	3
HDFS1-439	0.6959	$0.54^{0.22}_{0.10}$	982-1	3
HDFS1-177 <sup>c</sup>	0.76	$0.82^{0.06}_{0.14}$	55	1
HDFS1-527	1.23	$1.14^{0.12}_{0.08}$	60	1
HDFS1-379	1.27	$1.06^{0.10}_{0.06}$	39	1
HDFS1-334	1.283	$1.20^{0.08}_{0.18}$	....	4
HDFS1-360	1.439	$1.28^{0.66}_{0.18}$	....	4
HDFS1-104 <sup>c</sup>	1.558	$0.86^{0.02}_{0.06}$	....	4
HDFS1-386	2.028	$2.20^{0.08}_{2.04}$ <sup>d</sup>	....	4
HDFS1-160	2.79	$3.00^{0.12}_{0.12}$	EIS47	2
HDFS1-36	2.793	$3.02^{0.22}_{0.08}$	....	4
HDFS2-865	2.804	$0.02^{2.62}_{0.00}$ <sup>d</sup>	....	4
HDFS1-20 <sup>c</sup>	3.2	$3.28^{0.12}_{0.12}$	EIS43	2

<sup>a</sup> The ID from the source indicated in the last column.

<sup>b</sup> 1 - Rigopoulou et al. (2000); 2 - Cristiani et al. (2000);  
3 - Glazebrook (2001); 4 - Chapter 3

<sup>c</sup> Does not meet our good photometry requirement.

<sup>d</sup>  $\gamma_{\text{alt}} \geq 10\%$ ; Note. — HDFS1-406 was also observed by Rigopoulou et al. (2000) with  $z_{\text{spec}}$  identical to that measured by Glazebrook (2001).

TABLE A.7. Image Depths

Filter	AB <sub>lim</sub> 0'.7 Aperture	AB <sub>lim</sub> 2'.0 Aperture
<i>J<sub>s</sub></i>	27.1	26.0
<i>H</i>	26.5	25.4
<i>K<sub>s</sub></i>	26.5	25.5

Note. – All limits are  $5\sigma$  without aperture corrections.

Table A.8: Optical Photometry –  $K_{s,AB}^{\text{tot}} < 26$  Sample

ID	R.A.(22h) J2000	Decl.(-60°) J2000	$U_{300}^a$	$B_{450}^a$	$V_{606}^a$	$I_{814}^a$
HDFS2 – 61	33 : 2.59	34 : 24.0	$9.2 \pm 3.6$	$6.3 \pm 1.8$	$13.7 \pm 1.2$	$22.0 \pm 1.8$
HDFS2 – 75	33 : 2.99	34 : 23.2	$-2.4 \pm 3.4$	$13.0 \pm 1.8$	$13.6 \pm 1.2$	$24.7 \pm 1.6$
HDFS2 – 97	32 : 58.88	34 : 21.8	$9.0 \pm 3.4$	$3.9 \pm 1.8$	$10.7 \pm 1.2$	$22.4 \pm 1.7$
HDFS2 – 110	33 : 3.60	34 : 20.7	$-0.2 \pm 2.7$	$2.6 \pm 1.3$	$3.3 \pm 0.8$	$4.9 \pm 1.3$
HDFS2 – 107	33 : 2.84	34 : 20.7	$3.6 \pm 2.7$	$10.6 \pm 1.3$	$8.4 \pm 0.8$	$7.4 \pm 1.3$
HDFS2 – 66	32 : 59.57	34 : 20.4	$-4.3 \pm 3.2$	$7.2 \pm 1.6$	$20.8 \pm 1.0$	$87.1 \pm 1.5$
HDFS2 – 103	32 : 54.49	34 : 18.8	$8.2 \pm 4.2$	$19.1 \pm 2.0$	$23.8 \pm 1.3$	$22.3 \pm 1.9$
HDFS2 – 116	33 : 0.04	34 : 18.7	$2.3 \pm 2.7$	$5.0 \pm 1.3$	$7.1 \pm 0.8$	$10.2 \pm 1.3$
HDFS2 – 123	32 : 57.41	34 : 18.0	$1.1 \pm 2.9$	$5.9 \pm 1.4$	$9.5 \pm 0.9$	$8.2 \pm 1.4$
HDFS2 – 128	33 : 1.48	34 : 17.7	$3.2 \pm 2.4$	$4.4 \pm 1.1$	$4.8 \pm 0.7$	$15.0 \pm 1.2$
HDFS2 – 93	33 : 0.50	34 : 17.5	$8.8 \pm 2.5$	$6.9 \pm 1.1$	$38.8 \pm 0.7$	$162.8 \pm 1.2$
HDFS2 – 126	32 : 51.54	34 : 17.0	$-1.5 \pm 4.0$	$4.5 \pm 1.9$	$11.6 \pm 1.2$	$20.6 \pm 1.8$
HDFS2 – 125	33 : 1.55	34 : 17.0	$7.1 \pm 2.2$	$10.4 \pm 1.1$	$11.6 \pm 0.7$	$17.7 \pm 1.2$
HDFS2 – 134	32 : 52.66	34 : 16.7	$-1.2 \pm 3.9$	$4.7 \pm 1.8$	$6.3 \pm 1.2$	$9.0 \pm 1.6$
HDFS2 – 133	32 : 56.62	34 : 16.5	$-3.9 \pm 2.7$	$9.1 \pm 1.3$	$15.9 \pm 0.8$	$16.1 \pm 1.3$
HDFS2 – 124	32 : 58.70	34 : 16.3	$6.7 \pm 2.5$	$2.0 \pm 1.1$	$5.9 \pm 0.7$	$16.7 \pm 1.2$
HDFS2 – 119	33 : 3.92	34 : 16.3	$9.9 \pm 2.2$	$17.9 \pm 1.1$	$18.8 \pm 0.7$	$34.7 \pm 1.1$
HDFS2 – 127	33 : 3.67	34 : 16.2	$10.8 \pm 2.2$	$5.9 \pm 1.0$	$7.7 \pm 0.7$	$16.9 \pm 1.1$
HDFS2 – 120	32 : 50.96	34 : 15.2	$14.4 \pm 3.7$	$25.0 \pm 1.8$	$54.7 \pm 1.1$	$88.6 \pm 1.6$
HDFS2 – 149	33 : 4.32	34 : 14.7	$7.9 \pm 2.2$	$16.4 \pm 1.0$	$13.7 \pm 0.6$	$19.0 \pm 1.1$
HDFS2 – 130	32 : 59.10	34 : 14.6	$11.5 \pm 2.2$	$24.3 \pm 1.1$	$31.0 \pm 0.7$	$52.4 \pm 1.1$
HDFS2 – 155	33 : 1.12	34 : 14.2	$4.8 \pm 2.1$	$13.6 \pm 1.0$	$15.9 \pm 0.6$	$27.0 \pm 1.1$
HDFS2 – 144	33 : 3.35	34 : 14.1	$-0.3 \pm 2.2$	$27.7 \pm 1.0$	$30.2 \pm 0.6$	$31.7 \pm 1.1$
HDFS2 – 105	32 : 56.11	34 : 14.0	$90.6 \pm 2.5$	$149.3 \pm 1.1$	$272.2 \pm 0.7$	$466.0 \pm 1.2$
HDFS2 – 153	32 : 54.82	34 : 14.0	$-3.1 \pm 3.7$	$3.4 \pm 1.6$	$6.1 \pm 1.0$	$14.9 \pm 1.5$



Table A.8: Optical Photometry -- continued

ID	R.A.(22h) J2000	Decl.(-60°) J2000	$U_{300}^a$	$B_{450}^a$	$V_{606}^a$	$I_{814}^a$
HDFS2 – 146	32 : 52.76	34 : 13.5	$1.2 \pm 3.2$	$1.1 \pm 1.4$	$8.6 \pm 0.9$	$17.3 \pm 1.4$
HDFS2 – 162	33 : 4.90	34 : 13.3	$7.2 \pm 2.2$	$3.9 \pm 1.1$	$7.7 \pm 0.7$	$10.6 \pm 1.2$
HDFS2 – 49	33 : 1.80	34 : 13.3	$27.2 \pm 2.1$	$54.1 \pm 1.0$	$94.4 \pm 0.6$	$274.8 \pm 1.1$
HDFS2 – 112	32 : 49.81	34 : 13.2	$16.9 \pm 3.5$	$36.5 \pm 1.6$	$60.9 \pm 1.0$	$168.4 \pm 1.5$
HDFS2 – 98	33 : 5.18	34 : 13.0	$5.2 \pm 2.7$	$-3.1 \pm 1.3$	$10.2 \pm 0.8$	$15.4 \pm 1.4$
HDFS2 – 161	32 : 54.35	34 : 12.8	$-1.0 \pm 3.0$	$1.7 \pm 1.3$	$7.0 \pm 0.8$	$9.8 \pm 1.3$
HDFS2 – 156	32 : 52.48	34 : 12.5	$8.7 \pm 3.0$	$24.9 \pm 1.4$	$23.6 \pm 0.8$	$21.8 \pm 1.3$
HDFS2 – 136	32 : 46.36	34 : 12.2	$1.9 \pm 3.8$	$20.4 \pm 1.8$	$30.3 \pm 1.1$	$45.0 \pm 1.6$
HDFS2 – 159	33 : 1.40	34 : 12.0	$6.6 \pm 2.1$	$0.2 \pm 1.0$	$4.7 \pm 0.6$	$10.6 \pm 1.1$
HDFS2 – 167	32 : 51.14	34 : 11.8	$5.5 \pm 3.0$	$8.4 \pm 1.3$	$10.4 \pm 0.8$	$10.3 \pm 1.3$
HDFS2 – 175	33 : 2.66	34 : 11.6	$1.9 \pm 2.1$	$2.0 \pm 1.0$	$6.9 \pm 0.6$	$12.2 \pm 1.1$
HDFS2 – 166	32 : 56.18	34 : 11.5	$-0.2 \pm 2.1$	$13.7 \pm 1.0$	$19.5 \pm 0.7$	$17.0 \pm 1.1$
HDFS2 – 154	32 : 49.02	34 : 11.2	$12.4 \pm 3.1$	$24.8 \pm 1.4$	$31.4 \pm 0.9$	$53.0 \pm 1.4$
HDFS2 – 165	32 : 46.75	34 : 11.0	$3.3 \pm 3.6$	$1.1 \pm 1.6$	$9.3 \pm 1.0$	$16.0 \pm 1.5$
HDFS2 – 163	32 : 48.05	34 : 10.8	$6.2 \pm 3.2$	$4.3 \pm 1.4$	$6.9 \pm 0.9$	$10.2 \pm 1.4$
HDFS2 – 168	33 : 1.91	34 : 10.8	$8.0 \pm 2.1$	$7.4 \pm 1.0$	$18.2 \pm 0.6$	$28.9 \pm 1.1$
HDFS2 – 148	33 : 1.58	34 : 10.5	$23.9 \pm 2.0$	$39.6 \pm 1.0$	$60.2 \pm 0.6$	$132.7 \pm 1.1$
HDFS2 – 171	32 : 59.78	34 : 10.3	$15.1 \pm 2.1$	$21.8 \pm 1.0$	$25.0 \pm 0.6$	$27.0 \pm 1.1$
HDFS2 – 152	32 : 55.25	34 : 10.0	$27.0 \pm 3.7$	$49.4 \pm 1.6$	$69.2 \pm 0.9$	$147.1 \pm 1.6$
HDFS2 – 174	32 : 54.17	34 : 8.9	$10.5 \pm 2.4$	$33.4 \pm 1.1$	$46.5 \pm 0.7$	$54.7 \pm 1.2$
HDFS2 – 170	33 : 4.50	34 : 8.8	$10.9 \pm 2.1$	$25.6 \pm 1.0$	$53.3 \pm 0.6$	$101.1 \pm 1.1$
HDFS2 – 114	32 : 47.54	34 : 8.5	$74.7 \pm 2.9$	$162.4 \pm 1.3$	$390.9 \pm 0.8$	$803.4 \pm 1.3$
HDFS2 – 188	32 : 54.38	34 : 8.3	$3.1 \pm 2.4$	$10.8 \pm 1.1$	$15.1 \pm 0.7$	$11.9 \pm 1.2$
HDFS2 – 177	33 : 4.93	34 : 8.3	$19.8 \pm 2.1$	$48.7 \pm 1.1$	$57.2 \pm 0.7$	$63.8 \pm 1.1$
HDFS2 – 158	32 : 51.11	34 : 8.0	$4.5 \pm 2.5$	$25.8 \pm 1.1$	$74.2 \pm 0.7$	$128.7 \pm 1.2$
HDFS2 – 184	32 : 46.86	34 : 7.5	$-0.1 \pm 2.9$	$17.9 \pm 1.3$	$19.4 \pm 0.8$	$22.9 \pm 1.3$

Table A.8: Optical Photometry – continued

ID	R.A.(22h) J2000	Decl.(-60°) J2000	$U_{300}^a$	$B_{450}^a$	$V_{606}^a$	$I_{814}^a$
HDFS2 – 147	32 : 55.28	34 : 7.3	$43.7 \pm 3.7$	$64.4 \pm 1.5$	$119.9 \pm 0.9$	$176.4 \pm 1.6$
HDFS2 – 180	32 : 46.00	34 : 7.3	$42.7 \pm 3.0$	$57.6 \pm 1.4$	$75.4 \pm 0.8$	$122.6 \pm 1.3$
HDFS2 – 196	32 : 49.16	34 : 6.8	$7.2 \pm 2.5$	$8.3 \pm 1.1$	$8.1 \pm 0.7$	$9.7 \pm 1.2$
HDFS2 – 191	33 : 4.25	34 : 6.7	$13.8 \pm 2.0$	$22.0 \pm 1.0$	$26.0 \pm 0.6$	$45.5 \pm 1.1$
HDFS2 – 194	33 : 0.04	34 : 6.5	$0.7 \pm 2.0$	$3.4 \pm 1.0$	$3.7 \pm 0.6$	$4.5 \pm 1.1$
HDFS2 – 189	33 : 1.37	34 : 6.3	$5.4 \pm 2.0$	$10.4 \pm 1.0$	$16.7 \pm 0.6$	$40.2 \pm 1.1$
HDFS2 – 204	33 : 4.82	34 : 6.3	$1.6 \pm 2.1$	$3.3 \pm 1.0$	$5.6 \pm 0.6$	$5.0 \pm 1.1$
HDFS2 – 160	32 : 49.85	34 : 6.3	$30.5 \pm 2.4$	$58.6 \pm 1.1$	$90.2 \pm 0.7$	$175.5 \pm 1.2$
HDFS2 – 208	32 : 59.50	34 : 6.3	$2.2 \pm 2.0$	$10.2 \pm 1.0$	$13.8 \pm 0.6$	$12.9 \pm 1.1$
HDFS2 – 185	32 : 46.25	34 : 5.8	$13.0 \pm 2.8$	$14.4 \pm 1.2$	$31.4 \pm 0.8$	$57.2 \pm 1.3$
HDFS2 – 210	32 : 52.01	34 : 5.6	$8.3 \pm 2.3$	$5.5 \pm 1.1$	$7.9 \pm 0.7$	$16.1 \pm 1.1$
HDFS2 – 192	33 : 0.83	34 : 5.6	$8.3 \pm 2.0$	$18.7 \pm 1.0$	$20.3 \pm 0.6$	$25.8 \pm 1.1$
HDFS2 – 183	32 : 59.86	34 : 5.4	$4.5 \pm 2.0$	$33.5 \pm 1.0$	$45.8 \pm 0.6$	$85.4 \pm 1.1$
HDFS2 – 209	32 : 59.14	34 : 5.2	$-3.5 \pm 2.0$	$12.8 \pm 1.0$	$22.3 \pm 0.6$	$26.9 \pm 1.1$
HDFS2 – 207	32 : 56.44	34 : 5.2	$3.2 \pm 2.1$	$10.7 \pm 1.0$	$11.0 \pm 0.6$	$20.1 \pm 1.1$
HDFS2 – 199	32 : 45.56	34 : 5.0	$6.7 \pm 2.8$	$6.5 \pm 1.3$	$15.1 \pm 0.8$	$19.3 \pm 1.4$
HDFS2 – 195	32 : 47.72	34 : 5.0	$-0.2 \pm 2.5$	$1.1 \pm 1.1$	$4.9 \pm 0.7$	$11.7 \pm 1.2$
HDFS2 – 215	32 : 46.86	34 : 4.9	$10.6 \pm 2.6$	$5.5 \pm 1.2$	$10.2 \pm 0.7$	$16.5 \pm 1.2$
HDFS2 – 201	32 : 48.26	34 : 4.9	$13.3 \pm 2.4$	$21.6 \pm 1.1$	$22.4 \pm 0.7$	$28.0 \pm 1.2$
HDFS2 – 140	32 : 50.96	34 : 4.8	$44.8 \pm 2.3$	$69.8 \pm 1.1$	$88.4 \pm 0.6$	$161.8 \pm 1.1$
HDFS2 – 211	32 : 48.16	34 : 4.7	$-3.8 \pm 2.4$	$3.7 \pm 1.1$	$5.6 \pm 0.7$	$14.5 \pm 1.2$
HDFS2 – 206	32 : 47.54	34 : 4.7	$-6.5 \pm 2.4$	$0.5 \pm 1.1$	$8.1 \pm 0.7$	$19.0 \pm 1.2$
HDFS2 – 226	33 : 0.90	34 : 4.0	$2.8 \pm 2.0$	$2.1 \pm 1.0$	$6.4 \pm 0.6$	$11.0 \pm 1.1$
HDFS2 – 203	32 : 46.28	34 : 4.0	$2.6 \pm 2.6$	$12.1 \pm 1.1$	$23.3 \pm 0.7$	$34.9 \pm 1.2$
HDFS2 – 214	32 : 52.04	34 : 3.8	$3.9 \pm 2.3$	$4.3 \pm 1.0$	$11.3 \pm 0.6$	$26.8 \pm 1.1$
HDFS2 – 198	32 : 56.83	34 : 3.4	$11.8 \pm 2.0$	$33.4 \pm 1.0$	$54.5 \pm 0.6$	$80.2 \pm 1.1$

Table A.8: Optical Photometry – continued

ID	R.A.(22h) J2000	Decl.(-60°) J2000	$U_{300}^a$	$B_{450}^a$	$V_{606}^a$	$I_{814}^a$
HDFS2 – 222	32 : 53.66	34 : 3.1	$11.3 \pm 2.3$	$21.4 \pm 1.1$	$25.0 \pm 0.6$	$32.4 \pm 1.1$
HDFS2 – 221	32 : 49.42	34 : 3.0	$8.1 \pm 2.3$	$14.3 \pm 1.0$	$17.6 \pm 0.6$	$18.5 \pm 1.1$
HDFS2 – 172	32 : 52.22	34 : 2.6	$43.5 \pm 2.3$	$87.5 \pm 1.0$	$216.0 \pm 0.6$	$468.5 \pm 1.1$
HDFS2 – 225	32 : 53.92	34 : 1.8	$7.9 \pm 2.3$	$16.3 \pm 1.1$	$22.3 \pm 0.6$	$44.0 \pm 1.1$
HDFS2 – 227	32 : 45.60	34 : 1.7	$15.2 \pm 2.4$	$-0.9 \pm 1.1$	$6.9 \pm 0.7$	$15.3 \pm 1.2$
HDFS2 – 224	33 : 0.72	34 : 1.6	$1.4 \pm 1.9$	$9.2 \pm 0.9$	$12.9 \pm 0.6$	$19.7 \pm 1.1$
HDFS2 – 217	32 : 51.32	34 : 1.5	$17.8 \pm 2.3$	$27.0 \pm 1.0$	$40.5 \pm 0.6$	$53.8 \pm 1.1$
HDFS2 – 232	33 : 2.12	34 : 1.1	$6.3 \pm 2.0$	$8.4 \pm 1.0$	$7.6 \pm 0.6$	$9.9 \pm 1.1$
HDFS2 – 239	33 : 4.07	34 : 0.7	$3.0 \pm 2.0$	$3.7 \pm 1.0$	$13.2 \pm 0.6$	$19.8 \pm 1.1$
HDFS2 – 243	33 : 2.92	34 : 0.6	$1.8 \pm 2.0$	$5.3 \pm 1.0$	$7.2 \pm 0.6$	$10.3 \pm 1.1$
HDFS2 – 247	32 : 53.88	34 : 0.1	$-0.9 \pm 2.3$	$7.2 \pm 1.1$	$10.1 \pm 0.6$	$11.3 \pm 1.1$
HDFS2 – 242	32 : 56.18	34 : 0.0	$5.3 \pm 2.0$	$13.1 \pm 1.0$	$15.1 \pm 0.6$	$15.0 \pm 1.1$
HDFS2 – 238	32 : 52.73	33 : 59.9	$7.4 \pm 2.2$	$15.3 \pm 1.0$	$19.1 \pm 0.6$	$20.9 \pm 1.1$
HDFS2 – 246	32 : 56.00	33 : 59.5	$-2.3 \pm 2.0$	$7.8 \pm 1.0$	$13.7 \pm 0.6$	$20.9 \pm 1.1$
HDFS2 – 250	32 : 49.52	33 : 59.4	$-2.4 \pm 2.2$	$3.8 \pm 1.0$	$5.1 \pm 0.6$	$11.5 \pm 1.1$
HDFS2 – 150	32 : 52.15	33 : 59.4	$39.5 \pm 2.2$	$85.1 \pm 1.0$	$216.6 \pm 0.6$	$452.1 \pm 1.1$
HDFS2 – 234	32 : 46.79	33 : 58.9	$16.2 \pm 2.3$	$20.6 \pm 1.1$	$23.8 \pm 0.6$	$41.4 \pm 1.1$
HDFS2 – 241	32 : 45.46	33 : 58.3	$6.4 \pm 2.5$	$15.7 \pm 1.2$	$15.3 \pm 0.7$	$20.0 \pm 1.3$
HDFS2 – 236	32 : 51.54	33 : 58.2	$4.2 \pm 2.2$	$1.8 \pm 1.0$	$4.3 \pm 0.6$	$15.7 \pm 1.1$
HDFS2 – 252	33 : 2.99	33 : 58.2	$-2.5 \pm 2.0$	$12.6 \pm 1.0$	$24.0 \pm 0.6$	$31.7 \pm 1.1$
HDFS2 – 231	33 : 2.77	33 : 58.1	$2.9 \pm 1.9$	$31.4 \pm 0.9$	$38.3 \pm 0.6$	$51.4 \pm 1.1$
HDFS2 – 245	32 : 52.58	33 : 57.6	$14.7 \pm 2.2$	$20.4 \pm 1.0$	$28.0 \pm 0.6$	$44.7 \pm 1.1$
HDFS2 – 263	33 : 2.63	33 : 57.4	$3.0 \pm 1.9$	$9.5 \pm 0.9$	$14.3 \pm 0.6$	$16.5 \pm 1.0$
HDFS2 – 230	32 : 59.21	33 : 57.3	$5.1 \pm 2.0$	$10.9 \pm 1.0$	$23.4 \pm 0.6$	$42.4 \pm 1.1$
HDFS2 – 244	33 : 0.90	33 : 57.0	$24.7 \pm 1.9$	$45.5 \pm 0.9$	$54.6 \pm 0.6$	$89.5 \pm 1.1$
HDFS2 – 254	32 : 53.02	33 : 56.9	$-3.6 \pm 2.2$	$1.5 \pm 1.0$	$0.3 \pm 0.6$	$1.5 \pm 1.1$

Table A.8: Optical Photometry – continued

ID	R.A.(22h) J2000	Decl.(-60°) J2000	$U_{300}^a$	$B_{450}^a$	$V_{606}^a$	$I_{814}^a$
HDFS2 – 233	32 : 50.03	33 : 56.7	$3.6 \pm 2.2$	$34.3 \pm 1.0$	$61.0 \pm 0.6$	$86.5 \pm 1.1$
HDFS2 – 271	32 : 47.22	33 : 56.6	$11.2 \pm 2.2$	$12.4 \pm 1.0$	$10.3 \pm 0.6$	$15.7 \pm 1.1$
HDFS2 – 267	33 : 3.89	33 : 55.9	$2.7 \pm 2.0$	$24.3 \pm 1.0$	$28.7 \pm 0.6$	$32.9 \pm 1.1$
HDFS2 – 255	32 : 59.46	33 : 55.8	$22.2 \pm 2.0$	$34.2 \pm 1.0$	$38.0 \pm 0.6$	$65.4 \pm 1.1$
HDFS2 – 264	32 : 55.93	33 : 55.5	$1.5 \pm 2.0$	$11.3 \pm 1.0$	$16.8 \pm 0.6$	$23.7 \pm 1.1$
HDFS2 – 276	32 : 59.46	33 : 55.0	$3.8 \pm 1.8$	$15.1 \pm 0.9$	$16.6 \pm 0.5$	$18.6 \pm 1.0$
HDFS2 – 273	32 : 53.63	33 : 54.9	$7.0 \pm 2.2$	$14.7 \pm 1.0$	$17.0 \pm 0.6$	$27.1 \pm 1.1$
HDFS2 – 240	32 : 48.23	33 : 54.9	$9.5 \pm 2.2$	$34.1 \pm 1.0$	$68.9 \pm 0.6$	$154.2 \pm 1.1$
HDFS2 – 219	32 : 46.86	33 : 54.8	$3.8 \pm 2.2$	$59.0 \pm 1.1$	$323.4 \pm 0.6$	$1042.5 \pm 1.1$
HDFS2 – 294	33 : 1.76	33 : 54.6	$1.7 \pm 1.9$	$0.3 \pm 0.9$	$1.5 \pm 0.6$	$3.8 \pm 1.1$
HDFS2 – 279	32 : 49.02	33 : 54.5	$1.8 \pm 2.2$	$12.6 \pm 1.0$	$13.9 \pm 0.6$	$16.4 \pm 1.1$
HDFS2 – 283	32 : 52.37	33 : 53.9	$0.9 \pm 2.2$	$5.3 \pm 1.0$	$6.8 \pm 0.6$	$11.5 \pm 1.1$
HDFS2 – 295	32 : 59.10	33 : 53.5	$1.9 \pm 1.9$	$14.4 \pm 0.9$	$13.9 \pm 0.6$	$12.4 \pm 1.1$
HDFS2 – 299	32 : 59.89	33 : 53.3	$-1.2 \pm 1.9$	$0.8 \pm 0.9$	$2.8 \pm 0.6$	$0.1 \pm 1.1$
HDFS2 – 260	33 : 3.10	33 : 53.2	$-0.2 \pm 2.0$	$14.2 \pm 1.0$	$19.1 \pm 0.6$	$24.6 \pm 1.1$
HDFS2 – 291	32 : 51.54	33 : 53.2	$3.9 \pm 2.2$	$4.8 \pm 1.0$	$5.4 \pm 0.6$	$6.7 \pm 1.1$
HDFS2 – 280	32 : 54.31	33 : 52.1	$-1.3 \pm 2.2$	$10.4 \pm 1.0$	$23.6 \pm 0.6$	$28.6 \pm 1.1$
HDFS2 – 287	32 : 46.00	33 : 51.8	$15.1 \pm 2.3$	$14.1 \pm 1.1$	$19.3 \pm 0.6$	$27.6 \pm 1.2$
HDFS2 – 302	32 : 49.60	33 : 51.2	$-2.6 \pm 2.2$	$1.2 \pm 1.0$	$7.4 \pm 0.6$	$14.5 \pm 1.1$
HDFS2 – 307	33 : 3.85	33 : 51.1	$3.3 \pm 2.0$	$-1.0 \pm 1.0$	$1.3 \pm 0.6$	$4.9 \pm 1.1$
HDFS2 – 290	32 : 54.24	33 : 50.5	$1.7 \pm 2.2$	$15.7 \pm 1.0$	$38.1 \pm 0.6$	$48.4 \pm 1.1$
HDFS2 – 304	32 : 53.74	33 : 50.5	$7.7 \pm 2.2$	$16.4 \pm 1.0$	$15.5 \pm 0.6$	$28.2 \pm 1.1$
HDFS2 – 309	33 : 1.94	33 : 50.0	$1.0 \pm 2.0$	$4.9 \pm 1.0$	$8.6 \pm 0.6$	$15.2 \pm 1.1$
HDFS2 – 305	32 : 56.98	33 : 49.9	$6.9 \pm 2.0$	$6.5 \pm 0.9$	$10.3 \pm 0.6$	$20.5 \pm 1.1$
HDFS2 – 319	32 : 57.55	33 : 49.3	$1.2 \pm 2.0$	$1.8 \pm 0.9$	$7.5 \pm 0.6$	$12.5 \pm 1.1$
HDFS2 – 306	32 : 49.20	33 : 49.1	$-1.9 \pm 2.2$	$6.4 \pm 1.0$	$8.5 \pm 0.6$	$10.9 \pm 1.1$

Table A.8: Optical Photometry – continued

ID	R.A.(22h) J2000	Decl.(-60°) J2000	$U_{300}^a$	$B_{450}^a$	$V_{606}^a$	$I_{814}^a$
HDFS2 – 293	32 : 57.91	33 : 49.0	$24.0 \pm 2.0$	$31.1 \pm 0.9$	$74.6 \pm 0.6$	$120.9 \pm 1.1$
HDFS2 – 315	32 : 59.39	33 : 48.1	$-0.5 \pm 2.0$	$17.3 \pm 1.0$	$19.0 \pm 0.6$	$21.3 \pm 1.1$
HDFS2 – 303	32 : 45.56	33 : 47.4	$31.0 \pm 2.4$	$57.1 \pm 1.2$	$64.8 \pm 0.7$	$93.2 \pm 1.3$
HDFS2 – 314	32 : 46.64	33 : 47.3	$2.7 \pm 2.2$	$3.0 \pm 1.0$	$3.1 \pm 0.6$	$7.7 \pm 1.1$
HDFS2 – 323	32 : 52.87	33 : 47.2	$6.9 \pm 2.2$	$11.7 \pm 1.0$	$10.2 \pm 0.6$	$12.4 \pm 1.1$
HDFS2 – 316	32 : 58.34	33 : 46.7	$24.1 \pm 2.0$	$25.7 \pm 1.0$	$28.8 \pm 0.6$	$40.3 \pm 1.1$
HDFS2 – 292	33 : 2.48	33 : 46.4	$85.6 \pm 2.0$	$129.5 \pm 1.0$	$197.9 \pm 0.6$	$356.8 \pm 1.1$
HDFS2 – 301	32 : 58.63	33 : 46.3	$4.3 \pm 2.0$	$0.2 \pm 0.9$	$6.6 \pm 0.6$	$30.3 \pm 1.1$
HDFS2 – 337	33 : 2.12	33 : 46.3	$1.1 \pm 2.0$	$1.5 \pm 0.9$	$1.9 \pm 0.6$	$0.2 \pm 1.1$
HDFS2 – 333	32 : 53.92	33 : 46.2	$8.6 \pm 2.2$	$14.9 \pm 1.0$	$24.7 \pm 0.6$	$32.3 \pm 1.1$
HDFS2 – 317	33 : 5.15	33 : 46.1	$3.7 \pm 2.1$	$4.3 \pm 1.0$	$14.8 \pm 0.6$	$33.5 \pm 1.1$
HDFS2 – 313	33 : 5.65	33 : 46.1	$3.7 \pm 4.8$	$12.4 \pm 1.8$	$11.4 \pm 1.0$	$22.5 \pm 1.9$
HDFS2 – 336	32 : 49.24	33 : 45.9	$1.2 \pm 2.1$	$8.6 \pm 1.0$	$11.3 \pm 0.6$	$13.6 \pm 1.1$
HDFS2 – 335	32 : 52.26	33 : 45.3	$0.0 \pm 2.2$	$2.1 \pm 1.0$	$5.1 \pm 0.6$	$10.4 \pm 1.1$
HDFS2 – 312	32 : 49.99	33 : 45.0	$44.1 \pm 2.1$	$62.9 \pm 1.0$	$74.4 \pm 0.6$	$116.9 \pm 1.1$
HDFS2 – 342	32 : 47.18	33 : 44.6	$-1.0 \pm 2.2$	$1.8 \pm 1.0$	$5.6 \pm 0.6$	$13.1 \pm 1.1$
HDFS2 – 348	33 : 5.15	33 : 44.6	$1.8 \pm 2.1$	$14.5 \pm 1.0$	$23.1 \pm 0.6$	$33.7 \pm 1.1$
HDFS2 – 331	32 : 45.92	33 : 44.3	$2.1 \pm 2.2$	$23.9 \pm 1.0$	$31.3 \pm 0.6$	$35.1 \pm 1.2$
HDFS2 – 326	32 : 47.47	33 : 44.0	$4.9 \pm 2.2$	$12.8 \pm 1.0$	$35.2 \pm 0.6$	$82.1 \pm 1.1$
HDFS2 – 345	32 : 46.21	33 : 43.8	$0.6 \pm 2.2$	$4.2 \pm 1.0$	$6.1 \pm 0.6$	$4.7 \pm 1.1$
HDFS2 – 328	32 : 49.42	33 : 43.7	$15.1 \pm 2.2$	$14.6 \pm 1.0$	$37.7 \pm 0.6$	$78.2 \pm 1.1$
HDFS2 – 344	32 : 49.31	33 : 43.0	$13.7 \pm 2.1$	$11.8 \pm 1.0$	$22.0 \pm 0.6$	$42.2 \pm 1.1$
HDFS2 – 332	32 : 52.04	33 : 42.4	$-2.5 \pm 2.1$	$17.7 \pm 1.0$	$42.3 \pm 0.6$	$50.2 \pm 1.1$
HDFS2 – 358	32 : 54.89	33 : 42.1	$1.2 \pm 2.3$	$22.8 \pm 1.1$	$19.8 \pm 0.6$	$20.4 \pm 1.1$
HDFS2 – 339	33 : 0.79	33 : 42.0	$47.2 \pm 1.9$	$70.3 \pm 0.9$	$71.2 \pm 0.6$	$85.5 \pm 1.1$
HDFS2 – 352	32 : 50.53	33 : 42.0	$7.1 \pm 2.1$	$6.2 \pm 1.0$	$13.3 \pm 0.6$	$23.8 \pm 1.1$

Table A.8: Optical Photometry – continued

ID	R.A.(22h) J2000	Decl.(-60°) J2000	$U_{300}^a$	$B_{450}^a$	$V_{606}^a$	$I_{814}^a$
HDFS2 – 349	32 : 47.40	33 : 41.9	$22.1 \pm 2.2$	$32.0 \pm 1.0$	$41.5 \pm 0.6$	$65.7 \pm 1.1$
HDFS2 – 354	32 : 58.52	33 : 41.9	$10.8 \pm 2.0$	$16.2 \pm 0.9$	$15.5 \pm 0.6$	$18.6 \pm 1.1$
HDFS2 – 353	32 : 55.82	33 : 41.8	$2.7 \pm 2.3$	$3.4 \pm 1.1$	$6.5 \pm 0.7$	$9.8 \pm 1.2$
HDFS2 – 363	32 : 59.10	33 : 41.5	$5.5 \pm 2.0$	$8.6 \pm 1.0$	$19.4 \pm 0.6$	$27.2 \pm 1.1$
HDFS2 – 278	33 : 3.60	33 : 41.5	$114.0 \pm 2.0$	$398.6 \pm 1.0$	$1157.3 \pm 0.6$	$2309.2 \pm 1.1$
HDFS2 – 327	32 : 53.99	33 : 41.4	$10.9 \pm 2.2$	$14.6 \pm 1.0$	$31.9 \pm 0.6$	$78.6 \pm 1.1$
HDFS2 – 365	32 : 48.55	33 : 40.0	$15.8 \pm 2.1$	$21.3 \pm 1.0$	$22.8 \pm 0.6$	$26.8 \pm 1.1$
HDFS2 – 380	33 : 4.57	33 : 40.0	$-4.9 \pm 2.0$	$13.5 \pm 1.0$	$15.1 \pm 0.6$	$16.3 \pm 1.1$
HDFS2 – 356	33 : 0.83	33 : 39.8	$4.7 \pm 1.9$	$30.6 \pm 0.9$	$36.0 \pm 0.6$	$43.5 \pm 1.1$
HDFS2 – 340	32 : 59.46	33 : 39.5	$57.5 \pm 2.0$	$108.9 \pm 1.0$	$235.2 \pm 0.6$	$387.9 \pm 1.1$
HDFS2 – 388	32 : 54.60	33 : 39.3	$4.9 \pm 2.2$	$8.9 \pm 1.0$	$8.2 \pm 0.6$	$8.7 \pm 1.1$
HDFS2 – 374	32 : 49.56	33 : 38.8	$9.6 \pm 2.2$	$17.0 \pm 1.0$	$19.1 \pm 0.6$	$22.1 \pm 1.1$
HDFS2 – 368	32 : 50.06	33 : 38.8	$-3.0 \pm 2.1$	$10.6 \pm 1.0$	$17.0 \pm 0.6$	$15.6 \pm 1.1$
HDFS2 – 387	32 : 52.30	33 : 38.5	$2.9 \pm 2.2$	$8.1 \pm 1.0$	$10.0 \pm 0.6$	$9.4 \pm 1.1$
HDFS2 – 393	32 : 51.00	33 : 38.3	$2.0 \pm 2.1$	$-0.8 \pm 1.0$	$-0.1 \pm 0.6$	$1.8 \pm 1.1$
HDFS2 – 346	32 : 51.50	33 : 37.4	$23.9 \pm 2.1$	$81.7 \pm 1.0$	$217.8 \pm 0.6$	$483.2 \pm 1.1$
HDFS2 – 311	32 : 53.74	33 : 37.4	$78.0 \pm 2.2$	$134.0 \pm 1.0$	$263.9 \pm 0.6$	$454.8 \pm 1.1$
HDFS2 – 376	33 : 2.84	33 : 37.2	$9.3 \pm 2.0$	$15.6 \pm 0.9$	$20.5 \pm 0.6$	$40.3 \pm 1.1$
HDFS2 – 355	32 : 56.72	33 : 37.2	$1.4 \pm 2.0$	$10.2 \pm 0.9$	$20.6 \pm 0.6$	$31.1 \pm 1.1$
HDFS2 – 371	32 : 54.96	33 : 36.7	$10.2 \pm 2.3$	$6.0 \pm 1.1$	$15.2 \pm 0.6$	$37.7 \pm 1.2$
HDFS2 – 398	32 : 56.58	33 : 36.5	$8.2 \pm 1.9$	$18.2 \pm 1.0$	$29.9 \pm 0.6$	$38.8 \pm 1.1$
HDFS2 – 392	32 : 54.71	33 : 36.2	$0.5 \pm 2.2$	$3.2 \pm 1.0$	$9.8 \pm 0.6$	$20.2 \pm 1.1$
HDFS2 – 296	32 : 47.65	33 : 35.8	$111.5 \pm 2.2$	$319.1 \pm 1.0$	$1088.8 \pm 0.6$	$2995.7 \pm 1.1$
HDFS2 – 409	32 : 57.55	33 : 35.7	$-0.9 \pm 2.0$	$0.4 \pm 0.9$	$-0.5 \pm 0.6$	$0.7 \pm 1.1$
HDFS2 – 410	32 : 55.14	33 : 34.9	$1.9 \pm 2.5$	$4.5 \pm 1.2$	$8.3 \pm 0.7$	$17.2 \pm 1.2$
HDFS2 – 402	33 : 2.16	33 : 34.8	$18.9 \pm 2.0$	$25.9 \pm 0.9$	$52.3 \pm 0.6$	$88.3 \pm 1.1$

Table A.8: Optical Photometry – continued

ID	R.A.(22h) J2000	Decl.(-60°) J2000	$U_{300}^a$	$B_{450}^a$	$V_{606}^a$	$I_{814}^a$
HDFS2 – 370	32 : 53.30	33 : 34.7	$2.8 \pm 2.1$	$1.8 \pm 1.0$	$4.2 \pm 0.6$	$21.8 \pm 1.1$
HDFS2 – 407	32 : 48.88	33 : 34.3	$9.2 \pm 2.1$	$21.2 \pm 1.0$	$25.5 \pm 0.6$	$28.9 \pm 1.1$
HDFS2 – 406	33 : 5.44	33 : 34.3	$12.2 \pm 2.1$	$7.5 \pm 1.1$	$13.6 \pm 0.7$	$24.4 \pm 1.2$
HDFS2 – 414	33 : 5.18	33 : 34.0	$6.5 \pm 2.1$	$3.9 \pm 1.0$	$6.0 \pm 0.6$	$9.5 \pm 1.1$
HDFS2 – 377	33 : 0.04	33 : 33.8	$3.9 \pm 2.0$	$3.0 \pm 0.9$	$8.9 \pm 0.6$	$43.6 \pm 1.1$
HDFS2 – 390	32 : 55.75	33 : 33.6	$25.2 \pm 2.8$	$40.5 \pm 1.2$	$66.5 \pm 0.7$	$106.7 \pm 1.3$
HDFS2 – 405	33 : 3.49	33 : 33.2	$3.6 \pm 2.0$	$18.7 \pm 1.0$	$22.8 \pm 0.6$	$29.3 \pm 1.1$
HDFS2 – 359	32 : 53.41	33 : 33.0	$14.0 \pm 2.2$	$20.4 \pm 1.0$	$34.7 \pm 0.6$	$85.7 \pm 1.1$
HDFS2 – 361	32 : 54.67	33 : 33.0	$67.2 \pm 2.2$	$269.5 \pm 1.0$	$557.1 \pm 0.6$	$858.6 \pm 1.1$
HDFS2 – 383	32 : 52.37	33 : 32.9	$53.0 \pm 2.2$	$82.5 \pm 1.0$	$165.5 \pm 0.6$	$290.1 \pm 1.1$
HDFS2 – 411	32 : 58.78	33 : 32.9	$9.4 \pm 2.0$	$25.3 \pm 1.0$	$30.0 \pm 0.6$	$35.9 \pm 1.1$
HDFS2 – 413	32 : 53.99	33 : 32.7	$11.5 \pm 2.2$	$14.5 \pm 1.0$	$19.7 \pm 0.6$	$29.7 \pm 1.1$
HDFS2 – 426	33 : 2.77	33 : 32.6	$1.2 \pm 2.0$	$5.5 \pm 0.9$	$16.7 \pm 0.6$	$28.5 \pm 1.1$
HDFS2 – 415	32 : 48.37	33 : 32.4	$19.6 \pm 2.1$	$24.1 \pm 1.0$	$38.5 \pm 0.6$	$60.6 \pm 1.1$
HDFS2 – 430	32 : 48.16	33 : 32.4	$1.0 \pm 2.2$	$5.0 \pm 1.0$	$12.6 \pm 0.6$	$21.6 \pm 1.1$
HDFS2 – 394	33 : 1.80	33 : 31.8	$3.1 \pm 2.0$	$30.9 \pm 0.9$	$44.5 \pm 0.6$	$70.1 \pm 1.1$
HDFS2 – 418	33 : 4.32	33 : 31.7	$5.5 \pm 2.0$	$23.6 \pm 1.0$	$58.4 \pm 0.6$	$100.9 \pm 1.1$
HDFS2 – 421	32 : 56.83	33 : 31.5	$2.2 \pm 2.0$	$2.4 \pm 0.9$	$7.1 \pm 0.6$	$32.8 \pm 1.1$
HDFS2 – 379	32 : 58.24	33 : 31.4	$64.6 \pm 2.0$	$108.9 \pm 0.9$	$246.3 \pm 0.6$	$381.3 \pm 1.1$
HDFS2 – 428	32 : 53.12	33 : 30.9	$5.6 \pm 2.1$	$1.2 \pm 1.0$	$4.4 \pm 0.6$	$12.4 \pm 1.1$
HDFS2 – 423	33 : 4.97	33 : 30.5	$-0.8 \pm 2.1$	$54.8 \pm 1.0$	$68.7 \pm 0.6$	$74.4 \pm 1.1$
HDFS2 – 441	32 : 56.40	33 : 30.3	$1.9 \pm 2.0$	$4.9 \pm 1.0$	$6.9 \pm 0.6$	$14.3 \pm 1.1$
HDFS2 – 424	32 : 49.56	33 : 30.3	$3.0 \pm 2.1$	$4.0 \pm 1.0$	$8.5 \pm 0.6$	$14.2 \pm 1.1$
HDFS2 – 412	32 : 55.82	33 : 30.2	$9.5 \pm 2.6$	$34.2 \pm 1.1$	$66.8 \pm 0.7$	$92.6 \pm 1.3$
HDFS2 – 443	33 : 4.36	33 : 30.2	$-2.4 \pm 2.0$	$9.1 \pm 1.0$	$12.4 \pm 0.6$	$14.7 \pm 1.1$
HDFS2 – 439	32 : 46.03	33 : 30.1	$5.1 \pm 2.2$	$8.3 \pm 1.0$	$7.2 \pm 0.6$	$12.8 \pm 1.2$

Table A.8: Optical Photometry – continued

ID	R.A.(22h) J2000	Decl.(-60°) J2000	$U_{300}^a$	$B_{450}^a$	$V_{606}^a$	$I_{814}^a$
HDFS2 – 422	33 : 3.24	33 : 29.6	$14.4 \pm 2.0$	$92.3 \pm 1.0$	$127.4 \pm 0.6$	$173.4 \pm 1.1$
HDFS2 – 446	33 : 4.61	33 : 29.4	$7.3 \pm 2.1$	$19.0 \pm 1.0$	$16.8 \pm 0.6$	$17.0 \pm 1.1$
HDFS2 – 435	33 : 2.12	33 : 29.2	$-1.4 \pm 2.0$	$9.5 \pm 0.9$	$15.3 \pm 0.6$	$19.2 \pm 1.1$
HDFS2 – 404	32 : 55.00	33 : 28.9	$1.9 \pm 2.2$	$16.0 \pm 1.1$	$32.3 \pm 0.6$	$119.5 \pm 1.1$
HDFS2 – 433	32 : 58.31	33 : 28.9	$1.1 \pm 2.0$	$21.3 \pm 0.9$	$28.3 \pm 0.6$	$41.2 \pm 1.1$
HDFS2 – 431	32 : 59.50	33 : 28.8	$18.4 \pm 2.0$	$34.9 \pm 1.0$	$42.1 \pm 0.6$	$76.6 \pm 1.1$
HDFS2 – 427	32 : 57.12	33 : 28.7	$-4.0 \pm 2.0$	$8.3 \pm 0.9$	$21.1 \pm 0.6$	$93.4 \pm 1.1$
HDFS2 – 382	32 : 50.68	33 : 28.5	$7.2 \pm 2.1$	$64.7 \pm 1.0$	$90.6 \pm 0.6$	$118.4 \pm 1.1$
HDFS2 – 357	32 : 53.05	33 : 28.4	$34.3 \pm 2.2$	$62.2 \pm 1.0$	$114.4 \pm 0.6$	$317.9 \pm 1.1$
HDFS2 – 456	32 : 57.44	33 : 28.0	$1.0 \pm 2.0$	$15.4 \pm 0.9$	$13.6 \pm 0.6$	$15.9 \pm 1.1$
HDFS2 – 449	32 : 56.69	33 : 27.5	$11.4 \pm 2.0$	$15.1 \pm 1.0$	$13.9 \pm 0.6$	$18.0 \pm 1.1$
HDFS2 – 458	32 : 53.77	33 : 26.9	$-4.1 \pm 2.2$	$5.5 \pm 1.0$	$4.8 \pm 0.6$	$4.9 \pm 1.1$
HDFS2 – 464	32 : 58.67	33 : 26.9	$-0.6 \pm 2.0$	$3.6 \pm 0.9$	$9.1 \pm 0.6$	$14.0 \pm 1.1$
HDFS2 – 457	32 : 51.61	33 : 26.7	$3.2 \pm 2.2$	$4.7 \pm 1.0$	$6.4 \pm 0.6$	$8.4 \pm 1.1$
HDFS2 – 461	33 : 2.52	33 : 26.1	$4.2 \pm 2.0$	$9.9 \pm 1.0$	$8.5 \pm 0.6$	$16.3 \pm 1.1$
HDFS2 – 462	32 : 57.34	33 : 26.0	$0.3 \pm 2.0$	$15.4 \pm 0.9$	$24.9 \pm 0.6$	$31.1 \pm 1.1$
HDFS2 – 451	32 : 47.18	33 : 25.8	$10.5 \pm 2.2$	$16.7 \pm 1.0$	$24.4 \pm 0.6$	$41.9 \pm 1.1$
HDFS2 – 438	32 : 50.53	33 : 25.8	$30.9 \pm 2.1$	$75.5 \pm 1.0$	$174.3 \pm 0.6$	$341.2 \pm 1.1$
HDFS2 – 434	33 : 0.90	33 : 25.5	$32.4 \pm 2.0$	$55.0 \pm 0.9$	$62.0 \pm 0.6$	$114.5 \pm 1.1$
HDFS2 – 658	33 : 4.25	33 : 25.5	$1.7 \pm 2.1$	$9.7 \pm 1.0$	$11.3 \pm 0.6$	$12.4 \pm 1.1$
HDFS2 – 453	32 : 59.60	33 : 25.4	$-0.7 \pm 2.0$	$24.3 \pm 1.0$	$26.6 \pm 0.6$	$32.0 \pm 1.1$
HDFS2 – 654	33 : 5.08	33 : 25.4	$1.4 \pm 2.1$	$1.2 \pm 1.0$	$4.2 \pm 0.6$	$0.1 \pm 1.1$
HDFS2 – 660	32 : 59.10	33 : 25.3	$2.1 \pm 2.0$	$4.0 \pm 1.0$	$6.5 \pm 0.6$	$6.8 \pm 1.1$
HDFS2 – 448	32 : 55.03	33 : 25.3	$6.7 \pm 2.2$	$25.2 \pm 1.1$	$32.6 \pm 0.6$	$39.7 \pm 1.1$
HDFS2 – 436	33 : 2.84	33 : 25.0	$24.6 \pm 2.0$	$81.8 \pm 1.0$	$106.9 \pm 0.6$	$186.7 \pm 1.1$
HDFS2 – 459	33 : 4.43	33 : 24.6	$1.1 \pm 2.1$	$18.4 \pm 1.0$	$31.9 \pm 0.6$	$38.8 \pm 1.1$



Table A.8: Optical Photometry – continued

ID	R.A.(22h) J2000	Decl.(−60°) J2000	$U_{300}^a$	$B_{450}^a$	$V_{606}^a$	$I_{814}^a$
HDFS2 – 631	32 : 57.44	33 : 24.3	$1.0 \pm 2.0$	$1.5 \pm 0.9$	$3.3 \pm 0.6$	$11.8 \pm 1.1$
HDFS2 – 470	32 : 54.53	33 : 24.3	$8.8 \pm 2.2$	$10.2 \pm 1.0$	$20.6 \pm 0.6$	$34.0 \pm 1.1$
HDFS2 – 447	32 : 52.15	33 : 23.8	$45.7 \pm 2.2$	$105.2 \pm 1.0$	$145.1 \pm 0.6$	$246.6 \pm 1.1$
HDFS2 – 645	32 : 54.85	33 : 23.6	$5.4 \pm 2.2$	$8.6 \pm 1.0$	$9.5 \pm 0.6$	$15.2 \pm 1.1$
HDFS2 – 633	32 : 57.23	33 : 23.1	$3.1 \pm 1.7$	$12.5 \pm 0.8$	$15.8 \pm 0.5$	$28.3 \pm 0.9$
HDFS2 – 452	32 : 57.05	33 : 22.8	$74.0 \pm 2.0$	$106.8 \pm 1.0$	$150.3 \pm 0.6$	$251.5 \pm 1.1$
HDFS2 – 639	32 : 45.92	33 : 22.5	$0.8 \pm 2.3$	$1.8 \pm 1.1$	$5.3 \pm 0.7$	$12.5 \pm 1.2$
HDFS2 – 467	32 : 54.20	33 : 22.4	$2.5 \pm 2.2$	$3.7 \pm 1.0$	$5.3 \pm 0.6$	$11.1 \pm 1.1$
HDFS2 – 628	33 : 4.57	33 : 22.4	$-2.3 \pm 2.1$	$8.5 \pm 1.0$	$36.4 \pm 0.6$	$83.9 \pm 1.1$
HDFS2 – 469	33 : 5.00	33 : 22.0	$-0.0 \pm 2.1$	$3.4 \pm 1.0$	$8.3 \pm 0.6$	$18.5 \pm 1.1$
HDFS2 – 419	33 : 2.81	33 : 22.0	$36.5 \pm 2.0$	$191.4 \pm 1.0$	$758.7 \pm 0.6$	$1980.5 \pm 1.1$
HDFS2 – 626	32 : 52.91	33 : 21.6	$-3.8 \pm 2.1$	$19.4 \pm 1.0$	$33.1 \pm 0.6$	$40.0 \pm 1.1$
HDFS2 – 625	32 : 49.24	33 : 20.6	$13.0 \pm 2.1$	$12.1 \pm 1.0$	$10.6 \pm 0.6$	$11.2 \pm 1.1$
HDFS2 – 466	32 : 54.31	33 : 20.3	$28.3 \pm 2.2$	$43.5 \pm 1.0$	$86.4 \pm 0.6$	$131.1 \pm 1.1$
HDFS2 – 596	32 : 53.12	33 : 20.0	$4.0 \pm 2.2$	$20.0 \pm 1.0$	$40.7 \pm 0.6$	$52.1 \pm 1.1$
HDFS2 – 620	33 : 3.71	33 : 19.7	$-5.4 \pm 2.1$	$4.3 \pm 1.0$	$11.4 \pm 0.6$	$18.6 \pm 1.1$
HDFS2 – 638	32 : 55.00	33 : 19.4	$-0.4 \pm 2.3$	$-0.6 \pm 1.1$	$-0.7 \pm 0.6$	$0.4 \pm 1.2$
HDFS2 – 617	32 : 52.26	33 : 19.3	$36.2 \pm 2.2$	$54.9 \pm 1.0$	$91.8 \pm 0.6$	$103.0 \pm 1.1$
HDFS2 – 614	33 : 4.25	33 : 19.2	$2.0 \pm 2.1$	$1.0 \pm 1.0$	$4.7 \pm 0.6$	$3.3 \pm 1.1$
HDFS2 – 613	33 : 3.42	33 : 19.0	$2.8 \pm 2.1$	$3.6 \pm 1.0$	$10.4 \pm 0.6$	$16.9 \pm 1.1$
HDFS2 – 608	33 : 0.18	33 : 18.9	$47.3 \pm 2.0$	$63.1 \pm 1.0$	$93.0 \pm 0.6$	$177.7 \pm 1.1$
HDFS2 – 609	32 : 57.62	33 : 18.2	$10.1 \pm 2.0$	$9.7 \pm 1.0$	$22.1 \pm 0.6$	$33.8 \pm 1.1$
HDFS2 – 605	32 : 50.50	33 : 17.8	$2.0 \pm 2.2$	$6.2 \pm 1.0$	$9.7 \pm 0.6$	$20.0 \pm 1.1$
HDFS2 – 602	32 : 55.90	33 : 17.6	$36.8 \pm 4.1$	$62.9 \pm 1.4$	$121.6 \pm 0.8$	$212.4 \pm 1.6$
HDFS2 – 601	33 : 5.29	33 : 17.4	$11.5 \pm 2.2$	$26.7 \pm 1.1$	$46.2 \pm 0.6$	$61.5 \pm 1.1$
HDFS2 – 595	32 : 52.91	33 : 16.9	$6.9 \pm 2.2$	$34.5 \pm 1.0$	$79.1 \pm 0.6$	$211.1 \pm 1.1$

Table A.8: Optical Photometry – continued

ID	R.A.(22h) J2000	Decl.(-60°) J2000	$U_{300}^a$	$B_{450}^a$	$V_{606}^a$	$I_{814}^a$
HDFS2 – 618	32 : 46.28	33 : 16.5	$9.2 \pm 2.2$	$11.1 \pm 1.0$	$12.0 \pm 0.6$	$14.2 \pm 1.1$
HDFS2 – 592	33 : 1.91	33 : 16.2	$55.3 \pm 2.1$	$156.2 \pm 1.0$	$382.2 \pm 0.6$	$667.5 \pm 1.1$
HDFS2 – 606	32 : 46.57	33 : 16.1	$15.6 \pm 2.2$	$10.9 \pm 1.0$	$12.3 \pm 0.6$	$13.5 \pm 1.1$
HDFS2 – 594	32 : 52.55	33 : 16.0	$13.9 \pm 2.2$	$15.2 \pm 1.0$	$27.3 \pm 0.6$	$35.2 \pm 1.1$
HDFS2 – 587	33 : 5.08	33 : 15.9	$-2.7 \pm 2.3$	$7.6 \pm 1.1$	$16.2 \pm 0.7$	$22.4 \pm 1.2$
HDFS2 – 597	32 : 54.38	33 : 15.7	$1.4 \pm 2.2$	$7.1 \pm 1.0$	$8.3 \pm 0.6$	$9.7 \pm 1.1$
HDFS2 – 593	32 : 52.62	33 : 15.0	$-1.4 \pm 2.2$	$5.3 \pm 1.0$	$24.7 \pm 0.6$	$56.5 \pm 1.1$
HDFS2 – 591	32 : 58.24	33 : 14.9	$2.0 \pm 2.1$	$1.2 \pm 1.0$	$0.8 \pm 0.6$	$6.5 \pm 1.1$
HDFS2 – 590	32 : 51.43	33 : 14.9	$-1.8 \pm 2.2$	$23.5 \pm 1.0$	$32.2 \pm 0.6$	$34.0 \pm 1.1$
HDFS2 – 586	33 : 5.51	33 : 14.9	$-3.4 \pm 2.4$	$2.8 \pm 1.1$	$6.4 \pm 0.7$	$6.8 \pm 1.3$
HDFS2 – 585	32 : 51.72	33 : 14.5	$18.6 \pm 2.2$	$28.4 \pm 1.0$	$31.8 \pm 0.6$	$39.2 \pm 1.1$
HDFS2 – 588	32 : 47.04	33 : 14.3	$5.3 \pm 2.2$	$11.4 \pm 1.0$	$16.1 \pm 0.6$	$17.0 \pm 1.1$
HDFS2 – 583	32 : 50.64	33 : 14.3	$8.9 \pm 2.2$	$19.1 \pm 1.0$	$21.1 \pm 0.6$	$21.9 \pm 1.1$
HDFS2 – 579	33 : 0.86	33 : 14.3	$9.8 \pm 2.1$	$30.0 \pm 1.0$	$33.4 \pm 0.6$	$42.0 \pm 1.1$
HDFS2 – 582	32 : 50.46	33 : 14.1	$15.6 \pm 2.2$	$31.9 \pm 1.0$	$39.8 \pm 0.6$	$56.0 \pm 1.1$
HDFS2 – 581	32 : 48.55	33 : 13.9	$51.5 \pm 2.2$	$62.6 \pm 1.0$	$102.3 \pm 0.6$	$177.0 \pm 1.1$
HDFS2 – 578	32 : 50.96	33 : 13.9	$22.0 \pm 2.2$	$28.8 \pm 1.0$	$50.8 \pm 0.6$	$79.6 \pm 1.1$
HDFS2 – 574	33 : 3.96	33 : 13.7	$6.4 \pm 2.4$	$39.0 \pm 1.1$	$53.7 \pm 0.7$	$65.4 \pm 1.3$
HDFS2 – 566	32 : 53.92	33 : 13.4	$13.1 \pm 2.2$	$130.6 \pm 1.0$	$502.9 \pm 0.6$	$1044.2 \pm 1.1$
HDFS2 – 568	33 : 1.98	33 : 12.5	$-2.7 \pm 2.3$	$7.2 \pm 1.1$	$10.7 \pm 0.7$	$28.7 \pm 1.3$
HDFS2 – 572	32 : 46.86	33 : 12.3	$1.7 \pm 2.2$	$19.7 \pm 1.1$	$18.8 \pm 0.6$	$18.1 \pm 1.1$
HDFS2 – 571	32 : 53.45	33 : 12.0	$6.7 \pm 2.2$	$21.9 \pm 1.0$	$44.9 \pm 0.6$	$57.9 \pm 1.1$
HDFS2 – 567	32 : 51.68	33 : 11.9	$-3.1 \pm 2.2$	$2.9 \pm 1.0$	$7.3 \pm 0.6$	$14.3 \pm 1.1$
HDFS2 – 564	33 : 5.26	33 : 11.7	$2.7 \pm 2.8$	$1.5 \pm 1.3$	$3.3 \pm 0.8$	$3.9 \pm 1.6$
HDFS2 – 565	32 : 50.28	33 : 11.3	$-1.2 \pm 2.2$	$11.8 \pm 1.0$	$20.2 \pm 0.6$	$22.6 \pm 1.1$
HDFS2 – 561	32 : 49.49	33 : 11.1	$35.4 \pm 2.2$	$54.5 \pm 1.0$	$107.9 \pm 0.6$	$185.5 \pm 1.1$

Table A.8: Optical Photometry – continued

ID	R.A.(22h) J2000	Decl.(-60°) J2000	$U_{300}^a$	$B_{450}^a$	$V_{606}^a$	$I_{814}^a$
HDFS2 – 560	32 : 58.63	33 : 10.5	$4.3 \pm 2.3$	$16.4 \pm 1.1$	$18.4 \pm 0.7$	$21.7 \pm 1.3$
HDFS2 – 559	33 : 3.13	33 : 10.4	$0.0 \pm 2.7$	$7.5 \pm 1.2$	$12.2 \pm 0.7$	$11.4 \pm 1.6$
HDFS2 – 562	32 : 50.32	33 : 10.1	$-0.8 \pm 2.2$	$0.6 \pm 1.0$	$6.8 \pm 0.6$	$12.3 \pm 1.1$
HDFS2 – 558	32 : 53.48	33 : 9.5	$-1.7 \pm 2.2$	$11.5 \pm 1.0$	$21.0 \pm 0.6$	$24.2 \pm 1.1$
HDFS2 – 543	32 : 51.86	33 : 9.4	$15.5 \pm 2.2$	$16.4 \pm 1.0$	$26.9 \pm 0.6$	$59.1 \pm 1.1$
HDFS2 – 556	32 : 48.98	33 : 9.3	$10.6 \pm 2.2$	$18.4 \pm 1.0$	$43.3 \pm 0.6$	$64.0 \pm 1.1$
HDFS2 – 554	32 : 48.01	33 : 9.3	$-0.9 \pm 2.2$	$17.6 \pm 1.0$	$23.4 \pm 0.6$	$37.0 \pm 1.1$
HDFS2 – 542	32 : 52.30	33 : 8.3	$70.9 \pm 2.2$	$143.7 \pm 1.0$	$321.2 \pm 0.6$	$643.3 \pm 1.1$
HDFS2 – 550	33 : 0.90	33 : 8.0	$-0.3 \pm 2.7$	$5.8 \pm 1.3$	$12.7 \pm 0.8$	$14.1 \pm 1.7$
HDFS2 – 548	32 : 59.96	33 : 7.7	$8.8 \pm 2.6$	$18.9 \pm 1.2$	$35.4 \pm 0.7$	$44.6 \pm 1.5$
HDFS2 – 547	32 : 53.41	33 : 7.0	$5.5 \pm 2.4$	$7.0 \pm 1.1$	$8.9 \pm 0.6$	$9.7 \pm 1.2$
HDFS2 – 532	32 : 51.68	33 : 5.9	$-1.0 \pm 2.3$	$4.3 \pm 1.1$	$12.8 \pm 0.6$	$67.1 \pm 1.2$
HDFS2 – 517	32 : 57.55	33 : 5.9	$218.0 \pm 2.8$	$458.9 \pm 1.3$	$915.0 \pm 0.8$	$1769.8 \pm 1.6$
HDFS2 – 527	32 : 54.02	33 : 5.4	$10.5 \pm 2.5$	$31.4 \pm 1.1$	$109.5 \pm 0.7$	$283.5 \pm 1.4$
HDFS2 – 518	32 : 57.23	33 : 5.4	$62.0 \pm 2.8$	$89.4 \pm 1.4$	$126.8 \pm 0.8$	$260.0 \pm 1.7$
HDFS2 – 529	32 : 58.70	33 : 5.3	$-0.9 \pm 2.9$	$4.9 \pm 1.4$	$12.5 \pm 0.8$	$20.0 \pm 1.7$
HDFS2 – 528	32 : 52.04	33 : 4.7	$-0.2 \pm 2.4$	$1.3 \pm 1.1$	$0.2 \pm 0.7$	$1.2 \pm 1.3$
HDFS2 – 525	32 : 49.74	33 : 4.4	$5.5 \pm 2.4$	$10.9 \pm 1.1$	$16.6 \pm 0.7$	$32.0 \pm 1.2$
HDFS2 – 521	32 : 59.68	33 : 4.0	$9.7 \pm 3.3$	$1.9 \pm 1.6$	$2.9 \pm 0.8$	$11.8 \pm 1.6$
HDFS2 – 519	33 : 0.00	33 : 3.9	$26.8 \pm 3.5$	$48.9 \pm 1.7$	$51.0 \pm 0.8$	$78.0 \pm 1.7$
HDFS2 – 511	32 : 47.04	33 : 3.0	$11.7 \pm 2.4$	$29.2 \pm 1.1$	$40.0 \pm 0.7$	$65.0 \pm 1.3$
HDFS2 – 515	32 : 49.63	33 : 2.9	$5.0 \pm 2.5$	$35.0 \pm 1.1$	$36.2 \pm 0.7$	$39.1 \pm 1.4$
HDFS2 – 512	32 : 47.33	33 : 2.7	$7.9 \pm 2.4$	$8.9 \pm 1.1$	$16.1 \pm 0.7$	$26.7 \pm 1.3$
HDFS2 – 513	32 : 47.58	33 : 2.4	$3.7 \pm 2.5$	$9.4 \pm 1.1$	$14.3 \pm 0.7$	$29.9 \pm 1.3$
HDFS2 – 506	32 : 53.41	33 : 1.5	$-2.9 \pm 2.5$	$4.9 \pm 1.1$	$12.9 \pm 0.7$	$17.1 \pm 1.3$
HDFS2 – 502	32 : 53.70	33 : 1.4	$0.2 \pm 2.5$	$6.2 \pm 1.2$	$8.6 \pm 0.7$	$17.0 \pm 1.3$

Table A.8: Optical Photometry – continued

ID	R.A.(22h) J2000	Decl.(-60°) J2000	$U_{300}^a$	$B_{450}^a$	$V_{606}^a$	$I_{814}^a$
HDFS2 – 500	32 : 51.18	33 : 1.4	$11.5 \pm 2.5$	$33.7 \pm 1.1$	$42.6 \pm 0.7$	$70.9 \pm 1.4$
HDFS2 – 501	32 : 51.43	33 : 1.3	$2.1 \pm 2.5$	$2.4 \pm 1.1$	$3.8 \pm 0.7$	$4.0 \pm 1.4$
HDFS2 – 508	32 : 48.77	33 : 1.0	$3.8 \pm 2.6$	$2.1 \pm 1.1$	$2.5 \pm 0.7$	$3.3 \pm 1.5$
HDFS2 – 498	32 : 46.21	33 : 0.6	$2.4 \pm 2.7$	$10.6 \pm 1.3$	$8.6 \pm 0.8$	$8.1 \pm 1.6$
HDFS2 – 499	32 : 48.52	33 : 0.5	$3.0 \pm 2.5$	$3.1 \pm 1.1$	$4.4 \pm 0.7$	$6.9 \pm 1.5$
HDFS2 – 494	32 : 54.46	33 : 0.2	$3.8 \pm 2.6$	$12.4 \pm 1.2$	$10.4 \pm 0.7$	$15.3 \pm 1.3$
HDFS2 – 487	32 : 55.72	32 : 59.1	$-0.3 \pm 3.1$	$6.6 \pm 1.5$	$9.9 \pm 0.8$	$10.8 \pm 1.5$
HDFS2 – 486	32 : 54.35	32 : 59.0	$0.8 \pm 2.6$	$12.3 \pm 1.2$	$16.1 \pm 0.7$	$17.4 \pm 1.3$
HDFS2 – 481	32 : 53.81	32 : 58.5	$7.9 \pm 2.5$	$15.6 \pm 1.2$	$17.7 \pm 0.7$	$22.1 \pm 1.3$
HDFS2 – 482	32 : 46.75	32 : 58.3	$5.4 \pm 2.6$	$7.1 \pm 1.2$	$10.4 \pm 0.7$	$15.6 \pm 1.5$
HDFS2 – 484	32 : 48.05	32 : 58.3	$0.3 \pm 2.5$	$0.1 \pm 1.1$	$2.5 \pm 0.7$	$2.2 \pm 1.4$
HDFS2 – 475	32 : 47.04	32 : 58.1	$4.5 \pm 2.6$	$19.3 \pm 1.2$	$21.8 \pm 0.7$	$24.7 \pm 1.4$
HDFS2 – 478	32 : 46.39	32 : 57.5	$3.0 \pm 2.6$	$1.0 \pm 1.2$	$7.2 \pm 0.7$	$10.6 \pm 1.4$
HDFS2 – 483	32 : 54.31	32 : 57.5	$6.0 \pm 2.6$	$25.2 \pm 1.2$	$29.5 \pm 0.7$	$29.7 \pm 1.2$
HDFS2 – 641	32 : 50.10	32 : 57.4	$13.6 \pm 2.5$	$4.1 \pm 1.2$	$6.2 \pm 0.7$	$7.7 \pm 1.3$
HDFS2 – 493	32 : 46.86	32 : 56.6	$2.4 \pm 2.5$	$18.9 \pm 1.2$	$18.8 \pm 0.7$	$26.5 \pm 1.3$
HDFS2 – 657	32 : 47.76	32 : 56.0	$25.4 \pm 2.5$	$37.7 \pm 1.2$	$44.6 \pm 0.7$	$73.4 \pm 1.3$
HDFS2 – 669	32 : 47.33	32 : 56.0	$7.5 \pm 2.5$	$13.8 \pm 1.2$	$16.7 \pm 0.7$	$21.5 \pm 1.3$
HDFS2 – 677	32 : 53.84	32 : 55.5	$13.3 \pm 2.5$	$29.6 \pm 1.2$	$31.8 \pm 0.7$	$37.0 \pm 1.2$
HDFS2 – 671	32 : 58.67	32 : 55.0	$5.8 \pm 4.0$	$4.9 \pm 1.7$	$0.9 \pm 0.8$	$4.1 \pm 1.5$
HDFS2 – 644	32 : 50.28	32 : 54.7	$-0.4 \pm 2.5$	$8.1 \pm 1.1$	$7.2 \pm 0.7$	$15.0 \pm 1.2$
HDFS2 – 632	32 : 52.66	32 : 54.7	$-5.8 \pm 2.5$	$0.2 \pm 1.1$	$11.2 \pm 0.7$	$23.5 \pm 1.2$
HDFS2 – 674	32 : 54.85	32 : 54.5	$14.4 \pm 2.5$	$17.9 \pm 1.1$	$17.9 \pm 0.7$	$25.7 \pm 1.2$
HDFS2 – 683	32 : 46.79	32 : 54.2	$1.6 \pm 2.6$	$5.7 \pm 1.2$	$11.4 \pm 0.7$	$14.1 \pm 1.3$
HDFS2 – 696	32 : 49.24	32 : 53.4	$37.3 \pm 2.5$	$67.5 \pm 1.2$	$142.5 \pm 0.7$	$277.3 \pm 1.2$
HDFS2 – 687	32 : 51.25	32 : 52.8	$5.1 \pm 2.5$	$13.5 \pm 1.1$	$22.4 \pm 0.7$	$33.8 \pm 1.2$

Table A.8: Optical Photometry – continued

ID	R.A.(22h) J2000	Decl.(-60°) J2000	$U_{300}^a$	$B_{450}^a$	$V_{606}^a$	$I_{814}^a$
HDFS2 – 693	32 : 46.79	32 : 52.8	$5.0 \pm 2.6$	$5.7 \pm 1.2$	$8.8 \pm 0.7$	$13.5 \pm 1.3$
HDFS2 – 616	32 : 47.65	32 : 52.3	$40.2 \pm 2.6$	$54.1 \pm 1.2$	$102.7 \pm 0.7$	$163.6 \pm 1.2$
HDFS2 – 648	32 : 55.79	32 : 51.9	$2.1 \pm 2.4$	$12.5 \pm 1.2$	$23.7 \pm 0.7$	$27.0 \pm 1.2$
HDFS2 – 694	32 : 54.06	32 : 51.5	$87.7 \pm 2.2$	$137.1 \pm 1.0$	$283.7 \pm 0.6$	$459.5 \pm 1.1$
HDFS2 – 716	32 : 51.32	32 : 50.6	$13.3 \pm 2.3$	$12.9 \pm 1.0$	$14.9 \pm 0.7$	$21.8 \pm 1.1$
HDFS2 – 692	32 : 51.83	32 : 50.3	$3.3 \pm 2.2$	$6.2 \pm 1.0$	$9.4 \pm 0.6$	$9.6 \pm 1.1$
HDFS2 – 699	32 : 56.04	32 : 50.2	$-4.4 \pm 3.0$	$1.6 \pm 1.3$	$0.3 \pm 0.7$	$1.8 \pm 1.3$
HDFS2 – 668	32 : 47.15	32 : 49.7	$9.5 \pm 2.7$	$12.1 \pm 1.2$	$12.9 \pm 0.7$	$18.0 \pm 1.2$
HDFS2 – 652	32 : 46.75	32 : 49.0	$11.1 \pm 2.7$	$20.4 \pm 1.2$	$27.5 \pm 0.7$	$34.8 \pm 1.3$
HDFS2 – 725	32 : 47.65	32 : 49.0	$-2.2 \pm 2.5$	$5.4 \pm 1.1$	$10.1 \pm 0.7$	$11.9 \pm 1.2$
HDFS2 – 707	32 : 47.44	32 : 48.6	$0.6 \pm 2.5$	$11.8 \pm 1.1$	$17.1 \pm 0.7$	$17.9 \pm 1.2$
HDFS2 – 736	32 : 54.67	32 : 48.0	$2.3 \pm 2.1$	$14.5 \pm 1.0$	$17.7 \pm 0.6$	$16.7 \pm 1.1$
HDFS2 – 748	32 : 49.20	32 : 47.0	$-0.7 \pm 2.2$	$-0.3 \pm 1.0$	$6.1 \pm 0.6$	$12.4 \pm 1.1$
HDFS2 – 753	32 : 47.58	32 : 46.8	$-1.3 \pm 2.3$	$3.3 \pm 1.1$	$14.0 \pm 0.7$	$24.2 \pm 1.2$
HDFS2 – 749	32 : 49.34	32 : 46.5	$4.1 \pm 2.1$	$4.0 \pm 1.0$	$7.0 \pm 0.6$	$10.7 \pm 1.1$
HDFS2 – 773	32 : 54.56	32 : 44.1	$-0.8 \pm 2.0$	$3.7 \pm 1.0$	$8.8 \pm 0.6$	$12.3 \pm 1.1$
HDFS2 – 738	32 : 54.28	32 : 43.9	$-2.0 \pm 2.1$	$-0.3 \pm 1.0$	$3.1 \pm 0.6$	$7.6 \pm 1.1$
HDFS2 – 1051	32 : 50.89	32 : 42.9	$24.5 \pm 2.1$	$108.2 \pm 1.0$	$441.1 \pm 0.6$	$1320.9 \pm 1.1$
HDFS2 – 771	32 : 49.92	32 : 42.9	$-2.9 \pm 2.1$	$4.8 \pm 1.0$	$9.7 \pm 0.6$	$11.8 \pm 1.1$
HDFS2 – 907	32 : 49.24	32 : 42.6	$-4.1 \pm 2.1$	$14.0 \pm 1.0$	$18.5 \pm 0.6$	$18.5 \pm 1.1$
HDFS2 – 1023	32 : 54.56	32 : 41.1	$-3.8 \pm 2.0$	$5.8 \pm 1.0$	$15.6 \pm 0.6$	$16.9 \pm 1.1$
HDFS2 – 860	32 : 51.83	32 : 40.8	$8.6 \pm 2.0$	$10.0 \pm 1.0$	$14.3 \pm 0.6$	$20.1 \pm 1.1$
HDFS2 – 1042	32 : 46.82	32 : 40.4	$5.1 \pm 2.3$	$9.6 \pm 1.0$	$9.3 \pm 0.6$	$9.5 \pm 1.1$
HDFS2 – 1107	32 : 47.44	32 : 40.4	$15.3 \pm 2.2$	$21.5 \pm 1.0$	$21.6 \pm 0.6$	$32.5 \pm 1.1$
HDFS2 – 1041	32 : 48.01	32 : 39.6	$14.5 \pm 2.1$	$17.2 \pm 1.0$	$17.8 \pm 0.6$	$20.1 \pm 1.1$
HDFS2 – 1097	32 : 53.34	32 : 39.2	$30.2 \pm 2.0$	$64.5 \pm 1.0$	$126.8 \pm 0.6$	$294.2 \pm 1.1$

Table A.8: Optical Photometry -- continued

ID	R.A.(22h) J2000	Decl.(-60°) J2000	$U_{300}^a$	$B_{450}^a$	$V_{606}^a$	$I_{814}^a$
HDFS2 – 1100	32 : 53.09	32 : 38.9	$21.3 \pm 2.0$	$31.0 \pm 0.9$	$69.4 \pm 0.6$	$135.6 \pm 1.0$
HDFS2 – 1035	32 : 52.48	32 : 38.0	$8.9 \pm 2.0$	$15.7 \pm 1.0$	$29.6 \pm 0.6$	$42.7 \pm 1.1$
HDFS2 – 1105	32 : 48.34	32 : 38.0	$4.1 \pm 2.1$	$11.2 \pm 1.0$	$33.0 \pm 0.6$	$43.8 \pm 1.1$
HDFS2 – 1064	32 : 50.68	32 : 37.7	$5.0 \pm 2.0$	$3.7 \pm 1.0$	$5.0 \pm 0.6$	$12.2 \pm 1.1$
HDFS2 – 1086	32 : 52.22	32 : 37.1	$2.0 \pm 2.0$	$22.7 \pm 1.0$	$31.0 \pm 0.6$	$35.4 \pm 1.1$
HDFS2 – 1112	32 : 48.62	32 : 37.0	$1.2 \pm 2.0$	$20.2 \pm 1.0$	$25.1 \pm 0.6$	$27.1 \pm 1.1$
HDFS2 – 1104	32 : 53.63	32 : 35.9	$83.4 \pm 2.0$	$215.8 \pm 0.9$	$535.5 \pm 0.6$	$892.9 \pm 1.1$
HDFS2 – 1106	32 : 48.91	32 : 35.4	$0.7 \pm 2.0$	$23.1 \pm 1.0$	$29.2 \pm 0.6$	$32.6 \pm 1.1$
HDFS2 – 1111	32 : 51.18	32 : 33.9	$2.6 \pm 2.0$	$12.0 \pm 0.9$	$37.9 \pm 0.6$	$71.8 \pm 1.1$
HDFS2 – 1102	32 : 46.79	32 : 33.8	$1.3 \pm 2.2$	$-0.1 \pm 1.0$	$3.3 \pm 0.6$	$6.3 \pm 1.1$
HDFS2 – 1098	32 : 48.30	32 : 32.9	$-1.9 \pm 2.0$	$7.7 \pm 1.0$	$16.5 \pm 0.6$	$18.0 \pm 1.1$
HDFS2 – 1092	32 : 52.51	32 : 32.7	$4.0 \pm 2.0$	$15.0 \pm 0.9$	$17.5 \pm 0.6$	$18.4 \pm 1.1$
HDFS2 – 1074	32 : 55.86	32 : 32.5	$-0.9 \pm 2.0$	$23.2 \pm 1.0$	$31.9 \pm 0.6$	$39.6 \pm 1.1$
HDFS2 – 1088	32 : 53.52	32 : 32.0	$17.9 \pm 2.0$	$26.0 \pm 0.9$	$29.6 \pm 0.6$	$47.2 \pm 1.1$
HDFS2 – 1066	32 : 53.05	32 : 31.4	$8.2 \pm 2.0$	$23.4 \pm 0.9$	$29.2 \pm 0.6$	$28.5 \pm 1.1$
HDFS2 – 1078	32 : 54.13	32 : 30.0	$4.1 \pm 2.0$	$14.3 \pm 1.0$	$23.8 \pm 0.6$	$27.3 \pm 1.1$
HDFS2 – 1069	32 : 55.93	32 : 29.7	$-6.7 \pm 2.0$	$2.6 \pm 1.0$	$8.0 \pm 0.6$	$12.1 \pm 1.1$
HDFS2 – 1081	32 : 46.75	32 : 29.4	$19.4 \pm 2.1$	$28.0 \pm 1.0$	$33.2 \pm 0.6$	$58.0 \pm 1.1$
HDFS2 – 1080	32 : 52.01	32 : 29.4	$0.4 \pm 2.0$	$1.5 \pm 0.9$	$2.1 \pm 0.6$	$6.3 \pm 1.0$
HDFS2 – 985	32 : 54.82	32 : 29.0	$31.9 \pm 2.0$	$43.1 \pm 1.0$	$51.1 \pm 0.6$	$90.6 \pm 1.1$
HDFS2 – 1054	32 : 48.44	32 : 28.6	$10.7 \pm 2.0$	$38.7 \pm 1.0$	$50.6 \pm 0.6$	$97.1 \pm 1.1$
HDFS2 – 1065	32 : 48.12	32 : 28.2	$2.4 \pm 2.1$	$3.1 \pm 1.0$	$4.9 \pm 0.6$	$12.8 \pm 1.1$
HDFS2 – 1070	32 : 49.81	32 : 26.7	$3.4 \pm 2.0$	$0.1 \pm 1.0$	$3.3 \pm 0.6$	$13.9 \pm 1.1$
HDFS2 – 1038	32 : 49.16	32 : 25.9	$1.9 \pm 2.0$	$93.3 \pm 1.0$	$144.2 \pm 0.6$	$169.3 \pm 1.1$
HDFS2 – 1030	32 : 49.96	32 : 25.2	$-1.1 \pm 2.0$	$0.4 \pm 1.0$	$5.1 \pm 0.6$	$3.0 \pm 1.1$
HDFS2 – 1045	32 : 49.06	32 : 24.4	$16.1 \pm 2.0$	$31.3 \pm 1.0$	$39.1 \pm 0.6$	$56.2 \pm 1.1$

Table A.8: Optical Photometry – continued

ID	R.A.(22h) J2000	Decl.(-60°) J2000	$U_{300}^a$	$B_{450}^a$	$V_{606}^a$	$I_{814}^a$
HDFS2 – 1043	32 : 54.42	32 : 24.4	$4.8 \pm 2.0$	$7.6 \pm 1.0$	$6.1 \pm 0.6$	$7.1 \pm 1.1$
HDFS2 – 1044	32 : 52.01	32 : 24.1	$-1.1 \pm 2.0$	$10.4 \pm 0.9$	$29.1 \pm 0.6$	$37.9 \pm 1.0$
HDFS2 – 1018	32 : 54.78	32 : 23.7	$8.5 \pm 2.0$	$10.4 \pm 1.0$	$13.8 \pm 0.6$	$31.9 \pm 1.1$
HDFS2 – 1027	32 : 49.31	32 : 23.4	$7.5 \pm 2.0$	$10.7 \pm 0.9$	$9.2 \pm 0.6$	$10.5 \pm 1.1$
HDFS2 – 1033	32 : 52.19	32 : 23.2	$9.8 \pm 2.0$	$10.1 \pm 0.9$	$16.4 \pm 0.6$	$17.9 \pm 1.0$
HDFS2 – 1032	32 : 50.50	32 : 22.6	$-3.7 \pm 2.0$	$1.5 \pm 1.0$	$3.1 \pm 0.6$	$7.6 \pm 1.1$
HDFS2 – 966	32 : 47.15	32 : 21.5	$3.5 \pm 2.1$	$8.5 \pm 1.0$	$12.8 \pm 0.6$	$11.4 \pm 1.1$
HDFS2 – 1029	32 : 49.16	32 : 21.2	$-5.3 \pm 2.0$	$-0.6 \pm 1.0$	$3.6 \pm 0.6$	$2.7 \pm 1.1$
HDFS2 – 935	32 : 56.04	32 : 20.4	$63.5 \pm 2.0$	$93.0 \pm 1.0$	$169.2 \pm 0.6$	$270.5 \pm 1.1$
HDFS2 – 1019	32 : 48.26	32 : 19.8	$0.6 \pm 2.0$	$7.5 \pm 1.0$	$9.8 \pm 0.6$	$8.1 \pm 1.1$
HDFS2 – 1022	32 : 47.80	32 : 19.6	$2.7 \pm 2.0$	$34.6 \pm 1.0$	$49.1 \pm 0.6$	$70.9 \pm 1.1$
HDFS2 – 961	32 : 48.59	32 : 19.1	$-4.2 \pm 2.0$	$1.1 \pm 1.0$	$6.0 \pm 0.6$	$7.3 \pm 1.1$
HDFS2 – 999	32 : 53.77	32 : 18.5	$-3.3 \pm 2.0$	$5.2 \pm 1.0$	$10.1 \pm 0.6$	$11.7 \pm 1.1$
HDFS2 – 1005	32 : 52.08	32 : 18.5	$5.1 \pm 2.0$	$17.2 \pm 0.9$	$25.0 \pm 0.6$	$41.1 \pm 1.1$
HDFS2 – 978	32 : 48.16	32 : 17.7	$1.5 \pm 2.0$	$10.3 \pm 1.0$	$15.9 \pm 0.6$	$32.0 \pm 1.1$
HDFS2 – 983	32 : 46.97	32 : 17.5	$11.2 \pm 2.1$	$19.8 \pm 1.0$	$18.9 \pm 0.6$	$16.7 \pm 1.1$
HDFS2 – 989	32 : 49.81	32 : 17.4	$-5.3 \pm 2.0$	$1.8 \pm 1.0$	$7.0 \pm 0.6$	$6.9 \pm 1.1$
HDFS2 – 1000	32 : 55.54	32 : 17.3	$45.6 \pm 2.1$	$58.4 \pm 1.0$	$107.1 \pm 0.6$	$165.8 \pm 1.1$
HDFS2 – 975	32 : 53.05	32 : 17.0	$24.8 \pm 2.0$	$36.1 \pm 1.0$	$51.2 \pm 0.6$	$105.1 \pm 1.1$
HDFS2 – 1003	32 : 48.44	32 : 16.6	$4.4 \pm 2.0$	$2.8 \pm 1.0$	$9.2 \pm 0.6$	$16.6 \pm 1.1$
HDFS2 – 995	32 : 51.00	32 : 16.5	$5.9 \pm 2.0$	$7.7 \pm 0.9$	$15.6 \pm 0.6$	$22.4 \pm 1.1$
HDFS2 – 974	32 : 48.88	32 : 16.0	$19.0 \pm 2.0$	$45.7 \pm 1.0$	$104.3 \pm 0.6$	$210.5 \pm 1.1$
HDFS2 – 993	32 : 56.00	32 : 15.8	$2.4 \pm 2.0$	$5.8 \pm 1.0$	$7.6 \pm 0.6$	$12.7 \pm 1.1$
HDFS2 – 968	32 : 52.91	32 : 15.7	$6.3 \pm 2.0$	$4.8 \pm 1.0$	$4.9 \pm 0.6$	$11.0 \pm 1.1$
HDFS2 – 929	32 : 52.62	32 : 15.5	$0.3 \pm 2.0$	$10.4 \pm 0.9$	$18.4 \pm 0.6$	$34.7 \pm 1.1$
HDFS2 – 996	32 : 54.42	32 : 15.4	$13.4 \pm 2.0$	$40.6 \pm 1.0$	$48.6 \pm 0.6$	$58.9 \pm 1.1$

Table A.8: Optical Photometry – continued

ID	R.A.(22h) J2000	Decl.(-60°) J2000	$U_{300}^a$	$B_{450}^a$	$V_{606}^a$	$I_{814}^a$
HDFS2 – 969	32 : 54.78	32 : 15.4	$5.9 \pm 2.0$	$45.4 \pm 1.0$	$229.8 \pm 0.6$	$736.9 \pm 1.1$
HDFS2 – 959	32 : 52.01	32 : 14.9	$32.9 \pm 2.0$	$45.8 \pm 0.9$	$69.3 \pm 0.6$	$153.2 \pm 1.1$
HDFS2 – 868	32 : 47.90	32 : 14.5	$2.4 \pm 2.0$	$11.8 \pm 1.0$	$10.7 \pm 0.6$	$16.4 \pm 1.1$
HDFS2 – 925	32 : 55.75	32 : 13.4	$21.0 \pm 1.9$	$27.6 \pm 0.9$	$44.2 \pm 0.6$	$86.7 \pm 1.0$
HDFS2 – 943	32 : 53.88	32 : 13.1	$29.9 \pm 2.0$	$67.7 \pm 0.9$	$84.3 \pm 0.6$	$99.2 \pm 1.1$
HDFS2 – 962	32 : 51.65	32 : 12.6	$29.0 \pm 2.0$	$43.6 \pm 1.0$	$55.4 \pm 0.6$	$93.0 \pm 1.1$
HDFS2 – 908	32 : 49.24	32 : 11.6	$-2.2 \pm 2.0$	$2.6 \pm 1.0$	$1.8 \pm 0.6$	$6.8 \pm 1.1$
HDFS2 – 911	32 : 55.72	32 : 11.4	$7.3 \pm 2.1$	$35.4 \pm 1.0$	$203.5 \pm 0.6$	$778.8 \pm 1.1$
HDFS2 – 944	32 : 46.64	32 : 11.3	$0.0 \pm 3.0$	$6.0 \pm 1.2$	$15.0 \pm 0.8$	$22.9 \pm 1.5$
HDFS2 – 940	32 : 50.68	32 : 10.6	$6.4 \pm 2.0$	$12.0 \pm 1.0$	$20.0 \pm 0.6$	$35.9 \pm 1.1$
HDFS2 – 941	32 : 47.18	32 : 10.6	$-3.9 \pm 2.1$	$0.5 \pm 1.0$	$4.1 \pm 0.6$	$9.5 \pm 1.1$
HDFS2 – 949	32 : 56.26	32 : 9.4	$-19.5 \pm 2.1$	$15.7 \pm 1.0$	$20.9 \pm 0.6$	$32.5 \pm 1.1$
HDFS2 – 918	32 : 52.51	32 : 9.3	$17.5 \pm 2.0$	$16.0 \pm 0.9$	$27.0 \pm 0.6$	$39.5 \pm 1.1$
HDFS2 – 952	32 : 55.14	32 : 9.0	$10.6 \pm 2.0$	$17.1 \pm 1.0$	$19.2 \pm 0.6$	$22.1 \pm 1.1$
HDFS2 – 939	32 : 46.64	32 : 8.9	$0.8 \pm 3.3$	$3.5 \pm 1.3$	$10.7 \pm 0.9$	$19.2 \pm 1.6$
HDFS2 – 927	32 : 51.04	32 : 8.6	$-0.3 \pm 2.0$	$4.7 \pm 1.0$	$6.7 \pm 0.6$	$6.3 \pm 1.1$
HDFS2 – 947	32 : 54.78	32 : 8.2	$1.7 \pm 2.0$	$4.5 \pm 1.0$	$11.2 \pm 0.6$	$18.0 \pm 1.1$
HDFS2 – 923	32 : 50.64	32 : 7.9	$0.1 \pm 2.0$	$12.9 \pm 1.0$	$14.6 \pm 0.6$	$18.3 \pm 1.1$
HDFS2 – 919	32 : 48.23	32 : 7.5	$9.5 \pm 2.0$	$13.3 \pm 1.0$	$13.1 \pm 0.6$	$27.8 \pm 1.1$
HDFS2 – 934	32 : 52.69	32 : 7.3	$96.9 \pm 2.0$	$151.3 \pm 0.9$	$313.0 \pm 0.6$	$491.6 \pm 1.1$
HDFS2 – 910	32 : 47.72	32 : 6.6	$3.4 \pm 2.1$	$7.3 \pm 1.0$	$19.2 \pm 0.6$	$41.4 \pm 1.1$
HDFS2 – 926	32 : 50.10	32 : 6.5	$-0.7 \pm 2.0$	$16.2 \pm 1.0$	$20.2 \pm 0.6$	$27.4 \pm 1.1$
HDFS2 – 824	32 : 53.70	32 : 6.1	$8.0 \pm 2.0$	$19.7 \pm 0.9$	$47.4 \pm 0.6$	$152.8 \pm 1.1$
HDFS2 – 924	32 : 51.86	32 : 5.9	$-0.1 \pm 2.0$	$21.4 \pm 1.0$	$40.6 \pm 0.6$	$51.5 \pm 1.1$
HDFS2 – 921	32 : 49.06	32 : 5.8	$22.4 \pm 2.0$	$78.0 \pm 1.0$	$95.1 \pm 0.6$	$116.2 \pm 1.1$
HDFS2 – 836	32 : 54.17	32 : 5.2	$4.9 \pm 2.0$	$14.7 \pm 1.0$	$13.1 \pm 0.6$	$14.8 \pm 1.1$



Table A.8: Optical Photometry – continued

ID	R.A.(22h) J2000	Decl.(-60°) J2000	$U_{300}^a$	$B_{450}^a$	$V_{606}^a$	$I_{814}^a$
HDFS2 – 906	32 : 48.23	32 : 4.8	$0.7 \pm 2.1$	$5.7 \pm 1.0$	$9.6 \pm 0.6$	$22.3 \pm 1.1$
HDFS2 – 891	32 : 50.17	32 : 4.8	$8.4 \pm 2.0$	$17.4 \pm 1.0$	$24.0 \pm 0.6$	$42.9 \pm 1.1$
HDFS2 – 912	32 : 51.18	32 : 4.3	$1.7 \pm 2.0$	$6.6 \pm 1.0$	$6.9 \pm 0.6$	$9.7 \pm 1.1$
HDFS2 – 897	32 : 52.01	32 : 4.1	$5.9 \pm 2.0$	$13.1 \pm 1.0$	$12.9 \pm 0.6$	$16.1 \pm 1.1$
HDFS2 – 890	32 : 48.84	32 : 3.6	$19.9 \pm 2.0$	$30.3 \pm 1.0$	$43.0 \pm 0.6$	$85.5 \pm 1.1$
HDFS2 – 877	32 : 50.28	32 : 3.3	$57.5 \pm 2.0$	$112.8 \pm 1.0$	$263.6 \pm 0.6$	$451.2 \pm 1.1$
HDFS2 – 937	32 : 51.18	32 : 2.7	$7.6 \pm 2.0$	$12.9 \pm 1.0$	$13.7 \pm 0.6$	$13.4 \pm 1.1$
HDFS2 – 864	32 : 53.48	32 : 2.5	$1.4 \pm 1.5$	$14.5 \pm 0.7$	$24.1 \pm 0.4$	$37.1 \pm 0.8$
HDFS2 – 865	32 : 49.45	32 : 2.1	$-0.7 \pm 2.0$	$22.6 \pm 1.0$	$21.7 \pm 0.6$	$26.5 \pm 1.1$
HDFS2 – 901	32 : 55.39	32 : 1.8	$2.2 \pm 2.1$	$3.0 \pm 1.0$	$5.9 \pm 0.6$	$14.0 \pm 1.1$
HDFS2 – 885	32 : 54.31	32 : 1.5	$0.2 \pm 2.0$	$8.6 \pm 1.0$	$13.0 \pm 0.6$	$17.6 \pm 1.1$
HDFS2 – 863	32 : 53.38	32 : 1.2	$3.0 \pm 2.0$	$3.6 \pm 1.0$	$16.1 \pm 0.6$	$69.0 \pm 1.1$
HDFS2 – 843	32 : 50.35	32 : 1.1	$6.4 \pm 2.0$	$26.6 \pm 1.0$	$35.8 \pm 0.6$	$72.6 \pm 1.1$
HDFS2 – 883	32 : 54.46	32 : 0.6	$-1.1 \pm 2.0$	$3.0 \pm 1.0$	$7.3 \pm 0.6$	$17.8 \pm 1.1$
HDFS2 – 886	32 : 51.25	32 : 0.5	$7.8 \pm 2.0$	$6.8 \pm 1.0$	$13.9 \pm 0.6$	$22.1 \pm 1.1$
HDFS2 – 845	32 : 50.78	31 : 59.7	$27.7 \pm 2.0$	$37.4 \pm 1.0$	$64.4 \pm 0.6$	$87.7 \pm 1.1$
HDFS2 – 879	32 : 50.64	31 : 59.4	$8.5 \pm 2.0$	$10.4 \pm 1.0$	$18.9 \pm 0.6$	$28.2 \pm 1.1$
HDFS2 – 842	32 : 53.59	31 : 59.1	$2.2 \pm 2.0$	$4.1 \pm 1.0$	$15.9 \pm 0.6$	$20.2 \pm 1.1$
HDFS2 – 830	32 : 51.11	31 : 58.6	$4.2 \pm 2.0$	$8.1 \pm 1.0$	$8.3 \pm 0.6$	$18.6 \pm 1.1$
HDFS2 – 823	32 : 52.94	31 : 58.4	$14.5 \pm 2.0$	$20.8 \pm 1.0$	$28.7 \pm 0.6$	$47.0 \pm 1.1$
HDFS2 – 904	32 : 54.06	31 : 58.1	$27.8 \pm 2.0$	$48.9 \pm 1.0$	$54.8 \pm 0.6$	$78.7 \pm 1.1$
HDFS2 – 873	32 : 49.45	31 : 57.9	$-0.3 \pm 2.0$	$2.1 \pm 1.0$	$4.7 \pm 0.6$	$17.0 \pm 1.1$
HDFS2 – 851	32 : 51.97	31 : 56.8	$0.4 \pm 2.1$	$9.0 \pm 1.0$	$10.8 \pm 0.6$	$12.3 \pm 1.1$
HDFS2 – 828	32 : 47.65	31 : 56.7	$1.9 \pm 2.2$	$13.1 \pm 1.0$	$18.2 \pm 0.6$	$23.6 \pm 1.1$
HDFS2 – 867	32 : 55.07	31 : 56.7	$3.9 \pm 2.1$	$7.0 \pm 1.0$	$7.0 \pm 0.6$	$6.9 \pm 1.1$
HDFS2 – 813	32 : 56.18	31 : 56.5	$0.1 \pm 2.1$	$0.1 \pm 1.0$	$8.5 \pm 0.6$	$63.2 \pm 1.1$

Table A.8: Optical Photometry – continued

ID	R.A.(22h) J2000	Decl.(-60°) J2000	$U_{300}^a$	$B_{450}^a$	$V_{606}^a$	$I_{814}^a$
HDFS2 – 855	32 : 52.80	31 : 56.5	$0.4 \pm 2.0$	$3.9 \pm 1.0$	$10.6 \pm 0.6$	$9.6 \pm 1.1$
HDFS2 – 844	32 : 50.39	31 : 55.7	$1.9 \pm 2.1$	$6.6 \pm 1.0$	$12.7 \pm 0.6$	$14.1 \pm 1.1$
HDFS2 – 847	32 : 50.78	31 : 55.3	$0.7 \pm 2.1$	$4.1 \pm 1.0$	$5.7 \pm 0.6$	$6.5 \pm 1.1$
HDFS2 – 852	32 : 53.12	31 : 54.8	$6.8 \pm 2.1$	$19.6 \pm 1.0$	$20.9 \pm 0.6$	$22.4 \pm 1.1$
HDFS2 – 791	32 : 51.25	31 : 54.4	$10.6 \pm 2.0$	$25.6 \pm 1.0$	$32.7 \pm 0.6$	$52.9 \pm 1.1$
HDFS2 – 806	32 : 53.38	31 : 54.4	$1.7 \pm 2.1$	$0.4 \pm 1.0$	$2.8 \pm 0.6$	$5.6 \pm 1.1$
HDFS2 – 821	32 : 53.84	31 : 54.0	$-3.1 \pm 2.1$	$11.6 \pm 1.0$	$16.6 \pm 0.6$	$20.5 \pm 1.1$
HDFS2 – 803	32 : 52.04	31 : 53.9	$5.2 \pm 2.1$	$11.1 \pm 1.0$	$19.0 \pm 0.6$	$38.6 \pm 1.1$
HDFS2 – 812	32 : 48.84	31 : 53.8	$-0.7 \pm 2.1$	$31.7 \pm 1.0$	$68.1 \pm 0.6$	$83.7 \pm 1.1$
HDFS2 – 810	32 : 52.69	31 : 53.2	$17.3 \pm 2.0$	$33.6 \pm 1.0$	$41.3 \pm 0.6$	$85.5 \pm 1.1$
HDFS2 – 802	32 : 52.22	31 : 52.7	$14.4 \pm 2.1$	$56.9 \pm 1.0$	$74.9 \pm 0.6$	$128.7 \pm 1.1$
HDFS2 – 800	32 : 56.08	31 : 52.2	$7.0 \pm 2.3$	$6.2 \pm 1.1$	$15.2 \pm 0.7$	$23.9 \pm 1.2$
HDFS2 – 794	32 : 51.83	31 : 51.8	$4.0 \pm 2.1$	$16.3 \pm 1.0$	$14.9 \pm 0.6$	$16.5 \pm 1.1$
HDFS2 – 819	32 : 56.58	31 : 51.3	$7.8 \pm 2.5$	$27.3 \pm 1.3$	$28.6 \pm 0.7$	$36.8 \pm 1.4$
HDFS2 – 769	32 : 49.70	31 : 50.1	$4.9 \pm 2.2$	$4.1 \pm 1.1$	$7.3 \pm 0.6$	$13.4 \pm 1.1$
HDFS2 – 817	32 : 48.84	31 : 49.7	$6.6 \pm 2.1$	$11.2 \pm 1.0$	$26.4 \pm 0.6$	$33.8 \pm 1.1$
HDFS2 – 808	32 : 54.46	31 : 49.1	$3.9 \pm 2.4$	$11.0 \pm 1.1$	$20.9 \pm 0.7$	$38.8 \pm 1.4$
HDFS2 – 788	32 : 51.47	31 : 49.0	$-1.9 \pm 2.2$	$6.2 \pm 1.1$	$6.9 \pm 0.6$	$9.8 \pm 1.2$
HDFS2 – 792	32 : 56.08	31 : 48.9	$94.9 \pm 2.6$	$171.3 \pm 1.2$	$377.7 \pm 0.7$	$673.1 \pm 1.6$
HDFS2 – 796	32 : 48.84	31 : 48.6	$6.2 \pm 2.2$	$3.5 \pm 1.0$	$7.9 \pm 0.6$	$8.6 \pm 1.1$
HDFS2 – 801	32 : 52.55	31 : 47.3	$16.0 \pm 2.4$	$35.8 \pm 1.2$	$41.9 \pm 0.7$	$53.3 \pm 1.4$
HDFS2 – 764	32 : 49.42	31 : 46.6	$0.7 \pm 2.3$	$4.2 \pm 1.1$	$7.8 \pm 0.7$	$16.4 \pm 1.3$
HDFS2 – 740	32 : 53.34	31 : 46.5	$2.6 \pm 2.6$	$6.8 \pm 1.2$	$20.4 \pm 0.7$	$33.6 \pm 1.6$
HDFS2 – 781	32 : 56.33	31 : 46.4	$-4.7 \pm 3.0$	$2.0 \pm 1.5$	$1.8 \pm 0.9$	$2.2 \pm 2.0$
HDFS2 – 809	32 : 50.86	31 : 45.9	$15.0 \pm 2.5$	$29.8 \pm 1.2$	$30.1 \pm 0.7$	$43.3 \pm 1.5$
HDFS2 – 790	32 : 50.21	31 : 45.8	$40.7 \pm 2.6$	$60.4 \pm 1.2$	$79.2 \pm 0.7$	$147.7 \pm 1.5$

Table A.8: Optical Photometry – continued

ID	R.A.(22h) J2000	Decl.(-60°) J2000	$U_{300}$ <sup>a</sup>	$B_{450}$ <sup>a</sup>	$V_{606}$ <sup>a</sup>	$I_{814}$ <sup>a</sup>
HDFS2 – 786	32 : 49.24	31 : 44.9	$1.0 \pm 2.5$	$17.7 \pm 1.2$	$40.2 \pm 0.7$	$50.3 \pm 1.5$
HDFS2 – 776	32 : 48.95	31 : 42.0	$5.5 \pm 2.7$	$4.8 \pm 1.3$	$11.9 \pm 0.8$	$15.0 \pm 1.7$

<sup>a</sup> Flux measured with a 2''0 diameter aperture.

Note – All fluxes in units of  $10^{-31}$  ergs s<sup>-1</sup> Hz<sup>-1</sup> cm<sup>-2</sup>.

Note, – Units of right ascension are minutes and seconds, and units of declination are arcminutes and arcseconds

Table A.9: NIR Photometry --  $K_{s,AB}^{\text{tot}} < 26$  Sample

ID	$J_s^a$	$H^a$	$K_s^a$	$K_s^{\text{tot } b}$
HDFS2 – 61	$63.2 \pm 4.3$	$64.8 \pm 7.1$	$93.6 \pm 6.7$	$101.4 \pm 9.4$
HDFS2 – 75	$46.3 \pm 4.2$	$41.4 \pm 6.9$	$50.9 \pm 6.5$	$50.3 \pm 8.9$
HDFS2 – 97	$47.7 \pm 4.4$	$42.4 \pm 7.3$	$31.6 \pm 6.9$	$27.2 \pm 6.8$
HDFS2 – 110	$6.5 \pm 4.2$	$20.9 \pm 6.9$	$14.6 \pm 6.5$	$17.7 \pm 3.4$
HDFS2 – 107	$1.0 \pm 3.8$	$11.9 \pm 6.3$	$15.7 \pm 5.9$	$15.2 \pm 5.1$
HDFS2 – 66	$386.5 \pm 4.1$	$661.7 \pm 6.7$	$1087.7 \pm 6.4$	$1255.6 \pm 12.6$
HDFS2 – 103	$38.5 \pm 4.5$	$47.6 \pm 7.4$	$46.2 \pm 7.0$	$51.9 \pm 10.3$
HDFS2 – 116	$-0.5 \pm 3.9$	$-1.9 \pm 6.3$	$11.1 \pm 6.0$	$18.1 \pm 5.0$
HDFS2 – 123	$7.8 \pm 4.0$	$5.8 \pm 6.6$	$10.9 \pm 6.2$	$16.4 \pm 4.3$
HDFS2 – 128	$23.9 \pm 3.6$	$14.3 \pm 5.9$	$22.5 \pm 5.6$	$16.9 \pm 3.5$
HDFS2 – 93	$442.4 \pm 3.7$	$645.8 \pm 6.0$	$792.1 \pm 5.7$	$1004.1 \pm 12.7$
HDFS2 – 126	$26.3 \pm 4.6$	$17.4 \pm 7.6$	$20.0 \pm 7.2$	$25.2 \pm 5.0$
HDFS2 – 125	$17.0 \pm 3.5$	$20.5 \pm 5.7$	$29.3 \pm 5.5$	$27.1 \pm 4.9$
HDFS2 – 134	$0.5 \pm 4.4$	$5.3 \pm 7.2$	$10.3 \pm 6.8$	$17.7 \pm 5.8$
HDFS2 – 133	$18.7 \pm 3.9$	$23.8 \pm 6.4$	$15.6 \pm 6.0$	$17.6 \pm 4.5$
HDFS2 – 124	$35.7 \pm 3.7$	$31.8 \pm 6.0$	$42.3 \pm 5.7$	$46.1 \pm 6.3$
HDFS2 – 119	$44.6 \pm 4.0$	$51.3 \pm 6.5$	$80.2 \pm 6.3$	$90.0 \pm 8.7$
HDFS2 – 127	$16.2 \pm 3.8$	$53.2 \pm 6.2$	$63.0 \pm 6.0$	$75.6 \pm 7.2$
HDFS2 – 120	$120.5 \pm 4.4$	$129.9 \pm 7.2$	$158.4 \pm 6.8$	$167.0 \pm 9.6$
HDFS2 – 149	$27.1 \pm 4.2$	$22.5 \pm 6.9$	$33.4 \pm 6.7$	$31.7 \pm 5.4$
HDFS2 – 130	$82.2 \pm 3.5$	$100.4 \pm 5.7$	$128.8 \pm 5.4$	$146.7 \pm 8.4$
HDFS2 – 155	$21.0 \pm 3.4$	$25.7 \pm 5.6$	$13.0 \pm 5.3$	$15.8 \pm 3.0$
HDFS2 – 144	$56.3 \pm 3.4$	$70.2 \pm 5.6$	$55.0 \pm 5.4$	$58.3 \pm 7.2$
HDFS2 – 105	$620.5 \pm 3.7$	$824.7 \pm 6.0$	$933.0 \pm 5.7$	$1123.2 \pm 12.0$
HDFS2 – 153	$15.3 \pm 3.8$	$14.9 \pm 6.2$	$13.5 \pm 5.9$	$18.5 \pm 4.6$
HDFS2 – 146	$17.2 \pm 3.9$	$42.6 \pm 6.4$	$36.7 \pm 6.0$	$39.4 \pm 6.5$

Table A.9: NIR Photometry – continued

ID	$J_s^a$	$H^a$	$K_s^a$	$K_s^{\text{tot } b}$
HDFS2 – 162	$1.2 \pm 5.1$	$6.6 \pm 8.2$	$24.9 \pm 8.0$	$22.2 \pm 7.9$
HDFS2 – 49	$1118.3 \pm 3.3$	$1796.7 \pm 5.4$	$2689.3 \pm 5.2$	$3736.9 \pm 12.6$
HDFS2 – 112	$624.5 \pm 4.2$	$956.1 \pm 6.9$	$1412.3 \pm 6.5$	$1686.8 \pm 13.6$
HDFS2 – 98	$9.3 \pm 5.6$	$77.9 \pm 9.3$	$206.1 \pm 9.0$	$245.6 \pm 14.3$
HDFS2 – 161	$14.7 \pm 3.7$	$10.6 \pm 6.0$	$22.1 \pm 5.7$	$23.2 \pm 5.7$
HDFS2 – 156	$25.5 \pm 3.8$	$33.3 \pm 6.2$	$30.8 \pm 5.9$	$37.3 \pm 8.0$
HDFS2 – 136	$134.7 \pm 4.5$	$159.7 \pm 7.4$	$234.1 \pm 7.0$	$303.0 \pm 13.6$
HDFS2 – 159	$29.7 \pm 3.3$	$23.0 \pm 5.4$	$42.5 \pm 5.2$	$31.7 \pm 3.5$
HDFS2 – 167	$14.0 \pm 3.9$	$18.0 \pm 6.3$	$24.1 \pm 6.0$	$21.5 \pm 4.0$
HDFS2 – 175	$5.5 \pm 3.2$	$15.1 \pm 5.3$	$9.1 \pm 5.1$	$16.3 \pm 3.2$
HDFS2 – 166	$28.5 \pm 3.5$	$51.7 \pm 5.6$	$41.6 \pm 5.4$	$46.3 \pm 7.5$
HDFS2 – 154	$80.8 \pm 4.0$	$84.9 \pm 6.5$	$67.4 \pm 6.2$	$76.5 \pm 10.1$
HDFS2 – 165	$20.5 \pm 4.3$	$10.4 \pm 6.9$	$39.1 \pm 6.5$	$45.1 \pm 7.4$
HDFS2 – 163	$8.1 \pm 4.1$	$48.7 \pm 6.7$	$45.6 \pm 6.3$	$43.7 \pm 7.8$
HDFS2 – 168	$34.6 \pm 3.2$	$40.7 \pm 5.3$	$24.5 \pm 5.1$	$49.0 \pm 5.0$
HDFS2 – 148	$174.0 \pm 3.2$	$202.4 \pm 5.3$	$219.5 \pm 5.1$	$281.4 \pm 6.6$
HDFS2 – 171	$65.8 \pm 3.3$	$54.7 \pm 5.3$	$55.3 \pm 5.1$	$63.8 \pm 6.6$
HDFS2 – 152	$298.5 \pm 3.4$	$356.1 \pm 5.6$	$433.4 \pm 5.3$	$474.2 \pm 10.1$
HDFS2 – 174	$65.0 \pm 3.4$	$116.9 \pm 5.6$	$120.4 \pm 5.3$	$141.8 \pm 8.9$
HDFS2 – 170	$125.4 \pm 4.2$	$128.4 \pm 6.9$	$172.1 \pm 6.7$	$177.9 \pm 11.9$
HDFS2 – 114	$1438.8 \pm 3.8$	$1998.9 \pm 6.2$	$2475.8 \pm 5.9$	$3526.2 \pm 18.2$
HDFS2 – 188	$19.4 \pm 3.4$	$14.7 \pm 5.5$	$8.6 \pm 5.3$	$17.8 \pm 2.4$
HDFS2 – 177	$116.8 \pm 5.0$	$142.0 \pm 8.1$	$153.2 \pm 7.9$	$191.1 \pm 14.8$
HDFS2 – 158	$174.6 \pm 3.5$	$196.7 \pm 5.7$	$243.3 \pm 5.4$	$312.3 \pm 13.9$
HDFS2 – 184	$37.6 \pm 3.8$	$55.0 \pm 6.1$	$43.7 \pm 5.8$	$45.7 \pm 6.5$
HDFS2 – 147	$195.0 \pm 3.3$	$212.1 \pm 5.4$	$211.9 \pm 5.2$	$399.2 \pm 15.2$
HDFS2 – 180	$136.5 \pm 3.8$	$142.4 \pm 6.2$	$159.1 \pm 5.9$	$158.7 \pm 8.8$

Table A.9: NIR Photometry – continued

ID	$J_s^a$	$H^a$	$K_s^a$	$K_s^{\text{tot } b}$
HDFS2 – 196	$12.8 \pm 3.5$	$18.8 \pm 5.7$	$17.3 \pm 5.4$	$16.8 \pm 4.9$
HDFS2 – 191	$68.1 \pm 4.0$	$70.0 \pm 6.5$	$89.2 \pm 6.3$	$126.5 \pm 11.6$
HDFS2 – 194	$15.2 \pm 3.2$	$9.6 \pm 5.3$	$17.7 \pm 5.1$	$25.7 \pm 5.9$
HDFS2 – 189	$73.8 \pm 3.3$	$88.9 \pm 5.3$	$83.2 \pm 5.1$	$86.3 \pm 7.3$
HDFS2 – 204	$24.1 \pm 4.7$	$40.0 \pm 7.6$	$31.7 \pm 7.4$	$29.7 \pm 6.9$
HDFS2 – 160	$402.9 \pm 3.5$	$574.0 \pm 5.6$	$818.3 \pm 5.4$	$997.5 \pm 12.3$
HDFS2 – 208	$5.4 \pm 3.2$	$-4.1 \pm 5.3$	$22.4 \pm 5.1$	$30.5 \pm 6.8$
HDFS2 – 185	$59.5 \pm 3.6$	$78.9 \pm 5.9$	$80.9 \pm 5.6$	$99.6 \pm 9.6$
HDFS2 – 210	$22.9 \pm 3.3$	$22.4 \pm 5.4$	$19.1 \pm 5.2$	$19.4 \pm 4.1$
HDFS2 – 192	$55.4 \pm 3.3$	$56.8 \pm 5.3$	$55.4 \pm 5.1$	$64.4 \pm 7.0$
HDFS2 – 183	$249.6 \pm 3.2$	$361.3 \pm 5.3$	$395.3 \pm 5.1$	$498.4 \pm 10.5$
HDFS2 – 209	$33.9 \pm 3.2$	$49.8 \pm 5.3$	$57.9 \pm 5.1$	$73.8 \pm 7.7$
HDFS2 – 207	$22.3 \pm 3.2$	$33.8 \pm 5.3$	$40.6 \pm 5.1$	$44.1 \pm 5.7$
HDFS2 – 199	$18.1 \pm 3.7$	$35.2 \pm 6.0$	$44.5 \pm 5.7$	$44.4 \pm 8.2$
HDFS2 – 195	$11.5 \pm 3.5$	$22.9 \pm 5.7$	$47.3 \pm 5.4$	$60.6 \pm 5.5$
HDFS2 – 215	$10.0 \pm 3.5$	$9.6 \pm 5.7$	$11.1 \pm 5.4$	$23.8 \pm 4.1$
HDFS2 – 201	$59.1 \pm 3.4$	$47.1 \pm 5.6$	$45.9 \pm 5.4$	$53.8 \pm 4.4$
HDFS2 – 140	$442.2 \pm 3.3$	$619.2 \pm 5.4$	$816.8 \pm 5.2$	$1213.5 \pm 11.0$
HDFS2 – 211	$19.7 \pm 3.4$	$9.5 \pm 5.6$	$43.5 \pm 5.3$	$34.9 \pm 3.8$
HDFS2 – 206	$24.9 \pm 3.5$	$27.5 \pm 5.7$	$32.2 \pm 5.4$	$47.5 \pm 4.7$
HDFS2 – 226	$2.8 \pm 3.3$	$1.6 \pm 5.3$	$13.8 \pm 5.1$	$17.3 \pm 4.8$
HDFS2 – 203	$33.7 \pm 3.5$	$77.8 \pm 5.7$	$78.9 \pm 5.4$	$108.1 \pm 9.2$
HDFS2 – 214	$37.8 \pm 3.2$	$35.8 \pm 5.3$	$40.7 \pm 5.1$	$53.0 \pm 3.2$
HDFS2 – 198	$110.1 \pm 3.2$	$100.4 \pm 5.3$	$95.8 \pm 5.1$	$121.9 \pm 5.7$
HDFS2 – 222	$60.2 \pm 3.2$	$69.0 \pm 5.3$	$75.1 \pm 5.1$	$78.5 \pm 6.9$
HDFS2 – 221	$40.2 \pm 3.3$	$51.4 \pm 5.4$	$72.4 \pm 5.2$	$76.4 \pm 6.9$
HDFS2 – 172	$822.5 \pm 3.2$	$1125.9 \pm 5.3$	$1417.6 \pm 5.1$	$1761.5 \pm 8.8$

Table A.9: NIR Photometry – continued

ID	$J_s^a$	$H^a$	$K_s^a$	$K_s^{\text{tot } b}$
HDFS2 – 225	$62.9 \pm 3.2$	$72.0 \pm 5.3$	$75.5 \pm 5.1$	$82.6 \pm 7.0$
HDFS2 – 227	$32.0 \pm 3.5$	$37.6 \pm 5.7$	$37.8 \pm 5.4$	$39.6 \pm 5.5$
HDFS2 – 224	$29.9 \pm 3.2$	$37.0 \pm 5.3$	$39.4 \pm 5.1$	$38.8 \pm 7.2$
HDFS2 – 217	$73.0 \pm 3.2$	$120.8 \pm 5.3$	$131.7 \pm 5.1$	$163.5 \pm 8.6$
HDFS2 – 232	$28.8 \pm 3.3$	$37.0 \pm 5.3$	$49.7 \pm 5.1$	$53.8 \pm 6.2$
HDFS2 – 239	$6.3 \pm 3.7$	$23.2 \pm 6.1$	$36.5 \pm 5.9$	$38.8 \pm 7.3$
HDFS2 – 243	$14.7 \pm 3.2$	$9.6 \pm 5.3$	$18.1 \pm 5.1$	$18.4 \pm 5.4$
HDFS2 – 247	$3.3 \pm 3.2$	$26.6 \pm 5.3$	$15.6 \pm 5.1$	$16.3 \pm 3.1$
HDFS2 – 242	$20.7 \pm 3.2$	$27.0 \pm 5.3$	$23.0 \pm 5.1$	$22.5 \pm 4.8$
HDFS2 – 238	$26.9 \pm 3.2$	$37.5 \pm 5.3$	$34.3 \pm 5.1$	$34.8 \pm 5.4$
HDFS2 – 246	$24.2 \pm 3.2$	$18.6 \pm 5.3$	$27.7 \pm 5.1$	$35.3 \pm 7.1$
HDFS2 – 250	$7.6 \pm 3.2$	$18.2 \pm 5.3$	$12.6 \pm 5.1$	$17.5 \pm 3.2$
HDFS2 – 150	$776.4 \pm 3.2$	$1090.9 \pm 5.3$	$1401.6 \pm 5.1$	$2068.3 \pm 10.1$
HDFS2 – 234	$49.3 \pm 3.2$	$65.9 \pm 5.3$	$76.5 \pm 5.1$	$97.4 \pm 7.9$
HDFS2 – 241	$24.0 \pm 3.4$	$39.1 \pm 5.6$	$44.5 \pm 5.4$	$54.3 \pm 6.5$
HDFS2 – 236	$72.2 \pm 3.2$	$148.7 \pm 5.3$	$196.9 \pm 5.1$	$217.8 \pm 7.9$
HDFS2 – 252	$14.1 \pm 3.2$	$60.8 \pm 5.3$	$83.0 \pm 5.1$	$103.9 \pm 5.3$
HDFS2 – 231	$121.8 \pm 3.2$	$157.7 \pm 5.3$	$182.0 \pm 5.1$	$229.5 \pm 6.3$
HDFS2 – 245	$65.5 \pm 3.2$	$69.3 \pm 5.3$	$95.0 \pm 5.1$	$105.7 \pm 8.5$
HDFS2 – 263	$23.9 \pm 3.2$	$45.3 \pm 5.2$	$52.0 \pm 5.0$	$55.6 \pm 3.1$
HDFS2 – 230	$147.4 \pm 3.2$	$217.9 \pm 5.3$	$362.7 \pm 5.1$	$451.6 \pm 10.5$
HDFS2 – 244	$154.2 \pm 3.2$	$169.3 \pm 5.3$	$216.0 \pm 5.1$	$249.7 \pm 10.0$
HDFS2 – 254	$14.5 \pm 3.2$	$91.5 \pm 5.3$	$143.5 \pm 5.1$	$153.2 \pm 7.9$
HDFS2 – 233	$93.1 \pm 3.2$	$166.8 \pm 5.3$	$152.7 \pm 5.1$	$237.7 \pm 7.2$
HDFS2 – 271	$28.5 \pm 3.2$	$15.0 \pm 5.3$	$21.0 \pm 5.1$	$15.0 \pm 5.4$
HDFS2 – 267	$83.2 \pm 3.5$	$113.6 \pm 5.8$	$136.9 \pm 5.6$	$181.9 \pm 10.8$
HDFS2 – 255	$98.7 \pm 3.2$	$109.7 \pm 5.3$	$120.2 \pm 5.1$	$152.6 \pm 5.9$

Table A.9: NIR Photometry – continued

ID	$J_s^a$	$H^a$	$K_s^a$	$K_s^{\text{tot } b}$
HDFS2 – 264	$60.4 \pm 3.2$	$88.6 \pm 5.3$	$96.7 \pm 5.1$	$125.5 \pm 7.8$
HDFS2 – 276	$46.7 \pm 3.0$	$64.7 \pm 4.8$	$49.6 \pm 4.6$	$36.7 \pm 2.2$
HDFS2 – 273	$35.6 \pm 3.2$	$34.6 \pm 5.3$	$25.4 \pm 5.1$	$25.7 \pm 5.4$
HDFS2 – 240	$225.1 \pm 3.2$	$281.8 \pm 5.3$	$324.7 \pm 5.1$	$401.8 \pm 10.3$
HDFS2 – 219	$2129.8 \pm 3.2$	$2947.4 \pm 5.3$	$3722.8 \pm 5.1$	$4486.7 \pm 11.7$
HDFS2 – 294	$5.6 \pm 3.2$	$1.6 \pm 5.3$	$2.8 \pm 5.1$	$15.4 \pm 3.6$
HDFS2 – 279	$31.1 \pm 3.2$	$20.9 \pm 5.3$	$44.2 \pm 5.1$	$51.6 \pm 7.3$
HDFS2 – 283	$14.6 \pm 3.2$	$20.7 \pm 5.3$	$21.6 \pm 5.1$	$23.0 \pm 4.3$
HDFS2 – 295	$19.8 \pm 3.2$	$16.8 \pm 5.3$	$10.8 \pm 5.1$	$15.0 \pm 4.0$
HDFS2 – 299	$-0.4 \pm 3.2$	$16.4 \pm 5.3$	$14.7 \pm 5.1$	$16.2 \pm 3.9$
HDFS2 – 260	$52.9 \pm 3.2$	$133.0 \pm 5.3$	$193.3 \pm 5.1$	$277.1 \pm 11.3$
HDFS2 – 291	$12.5 \pm 3.2$	$4.0 \pm 5.3$	$22.9 \pm 5.1$	$21.6 \pm 4.5$
HDFS2 – 280	$26.1 \pm 3.2$	$60.1 \pm 5.3$	$74.5 \pm 5.1$	$91.3 \pm 5.1$
HDFS2 – 287	$47.4 \pm 3.2$	$50.0 \pm 5.3$	$61.4 \pm 5.1$	$66.3 \pm 7.3$
HDFS2 – 302	$20.2 \pm 3.2$	$30.6 \pm 5.3$	$21.2 \pm 5.1$	$23.6 \pm 5.4$
HDFS2 – 307	$-10.0 \pm 3.4$	$-0.8 \pm 5.7$	$14.5 \pm 5.5$	$15.6 \pm 5.0$
HDFS2 – 290	$56.4 \pm 3.2$	$100.8 \pm 5.3$	$85.2 \pm 5.1$	$105.9 \pm 5.1$
HDFS2 – 304	$50.7 \pm 3.2$	$43.2 \pm 5.3$	$31.1 \pm 5.1$	$30.1 \pm 6.4$
HDFS2 – 309	$22.6 \pm 3.2$	$20.4 \pm 5.3$	$13.8 \pm 5.1$	$16.3 \pm 4.5$
HDFS2 – 305	$20.1 \pm 3.2$	$12.4 \pm 5.3$	$25.4 \pm 5.1$	$25.7 \pm 5.2$
HDFS2 – 319	$1.1 \pm 3.2$	$10.1 \pm 5.3$	$11.6 \pm 5.1$	$15.2 \pm 4.5$
HDFS2 – 306	$15.8 \pm 3.2$	$28.2 \pm 5.3$	$21.1 \pm 5.1$	$24.4 \pm 4.9$
HDFS2 – 293	$140.8 \pm 3.2$	$147.5 \pm 5.3$	$184.3 \pm 5.1$	$262.2 \pm 11.6$
HDFS2 – 315	$38.5 \pm 3.3$	$52.0 \pm 5.3$	$41.6 \pm 5.1$	$46.0 \pm 5.6$
HDFS2 – 303	$184.8 \pm 3.5$	$206.9 \pm 5.7$	$201.2 \pm 5.4$	$231.5 \pm 9.9$
HDFS2 – 314	$28.0 \pm 3.2$	$51.8 \pm 5.3$	$47.6 \pm 5.1$	$48.4 \pm 7.1$
HDFS2 – 323	$14.0 \pm 3.2$	$34.7 \pm 5.3$	$35.4 \pm 5.1$	$33.8 \pm 5.2$



Table A.9: NIR Photometry – continued

ID	$J_s^a$	H <sup>a</sup>	$K_s^a$	$K_s^{\text{tot } b}$
HDFS2 – 316	$60.9 \pm 3.2$	$81.6 \pm 5.3$	$92.7 \pm 5.1$	$103.7 \pm 5.0$
HDFS2 – 292	$441.9 \pm 3.2$	$554.6 \pm 5.3$	$599.8 \pm 5.1$	$786.0 \pm 13.1$
HDFS2 – 301	$253.1 \pm 3.2$	$490.0 \pm 5.3$	$733.0 \pm 5.1$	$948.9 \pm 11.8$
HDFS2 – 337	$15.8 \pm 3.2$	$14.2 \pm 5.3$	$17.9 \pm 5.1$	$40.1 \pm 4.7$
HDFS2 – 333	$38.6 \pm 3.2$	$30.6 \pm 5.3$	$35.2 \pm 5.1$	$33.8 \pm 6.0$
HDFS2 – 317	$159.1 \pm 4.7$	$267.2 \pm 7.6$	$402.9 \pm 7.4$	$437.3 \pm 11.8$
HDFS2 – 313	$36.5 \pm 5.8$	$75.0 \pm 9.5$	$297.2 \pm 9.3$	$361.1 \pm 8.8$
HDFS2 – 336	$26.1 \pm 3.2$	$26.2 \pm 5.3$	$20.2 \pm 5.1$	$24.6 \pm 5.2$
HDFS2 – 335	$11.9 \pm 3.2$	$36.9 \pm 5.3$	$53.7 \pm 5.1$	$57.1 \pm 7.0$
HDFS2 – 312	$184.1 \pm 3.2$	$199.8 \pm 5.3$	$254.7 \pm 5.1$	$304.3 \pm 9.9$
HDFS2 – 342	$13.8 \pm 3.2$	$10.4 \pm 5.3$	$21.5 \pm 5.1$	$23.0 \pm 4.1$
HDFS2 – 348	$18.0 \pm 4.7$	$35.6 \pm 7.6$	$33.4 \pm 7.4$	$25.7 \pm 4.0$
HDFS2 – 331	$75.5 \pm 3.3$	$107.3 \pm 5.4$	$154.2 \pm 5.2$	$155.8 \pm 8.7$
HDFS2 – 326	$142.3 \pm 3.2$	$173.5 \pm 5.3$	$185.4 \pm 5.1$	$192.2 \pm 9.0$
HDFS2 – 345	$7.2 \pm 3.2$	$19.8 \pm 5.3$	$12.8 \pm 5.1$	$16.2 \pm 3.8$
HDFS2 – 328	$120.0 \pm 3.2$	$127.1 \pm 5.3$	$148.1 \pm 5.1$	$164.3 \pm 9.6$
HDFS2 – 344	$38.6 \pm 3.1$	$63.4 \pm 5.1$	$65.8 \pm 4.9$	$58.3 \pm 3.4$
HDFS2 – 332	$47.9 \pm 3.2$	$69.2 \pm 5.3$	$102.8 \pm 5.1$	$125.6 \pm 8.1$
HDFS2 – 358	$13.9 \pm 3.3$	$11.1 \pm 5.3$	$15.2 \pm 5.1$	$18.4 \pm 3.8$
HDFS2 – 339	$96.7 \pm 3.2$	$135.9 \pm 5.3$	$137.2 \pm 5.1$	$155.2 \pm 8.3$
HDFS2 – 352	$17.4 \pm 3.2$	$6.1 \pm 5.3$	$28.6 \pm 5.1$	$30.8 \pm 5.2$
HDFS2 – 349	$55.9 \pm 3.2$	$70.1 \pm 5.3$	$36.8 \pm 5.1$	$38.3 \pm 5.6$
HDFS2 – 354	$50.7 \pm 3.2$	$44.3 \pm 5.3$	$46.0 \pm 5.1$	$53.2 \pm 6.1$
HDFS2 – 353	$7.5 \pm 3.3$	$8.1 \pm 5.3$	$35.4 \pm 5.1$	$51.3 \pm 8.4$
HDFS2 – 363	$26.0 \pm 3.2$	$24.6 \pm 5.3$	$27.1 \pm 5.1$	$28.0 \pm 4.6$
HDFS2 – 278	$4186.3 \pm 3.3$	$5609.9 \pm 5.3$	$7078.1 \pm 5.2$	$10738.5 \pm 17.5$
HDFS2 – 327	$234.2 \pm 3.2$	$399.9 \pm 5.3$	$608.1 \pm 5.1$	$730.4 \pm 10.1$

Table A.9: NIR Photometry – continued

ID	$J_s^a$	$H^a$	$K_s^a$	$K_s^{\text{tot } b}$
HDFS2 – 365	$52.3 \pm 3.2$	$39.2 \pm 5.3$	$46.5 \pm 5.1$	$60.6 \pm 6.4$
HDFS2 – 380	$3.0 \pm 3.9$	$35.9 \pm 6.4$	$33.1 \pm 6.2$	$29.7 \pm 4.8$
HDFS2 – 356	$94.0 \pm 3.2$	$108.9 \pm 5.3$	$127.5 \pm 5.1$	$150.0 \pm 9.0$
HDFS2 – 340	$495.9 \pm 3.2$	$580.4 \pm 5.3$	$632.8 \pm 5.1$	$970.0 \pm 14.8$
HDFS2 – 388	$13.4 \pm 3.2$	$10.9 \pm 5.3$	$14.8 \pm 5.1$	$15.1 \pm 3.9$
HDFS2 – 374	$32.2 \pm 3.2$	$21.6 \pm 5.3$	$32.9 \pm 5.1$	$41.1 \pm 7.8$
HDFS2 – 368	$34.8 \pm 3.2$	$2.6 \pm 5.3$	$58.2 \pm 5.1$	$57.8 \pm 7.1$
HDFS2 – 387	$18.6 \pm 3.2$	$23.8 \pm 5.3$	$16.8 \pm 5.1$	$20.9 \pm 4.9$
HDFS2 – 393	$-2.2 \pm 3.2$	$0.5 \pm 5.3$	$12.9 \pm 5.1$	$14.8 \pm 4.6$
HDFS2 – 346	$1077.4 \pm 3.2$	$1773.1 \pm 5.3$	$2500.8 \pm 5.1$	$2988.5 \pm 11.4$
HDFS2 – 311	$612.0 \pm 3.2$	$708.1 \pm 5.3$	$823.5 \pm 5.1$	$1716.7 \pm 12.9$
HDFS2 – 376	$130.0 \pm 3.2$	$184.9 \pm 5.3$	$242.6 \pm 5.1$	$299.0 \pm 10.3$
HDFS2 – 355	$43.2 \pm 3.3$	$57.5 \pm 5.3$	$47.3 \pm 5.1$	$51.1 \pm 6.4$
HDFS2 – 371	$127.2 \pm 3.2$	$202.9 \pm 5.3$	$340.8 \pm 5.1$	$423.5 \pm 10.8$
HDFS2 – 398	$48.9 \pm 3.2$	$31.5 \pm 5.3$	$35.3 \pm 5.1$	$42.7 \pm 6.4$
HDFS2 – 392	$28.2 \pm 3.2$	$44.6 \pm 5.3$	$51.5 \pm 5.1$	$58.9 \pm 4.4$
HDFS2 – 296	$6361.1 \pm 3.2$	$9484.5 \pm 5.3$	$12520.4 \pm 5.1$	$22057.5 \pm 19.7$
HDFS2 – 409	$3.4 \pm 3.3$	$19.3 \pm 5.3$	$19.4 \pm 5.1$	$22.5 \pm 4.9$
HDFS2 – 410	$15.1 \pm 3.2$	$30.0 \pm 5.3$	$13.1 \pm 5.1$	$18.7 \pm 4.4$
HDFS2 – 402	$113.4 \pm 3.2$	$119.1 \pm 5.3$	$123.6 \pm 5.1$	$140.7 \pm 9.6$
HDFS2 – 370	$95.3 \pm 3.2$	$143.0 \pm 5.2$	$225.4 \pm 5.0$	$244.4 \pm 5.3$
HDFS2 – 407	$56.7 \pm 3.2$	$52.5 \pm 5.3$	$33.5 \pm 5.1$	$38.2 \pm 5.1$
HDFS2 – 406	$23.0 \pm 5.0$	$26.3 \pm 8.0$	$44.8 \pm 7.8$	$50.1 \pm 14.3$
HDFS2 – 414	$7.2 \pm 4.4$	$3.1 \pm 7.3$	$34.6 \pm 7.1$	$56.2 \pm 12.7$
HDFS2 – 377	$201.7 \pm 3.2$	$296.2 \pm 5.3$	$457.1 \pm 5.1$	$543.6 \pm 9.4$
HDFS2 – 390	$134.7 \pm 3.2$	$154.2 \pm 5.3$	$167.8 \pm 5.1$	$232.1 \pm 12.8$
HDFS2 – 405	$42.4 \pm 3.3$	$56.5 \pm 5.3$	$84.6 \pm 5.1$	$101.5 \pm 10.4$

Table A.9: NIR Photometry – continued

ID	$J_s^a$	$H^a$	$K_s^a$	$K_s^{\text{tot } b}$
HDFS2 – 359	$288.9 \pm 3.2$	$450.0 \pm 5.3$	$693.8 \pm 5.1$	$978.6 \pm 8.8$
HDFS2 – 361	$1173.7 \pm 3.2$	$1329.8 \pm 5.3$	$1389.0 \pm 5.1$	$1975.7 \pm 13.9$
HDFS2 – 383	$379.8 \pm 3.2$	$480.5 \pm 5.3$	$551.3 \pm 5.1$	$641.0 \pm 9.2$
HDFS2 – 411	$58.7 \pm 3.2$	$64.6 \pm 5.3$	$91.5 \pm 5.1$	$117.4 \pm 8.8$
HDFS2 – 413	$61.7 \pm 3.2$	$72.7 \pm 5.3$	$90.6 \pm 5.1$	$97.2 \pm 7.5$
HDFS2 – 426	$36.1 \pm 3.2$	$58.8 \pm 5.3$	$53.8 \pm 5.1$	$61.7 \pm 6.1$
HDFS2 – 415	$67.2 \pm 3.2$	$62.5 \pm 5.3$	$64.6 \pm 5.1$	$68.2 \pm 6.8$
HDFS2 – 430	$23.1 \pm 3.2$	$19.0 \pm 5.3$	$15.1 \pm 5.1$	$17.2 \pm 3.9$
HDFS2 – 394	$246.3 \pm 3.2$	$331.4 \pm 5.3$	$475.3 \pm 5.1$	$705.0 \pm 14.1$
HDFS2 – 418	$124.2 \pm 3.6$	$135.4 \pm 5.9$	$157.3 \pm 5.6$	$192.8 \pm 10.0$
HDFS2 – 421	$69.0 \pm 3.2$	$66.0 \pm 5.3$	$98.3 \pm 5.1$	$108.9 \pm 7.7$
HDFS2 – 379	$486.5 \pm 3.2$	$529.5 \pm 5.3$	$600.4 \pm 5.1$	$944.3 \pm 15.8$
HDFS2 – 428	$48.3 \pm 3.1$	$59.7 \pm 5.1$	$75.5 \pm 4.9$	$75.7 \pm 4.5$
HDFS2 – 423	$85.0 \pm 4.1$	$149.5 \pm 6.7$	$176.0 \pm 6.5$	$175.7 \pm 12.5$
HDFS2 – 441	$13.8 \pm 3.2$	$-3.3 \pm 5.3$	$18.5 \pm 5.1$	$16.8 \pm 3.9$
HDFS2 – 424	$39.5 \pm 3.2$	$72.1 \pm 5.3$	$121.2 \pm 5.1$	$141.3 \pm 7.9$
HDFS2 – 412	$121.5 \pm 3.2$	$128.5 \pm 5.3$	$128.8 \pm 5.1$	$165.5 \pm 9.6$
HDFS2 – 443	$24.6 \pm 3.6$	$11.7 \pm 5.9$	$11.0 \pm 5.7$	$16.5 \pm 3.7$
HDFS2 – 439	$5.4 \pm 3.3$	$12.4 \pm 5.4$	$21.7 \pm 5.2$	$16.6 \pm 4.3$
HDFS2 – 422	$398.5 \pm 3.2$	$478.3 \pm 5.3$	$574.8 \pm 5.1$	$663.4 \pm 10.0$
HDFS2 – 446	$17.8 \pm 3.8$	$23.7 \pm 6.2$	$30.2 \pm 6.0$	$27.2 \pm 6.7$
HDFS2 – 435	$54.9 \pm 3.2$	$40.5 \pm 5.3$	$66.0 \pm 5.1$	$72.3 \pm 6.7$
HDFS2 – 404	$601.8 \pm 3.2$	$949.5 \pm 5.3$	$1426.4 \pm 5.1$	$1662.6 \pm 10.5$
HDFS2 – 433	$95.3 \pm 3.2$	$112.9 \pm 5.3$	$161.7 \pm 5.1$	$194.1 \pm 5.8$
HDFS2 – 431	$120.3 \pm 3.2$	$146.9 \pm 5.3$	$189.1 \pm 5.1$	$200.3 \pm 8.2$
HDFS2 – 427	$248.5 \pm 3.2$	$390.1 \pm 5.3$	$495.8 \pm 5.1$	$566.6 \pm 9.5$
HDFS2 – 382	$298.2 \pm 3.2$	$374.7 \pm 5.3$	$466.7 \pm 5.1$	$837.1 \pm 10.2$

Table A.9: NIR Photometry – continued

ID	$J_s^a$	$H^a$	$K_s^a$	$K_s^{\text{tot } b}$
HDFS2 – 357	$1198.7 \pm 3.2$	$1830.4 \pm 5.3$	$2501.8 \pm 5.1$	$3198.7 \pm 13.1$
HDFS2 – 456	$10.2 \pm 3.2$	$36.1 \pm 5.3$	$13.5 \pm 5.1$	$16.0 \pm 4.8$
HDFS2 – 449	$36.9 \pm 3.2$	$39.3 \pm 5.3$	$44.1 \pm 5.1$	$49.9 \pm 6.0$
HDFS2 – 458	$12.5 \pm 3.2$	$20.8 \pm 5.3$	$37.0 \pm 5.1$	$36.7 \pm 5.4$
HDFS2 – 464	$12.9 \pm 3.2$	$5.9 \pm 5.3$	$11.7 \pm 5.1$	$15.5 \pm 4.8$
HDFS2 – 457	$18.4 \pm 3.2$	$17.8 \pm 5.3$	$25.1 \pm 5.1$	$27.4 \pm 5.0$
HDFS2 – 461	$15.3 \pm 3.2$	$12.0 \pm 5.3$	$24.5 \pm 5.1$	$31.3 \pm 5.2$
HDFS2 – 462	$35.6 \pm 3.2$	$47.8 \pm 5.3$	$23.3 \pm 5.1$	$23.3 \pm 5.6$
HDFS2 – 451	$44.5 \pm 3.2$	$65.6 \pm 5.3$	$56.7 \pm 5.1$	$60.6 \pm 8.2$
HDFS2 – 438	$486.9 \pm 3.2$	$614.4 \pm 5.3$	$713.1 \pm 5.1$	$735.9 \pm 6.2$
HDFS2 – 434	$161.8 \pm 3.2$	$149.6 \pm 5.3$	$197.1 \pm 5.1$	$277.4 \pm 12.0$
HDFS2 – 658	$6.9 \pm 3.4$	$-3.7 \pm 5.7$	$25.3 \pm 5.5$	$25.4 \pm 4.7$
HDFS2 – 453	$62.3 \pm 3.2$	$57.7 \pm 5.3$	$74.3 \pm 5.1$	$79.5 \pm 8.1$
HDFS2 – 654	$9.2 \pm 4.1$	$10.6 \pm 6.8$	$16.5 \pm 6.6$	$24.4 \pm 4.8$
HDFS2 – 660	$4.3 \pm 3.2$	$11.6 \pm 5.3$	$17.4 \pm 5.1$	$22.0 \pm 4.1$
HDFS2 – 448	$91.0 \pm 3.2$	$103.2 \pm 5.3$	$117.3 \pm 5.1$	$116.2 \pm 8.0$
HDFS2 – 436	$505.5 \pm 3.2$	$703.5 \pm 5.3$	$785.1 \pm 5.1$	$1114.7 \pm 8.9$
HDFS2 – 459	$47.6 \pm 3.6$	$75.6 \pm 5.9$	$87.3 \pm 5.7$	$104.6 \pm 8.6$
HDFS2 – 631	$20.1 \pm 3.2$	$12.9 \pm 5.3$	$7.6 \pm 5.1$	$15.3 \pm 2.8$
HDFS2 – 470	$33.3 \pm 3.2$	$35.9 \pm 5.3$	$41.1 \pm 5.1$	$44.0 \pm 6.2$
HDFS2 – 447	$492.0 \pm 3.2$	$626.5 \pm 5.3$	$730.4 \pm 5.1$	$850.6 \pm 10.2$
HDFS2 – 645	$14.2 \pm 3.2$	$5.9 \pm 5.3$	$20.1 \pm 5.1$	$17.0 \pm 3.7$
HDFS2 – 633	$100.3 \pm 2.8$	$161.0 \pm 4.6$	$218.1 \pm 4.4$	$197.0 \pm 4.3$
HDFS2 – 452	$334.2 \pm 3.2$	$421.3 \pm 5.3$	$475.7 \pm 5.1$	$589.1 \pm 7.1$
HDFS2 – 639	$35.3 \pm 3.4$	$20.0 \pm 5.6$	$34.6 \pm 5.4$	$55.0 \pm 9.6$
HDFS2 – 467	$38.1 \pm 3.3$	$88.5 \pm 5.3$	$173.8 \pm 5.1$	$201.0 \pm 5.5$
HDFS2 – 628	$137.9 \pm 3.7$	$109.8 \pm 6.0$	$92.1 \pm 5.8$	$99.3 \pm 7.2$

Table A.9: NIR Photometry – continued

ID	$J_s^a$	$H^a$	$K_s^a$	$K_s^{\text{tot } b}$
HDFS2 – 469	$89.1 \pm 4.0$	$188.4 \pm 6.6$	$339.5 \pm 6.4$	$397.1 \pm 11.7$
HDFS2 – 419	$4513.4 \pm 3.2$	$7058.2 \pm 5.3$	$9362.4 \pm 5.1$	$13407.9 \pm 15.7$
HDFS2 – 626	$37.2 \pm 3.2$	$65.5 \pm 5.3$	$64.9 \pm 5.1$	$56.7 \pm 6.8$
HDFS2 – 625	$20.9 \pm 3.2$	$21.7 \pm 5.3$	$18.8 \pm 5.1$	$22.0 \pm 5.0$
HDFS2 – 466	$157.5 \pm 3.2$	$178.6 \pm 5.3$	$193.8 \pm 5.1$	$302.3 \pm 12.4$
HDFS2 – 596	$76.3 \pm 3.2$	$151.2 \pm 5.3$	$173.1 \pm 5.1$	$230.6 \pm 6.7$
HDFS2 – 620	$18.9 \pm 3.2$	$3.2 \pm 5.3$	$18.6 \pm 5.1$	$17.8 \pm 3.6$
HDFS2 – 638	$-6.4 \pm 3.3$	$2.2 \pm 5.3$	$14.5 \pm 5.1$	$16.0 \pm 3.3$
HDFS2 – 617	$118.1 \pm 3.3$	$106.7 \pm 5.3$	$110.2 \pm 5.1$	$110.0 \pm 8.3$
HDFS2 – 614	$6.2 \pm 3.4$	$6.6 \pm 5.6$	$36.2 \pm 5.4$	$42.9 \pm 7.3$
HDFS2 – 613	$12.8 \pm 3.2$	$8.1 \pm 5.3$	$4.7 \pm 5.1$	$14.8 \pm 3.0$
HDFS2 – 608	$214.4 \pm 3.2$	$266.2 \pm 5.3$	$290.7 \pm 5.1$	$342.7 \pm 9.9$
HDFS2 – 609	$34.4 \pm 3.2$	$29.2 \pm 5.3$	$27.1 \pm 5.1$	$33.1 \pm 5.1$
HDFS2 – 605	$27.6 \pm 3.2$	$24.8 \pm 5.3$	$36.0 \pm 5.1$	$42.8 \pm 6.6$
HDFS2 – 602	$286.8 \pm 3.2$	$322.4 \pm 5.3$	$360.0 \pm 5.1$	$460.3 \pm 11.1$
HDFS2 – 601	$65.4 \pm 4.2$	$71.9 \pm 7.0$	$58.0 \pm 6.8$	$58.7 \pm 8.2$
HDFS2 – 595	$770.8 \pm 3.2$	$1312.3 \pm 5.3$	$2035.1 \pm 5.1$	$2719.6 \pm 13.9$
HDFS2 – 618	$35.1 \pm 3.3$	$28.3 \pm 5.4$	$26.5 \pm 5.2$	$26.3 \pm 5.5$
HDFS2 – 592	$1023.5 \pm 3.2$	$1290.0 \pm 5.3$	$1551.4 \pm 5.1$	$1924.4 \pm 11.9$
HDFS2 – 606	$19.3 \pm 3.2$	$30.3 \pm 5.3$	$18.7 \pm 5.1$	$22.0 \pm 4.3$
HDFS2 – 594	$27.3 \pm 3.2$	$33.5 \pm 5.3$	$31.0 \pm 5.1$	$20.7 \pm 2.5$
HDFS2 – 587	$57.7 \pm 4.0$	$85.7 \pm 6.6$	$137.1 \pm 6.4$	$180.0 \pm 11.7$
HDFS2 – 597	$4.0 \pm 3.2$	$16.0 \pm 5.3$	$25.0 \pm 5.1$	$27.9 \pm 4.6$
HDFS2 – 593	$72.8 \pm 3.2$	$70.3 \pm 5.3$	$64.8 \pm 5.1$	$84.2 \pm 7.6$
HDFS2 – 591	$18.8 \pm 3.2$	$28.3 \pm 5.3$	$19.0 \pm 5.1$	$18.0 \pm 5.4$
HDFS2 – 590	$41.0 \pm 3.2$	$63.9 \pm 5.3$	$88.7 \pm 5.1$	$80.4 \pm 8.4$
HDFS2 – 586	$12.9 \pm 4.6$	$5.3 \pm 7.4$	$15.4 \pm 7.2$	$15.6 \pm 3.5$

Table A.9: NIR Photometry – continued

ID	$J_s^a$	H <sup>a</sup>	$K_s^a$	$K_s^{\text{tot } b}$
HDFS2 – 585	$57.2 \pm 3.2$	$67.8 \pm 5.3$	$84.1 \pm 5.1$	$132.9 \pm 9.9$
HDFS2 – 588	$26.1 \pm 3.2$	$26.9 \pm 5.3$	$35.8 \pm 5.1$	$35.7 \pm 5.2$
HDFS2 – 583	$37.2 \pm 3.2$	$16.7 \pm 5.3$	$26.0 \pm 5.1$	$25.5 \pm 3.1$
HDFS2 – 579	$80.2 \pm 3.2$	$83.7 \pm 5.3$	$95.6 \pm 5.1$	$89.8 \pm 7.2$
HDFS2 – 582	$116.6 \pm 3.2$	$142.5 \pm 5.3$	$152.1 \pm 5.1$	$177.1 \pm 8.6$
HDFS2 – 581	$147.8 \pm 3.2$	$185.1 \pm 5.3$	$182.6 \pm 5.1$	$202.2 \pm 8.4$
HDFS2 – 578	$75.3 \pm 3.2$	$86.7 \pm 5.3$	$101.7 \pm 5.1$	$104.5 \pm 8.0$
HDFS2 – 574	$102.9 \pm 3.3$	$153.5 \pm 5.3$	$198.0 \pm 5.1$	$264.5 \pm 10.8$
HDFS2 – 566	$1761.3 \pm 3.2$	$2155.5 \pm 5.3$	$2600.8 \pm 5.1$	$3616.7 \pm 14.8$
HDFS2 – 568	$51.1 \pm 3.2$	$55.2 \pm 5.3$	$58.8 \pm 5.1$	$68.6 \pm 8.4$
HDFS2 – 572	$24.4 \pm 3.2$	$36.5 \pm 5.3$	$52.9 \pm 5.1$	$60.0 \pm 7.1$
HDFS2 – 571	$64.2 \pm 3.2$	$127.4 \pm 5.3$	$148.0 \pm 5.1$	$141.2 \pm 8.2$
HDFS2 – 567	$19.8 \pm 3.2$	$17.8 \pm 5.3$	$67.5 \pm 5.1$	$71.3 \pm 7.1$
HDFS2 – 564	$12.3 \pm 4.1$	$-7.4 \pm 6.8$	$16.6 \pm 6.6$	$19.6 \pm 4.1$
HDFS2 – 565	$4.1 \pm 3.2$	$36.5 \pm 5.3$	$25.0 \pm 5.1$	$24.3 \pm 4.5$
HDFS2 – 561	$231.2 \pm 3.2$	$284.3 \pm 5.3$	$302.9 \pm 5.1$	$409.9 \pm 11.9$
HDFS2 – 560	$41.5 \pm 3.2$	$31.6 \pm 5.3$	$36.9 \pm 5.1$	$50.4 \pm 8.1$
HDFS2 – 559	$12.5 \pm 3.2$	$16.6 \pm 5.3$	$43.2 \pm 5.1$	$53.8 \pm 6.7$
HDFS2 – 562	$9.6 \pm 3.2$	$26.7 \pm 5.3$	$31.0 \pm 5.1$	$32.5 \pm 6.1$
HDFS2 – 558	$30.3 \pm 3.2$	$55.2 \pm 5.3$	$58.4 \pm 5.1$	$60.4 \pm 6.6$
HDFS2 – 543	$68.1 \pm 3.2$	$77.9 \pm 5.3$	$65.8 \pm 5.1$	$82.3 \pm 5.2$
HDFS2 – 556	$77.0 \pm 3.2$	$81.4 \pm 5.3$	$90.2 \pm 5.1$	$103.3 \pm 7.7$
HDFS2 – 554	$100.2 \pm 3.2$	$132.5 \pm 5.3$	$165.9 \pm 5.1$	$203.5 \pm 11.0$
HDFS2 – 542	$1002.9 \pm 3.2$	$1259.8 \pm 5.3$	$1498.4 \pm 5.1$	$2984.8 \pm 19.6$
HDFS2 – 550	$10.6 \pm 3.2$	$1.0 \pm 5.3$	$14.2 \pm 5.1$	$16.1 \pm 3.9$
HDFS2 – 548	$53.1 \pm 3.2$	$64.7 \pm 5.3$	$59.2 \pm 5.1$	$57.7 \pm 6.5$
HDFS2 – 547	$16.2 \pm 3.2$	$14.5 \pm 5.3$	$31.5 \pm 5.1$	$31.8 \pm 4.5$

Table A.9: NIR Photometry – continued

ID	$J_s^a$	$H^a$	$K_s^a$	$K_s^{\text{tot } b}$
HDFS2 – 532	$321.3 \pm 3.2$	$489.8 \pm 5.3$	$713.0 \pm 5.1$	$799.5 \pm 9.3$
HDFS2 – 517	$3019.4 \pm 3.2$	$4319.0 \pm 5.3$	$5467.8 \pm 5.1$	$7691.9 \pm 15.6$
HDFS2 – 527	$527.8 \pm 3.3$	$742.7 \pm 5.3$	$952.1 \pm 5.1$	$1105.9 \pm 10.1$
HDFS2 – 518	$443.1 \pm 3.2$	$474.8 \pm 5.3$	$563.4 \pm 5.1$	$662.6 \pm 6.9$
HDFS2 – 529	$23.3 \pm 3.2$	$29.7 \pm 5.3$	$41.3 \pm 5.1$	$52.2 \pm 7.6$
HDFS2 – 528	$0.8 \pm 3.2$	$-12.7 \pm 5.3$	$6.8 \pm 5.1$	$14.9 \pm 3.4$
HDFS2 – 525	$44.0 \pm 3.2$	$40.4 \pm 5.3$	$49.4 \pm 5.1$	$54.9 \pm 6.6$
HDFS2 – 521	$16.4 \pm 3.2$	$23.7 \pm 5.3$	$21.3 \pm 5.1$	$26.2 \pm 6.1$
HDFS2 – 519	$149.3 \pm 3.2$	$179.3 \pm 5.3$	$190.1 \pm 5.1$	$193.7 \pm 8.2$
HDFS2 – 511	$149.0 \pm 3.2$	$210.2 \pm 5.3$	$242.4 \pm 5.1$	$300.0 \pm 10.9$
HDFS2 – 515	$42.7 \pm 3.2$	$76.3 \pm 5.3$	$63.0 \pm 5.1$	$63.7 \pm 7.2$
HDFS2 – 512	$25.4 \pm 3.2$	$39.8 \pm 5.3$	$34.7 \pm 5.1$	$35.4 \pm 4.2$
HDFS2 – 513	$35.8 \pm 3.2$	$38.9 \pm 5.3$	$50.4 \pm 5.1$	$54.9 \pm 6.1$
HDFS2 – 506	$17.4 \pm 3.2$	$33.0 \pm 5.3$	$43.3 \pm 5.1$	$47.4 \pm 6.2$
HDFS2 – 502	$31.3 \pm 3.2$	$73.4 \pm 5.3$	$142.9 \pm 5.1$	$142.1 \pm 8.7$
HDFS2 – 500	$183.2 \pm 3.3$	$257.7 \pm 5.3$	$277.4 \pm 5.1$	$334.3 \pm 9.6$
HDFS2 – 501	$8.6 \pm 3.3$	$6.6 \pm 5.3$	$22.0 \pm 5.1$	$20.9 \pm 2.7$
HDFS2 – 508	$0.4 \pm 3.2$	$-2.4 \pm 5.3$	$5.8 \pm 5.1$	$15.5 \pm 3.6$
HDFS2 – 498	$16.9 \pm 3.4$	$9.8 \pm 5.6$	$35.1 \pm 5.4$	$39.1 \pm 6.0$
HDFS2 – 499	$5.0 \pm 3.2$	$10.0 \pm 5.3$	$25.0 \pm 5.1$	$26.8 \pm 5.5$
HDFS2 – 494	$17.1 \pm 3.3$	$23.6 \pm 5.3$	$20.3 \pm 5.1$	$22.4 \pm 4.7$
HDFS2 – 487	$15.9 \pm 3.2$	$27.8 \pm 5.3$	$32.4 \pm 5.1$	$37.1 \pm 7.4$
HDFS2 – 486	$15.7 \pm 3.3$	$31.0 \pm 5.3$	$28.0 \pm 5.1$	$29.2 \pm 3.5$
HDFS2 – 481	$34.2 \pm 3.2$	$42.7 \pm 5.3$	$39.0 \pm 5.1$	$39.9 \pm 5.8$
HDFS2 – 482	$11.9 \pm 3.2$	$26.6 \pm 5.3$	$21.6 \pm 5.1$	$24.9 \pm 6.2$
HDFS2 – 484	$-0.2 \pm 3.2$	$-0.5 \pm 5.3$	$20.7 \pm 5.1$	$17.9 \pm 4.2$
HDFS2 – 475	$49.9 \pm 3.2$	$57.6 \pm 5.3$	$74.4 \pm 5.1$	$95.1 \pm 8.0$

Table A.9: NIR Photometry – continued

ID	$J_s^a$	$H^a$	$K_s^a$	$K_s^{\text{tot } b}$
HDFS2 – 478	$-0.9 \pm 3.4$	$6.1 \pm 5.5$	$22.8 \pm 5.3$	$25.7 \pm 4.7$
HDFS2 – 483	$31.3 \pm 3.3$	$44.2 \pm 5.3$	$52.1 \pm 5.1$	$58.5 \pm 6.0$
HDFS2 – 641	$15.1 \pm 3.2$	$10.0 \pm 5.3$	$28.6 \pm 5.1$	$28.9 \pm 5.9$
HDFS2 – 493	$38.9 \pm 3.2$	$50.3 \pm 5.3$	$61.3 \pm 5.1$	$61.7 \pm 6.8$
HDFS2 – 657	$113.7 \pm 3.2$	$125.7 \pm 5.3$	$151.6 \pm 5.1$	$197.1 \pm 11.3$
HDFS2 – 669	$52.1 \pm 3.2$	$66.6 \pm 5.3$	$73.1 \pm 5.1$	$76.7 \pm 6.9$
HDFS2 – 677	$68.2 \pm 3.2$	$67.4 \pm 5.3$	$70.1 \pm 5.1$	$76.3 \pm 7.5$
HDFS2 – 671	$-0.0 \pm 3.2$	$8.9 \pm 5.3$	$28.3 \pm 5.1$	$31.1 \pm 5.2$
HDFS2 – 644	$18.4 \pm 3.2$	$18.0 \pm 5.3$	$11.5 \pm 5.1$	$16.5 \pm 4.3$
HDFS2 – 632	$23.3 \pm 3.2$	$18.5 \pm 5.3$	$33.5 \pm 5.1$	$39.2 \pm 6.1$
HDFS2 – 674	$54.2 \pm 3.2$	$55.8 \pm 5.3$	$45.6 \pm 5.1$	$51.7 \pm 6.0$
HDFS2 – 683	$13.7 \pm 3.2$	$12.2 \pm 5.3$	$25.1 \pm 5.1$	$22.1 \pm 4.2$
HDFS2 – 696	$388.0 \pm 3.2$	$450.6 \pm 5.3$	$532.9 \pm 5.1$	$794.4 \pm 14.3$
HDFS2 – 687	$40.0 \pm 3.2$	$54.1 \pm 5.3$	$60.1 \pm 5.1$	$81.6 \pm 7.6$
HDFS2 – 693	$17.4 \pm 3.2$	$22.6 \pm 5.3$	$37.4 \pm 5.1$	$36.9 \pm 3.8$
HDFS2 – 616	$206.9 \pm 3.2$	$215.3 \pm 5.3$	$245.1 \pm 5.1$	$280.4 \pm 10.8$
HDFS2 – 648	$21.4 \pm 3.2$	$23.9 \pm 5.3$	$35.8 \pm 5.1$	$34.5 \pm 5.5$
HDFS2 – 694	$569.5 \pm 3.2$	$648.7 \pm 5.3$	$680.9 \pm 5.1$	$891.1 \pm 11.8$
HDFS2 – 716	$34.6 \pm 3.2$	$49.7 \pm 5.3$	$34.0 \pm 5.1$	$51.3 \pm 8.2$
HDFS2 – 692	$10.8 \pm 3.2$	$40.0 \pm 5.3$	$14.6 \pm 5.1$	$19.6 \pm 4.1$
HDFS2 – 699	$18.2 \pm 3.2$	$60.3 \pm 5.3$	$116.6 \pm 5.1$	$130.5 \pm 7.5$
HDFS2 – 668	$46.0 \pm 3.2$	$42.6 \pm 5.3$	$62.5 \pm 5.1$	$61.1 \pm 6.9$
HDFS2 – 652	$69.0 \pm 3.3$	$96.7 \pm 5.3$	$130.3 \pm 5.1$	$165.7 \pm 9.7$
HDFS2 – 725	$13.4 \pm 3.2$	$25.6 \pm 5.3$	$51.2 \pm 5.1$	$50.8 \pm 6.3$
HDFS2 – 707	$25.2 \pm 3.2$	$63.2 \pm 5.3$	$53.8 \pm 5.1$	$67.5 \pm 4.1$
HDFS2 – 736	$23.6 \pm 3.2$	$33.6 \pm 5.3$	$37.2 \pm 5.1$	$44.0 \pm 6.0$
HDFS2 – 748	$14.1 \pm 3.2$	$12.5 \pm 5.3$	$30.8 \pm 5.1$	$35.1 \pm 8.0$



Table A.9: NIR Photometry – continued

ID	$J_s^a$	$H^a$	$K_s^a$	$K_s^{\text{tot } b}$
HDFS2 – 753	$12.0 \pm 3.2$	$22.8 \pm 5.3$	$33.1 \pm 5.1$	$35.9 \pm 5.8$
HDFS2 – 749	$21.6 \pm 3.2$	$25.1 \pm 5.3$	$22.5 \pm 5.1$	$24.4 \pm 5.5$
HDFS2 – 773	$12.5 \pm 3.2$	$13.5 \pm 5.3$	$28.9 \pm 5.1$	$37.2 \pm 6.6$
HDFS2 – 738	$8.9 \pm 3.2$	$12.3 \pm 5.3$	$26.6 \pm 5.1$	$26.3 \pm 4.9$
HDFS2 – 1051	$2740.7 \pm 3.2$	$3700.1 \pm 5.3$	$4508.3 \pm 5.1$	$5892.1 \pm 14.2$
HDFS2 – 771	$17.4 \pm 3.2$	$40.6 \pm 5.3$	$52.1 \pm 5.1$	$50.4 \pm 6.3$
HDFS2 – 907	$14.2 \pm 3.2$	$54.3 \pm 5.3$	$25.9 \pm 5.1$	$26.7 \pm 4.6$
HDFS2 – 1023	$12.3 \pm 3.2$	$20.6 \pm 5.3$	$44.9 \pm 5.1$	$55.5 \pm 6.8$
HDFS2 – 860	$17.6 \pm 3.2$	$10.1 \pm 5.3$	$15.1 \pm 5.1$	$16.2 \pm 3.6$
HDFS2 – 1042	$11.0 \pm 3.3$	$7.8 \pm 5.4$	$13.9 \pm 5.2$	$15.5 \pm 4.5$
HDFS2 – 1107	$49.3 \pm 3.2$	$41.6 \pm 5.3$	$41.2 \pm 5.1$	$43.1 \pm 6.8$
HDFS2 – 1041	$46.0 \pm 3.2$	$57.7 \pm 5.3$	$49.8 \pm 5.1$	$55.1 \pm 7.0$
HDFS2 – 1097	$770.8 \pm 3.2$	$1093.1 \pm 5.3$	$1661.4 \pm 5.1$	$2397.3 \pm 10.7$
HDFS2 – 1100	$188.9 \pm 3.2$	$218.0 \pm 5.3$	$270.5 \pm 5.1$	$271.7 \pm 5.3$
HDFS2 – 1035	$42.8 \pm 3.2$	$55.9 \pm 5.3$	$43.1 \pm 5.1$	$44.9 \pm 6.6$
HDFS2 – 1105	$90.6 \pm 3.2$	$172.9 \pm 5.3$	$245.4 \pm 5.1$	$281.5 \pm 9.8$
HDFS2 – 1064	$21.7 \pm 3.2$	$-1.8 \pm 5.3$	$15.3 \pm 5.1$	$23.2 \pm 4.5$
HDFS2 – 1086	$47.7 \pm 3.2$	$95.6 \pm 5.3$	$93.5 \pm 5.1$	$108.6 \pm 8.4$
HDFS2 – 1112	$40.1 \pm 3.2$	$43.2 \pm 5.3$	$37.1 \pm 5.1$	$37.5 \pm 6.1$
HDFS2 – 1104	$1394.0 \pm 3.2$	$1681.0 \pm 5.3$	$2026.3 \pm 5.1$	$3120.5 \pm 15.7$
HDFS2 – 1106	$30.4 \pm 3.2$	$36.6 \pm 5.3$	$34.1 \pm 5.1$	$36.5 \pm 6.8$
HDFS2 – 1111	$88.5 \pm 3.2$	$106.4 \pm 5.3$	$77.5 \pm 5.1$	$82.3 \pm 6.7$
HDFS2 – 1102	$88.2 \pm 3.4$	$163.0 \pm 5.5$	$231.3 \pm 5.3$	$260.0 \pm 8.6$
HDFS2 – 1098	$18.2 \pm 3.2$	$38.0 \pm 5.3$	$29.1 \pm 5.1$	$32.6 \pm 5.5$
HDFS2 – 1092	$20.7 \pm 3.2$	$33.0 \pm 5.3$	$36.5 \pm 5.1$	$47.3 \pm 8.6$
HDFS2 – 1074	$67.5 \pm 3.2$	$123.2 \pm 5.3$	$144.1 \pm 5.1$	$154.6 \pm 8.4$
HDFS2 – 1088	$78.8 \pm 3.2$	$92.3 \pm 5.3$	$107.5 \pm 5.1$	$121.7 \pm 8.2$

Table A.9: NIR Photometry – continued

ID	$J_s^a$	$H^a$	$K_s^a$	$K_s^{\text{tot } b}$
HDFS2 – 1066	$44.6 \pm 3.2$	$51.3 \pm 5.3$	$47.0 \pm 5.1$	$41.6 \pm 6.3$
HDFS2 – 1078	$21.2 \pm 3.2$	$40.9 \pm 5.3$	$56.7 \pm 5.1$	$55.4 \pm 7.1$
HDFS2 – 1069	$24.4 \pm 3.2$	$35.3 \pm 5.3$	$43.2 \pm 5.1$	$45.6 \pm 5.7$
HDFS2 – 1081	$60.3 \pm 3.4$	$66.3 \pm 5.5$	$70.9 \pm 5.3$	$74.6 \pm 8.1$
HDFS2 – 1080	$9.0 \pm 3.2$	$8.6 \pm 5.3$	$12.5 \pm 5.1$	$16.2 \pm 3.6$
HDFS2 – 985	$102.6 \pm 3.2$	$117.9 \pm 5.3$	$125.0 \pm 5.1$	$155.7 \pm 10.7$
HDFS2 – 1054	$332.4 \pm 3.2$	$562.7 \pm 5.3$	$707.4 \pm 5.1$	$879.8 \pm 11.8$
HDFS2 – 1065	$56.7 \pm 3.3$	$100.4 \pm 5.3$	$104.8 \pm 5.1$	$125.6 \pm 5.3$
HDFS2 – 1070	$14.5 \pm 3.2$	$7.7 \pm 5.3$	$8.9 \pm 5.1$	$15.8 \pm 3.6$
HDFS2 – 1038	$202.0 \pm 3.3$	$304.9 \pm 5.3$	$314.8 \pm 5.1$	$357.2 \pm 5.9$
HDFS2 – 1030	$5.7 \pm 3.2$	$26.3 \pm 5.3$	$18.0 \pm 5.1$	$19.9 \pm 5.0$
HDFS2 – 1045	$104.0 \pm 3.2$	$119.9 \pm 5.3$	$130.5 \pm 5.1$	$167.4 \pm 6.0$
HDFS2 – 1043	$-0.2 \pm 3.2$	$21.8 \pm 5.3$	$7.4 \pm 5.1$	$17.6 \pm 3.6$
HDFS2 – 1044	$66.5 \pm 3.2$	$115.7 \pm 5.3$	$149.4 \pm 5.1$	$182.6 \pm 9.6$
HDFS2 – 1018	$39.9 \pm 3.2$	$32.7 \pm 5.3$	$59.8 \pm 5.1$	$61.6 \pm 6.6$
HDFS2 – 1027	$24.4 \pm 3.2$	$20.2 \pm 5.3$	$28.3 \pm 5.1$	$16.2 \pm 3.6$
HDFS2 – 1033	$14.5 \pm 3.2$	$30.0 \pm 5.3$	$28.9 \pm 5.1$	$33.5 \pm 3.6$
HDFS2 – 1032	$71.7 \pm 3.2$	$132.1 \pm 5.3$	$240.0 \pm 5.1$	$264.4 \pm 8.4$
HDFS2 – 966	$28.4 \pm 3.3$	$28.2 \pm 5.4$	$30.5 \pm 5.1$	$30.6 \pm 5.3$
HDFS2 – 1029	$22.0 \pm 3.2$	$39.3 \pm 5.3$	$64.9 \pm 5.1$	$67.3 \pm 7.2$
HDFS2 – 935	$322.0 \pm 3.2$	$355.0 \pm 5.3$	$387.2 \pm 5.1$	$549.2 \pm 13.5$
HDFS2 – 1019	$15.3 \pm 3.2$	$18.7 \pm 5.3$	$23.9 \pm 5.1$	$25.5 \pm 4.8$
HDFS2 – 1022	$190.5 \pm 3.2$	$263.3 \pm 5.3$	$333.8 \pm 5.1$	$385.0 \pm 9.7$
HDFS2 – 961	$-6.3 \pm 3.2$	$1.8 \pm 5.3$	$10.2 \pm 5.1$	$15.9 \pm 3.6$
HDFS2 – 999	$2.1 \pm 3.2$	$15.9 \pm 5.3$	$20.3 \pm 5.1$	$22.6 \pm 4.6$
HDFS2 – 1005	$125.4 \pm 3.2$	$166.4 \pm 5.3$	$218.8 \pm 5.1$	$237.4 \pm 9.2$
HDFS2 – 978	$121.6 \pm 3.2$	$197.5 \pm 5.3$	$275.3 \pm 5.1$	$347.9 \pm 6.7$

Table A.9: NIR Photometry – continued

ID	$J_s^a$	$H^a$	$K_s^a$	$K_s^{\text{tot } b}$
HDFS2 – 983	$32.5 \pm 3.4$	$35.6 \pm 5.5$	$10.7 \pm 5.3$	$15.7 \pm 4.1$
HDFS2 – 989	$5.5 \pm 3.2$	$16.6 \pm 5.3$	$11.2 \pm 5.1$	$16.7 \pm 4.5$
HDFS2 – 1000	$191.9 \pm 3.2$	$210.1 \pm 5.3$	$229.4 \pm 5.1$	$258.8 \pm 9.6$
HDFS2 – 975	$133.7 \pm 3.2$	$147.7 \pm 5.3$	$180.1 \pm 5.1$	$278.1 \pm 12.3$
HDFS2 – 1003	$15.4 \pm 3.2$	$20.3 \pm 5.3$	$31.2 \pm 5.1$	$32.7 \pm 5.6$
HDFS2 – 995	$23.2 \pm 3.2$	$4.8 \pm 5.3$	$26.0 \pm 5.1$	$24.0 \pm 5.3$
HDFS2 – 974	$319.4 \pm 3.2$	$425.6 \pm 5.3$	$504.2 \pm 5.1$	$587.6 \pm 10.6$
HDFS2 – 993	$11.8 \pm 3.2$	$16.3 \pm 5.3$	$12.6 \pm 5.1$	$14.9 \pm 4.0$
HDFS2 – 968	$63.4 \pm 3.2$	$132.9 \pm 5.3$	$187.7 \pm 5.1$	$213.3 \pm 5.2$
HDFS2 – 929	$140.5 \pm 3.2$	$202.6 \pm 5.3$	$324.6 \pm 5.1$	$364.5 \pm 9.4$
HDFS2 – 996	$118.0 \pm 3.2$	$140.2 \pm 5.3$	$141.0 \pm 5.1$	$175.6 \pm 5.9$
HDFS2 – 969	$1659.3 \pm 3.2$	$2409.4 \pm 5.3$	$2973.9 \pm 5.1$	$3502.0 \pm 11.3$
HDFS2 – 959	$235.1 \pm 3.2$	$258.5 \pm 5.3$	$317.9 \pm 5.1$	$369.0 \pm 10.5$
HDFS2 – 868	$20.5 \pm 3.2$	$39.9 \pm 5.3$	$32.4 \pm 5.1$	$30.4 \pm 6.5$
HDFS2 – 925	$121.8 \pm 3.1$	$140.0 \pm 5.1$	$159.0 \pm 4.9$	$165.5 \pm 4.7$
HDFS2 – 943	$93.2 \pm 3.2$	$100.8 \pm 5.3$	$79.8 \pm 5.1$	$92.0 \pm 8.0$
HDFS2 – 962	$152.8 \pm 3.2$	$191.0 \pm 5.3$	$219.6 \pm 5.1$	$242.7 \pm 8.5$
HDFS2 – 908	$44.8 \pm 3.2$	$203.1 \pm 5.3$	$315.1 \pm 5.1$	$372.0 \pm 9.5$
HDFS2 – 911	$1770.7 \pm 3.2$	$2518.7 \pm 5.3$	$3262.7 \pm 5.1$	$4036.4 \pm 12.8$
HDFS2 – 944	$35.3 \pm 3.7$	$31.5 \pm 6.0$	$30.5 \pm 5.8$	$33.1 \pm 5.9$
HDFS2 – 940	$44.1 \pm 3.2$	$36.4 \pm 5.3$	$33.9 \pm 5.1$	$36.6 \pm 6.2$
HDFS2 – 941	$6.8 \pm 3.3$	$3.8 \pm 5.4$	$16.8 \pm 5.2$	$18.3 \pm 4.6$
HDFS2 – 949	$119.6 \pm 3.2$	$165.9 \pm 5.3$	$188.5 \pm 5.1$	$203.0 \pm 8.4$
HDFS2 – 918	$40.9 \pm 3.2$	$35.1 \pm 5.3$	$51.2 \pm 5.1$	$64.1 \pm 4.6$
HDFS2 – 952	$32.6 \pm 3.2$	$37.1 \pm 5.3$	$26.9 \pm 5.1$	$26.4 \pm 5.0$
HDFS2 – 939	$37.0 \pm 3.7$	$31.6 \pm 6.0$	$42.5 \pm 5.8$	$53.4 \pm 5.3$
HDFS2 – 927	$11.0 \pm 3.2$	$4.8 \pm 5.3$	$19.5 \pm 5.1$	$19.8 \pm 4.7$

Table A.9: NIR Photometry -- continued

ID	$J_s^a$	$H^a$	$K_s^a$	$K_s^{\text{tot } b}$
HDFS2 – 947	$74.6 \pm 3.2$	$112.4 \pm 5.3$	$158.3 \pm 5.1$	$173.5 \pm 8.4$
HDFS2 – 923	$17.4 \pm 3.2$	$20.9 \pm 5.3$	$27.7 \pm 5.1$	$29.4 \pm 6.8$
HDFS2 – 919	$34.0 \pm 3.2$	$26.8 \pm 5.3$	$49.6 \pm 5.1$	$55.4 \pm 7.0$
HDFS2 – 934	$641.8 \pm 3.2$	$714.0 \pm 5.3$	$805.1 \pm 5.1$	$1196.6 \pm 14.7$
HDFS2 – 910	$64.3 \pm 3.2$	$64.2 \pm 5.3$	$77.1 \pm 5.1$	$81.9 \pm 7.8$
HDFS2 – 926	$30.5 \pm 3.2$	$37.3 \pm 5.3$	$33.3 \pm 5.1$	$40.1 \pm 6.0$
HDFS2 – 824	$495.4 \pm 3.2$	$770.9 \pm 5.3$	$1154.5 \pm 5.1$	$1398.6 \pm 11.4$
HDFS2 – 924	$63.7 \pm 3.2$	$106.2 \pm 5.3$	$105.2 \pm 5.1$	$121.7 \pm 8.4$
HDFS2 – 921	$181.8 \pm 3.2$	$198.1 \pm 5.3$	$213.3 \pm 5.1$	$291.5 \pm 11.5$
HDFS2 – 836	$18.7 \pm 3.2$	$26.1 \pm 5.3$	$18.0 \pm 5.1$	$19.9 \pm 4.3$
HDFS2 – 906	$20.8 \pm 3.2$	$25.5 \pm 5.3$	$26.5 \pm 5.1$	$26.6 \pm 4.8$
HDFS2 – 891	$59.4 \pm 3.2$	$81.9 \pm 5.3$	$74.7 \pm 5.1$	$81.2 \pm 3.9$
HDFS2 – 912	$2.5 \pm 3.2$	$22.0 \pm 5.3$	$6.2 \pm 5.1$	$18.9 \pm 3.8$
HDFS2 – 897	$24.9 \pm 3.2$	$33.1 \pm 5.3$	$26.6 \pm 5.1$	$28.7 \pm 5.1$
HDFS2 – 890	$179.8 \pm 3.2$	$208.4 \pm 5.3$	$282.5 \pm 5.1$	$327.6 \pm 9.2$
HDFS2 – 877	$711.6 \pm 3.2$	$882.2 \pm 5.3$	$1029.9 \pm 5.1$	$1187.1 \pm 7.4$
HDFS2 – 937	$26.3 \pm 3.2$	$18.4 \pm 5.3$	$20.9 \pm 5.1$	$25.8 \pm 5.0$
HDFS2 – 864	$76.2 \pm 2.4$	$96.1 \pm 3.9$	$99.0 \pm 3.8$	$83.3 \pm 2.4$
HDFS2 – 865	$21.7 \pm 3.2$	$22.0 \pm 5.3$	$15.4 \pm 5.1$	$21.0 \pm 4.6$
HDFS2 – 901	$15.2 \pm 3.4$	$13.6 \pm 5.5$	$20.4 \pm 5.4$	$20.6 \pm 4.7$
HDFS2 – 885	$19.1 \pm 3.3$	$10.1 \pm 5.5$	$36.5 \pm 5.3$	$38.0 \pm 5.8$
HDFS2 – 863	$347.8 \pm 3.3$	$541.9 \pm 5.4$	$727.7 \pm 5.3$	$986.6 \pm 13.7$
HDFS2 – 843	$120.5 \pm 3.2$	$129.0 \pm 5.3$	$154.5 \pm 5.1$	$202.4 \pm 6.5$
HDFS2 – 883	$24.2 \pm 3.4$	$29.2 \pm 5.5$	$35.7 \pm 5.4$	$45.6 \pm 4.6$
HDFS2 – 886	$21.1 \pm 3.3$	$27.1 \pm 5.4$	$26.1 \pm 5.2$	$35.6 \pm 6.6$
HDFS2 – 845	$92.6 \pm 3.3$	$118.7 \pm 5.4$	$110.1 \pm 5.2$	$131.3 \pm 8.6$
HDFS2 – 879	$36.4 \pm 3.3$	$28.7 \pm 5.4$	$31.5 \pm 5.2$	$29.9 \pm 3.2$

Table A.9: NIR Photometry – continued

ID	$J_s$ <sup>a</sup>	H <sup>a</sup>	$K_s$ <sup>a</sup>	$K_s^{\text{tot}}$ <sup>b</sup>
HDFS2 – 842	$24.9 \pm 3.4$	$39.5 \pm 5.6$	$39.6 \pm 5.5$	$44.9 \pm 6.7$
HDFS2 – 830	$36.9 \pm 3.4$	$29.5 \pm 5.5$	$43.5 \pm 5.4$	$42.9 \pm 6.9$
HDFS2 – 823	$85.1 \pm 3.5$	$99.7 \pm 5.6$	$142.2 \pm 5.5$	$136.2 \pm 8.2$
HDFS2 – 904	$119.9 \pm 3.5$	$151.2 \pm 5.7$	$154.2 \pm 5.6$	$157.9 \pm 11.3$
HDFS2 – 873	$114.5 \pm 3.4$	$191.0 \pm 5.5$	$264.2 \pm 5.3$	$321.5 \pm 10.5$
HDFS2 – 851	$35.9 \pm 3.5$	$23.4 \pm 5.7$	$21.1 \pm 5.6$	$22.8 \pm 5.5$
HDFS2 – 828	$35.4 \pm 3.3$	$61.6 \pm 5.5$	$60.4 \pm 5.3$	$73.7 \pm 5.5$
HDFS2 – 867	$7.2 \pm 3.7$	$22.5 \pm 6.2$	$20.9 \pm 6.0$	$26.0 \pm 5.7$
HDFS2 – 813	$198.8 \pm 3.9$	$180.6 \pm 6.3$	$155.5 \pm 6.2$	$168.6 \pm 8.8$
HDFS2 – 855	$12.8 \pm 3.6$	$9.8 \pm 5.9$	$24.8 \pm 5.7$	$26.6 \pm 5.7$
HDFS2 – 844	$15.7 \pm 3.5$	$27.1 \pm 5.7$	$37.9 \pm 5.5$	$35.2 \pm 6.5$
HDFS2 – 847	$4.4 \pm 3.5$	$13.7 \pm 5.8$	$9.2 \pm 5.6$	$15.3 \pm 3.4$
HDFS2 – 852	$36.8 \pm 3.8$	$36.2 \pm 6.3$	$21.4 \pm 6.1$	$31.4 \pm 6.0$
HDFS2 – 791	$75.4 \pm 3.7$	$70.9 \pm 6.1$	$97.2 \pm 5.9$	$100.0 \pm 9.0$
HDFS2 – 806	$29.2 \pm 3.9$	$135.9 \pm 6.3$	$261.6 \pm 6.2$	$303.2 \pm 11.6$
HDFS2 – 821	$16.0 \pm 3.9$	$21.5 \pm 6.5$	$13.8 \pm 6.4$	$17.7 \pm 4.7$
HDFS2 – 803	$59.1 \pm 3.8$	$83.6 \pm 6.3$	$113.7 \pm 6.1$	$133.0 \pm 6.1$
HDFS2 – 812	$112.4 \pm 3.5$	$233.7 \pm 5.8$	$269.8 \pm 5.7$	$365.8 \pm 15.1$
HDFS2 – 810	$140.1 \pm 3.9$	$166.2 \pm 6.5$	$200.6 \pm 6.4$	$225.3 \pm 10.9$
HDFS2 – 802	$367.0 \pm 4.0$	$526.2 \pm 6.5$	$585.7 \pm 6.4$	$709.0 \pm 13.5$
HDFS2 – 800	$4.6 \pm 4.6$	$16.8 \pm 7.4$	$28.7 \pm 7.3$	$36.4 \pm 6.8$
HDFS2 – 794	$28.5 \pm 4.0$	$34.0 \pm 6.7$	$26.3 \pm 6.6$	$31.9 \pm 5.8$
HDFS2 – 819	$39.0 \pm 4.9$	$55.2 \pm 8.0$	$47.0 \pm 7.9$	$31.1 \pm 4.1$
HDFS2 – 769	$5.1 \pm 4.0$	$18.0 \pm 6.6$	$37.0 \pm 6.6$	$36.1 \pm 6.7$
HDFS2 – 817	$43.7 \pm 4.0$	$55.9 \pm 6.6$	$60.0 \pm 6.5$	$70.4 \pm 8.7$
HDFS2 – 808	$48.9 \pm 4.9$	$34.9 \pm 8.1$	$70.6 \pm 8.0$	$74.3 \pm 10.0$
HDFS2 – 788	$10.7 \pm 4.5$	$1.8 \pm 7.4$	$25.8 \pm 7.2$	$27.5 \pm 5.9$

Table A.9: NIR Photometry – continued

ID	$J_s^a$	$H^a$	$K_s^a$	$K_s^{\text{tot } b}$
HDFS2 – 792	$972.9 \pm 5.4$	$1276.1 \pm 8.9$	$1435.3 \pm 8.8$	$2328.1 \pm 28.5$
HDFS2 – 796	$8.8 \pm 4.3$	$21.2 \pm 7.0$	$24.9 \pm 6.9$	$24.9 \pm 3.9$
HDFS2 – 801	$67.9 \pm 5.1$	$76.7 \pm 8.3$	$94.5 \pm 8.2$	$105.5 \pm 11.1$
HDFS2 – 764	$128.8 \pm 4.7$	$232.7 \pm 7.7$	$357.2 \pm 7.5$	$414.3 \pm 8.6$
HDFS2 – 740	$78.7 \pm 5.5$	$188.3 \pm 9.1$	$313.0 \pm 9.1$	$421.1 \pm 20.2$
HDFS2 – 781	$-7.3 \pm 6.5$	$-27.2 \pm 10.7$	$14.8 \pm 10.9$	$29.2 \pm 7.3$
HDFS2 – 809	$63.1 \pm 5.1$	$73.0 \pm 8.4$	$84.2 \pm 8.3$	$91.8 \pm 10.6$
HDFS2 – 790	$278.3 \pm 5.0$	$340.0 \pm 8.2$	$416.9 \pm 8.1$	$473.9 \pm 16.8$
HDFS2 – 786	$70.0 \pm 5.0$	$141.8 \pm 8.3$	$153.7 \pm 8.2$	$198.1 \pm 13.3$
HDFS2 – 776	$25.5 \pm 5.9$	$52.6 \pm 9.8$	$42.1 \pm 9.8$	$45.6 \pm 8.0$

<sup>a</sup> Flux measured with a  $2''.0$  diameter aperture.

<sup>b</sup> Flux measured from SExtractor BEST aperture with a  $2''.0$  minimum diameter

Note – All fluxes in units of  $10^{-31}$  ergs s $^{-1}$ Hz $^{-1}$ cm $^{-2}$ .

Table A.10:  $z_{\text{phot}}$  and  $L^{\text{rest}} - K_{s,AB}^{\text{tot}} < 25$  Sample

ID	$z_{\text{phot}}$	$L_U^{\text{rest}}$	$L_B^{\text{rest}}$	$L_V^{\text{rest}}$
		$10^{10} h^{-2} L_{\odot}$	$10^{10} h^{-2} L_{\odot}$	$10^{10} h^{-2} L_{\odot}$
HDFS2 – 49	1.230	4.68	4.30	4.17
HDFS2 – 61	$0.96^{0.60}_{0.52}$	$0.18^{0.67}_{0.16}$	$0.12^{0.42}_{0.11}$	$0.12^{0.25}_{0.11}$
HDFS2 – 66	$1.10^{0.18}_{0.06}$	$0.84^{0.91}_{0.19}$	$0.93^{0.73}_{0.18}$	$1.03^{0.60}_{0.16}$
HDFS2 – 75	$0.96^{0.00}_{0.94}$	$0.18^{0.00}_{0.18}$	$0.11^{0.00}_{0.11}$	$0.08^{0.00}_{0.08}$
HDFS2 – 93	$0.62^{0.10}_{0.02}$	$0.12^{0.12}_{0.02}$	$0.17^{0.13}_{0.02}$	$0.23^{0.13}_{0.02}$
HDFS2 – 98	$4.20^{0.08}_{0.08}$	$19.33^{1.49}_{1.36}$	.....	.....
HDFS2 – 103	$2.52^{0.20}_{2.18}$ a	$3.46^{0.59}_{3.43}$	$1.50^{0.34}_{1.48}$	$0.86^{0.17}_{0.85}$
HDFS2 – 105	$0.50^{0.02}_{0.26}$	$0.59^{0.06}_{0.51}$	$0.37^{0.04}_{0.32}$	$0.30^{0.02}_{0.25}$
HDFS2 – 112	$1.12^{0.12}_{0.16}$	$1.94^{1.04}_{0.86}$	$1.78^{0.81}_{0.80}$	$1.79^{0.63}_{0.67}$
HDFS2 – 114	0.560	1.03	0.80	0.71
HDFS2 – 119	$0.94^{0.04}_{0.06}$	$0.29^{0.04}_{0.05}$	$0.17^{0.02}_{0.03}$	$0.11^{0.01}_{0.02}$
HDFS2 – 120	$0.46^{3.40}_{0.14}$ a	$0.08^{17.25}_{0.05}$	$0.06^{7.73}_{0.04}$	$0.05^{4.83}_{0.03}$
HDFS2 – 124	$0.82^{0.06}_{0.06}$	$0.07^{0.02}_{0.02}$	$0.06^{0.02}_{0.01}$	$0.05^{0.01}_{0.01}$
HDFS2 – 127	$0.88^{0.04}_{0.04}$	$0.12^{0.02}_{0.02}$	$0.07^{0.01}_{0.01}$	$0.04^{0.00}_{0.00}$
HDFS2 – 130	$1.00^{0.10}_{0.50}$	$0.53^{0.19}_{0.44}$	$0.32^{0.12}_{0.27}$	$0.22^{0.06}_{0.18}$
HDFS2 – 136 b	$1.42^{0.22}_{0.18}$	$1.46^{0.79}_{0.57}$	$1.00^{0.44}_{0.31}$	$0.77^{0.29}_{0.18}$
HDFS2 – 140	$1.18^{0.14}_{0.12}$	$2.46^{1.20}_{0.72}$	$1.82^{0.75}_{0.56}$	$1.56^{0.55}_{0.41}$
HDFS2 – 144 b	$2.52^{0.18}_{0.48}$ a	$3.84^{0.59}_{1.75}$	$1.67^{0.19}_{0.62}$	$0.79^{0.25}_{0.13}$
HDFS2 – 146	$4.28^{0.08}_{3.66}$ a	$5.93^{0.05}_{5.90}$	.....	.....
HDFS2 – 147	$0.46^{0.04}_{0.24}$	$0.24^{0.06}_{0.20}$	$0.14^{0.04}_{0.12}$	$0.11^{0.02}_{0.09}$
HDFS2 – 148	$0.72^{0.06}_{0.14}$	$0.40^{0.12}_{0.19}$	$0.29^{0.07}_{0.13}$	$0.20^{0.04}_{0.08}$
HDFS2 – 150	$0.44^{0.10}_{0.16}$	$0.27^{0.23}_{0.20}$	$0.21^{0.19}_{0.15}$	$0.22^{0.14}_{0.15}$
HDFS2 – 152	$0.98^{0.04}_{0.18}$	$1.11^{0.15}_{0.52}$	$0.75^{0.12}_{0.36}$	$0.60^{0.10}_{0.25}$
HDFS2 – 154	$0.84^{0.02}_{0.82}$	$0.34^{0.02}_{0.34}$	$0.20^{0.01}_{0.20}$	$0.14^{0.01}_{0.14}$
HDFS2 – 156	$2.18^{0.36}_{0.22}$	$1.19^{0.64}_{0.20}$	$0.54^{0.27}_{0.09}$	$0.45^{0.02}_{0.12}$
HDFS2 – 158	$0.38^{3.60}_{0.04}$ a	$0.06^{28.26}_{0.02}$	$0.05^{12.75}_{0.01}$	$0.04^{7.94}_{0.01}$
HDFS2 – 160	$1.06^{0.12}_{0.24}$	$1.76^{0.76}_{0.94}$	$1.23^{0.50}_{0.73}$	$1.04^{0.35}_{0.55}$
HDFS2 – 163 b,d	$2.56^{0.32}_{0.02}$	$0.59^{0.45}_{0.02}$	$0.91^{0.56}_{0.03}$	$0.70^{0.14}_{0.02}$
HDFS2 – 165	$4.14^{0.16}_{0.16}$	$3.44^{0.77}_{0.68}$	.....	.....
HDFS2 – 166 b	$2.56^{0.40}_{0.02}$	$3.71^{1.58}_{0.19}$	$1.97^{0.62}_{0.03}$	$1.23^{0.00}_{0.12}$
HDFS2 – 168	$0.48^{3.30}_{0.02}$ a	$0.06^{7.00}_{0.01}$	$0.04^{1.52}_{0.00}$	$0.03^{0.42}_{0.00}$
HDFS2 – 170	$0.50^{0.14}_{0.04}$ a	$0.10^{0.11}_{0.02}$	$0.07^{0.07}_{0.02}$	$0.06^{0.04}_{0.01}$
HDFS2 – 171	$1.62^{0.00}_{0.08}$ a	$1.36^{0.00}_{0.14}$	$0.82^{0.00}_{0.09}$	$0.53^{0.00}_{0.14}$
HDFS2 – 172	$0.48^{0.20}_{0.16}$	$0.35^{0.74}_{0.24}$	$0.28^{0.52}_{0.20}$	$0.28^{0.41}_{0.18}$
HDFS2 – 174	$2.78^{0.20}_{1.54}$ a	$6.00^{1.26}_{4.99}$	$3.58^{0.67}_{3.11}$	$2.22^{0.43}_{1.92}$
HDFS2 – 177	$2.06^{0.28}_{0.44}$	$4.92^{2.13}_{2.21}$	$2.65^{0.73}_{1.38}$	$1.65^{0.43}_{0.73}$

Table A.10:  $z_{\text{phot}}$  and  $L^{\text{rest}}$  – continued

ID	$z_{\text{phot}}$	$L_U^{\text{rest}}$	$L_B^{\text{rest}}$	$L_V^{\text{rest}}$
HDFS2 – 180	$0.64^{+0.12}_{-0.46}$	$0.30^{+0.19}_{-0.29}$	$0.18^{+0.10}_{-0.18}$	$0.12^{+0.05}_{-0.11}$
HDFS2 – 183	$1.28^{+0.08}_{-0.12}$	$1.76^{+0.44}_{-0.51}$	$1.32^{+0.23}_{-0.36}$	$1.12^{+0.18}_{-0.27}$
HDFS2 – 184 <sup>b</sup>	$2.28^{+0.26}_{-2.24}$ a	$2.34^{+1.13}_{-2.34}$	$1.23^{+0.38}_{-1.23}$	$1.05^{+0.01}_{-1.05}$
HDFS2 – 185	$0.52^{+3.44}_{-0.02}$ a	$0.08^{+12.01}_{-0.01}$	$0.06^{+4.65}_{-0.01}$	$0.04^{+2.54}_{-0.00}$
HDFS2 – 189	$0.80^{+0.08}_{-0.08}$	$0.15^{+0.05}_{-0.04}$	$0.11^{+0.04}_{-0.03}$	$0.09^{+0.02}_{-0.02}$
HDFS2 – 191	$0.94^{+0.04}_{-0.20}$	$0.46^{+0.07}_{-0.22}$	$0.27^{+0.05}_{-0.13}$	$0.20^{+0.02}_{-0.09}$
HDFS2 – 192	$1.54^{+0.16}_{-0.44}$ a	$1.09^{+0.23}_{-0.64}$	$0.54^{+0.24}_{-0.27}$	$0.40^{+0.11}_{-0.18}$
HDFS2 – 195	$4.38^{+0.12}_{-0.20}$	$8.58^{+0.64}_{-1.08}$	.....	.....
HDFS2 – 198	$0.10^{+0.38}_{-0.02}$	$0.00^{+0.12}_{-0.00}$	$0.00^{+0.07}_{-0.00}$	$0.00^{+0.06}_{-0.00}$
HDFS2 – 199	$3.58^{+0.06}_{-3.16}$ a	$3.80^{+0.16}_{-3.78}$	$1.69^{+0.11}_{-1.68}$	.....
HDFS2 – 201	$1.54^{+0.08}_{-1.48}$ a	$1.20^{+0.18}_{-1.20}$	$0.58^{+0.08}_{-0.58}$	$0.33^{+0.13}_{-0.33}$
HDFS2 – 203	$3.64^{+0.10}_{-3.06}$ a	$13.69^{+0.85}_{-13.58}$	$5.41^{+0.00}_{-5.34}$	.....
HDFS2 – 206	$4.40^{+0.08}_{-0.06}$	$6.94^{+0.23}_{-0.12}$	.....	.....
HDFS2 – 207	$0.90^{+0.36}_{-0.08}$	$0.18^{+0.34}_{-0.04}$	$0.10^{+0.12}_{-0.02}$	$0.06^{+0.08}_{-0.01}$
HDFS2 – 209	$3.12^{+0.24}_{-0.28}$ a	$5.05^{+0.89}_{-1.14}$	$2.39^{+0.39}_{-0.37}$	$1.53^{+0.15}_{-0.13}$
HDFS2 – 214	$0.64^{+3.78}_{-0.06}$ a	$0.05^{+6.35}_{-0.01}$	$0.04^{+2.63}_{-0.01}$	$0.03^{+1.53}_{-0.01}$
HDFS2 – 217	$0.46^{+2.16}_{-0.10}$ a	$0.09^{+6.44}_{-0.04}$	$0.05^{+3.39}_{-0.02}$	$0.03^{+2.24}_{-0.01}$
HDFS2 – 219	$0.44^{+0.06}_{-0.02}$	$0.23^{+0.15}_{-0.04}$	$0.34^{+0.20}_{-0.05}$	$0.49^{+0.19}_{-0.06}$
HDFS2 – 221	$1.90^{+6.28}_{-0.26}$	$1.01^{+0.47}_{-0.33}$	$0.61^{+0.20}_{-0.23}$	$0.46^{+0.17}_{-0.17}$
HDFS2 – 222	$1.38^{+0.54}_{-1.18}$ a	$0.75^{+1.03}_{-0.75}$	$0.44^{+0.51}_{-0.44}$	$0.30^{+0.35}_{-0.30}$
HDFS2 – 224	$0.10^{+0.92}_{-0.08}$ a	$0.00^{+0.25}_{-0.00}$	$0.00^{+0.15}_{-0.00}$	$0.00^{+0.10}_{-0.00}$
HDFS2 – 225	$0.78^{+0.08}_{-0.24}$	$0.20^{+0.07}_{-0.13}$	$0.13^{+0.04}_{-0.08}$	$0.09^{+0.03}_{-0.06}$
HDFS2 – 227	$0.60^{+0.20}_{-0.16}$ a	$0.03^{+0.06}_{-0.02}$	$0.03^{+0.03}_{-0.02}$	$0.02^{+0.03}_{-0.01}$
HDFS2 – 230	$1.34^{+0.62}_{-0.12}$	$1.06^{+2.52}_{-0.32}$	$0.84^{+1.75}_{-0.22}$	$0.74^{+1.37}_{-0.17}$
HDFS2 – 231 <sup>b</sup>	$2.04^{+0.18}_{-0.68}$	$4.04^{+1.12}_{-2.68}$	$2.44^{+0.36}_{-1.60}$	$1.72^{+0.24}_{-1.11}$
HDFS2 – 232	$1.58^{+0.06}_{-0.18}$	$0.49^{+0.06}_{-0.15}$	$0.31^{+0.04}_{-0.08}$	$0.25^{+0.02}_{-0.06}$
HDFS2 – 233 <sup>b</sup>	$0.16^{+3.46}_{-0.04}$ a	$0.01^{+22.05}_{-0.00}$	$0.01^{+7.72}_{-0.00}$	$0.00^{+3.95}_{-0.00}$
HDFS2 – 234	$0.88^{+0.08}_{-0.12}$	$0.33^{+0.07}_{-0.11}$	$0.19^{+0.04}_{-0.06}$	$0.12^{+0.02}_{-0.03}$
HDFS2 – 236	$1.30^{+0.02}_{-0.24}$	$0.36^{+0.03}_{-0.22}$	$0.34^{+0.02}_{-0.19}$	$0.35^{+0.02}_{-0.17}$
HDFS2 – 239	$3.94^{+0.14}_{-0.16}$	$7.15^{+0.46}_{-0.81}$	$3.94^{+0.27}_{-0.36}$	.....
HDFS2 – 240	$0.62^{+0.08}_{-0.44}$	$0.27^{+0.13}_{-0.27}$	$0.21^{+0.09}_{-0.20}$	$0.17^{+0.06}_{-0.16}$
HDFS2 – 241	$2.30^{+0.14}_{-1.04}$ a	$1.79^{+0.37}_{-1.26}$	$1.02^{+0.09}_{-0.77}$	$0.71^{+0.11}_{-0.56}$
HDFS2 – 244	$1.00^{+0.16}_{-0.24}$	$0.81^{+0.50}_{-0.42}$	$0.46^{+0.33}_{-0.24}$	$0.31^{+0.24}_{-0.13}$
HDFS2 – 245	$0.60^{+0.40}_{-0.16}$	$0.12^{+0.31}_{-0.06}$	$0.07^{+0.19}_{-0.04}$	$0.05^{+0.12}_{-0.02}$
HDFS2 – 252	$3.32^{+0.20}_{-0.22}$	$5.35^{+2.39}_{-1.74}$	$3.20^{+8.46}_{-0.31}$	.....
HDFS2 – 254 <sup>c</sup>	$9.62^{+0.14}_{-7.30}$ a	.....	.....	.....
HDFS2 – 255	$0.98^{+0.04}_{-0.20}$	$0.62^{+0.09}_{-0.30}$	$0.38^{+0.06}_{-0.18}$	$0.26^{+0.03}_{-0.12}$
HDFS2 – 260 <sup>b</sup>	$2.54^{+0.22}_{-0.26}$	$4.40^{+1.63}_{-1.71}$	$3.25^{+1.06}_{-0.99}$	$2.87^{+0.75}_{-0.76}$



Table A.10:  $z_{phot}$  and  $L^{rest}$ – continued

ID	$z_{phot}$	$L_U^{rest}$	$L_B^{rest}$	$L_V^{rest}$
HDFS2 – 263	$2.60^{0.40}_a$	$1.98^{0.99}_{0.84}$	$1.16^{0.59}_{0.46}$	$0.83^{0.32}_{0.28}$
HDFS2 – 264 <sup>b</sup>	$2.14^{0.02}_a$	$2.51^{0.07}_{2.06}$	$1.58^{0.04}_{1.27}$	$1.21^{0.01}_{0.96}$
HDFS2 – 267 <sup>b</sup>	$2.14^{0.06}_{0.48}$	$3.15^{0.31}_{1.56}$	$1.98^{0.01}_{1.03}$	$1.33^{0.07}_{0.58}$
HDFS2 – 278	$0.26^{0.06}_{0.04}$	$0.26^{0.25}_{0.10}$	$0.25^{0.20}_{0.09}$	$0.28^{0.20}_{0.10}$
HDFS2 – 279 <sup>b</sup>	$1.98^{0.78}_a$	$1.69^{1.47}_{0.17}$	$0.72^{0.31}_{0.07}$	$0.31^{0.89}_{0.06}$
HDFS2 – 280	$3.26^{0.36}_{0.10}$	$5.47^{3.17}_{0.63}$	$3.01^{0.87}_{0.08}$	.....
HDFS2 – 287	$0.80^{0.22}_{0.40}$	$0.17^{0.15}_{0.14}$	$0.08^{0.09}_{0.07}$	$0.06^{0.06}_{0.05}$
HDFS2 – 290 <sup>b</sup>	$3.64^{0.10}_a$	$13.86^{0.83}_{13.86}$	$4.87^{0.00}_{4.87}$	.....
HDFS2 – 292	0.696	1.11	0.68	0.46
HDFS2 – 293	$0.46^{3.24}_a$	$0.13^{20.49}_{0.03}$	$0.09^{9.24}_{0.02}$	$0.07^{5.76}_{0.01}$
HDFS2 – 296	0.580	2.99	2.86	2.94
HDFS2 – 301	$1.36^{0.32}_{0.04}$	$0.83^{1.53}_{0.13}$	$1.11^{1.33}_{0.13}$	$1.40^{1.37}_{0.14}$
HDFS2 – 303	$1.42^{0.16}_a$	$2.42^{0.88}_{2.42}$	$1.30^{0.28}_{1.30}$	$0.88^{0.34}_{0.87}$
HDFS2 – 311	0.565	0.81	0.53	0.39
HDFS2 – 312	$1.00^{0.20}_{0.66}$	$1.09^{0.87}_{1.01}$	$0.65^{0.49}_{0.61}$	$0.46^{0.29}_{0.43}$
HDFS2 – 313	$3.48^{0.10}_{0.30}$	$7.74^{1.06}_{2.33}$	$8.87^{1.05}_{2.97}$	.....
HDFS2 – 314	$1.30^{0.10}_{0.28}$	$0.19^{0.06}_{0.12}$	$0.16^{0.04}_{0.09}$	$0.15^{0.04}_{0.08}$
HDFS2 – 315 <sup>b</sup>	$2.52^{0.18}_{0.38}$	$3.29^{0.63}_{1.33}$	$1.48^{0.32}_{0.45}$	$0.75^{0.21}_{0.00}$
HDFS2 – 316	$1.16^{0.14}_{0.62}$	$0.68^{0.25}_{0.57}$	$0.39^{0.12}_{0.34}$	$0.26^{0.07}_{0.22}$
HDFS2 – 317	$1.44^{0.24}_{0.34}$	$1.18^{0.79}_{0.81}$	$1.02^{0.56}_{0.65}$	$0.97^{0.55}_{0.55}$
HDFS2 – 326	$0.64^{0.10}_{0.46}$	$0.14^{0.09}_{0.13}$	$0.11^{0.06}_{0.11}$	$0.10^{0.05}_{0.09}$
HDFS2 – 327	$1.06^{0.20}_{0.10}$	$0.77^{0.73}_{0.22}$	$0.63^{0.51}_{0.19}$	$0.60^{0.38}_{0.15}$
HDFS2 – 328	$0.58^{0.12}_{0.04}$	$0.11^{0.10}_{0.02}$	$0.08^{0.06}_{0.02}$	$0.07^{0.04}_{0.01}$
HDFS2 – 331 <sup>b</sup>	$2.22^{0.64}_{0.20}$	$2.81^{3.54}_{0.69}$	$1.65^{1.56}_{0.34}$	$1.29^{1.32}_{0.29}$
HDFS2 – 332	$3.52^{0.16}_{0.18}$	$8.61^{1.10}_{1.63}$	$4.04^{0.90}_{0.49}$	.....
HDFS2 – 335	$3.20^{0.56}_a$	$2.53^{2.61}_{0.96}$	$1.77^{0.98}_{0.51}$	$1.16^{0.67}_{0.12}$
HDFS2 – 337	$1.64^{6.80}_a$	$0.10^{77.64}_{0.01}$	$0.36^{4.88}_{0.03}$	$0.40^{28.98}_{0.00}$
HDFS2 – 339	$1.74^{0.12}_a$	$3.00^{0.38}_{2.99}$	$1.26^{0.16}_{1.26}$	$0.96^{0.19}_{0.96}$
HDFS2 – 340	$0.34^{0.12}_{0.10}$	$0.16^{0.22}_{0.10}$	$0.11^{0.15}_{0.07}$	$0.10^{0.11}_{0.06}$
HDFS2 – 344	$0.58^{0.18}_{0.06}$	$0.08^{0.10}_{0.02}$	$0.05^{0.06}_{0.01}$	$0.04^{0.02}_{0.01}$
HDFS2 – 346	$0.68^{0.10}_{0.26}$	$1.09^{0.65}_{0.86}$	$0.81^{0.39}_{0.63}$	$0.77^{0.37}_{0.56}$
HDFS2 – 349	$0.10^{0.38}_{0.00}$	$0.00^{0.08}_{0.00}$	$0.00^{0.04}_{0.00}$	$0.00^{0.03}_{0.00}$
HDFS2 – 353	$3.54^{0.34}_{0.18}$	$1.30^{0.71}_{0.15}$	$1.56^{0.82}_{0.31}$	.....
HDFS2 – 354	$1.60^{0.02}_{0.06}$	$0.97^{0.03}_{0.10}$	$0.59^{0.02}_{0.05}$	$0.34^{0.06}_{0.04}$
HDFS2 – 355	$0.10^{0.38}_a$	$0.00^{0.05}_{0.00}$	$0.00^{0.03}_{0.00}$	$0.00^{0.02}_{0.00}$
HDFS2 – 356 <sup>b</sup>	$2.04^{0.18}_{0.50}$	$3.09^{0.86}_{1.60}$	$1.79^{0.25}_{1.03}$	$1.16^{0.19}_{0.55}$
HDFS2 – 357	1.270	6.24	5.34	4.91
HDFS2 – 359	$1.08^{0.22}_{0.10}$	$0.88^{0.96}_{0.26}$	$0.77^{0.70}_{0.24}$	$0.76^{0.53}_{0.19}$

Table A.10:  $z_{phot}$  and  $L^{rest}$  – continued

ID	$z_{phot}$	$L_U^{rest}$	$L_B^{rest}$	$L_V^{rest}$
HDFS2 – 361	$0.14_{-0.06}^{+0.02}$	$0.03_{-0.02}^{+0.01}$	$0.03_{-0.02}^{+0.01}$	$0.03_{-0.02}^{+0.01}$
HDFS2 – 365	$1.62_{-1.46}^{+0.00} \text{ a}$	$1.55_{-1.54}^{+0.00}$	$0.74_{-0.73}^{+0.00}$	$0.47_{-0.47}^{+0.00}$
HDFS2 – 368 <sup>b,d</sup>	$3.12_{-0.16}^{+0.10}$	$0.56_{-0.06}^{+0.42}$	$0.58_{-0.27}^{+0.18}$	$2.06_{-0.58}^{+0.30}$
HDFS2 – 370	$0.98_{-0.04}^{+4.58} \text{ a}$	$0.11_{-0.02}^{+61.86}$	$0.15_{-0.02}^{+37.16}$	$0.19_{-0.02}^{+27.20}$
HDFS2 – 371	$1.20_{-0.18}^{+0.04}$	$0.59_{-0.27}^{+0.09}$	$0.50_{-0.22}^{+0.06}$	$0.46_{-0.17}^{+0.05}$
HDFS2 – 374	$0.14_{-0.12}^{+1.80} \text{ a}$	$0.00_{-0.00}^{+1.55}$	$0.00_{-0.00}^{+0.58}$	$0.00_{-0.00}^{+0.23}$
HDFS2 – 376	$1.26_{-0.20}^{+0.14}$	$0.78_{-0.36}^{+0.37}$	$0.63_{-0.29}^{+0.22}$	$0.55_{-0.22}^{+0.17}$
HDFS2 – 377	$0.96_{-0.04}^{+0.20} \text{ a}$	$0.21_{-0.04}^{+0.33}$	$0.28_{-0.05}^{+0.32}$	$0.36_{-0.05}^{+0.29}$
HDFS2 – 379	$0.42_{-0.18}^{+0.04}$	$0.29_{-0.23}^{+0.08}$	$0.20_{-0.15}^{+0.06}$	$0.16_{-0.12}^{+0.03}$
HDFS2 – 382 <sup>b</sup>	$2.16_{-0.82}^{+0.10} \text{ a}$	$10.82_{-7.94}^{+2.15}$	$6.09_{-4.20}^{+0.76}$	$4.03_{-2.58}^{+0.34}$
HDFS2 – 383	$0.50_{-0.14}^{+0.08}$	$0.35_{-0.21}^{+0.18}$	$0.24_{-0.14}^{+0.12}$	$0.19_{-0.10}^{+0.07}$
HDFS2 – 390	$0.52_{-0.34}^{+0.14}$	$0.17_{-0.15}^{+0.16}$	$0.10_{-0.09}^{+0.09}$	$0.07_{-0.07}^{+0.05}$
HDFS2 – 392	$0.54_{-0.08}^{+3.74} \text{ a}$	$0.03_{-0.01}^{+9.03}$	$0.02_{-0.01}^{+3.84}$	$0.02_{-0.01}^{+2.28}$
HDFS2 – 394 <sup>b</sup>	$1.46_{-0.16}^{+0.54}$	$2.36_{-0.79}^{+4.01}$	$1.76_{-0.49}^{+2.75}$	$1.51_{-0.35}^{+1.85}$
HDFS2 – 398	$0.20_{-0.12}^{+0.26}$	$0.01_{-0.01}^{+0.06}$	$0.01_{-0.01}^{+0.04}$	$0.00_{-0.00}^{+0.02}$
HDFS2 – 402	$0.48_{-0.06}^{+0.10}$	$0.10_{-0.03}^{+0.07}$	$0.06_{-0.02}^{+0.04}$	$0.05_{-0.01}^{+0.02}$
HDFS2 – 404	$1.16_{-0.10}^{+0.12}$	$1.49_{-0.49}^{+0.85}$	$1.65_{-0.50}^{+0.76}$	$1.84_{-0.45}^{+0.67}$
HDFS2 – 405 <sup>b</sup>	$2.42_{-1.18}^{+0.44} \text{ a}$	$2.90_{-2.31}^{+1.50}$	$1.32_{-1.00}^{+0.75}$	$1.08_{-0.87}^{+0.66}$
HDFS2 – 406	$0.72_{-0.14}^{+0.04}$	$0.11_{-0.05}^{+0.02}$	$0.07_{-0.03}^{+0.01}$	$0.04_{-0.01}^{+0.00}$
HDFS2 – 407	$0.02_{-0.00}^{+1.60} \text{ a}$	$0.00_{-0.00}^{+1.23}$	$0.00_{-0.00}^{+0.59}$	$0.00_{-0.00}^{+0.41}$
HDFS2 – 409 <sup>c</sup>	$9.70_{-3.64}^{+0.26} \text{ a}$	.....	.....	.....
HDFS2 – 411	$2.08_{-1.72}^{+0.46} \text{ a}$	$2.91_{-2.86}^{+1.99}$	$1.32_{-1.30}^{+0.68}$	$0.85_{-0.84}^{+0.61}$
HDFS2 – 412	$0.16_{-0.06}^{+0.32}$	$0.01_{-0.00}^{+0.13}$	$0.01_{-0.00}^{+0.08}$	$0.00_{-0.00}^{+0.06}$
HDFS2 – 413	$1.08_{-0.54}^{+0.38}$	$0.35_{-0.28}^{+0.46}$	$0.22_{-0.19}^{+0.23}$	$0.18_{-0.15}^{+0.16}$
HDFS2 – 414	$0.88_{-0.14}^{+2.62} \text{ a}$	$0.12_{-0.05}^{+0.55}$	$0.06_{-0.02}^{+1.44}$	$0.03_{-0.01}^{+2.66}$
HDFS2 – 415	$0.54_{-0.06}^{+0.10}$	$0.12_{-0.03}^{+0.08}$	$0.07_{-0.02}^{+0.04}$	$0.05_{-0.01}^{+0.02}$
HDFS2 – 418	$0.46_{-0.24}^{+3.40} \text{ a}$	$0.10_{-0.09}^{+20.82}$	$0.07_{-0.06}^{+8.88}$	$0.06_{-0.05}^{+5.28}$
HDFS2 – 419	0.465	0.92	0.97	1.12
HDFS2 – 421	$4.86_{-0.18}^{+0.32} \text{ a}$	$18.65_{-2.65}^{+4.11}$	.....	.....
HDFS2 – 422 <sup>b</sup>	2.028	11.99	7.08	4.66
HDFS2 – 423 <sup>b</sup>	$2.76_{-0.20}^{+0.18}$	$6.50_{-0.81}^{+1.21}$	$3.94_{-1.03}^{+0.71}$	$2.83_{-0.57}^{+0.39}$
HDFS2 – 424	$2.28_{-1.08}^{+0.72} \text{ a}$	$1.94_{-1.68}^{+2.99}$	$1.36_{-1.17}^{+1.81}$	$1.20_{-1.04}^{+1.58}$
HDFS2 – 426	$0.42_{-0.06}^{+3.70} \text{ a}$	$0.03_{-0.01}^{+12.94}$	$0.02_{-0.01}^{+4.72}$	$0.02_{-0.01}^{+2.45}$
HDFS2 – 427	$0.68_{-0.02}^{+0.12}$	$0.11_{-0.01}^{+0.11}$	$0.14_{-0.01}^{+0.12}$	$0.17_{-0.01}^{+0.11}$
HDFS2 – 428	$0.94_{-0.06}^{+0.16}$	$0.09_{-0.02}^{+0.07}$	$0.08_{-0.02}^{+0.07}$	$0.10_{-0.02}^{+0.06}$
HDFS2 – 431	$0.98_{-0.28}^{+0.10}$	$0.61_{-0.38}^{+0.22}$	$0.36_{-0.22}^{+0.15}$	$0.27_{-0.15}^{+0.07}$
HDFS2 – 433 <sup>b</sup>	$1.34_{-0.84}^{+0.68} \text{ a}$	$1.04_{-0.97}^{+2.06}$	$0.65_{-0.61}^{+1.19}$	$0.48_{-0.45}^{+0.73}$
HDFS2 – 434	$0.92_{-0.16}^{+0.04}$	$0.82_{-0.33}^{+0.12}$	$0.50_{-0.20}^{+0.07}$	$0.34_{-0.12}^{+0.03}$

Table A.10:  $z_{\text{phot}}$  and  $L^{\text{rest}}$  – continued

ID	$z_{\text{phot}}$	$L_U^{\text{rest}}$	$L_B^{\text{rest}}$	$L_V^{\text{rest}}$
HDFS2 – 435	0.20 <sup>1.74</sup> <sub>0.00</sub> a	0.00 <sup>1.51</sup> <sub>0.00</sub>	0.00 <sup>0.79</sup> <sub>0.00</sub>	0.00 <sup>0.34</sup> <sub>0.00</sub>
HDFS2 – 436	1.439	5.52	3.52	2.92
HDFS2 – 438	0.46 <sup>0.06</sup> <sub>0.26</sub>	0.26 <sup>0.11</sup> <sub>0.24</sub>	0.20 <sup>0.09</sup> <sub>0.17</sub>	0.19 <sup>0.05</sup> <sub>0.16</sub>
HDFS2 – 447	0.22 <sup>1.40</sup> <sub>0.04</sub> a	0.05 <sup>8.87</sup> <sub>0.02</sub>	0.03 <sup>4.23</sup> <sub>0.01</sub>	0.02 <sup>3.45</sup> <sub>0.01</sub>
HDFS2 – 448	2.04 <sup>0.12</sup> <sub>1.80</sub> a	2.59 <sup>0.39</sup> <sub>2.58</sub>	1.49 <sup>0.11</sup> <sub>1.49</sub>	0.96 <sup>0.06</sup> <sub>0.95</sub>
HDFS2 – 449	1.52 <sup>0.10</sup> <sub>0.14</sub>	0.90 <sup>0.17</sup> <sub>0.21</sub>	0.44 <sup>0.08</sup> <sub>0.02</sub>	0.38 <sup>0.00</sup> <sub>0.07</sub>
HDFS2 – 451	0.64 <sup>0.12</sup> <sub>0.12</sub>	0.13 <sup>0.07</sup> <sub>0.06</sub>	0.08 <sup>0.04</sup> <sub>0.03</sub>	0.05 <sup>0.02</sup> <sub>0.02</sub>
HDFS2 – 452	0.50 <sup>0.40</sup> <sub>0.24</sub>	0.38 <sup>1.28</sup> <sub>0.31</sub>	0.21 <sup>0.75</sup> <sub>0.17</sub>	0.16 <sup>0.46</sup> <sub>0.13</sub>
HDFS2 – 453 b	2.14 <sup>0.60</sup> <sub>1.92</sub> a	2.19 <sup>2.07</sup> <sub>2.18</sub>	1.09 <sup>0.41</sup> <sub>1.09</sub>	0.61 <sup>0.61</sup> <sub>0.61</sub>
HDFS2 – 459 b	3.12 <sup>0.14</sup> <sub>2.78</sub> a	5.79 <sup>1.84</sup> <sub>5.76</sub>	3.17 <sup>0.29</sup> <sub>3.15</sub>	2.02 <sup>0.09</sup> <sub>2.01</sub>
HDFS2 – 466	0.46 <sup>0.06</sup> <sub>0.12</sub>	0.17 <sup>0.06</sup> <sub>0.09</sub>	0.10 <sup>0.04</sup> <sub>0.06</sub>	0.08 <sup>0.02</sup> <sub>0.04</sub>
HDFS2 – 467	2.26 <sup>0.84</sup> <sub>0.26</sub> a	1.64 <sup>4.10</sup> <sub>0.62</sub>	1.38 <sup>2.98</sup> <sub>0.54</sub>	1.42 <sup>2.67</sup> <sub>0.51</sub>
HDFS2 – 469 c	2.22 <sup>0.12</sup> <sub>0.28</sub>	.....	.....	.....
HDFS2 – 470	0.50 <sup>3.36</sup> <sub>0.02</sub> a	0.05 <sup>5.19</sup> <sub>0.00</sub>	0.03 <sup>2.18</sup> <sub>0.00</sub>	0.02 <sup>1.28</sup> <sub>0.00</sub>
HDFS2 – 475 b	2.04 <sup>0.20</sup> <sub>0.42</sub>	1.99 <sup>0.74</sup> <sub>0.79</sub>	1.18 <sup>0.20</sup> <sub>0.61</sub>	0.77 <sup>0.09</sup> <sub>0.32</sub>
HDFS2 – 481	0.10 <sup>1.94</sup> <sub>0.08</sub> a	0.00 <sup>1.24</sup> <sub>0.00</sub>	0.00 <sup>0.60</sup> <sub>0.00</sub>	0.00 <sup>0.39</sup> <sub>0.00</sub>
HDFS2 – 483 b	2.74 <sup>0.18</sup> <sub>2.38</sub> a	3.06 <sup>0.41</sup> <sub>3.02</sub>	1.57 <sup>0.20</sup> <sub>1.55</sub>	1.07 <sup>0.15</sup> <sub>1.06</sub>
HDFS2 – 487	2.92 <sup>0.20</sup> <sub>0.40</sub>	2.50 <sup>0.52</sup> <sub>0.79</sub>	1.51 <sup>0.16</sup> <sub>0.58</sub>	1.04 <sup>0.06</sup> <sub>0.33</sub>
HDFS2 – 493 b	2.24 <sup>0.16</sup> <sub>1.20</sub> a	1.78 <sup>0.43</sup> <sub>1.48</sub>	0.83 <sup>0.17</sup> <sub>0.68</sub>	0.56 <sup>0.08</sup> <sub>0.46</sub>
HDFS2 – 498 b	2.08 <sup>0.20</sup> <sub>0.24</sub>	1.01 <sup>0.35</sup> <sub>0.30</sub>	0.40 <sup>0.11</sup> <sub>0.03</sub>	0.23 <sup>0.13</sup> <sub>0.09</sub>
HDFS2 – 500	1.30 <sup>0.26</sup> <sub>0.16</sub>	1.58 <sup>1.13</sup> <sub>0.56</sub>	1.09 <sup>0.53</sup> <sub>0.37</sub>	0.90 <sup>0.47</sup> <sub>0.28</sub>
HDFS2 – 502	3.16 <sup>0.22</sup> <sub>0.34</sub>	4.41 <sup>1.43</sup> <sub>1.38</sub>	3.36 <sup>0.79</sup> <sub>1.28</sub>	3.06 <sup>0.13</sup> <sub>0.88</sub>
HDFS2 – 506	3.62 <sup>0.12</sup> <sub>0.32</sub>	4.63 <sup>0.36</sup> <sub>1.40</sub>	2.15 <sup>0.31</sup> <sub>0.47</sub>	.....
HDFS2 – 511	1.24 <sup>0.12</sup> <sub>0.76</sub>	1.21 <sup>0.44</sup> <sub>1.11</sub>	0.80 <sup>0.19</sup> <sub>0.75</sub>	0.63 <sup>0.15</sup> <sub>0.59</sub>
HDFS2 – 513	0.76 <sup>0.02</sup> <sub>0.12</sub>	0.14 <sup>0.01</sup> <sub>0.06</sub>	0.09 <sup>0.01</sup> <sub>0.04</sub>	0.06 <sup>0.00</sup> <sub>0.02</sub>
HDFS2 – 515 b	2.52 <sup>0.10</sup> <sub>0.20</sub>	3.08 <sup>0.48</sup> <sub>0.64</sub>	1.72 <sup>0.30</sup> <sub>0.25</sub>	0.95 <sup>0.17</sup> <sub>0.00</sub>
HDFS2 – 517	0.580	2.82	1.98	1.68
HDFS2 – 518	0.582	0.46	0.30	0.26
HDFS2 – 519	1.40 <sup>0.06</sup> <sub>0.44</sub>	1.74 <sup>0.24</sup> <sub>1.10</sub>	0.96 <sup>0.01</sup> <sub>0.62</sub>	0.69 <sup>0.07</sup> <sub>0.43</sub>
HDFS2 – 525	0.70 <sup>0.08</sup> <sub>0.12</sub>	0.13 <sup>0.05</sup> <sub>0.06</sub>	0.08 <sup>0.03</sup> <sub>0.03</sub>	0.06 <sup>0.02</sup> <sub>0.02</sub>
HDFS2 – 527	0.48 <sup>0.10</sup> <sub>0.18</sub>	0.16 <sup>0.14</sup> <sub>0.13</sub>	0.15 <sup>0.13</sup> <sub>0.12</sub>	0.17 <sup>0.11</sup> <sub>0.12</sub>
HDFS2 – 529	3.84 <sup>0.08</sup> <sub>3.32</sub> a	6.51 <sup>0.42</sup> <sub>6.47</sub>	3.32 <sup>0.15</sup> <sub>3.29</sub>	.....
HDFS2 – 532	0.98 <sup>0.12</sup> <sub>0.04</sub>	0.33 <sup>0.27</sup> <sub>0.06</sub>	0.45 <sup>0.28</sup> <sub>0.08</sub>	0.58 <sup>0.26</sup> <sub>0.07</sub>
HDFS2 – 542	0.48 <sup>0.08</sup> <sub>0.28</sub>	0.56 <sup>0.32</sup> <sub>0.51</sub>	0.42 <sup>0.24</sup> <sub>0.38</sub>	0.39 <sup>0.17</sup> <sub>0.34</sub>
HDFS2 – 543	0.76 <sup>0.02</sup> <sub>0.12</sub>	0.26 <sup>0.02</sup> <sub>0.11</sub>	0.18 <sup>0.01</sup> <sub>0.07</sub>	0.12 <sup>0.01</sup> <sub>0.04</sub>
HDFS2 – 548	0.28 <sup>2.80</sup> <sub>0.18</sub> a	0.02 <sup>4.81</sup> <sub>0.01</sub>	0.01 <sup>2.03</sup> <sub>0.01</sub>	0.01 <sup>1.15</sup> <sub>0.01</sub>
HDFS2 – 554 b	1.34 <sup>0.34</sup> <sub>0.18</sub>	0.86 <sup>0.83</sup> <sub>0.33</sub>	0.59 <sup>0.47</sup> <sub>0.21</sub>	0.45 <sup>0.32</sup> <sub>0.13</sub>
HDFS2 – 556	0.46 <sup>3.36</sup> <sub>0.12</sub> a	0.07 <sup>11.72</sup> <sub>0.04</sub>	0.05 <sup>4.77</sup> <sub>0.03</sub>	0.04 <sup>2.73</sup> <sub>0.02</sub>

Table A.10:  $z_{\text{phot}}$  and  $L^{\text{rest}}$  – continued

ID	$z_{\text{phot}}$	$L^{\text{rest}}_{\text{U}}$	$L^{\text{rest}}_{\text{B}}$	$L^{\text{rest}}_{\text{V}}$
HDFS2 – 558	$3.10^{+0.10}_{-0.16}$	$4.00^{+0.63}_{-0.53}$	$2.15^{+0.19}_{-0.05}$	$1.32^{+0.09}_{-0.02}$
HDFS2 – 559 <sup>b</sup>	$3.12^{+0.18}_{-0.10}$	$1.63^{+0.16}_{-0.10}$	$1.13^{+0.30}_{-0.16}$	$1.23^{+0.21}_{-0.12}$
HDFS2 – 560	$0.02^{+2.04}_{-0.00}$ <sup>a</sup>	$0.00^{+1.94}_{-0.00}$	$0.00^{+0.88}_{-0.00}$	$0.00^{+0.46}_{-0.00}$
HDFS2 – 561	$0.48^{+0.08}_{-0.16}$	$0.21^{+0.11}_{-0.14}$	$0.14^{+0.07}_{-0.09}$	$0.11^{+0.04}_{-0.07}$
HDFS2 – 566	$0.18^{+3.86}_{-0.00}$ <sup>a</sup>	$0.03^{+311.97}_{-0.00}$	$0.04^{+138.34}_{-0.00}$	$0.05^{+84.90}_{-0.00}$
HDFS2 – 567	$3.90^{+0.26}_{-0.02}$	$3.32^{+1.43}_{-0.10}$	$3.30^{+1.10}_{-0.08}$	.....
HDFS2 – 568	$0.78^{+0.08}_{-0.04}$	$0.12^{+0.05}_{-0.02}$	$0.10^{+0.03}_{-0.01}$	$0.09^{+0.02}_{-0.01}$
HDFS2 – 571	$3.16^{+2.44}_{-2.44}$ <sup>a</sup>	$7.97^{+5.39}_{-7.72}$	$4.52^{+1.16}_{-4.40}$	$2.80^{+0.59}_{-2.73}$
HDFS2 – 572 <sup>b</sup>	$2.42^{+0.28}_{-0.22}$	$1.75^{+0.61}_{-0.44}$	$0.83^{+0.38}_{-0.15}$	$0.72^{+0.26}_{-0.17}$
HDFS2 – 574 <sup>b</sup>	$2.86^{+0.10}_{-0.66}$	$10.00^{+0.70}_{-5.12}$	$5.30^{+0.56}_{-2.69}$	$3.98^{+0.33}_{-2.17}$
HDFS2 – 578	$0.48^{+0.04}_{-0.02}$	$0.10^{+0.03}_{-0.01}$	$0.06^{+0.01}_{-0.01}$	$0.04^{+0.01}_{-0.00}$
HDFS2 – 579	$2.04^{+1.68}_{-0.02}$ <sup>a</sup>	$2.41^{+0.20}_{-2.37}$	$1.26^{+0.08}_{-1.24}$	$0.77^{+0.03}_{-0.76}$
HDFS2 – 581	$0.50^{+0.02}_{-0.04}$	$0.22^{+0.02}_{-0.05}$	$0.14^{+0.02}_{-0.03}$	$0.09^{+0.01}_{-0.02}$
HDFS2 – 582	$1.34^{+0.28}_{-1.06}$ <sup>a</sup>	$1.37^{+0.87}_{-1.34}$	$0.82^{+0.26}_{-0.81}$	$0.59^{+0.31}_{-0.58}$
HDFS2 – 585	$1.86^{+0.06}_{-1.62}$ <sup>a</sup>	$2.82^{+0.17}_{-2.80}$	$1.30^{+0.07}_{-1.29}$	$0.91^{+0.04}_{-0.90}$
HDFS2 – 587	$2.26^{+0.86}_{-0.28}$ <sup>a</sup>	$2.98^{+5.21}_{-1.03}$	$1.75^{+2.80}_{-0.49}$	$1.48^{+2.13}_{-0.47}$
HDFS2 – 590 <sup>b</sup>	$2.92^{+0.14}_{-0.22}$	$3.46^{+0.39}_{-0.44}$	$1.99^{+0.25}_{-0.38}$	$1.56^{+0.11}_{-0.30}$
HDFS2 – 592	$0.28^{+0.06}_{-0.10}$	$0.13^{+0.10}_{-0.09}$	$0.11^{+0.07}_{-0.07}$	$0.10^{+0.06}_{-0.07}$
HDFS2 – 593	$4.38^{+0.06}_{-0.04}$	$11.51^{+0.57}_{-0.12}$	.....	.....
HDFS2 – 595	1.283	4.40	3.65	3.30
HDFS2 – 596	$3.00^{+0.14}_{-0.52}$ <sup>a</sup>	$10.16^{+1.29}_{-4.71}$	$6.04^{+0.16}_{-2.60}$	$4.02^{+0.02}_{-1.59}$
HDFS2 – 601	$0.46^{+0.02}_{-0.38}$ <sup>a</sup>	$0.08^{+0.01}_{-0.08}$	$0.05^{+0.01}_{-0.05}$	$0.03^{+0.00}_{-0.03}$
HDFS2 – 602	$0.50^{+0.08}_{-0.32}$	$0.27^{+0.14}_{-0.25}$	$0.18^{+0.09}_{-0.16}$	$0.14^{+0.05}_{-0.13}$
HDFS2 – 605	$0.70^{+0.12}_{-0.12}$	$0.06^{+0.04}_{-0.03}$	$0.04^{+0.02}_{-0.02}$	$0.03^{+0.02}_{-0.01}$
HDFS2 – 608	0.540	0.26	0.17	0.13
HDFS2 – 614	$3.52^{+0.20}_{-0.22}$	$1.29^{+0.31}_{-0.18}$	$1.80^{+0.49}_{-0.48}$	.....
HDFS2 – 616	$0.48^{+0.12}_{-0.08}$	$0.19^{+0.16}_{-0.07}$	$0.12^{+0.09}_{-0.05}$	$0.09^{+0.05}_{-0.03}$
HDFS2 – 617	$0.26^{+0.08}_{-0.12}$	$0.03^{+0.03}_{-0.02}$	$0.02^{+0.02}_{-0.02}$	$0.01^{+0.01}_{-0.01}$
HDFS2 – 626 <sup>b</sup>	$3.14^{+0.22}_{-0.14}$ <sup>a</sup>	$4.06^{+1.18}_{-0.52}$	$2.10^{+0.31}_{-0.11}$	$1.23^{+0.15}_{-0.05}$
HDFS2 – 628	$4.38^{+0.10}_{-4.36}$ <sup>a</sup>	$12.91^{+1.14}_{-12.91}$	.....	.....
HDFS2 – 632	$4.34^{+0.06}_{-0.06}$	$6.00^{+0.22}_{-0.31}$	.....	.....
HDFS2 – 633	$1.32^{+0.60}_{-0.02}$	$0.66^{+1.56}_{-0.04}$	$0.53^{+1.08}_{-0.02}$	$0.48^{+0.95}_{-0.02}$
HDFS2 – 639	$0.88^{+0.08}_{-0.68}$	$0.15^{+0.05}_{-0.15}$	$0.11^{+0.04}_{-0.11}$	$0.12^{+0.03}_{-0.11}$
HDFS2 – 652	$2.08^{+0.28}_{-0.96}$ <sup>a</sup>	$2.61^{+1.50}_{-2.05}$	$1.58^{+0.49}_{-1.25}$	$1.19^{+0.45}_{-0.94}$
HDFS2 – 657	$1.00^{+0.04}_{-0.24}$	$0.69^{+0.09}_{-0.36}$	$0.41^{+0.06}_{-0.23}$	$0.28^{+0.03}_{-0.14}$
HDFS2 – 668	$1.48^{+0.10}_{-0.32}$	$0.63^{+0.10}_{-0.35}$	$0.38^{+0.06}_{-0.18}$	$0.23^{+0.04}_{-0.06}$
HDFS2 – 669	$1.66^{+0.16}_{-0.50}$ <sup>a</sup>	$0.95^{+0.30}_{-0.62}$	$0.57^{+0.18}_{-0.34}$	$0.39^{+0.17}_{-0.20}$
HDFS2 – 674	$1.48^{+0.06}_{-0.52}$	$0.95^{+0.16}_{-0.64}$	$0.53^{+0.01}_{-0.36}$	$0.36^{+0.04}_{-0.21}$

Table A.10:  $z_{phot}$  and  $L^{rest}$  – continued

ID	$z_{phot}$	$L_U^{rest}$	$L_B^{rest}$	$L_V^{rest}$
HDFS2 – 677	1.98 <sup>0.06</sup> <sub>1.84</sub> a	2.64 <sup>0.20</sup> <sub>2.63</sub>	1.33 <sup>0.05</sup> <sub>1.32</sub>	0.79 <sup>0.00</sup> <sub>0.79</sub>
HDFS2 – 687	0.48 <sup>0.56</sup> <sub>0.38</sub> a	0.07 <sup>0.48</sup> <sub>0.07</sub>	0.04 <sup>0.24</sup> <sub>0.04</sub>	0.03 <sup>0.15</sup> <sub>0.03</sub>
HDFS2 – 694	0.46 <sup>0.02</sup> <sub>0.26</sub>	0.47 <sup>0.06</sup> <sub>0.41</sub>	0.31 <sup>0.04</sup> <sub>0.27</sub>	0.25 <sup>0.02</sup> <sub>0.22</sub>
HDFS2 – 696	0.52 <sup>0.08</sup> <sub>0.30</sub>	0.33 <sup>0.17</sup> <sub>0.30</sub>	0.24 <sup>0.12</sup> <sub>0.22</sub>	0.20 <sup>0.08</sup> <sub>0.17</sub>
HDFS2 – 699	2.10 <sup>7.22</sup> <sub>0.00</sub> a	0.49 <sup>174.34</sup> <sub>0.00</sub>	0.61 <sup>124.30</sup> <sub>0.00</sub>	0.76 <sup>101.94</sup> <sub>0.00</sub>
HDFS2 – 707 <sup>b</sup>	2.56 <sup>0.04</sup> <sub>0.02</sub>	2.22 <sup>0.18</sup> <sub>0.08</sub>	1.61 <sup>0.10</sup> <sub>0.04</sub>	1.02 <sup>0.01</sup> <sub>0.07</sub>
HDFS2 – 716	1.34 <sup>0.00</sup> <sub>1.30</sub> a	0.57 <sup>0.00</sup> <sub>0.57</sub>	0.28 <sup>0.02</sup> <sub>0.28</sub>	0.20 <sup>0.00</sup> <sub>0.20</sub>
HDFS2 – 725	3.26 <sup>0.20</sup> <sub>0.16</sub>	2.10 <sup>0.54</sup> <sub>0.34</sub>	1.51 <sup>0.28</sup> <sub>0.25</sub>	.....
HDFS2 – 736 <sup>b</sup>	2.66 <sup>0.22</sup> <sub>0.22</sub>	2.53 <sup>0.41</sup> <sub>0.54</sub>	1.22 <sup>0.27</sup> <sub>0.30</sub>	0.80 <sup>0.19</sup> <sub>0.16</sub>
HDFS2 – 740	2.98 <sup>0.26</sup> <sub>0.30</sub>	10.99 <sup>3.87</sup> <sub>3.19</sub>	7.84 <sup>2.24</sup> <sub>2.47</sub>	6.85 <sup>0.80</sup> <sub>1.85</sub>
HDFS2 – 764	1.74 <sup>0.14</sup> <sub>0.26</sub>	1.48 <sup>0.58</sup> <sub>0.78</sub>	1.45 <sup>0.52</sup> <sub>0.64</sub>	1.52 <sup>0.42</sup> <sub>0.60</sub>
HDFS2 – 771	3.00 <sup>0.14</sup> <sub>0.20</sub>	2.31 <sup>0.37</sup> <sub>0.46</sub>	1.52 <sup>0.18</sup> <sub>0.27</sub>	1.11 <sup>0.01</sup> <sub>0.17</sub>
HDFS2 – 773	3.66 <sup>0.14</sup> <sub>0.38</sub> a	2.96 <sup>0.52</sup> <sub>0.77</sub>	2.02 <sup>0.30</sup> <sub>0.59</sub>	.....
HDFS2 – 776	0.40 <sup>1.72</sup> <sub>0.02</sub> a	0.02 <sup>1.69</sup> <sub>0.00</sub>	0.01 <sup>1.04</sup> <sub>0.00</sub>	0.01 <sup>1.03</sup> <sub>0.00</sub>
HDFS2 – 786 <sup>b</sup>	3.14 <sup>0.18</sup> <sub>2.68</sub> a	12.10 <sup>2.63</sup> <sub>12.02</sub>	6.52 <sup>0.79</sup> <sub>6.47</sub>	3.99 <sup>0.35</sup> <sub>3.95</sub>
HDFS2 – 790	1.00 <sup>0.04</sup> <sub>0.24</sub>	1.26 <sup>0.15</sup> <sub>0.70</sub>	0.76 <sup>0.14</sup> <sub>0.42</sub>	0.56 <sup>0.14</sup> <sub>0.26</sub>
HDFS2 – 791	0.66 <sup>0.28</sup> <sub>0.56</sub>	0.15 <sup>0.26</sup> <sub>0.15</sub>	0.09 <sup>0.14</sup> <sub>0.09</sub>	0.07 <sup>0.09</sup> <sub>0.07</sub>
HDFS2 – 792	0.46 <sup>0.06</sup> <sub>0.22</sub>	0.58 <sup>0.24</sup> <sub>0.49</sub>	0.41 <sup>0.17</sup> <sub>0.34</sub>	0.36 <sup>0.10</sup> <sub>0.29</sub>
HDFS2 – 801	0.04 <sup>2.04</sup> <sub>0.02</sub> a	0.00 <sup>3.43</sup> <sub>0.00</sub>	0.00 <sup>1.57</sup> <sub>0.00</sub>	0.00 <sup>0.97</sup> <sub>0.00</sub>
HDFS2 – 802	1.32 <sup>0.40</sup> <sub>0.12</sub>	2.90 <sup>3.67</sup> <sub>0.82</sub>	2.09 <sup>2.14</sup> <sub>0.53</sub>	1.75 <sup>1.75</sup> <sub>0.41</sub>
HDFS2 – 803	0.70 <sup>0.20</sup> <sub>0.18</sub>	0.13 <sup>0.15</sup> <sub>0.07</sub>	0.09 <sup>0.08</sup> <sub>0.05</sub>	0.07 <sup>0.05</sup> <sub>0.03</sub>
HDFS2 – 806	2.64 <sup>0.12</sup> <sub>0.34</sub>	2.63 <sup>0.64</sup> <sub>1.31</sub>	3.17 <sup>0.73</sup> <sub>1.37</sub>	3.62 <sup>0.56</sup> <sub>1.35</sub>
HDFS2 – 808	0.54 <sup>3.32</sup> <sub>0.06</sub> a	0.06 <sup>5.38</sup> <sub>0.02</sub>	0.04 <sup>3.95</sup> <sub>0.01</sub>	0.03 <sup>2.95</sup> <sub>0.01</sub>
HDFS2 – 809	1.26 <sup>0.66</sup> <sub>1.22</sub> a	0.89 <sup>1.54</sup> <sub>0.89</sub>	0.49 <sup>0.62</sup> <sub>0.49</sub>	0.32 <sup>0.44</sup> <sub>0.32</sub>
HDFS2 – 810	0.94 <sup>0.02</sup> <sub>0.18</sub>	0.61 <sup>0.04</sup> <sub>0.29</sub>	0.36 <sup>0.03</sup> <sub>0.15</sub>	0.25 <sup>0.02</sup> <sub>0.08</sub>
HDFS2 – 812 <sup>b</sup>	2.793	10.99	7.00	4.86
HDFS2 – 813 <sup>c</sup>	5.90 <sup>0.12</sup> <sub>0.18</sub>	.....	.....	.....
HDFS2 – 817	0.34 <sup>3.36</sup> <sub>0.04</sub> a	0.02 <sup>8.03</sup> <sub>0.01</sub>	0.01 <sup>3.27</sup> <sub>0.00</sub>	0.01 <sup>1.81</sup> <sub>0.00</sub>
HDFS2 – 823	1.06 <sup>0.04</sup> <sub>0.72</sub>	0.45 <sup>0.06</sup> <sub>0.42</sub>	0.28 <sup>0.03</sup> <sub>0.26</sub>	0.21 <sup>0.02</sup> <sub>0.20</sub>
HDFS2 – 824	0.96 <sup>0.10</sup> <sub>0.10</sub>	0.93 <sup>0.43</sup> <sub>0.31</sub>	0.85 <sup>0.39</sup> <sub>0.30</sub>	0.90 <sup>0.32</sup> <sub>0.26</sub>
HDFS2 – 828 <sup>b</sup>	2.70 <sup>0.22</sup> <sub>2.36</sub> a	4.11 <sup>0.79</sup> <sub>4.08</sub>	2.37 <sup>0.43</sup> <sub>2.36</sub>	1.41 <sup>0.28</sup> <sub>1.40</sub>
HDFS2 – 830	0.94 <sup>0.02</sup> <sub>0.06</sub>	0.14 <sup>0.01</sup> <sub>0.03</sub>	0.10 <sup>0.01</sup> <sub>0.02</sub>	0.08 <sup>0.00</sup> <sub>0.01</sub>
HDFS2 – 842	3.76 <sup>0.14</sup> <sub>0.62</sub> a	5.68 <sup>0.02</sup> <sub>2.59</sub>	2.06 <sup>0.08</sup> <sub>0.46</sub>	.....
HDFS2 – 843	0.86 <sup>0.06</sup> <sub>0.68</sub>	0.44 <sup>0.09</sup> <sub>0.44</sub>	0.27 <sup>0.04</sup> <sub>0.27</sub>	0.20 <sup>0.02</sup> <sub>0.19</sub>
HDFS2 – 845	0.46 <sup>0.04</sup> <sub>0.12</sub>	0.12 <sup>0.03</sup> <sub>0.07</sub>	0.07 <sup>0.02</sup> <sub>0.04</sub>	0.05 <sup>0.01</sup> <sub>0.02</sub>
HDFS2 – 863	1.02 <sup>0.08</sup> <sub>0.08</sub>	0.47 <sup>0.20</sup> <sub>0.14</sub>	0.58 <sup>0.21</sup> <sub>0.18</sub>	0.73 <sup>0.19</sup> <sub>0.18</sub>
HDFS2 – 864 <sup>b</sup>	0.16 <sup>0.84</sup> <sub>0.04</sub> a	0.00 <sup>0.34</sup> <sub>0.00</sub>	0.00 <sup>0.21</sup> <sub>0.00</sub>	0.00 <sup>0.16</sup> <sub>0.00</sub>
HDFS2 – 873	1.20 <sup>0.40</sup> <sub>0.06</sub>	0.26 <sup>0.76</sup> <sub>0.05</sub>	0.33 <sup>0.65</sup> <sub>0.06</sub>	0.41 <sup>0.58</sup> <sub>0.07</sub>

Table A.10:  $z_{\text{phot}}$  and  $L^{\text{rest}}$  – continued

ID	$z_{\text{phot}}$	$L_U^{\text{rest}}$	$L_B^{\text{rest}}$	$L_V^{\text{rest}}$
HDFS2 – 877	$0.42^{0.10}_{-0.20}$	$0.31^{0.25}_{-0.26}$	$0.22^{0.18}_{-0.18}$	$0.19^{0.13}_{-0.16}$
HDFS2 – 883	$0.62^{3.76}_{-0.00}$ <sup>a</sup>	$0.04^{7.55}_{-0.00}$	$0.04^{3.32}_{-0.00}$	$0.03^{2.03}_{-0.00}$
HDFS2 – 885 <sup>b</sup>	$3.22^{0.18}_{-3.04}$ <sup>a</sup>	$1.55^{0.00}_{-1.55}$	$0.99^{0.27}_{-0.99}$	.....
HDFS2 – 890	$0.96^{0.04}_{-0.16}$	$0.67^{0.09}_{-0.28}$	$0.45^{0.06}_{-0.20}$	$0.38^{0.03}_{-0.16}$
HDFS2 – 891	$0.72^{0.10}_{-0.62}$	$0.17^{0.07}_{-0.17}$	$0.10^{0.04}_{-0.10}$	$0.07^{0.03}_{-0.07}$
HDFS2 – 904	$1.18^{0.50}_{-1.02}$ <sup>a</sup>	$1.12^{1.55}_{-1.11}$	$0.63^{0.61}_{-0.62}$	$0.41^{0.40}_{-0.41}$
HDFS2 – 908	$2.28^{7.26}_{-0.16}$ <sup>a</sup>	$1.86^{473.08}_{-0.61}$	$2.53^{275.55}_{-0.77}$	$2.92^{198.25}_{-0.56}$
HDFS2 – 910	$0.58^{3.64}_{-0.08}$ <sup>a</sup>	$0.06^{11.29}_{-0.02}$	$0.05^{4.94}_{-0.02}$	$0.04^{3.00}_{-0.01}$
HDFS2 – 911	$0.56^{0.02}_{-0.02}$	$0.38^{0.07}_{-0.06}$	$0.56^{0.08}_{-0.07}$	$0.72^{0.07}_{-0.07}$
HDFS2 – 918	$0.48^{0.22}_{-0.02}$	$0.07^{0.13}_{-0.01}$	$0.04^{0.06}_{-0.00}$	$0.03^{0.04}_{-0.00}$
HDFS2 – 919	$0.88^{0.04}_{-0.04}$	$0.23^{0.03}_{-0.03}$	$0.14^{0.02}_{-0.02}$	$0.09^{0.01}_{-0.01}$
HDFS2 – 921	$0.06^{2.08}_{-0.02}$ <sup>a</sup>	$0.00^{7.78}_{-0.00}$	$0.00^{3.58}_{-0.00}$	$0.00^{2.35}_{-0.00}$
HDFS2 – 924 <sup>b</sup>	$3.12^{0.14}_{-2.96}$ <sup>a</sup>	$7.82^{2.13}_{-7.81}$	$4.10^{0.38}_{-4.09}$	$2.41^{0.19}_{-2.41}$
HDFS2 – 925	$0.70^{0.08}_{-0.16}$	$0.27^{0.11}_{-0.14}$	$0.17^{0.06}_{-0.09}$	$0.13^{0.04}_{-0.06}$
HDFS2 – 926 <sup>b</sup>	$0.02^{2.14}_{-0.00}$ <sup>a</sup>	$0.00^{1.61}_{-0.00}$	$0.00^{0.71}_{-0.00}$	$0.00^{0.59}_{-0.00}$
HDFS2 – 929 <sup>b</sup>	$1.42^{0.52}_{-0.18}$	$1.08^{1.90}_{-0.48}$	$0.88^{1.39}_{-0.32}$	$0.79^{1.05}_{-0.24}$
HDFS2 – 934	$0.42^{0.06}_{-0.12}$	$0.40^{0.17}_{-0.25}$	$0.26^{0.11}_{-0.15}$	$0.22^{0.07}_{-0.12}$
HDFS2 – 935	$0.48^{0.04}_{-0.24}$	$0.33^{0.08}_{-0.28}$	$0.20^{0.05}_{-0.17}$	$0.15^{0.03}_{-0.12}$
HDFS2 – 939	$0.16^{0.58}_{-0.02}$ <sup>a</sup>	$0.00^{0.12}_{-0.00}$	$0.00^{0.07}_{-0.00}$	$0.00^{0.06}_{-0.00}$
HDFS2 – 943	$0.06^{0.02}_{-0.04}$	$0.00^{0.00}_{-0.00}$	$0.00^{0.00}_{-0.00}$	$0.00^{0.00}_{-0.00}$
HDFS2 – 947	$1.54^{0.40}_{-0.38}$	$0.75^{0.84}_{-0.48}$	$0.58^{0.64}_{-0.35}$	$0.53^{0.49}_{-0.29}$
HDFS2 – 949 <sup>b</sup>	$1.56^{0.24}_{-0.18}$	$1.31^{0.76}_{-0.43}$	$0.96^{0.55}_{-0.26}$	$0.83^{0.40}_{-0.22}$
HDFS2 – 959	$0.78^{0.14}_{-0.08}$	$0.56^{0.38}_{-0.17}$	$0.39^{0.20}_{-0.10}$	$0.27^{0.14}_{-0.04}$
HDFS2 – 962	$1.02^{0.10}_{-0.70}$	$0.89^{0.31}_{-0.84}$	$0.53^{0.19}_{-0.51}$	$0.39^{0.11}_{-0.37}$
HDFS2 – 968	$1.52^{0.32}_{-0.18}$	$0.53^{0.53}_{-0.24}$	$0.48^{0.41}_{-0.18}$	$0.53^{0.49}_{-0.19}$
HDFS2 – 969	$0.50^{0.06}_{-0.04}$	$0.29^{0.17}_{-0.08}$	$0.39^{0.20}_{-0.10}$	$0.50^{0.18}_{-0.10}$
HDFS2 – 974	$0.50^{0.12}_{-0.26}$	$0.20^{0.18}_{-0.17}$	$0.15^{0.13}_{-0.13}$	$0.13^{0.09}_{-0.11}$
HDFS2 – 975	$0.76^{0.10}_{-0.12}$	$0.44^{0.21}_{-0.19}$	$0.29^{0.11}_{-0.11}$	$0.20^{0.06}_{-0.06}$
HDFS2 – 978	$1.34^{0.44}_{-0.08}$	$0.83^{1.28}_{-0.19}$	$0.68^{0.88}_{-0.13}$	$0.62^{0.80}_{-0.11}$
HDFS2 – 985	$0.82^{0.06}_{-0.24}$	$0.46^{0.10}_{-0.26}$	$0.28^{0.05}_{-0.17}$	$0.17^{0.03}_{-0.09}$
HDFS2 – 996	$2.04^{0.14}_{-1.90}$ <sup>a</sup>	$4.01^{0.92}_{-4.00}$	$2.38^{0.21}_{-2.38}$	$1.50^{0.40}_{-1.49}$
HDFS2 – 1000	$0.48^{0.04}_{-0.08}$	$0.21^{0.05}_{-0.08}$	$0.13^{0.03}_{-0.05}$	$0.09^{0.01}_{-0.03}$
HDFS2 – 1005	$1.38^{0.28}_{-0.18}$	$1.05^{0.81}_{-0.41}$	$0.75^{0.47}_{-0.25}$	$0.61^{0.31}_{-0.17}$
HDFS2 – 1018	$0.78^{0.08}_{-0.02}$	$0.13^{0.05}_{-0.01}$	$0.09^{0.03}_{-0.01}$	$0.06^{0.02}_{-0.00}$
HDFS2 – 1022 <sup>b</sup>	$1.98^{0.18}_{-0.70}$	$5.10^{1.44}_{-3.70}$	$3.30^{0.90}_{-2.29}$	$2.53^{0.16}_{-1.71}$
HDFS2 – 1023	$3.56^{0.10}_{-0.14}$	$2.72^{0.33}_{-0.37}$	$1.90^{0.21}_{-0.21}$	.....
HDFS2 – 1029	$2.16^{0.12}_{-0.14}$	$0.66^{0.25}_{-0.19}$	$0.55^{0.12}_{-0.11}$	$0.49^{0.09}_{-0.09}$
HDFS2 – 1032	$1.88^{4.36}_{-0.14}$ <sup>a</sup>	$1.03^{92.48}_{-0.32}$	$1.07^{62.37}_{-0.30}$	$1.07^{49.33}_{-0.23}$

Table A.10:  $z_{phot}$  and  $L^{rest}$  – continued

ID	$z_{phot}$	$L_U^{rest}$	$L_B^{rest}$	$L_V^{rest}$
HDFS2 – 1035	$0.46^{0.18}_{0.36}$ <sup>a</sup>	$0.05^{0.08}_{0.05}$	$0.03^{0.04}_{0.03}$	$0.02^{0.02}_{0.02}$
HDFS2 – 1038 <sup>b</sup>	2.790	17.47	9.05	5.64
HDFS2 – 1041	$1.62^{0.02}_{0.26}$	$0.83^{0.03}_{0.26}$	$0.48^{0.04}_{0.14}$	$0.39^{0.00}_{0.14}$
HDFS2 – 1044	$3.14^{0.26}_{2.80}$ <sup>a</sup>	$8.66^{2.99}_{8.64}$	$4.82^{0.88}_{4.80}$	$3.19^{0.35}_{3.18}$
HDFS2 – 1045	$0.16^{1.20}_{0.04}$ <sup>a</sup>	$0.01^{1.40}_{0.00}$	$0.00^{0.82}_{0.00}$	$0.00^{0.55}_{0.00}$
HDFS2 – 1051	$0.46^{0.04}_{0.08}$	$0.48^{0.17}_{0.23}$	$0.54^{0.19}_{0.26}$	$0.71^{0.16}_{0.30}$
HDFS2 – 1054	$1.32^{0.42}_{0.06}$	$2.23^{3.28}_{0.38}$	$1.77^{2.11}_{0.24}$	$1.58^{2.04}_{0.21}$
HDFS2 – 1065	$1.22^{0.16}_{0.16}$	$0.24^{0.19}_{0.10}$	$0.24^{0.14}_{0.10}$	$0.24^{0.12}_{0.08}$
HDFS2 – 1066	$2.70^{0.06}_{2.66}$ <sup>a</sup>	$2.98^{0.11}_{2.98}$	$1.27^{0.05}_{1.27}$	$0.68^{0.02}_{0.68}$
HDFS2 – 1069	$0.28^{3.36}_{0.10}$ <sup>a</sup>	$0.00^{4.07}_{0.00}$	$0.00^{1.81}_{0.00}$	$0.00^{1.12}_{0.00}$
HDFS2 – 1074 <sup>b</sup>	$2.48^{0.40}_{0.22}$	$4.32^{2.35}_{1.22}$	$2.54^{1.47}_{0.54}$	$1.64^{1.14}_{0.15}$
HDFS2 – 1078	$3.10^{0.20}_{2.68}$ <sup>a</sup>	$3.09^{0.75}_{3.05}$	$1.85^{0.21}_{1.83}$	$1.35^{0.00}_{1.34}$
HDFS2 – 1081	$0.76^{0.08}_{0.12}$	$0.25^{0.07}_{0.09}$	$0.15^{0.04}_{0.05}$	$0.09^{0.02}_{0.03}$
HDFS2 – 1086 <sup>b</sup>	$2.58^{0.34}_{0.06}$	$4.05^{1.97}_{0.34}$	$2.45^{0.96}_{0.17}$	$1.59^{0.47}_{0.09}$
HDFS2 – 1088	$1.06^{0.20}_{0.34}$	$0.53^{0.36}_{0.34}$	$0.31^{0.22}_{0.21}$	$0.23^{0.13}_{0.14}$
HDFS2 – 1092 <sup>b</sup>	$2.60^{0.14}_{2.22}$ <sup>a</sup>	$2.60^{0.19}_{2.56}$	$1.28^{0.28}_{1.27}$	$0.88^{0.19}_{0.86}$
HDFS2 – 1097	$1.02^{0.06}_{0.22}$	$2.48^{0.54}_{1.36}$	$1.91^{0.43}_{1.11}$	$1.75^{0.32}_{0.91}$
HDFS2 – 1100	$0.54^{0.08}_{0.14}$	$0.17^{0.09}_{0.10}$	$0.13^{0.06}_{0.08}$	$0.11^{0.04}_{0.05}$
HDFS2 – 1102	$1.64^{5.06}_{0.08}$ <sup>a</sup>	$0.48^{14.50}_{0.12}$	$0.69^{59.08}_{0.13}$	$0.86^{38.86}_{0.12}$
HDFS2 – 1104	$0.30^{0.04}_{0.12}$	$0.22^{0.10}_{0.17}$	$0.18^{0.07}_{0.13}$	$0.17^{0.06}_{0.12}$
HDFS2 – 1105	$3.00^{0.14}_{0.78}$ <sup>a</sup>	$10.49^{1.43}_{6.86}$	$6.45^{0.67}_{3.90}$	$5.04^{0.06}_{2.82}$
HDFS2 – 1107	$0.94^{0.00}_{0.92}$	$0.34^{0.00}_{0.34}$	$0.17^{0.00}_{0.17}$	$0.12^{0.00}_{0.12}$
HDFS2 – 1111	$4.16^{0.16}_{3.70}$ <sup>a</sup>	$12.28^{0.00}_{12.23}$	.....	.....
HDFS2 – 1112 <sup>b</sup>	$2.84^{0.06}_{2.82}$ <sup>a</sup>	$3.48^{0.10}_{3.48}$	$1.32^{0.03}_{1.32}$	$0.68^{0.02}_{0.68}$

<sup>a</sup>  $\geq 1\%$  of Monte-Carlo realizations have  $z \geq 1$  away from  $z_{phot}$

<sup>b</sup> Meets U-dropout color criteria

<sup>c</sup> Redshift is likely in error

Note. – Objects with  $z_{phot} < 5.2$  and no luminosity or color measurements have  $25 \geq K_{s,AB} < 26$ .

Note. – Objects with no redshift, color, and luminosity errors have spectroscopic redshifts

Table A.11: Colors,  $\mathcal{M}/L$ 's, and  $\mathcal{M}-K_{s,AB}^{\text{tot}} < 25$  Sample

ID	$(U - B)_{\text{rest}}$	$(B - V)_{\text{rest}}$	$\log_{10} \mathcal{M}/L_V$	$\mathcal{M}$ $10^{10} h^{-2} M_{\odot}$
HDFS2 - 49	1.230	0.06	0.06	$0.28^{0.15}_{0.15}$
HDFS2 - 61	$0.96^{0.60}_{0.52}$	$-0.28^{0.06}_{0.08}$	$-0.28^{0.06}_{0.08}$	$0.33^{0.11}_{0.49}$
HDFS2 - 66	$1.10^{0.18}_{0.06}$	$0.27^{0.04}_{0.17}$	$0.27^{0.04}_{0.17}$	$0.48^{0.15}_{0.26}$
HDFS2 - 75	$0.96^{0.00}_{0.94}$	$-0.39^{0.23}_{0.00}$	$-0.39^{0.23}_{0.00}$	$-0.11^{0.13}_{0.33}$
HDFS2 - 93	$0.62^{0.10}_{0.02}$	$0.50^{0.04}_{0.11}$	$0.50^{0.04}_{0.11}$	$0.76^{0.12}_{0.25}$
HDFS2 - 98	$4.20^{0.08}_{0.08}$	.....	.....	.....
HDFS2 - 103	$2.52^{0.20}_{2.18}$ a	$-0.76^{0.13}_{0.00}$	$-0.76^{0.13}_{0.00}$	$-0.52^{0.37}_{0.10}$
HDFS2 - 105	$0.50^{0.02}_{0.26}$	$-0.35^{0.01}_{0.05}$	$-0.35^{0.01}_{0.05}$	$-0.01^{0.28}_{0.14}$
HDFS2 - 112	$1.12^{0.12}_{0.16}$	$0.06^{0.01}_{0.06}$	$0.06^{0.01}_{0.06}$	$0.34^{0.22}_{0.17}$
HDFS2 - 114	0.560	-0.12	-0.12	$0.14^{0.15}_{0.14}$
HDFS2 - 119	$0.94^{0.04}_{0.06}$	$-0.43^{0.02}_{0.03}$	$-0.43^{0.02}_{0.03}$	$-0.37^{0.18}_{0.12}$
HDFS2 - 120	$0.46^{3.40}_{0.14}$ a	$-0.27^{0.00}_{0.45}$	$-0.27^{0.00}_{0.45}$	$-0.00^{0.19}_{0.36}$
HDFS2 - 124	$0.82^{0.06}_{0.06}$	$-0.08^{0.04}_{0.01}$	$-0.08^{0.04}_{0.01}$	$0.20^{0.14}_{0.21}$
HDFS2 - 127	$0.88^{0.04}_{0.04}$	$-0.41^{0.12}_{0.01}$	$-0.41^{0.12}_{0.01}$	$-0.55^{0.15}_{0.15}$
HDFS2 - 130	$1.00^{0.10}_{0.50}$	$-0.41^{0.01}_{0.13}$	$-0.41^{0.01}_{0.13}$	$-0.21^{0.23}_{0.15}$
HDFS2 - 136 b	$1.42^{0.22}_{0.18}$	$-0.26^{0.09}_{0.08}$	$-0.26^{0.09}_{0.08}$	$-0.06^{0.25}_{0.16}$
HDFS2 - 140	$1.18^{0.14}_{0.12}$	$-0.18^{0.00}_{0.08}$	$-0.18^{0.00}_{0.08}$	$0.09^{0.19}_{0.15}$
HDFS2 - 144 b	$2.52^{0.18}_{0.48}$ a	$-0.75^{0.17}_{0.01}$	$-0.75^{0.17}_{0.01}$	$-0.81^{0.81}_{0.08}$
HDFS2 - 146	$4.28^{0.08}_{3.66}$ a	.....	.....	.....
HDFS2 - 147	$0.46^{0.04}_{0.24}$	$-0.40^{0.02}_{0.11}$	$-0.40^{0.02}_{0.11}$	$-0.13^{0.28}_{0.24}$
HDFS2 - 148	$0.72^{0.06}_{0.14}$	$-0.21^{0.02}_{0.05}$	$-0.21^{0.02}_{0.05}$	$-0.21^{0.27}_{0.16}$
HDFS2 - 150	$0.44^{0.10}_{0.16}$	$-0.10^{0.07}_{0.02}$	$-0.10^{0.07}_{0.02}$	$0.36^{0.20}_{0.22}$
HDFS2 - 152	$0.98^{0.04}_{0.18}$	$-0.28^{0.01}_{0.02}$	$-0.28^{0.01}_{0.02}$	$-0.00^{0.27}_{0.09}$
HDFS2 - 154	$0.84^{0.02}_{0.82}$	$-0.45^{0.03}_{0.09}$	$-0.45^{0.03}_{0.09}$	$-0.23^{0.26}_{0.09}$
HDFS2 - 156	$2.18^{0.36}_{0.22}$	$-0.71^{0.04}_{0.04}$	$-0.71^{0.04}_{0.04}$	$0.05^{0.00}_{0.55}$
HDFS2 - 158	$0.38^{3.60}_{0.04}$ a	$-0.06^{0.07}_{0.65}$	$-0.06^{0.07}_{0.65}$	$0.21^{0.10}_{0.66}$
HDFS2 - 160	$1.06^{0.12}_{0.24}$	$-0.24^{0.00}_{0.09}$	$-0.24^{0.00}_{0.09}$	$0.07^{0.20}_{0.14}$
HDFS2 - 163 b,d	.....	.....	.....	.....
HDFS2 - 165	$4.14^{0.16}_{0.16}$	.....	.....	.....
HDFS2 - 166 b	$2.56^{0.40}_{0.02}$	$-0.54^{0.04}_{0.11}$	$-0.54^{0.04}_{0.11}$	$-0.39^{0.03}_{0.46}$
HDFS2 - 168	$0.48^{3.30}_{0.02}$ a	$-0.21^{0.00}_{0.65}$	$-0.21^{0.00}_{0.65}$	$-0.11^{0.17}_{0.58}$
HDFS2 - 170	$0.50^{0.14}_{0.04}$ a	$-0.23^{0.00}_{0.04}$	$-0.23^{0.00}_{0.04}$	$0.02^{0.21}_{0.26}$
HDFS2 - 171	$1.62^{0.00}_{0.08}$ a	$-0.40^{0.00}_{0.14}$	$-0.40^{0.00}_{0.14}$	$-0.34^{0.09}_{0.31}$
HDFS2 - 172	$0.48^{0.20}_{0.16}$	$-0.09^{0.02}_{0.09}$	$-0.09^{0.02}_{0.09}$	$0.31^{0.19}_{0.30}$
HDFS2 - 174	$2.78^{0.20}_{1.54}$ a	$-0.41^{0.01}_{0.14}$	$-0.41^{0.01}_{0.14}$	$-0.40^{0.25}_{0.10}$
HDFS2 - 177	$2.06^{0.28}_{0.44}$	$-0.52^{0.01}_{0.15}$	$-0.52^{0.01}_{0.15}$	$-0.39^{0.29}_{0.07}$



Table A.11: Colors,  $\mathcal{M}/L$ 's, and  $\mathcal{M}$ - continued

ID	$(U - B)_{\text{rest}}$	$(B - V)_{\text{rest}}$	$\log_{10} \mathcal{M}/L_V$	$\mathcal{M}$
HDFS2 - 180	$0.64^{+0.12}_{-0.46}$	$-0.40^{+0.00}_{-0.23}$	$-0.40^{+0.00}_{-0.23}$	$-0.34^{+0.25}_{-0.15}$
HDFS2 - 183	$1.28^{+0.08}_{-0.12}$	$-0.16^{+0.02}_{-0.11}$	$-0.16^{+0.02}_{-0.11}$	$0.08^{+0.19}_{-0.13}$
HDFS2 - 184 <sup>b</sup>	$2.28^{+0.26}_{-2.24}$ <sup>a</sup>	$-0.55^{+0.44}_{-0.13}$	$-0.55^{+0.44}_{-0.13}$	$0.09^{+0.06}_{-0.82}$
HDFS2 - 185	$0.52^{+3.44}_{-0.02}$ <sup>a</sup>	$-0.22^{+0.00}_{-0.64}$	$-0.22^{+0.00}_{-0.64}$	$-0.13^{+0.12}_{-0.46}$
HDFS2 - 189	$0.80^{+0.08}_{-0.08}$	$-0.19^{+0.04}_{-0.03}$	$-0.19^{+0.04}_{-0.03}$	$0.11^{+0.13}_{-0.19}$
HDFS2 - 191	$0.94^{+0.04}_{-0.20}$	$-0.42^{+0.02}_{-0.01}$	$-0.42^{+0.02}_{-0.01}$	$-0.16^{+0.13}_{-0.21}$
HDFS2 - 192	$1.54^{+0.16}_{-0.44}$ <sup>a</sup>	$-0.62^{+0.22}_{-0.02}$	$-0.62^{+0.22}_{-0.02}$	$-0.14^{+0.09}_{-0.31}$
HDFS2 - 195	$4.38^{+0.12}_{-0.20}$	.....	.....	.....
HDFS2 - 198	$0.10^{+0.38}_{-0.02}$	$-0.24^{+0.00}_{-0.16}$	$-0.24^{+0.00}_{-0.16}$	$0.08^{+0.15}_{-0.25}$
HDFS2 - 199	$3.58^{+0.06}_{-3.16}$ <sup>a</sup>	$-0.73^{+0.42}_{-0.00}$	.....	.....
HDFS2 - 201	$1.54^{+0.06}_{-1.48}$ <sup>a</sup>	$-0.63^{+0.10}_{-0.05}$	$-0.63^{+0.10}_{-0.05}$	$-0.56^{+0.43}_{-0.08}$
HDFS2 - 203	$3.64^{+0.10}_{-3.06}$ <sup>a</sup>	$-0.86^{+0.49}_{-0.02}$	.....	.....
HDFS2 - 206	$4.40^{+0.08}_{-0.06}$	.....	.....	.....
HDFS2 - 207	$0.90^{+0.36}_{-0.08}$	$-0.46^{+0.02}_{-0.21}$	$-0.46^{+0.02}_{-0.21}$	$-0.44^{+0.22}_{-0.13}$
HDFS2 - 209	$3.12^{+0.24}_{-0.28}$ <sup>a</sup>	$-0.66^{+0.13}_{-0.01}$	$-0.66^{+0.13}_{-0.01}$	$-0.35^{+0.24}_{-0.16}$
HDFS2 - 214	$0.64^{+3.78}_{-0.06}$ <sup>a</sup>	$-0.07^{+0.04}_{-0.73}$	$-0.07^{+0.04}_{-0.73}$	$-0.02^{+0.14}_{-0.48}$
HDFS2 - 217	$0.46^{+2.16}_{-0.10}$ <sup>a</sup>	$-0.54^{+0.06}_{-0.06}$	$-0.54^{+0.06}_{-0.06}$	$-0.32^{+0.30}_{-0.09}$
HDFS2 - 219	$0.44^{+0.06}_{-0.02}$	$0.58^{+0.00}_{-0.04}$	$0.58^{+0.00}_{-0.04}$	$0.90^{+0.12}_{-0.28}$
HDFS2 - 221	$1.90^{+0.28}_{-0.26}$	$-0.40^{+0.00}_{-0.23}$	$-0.40^{+0.00}_{-0.23}$	$-0.12^{+0.18}_{-0.15}$
HDFS2 - 222	$1.38^{+0.54}_{-1.18}$ <sup>a</sup>	$-0.43^{+0.00}_{-0.24}$	$-0.43^{+0.00}_{-0.24}$	$-0.27^{+0.22}_{-0.15}$
HDFS2 - 224	$0.10^{+0.92}_{-0.08}$ <sup>a</sup>	$-0.01^{+0.10}_{-0.56}$	$-0.01^{+0.10}_{-0.56}$	$-0.12^{+0.21}_{-0.18}$
HDFS2 - 225	$0.78^{+0.08}_{-0.24}$	$-0.35^{+0.04}_{-0.04}$	$-0.35^{+0.04}_{-0.04}$	$-0.15^{+0.19}_{-0.16}$
HDFS2 - 227	$0.60^{+0.20}_{-0.16}$ <sup>a</sup>	$0.16^{+0.34}_{-0.41}$	$0.16^{+0.34}_{-0.41}$	$0.21^{+0.30}_{-0.23}$
HDFS2 - 230	$1.34^{+0.62}_{-0.12}$	$-0.11^{+0.05}_{-0.11}$	$-0.11^{+0.05}_{-0.11}$	$0.14^{+0.19}_{-0.16}$
HDFS2 - 231 <sup>b</sup>	$2.04^{+0.18}_{-0.68}$	$-0.40^{+0.02}_{-0.12}$	$-0.40^{+0.02}_{-0.12}$	$-0.20^{+0.25}_{-0.11}$
HDFS2 - 232	$1.58^{+0.06}_{-0.18}$	$-0.35^{+0.08}_{-0.01}$	$-0.35^{+0.08}_{-0.01}$	$0.01^{+0.14}_{-0.18}$
HDFS2 - 233 <sup>b</sup>	$0.16^{+3.46}_{-0.04}$ <sup>a</sup>	$0.06^{+0.11}_{-0.98}$	$0.06^{+0.11}_{-0.98}$	$0.08^{+0.11}_{-0.75}$
HDFS2 - 234	$0.88^{+0.06}_{-0.12}$	$-0.43^{+0.03}_{-0.05}$	$-0.43^{+0.03}_{-0.05}$	$-0.39^{+0.19}_{-0.14}$
HDFS2 - 236	$1.30^{+0.02}_{-0.24}$	$0.10^{+0.15}_{-0.02}$	$0.10^{+0.15}_{-0.02}$	$0.36^{+0.27}_{-0.11}$
HDFS2 - 239	$3.94^{+0.14}_{-0.16}$	$-0.50^{+0.01}_{-0.00}$	.....	.....
HDFS2 - 240	$0.62^{+0.08}_{-0.44}$	$-0.14^{+0.04}_{-0.06}$	$-0.14^{+0.04}_{-0.06}$	$0.02^{+0.40}_{-0.14}$
HDFS2 - 241	$2.30^{+0.14}_{-1.04}$ <sup>a</sup>	$-0.47^{+0.00}_{-0.24}$	$-0.47^{+0.00}_{-0.24}$	$-0.21^{+0.29}_{-0.22}$
HDFS2 - 244	$1.00^{+0.16}_{-0.24}$	$-0.47^{+0.07}_{-0.08}$	$-0.47^{+0.07}_{-0.08}$	$-0.27^{+0.27}_{-0.10}$
HDFS2 - 245	$0.60^{+0.40}_{-0.16}$	$-0.50^{+0.04}_{-0.09}$	$-0.50^{+0.04}_{-0.09}$	$-0.15^{+0.18}_{-0.19}$
HDFS2 - 252	$3.32^{+0.20}_{-0.22}$	$-0.41^{+0.32}_{-0.23}$	.....	.....
HDFS2 - 254 <sup>c</sup>	.....	.....	.....	.....
HDFS2 - 255	$0.98^{+0.04}_{-0.20}$	$-0.40^{+0.00}_{-0.09}$	$-0.40^{+0.00}_{-0.09}$	$-0.26^{+0.22}_{-0.13}$
HDFS2 - 260 <sup>b</sup>	$2.54^{+0.22}_{-0.26}$	$-0.18^{+0.13}_{-0.03}$	$-0.18^{+0.13}_{-0.03}$	$0.14^{+0.19}_{-0.17}$

Table A.11: Colors,  $\mathcal{M}/L$ 's, and  $\mathcal{M}$ - continued

ID	$(U - B)_{\text{rest}}$	$(B - V)_{\text{rest}}$	$\log_{10} \mathcal{M}/L_V$	$\mathcal{M}$
HDFS2 - 263	$2.60^{0.40}_{0.40}^a$	$-0.43^{0.04}_{0.09}$	$-0.43^{0.04}_{0.09}$	$-0.18^{0.16}_{0.22}$
HDFS2 - 264 <sup>b</sup>	$2.14^{0.02}_{0.96}^a$	$-0.35^{0.09}_{0.06}$	$-0.35^{0.09}_{0.06}$	$-0.07^{0.22}_{0.13}$
HDFS2 - 267 <sup>b</sup>	$2.14^{0.06}_{0.48}$	$-0.35^{0.00}_{0.10}$	$-0.35^{0.00}_{0.10}$	$-0.28^{0.31}_{0.06}$
HDFS2 - 278	$0.26^{0.06}_{0.04}$	$0.11^{0.02}_{0.10}$	$0.11^{0.02}_{0.10}$	$0.48^{0.15}_{0.17}$
HDFS2 - 279 <sup>b</sup>	$1.98^{0.78}_{0.08}^a$	$-0.78^{0.08}_{0.06}$	$-0.78^{0.08}_{0.06}$	$-0.97^{1.21}_{0.18}$
HDFS2 - 280	$3.26^{0.36}_{0.10}$	$-0.50^{0.08}_{0.22}$	.....	.....
HDFS2 - 287	$0.80^{0.22}_{0.40}$	$-0.64^{0.04}_{0.00}$	$-0.64^{0.04}_{0.00}$	$-0.03^{0.10}_{0.29}$
HDFS2 - 290 <sup>b</sup>	$3.64^{0.10}_{3.50}^a$	$-0.99^{1.26}_{0.12}$	.....	.....
HDFS2 - 292	0.696	-0.38	-0.38	$-0.27^{0.16}_{0.14}$
HDFS2 - 293	$0.46^{3.24}_{0.04}^a$	$-0.21^{0.00}_{0.43}$	$-0.21^{0.00}_{0.43}$	$0.00^{0.17}_{0.29}$
HDFS2 - 296	0.580	0.10	0.10	$0.37^{0.16}_{0.14}$
HDFS2 - 301	$1.36^{0.32}_{0.04}$	$0.47^{0.04}_{0.27}$	$0.47^{0.04}_{0.27}$	$0.68^{0.12}_{0.24}$
HDFS2 - 303	$1.42^{0.16}_{1.32}^a$	$-0.53^{0.09}_{0.12}$	$-0.53^{0.09}_{0.12}$	$-0.27^{0.29}_{0.11}$
HDFS2 - 311	0.565	-0.32	-0.32	$-0.14^{0.16}_{0.14}$
HDFS2 - 312	$1.00^{0.20}_{0.66}$	$-0.41^{0.00}_{0.28}$	$-0.41^{0.00}_{0.28}$	$-0.20^{0.21}_{0.17}$
HDFS2 - 313	$3.48^{0.10}_{0.30}$	$0.30^{0.00}_{0.09}$	.....	.....
HDFS2 - 314	$1.30^{0.10}_{0.28}$	$-0.06^{0.07}_{0.08}$	$-0.06^{0.07}_{0.08}$	$0.20^{0.33}_{0.10}$
HDFS2 - 315 <sup>b</sup>	$2.52^{0.18}_{0.38}$	$-0.71^{0.18}_{0.01}$	$-0.71^{0.18}_{0.01}$	$-0.71^{0.89}_{0.11}$
HDFS2 - 316	$1.16^{0.14}_{0.62}$	$-0.45^{0.00}_{0.22}$	$-0.45^{0.00}_{0.22}$	$-0.30^{0.26}_{0.11}$
HDFS2 - 317	$1.44^{0.24}_{0.34}$	$-0.01^{0.15}_{0.08}$	$-0.01^{0.15}_{0.08}$	$0.26^{0.31}_{0.12}$
HDFS2 - 326	$0.64^{0.10}_{0.46}$	$-0.08^{0.08}_{0.10}$	$-0.08^{0.08}_{0.10}$	$0.14^{0.45}_{0.17}$
HDFS2 - 327	$1.06^{0.20}_{0.10}$	$-0.06^{0.00}_{0.08}$	$-0.06^{0.00}_{0.08}$	$0.25^{0.19}_{0.20}$
HDFS2 - 328	$0.58^{0.12}_{0.04}$	$-0.12^{0.03}_{0.15}$	$-0.12^{0.03}_{0.15}$	$0.07^{0.15}_{0.23}$
HDFS2 - 331 <sup>b</sup>	$2.22^{0.64}_{0.20}$	$-0.43^{0.05}_{0.16}$	$-0.43^{0.05}_{0.16}$	$-0.04^{0.19}_{0.13}$
HDFS2 - 332	$3.52^{0.16}_{0.18}$	$-0.67^{0.12}_{0.00}$	.....	.....
HDFS2 - 335	$3.20^{0.56}_{0.34}^a$	$-0.24^{0.08}_{0.29}$	$-0.24^{0.08}_{0.29}$	$-0.32^{0.32}_{0.09}$
HDFS2 - 337	$1.64^{6.80}_{0.02}^a$	$1.59^{0.04}_{2.03}$	$1.59^{0.04}_{2.03}$	$0.51^{0.15}_{0.98}$
HDFS2 - 339	$1.74^{0.12}_{1.64}^a$	$-0.79^{0.08}_{0.00}$	$-0.79^{0.08}_{0.00}$	$-0.09^{0.09}_{0.41}$
HDFS2 - 340	$0.34^{0.12}_{0.10}$	$-0.25^{0.07}_{0.03}$	$-0.25^{0.07}_{0.03}$	$0.18^{0.16}_{0.23}$
HDFS2 - 344	$0.58^{0.18}_{0.06}$	$-0.27^{0.00}_{0.10}$	$-0.27^{0.00}_{0.10}$	$-0.27^{0.09}_{0.42}$
HDFS2 - 346	$0.68^{0.10}_{0.26}$	$-0.17^{0.08}_{0.06}$	$-0.17^{0.08}_{0.06}$	$0.24^{0.26}_{0.13}$
HDFS2 - 349	$0.10^{0.38}_{0.00}$	$-0.63^{0.05}_{0.00}$	$-0.63^{0.05}_{0.00}$	$-0.29^{0.16}_{0.21}$
HDFS2 - 353	$3.54^{0.34}_{0.18}$	$0.35^{0.00}_{0.10}$	.....	.....
HDFS2 - 354	$1.60^{0.02}_{0.06}$	$-0.40^{0.02}_{0.00}$	$-0.40^{0.02}_{0.00}$	$-0.49^{0.24}_{0.13}$
HDFS2 - 355	$0.10^{0.38}_{0.08}^a$	$0.12^{0.04}_{0.48}$	$0.12^{0.04}_{0.48}$	$0.33^{0.20}_{0.54}$
HDFS2 - 356 <sup>b</sup>	$2.04^{0.18}_{0.50}$	$-0.44^{0.04}_{0.19}$	$-0.44^{0.04}_{0.19}$	$-0.33^{0.28}_{0.09}$
HDFS2 - 357	1.270	-0.02	-0.02	$0.20^{0.16}_{0.15}$
HDFS2 - 359	$1.08^{0.22}_{0.10}$	$-0.00^{0.00}_{0.09}$	$-0.00^{0.00}_{0.09}$	$0.32^{0.17}_{0.23}$

Table A.11: Colors,  $\mathcal{M}/L$ 's, and  $\mathcal{M}$ - continued

ID	$(U - B)_{\text{rest}}$	$(B - V)_{\text{rest}}$	$\log_{10} \mathcal{M}/L_V$	$\mathcal{M}$
HDFS2 - 361	$0.14^{+0.02}_{-0.06}$	$-0.04^{+0.00}_{-0.06}$	$-0.04^{+0.00}_{-0.06}$	$0.26^{+0.23}_{-0.13}$
HDFS2 - 365	$1.62^{+0.00}_{-1.46}$ <sup>a</sup>	$-0.66^{+0.02}_{-0.08}$	$-0.66^{+0.02}_{-0.08}$	$-0.35^{+0.14}_{-0.41}$
HDFS2 - 368 <sup>b,d</sup>	.....	.....	.....	.....
HDFS2 - 370	$0.98^{+4.58}_{-0.04}$ <sup>a</sup>	$0.47^{+0.03}_{-0.87}$	$0.47^{+0.03}_{-0.87}$	$0.63^{+0.13}_{-0.66}$
HDFS2 - 371	$1.20^{+0.04}_{-0.18}$	$-0.03^{+0.03}_{-0.03}$	$-0.03^{+0.03}_{-0.03}$	$0.20^{+0.28}_{-0.10}$
HDFS2 - 374	$0.14^{+1.80}_{-0.12}$ <sup>a</sup>	$-0.54^{+0.00}_{-0.42}$	$-0.54^{+0.00}_{-0.42}$	$-0.41^{+0.22}_{-0.54}$
HDFS2 - 376	$1.26^{+0.14}_{-0.20}$	$-0.09^{+0.02}_{-0.11}$	$-0.09^{+0.02}_{-0.11}$	$0.14^{+0.25}_{-0.14}$
HDFS2 - 377	$0.96^{+0.20}_{-0.04}$ <sup>a</sup>	$0.47^{+0.02}_{-0.20}$	$0.47^{+0.02}_{-0.20}$	$0.70^{+0.14}_{-0.37}$
HDFS2 - 379	$0.42^{+0.04}_{-0.18}$	$-0.26^{+0.10}_{-0.01}$	$-0.26^{+0.10}_{-0.01}$	$0.03^{+0.28}_{-0.13}$
HDFS2 - 382 <sup>b</sup>	$2.16^{+0.10}_{-0.82}$ <sup>a</sup>	$-0.48^{+0.11}_{-0.05}$	$-0.48^{+0.11}_{-0.05}$	$-0.30^{+0.24}_{-0.13}$
HDFS2 - 383	$0.50^{+0.08}_{-0.14}$	$-0.29^{+0.00}_{-0.05}$	$-0.29^{+0.00}_{-0.05}$	$-0.00^{+0.29}_{-0.16}$
HDFS2 - 390	$0.52^{+0.14}_{-0.34}$	$-0.38^{+0.01}_{-0.12}$	$-0.38^{+0.01}_{-0.12}$	$-0.14^{+0.29}_{-0.14}$
HDFS2 - 392	$0.54^{+3.74}_{-0.08}$ <sup>a</sup>	$-0.06^{+0.03}_{-0.72}$	$-0.06^{+0.03}_{-0.72}$	$0.05^{+0.30}_{-0.52}$
HDFS2 - 394 <sup>b</sup>	$1.46^{+0.54}_{-0.16}$	$-0.17^{+0.09}_{-0.07}$	$-0.17^{+0.09}_{-0.07}$	$0.09^{+0.16}_{-0.22}$
HDFS2 - 398	$0.20^{+0.26}_{-0.12}$	$-0.33^{+0.00}_{-0.12}$	$-0.33^{+0.00}_{-0.12}$	$-0.13^{+0.31}_{-0.18}$
HDFS2 - 402	$0.48^{+0.10}_{-0.06}$	$-0.30^{+0.00}_{-0.06}$	$-0.30^{+0.00}_{-0.06}$	$-0.01^{+0.21}_{-0.22}$
HDFS2 - 404	$1.16^{+0.12}_{-0.10}$	$0.26^{+0.03}_{-0.07}$	$0.26^{+0.03}_{-0.07}$	$0.50^{+0.20}_{-0.18}$
HDFS2 - 405 <sup>b</sup>	$2.42^{+0.44}_{-1.18}$ <sup>a</sup>	$-0.70^{+0.17}_{-0.01}$	$-0.70^{+0.17}_{-0.01}$	$0.03^{+0.11}_{-0.30}$
HDFS2 - 406	$0.72^{+0.04}_{-0.14}$	$-0.40^{+0.07}_{-0.01}$	$-0.40^{+0.07}_{-0.01}$	$-0.51^{+0.24}_{-0.17}$
HDFS2 - 407	$0.02^{+1.60}_{-0.00}$ <sup>a</sup>	$-0.40^{+0.00}_{-0.24}$	$-0.40^{+0.00}_{-0.24}$	$-0.15^{+0.10}_{-0.35}$
HDFS2 - 409 <sup>c</sup>	.....	.....	.....	.....
HDFS2 - 411	$2.08^{+0.46}_{-1.72}$ <sup>a</sup>	$-0.71^{+0.06}_{-0.05}$	$-0.71^{+0.06}_{-0.05}$	$-0.34^{+0.28}_{-0.10}$
HDFS2 - 412	$0.16^{+0.32}_{-0.06}$	$-0.09^{+0.00}_{-0.30}$	$-0.09^{+0.00}_{-0.30}$	$0.15^{+0.18}_{-0.44}$
HDFS2 - 413	$1.08^{+0.38}_{-0.54}$	$-0.33^{+0.00}_{-0.28}$	$-0.33^{+0.00}_{-0.28}$	$-0.01^{+0.15}_{-0.24}$
HDFS2 - 414	$0.88^{+2.62}_{-0.14}$ <sup>a</sup>	$-0.68^{+1.70}_{-0.11}$	$-0.68^{+1.70}_{-0.11}$	$-0.71^{+1.88}_{-0.15}$
HDFS2 - 415	$0.54^{+0.10}_{-0.06}$	$-0.39^{+0.02}_{-0.08}$	$-0.39^{+0.02}_{-0.08}$	$-0.28^{+0.26}_{-0.14}$
HDFS2 - 418	$0.46^{+3.40}_{-0.24}$ <sup>a</sup>	$-0.16^{+0.18}_{-0.61}$	$-0.16^{+0.18}_{-0.61}$	$0.09^{+0.25}_{-0.59}$
HDFS2 - 419	0.465	0.21	0.21	$0.54^{+0.16}_{-0.15}$
HDFS2 - 421	$4.86^{+0.32}_{-0.18}$ <sup>a</sup>	.....	.....	.....
HDFS2 - 422 <sup>b</sup>	2.028	-0.42	-0.42	$-0.31^{+0.15}_{-0.14}$
HDFS2 - 423 <sup>b</sup>	$2.76^{+0.18}_{-0.20}$	$-0.39^{+0.00}_{-0.11}$	$-0.39^{+0.00}_{-0.11}$	$-0.17^{+0.14}_{-0.19}$
HDFS2 - 424	$2.28^{+0.72}_{-1.98}$ <sup>a</sup>	$-0.24^{+0.04}_{-0.10}$	$-0.24^{+0.04}_{-0.10}$	$0.14^{+0.17}_{-0.17}$
HDFS2 - 426	$0.42^{+3.70}_{-0.06}$ <sup>a</sup>	$-0.06^{+0.01}_{-0.91}$	$-0.06^{+0.01}_{-0.91}$	$0.14^{+0.27}_{-0.92}$
HDFS2 - 427	$0.68^{+0.12}_{-0.02}$	$0.40^{+0.00}_{-0.08}$	$0.40^{+0.00}_{-0.08}$	$0.65^{+0.14}_{-0.25}$
HDFS2 - 428	$0.94^{+0.16}_{-0.06}$	$0.05^{+0.04}_{-0.04}$	$0.05^{+0.04}_{-0.04}$	$0.60^{+0.17}_{-0.26}$
HDFS2 - 431	$0.98^{+0.10}_{-0.28}$	$-0.41^{+0.04}_{-0.03}$	$-0.41^{+0.04}_{-0.03}$	$-0.16^{+0.16}_{-0.22}$
HDFS2 - 433 <sup>b</sup>	$1.34^{+0.68}_{-0.84}$ <sup>a</sup>	$-0.37^{+0.07}_{-0.18}$	$-0.37^{+0.07}_{-0.18}$	$-0.12^{+0.20}_{-0.15}$
HDFS2 - 434	$0.92^{+0.04}_{-0.16}$	$-0.40^{+0.01}_{-0.01}$	$-0.40^{+0.01}_{-0.01}$	$-0.26^{+0.20}_{-0.16}$

Table A.11: Colors,  $\mathcal{M}/L$ 's, and  $\mathcal{M}$ - continued

ID	$(U - B)_{\text{rest}}$	$(B - V)_{\text{rest}}$	$\log_{10}\mathcal{M}/L_V$	$\mathcal{M}$
HDFS2 - 435	$0.20^{1.74}_{0.00}$ <sup>a</sup>	$-0.28^{0.02}_{0.27}$	$-0.28^{0.02}_{0.27}$	$-0.19^{0.13}_{0.55}$
HDFS2 - 436	1.439	-0.34	-0.34	$0.04^{0.14}_{0.15}$
HDFS2 - 438	$0.46^{0.06}_{0.26}$	$-0.17^{0.09}_{0.02}$	$-0.17^{0.09}_{0.02}$	$0.25^{0.26}_{0.18}$
HDFS2 - 447	$0.22^{1.40}_{0.04}$ <sup>a</sup>	$-0.48^{0.13}_{0.09}$	$-0.48^{0.13}_{0.09}$	$0.04^{0.12}_{0.26}$
HDFS2 - 448	$2.04^{0.12}_{1.80}$ <sup>a</sup>	$-0.45^{0.08}_{0.09}$	$-0.45^{0.08}_{0.09}$	$-0.35^{0.30}_{0.06}$
HDFS2 - 449	$1.52^{0.10}_{0.14}$	$-0.63^{0.23}_{0.01}$	$-0.63^{0.23}_{0.01}$	$-0.02^{0.00}_{0.39}$
HDFS2 - 451	$0.64^{0.12}_{0.12}$	$-0.43^{0.03}_{0.04}$	$-0.43^{0.03}_{0.04}$	$-0.34^{0.25}_{0.20}$
HDFS2 - 452	$0.50^{0.40}_{0.24}$	$-0.51^{0.08}_{0.03}$	$-0.51^{0.08}_{0.03}$	$-0.03^{0.10}_{0.35}$
HDFS2 - 453 <sup>b</sup>	$2.14^{0.60}_{1.92}$ <sup>a</sup>	$-0.60^{0.41}_{0.28}$	$-0.60^{0.41}_{0.28}$	$-0.56^{0.46}_{0.10}$
HDFS2 - 459 <sup>b</sup>	$3.12^{0.14}_{2.78}$ <sup>a</sup>	$-0.51^{0.32}_{0.21}$	$-0.51^{0.32}_{0.21}$	$-0.36^{0.30}_{0.14}$
HDFS2 - 466	$0.46^{0.06}_{0.12}$	$-0.35^{0.02}_{0.01}$	$-0.35^{0.02}_{0.01}$	$-0.09^{0.21}_{0.22}$
HDFS2 - 467	$2.26^{0.84}_{0.26}$ <sup>a</sup>	$-0.04^{0.00}_{0.20}$	$-0.04^{0.00}_{0.20}$	$0.38^{0.16}_{0.24}$
HDFS2 - 469 <sup>c</sup>	.....	.....	.....	.....
HDFS2 - 470	$0.50^{3.36}_{0.02}$ <sup>a</sup>	$-0.31^{0.00}_{0.47}$	$-0.31^{0.00}_{0.47}$	$-0.23^{0.17}_{0.30}$
HDFS2 - 475 <sup>b</sup>	$2.04^{0.20}_{0.42}$ <sup>a</sup>	$-0.41^{0.00}_{0.24}$	$-0.41^{0.00}_{0.24}$	$-0.33^{0.25}_{0.14}$
HDFS2 - 481	$0.10^{1.94}_{0.08}$ <sup>a</sup>	$-0.46^{0.00}_{0.24}$	$-0.46^{0.00}_{0.24}$	$-0.38^{0.27}_{0.11}$
HDFS2 - 483 <sup>b</sup>	$2.74^{0.18}_{2.38}$ <sup>a</sup>	$-0.58^{0.00}_{0.13}$	$-0.58^{0.00}_{0.13}$	$-0.25^{0.17}_{0.17}$
HDFS2 - 487	$2.92^{0.20}_{0.40}$	$-0.40^{0.00}_{0.19}$	$-0.40^{0.00}_{0.19}$	$-0.24^{0.20}_{0.19}$
HDFS2 - 493 <sup>b</sup>	$2.24^{0.16}_{1.20}$ <sup>a</sup>	$-0.67^{0.17}_{0.03}$	$-0.67^{0.17}_{0.03}$	$-0.28^{0.17}_{0.19}$
HDFS2 - 498 <sup>b</sup>	$2.08^{0.20}_{0.24}$ <sup>a</sup>	$-0.86^{0.28}_{0.00}$	$-0.86^{0.28}_{0.00}$	$-0.54^{0.38}_{0.67}$
HDFS2 - 500	$1.30^{0.26}_{0.16}$	$-0.25^{0.03}_{0.15}$	$-0.25^{0.03}_{0.15}$	$0.04^{0.17}_{0.16}$
HDFS2 - 502	$3.16^{0.22}_{0.34}$	$-0.15^{0.00}_{0.13}$	$-0.15^{0.00}_{0.13}$	$0.19^{0.20}_{0.28}$
HDFS2 - 506	$3.62^{0.12}_{0.32}$	$-0.68^{0.12}_{0.00}$	.....	.....
HDFS2 - 511	$1.24^{0.12}_{0.76}$	$-0.29^{0.00}_{0.23}$	$-0.29^{0.00}_{0.23}$	$-0.04^{0.24}_{0.12}$
HDFS2 - 513	$0.76^{0.02}_{0.12}$	$-0.29^{0.04}_{0.01}$	$-0.29^{0.04}_{0.01}$	$-0.30^{0.23}_{0.12}$
HDFS2 - 515 <sup>b</sup>	$2.52^{0.10}_{0.20}$	$-0.48^{0.08}_{0.07}$	$-0.48^{0.08}_{0.07}$	$-0.58^{0.36}_{0.11}$
HDFS2 - 517	0.580	-0.24	-0.24	$0.08^{0.15}_{0.15}$
HDFS2 - 518	0.582	-0.31	-0.31	$0.10^{0.15}_{0.15}$
HDFS2 - 519	$1.40^{0.06}_{0.44}$	$-0.49^{0.09}_{0.15}$	$-0.49^{0.09}_{0.15}$	$-0.18^{0.25}_{0.13}$
HDFS2 - 525	$0.70^{0.08}_{0.12}$	$-0.32^{0.00}_{0.06}$	$-0.32^{0.00}_{0.06}$	$-0.17^{0.20}_{0.15}$
HDFS2 - 527	$0.48^{0.10}_{0.18}$	$0.09^{0.11}_{0.01}$	$0.09^{0.11}_{0.01}$	$0.51^{0.32}_{0.27}$
HDFS2 - 529	$3.84^{0.08}_{3.32}$ <sup>a</sup>	$-0.58^{0.37}_{0.04}$	.....	.....
HDFS2 - 532	$0.98^{0.12}_{0.04}$	$0.51^{0.03}_{0.13}$	$0.51^{0.03}_{0.13}$	$0.70^{0.15}_{0.23}$
HDFS2 - 542	$0.48^{0.08}_{0.28}$	$-0.18^{0.04}_{0.03}$	$-0.18^{0.04}_{0.03}$	$0.21^{0.25}_{0.16}$
HDFS2 - 543	$0.76^{0.02}_{0.12}$	$-0.24^{0.05}_{0.01}$	$-0.24^{0.05}_{0.01}$	$-0.34^{0.19}_{0.18}$
HDFS2 - 548	$0.28^{2.80}_{0.18}$ <sup>a</sup>	$-0.32^{0.05}_{0.17}$	$-0.32^{0.05}_{0.17}$	$-0.09^{0.29}_{0.39}$
HDFS2 - 554 <sup>b</sup>	$1.34^{0.34}_{0.18}$	$-0.26^{0.06}_{0.13}$	$-0.26^{0.06}_{0.13}$	$-0.06^{0.25}_{0.12}$
HDFS2 - 556	$0.46^{3.36}_{0.12}$ <sup>a</sup>	$-0.25^{0.01}_{0.57}$	$-0.25^{0.01}_{0.57}$	$-0.12^{0.26}_{0.37}$

Table A.11: Colors,  $\mathcal{M}/L$ 's, and  $\mathcal{M}$ - continued

ID	$(U - B)_{\text{rest}}$	$(B - V)_{\text{rest}}$	$\log_{10} \mathcal{M}/L_V$	$\mathcal{M}$
HDFS2 - 558	$3.10^{0.10}_{0.16}$	$-0.52^{0.13}_{0.07}$	$-0.52^{0.13}_{0.07}$	$-0.42^{0.22}_{0.13}$
HDFS2 - 559 <sup>b</sup>	$3.12^{0.18}_{0.10}$	$-0.25^{0.15}_{0.10}$	$-0.25^{0.15}_{0.10}$	$0.46^{0.19}_{0.17}$
HDFS2 - 560	$0.02^{2.04}_{0.00}$ <sup>a</sup>	$-0.14^{0.00}_{0.57}$	$-0.14^{0.00}_{0.57}$	$-0.35^{0.15}_{0.42}$
HDFS2 - 561	$0.48^{0.08}_{0.16}$	$-0.31^{0.01}_{0.05}$	$-0.31^{0.01}_{0.05}$	$-0.01^{0.24}_{0.21}$
HDFS2 - 566	$0.18^{3.86}_{0.00}$ <sup>a</sup>	$0.47^{0.01}_{1.20}$	$0.47^{0.01}_{1.20}$	$0.79^{0.11}_{1.07}$
HDFS2 - 567	$3.90^{0.26}_{0.02}$	$0.14^{0.01}_{0.07}$	.....	.....
HDFS2 - 568	$0.78^{0.08}_{0.04}$	$-0.09^{0.03}_{0.05}$	$-0.09^{0.03}_{0.05}$	$0.11^{0.13}_{0.22}$
HDFS2 - 571	$3.16^{0.44}_{2.44}$ <sup>a</sup>	$-0.47^{0.07}_{0.29}$	$-0.47^{0.07}_{0.29}$	$-0.40^{0.24}_{0.14}$
HDFS2 - 572 <sup>b</sup>	$2.42^{0.28}_{0.22}$	$-0.65^{0.11}_{0.01}$	$-0.65^{0.11}_{0.01}$	$0.11^{0.11}_{0.22}$
HDFS2 - 574 <sup>b</sup>	$2.86^{0.10}_{0.66}$	$-0.54^{0.03}_{0.10}$	$-0.54^{0.03}_{0.10}$	$-0.11^{0.11}_{0.24}$
HDFS2 - 578	$0.48^{0.04}_{0.02}$	$-0.38^{0.01}_{0.02}$	$-0.38^{0.01}_{0.02}$	$-0.40^{0.45}_{0.09}$
HDFS2 - 579	$2.04^{0.10}_{1.68}$ <sup>a</sup>	$-0.55^{0.15}_{0.11}$	$-0.55^{0.15}_{0.11}$	$-0.42^{0.28}_{0.10}$
HDFS2 - 581	$0.50^{0.02}_{0.04}$	$-0.34^{0.01}_{0.00}$	$-0.34^{0.01}_{0.00}$	$-0.28^{0.30}_{0.25}$
HDFS2 - 582	$1.34^{0.28}_{1.06}$ <sup>a</sup>	$-0.41^{0.02}_{0.23}$	$-0.41^{0.02}_{0.23}$	$-0.19^{0.29}_{0.08}$
HDFS2 - 585	$1.86^{0.06}_{1.62}$ <sup>a</sup>	$-0.69^{0.17}_{0.03}$	$-0.69^{0.17}_{0.03}$	$-0.21^{0.08}_{0.25}$
HDFS2 - 587	$2.26^{0.86}_{0.28}$ <sup>a</sup>	$-0.43^{0.09}_{0.08}$	$-0.43^{0.09}_{0.08}$	$0.08^{0.13}_{0.23}$
HDFS2 - 590 <sup>b</sup>	$2.92^{0.14}_{0.22}$	$-0.45^{0.03}_{0.09}$	$-0.45^{0.03}_{0.09}$	$-0.04^{0.16}_{0.19}$
HDFS2 - 592	$0.28^{0.06}_{0.10}$	$-0.07^{0.06}_{0.07}$	$-0.07^{0.06}_{0.07}$	$0.27^{0.21}_{0.13}$
HDFS2 - 593	$4.38^{0.06}_{0.04}$	.....	.....	.....
HDFS2 - 595	1.283	-0.05	-0.05	$0.17^{0.14}_{0.14}$
HDFS2 - 596	$3.00^{0.14}_{0.52}$ <sup>a</sup>	$-0.41^{0.03}_{0.09}$	$-0.41^{0.03}_{0.09}$	$-0.29^{0.19}_{0.17}$
HDFS2 - 601	$0.46^{0.02}_{0.38}$ <sup>a</sup>	$-0.41^{0.09}_{0.02}$	$-0.41^{0.09}_{0.02}$	$-0.31^{0.52}_{0.17}$
HDFS2 - 602	$0.50^{0.08}_{0.32}$	$-0.31^{0.00}_{0.07}$	$-0.31^{0.00}_{0.07}$	$0.01^{0.26}_{0.19}$
HDFS2 - 605	$0.70^{0.12}_{0.12}$	$-0.26^{0.03}_{0.07}$	$-0.26^{0.03}_{0.07}$	$-0.14^{0.19}_{0.17}$
HDFS2 - 608	0.540	-0.31	-0.31	$-0.05^{0.16}_{0.15}$
HDFS2 - 614	$3.52^{0.20}_{0.22}$	$0.51^{0.03}_{0.17}$	.....	.....
HDFS2 - 616	$0.48^{0.12}_{0.08}$	$-0.36^{0.00}_{0.05}$	$-0.36^{0.00}_{0.05}$	$-0.07^{0.24}_{0.19}$
HDFS2 - 617	$0.26^{0.08}_{0.12}$	$-0.37^{0.00}_{0.15}$	$-0.37^{0.00}_{0.15}$	$-0.27^{0.28}_{0.14}$
HDFS2 - 626 <sup>b</sup>	$3.14^{0.22}_{0.14}$ <sup>a</sup>	$-0.57^{0.09}_{0.12}$	$-0.57^{0.09}_{0.12}$	$-0.48^{0.21}_{0.14}$
HDFS2 - 628	$4.38^{0.10}_{4.36}$ <sup>a</sup>	.....	.....	.....
HDFS2 - 632	$4.34^{0.06}_{0.06}$	.....	.....	.....
HDFS2 - 633	$1.32^{0.60}_{0.02}$	$-0.08^{0.01}_{0.13}$	$-0.08^{0.01}_{0.13}$	$0.16^{0.16}_{0.16}$
HDFS2 - 639	$0.88^{0.08}_{0.68}$	$-0.16^{0.24}_{0.04}$	$-0.16^{0.24}_{0.04}$	$0.40^{0.32}_{0.19}$
HDFS2 - 652	$2.08^{0.28}_{0.96}$ <sup>a</sup>	$-0.40^{0.00}_{0.24}$	$-0.40^{0.00}_{0.24}$	$-0.10^{0.20}_{0.14}$
HDFS2 - 657	$1.00^{0.04}_{0.24}$	$-0.40^{0.00}_{0.12}$	$-0.40^{0.00}_{0.12}$	$-0.25^{0.20}_{0.13}$
HDFS2 - 668	$1.48^{0.10}_{0.32}$	$-0.40^{0.03}_{0.01}$	$-0.40^{0.03}_{0.01}$	$-0.42^{0.53}_{0.12}$
HDFS2 - 669	$1.66^{0.16}_{0.50}$ <sup>a</sup>	$-0.40^{0.02}_{0.06}$	$-0.40^{0.02}_{0.06}$	$-0.24^{0.35}_{0.02}$
HDFS2 - 674	$1.48^{0.06}_{0.52}$	$-0.48^{0.06}_{0.15}$	$-0.48^{0.06}_{0.15}$	$-0.27^{0.36}_{0.12}$

Table A.11: Colors,  $\mathcal{M}/L$ 's, and  $\mathcal{M}$ - continued

ID	$(U - B)_{\text{rest}}$	$(B - V)_{\text{rest}}$	$\log_{10} \mathcal{M}/L_V$	$\mathcal{M}$
HDFS2 - 677	$1.98^{0.06}_{1.84}^a$	$-0.59^{0.12}_{0.08}$	$-0.59^{0.12}_{0.08}$	$-0.46^{0.28}_{0.10}$
HDFS2 - 687	$0.48^{0.56}_{0.38}^a$	$-0.40^{0.13}_{0.17}$	$-0.40^{0.13}_{0.17}$	$-0.17^{0.35}_{0.23}$
HDFS2 - 694	$0.46^{0.02}_{0.26}$	$-0.30^{0.02}_{0.05}$	$-0.30^{0.02}_{0.05}$	$-0.00^{0.30}_{0.12}$
HDFS2 - 696	$0.52^{0.08}_{0.30}$	$-0.21^{0.00}_{0.06}$	$-0.21^{0.00}_{0.06}$	$0.05^{0.35}_{0.16}$
HDFS2 - 699	$2.10^{7.22}_{0.00}^a$	$0.38^{0.00}_{0.60}$	$0.38^{0.00}_{0.60}$	$0.67^{0.02}_{0.68}$
HDFS2 - 707 <sup>b</sup>	$2.56^{0.04}_{0.02}$	$-0.20^{0.01}_{0.02}$	$-0.20^{0.01}_{0.02}$	$-0.38^{0.11}_{0.23}$
HDFS2 - 716	$1.34^{0.00}_{1.30}^a$	$-0.63^{0.09}_{0.21}$	$-0.63^{0.09}_{0.21}$	$-0.16^{0.14}_{0.26}$
HDFS2 - 725	$3.26^{0.20}_{0.16}$	$-0.21^{0.00}_{0.09}$	.....	.....
HDFS2 - 736 <sup>b</sup>	$2.66^{0.22}_{0.22}$	$-0.64^{0.08}_{0.05}$	$-0.64^{0.08}_{0.05}$	$-0.31^{0.22}_{0.11}$
HDFS2 - 740	$2.98^{0.26}_{0.30}$	$-0.22^{0.01}_{0.05}$	$-0.22^{0.01}_{0.05}$	$0.12^{0.17}_{0.25}$
HDFS2 - 764	$1.74^{0.14}_{0.26}$	$0.13^{0.20}_{0.03}$	$0.13^{0.20}_{0.03}$	$0.40^{0.21}_{0.17}$
HDFS2 - 771	$3.00^{0.14}_{0.20}$	$-0.30^{0.02}_{0.06}$	$-0.30^{0.02}_{0.06}$	$-0.15^{0.14}_{0.23}$
HDFS2 - 773	$3.66^{0.14}_{0.38}^a$	$-0.27^{0.01}_{0.05}$	.....	.....
HDFS2 - 776	$0.40^{1.72}_{0.02}^a$	$-0.21^{0.04}_{0.18}$	$-0.21^{0.04}_{0.18}$	$-0.17^{0.19}_{0.26}$
HDFS2 - 786 <sup>b</sup>	$3.14^{0.18}_{2.68}^a$	$-0.52^{0.17}_{0.08}$	$-0.52^{0.17}_{0.08}$	$-0.42^{0.26}_{0.13}$
HDFS2 - 790	$1.00^{0.04}_{0.24}$	$-0.40^{0.04}_{0.01}$	$-0.40^{0.04}_{0.01}$	$-0.14^{0.32}_{0.06}$
HDFS2 - 791	$0.66^{0.28}_{0.56}$	$-0.40^{0.00}_{0.13}$	$-0.40^{0.00}_{0.13}$	$-0.18^{0.20}_{0.18}$
HDFS2 - 792	$0.46^{0.06}_{0.22}$	$-0.23^{0.06}_{0.03}$	$-0.23^{0.06}_{0.03}$	$0.13^{0.25}_{0.18}$
HDFS2 - 801	$0.04^{2.04}_{0.02}^a$	$-0.40^{0.00}_{0.33}$	$-0.40^{0.00}_{0.33}$	$-0.32^{0.20}_{0.14}$
HDFS2 - 802	$1.32^{0.40}_{0.12}$	$-0.21^{0.04}_{0.12}$	$-0.21^{0.04}_{0.12}$	$0.06^{0.18}_{0.16}$
HDFS2 - 803	$0.70^{0.20}_{0.18}$	$-0.27^{0.01}_{0.12}$	$-0.27^{0.01}_{0.12}$	$-0.04^{0.26}_{0.25}$
HDFS2 - 806	$2.64^{0.12}_{0.34}$	$0.35^{0.14}_{0.01}$	$0.35^{0.14}_{0.01}$	$0.53^{0.25}_{0.16}$
HDFS2 - 808	$0.54^{3.32}_{0.06}^a$	$-0.28^{0.00}_{0.10}$	$-0.28^{0.00}_{0.10}$	$-0.05^{0.19}_{0.22}$
HDFS2 - 809	$1.26^{0.66}_{1.22}^a$	$-0.50^{0.00}_{0.20}$	$-0.50^{0.00}_{0.20}$	$-0.30^{0.17}_{0.16}$
HDFS2 - 810	$0.94^{0.02}_{0.18}$	$-0.41^{0.09}_{0.00}$	$-0.41^{0.09}_{0.00}$	$-0.26^{0.27}_{0.10}$
HDFS2 - 812 <sup>b</sup>	2.793	-0.34	-0.34	$-0.23^{0.14}_{0.15}$
HDFS2 - 813 <sup>c</sup>	.....	.....	.....	.....
HDFS2 - 817	$0.34^{3.36}_{0.04}^a$	$-0.17^{0.00}_{0.65}$	$-0.17^{0.00}_{0.65}$	$-0.10^{0.14}_{0.43}$
HDFS2 - 823	$1.06^{0.04}_{0.72}$	$-0.38^{0.00}_{0.26}$	$-0.38^{0.00}_{0.26}$	$-0.09^{0.28}_{0.15}$
HDFS2 - 824	$0.96^{0.10}_{0.10}$	$0.05^{0.00}_{0.03}$	$0.05^{0.00}_{0.03}$	$0.42^{0.20}_{0.19}$
HDFS2 - 828 <sup>b</sup>	$2.70^{0.22}_{2.36}^a$	$-0.44^{0.08}_{0.13}$	$-0.44^{0.08}_{0.13}$	$-0.46^{0.45}_{0.02}$
HDFS2 - 830	$0.94^{0.02}_{0.06}$	$-0.26^{0.00}_{0.01}$	$-0.26^{0.00}_{0.01}$	$0.03^{0.17}_{0.14}$
HDFS2 - 842	$3.76^{0.14}_{0.62}^a$	$-0.95^{0.70}_{0.00}$	.....	.....
HDFS2 - 843	$0.86^{0.06}_{0.68}$	$-0.37^{0.15}_{0.04}$	$-0.37^{0.15}_{0.04}$	$-0.17^{0.27}_{0.13}$
HDFS2 - 845	$0.46^{0.04}_{0.12}$	$-0.43^{0.03}_{0.07}$	$-0.43^{0.03}_{0.07}$	$-0.30^{0.32}_{0.16}$
HDFS2 - 863	$1.02^{0.08}_{0.08}$	$0.38^{0.00}_{0.04}$	$0.38^{0.00}_{0.04}$	$0.68^{0.19}_{0.17}$
HDFS2 - 864 <sup>b</sup>	$0.16^{0.84}_{0.04}^a$	$0.04^{0.19}_{0.45}$	$0.04^{0.19}_{0.45}$	$0.05^{0.19}_{0.17}$
HDFS2 - 873	$1.20^{0.40}_{0.06}$	$0.39^{0.02}_{0.30}$	$0.39^{0.02}_{0.30}$	$0.65^{0.15}_{0.33}$

Table A.11: Colors,  $\mathcal{M}/L$ 's, and  $\mathcal{M}$ - continued

ID	$(U - B)_{\text{rest}}$	$(B - V)_{\text{rest}}$	$\log_{10}\mathcal{M}/L_V$	$\mathcal{M}$
HDFS2 - 877	$0.42^{0.10}_{0.20}$	$-0.21^{0.10}_{0.01}$	$-0.21^{0.10}_{0.01}$	$0.14^{0.24}_{0.15}$
HDFS2 - 883	$0.62^{3.76}_{0.00}$ a	$-0.04^{0.00}_{0.70}$	$-0.04^{0.00}_{0.70}$	$0.00^{0.07}_{0.49}$
HDFS2 - 885 b	$3.22^{0.18}_{3.04}$ a	$-0.34^{0.52}_{0.07}$	.....	.....
HDFS2 - 890	$0.96^{0.04}_{0.16}$	$-0.29^{0.00}_{0.06}$	$-0.29^{0.00}_{0.06}$	$0.09^{0.20}_{0.15}$
HDFS2 - 891	$0.72^{0.10}_{0.62}$	$-0.40^{0.08}_{0.04}$	$-0.40^{0.08}_{0.04}$	$-0.19^{0.21}_{0.15}$
HDFS2 - 904	$1.18^{0.50}_{1.02}$ a	$-0.48^{0.00}_{0.21}$	$-0.48^{0.00}_{0.21}$	$-0.30^{0.21}_{0.12}$
HDFS2 - 908	$2.28^{7.26}_{0.16}$ a	$0.48^{0.04}_{0.91}$	$0.48^{0.04}_{0.91}$	$0.55^{0.29}_{0.62}$
HDFS2 - 910	$0.58^{3.64}_{0.08}$ a	$-0.09^{0.01}_{0.65}$	$-0.09^{0.01}_{0.65}$	$0.11^{0.25}_{0.46}$
HDFS2 - 911	$0.56^{0.02}_{0.02}$	$0.57^{0.06}_{0.04}$	$0.57^{0.06}_{0.04}$	$0.70^{0.18}_{0.16}$
HDFS2 - 918	$0.48^{0.22}_{0.02}$	$-0.42^{0.03}_{0.17}$	$-0.42^{0.03}_{0.17}$	$-0.36^{0.33}_{0.13}$
HDFS2 - 919	$0.88^{0.04}_{0.04}$	$-0.36^{0.03}_{0.01}$	$-0.36^{0.03}_{0.01}$	$-0.37^{0.15}_{0.15}$
HDFS2 - 921	$0.06^{2.08}_{0.02}$ a	$-0.18^{0.00}_{0.53}$	$-0.18^{0.00}_{0.53}$	$-0.30^{0.17}_{0.17}$
HDFS2 - 924 b	$3.12^{0.14}_{2.96}$ a	$-0.55^{0.33}_{0.17}$	$-0.55^{0.33}_{0.17}$	$-0.48^{0.57}_{0.13}$
HDFS2 - 925	$0.70^{0.08}_{0.16}$	$-0.30^{0.03}_{0.07}$	$-0.30^{0.03}_{0.07}$	$-0.14^{0.22}_{0.14}$
HDFS2 - 926 b	$0.02^{2.14}_{0.00}$ a	$-0.11^{0.00}_{0.51}$	$-0.11^{0.00}_{0.51}$	$-0.12^{0.11}_{0.34}$
HDFS2 - 929 b	$1.42^{0.52}_{0.18}$	$-0.07^{0.08}_{0.07}$	$-0.07^{0.08}_{0.07}$	$0.15^{0.25}_{0.17}$
HDFS2 - 934	$0.42^{0.06}_{0.12}$	$-0.32^{0.05}_{0.00}$	$-0.32^{0.05}_{0.00}$	$0.04^{0.19}_{0.19}$
HDFS2 - 935	$0.48^{0.04}_{0.24}$	$-0.38^{0.02}_{0.02}$	$-0.38^{0.02}_{0.02}$	$-0.11^{0.29}_{0.13}$
HDFS2 - 939	$0.16^{0.58}_{0.02}$ a	$0.19^{0.01}_{0.55}$	$0.19^{0.01}_{0.55}$	$0.60^{0.15}_{0.66}$
HDFS2 - 943	$0.06^{0.02}_{0.04}$	$-0.40^{0.02}_{0.00}$	$-0.40^{0.02}_{0.00}$	$-0.30^{0.25}_{0.13}$
HDFS2 - 947	$1.54^{0.40}_{0.38}$	$-0.12^{0.09}_{0.02}$	$-0.12^{0.09}_{0.02}$	$0.18^{0.25}_{0.19}$
HDFS2 - 949 b	$1.56^{0.24}_{0.18}$	$-0.19^{0.09}_{0.02}$	$-0.19^{0.09}_{0.02}$	$0.11^{0.14}_{0.19}$
HDFS2 - 959	$0.78^{0.14}_{0.08}$	$-0.25^{0.04}_{0.07}$	$-0.25^{0.04}_{0.07}$	$-0.21^{0.27}_{0.12}$
HDFS2 - 962	$1.02^{0.10}_{0.70}$	$-0.41^{0.01}_{0.23}$	$-0.41^{0.01}_{0.23}$	$-0.14^{0.19}_{0.20}$
HDFS2 - 968	$1.52^{0.32}_{0.18}$	$0.05^{0.19}_{0.08}$	$0.05^{0.19}_{0.08}$	$0.48^{0.18}_{0.16}$
HDFS2 - 969	$0.50^{0.06}_{0.04}$	$0.48^{0.02}_{0.04}$	$0.48^{0.02}_{0.04}$	$0.71^{0.20}_{0.20}$
HDFS2 - 974	$0.50^{0.12}_{0.26}$	$-0.15^{0.05}_{0.05}$	$-0.15^{0.05}_{0.05}$	$0.16^{0.30}_{0.21}$
HDFS2 - 975	$0.76^{0.10}_{0.12}$	$-0.30^{0.03}_{0.06}$	$-0.30^{0.03}_{0.06}$	$-0.27^{0.22}_{0.15}$
HDFS2 - 978	$1.34^{0.44}_{0.08}$	$-0.06^{0.04}_{0.10}$	$-0.06^{0.04}_{0.10}$	$0.19^{0.20}_{0.14}$
HDFS2 - 985	$0.82^{0.06}_{0.24}$	$-0.40^{0.00}_{0.27}$	$-0.40^{0.00}_{0.27}$	$-0.45^{0.24}_{0.10}$
HDFS2 - 996	$2.04^{0.14}_{1.90}$ a	$-0.41^{0.09}_{0.23}$	$-0.41^{0.09}_{0.23}$	$-0.38^{0.34}_{0.06}$
HDFS2 - 1000	$0.48^{0.04}_{0.08}$	$-0.39^{0.02}_{0.00}$	$-0.39^{0.02}_{0.00}$	$-0.16^{0.28}_{0.15}$
HDFS2 - 1005	$1.38^{0.28}_{0.18}$	$-0.22^{0.08}_{0.08}$	$-0.22^{0.08}_{0.08}$	$0.03^{0.24}_{0.14}$
HDFS2 - 1018	$0.78^{0.08}_{0.02}$	$-0.22^{0.01}_{0.07}$	$-0.22^{0.01}_{0.07}$	$-0.31^{0.16}_{0.16}$
HDFS2 - 1022 b	$1.98^{0.18}_{0.70}$	$-0.32^{0.09}_{0.08}$	$-0.32^{0.09}_{0.08}$	$-0.07^{0.21}_{0.26}$
HDFS2 - 1023	$3.56^{0.10}_{0.14}$	$-0.24^{0.03}_{0.02}$	.....	.....
HDFS2 - 1029	$2.16^{0.12}_{0.14}$	$-0.05^{0.12}_{0.14}$	$-0.05^{0.12}_{0.14}$	$0.16^{0.18}_{0.15}$
HDFS2 - 1032	$1.88^{4.36}_{0.14}$ a	$0.19^{0.05}_{0.46}$	$0.19^{0.05}_{0.46}$	$0.33^{0.21}_{0.35}$

Table A.11: Colors,  $\mathcal{M}/L$ 's, and  $\mathcal{M}$ - continued

ID	$(U - B)_{\text{rest}}$	$(B - V)_{\text{rest}}$	$\log_{10} \mathcal{M}/L_V$	$\mathcal{M}$
HDFS2 – 1035	$0.46^{0.18}_{0.36}$ <sup>a</sup>	$-0.41^{0.02}_{0.23}$	$-0.41^{0.02}_{0.23}$	$-0.16^{0.36}_{0.38}$
HDFS2 – 1038 <sup>b</sup>	2.790	-0.56	-0.56	$-0.39^{0.15}_{0.15}$
HDFS2 – 1041	$1.62^{0.02}_{0.26}$	$-0.43^{0.04}_{0.00}$	$-0.43^{0.04}_{0.00}$	$0.00^{0.11}_{0.28}$
HDFS2 – 1044	$3.14^{0.26}_{2.80}$ <sup>a</sup>	$-0.49^{0.44}_{0.13}$	$-0.49^{0.44}_{0.13}$	$-0.30^{0.31}_{0.13}$
HDFS2 – 1045	$0.16^{1.20}_{0.04}$ <sup>a</sup>	$-0.50^{0.10}_{0.12}$	$-0.50^{0.10}_{0.12}$	$-0.17^{0.18}_{0.19}$
HDFS2 – 1051	$0.46^{0.04}_{0.08}$	$0.28^{0.00}_{0.01}$	$0.28^{0.00}_{0.01}$	$0.75^{0.21}_{0.21}$
HDFS2 – 1054	$1.32^{0.42}_{0.06}$	$-0.10^{0.04}_{0.11}$	$-0.10^{0.04}_{0.11}$	$0.16^{0.19}_{0.15}$
HDFS2 – 1065	$1.22^{0.16}_{0.16}$	$0.12^{0.02}_{0.14}$	$0.12^{0.02}_{0.14}$	$0.36^{0.24}_{0.14}$
HDFS2 – 1066	$2.70^{0.06}_{2.66}$ <sup>a</sup>	$-0.78^{0.46}_{0.02}$	$-0.78^{0.46}_{0.02}$	$-0.62^{0.48}_{0.05}$
HDFS2 – 1069	$0.28^{3.36}_{0.10}$ <sup>a</sup>	$0.13^{0.00}_{0.80}$	$0.13^{0.00}_{0.80}$	$0.20^{0.27}_{0.53}$
HDFS2 – 1074 <sup>b</sup>	$2.48^{0.40}_{0.22}$	$-0.43^{0.07}_{0.06}$	$-0.43^{0.07}_{0.06}$	$-0.34^{0.35}_{0.00}$
HDFS2 – 1078	$3.10^{0.20}_{2.68}$ <sup>a</sup>	$-0.41^{0.02}_{0.13}$	$-0.41^{0.02}_{0.13}$	$-0.15^{0.12}_{0.28}$
HDFS2 – 1081	$0.76^{0.08}_{0.12}$	$-0.40^{0.00}_{0.09}$	$-0.40^{0.00}_{0.09}$	$-0.49^{0.22}_{0.12}$
HDFS2 – 1086 <sup>b</sup>	$2.58^{0.34}_{0.06}$	$-0.40^{0.00}_{0.08}$	$-0.40^{0.00}_{0.08}$	$-0.33^{0.16}_{0.21}$
HDFS2 – 1088	$1.06^{0.20}_{0.34}$	$-0.42^{0.00}_{0.22}$	$-0.42^{0.00}_{0.22}$	$-0.15^{0.11}_{0.24}$
HDFS2 – 1092 <sup>b</sup>	$2.60^{0.14}_{2.22}$ <sup>a</sup>	$-0.62^{0.18}_{0.04}$	$-0.62^{0.18}_{0.04}$	$-0.25^{0.23}_{0.15}$
HDFS2 – 1097	$1.02^{0.06}_{0.22}$	$-0.13^{0.00}_{0.07}$	$-0.13^{0.00}_{0.07}$	$0.20^{0.27}_{0.12}$
HDFS2 – 1100	$0.54^{0.08}_{0.14}$	$-0.18^{0.00}_{0.06}$	$-0.18^{0.00}_{0.06}$	$0.01^{0.34}_{0.14}$
HDFS2 – 1102	$1.64^{5.06}_{0.08}$ <sup>a</sup>	$0.55^{0.10}_{1.11}$	$0.55^{0.10}_{1.11}$	$0.66^{0.17}_{0.90}$
HDFS2 – 1104	$0.30^{0.04}_{0.12}$	$-0.09^{0.07}_{0.04}$	$-0.09^{0.07}_{0.04}$	$0.21^{0.25}_{0.12}$
HDFS2 – 1105	$3.00^{0.14}_{0.78}$ <sup>a</sup>	$-0.38^{0.15}_{0.04}$	$-0.38^{0.15}_{0.04}$	$-0.05^{0.19}_{0.21}$
HDFS2 – 1107	$0.94^{0.00}_{0.92}$	$-0.59^{0.00}_{0.14}$	$-0.59^{0.00}_{0.14}$	$-0.16^{0.08}_{0.33}$
HDFS2 – 1111	$4.16^{0.16}_{3.70}$ <sup>a</sup>	.....	.....	.....
HDFS2 – 1112 <sup>b</sup>	$2.84^{0.06}_{2.82}$ <sup>a</sup>	$-0.90^{1.64}_{0.00}$	$-0.90^{1.64}_{0.00}$	$-0.67^{0.63}_{0.10}$

<sup>a</sup>  $\geq 1\%$  of Monte-Carlo realizations have  $z \geq 1$  away from  $z_{\text{phot}}$

<sup>b</sup> Meets U-dropout color criteria

<sup>c</sup> Redshift is likely in error

<sup>d</sup> Rest-frame colors are likely in error

Note. – Objects with  $z_{\text{phot}} < 5.2$  and no luminosity or color measurements have  $25 \geq K_{s,AB} < 26$ .

Note. – Objects with no redshift, color, and luminosity errors have spectroscopic redshifts



## REFERENCES

- Adelberger, K. L. & Steidel, C. C. 2000, *ApJ*, 544, 218
- Arp, H. 1966, *ApJS*, 14, 1
- Barger, A. J., Cowie, L. L., Sanders, D. B., Fulton, E., Taniguchi, Y., Sato, Y., Kawara, K., & Okuda, H. 1998, *Nature*, 394, 248
- Barger, A. J., Cowie, L. L., Smail, I., Ivison, R. J., Blain, A. W., & Kneib, J.-P. 1999, *AJ*, 117, 2656
- Baugh, C. M., Cole, S., Frenk, C. S., & Lacey, C. G. 1998, *ApJ*, 498, 504
- Baum, W. A. 1962, *IAU Symposium* 15, 390
- Bell, E. F. & de Jong, R. S. 2001, *ApJ*, 550, 212
- Benítez, N. 2000, *ApJ*, 536, 571
- Benítez, N., Broadhurst, T., Bouwens, R., Silk, J., & Rosati, P. 1999, *ApJ*, 515, L65
- Bertin, E. & Arnouts, S. 1996, *A&AS*, 117, 393
- Bessell, M. S. & Brett, J. M. 1988, *PASP*, 100, 1134
- Bessell, M. S. 1990, *PASP*, 102, 1181
- Blanton, M. R. et al. 2001, *AJ*, 121, 2358
- Bolzonella, M., Miralles, J.-M., & Pelló, R. 2000, *A&A*, 363, 476
- Bonatto, C., Bica, E., & Alloin, D. 1995, *A&AS*, 112, 71
- Brinchmann, J. & Ellis, R. S. 2000, *ApJ*, 536, L77
- Broadhurst, T. J., Ellis, R. S., & Shanks, T. 1988, *MNRAS*, 235, 827
- Broadhurst, T. & Bouwens, R. J. 2000, *ApJ*, 530, L53
- Bruzual A., G. & Charlot, S. 1993, *ApJ*, 405, 538
- Bruzual, G. & Charlot, S. 2001, in preparation
- Budavári, T. ;., Szalay, A. S., Connolly, A. J., Csabai, I. ;., & Dickinson, M. 2000, *AJ*, 120, 1588

- Casertano, S. et al. 2000, AJ, 120, 2747
- Cohen, J. G., Cowie, L. L., Hogg, D. W., Songaila, A., Blandford, R., Hu, E. M., & Shopbell, P. 1996, ApJ, 471, L5
- Cohen, J. G., Hogg, D. W., Blandford, R., Cowie, L. L., Hu, E., Songaila, A., Shopbell, P., & Richberg, K. 2000, ApJ, 538, 29
- Cole, S., Aragon-Salamanca, A., Frenk, C. S., Navarro, J. F., & Zepf, S. E. 1994, MNRAS, 271, 781
- Cole, S., Lacey, C. G., Baugh, C. M., & Frenk, C. S. 2000, MNRAS, 319, 168
- Cole, S. et al. 2001, MNRAS, 326, 255
- Coleman, G. D., Wu, C. -C., & Weedman, D. W. 1980, ApJS, 43, 393
- Colless, M., Ellis, R. S., Taylor, K., & Hook, R. N. 1990, MNRAS, 244, 408
- Connolly, A. J., Csabai, I., Szalay, A. S., Koo, D. C., Kron, R. G., & Munn, J. A. 1995, AJ, 110, 2655
- Cowie, L. L., Gardner, J. P., Lilly, S. J., & McLean, I. 1990, ApJ, 360, L1
- Cowie, L. L., Gardner, J. P., Hu, E. M., Songaila, A., Hodapp, K.-W., & Wainscoat, R. J. 1994, ApJ, 434, 114
- Cox, A. N. 2000, Allen's astrophysical quantities, (4th ed. New York: AIP Press; Springer)
- Cristiani, S. et al. 2000, A&A, 359, 489
- Csabai, I., Connolly, A. J., Szalay, A. S., & Budavári, T. 2000, AJ, 119, 69
- da Costa et al. 1998 submitted to A & A
- Dickinson, M. et al. 2000, ApJ, 531, 624
- Dickinson, M. 2001, in preparation
- Dickinson, M., 2001b, to appear in XIXth Moriond Astrophysics Meeting, Building Galaxies: From the Primordial Universe to the Present, ed. Cayatte, T. V., Guideroni, B., & Trinh Than Van, J., (Paris:Ed. Frontieres), 257, *astro-ph/0004027*
- Eisenhardt, P. & Dickinson, M. 1992, ApJ, 399, L47

- Ellis, R. 2001, updated lectures from the XIth Canary Islands Winter School of Astrophysics "Galaxies at High Redshift", astro-ph/0102056
- Fernández-Soto, A., Lanzetta, K. M., & Yahil, A. 1999, *ApJ*, 513, 34
- Fernández-Soto, A., Lanzetta, K. M., Chen, H., Pascarelle, S. M., & Yahata, N. 2001, *ApJS*, 135, 41
- Fioc, M. & Rocca-Volmerange, B. 1997, *A&A*, 326, 950
- Folkes, S. et al. 1999, *MNRAS*, 308, 459
- Fontana, A., Menci, N., D'Odorico, S., Giallongo, E., Poli, F., Cristiani, S., Moorwood, A., & Saracco, P. 1999, *MNRAS*, 310, L27
- Fontana, A., D'Odorico, S., Poli, F., Giallongo, E., Arnouts, S., Cristiani, S., Moorwood, A., & Saracco, P. 2000, *AJ*, 120, 2206
- Franx, M. et al. 2000, *The Messenger*, 99, 20
- Fried, J. W. et al. 2001, *A&A*, 367, 788
- Fukugita, M., Hogan, C. J., & Peebles, P. J. E. 1998, *ApJ*, 503, 518
- Huchra, J. P. 1977, *ApJ*, 217, 928
- Giallongo, E., D'Odorico, S., Fontana, A., Cristiani, S., Egami, E., Hu, E., & McMahon, R. G. 1998, *AJ*, 115, 2169
- Giallongo, E., Menci, N., Poli, F., D'Odorico, S., & Fontana, A. 2000, *ApJ*, 530, L73
- Giavalisco, M., Steidel, C. C., & Macchetto, F. D. 1996, *ApJ*, 470, 189
- Giavalisco, M., Steidel, C. C., Adelberger, K. L., Dickinson, M. E., Pettini, M., & Kellogg, M. 1998, *ApJ*, 503, 543
- Glazebrook, K. et al. 2001, in preparation
- González Delgado, R. M., García-Vargas, M. ;., Goldader, J., Leitherer, C., & Pasquali, A. 1999, *ApJ*, 513, 707
- Guhathakurta, P., Tyson, J. A., & Majewski, S. R. 1990, *ApJ*, 357, L9
- Gwyn, S. D. J. & Hartwick, F. D. A. 1996, *ApJ*, 468, L77
- Haehnelt, M. G., Steinmetz, M., & Rauch, M. 1998, *ApJ*, 495, 647

- Hogg, D. W., Neugebauer, G., Armus, L., Matthews, K., Pahre, M. A., Soifer, B. T., & Weinberger, A. J. 1997, *AJ*, 113, 2338
- Hogg, D. W. et al. 1998, *AJ*, 115, 1418
- Hu, E. M., Songaila, A., Cowie, L. L., & Stockton, A. 1991, *ApJ*, 368, 28
- Hu, E. M., McMahon, R. G., & Cowie, L. L. 1999, *ApJ*, 522, L9
- Kauffmann, G. & Charlot, S. 1998, *MNRAS*, 297, L23
- Kauffmann, G. & White, S. D. M. 1993, *MNRAS*, 261, 921
- Kauffmann, G., White, S. D. M., & Guiderdoni, B. 1993, *MNRAS*, 264, 201
- Kinney, A. L., Calzetti, D., Bohlin, R. C., McQuade, K., Storchi-Bergmann, T., & Schmitt, H. R. 1996, *ApJ*, 467, 38
- Koo, D. C. 1985, *AJ*, 90, 418
- Koo, D. C. 1986, *ApJ*, 311, 651
- Kron, R. G. 1980, *ApJS*, 43, 305
- Kulkarni, S. R. et al. 1999, *Nature*, 398, 389
- Labbé, I. et al. 2001, in preparation
- Lanzetta, K. M., Yahil, A., & Fernandez-Soto, A. 1996, *Nature*, 381, 759
- Larson, R. B. & Tinsley, B. M. 1978, *ApJ*, 219, 46
- Lilly, S. J., Le Fevre, O., Crampton, D., Hammer, F., & Tresse, L. 1995, *ApJ*, 455, 50
- Lilly, S. J., Tresse, L., Hammer, F., Crampton, D., & Le Fevre, O. 1995, *ApJ*, 455, 108
- Lilly, S. J., Le Fevre, O., Hammer, F., & Crampton, D. 1996, *ApJ*, 460, L1
- Lilly, S. et al. 1998, *ApJ*, 500, 75
- Liu, M. C., Charlot, S. ;., & Graham, J. R. 2000, *ApJ*, 543, 644
- Loh, E. D. & Spillar, E. J. 1986, *ApJ*, 303, 154
- Lowenthal, J. D., Hogan, C. J., Green, R. F., Caulet, A., Woodgate, B. E., Brown, L., & Foltz, C. B. 1991, *ApJ*, 377, L73

- Madau, P. 1995, *ApJ*, 441, 18
- Madau, P., Ferguson, H. C., Dickinson, M. E., Giavalisco, M., Steidel, C. C., & Fruchter, A. 1996, *MNRAS*, 283, 1388
- Mobasher, B. & Mazzei, P. 2000, *A&A*, 363, 517
- Moore, B., Quinn, T., Governato, F., Stadel, J., & Lake, G. 1999, *MNRAS*, 310, 1147
- Moorwood, A. F. 1997, *Proc. SPIE*, 2871, 1146
- Papovich, C., Dickinson, M., Ferguson, H. C., 2001, *ApJ*, 559, 620
- Pascarelle, S. M., Lanzetta, K. M., & Fernández-Soto, A. 1998, *ApJ*, 508, L1
- Pearce, F. R. et al. 1999, *ApJ*, 521, L99
- Persson, S. E., Murphy, D. C., Krzeminski, W., Roth, M., & Rieke, M. J. 1998, *AJ*, 116, 2475
- Pettini, M., Steidel, C. C., Adelberger, K. L., Dickinson, M., & Giavalisco, M. 2000, *ApJ*, 528, 96
- Pettini, M., Shapley, A. E., Steidel, C. C., Cuby, J., Dickinson, M., Moorwood, A. F. M., Adelberger, K. L., & Giavalisco, M. 2001, *ApJ*, 554, 981
- Poli, F., Giallongo, E., Menci, N., D'Odorico, S., & Fontana, A. 1999, *ApJ*, 527, 662
- Ponder, J. M. et al. 1998, *AJ*, 116, 2297
- Porciani, C., Giavalisco, M. 2001, *ApJ*, astro-ph/0107447
- Pozzetti, L., Bruzual A., G., & Zamorani, G. 1996, *MNRAS*, 281, 953
- Press, W. H., Vetterling, W. T., Teukolsky, S. A., Flannery, B. P., 1992, "Numerical Recipes in Fortran 77: 2nd edition", Cambridge University Press: New York.
- Puschell, J. J., Owen, F. N., & Laing, R. A. 1982, *ApJ*, 257, L57
- Rigopoulou, D. et al. 2000, *ApJ*, 537, L85
- Rudnick, G., Rix, H.-W., & Kennicutt, R. C. 2000, *ApJ*, 538, 569
- Salpeter, E. E. 1955, *ApJ*, 121, 161
- Sandage, A. 1961, *ApJ*, 134, 916
- Sawicki, M. J., Lin, H., & Yee, H. K. C. 1997, *AJ*, 113, 1

- Sawicki, M. & Yee, H. K. C. 1998, *AJ*, 115, 1329
- Schade, D., Lilly, S. J., Le Fevre, O., Hammer, F., & Crampton, D. 1996, *ApJ*, 464, 79
- Shapley, A. E., Steidel, C. C., Adelberger, K. L., Dickinson, M., Giavalisco, M., & Pettini, M. 2001, *ApJ*, astro-ph/0107324
- Somerville, R. S. & Primack, J. R. 1999, *MNRAS*, 310, 1087
- Somerville, R. S., Primack, J. R., & Faber, S. M. 2001, *MNRAS*, 320, 504
- Songaila, A., Cowie, L. L., Hu, E. M., & Gardner, J. P. 1994, *ApJS*, 94, 461
- Stanford, S. A., Eisenhardt, P. R. M., & Dickinson, M. 1995, *ApJ*, 450, 512
- Steidel, C. C. & Hamilton, D. 1992, *AJ*, 104, 941
- Steidel, C. C., Giavalisco, M., Pettini, M., Dickinson, M., & Adelberger, K. L. 1996, *ApJ*, 462, L17
- Steidel, C. C., Adelberger, K. L., Giavalisco, M., Dickinson, M., & Pettini, M. 1999, *ApJ*, 519, 1
- Steinmetz, M. & Navarro, J. F. 1999, *ApJ*, 513, 555
- Tinsley, B. M. 1980, *Fundamentals of Cosmic Physics*, 5, 287
- Thompson, R. I., Weymann, R. J., & Storrie-Lombardi, L. J. 2001, *ApJ*, 546, 694
- Tyson, J. A. 1988, *AJ*, 96, 1
- Walborn, N. R., Lennon, D. J., Heap, S. R., Lindler, D. J., Smith, L. J., Evans, C. J., & Parker, J. W. 2000, *PASP*, 112, 1243
- Wang, Y., Bahcall, N., & Turner, E. L. 1998, *AJ*, 116, 2081
- ed. Weymann, L. Storrie-Lombardi, M. Sawicki, & R. Brunner, 1999, in *ASP Conf. Ser.* 191, *Photometric Redshifts and High Redshift Galaxies*
- White, S. D. M. & Frenk, C. S. 1991, *ApJ*, 379, 52
- Williams, R. E. et al. 1996, *AJ*, 112, 1335
- Wolf, C. 1999, *PASP*, 111, 1048
- Wolf, C., Meisenheimer, K., & Röser, H.-J. 2001, *A&A*, 365, 660
- Zepf, S. E. 1997, *Nature*, 390, 377